

**Volcanic glass geochemistry of Italian proximal deposits linked to
distal archives in the central Mediterranean region.**

Paul Graham Albert

Thesis submitted for the degree of Doctor of Philosophy at the
University of London

August 2012

Institution of study
Department of Earth Sciences
Royal Holloway, University of London

Declaration

This thesis presents the results of original research undertaken by the author and none of the results, illustrations and text are based on published or unpublished work of others, except where specified and acknowledged.

Signature:Date.....

Abstract

Distal tephrochronology relies on the synchronous dispersal and deposition of volcanic ash or tephra (i.e. < 2mm) from explosive volcanic eruptions (Plinian/sub-Plinian). Tephrochronology correlates tephra layers to proximal source volcanic eruptions, where proximal age is well constrained, allowing tephra layers to be used as robust age markers. Tephra layers are recorded in a variety of distal environmental archives, thus tephrochronology provides an independent time framework for interpreting palaeoenvironmental proxies in marine and lacustrine cores.

Tephrochronology is dependent on precise correlations of distal glass geochemistries with proximal source volcanics. Proximal volcanic deposits have been subject to detailed sampling and glass analyses revealing spatial and temporal changes in magmatic compositions during individual eruptions. Geochemical ‘fingerprints’ have been determined for Italian explosive proximal deposits using electron probe micro analysis (EMPA) and laser ablation-inductively coupled plasma-mass spectrometry (LA-ICP-MS). Presented are detailed volcanic glass major, minor and trace element compositions for proximal deposits outcropping on the Aeolian Islands, Mount Etna and Ischia. These proximal glass compositions are used to test proximal-distal correlations, linking visible and crypto-tephra layers from marine (Tyrrhenian, Ionian and Adriatic Seas) and lacustrine (Lago Grande di Monticchio, Italy) cores to their volcanic source.

Combined major, minor and trace element characterisation of proximal and distal glasses has validated the provenance and age of numerous distal tephra layers. Precise tephra correlations have allowed for the exchange of tephrochronological information over wide geographical distances (up to 800 km). Correlations based solely on major element analyses can be erroneous due to repeated chemistries produced at many of the volcanic centres investigated. Trace element concentrations enable the identification of additional diagnostic features necessary for distinguishing tephra produced from a single volcanic centre. However, in some instances volcanic systems repeatedly produce glass geochemistries that are indistinguishable at a multi-element level demonstrating the importance of good stratigraphic control distally when assigning provenance. Some tephra identified in the Tyrrhenian Sea (Marsili basin) have no currently identified proximal counterparts. This research demonstrates that proximal stratigraphies are not always fully representative of event stratigraphies due to resurgent activity and in the case of volcanic islands flank collapse and limited on-land deposits.

Acknowledgements

I owe a number of people significant gratitude, without them completion of this thesis would not have been possible.

I would like to thank my supervisors at Royal Holloway, Prof. Martin Menzies and Dr Emma Tomlinson, for their guidance and support over the last four years. Particularly for helping me acquire and interpret the geochemical data presented in this research.

To Prof. Mauro Rosi who's knowledge of the Aeolian Islands was instrumental in enabling me to collect the relevant proximal samples.

To Dr Victoria Smith for her assistance in the acquisition of major element geochemical glass data presented in this thesis.

To Dr Sabine Wulf for providing crucial distal samples from both Lago Grande di Monticchio and the Ionian Sea in order to test proximal-distal tephra correlations and for fruitful discussions.

To Marco Pistolesi, Federico Di Traglia, Anna Todman and Celine Fourmentraux for their help in the field.

To Alessio Di Roberto for useful and helpful discussions regarding the Marsili Basin core.

To Christina Manning, Anna Bird, Jo Cross, Vicki Hudspith, John Fisher for their support and encouragement.

To Dr Rosanna De Rosa and Dr Paola Donato for introducing me to the Palinuro and Tarsia pyroclastic outcrops.

To Dr Michael Marani and Prof. Jörg Keller for providing access to marine core material.

To Dr Anna Bourne for fruitful discussions and making Adriatic marine core material available for analysis.

To Dr Ian Matthews for many useful and insightful discussions, plus some much need encouragement.

I would like to thank the NERC RESET consortium for contributing financially to this research, whilst also the members of the consortium for the ongoing exchange of information and ideas.

This PhD studentship was funded by the Royal Holloway Reid scholarship, without this financial support the research would not have been possible.

Thank you to my Mum and Dad for their continued support and encouragement during this process. Thank you for housing me, feeding me and putting up with me for the last couple of weeks of writing up.

Finally, thank you to Holly for your support and putting up with Eeyore over the last couple of months, I know it hasn't been easy!

| | |
|--|----|
| Declaration..... | 1 |
| Abstract..... | 2 |
| Acknowledgements..... | 3 |
| Table of Contents..... | 5 |
| List of Figures..... | 12 |
| List of Tables..... | 16 |
| List of Appendix..... | 19 |
| Chapter 1: Introduction..... | 20 |
| 1.1 Principles of Tephrochronology..... | 22 |
| 1.2 A review of central Mediterranean distal tephrochronology..... | 25 |
| 1.3 Thesis Objectives..... | 30 |
| Chapter 2: Methodology..... | 31 |
| 2.1 Samples..... | 31 |
| 2.2 Analytical Method..... | 31 |
| 2.2.1 Electron Micro-Probe Analysis (EPMA)..... | 31 |
| 2.2.2 Laser Ablation Inductively Coupled Plasma Mass Spectrometry (LA-ICP-MS)..... | 33 |
| 2.2.3 Inductively Coupled Plasma Atomic Emissions Spectroscopy (ICP-AES)..... | 34 |
| 2.2.4 Inductively Coupled Plasma Mass Spectrometry (ICP-MS)..... | 34 |
| 2.3 Statistical analysis of geochemical data..... | 35 |
| Chapter 3: The tephrostratigraphy & glass compositions of explosive volcanism on the Aeolian islands: Geochemical variability & chronostratigraphic markers..... | 36 |
| Abstract..... | 36 |

| | |
|--|-----|
| 3.4.3.2 Palisi Pumices..... | 93 |
| 3.4.4 Vulcano..... | 94 |
| 3.4.4.1 Quadrara Formation..... | 94 |
| 3.4.4.2 Casa Lentia..... | 99 |
| 3.4.4.3 Monte Saraceno..... | 101 |
| 3.4.4.4 TGR Scoria..... | 102 |
| 3.4.4.5 La Fossa Activity..... | 102 |
| 3.4.5 Stromboli..... | 104 |
| 3.4.5.1 Upper Vancori..... | 104 |
| 3.4.5.2 Secche di Lazzaro..... | 107 |
| 3.5 Discussion: Tephrochronological implications..... | 109 |
| 3.5.1 Lipari proximal explosive deposits..... | 109 |
| 3.5.1.1 Cycle VII P.dei Perciato & Falcone Formations..... | 109 |
| 3.5.1.2 Cycle VII Monte Guardia..... | 112 |
| 3.5.1.3 Cycle IX Gabelotto-Fiume Bianco..... | 113 |
| 3.5.1.4 Cycle X Monte Pilato..... | 114 |
| 3.5.1.5 Distal Lipari deposits recorded in the Aeolian Islands & the central Mediterranean..... | 115 |
| 3.5.1.6 Lipari Summary..... | 123 |
| 3.5.2 Salina proximal explosive deposits..... | 124 |
| 3.5.2.1 Lower Pollara..... | 124 |
| 3.5.2.2 Upper Pollara..... | 125 |
| 3.5.2.3 Distinguishing Pollara activity..... | 125 |
| 3.5.2.4 Distal Salina deposits in the central Mediterranean..... | 127 |
| 3.5.3 Panarea proximal explosive deposits..... | 127 |
| 3.5.4 Lipari – Salina rhyolitic activity..... | 128 |
| 3.5.5 Vulcano proximal explosive deposits..... | 128 |
| 3.5.5.1 Southern Vulcano..... | 129 |

| | |
|---|-----|
| 3.5.4.2 Casa Lentia..... | 130 |
| 3.5.5.3 TGR scoria & Monte Saraceno..... | 130 |
| 3.5.5.4 La Fossa..... | 131 |
| 3.5.6 Stromboli proximal explosive deposits..... | 134 |
| 3.5.6.1 Upper Vancori..... | 134 |
| 3.5.6.2 Secche di Lazzaro..... | 136 |
| 3.5.7 Distinguishing Vulcano & Stromboli glasses as distal tool..... | 139 |
| 3.5.7.1 Medial-distal Vulcano & Stromboli deposits..... | 140 |
| 3.5.7.2 Distal marine tephra..... | 143 |
| 3.6 Conclusions..... | 144 |
| Chapter 4: Marine-continental tephra correlations: volcanic glass geochemistry from the Marsili Basin & the Aeolian Islands, Southern Tyrrhenian Sea, Italy..... | 146 |
| Abstract..... | 146 |
| 4.1 Introduction..... | 147 |
| 4.2 Marsili Basin core (TIR2000-C01)..... | 147 |
| 4.3 Results..... | 150 |
| 4.3.1 TIR2000-C01 (Marsili Basin)..... | 150 |
| 4.3.2 TIR2000-7 (7 cm b.s.f.)..... | 154 |
| 4.3.3 TIR2000-50 (50 cm b.s.f.)..... | 157 |
| 4.3.4 TIR2000-93 (93 cm b.s.f.)..... | 160 |
| 4.3.5 TIR2000-398 (398 cm b.s.f.)..... | 162 |
| 4.3.6 TIR2000-417 (417 cm b.s.f.)..... | 164 |
| 4.4 Discussion..... | 167 |
| 4.4.1 Proximal-distal correlations/Tephrochronology..... | 167 |
| 4.4.1.1 TIR2000-7 (7 cm b.s.f.)/Lipari 776 cal AD..... | 167 |
| 4.4.1.2 TIR2000-50 (50 cm b.s.f.)/K-series activity Stromboli/Vulcano..... | 169 |
| 4.4.1.3 TIR2000-93 (93cm b.s.f.)/Campi Flegrei | |

| | |
|---|-----|
| 11915-12721 cal yrs BP..... | 171 |
| 4.4.1.4 TIR2000-398 (398 cm b.s.f.)/CA/HKCA activity, Aeolian Islands..... | 173 |
| 4.4.1.5 TIR2000-417 (417 cm b.s.f.)/HKCA of the Aeolian Island Activity..... | 175 |
| 4.4.2 Implications for tephra correlations..... | 178 |
| 4.4.3 Primary tephra V s Turbidites..... | 179 |
| 4.4.4 Chronological implications for the Marsili basin core..... | 180 |
| 4.5 Conclusions..... | 181 |
| Chapter 5: Ionian Sea Marine Core (M25-4-12)..... | 183 |
| Abstract..... | 183 |
| 5.1 Introduction..... | 184 |
| 5.2 Site..... | 185 |
| 5.3 Methodology..... | 186 |
| 5.4 Results..... | 187 |
| 5.4.1 Stratigraphy & Visible tephra layers..... | 187 |
| 5.4.2 Cryptotephra layers..... | 189 |
| 5.4.3 Geochemistry..... | 190 |
| 5.5 Discussion- Tephra correlations..... | 196 |
| 5.5.1 M25/4-12_28cm & M25/4-12_44cm b.s.f..... | 196 |
| 5.5.2 M25/4-12_118.5cm b.s.f ‘Y-3’..... | 205 |
| 5.5.2.1 Proximal Tufi Biancastri & distal Y-3 Ionian Sea correlations..... | 207 |
| 5.5.2.2 Distal-distal Y-3 correlations..... | 210 |
| 5.5.2.3 Implications..... | 212 |
| 5.5.3 M25/4-12_184.5cm b.s.f ‘Y-5’..... | 213 |
| 5.6 Conclusions..... | 217 |

| | |
|---|-----|
| Chapter 6: External ash layers recorded in the volcanic stratigraphies of the Aeolian Islands implications for tephrochronology & Mediterranean ash dispersals..... | 220 |
| Abstract..... | 220 |
| 6.1 Introduction..... | 221 |
| 6.2 ' <i>Ischia tephra</i> '..... | 223 |
| 6.2.1 Samples..... | 227 |
| 6.2.2 Results..... | 232 |
| 6.2.2.1 Proximal Ischia..... | 232 |
| 6.2.2.2 ' <i>Ischia tephra</i> ' layer Stromboli..... | 232 |
| 6.2.2.3 Group 1..... | 236 |
| 6.2.2.4 Group 2..... | 237 |
| 6.2.3 Discussion..... | 237 |
| 6.2.3.1 Proximal-distal correlations..... | 242 |
| 6.2.3.2 Further proximal-distal tephrocorrelations & implications..... | 245 |
| 6.2.3.3 Tephrochronological implications..... | 248 |
| 6.2.4 Summary..... | 251 |
| 6.3 MIS 5 external tephra outcropping in the Aeolian Islands..... | 253 |
| 6.3.1 Samples..... | 255 |
| 6.3.2 Results..... | 259 |
| 6.3.2.1 Panarea Pink Ash, Punta Falcone..... | 259 |
| 6.3.2.2 Barone tephra layer, Salina..... | 259 |
| 6.3.2.3 Italian Mainland..... | 262 |
| 6.3.2.4 Central Adriatic: PRAD 1-2..... | 263 |
| 6.3.2.5 Southern Adriatic..... | 263 |
| 6.3.3 Discussion..... | 266 |
| 6.3.4 Summary..... | 278 |

Chapter 1

Figure 1.1 A map showing central Mediterranean volcanic centres.....21

Chapter 2

Figure 2.1.Epoxy resin mount showing arrangement of juvenile cl.....32

Figure 2.2 SEM image of a LA-ICP-MS ablation analysis pit.....34

Chapter 3

Figure 3.1 Location of Aeolian Islands, southern Tyrrhenian Sea.....38

Figure 3.2 Geological map of Lipari & sampled localities.....41

Figure 3.3 Geological map of Salina & sampled localities.....42

Figure 3.4 Geological map of Vulcano & sampled localities.....43

Figure 3.5 Geological map of Stromboli & sampled localities.....44

Figure 3.6 P.del Perciato & Falcone stratigraphy.....47

Figure 3.7 Complete southern Lipari succession.....48

Figure 3.8 Sampled stratigraphy of Monte Guardia.....49

Figure 3.9 Sampled stratigraphy of Gabellotto-Fiume Bianco.....51

Figure 3.10 Sampled stratigraphy of the Monte Pilato eruption.....54

Figure 3.11 Sampled stratigraphy of the Lower Pollara eruption.....56

Figure 3.12 Sampled Upper Pollara stratigraphy.....57

Figure 3.13 A map showing the sampled localities on Panarea.....60

Figure 3.14 The Punta Falcone stratigraphy Panarea.....61

Figure 3.15 Sampled stratigraphy of the Quadrara formation.....64

Figure 3.16 Composite stratigraphic log of the La Fossa stratigraphy...65

Figure 3.17 Sampled stratigraphy of the Upper Vancori.....67

Figure 3.18 Sampled stratigraphy of Secche di Lazzaro (Semaforo)....68

| | |
|--|-----|
| Figure 3.19 Sampled stratigraphy of Secche di Lazzaro (COA)..... | 69 |
| Figure 3.20 Major element classification of Aeolian Islands glasses..... | 71 |
| Figure 3.21 Mantle normalised Aeolian Islands glasses..... | 72 |
| Figure 3.22 Major element bi-plots of the HKCA rhyolites, Lipari..... | 73 |
| Figure 3.23 Trace element bi-plots, Lipari.. .. | 76 |
| Figure 3.24 Chondrite normalised REE Aeolian Island glasses..... | 77 |
| Figure 3.25 Stratigraphic major element variation Monte Guardia..... | 81 |
| Figure 3.26 Major element bi-plots, Salina & Panarea..... | 85 |
| Figure 3.27 Trace element bi-plots, Salina & Panarea..... | 86 |
| Figure 3.28 Chemostratigraphy of the Upper Pollara tuff deposits..... | 90 |
| Figure 3.29 Major element bi-plots, Vulcano & Stromboli..... | 95 |
| Figure 3.30 Major element bi-plots, Quadrara..... | 96 |
| Figure 3.31 Trace element bi-plots, Vulcano & Stromboli..... | 98 |
| Figure 3.32 Trace element bi-plots, Quadrara..... | 100 |
| Figure 3.33 Major element bi-plots, Upper Vancori..... | 100 |
| Figure 3.34 Major element bi-plots, Secche di Lazzaro..... | 105 |
| Figure 3.35 Medial Monte Guardia stratigraphy, Nr Gelso, Vulcano... | 117 |
| Figure 3.36 SiO ₂ vs K ₂ O diagram, medial & distal Lipari deposits..... | 118 |
| Figure 3.37 Diagnostic trace element bi-plots, Lipari rhyolites..... | 122 |
| Figure 3.38 Trace element bi-plots, Upper Vancori, EL4..... | 135 |
| Figure 3.39 'Exotic' lapilli pumice fall (EL4), Drauto, Panarea..... | 141 |

Chapter 4

| | |
|--|-----|
| Figure 4.1 Marsili Basin Core & site locations..... | 151 |
| Figure 4.2 SEM images of shards from TIR2000-01 tephra layers..... | 152 |
| Figure 4.3 TAS & SiO ₂ vs FeO bi-plots for Marsili tephra layers..... | 155 |
| Figure 4.4 TIR2000-7 Mantle & average normalised diagrams..... | 156 |
| Figure 4.5 TIR2000-7 Trace element bi-plots, Monte Pilato & GFB... | 157 |

| | |
|---|-----|
| Figure 4.6 TIR2000-50 Mantle & average normalised diagrams..... | 158 |
| Figure 4.7 TIR2000-50 Major & trace element bi-plots, SDL, Pal A... | 159 |
| Figure 4.8 TIR2000-93 Mantle & average normalised diagrams..... | 160 |
| Figure 4.9 TIR2000-93 Trace element bi-plots, Soccavo 1..... | 161 |
| Figure 4.10 TIR2000-398 Mantle & average normalised diagrams..... | 163 |
| Figure 4.11 TIR2000-417 Mantle & average normalised diagrams..... | 165 |
| Figure 4.12 TIR2000-398 & TIR2000-417 trace element bi-plots..... | 166 |

Chapter 5

| | |
|---|-----|
| Figure 5.1 Location map for M25/4-12..... | 186 |
| Figure 5.2 Tephrostratigraphy of upper 180 cm of core M25/4-12..... | 187 |
| Figure 5.3 Shards extracted for the investigated tephra layers..... | 188 |
| Figure 5.4 Major element & TAS (M25/4-12 28 & 44cm)..... | 191 |
| Figure 5.5 M25/4-12 28 & 44cm Mantle normalised diagrams..... | 192 |
| Figure 5.6 Y-3/ Tufi Biancastri, TAS & major element bi-plots..... | 194 |
| Figure 5.7 Y-3 & Y-5 Mantle normalised diagrams..... | 195 |
| Figure 5.8 Y-3/Tufi Biancastri, trace element bi-plots..... | 198 |
| Figure 5.9 Y-5/Campanian Ignimbrite, TAS & major element..... | 201 |
| Figure 5.10 Y-5/Campanian Ignimbrite, trace element bi-plots..... | 202 |
| Figure 5.11 Y-3 & Y-5, Th vs. Nb Campanian magmatic series..... | 206 |

Chapter 6

| | |
|---|-----|
| Figure 6.1 Location Map, distal archives & external tephras..... | 221 |
| Figure 6.2 Sampled stratigraphy of ' <i>Ischia tephra</i> ', Stromboli..... | 222 |
| Figure 6.3 Composite volcanic stratigraphy, Ischia..... | 224 |
| Figure 6.4 Tephrostratigraphy, LGdM..... | 226 |
| Figure 6.5 Tephrostratigraphy, PRAD 1-2 & SA03-03..... | 228 |
| Figure 6.6 SEM images, Ischia tephra, Y-7, TM-19 & TM-20 layers.. | 229 |
| Figure 6.7 ' <i>Ischia tephra</i> ', Stromboli, Major element bi-plots..... | 235 |
| Figure 6.8 K ₂ O/N ₂ O, Ischia stratigraphy..... | 236 |

| | |
|---|-----|
| Figure 6.9 ‘ <i>Ischia tephra</i> ’, Group 1&2 tephra, TAS & Mantle norm. | 238 |
| Figure 6.10 Major & trace element bi-plots, Ischia & distal tephra. | 239 |
| Figure 6.11 Distribution map tephra for MEGT eruption of Ischia. | 250 |
| Figure 6.12 Panarea Pink Ash (PPA), Punta Falcone, Panarea. | 256 |
| Figure 6.13 Sampled stratigraphy, Barone tephra, LeS2, Tarsia. | 257 |
| Figure 6.14 TAS diagram PPA, Barone tephra & MIS 5 tephras. | 260 |
| Figure 6.15 Major element bi-plots, PPA, Barone, LeS1/2, LGdM. | 261 |
| Figure 6.16 Major element bi-plots, PPA & HAR MIS5 tephras. | 268 |
| Figure 6.17 Trace element bi-plots, PPA & HAR MIS5 tephras. | 269 |
| Figure 6.18 Major element bi-plots, Barone & LAR MIS 5 tephras. | 274 |
| Figure 6.19 Trace element bi-plots, Barone & LAR MIS 5 tephras. | 275 |
| Figure 6.20 Distribution map of tephras correlated to TM-27 LGdM. | 277 |

Chapter 7

| | |
|---|-----|
| Figure 7.1 Mount Etna locations maps & stratigraphy. | 284 |
| Figure 7.2 Deposits/samples (Biancavilla/Giarre/Acireale/Haua..) | 289 |
| Figure 7.3 Major element bi-plots (Biancavilla flow & fall deposits). | 300 |
| Figure 7.4 Normalised (Proximal, Biancavilla, Y-1, Haua Fteah). | 302 |
| Figure 7.5 Trace element bi-plots (Biancavilla flow & fall deposits). | 304 |
| Figure 7.6 Major element bi-plots (Etna tephras & proximal). | 307 |
| Figure 7.7 Trace element bi-plots (Etna tephras & proximal). | 312 |
| Figure 7.8 Map showing extent of Biancavilla fall footprint. | 321 |

Chapter 1

| | |
|---|----|
| Table 1.1 The most prominent tephrochronological markers..... | 29 |
|---|----|

Chapter 3

| | |
|--|-----|
| Table 3.1 Investigated major explosive eruptions, Aeolian Islands..... | 46 |
| Table 3.2 Sampled proximal stratigraphy of Lipari, last 42 ka..... | 52 |
| Table 3.3 Sampled proximal stratigraphy of Pollara activity, Salina..... | 59 |
| Table 3.4 Sampled stratigraphy of Vulcano over the last 21 ka..... | 62 |
| Table 3.5 Sampled stratigraphy of Stromboli over the last 13 ka..... | 66 |
| Table 3.6 Major, minor & trace element glass data (cycle VII)..... | 74 |
| Table 3.7 Major, minor & trace element glass data, Monte Guardia..... | 78 |
| Table 3.8 Major, minor & trace element glass data, Gabelotto..... | 82 |
| Table 3.9 Major, minor & trace element glass data, Monte Pilato..... | 83 |
| Table 3.10 Major, minor & trace element glass data, Lower Pollara..... | 88 |
| Table 3.11 Major, minor & trace element glass data, Upper Pollara..... | 89 |
| Table 3.12 Major, minor & trace element glass data, Panarea..... | 93 |
| Table 3.13 Major, minor & trace element glass data, Quadrara..... | 97 |
| Table 3.14 Major, minor & trace element glass data, Casa Lentia,..... | 101 |
| Table 3.15 Major, minor & trace element glass data, La Fossa..... | 103 |
| Table 3.16 Major, minor & trace element glass data, Upper Vancori... | 106 |
| Table 3.17 Major, minor & trace element glass data, SDL..... | 108 |
| Table 3.18 D^2 values between Lipari deposits..... | 111 |
| Table 3.19 Major, minor & trace element glass data, external tephras. | 115 |
| Table 3.20 Diagnostics used to distinguish Pollara activity, Salina..... | 126 |
| Table 3.21 D^2 values between La Fossa deposits, Vulcano..... | 133 |
| Table 3.22 D^2 values between Secche di Lazzaro deposits, Stromboli. | 138 |

| | |
|--|-----|
| Table 3.23 D ² values between U. Vancori, Quadrara & EL4 pumices.. | 141 |
| Chapter 4 | |
| Table 4.1 Major, minor & trace element data, TIR2000-C01 tephras... | 151 |
| Table 4.2 Diagnostic trace element ration, distal & proximal tephras.. | 153 |
| Chapter 5 | |
| Table 5.1 Major, minor & trace element data M25/4-12 tephras..... | 190 |
| Table 5.2 Y-3 & Y-5 – Proximal elemental ratios..... | 199 |
| Table 5.3 D ² values Y-3 & Tufi Biancastri..... | 209 |
| Table 5.4 D ² values (majors elements) Y-5/Campanian Ignimbrite.... | 214 |
| Table 5.5 D ² values (trace elements) Y-5/Campanian Ignimbrite..... | 215 |
| Chapter 6 | |
| Table 6.1 Investigated distal Ischia tephras..... | 225 |
| Table 6.2 Major, minor & trace element data, proximal Ischia..... | 230 |
| Table 6.3 Major, minor & trace element data, distal Ischia tephras.... | 233 |
| Table 6.4 Investigated MIS 5 tephras, external to Aeolian Islands..... | 254 |
| Table 6.5 Major, Minor & trace element data for external tephra..... | 258 |
| Table 6.6 Trace element data for MIS5 tephra, PRAD 1-2,..... | 264 |
| Table 6.7 Major, minor & trace element data for MIS 5 LGdM..... | 265 |
| Table 6.8 Alkali ratio groupings of prominent MIS 5 tephras..... | 266 |
| Chapter 7 | |
| Table 7.1 Stratigraphic info.. for Biancavilla flows & Unit D fall..... | 287 |
| Table 7.2 Major, minor & trace element data, Biancavilla flow & | 291 |
| Table 7.3 ICP-AES whole rock data, Biancavilla, Unit D..... | 294 |
| Table 7.4 Diagnostic incompatible trace element ratios, Etna tephras.. | 295 |
| Table 7.5 D ² values for Biancavilla flow & Unit D fall..... | 297 |
| Table 7.6 Revised nomenclatures, for Unit D/Biancavilla | 306 |
| Table 7.7 Reported Etnean tephras form the Mediterranean Region.... | 308 |
| Table 7.8 Major, minor & trace element date, distal Etnean tephra.... | 309 |

Table 7.9 D^2 values for major & minor elements, Etnean tephra.....313

Table 7.10 Suggested event stratigraphy for Biancavilla ignimbrite...319

| | |
|-------------|--|
| Appendix I | JVGR paper Albert et al., 2012 |
| Appendix II | Geochemical results/descriptions of Ischia tephra (Chapter 6.2). |

The following electronic appendixes are found on the accompanying CD:

| | |
|---------------|--|
| Appendix eI | Major, minor & trace element secondary standards (Chapter 2) . |
| Appendix eII | Full geochemical data set for Aeolian Proximal tephra |
| Appendix eIII | Full geochemical data set for Marsili Basin core (TIR2000-C01) tephra. |
| Appendix eIV | Full geochemical data set for Ionian Sea core (M25/4-12), tephra . |
| Appendix eV | Full geochemical data sets for tephra reported in Chapter 6. |
| Appendix eVI | Full geochemical data sets for Etnean proximal & distal tephra. |

Chapter 1: Introduction

1. Introduction

The oxygen isotope records from Greenland demonstrate that numerous, rapid climatic fluctuations occurred during the last glacial-interglacial cycle, with some of these climatic transitions occurring within centennial to millennial timescales (e.g. Dansgaard 1985; Alley et al., 1993; Dansgaard et al., 1993; Rasmussen et al., 2006). Such millennial-scale climatic oscillations have been recognised in the marine sequences of the Mediterranean region (Rohling et al., 1998; Paterne et al., 1999). Continentally this has been manifested in rapid alternations between steppe and forest dominated vegetation, Allen (2003) recognised that these vegetation changes responded to the more abrupt climatic variability observed in the Greenland ice record. Indeed millennial-scale oscillations in pollen concentrations are observed at numerous sites within the Mediterranean region (e.g., Tzedakis et al., 1997; Margri et al., 1999; Tzedakis et al., 2003). One of the most important terrestrial records in the central Mediterranean is Lago Grande di Monticchio, Italy, where the varved sediments provide the first independently dated record of millennial-scale vegetation response to climatic change (Watts, 1996). Thus the challenge remains to link the observed millennial-scale oscillations directly between marine and terrestrial archives to assess whether these climatic proxies are in phase or whether leads and/or lags exist. Consequently, this has led to the emergence of tephrostratigraphy as the preferred tool to precisely correlate these archives.

Explosive volcanism is responsible for the widespread dispersal of volcanic ash or tephra (< 2 mm). During sub-Plinian/Plinian eruptions tephras may be transported into the high atmosphere/lower stratosphere resulting in their dispersal over wide geographical areas. The synchronous deposition of tephras from individual eruptions provides invaluable isochronous markers (i.e., visible and crypto-tephra layers), which are recorded in a variety of environmental archives. Tephrochronology correlates tephras to proximal source volcanic eruptions and where the proximal age of the eruption is well constrained tephra layers provide precise age markers. Owing to the synchronous deposition of tephras, where they are correlated between archives they present useful tie points for the synchronisation of archives and the exchange of age constraints. Consequently, tephrochronology provides an independent time framework for interpreting palaeoenvironmental proxies in marine and lacustrine archives and so

has a pivotal role to play in understanding the timing and rates of rapid environmental transitions. A more recent focus has extended to using tephras within archaeological settings, the potential to link environmental archives to cultural evolutionary changes in the archaeological record provides an exciting opportunity to assess human responses to abrupt climatic change (Giaccio et al., 2006; Anikovich et al., 2007; Lowe et al., 2012).

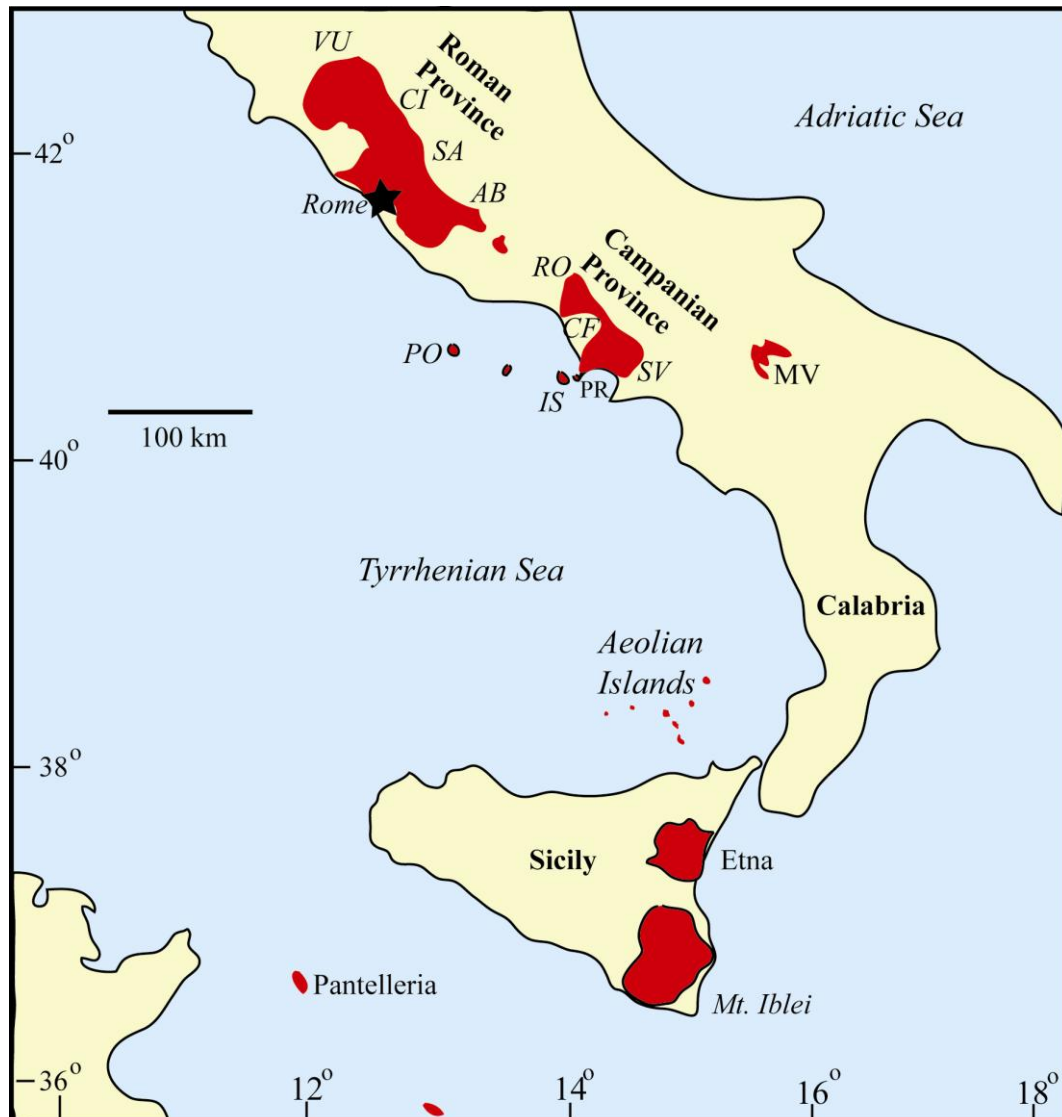


Figure 1.1: A map displaying the Italian volcanic centres within the central Mediterranean region (Adapted from Wulf, 2000). Roman Province; VU= Vulsini; CI = Cimini district (includes Vico); SA = Sabatini Volcanic distinct; AB Alban Hills. Campanian Province; PO =Ponza Island, RO = Roccomonfina; CF = Phlegrean Fields; SV= Somma-Vesuvius, IS= Ischia Island. PR = Prodi-a-Vivara; MV= Monte Vulture.

The central Mediterranean is uniquely placed to established detailed tephrostratigraphies and the application of tephrochronology due to;

(i) The regions proximity to a number of volcanic centres which have been persistently active during the last 200 ka (Keller et al., 1978; Paterne et al., 1988; 2008; Narcisi and Vezzoli., 1999) (Fig. 1.1).

(ii) Many of these centres are characterised by frequent large magnitude eruptive events (Narcisi and Vezzoli, 1999);

(iii) Many of the eruptive centres have distinct magma chemistries (Wulf et al., 2004).

1.1 Principles of Tephrochronology

The establishment of an individual proximal tephra's identity is essential to determine a precise tephrostratigraphy. The identity of a proximal tephra can be established by investigating physical and chemical characteristics, determining stratigraphy and establishing chronology. Physical characteristics include tephra colour, unit thickness, grain size variations, clast morphology, vesicularity and phenocryst content (Cas and Wright, 1987). Many central Mediterranean volcanic centres have been subject to detailed proximal investigations and the assessment of the physical parameters of erupted deposits has enabled the determination of proximal event stratigraphies. Examples include the Campanian Plain (Di Vito et al., 2008), Ischia (Brown et al., 2008), Mount Etna (Coltelli et al., 2000) and the Aeolian islands (Sulpizio et al., 2008; Dellino et al., 2011). These parameters can be used to link proximal stratigraphies over significant distances around the volcano and are integrated with chronological investigations of individual tephra's. Unfortunately the physical parameters of tephra's are often less reliable for linking tephra's in more distal localities, where many of the characteristics of a proximal tephra deposit may be absent. For instance atmospheric sorting of erupted ejecta during transport can in many cases result in tephra's being phenocryst poor with distance from the source (Carey and Sigurdsson 1992). It is often only the ash (< 2 mm) component that is recorded in the distal setting.

The chemical classification of the volcanic glass produced during an eruption can be used to underpin tephrochronology. Chemical characterisation of tephra's can include bulk rock analyses; but whole rock data is not representative of the magma compositions at the time of the eruption because it is a bulk average of clasts which may be geochemically heterogeneous. This can be particularly problematic for

compositionally bi-modal tephra deposits. Heterogeneity may originate due to variable proportions of phenocrysts, xenocrysts and lithic material entrained within the juvenile (i.e., magmatic) component of the tephra. Indeed “bulk” chemistries may be unrepresentative of actual magma compositions and as such markedly differ from the glasses found distally (Pearce et al., 2004). The compositions of juvenile deposits are frequently heterogeneous within the proximal settings (both laterally and stratigraphically) and even within a single glass shard (Ukstins Peate et al., 2008). Identification of this compositional heterogeneity is essential for proximal-distal correlations, particularly where it is the compositional range of tephtras that may be diagnostic of an individual eruption. Tomlinson et al., (2012) demonstrated that whole rock analyses of the Upper and Lower pumice eruptions of Nisyros mask the compositional variation between these two eruptions. High phenocryst contents in the pumices of the two eruptions meant that glass compositions are significantly different from the whole rock compositions. Consequently, erroneous distal correlations were established using whole rock proximal data, where glass data clearly would have resolved the precise provenance of the distal tephtras sourcing from this volcanic centre.

Electron microprobe analysis (EMPA) is the preferred micron-scale analytical technique underpinning tephrochronology (Hunt and Hill, 1993; Turney et al., 2004). Grain specific analysis of proximal glasses enabled the determination of stratigraphic compositional variations in eruptive sequences. Accepting that bulk-rock analysis of tephtras is not suitable for tephrochronological studies coupled there has been an increase in the number of proximal investigations detailing and characterising proximal glasses. These investigations largely build on the previously determined volcanostratigraphies established at many volcanic centres and provide an invaluable tool for distal tephrochronology. Specifically within the central Mediterranean region these include Campi Flegrei (Di Vito et al., 2008; Smith et al., 2011; Tomlinson et al., 2012) and Vesuvius (Santacroce et al., 2007). However, many of these volcanic centres still lack grain-specific glass analyses of proximal tephtras essential for precise proximal-distal correlations. Hence many of the established tephra correlations in the central Mediterranean remain untested using grain-specific glass correlations. Furthermore numerous unidentified tephtras are recorded within Central Mediterranean archives largely due to absence of complete proximal glass data sets (Giaccio et al., 2008).

A major obstacle that complicates the application of major element grain-specific analyses as tool for tephrochronology is that many evolved magmas, especially those erupted from the same volcano, are compositionally indistinguishable using major element geochemistries (Allan et al., 2008; Giaccio et al., 2008). This is a problem in the central Mediterranean, where volcanic centres within the Campanian volcanic zone produce geochemically similar trachytic glass compositions systematically over time (i.e., Campi Flegrei, Ischia and Somma-Vesuvius). This same problem is identified in the calc alkaline rhyolites produced in the Aeolian Islands (Giaccio et al., 2008).

An additional problem associated with the use of major element glass geochemistry is inter- and intra-laboratory comparison. Different operating conditions can make comparisons of glass data very difficult (Hunt and Hill, 1993). The most reliable correlations of proximal-distal tephtras are achieved where glass analysis of both proximal and distal tephtra is undertaken using the same instrument. Furthermore much of the published glass data was produced using Scanning electron microprobe-energy dispersive X-ray (SEM-EDX), and these glass analyses are not always comparable with EPMA. This is particularly problematic for comparisons with some of the earlier tephrochronological studies (Paterne et al., 1988).

Trace element concentrations in magmas often show wider variability than major elements because they are more strongly controlled by subtle variations in source composition and by magmatic processes (Allan et al., 2008). In the last ten or so years the trace element compositions of tephtras has been determined using grain-specific Laser Ablation Inductively Coupled Plasma Mass Spectrometry (LA-ICP-MS). A number of studies have applied single grain LA-ICP-MS analysis to establishing precise proximal glass geochemistries essential to proximal-distal correlations (Allan et al., 2008; Pearce et al., 2004; 2007; Ukstins-Peat et al., 2003; 2008; Tomlinson et al., 2010; 2012a; 2012b; Smith et al., 2011; Albert et al., 2012; Tamburrino et al., 2012). The application of grain-specific trace element analyses becomes a major focus of this research, assessing its potential as a tool to geochemically distinguish tephtras and robustly test proximal-distal correlations.

Once the stratigraphic, physical and chemical characteristics of a tephtra are determined the next challenge is to establish the age of the tephtra. The age of the tephtra deposit becomes essential for its use within distal tephrochronological studies. Proximal age constraints for tephtras can be derived either directly or indirectly. Proximal deposits can

be directly dated by radiometric determinations on primary phenocryst based on K-Ar dating (i.e. Frazzetta et al., 1984; Vezzoli, 1988). However, the errors are particularly large on volcanic deposits that are young > 15 ka. $^{40}\text{Ar}/^{39}\text{Ar}$ relies on the presence of K-rich mineral phases such as sanidine and orthoclase. Consequently, such methods are difficult to apply to calc-alkaline volcanic settings (i.e., Aeolian Islands). However, $^{40}\text{Ar}/^{39}\text{Ar}$ dating has been successfully applied to products of explosive eruptions in the highly potassic campanian region (i.e., De Vivo et al., 2001; Deino et al., 2004). For younger volcanic deposits, historical records present useful information on the most recent eruptive histories of volcanic centres.

The most frequently adopted indirect method of dating proximal deposits is by radiocarbon dating. Organic material from beneath or above pyroclastic deposits can be dated, presenting a maximum or minimum age of the tephra respectively. The more precise proximal radiocarbon ages are derived from charcoal formed and preserved within high temperature pyroclastic density currents (PDCs). Radiocarbon ages require calibration, the calculation of a radiocarbon age assumes that the ^{14}C in the atmosphere has been constant since the time of which the dated material was living (Reimer and Reimer, 2007). However, this is not case, ^{14}C in the atmosphere varies over time. Radiocarbon dates therefore need to be calibrated to determine the true age and so enabling comparisons with calendar ages derived from incremental records such as varve counting or ice core records. IntCal09 is the currently internationally recognised standard model for radiocarbon calibration. ^{14}C spanning the last 12,550 cal years BP is determined based on dated tree ring samples. Beyond 12, 550 cal. BP, the calibration curve is based on a range of marine coral data sets (Reimer et al., 2009). Calibration will reduce the precision of a radiocarbon age, however, will improve its accuracy. Consequently, calibrated ages are more likely to represent the true age of the sample (Lowe et al., 2007). Consequently, all radiocarbon ages derived from the literature associated with tephtras presented in this research have been calibrated using IntCal09.

1.2 A review of central Mediterranean distal tephrostratigraphy

The first distal visible tephtras recognised and described in the central-eastern Mediterranean region were recovered from the marine sediments extracted during Swedish deep sea exploration (Norin, 1958). Subsequent systematic investigations of deep-sea sediments led to the development of a marine tephrostratigraphic framework spanning the last 200,000 years (Keller et al., 1978; McCoy, 1980). Widespread tephtras were identified in multiple marine cores from the Ionian, Aegean Levantine Seas. These

tephras were attributed to eruptions from the Italian, Aegean and Central Anatolian volcanic centres. Tephras were largely dated using oxygen isotope and sapropel chronology to establish a record of large scale eruptive histories (i.e., Keller et al., 1978; McCoy 1980; Vinci, 1985; Narcisi and Vezzoli, 1999). Keller et al., (1978) established a detailed tephrostratigraphy for the central-eastern Mediterranean which still underpins marine tephrochronology in the region. Tephras were identified on the basis of their positions within palaeoclimatic zones (V, W, X, Y and Z), where V is the oldest and Z the youngest. Within each climatic zone, each tephra was successively numbered 1 being the youngest, for instance Y-1 is younger than Y-2 (Narcisi and Vezzoli 1999). Approximately 30 major tephra horizons were recognised across the central-Mediterranean following these pioneering investigations (Keller et al., 1978; McCoy 1980; Vinci, 1985). The main markers relevant to the central Mediterranean tephrostratigraphy are presented in Table 1.1.

Investigations within the Tyrrhenian and Adriatic Sea were undertaken by Paterne et al., (1986; 1988) for sequences spanning the last 80,000 years. These tephras were labelled according to their geochemical affinity to a particular volcanic system, for instance C = Campanian, E=Aeolian, Et = Etna, V=Vesuvius and P = Pantelleria. The youngest tephra from each volcanic centre was numbered as 1, 2 and so on. Most tephras identified were attributed to a volcanic provenance, however, only some were recognised as regional markers and attributed to specific source eruptions (Table 1). Paterne et al., (2008) have extended the Tyrrhenian Sea record back over the last 200,000 years, using the existing nomenclature. According to Narcisi and Vezzoli (1999) tephrostratigraphies in the Tyrrhenian Sea are more complex than the other central Mediterranean marine basins due to their proximity to active volcanism, suggesting primary tephra layers representative of volcanic events are diluted by a high numbers of turbidites that result in re-working of volcanoclastic material.

Multiple tephrochronological investigations have concentrated on the Adriatic marine basin, with initial investigations focusing on visible tephras (Calanchi et al., 1998). A comprehensive tephrostratigraphy in the Adriatic for the last 170 ka is presented by Calanchi and Dinelli (2008). Furthermore cryptotephra studies have been conducted in this marine basin significantly increasing the number of tephras identified in the Adriatic (Siani et al., 2004; Lowe et al., 2007; Bourne et al., 2010). The main regional tephrostratigraphic markers identified in the Adriatic are shown in Table 1.1.

Central Mediterranean tephra studies have also been undertaken on terrestrial sequences on the Italian mainland owing to their proximity to active volcanic centres. The most detailed record to date has been constructed through the long sedimentary sequence of Lago Grande di Monticchio (LGdM). Due to a high sedimentation rate, clear stratigraphic super position and a annually resolved varved chronology LGdM offers independent dating of tephras (Wulf et al., 2004; Wulf et al., 2008; Wulf et al., submitted). The initial investigations target tephras greater than 3 mm in thickness and 14 tephras were correlated to known eruptions (Narcisi, 1996). Results of the most recent investigations have characterised 349 tephra layers within the most complete record (Wulf et al., 2004; 2008; submitted). Tephras recorded in the LGdM record have been chemically characterised using major element and minor element data (EPMA-WDS) and each analysed tephra is labelled TM and numbered accordingly to its relevant stratigraphic position in the LGdM core.

Wulf et al., (2004) presented the results of the most prominent tephra layers spanning the last 105 ka years and more recently Wulf et al., (submitted) has extended the record back to 133 ka. The dating offered by the varve chronology of LGdM provides an invaluable tephrochronological record for Italian volcanism. Correlatives of tephras recorded within this archive are still being refined with the most recent contribution revising some earlier correlations (Wulf et al., submitted). Due to its comprehensive record of central Mediterranean explosive volcanism, the LGdM archive has become a central tephrostratigraphical reference for the region. With often incomplete and uncharacterised proximal stratigraphies other distal stratigraphies are correlated directly to LGdM tephras (Munno and Petrosino, 2007; Bourne et al., 2010).

Furthermore, within this research contribution some of the relevant TM tephra layers are re-investigated and in some instances new trace element data is presented to help refine proximal-distal and distal-distal tephra correlations. Most tephra layers recorded in LGdM derive from eruptions of volcanoes within the Campanian volcanic zone (313; Campi Flegrei, Ischia, Vesuvius, Ischia, Prodi). The remaining tephras derive from the Roman province, Etna, the Aeolian Islands and Pantelleria (Wulf et al., 2004). The prominent tephra layers that have been linked into the overall central Mediterranean tephrostratigraphy are given in Table 1.1.

Other key terrestrial archives include the San Gregorio Magno basin (SGMB), located in the southern Apennines, Italy (Munno and Petrosino, 2007) and Lake Ohrid, in the Balkans (Wager et al., 2009; Vogel et al., 2010). Both present tephrostratigraphic records that extended back over the last 100 ka. Only visible tephtras were characterised in the SGMB record. The main tephrostratigraphic markers from these two terrestrial markers are integrated into the broader central Mediterranean record (Table 1.1). The linking of distal archives in Table 1.1 demonstrates that numerous tephtras are recorded across the central Mediterranean region. This existing tephrostratigraphical framework is tested through the course of this research.

| Age Ka (approx) | Marine Archives | | | | | | Terrestrial archives | | | Source | Eruption | |
|-----------------|-------------------------------------|--|-----------|--------|--------|--------------------------------|----------------------------------|---|---------------------------------------|-----------|-----------------------------------|---|
| | Ionian Sea Keller et al., (1978) | Tyrrhenian Sea Paterne et al., (1988; 2008) | Adriatic | | | Siani et al.(2004) MD90-917 | Bourne 2010; 2012 PRAD 1-2 | LGdM Wulf et al., (2004); (submitted) | S.G.M.B Munno and Petrosino (2007) | | | Ohrid Vogel et al., (2010) OT0702 |
| | | | Pal 94-66 | RF95-7 | IN68-9 | | | | | | | |
| 7 | Z-1 | E-1 | | | | 275cm | | ? | | SV | Avellino/Pompeii? | |
| 9 | | V-1 | | 125cm | | | TM-6 | | OT0702-3 | AO: L | Gabellotto-Fiume bianco | |
| 12 | | C-1 | 214cm | 178cm | | 305cm | TM-7 | | | SV | Mercato | |
| 14 | | C-2 | | | | 395cm | TM-8 | S21 | | CF | Pomici Principale | |
| 16 | Y-1 | Et-1 | | | | 490cm | TM-11 | | | CF | NYT | |
| 17 | | | | | | 530cm | TM-12 | S20 | | Et | Biancavilla | |
| 19 | | | | 525cm | | 595cm | TM-13 | | | SV | Greenish | |
| | | C-4 | | | | | TM-14 | | | SV | Pomici di Base | |
| 30 | Y-3 | C-7 | | | | 1332cm | TM-15 | S19 | OT0702-4 | PR | Solchiaro | |
| 33 | | C-10 | | | | 1494cm | TM-16 | | | CF | VRa (Zanchetta et al.2003) | |
| | | C-9 | | | | | TM-17-2 | | | SV? | Codola | |
| 40 | Y-5 | C-13 | | | | 1653cm | TM-18 | S17 | OT0702-6 | CF | Schiava | |
| | Y-6 | | | | | | | | OT0702-7 | P | Campanian Ignimbrite | |
| 56 | | C-16 | | | | 1870cm | TM-19 | S-16 | | IS | Green Tuff | |
| | Y-7 | C-18 | | | | 1870cm | TM-20 | S15 | | IS | MEGT | |
| 70 | Y-9 | | | | | | TM-21 | | | AO: St | S. Angelo tephra/U.M.S.A | |
| | | P-10 | | | | | | | | P | Petrazza Tuff | |
| | X-2 | | | 80cm | | | | | | Camp | Ante Green Ignimbrite | |
| | X-3 | | | | | | | | | EO | | |
| | X-4 | | | | | | | | | Et | Acireale | |
| 105 | X-5 | C-27 | | | | 2525cm | TM-24 | S11 | | CVZ | Unknown | |
| | | | | | | 2525cm | TM-25 | | OT0702-8 | CVZ | Unknown | |
| | | | | | | | TM-26 | | | Et | | |
| 108 | X-6 | C-31 | | | | 2812cm | TM-27 | S10 | OT0702-9 | CVZ | Unknown | |
| | | C-36 | | | | | | S9 | | | | |
| 131 | W-0 | P-11 | | | | | | | OT0702-10 | P | Unknown | |
| 145 | W-1 | C-41 | | 350 | | | | S7 | | Rom/Vico? | Ignimbrite A, B, or C | |
| | V-2 | | | 450 | | | | | | | | |

Table 1.1: The most prominent and widespread tephra layers recorded in the central Mediterranean marine and terrestrial archives, those highlighted in bold are tephras that are included within the context of this thesis. (SV= Somma-Vesuvius; AO: L = Aeolian Islands, Lipari; CF = Campi Flegrei; Et = Mount Etna; PR = Prodigia; P = Pantelleria; AO: St = Aeolian Islands, Stromboli; CVZ = Campanian Volcanic Zone).

1.3 Thesis Objectives:

The overall aim of this research is to test proximal-distal tephra correlations within the central Mediterranean region using grain-specific trace element geochemistry of volcanic glasses. The specific objectives of this research are to;

(1) Demonstrate the potential and importance of defining detailed multi-elemental proximal geochemical data sets;

- Establishing stratigraphic, spatial and temporal variations in glass geochemistries produced during individual eruptions (i.e., Aeolian Islands, Ischia and Mount Etna).
- Using a multi-elemental approach to establish diagnostic geochemistries for distinguishing between different eruptions.

(2) Use tephras recorded in distal marine archives as a test-bed for precise proximal-distal tephra correlations.

(3) Demonstrate the benefits of integrating major, minor and trace element data to establish more reliable proximal-distal correlations.

(4) Revise and extend the fall footprints of tephras recorded in the central Mediterranean.

(5) Highlight the two way flow of stratigraphic and chronological information between proximal and distal settings.

2.1 Samples

Exposed proximal fall, flow and surge deposits were investigated with juvenile clasts sampled from individual stratigraphic units to capture vertical heterogeneities within the eruptive sequences at source. Pumice and scoria lapilli (2-64 mm) were the preferred proximal material sampled. The clasts were washed with distilled water and dried. Representative pumice/scoria samples from individual eruptive units were selected to encompass the full range in colour and morphology. These clasts were individually crushed and representative fragments were then picked and arranged on a glass disc using double sided tape. Once arranged and referenced these samples were mounted in Struers Epofix epoxy resin (Fig. 2.1). Mounts were sectioned and polished ready for micro-analyses. Scanning Electron Microscope (SEM) imagery was conducted to determine suitable glass locations for analysis avoiding phenocryst and microcryst phases. Distal ash deposits were washed with distilled water, dried and typically sieved between 63-125 μm , 125-250 μm and 250-500 μm . Shards from the largest grain size available were handpicked under a microscope, arranged in a grid formation and again mounted in Steurs Epofix resin, sectioned and polished. Shards were then catalogued and I.D using Scanning Electron Microscope (SEM) imagery to ensure that grain-specific major element analysis and trace element analyses were coupled to the same shard of glass. The sampling and extraction procedure used for cryptotephra investigations are referred to in chapter 5.

2.2 Analytical method

2.2.1 Electron microprobe analysis (EPMA)

Major and minor element chemistry was determined using a wavelength-dispersive JEOL 8600 electron microprobe (EPMA) in the Research Laboratory for Archaeology and the History of Art, University of Oxford. A beam accelerating voltage of 15kV was used with a 6nA current and a beam diameter of 10 μm . The instrument was calibrated with a suite of appropriate mineral standards; peak count times were 30 s for most elements, 10 s for Na and 60 s for P and Cl. Secondary glass standards from the Max Plank institute (MPI-DING suite; Jochum et al., 2006) bracketing the possible

chemistries were also analysed alongside the unknown tephra. These included evolved felsic [ATHO-G (rhyolite)], through intermediate [StHs6/80-G (andesite)] to mafic [GOR128-G (Komatiite)] glasses.



Figure 2.1: Epoxy resin mount showing the arrangement of juvenile pumice fragments from a pumice fall deposits associated with the Monte Guardia eruption, Lipari. Note the colour variation between white and grey pumice fragments.

Analytical totals $< 95\%$ were discarded, except in the case of highly evolved rhyolites and trachytes where dissolved volatile components (e.g., H_2O) can reach $> 5\%$ (Pearce et al., 1999) so totals of $\geq 93\%$ were deemed acceptable. All major element data was normalised to 100% for comparative purposes. This is of paramount importance for marine tephra, as glass shards absorb water from their surroundings, which is reflected in lower analytical totals. Errors are typically $< \pm 0.7\%$ RSD for Si; $\sim \pm 3\%$ for most other major elements, except for the low abundance elements: Ti ($\sim \pm 7\%$), Mn ($\sim \pm 30\%$). Standard glass analyses run alongside tephra samples are reported in Appendix eI. Error bars on plots represent reproducibility, calculated as a 2 x standard deviation of replicate analysis of MPI-DING StHs6/80-G.

2.2.2 Laser Ablation Inductively Coupled Plasma Mass Spectrometry (LA-ICP-MS)

Analyses of both distal and proximal tephra deposits were performed using an Agilent 7500es ICP-MS coupled to a Resonetics 193nm ArF excimer laser-ablation in the Department of Earth Sciences, Royal Holloway, University of London. Analytical procedures and operating conditions for tephra analysis are reported in Tomlinson et al. (2010). 20 μ m, 25 μ m and 34 μ m spot sizes were used depending on vesicularity of pumices/scoria and shard sizes, distal tephtras often require a smaller laser spots. Figure 2.2 demonstrates the laser ablation pit following a single spot analysis. The repetition rate was 5 Hz and the count time was 40 s on the sample and 40s on the gas blank to allow for the subtraction of the background signal. Ablation through the glass into the resin mounts do not contribute to the background signal. Blocks of eight sample/shards of glass and one MPI-DING reference glass were bracketed by NIST612 glass calibration standard (GeoREM 11/2006). In addition MPI-DING reference glasses (Jochum et al., 2006) were used to monitor analytical accuracy.

The internal standard used was ^{29}Si (determined by EPMA analysis). Since the explosive deposits of the many of the tephra in this research are highly evolved magmas, low concentrations of CaO do not permit the use of ^{43}Ca as an internal standard. Three geochemically distinct reference glasses were used to cover the possible geochemical spectrum often observed within the tephra deposits. Evolved felsic [ATHO-G (rhyolite)], through intermediate [StHs6/80-G (andesite)] to mafic [GOR128-G (Komatiite)] standards were used. LA-ICP-MS data reduction was performed manually using Microsoft Excel allowing for the removal of signal compromised by the occurrence of microcrysts. Full details of a time slice data reduction methods are given in Tomlinson et al. (2010). Accuracies of analyses of ATHO-G and StHs6/80-G MPI-DING glasses are typically $\leq 5\%$. Relative standard deviations (% RSD) of LA-ICP-MS analyses are 5-10% for Rb, Sr, Y, Zr, Nb, Ba, La, Ce, Pr, Nd, Th, U; 10-20 % RSD for mid to heavy rare earth elements (Sm-Yb), Ta, Pb and; 20-30% RSD for Gd and Lu. RSD increases with smaller spot (25 and 20 μ m) analyses. Secondary standards analyses run alongside individual tephtras are reported in Appendix eI. For consistency with EPMA error reporting, error bars on plots show 2 x the standard deviation of replicate analyses of MPI-DING StHs6/80-G.

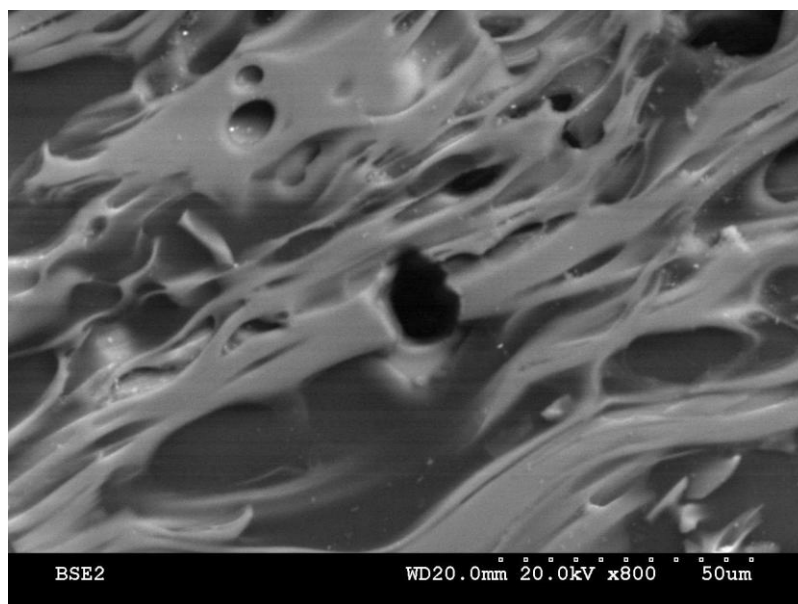


Figure 2.2: SEM image of a LA-ICP-MS ablation pit following glass analyses of a highly vesicular stretched pumice sample.

2.2.3 Inductively Coupled Plasma Atomic Emission Spectroscopy (ICP-AES)

Where glass analysis was not possible due to the high crystallinity of tephtras, ICP-AES (Department of Earth Science, Royal Holloway) was used to determine the major and minor element concentrations in the pumice and scoria. Individual pumices or scoria were ground into fine powders within a tungsten barrel using a TEMA grinding mill. Total digestion of samples was carried out using Ga as an internal standard. Powdered samples were mixed at ratio of 1:5 with LiBO₂ + Ga (Lithium Metaborate and Gallium). Fusions were digested in 5% nitric acid. Accuracies of analyses of the AVG-1 standard are typically < 5% for all elements analysed. Relative standard deviations (%RSD) are < 3 % for Si, Al, Fe, Mg, Ca, Sr, and < 5% for Na, K, and Mn.

2.2.4 Inductively Coupled Plasma Mass Spectrometry (ICP-MS)

Where glass analysis was again not possible due to the high crystallinity of tephtras ICP-MS (Department of Earth Sciences, Royal Holloway) fusions were used to determine trace element concentration in the pumice and scoria. Individual pumices or scoria were ground into fine powders within a tungsten barrel using a TEMA grinding mill. Total dissolution of samples was conducted using hydrofluoric and Perchloric acid. A 6 ml, 1:2 mixture of HClO₄ and HF are added to each sample. Accuracies of analyses of the AVG-2 standard are < 5 % for all most elements; with Nb, Sm and Gd typically < 10 %.

Relative standard deviation (%RSD) are < 1% Y, Ba, La, Ce, Pr, Nd, Dy, Er, Yb, Lu, Ta, Pb, Th; < 2% Rb, Zr, Nb, Sm, Gd; ≤ 3% for Eu.

2.3 Statistical analysis of geochemical data

Further to conventional graphical inspection of the glass data presented in this thesis (bi-plots and mantle normalised diagrams), statistical approaches are being more readily adopted to validate tephra correlations. Numerical correlation techniques are widely adopted in particular similarity coefficients (SC) (i.e., Borchardt et al., 1971; Tomlinson et al., 2012), this only considers the sample average which can be problematic given the important and natural variation seen in some tephra deposits. Herein statistical distance is used as an additional tool (D^2 ; Perkins et al., 1995, 1998; Pearce et al., 2008) for assessing tephra correlations. Statistical distance measures the difference between sample pairs, based on their mean and standard deviations. Providing the data has a normal distribution, the $D^2_{\text{calculated}}$ value has a Chi-squared distribution between compositionally identical sample pairs. Where glass populations display non-normally distributed populations, it may, in some instances, be possible to identify distinct normally distributed groupings, for instance in a compositionally bi-modal tephra, thus enabling statistical treatment of the two end-members separately. However where a tephra deposit contains significant background shard populations, numerous compositional groups or significant heterogeneity, then this approach is not applicable and has consequently not been applied to all tephra correlations within this thesis.

Where applicable, if the $D^2_{\text{calculated}} > \text{the } D^2_{\text{critical}}$ then the null hypothesis (the same pairs are identical) can be rejected. D^2_{critical} , is defined from the Chi squared tables depending on the degrees of freedom (f), where $f = \text{number of elements}$ used. Thus, where $f = 8$ (elements), at a 95% confidence limit, the $D^2_{\text{calculated}}$ would need to exceed the D^2_{critical} value of 18.307 for the sample pair to be significantly different. A $D^2_{\text{calculated}}$ value less than the D^2_{critical} means that the sample pair cannot be distinguished, however it does not indicate that they are identical. Compositionally identical samples can only be determined if $D^2 = 0$. Lower D^2 values do indicate greater compositional similarities between sample pairs and provide greater confidence in possible correlations (Pearce et al., 2008). Whilst this offers a useful tool for quantifying geochemical difference between tephras, determining correlations remain best constrained through detail investigation of multiple bi-plots where important trends can be identified.

Chapter 3: The tephrostratigraphy and glass compositions of explosive volcanism on the Aeolian Islands: Geochemical variability and chronostratigraphic markers.

Abstract

Tephra (volcanic ash < 2mm) from explosive volcanic activity on the Aeolian Islands are recorded distally in sedimentary archives within the central Mediterranean region. Tephrochronology requires that these ash layers can be robustly correlated to dated proximal deposits. Proximal stratigraphies of major explosive activity on the Aeolian Islands spanning the last 42 ka have been subject to detailed sampling. Determined here are major, minor and trace element compositions of volcanic glass to aid in proximal-distal correlations and to facilitate the re-assessment of existing distal tephrostratigraphies. Glass data from Lipari, Salina, Panarea Vulcano and Stromboli are presented.

Magmas erupted from the Aeolian Islands are geochemically diverse, reflecting variable petrological processes. The explosive products of Lipari (Monte Guardia) and Salina (Lower and Upper Pollara) demonstrate significant stratigraphic geochemical heterogeneity resulting from the mixing of discrete silicic melts. Island specific explosive activities often produce major and minor element compositions that are statistically indistinguishable through time. In certain instances glasses are best distinguished with careful assessment of the major and minor element variations (i.e. Vulcano, Stromboli), whilst in other cases trace element variations are more diagnostic of individual eruptions (Lipari and Salina).

Petrogenetic processes operating beneath Vulcano and Stromboli mean that their products can be separated using HFSE/Th ratios, despite the overlapping major element geochemistries of tephras from these two islands. Thus, in the absence of precise proximal equivalents of distal ash layers it is still possible to assign a volcanic source. On Lipari, HKCA rhyolitic glass geochemistries produced repeatedly over the last 42 ka are defined by increased concentrations of LREE and Th over time. On Stromboli, spatial geochemical variations observed in the Secche di Lazzaro deposits demonstrate the importance of detailed sampling at numerous localities in order to fully define diagnostic geochemistries at source.

3.1 Introduction

Distal occurrences of Aeolian island tephra are reported in marine archives in the Tyrrhenian Sea (Paterne et al., 1988; Di Roberto et al., 2008; Albert et al. 2012), Adriatic (Siani et al., 2004) and the Ionian Sea (Clift and Blusztajn, 1999; Caron et al., 2012). Additionally these tephra are identified in lacustrine cores (Narcisi, 2002) and the continental stratigraphies at Capo Milazzo (Morche 1988) on Sicily and more distally in the lacustrine sediments of Ioannina NW Greece (T. Jones 2012 *pers comm.*). With the continued application of micro-tephra investigation in the distal archives of the Central Mediterranean it is likely that more distal equivalents of major explosive eruptions will be identified. The purpose of this chapter is to;

- (1) Define the major and minor and trace element glass geochemistries of proximal deposits of some of the largest explosive episodes on the Aeolian Islands.
- (2) Assess the chemical variability of the glass compositions produced, both temporally and spatially (correlating proximal/medial stratigraphies);
- (3) Identify diagnostic features useful in assigning provenance solutions to distal tephras derived from the Aeolian Islands.

3.2 Geological background

The Aeolian volcanic arc comprises seven volcanic islands (Alicudi, Filicudi, Salina, Lipari, Vulcano, Panarea and Stromboli) and seven seamounts (Fig. 3.1). The Archipelago formed as a result of subduction of the Ionian plate beneath Calabria, a consequence of convergence of the African and Eurasian plates (e.g. Wortel and Spakman, 2000). Effusive and explosive eruptions on the Aeolian Islands have produced a large variety of products with differing magmatic associations. These range from calc-alkaline (CA) to high-K calc-alkaline (HKCA), shoshonitic (SHO) to High-K series (KS) suites (Ellam et al., 1988; Francalanci et al., 1993; Gioncada et al., 2003). A brief summary of the overall volcanic histories of the five Aeolian Islands investigated in this research are given below.

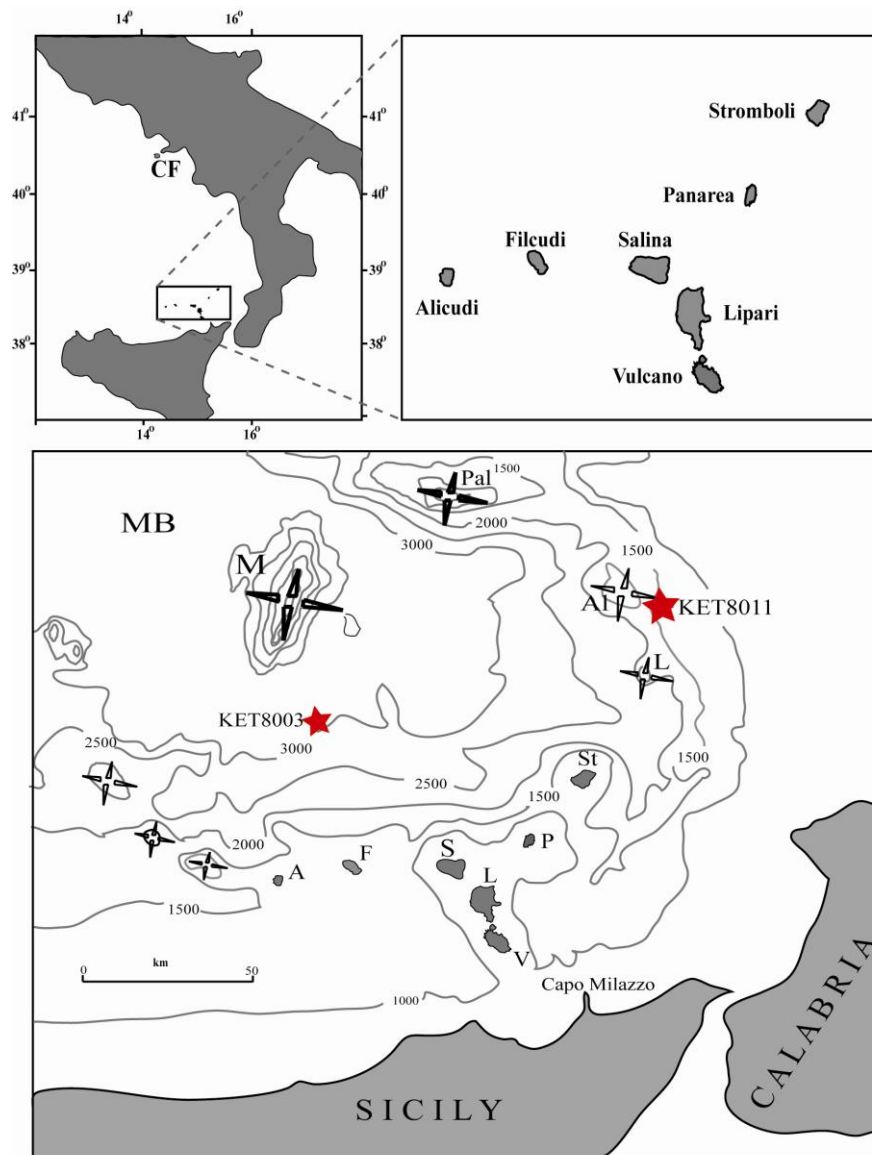


Figure 3.1: A map of the Aeolian Islands location in the southern Tyrrhenian Sea. From left to right; A= Alicudi; F=Filicudi; S = Salina; L=Lipari; V= Vulcano; P= Panarea; St= Stromboli. MB = Marsili Basin. Also given at the locations of two marine cores referred to; KET8003 and KET8011 (Paterne et al., 1988)

3.2.1 Lipari

Lipari is the largest of the Aeolian Islands (Fig. 3.2), the eruptive history is divided into 10 cycles separated by periods of quiescence (Crisci et al., 1991). The older cycles spanning I-VI (220-92 ka) are characterised by basaltic andesite to high K-andesites (Crisci et al., 1991).

Following a significant period of quiescence activity resumes on the Island at 42 ± 3 ka and sees the introduction of more evolved rhyolitic compositions (Gioncada et al., 2003). This post-42 ka stratigraphy is geochemically characterised in this chapter.

3.2.2 Salina

Salina is the second largest island; six volcanic centres can be identified ranging in age from 500-13 ka (Gertisser and Keller, 2000) (Fig. 3.3). Two clearly separate volcanic cycles can be distinguished on Salina, (1) characterised by eruption of high aluminium basalts ranging to dacites, these products were erupted from centres Capo, Rivi, Corvo and Fossa delle Felisi (oldest to youngest). An erosional unconformity separates these deposits from the younger cycle. This erosional unconformity is characterised by raised beach terraces associated with the last interglacial (Keller, 1980). (2) Younger activity (67-13 ka) built the andesitic cone of Monte dei Porri and ended with activity at the Pollara explosion crater. The activity at the Pollara centre, in the north-west of the island is the focus of geochemical characterisation in this study (Fig. 3.3).

3.2.3 Panarea

The formation of Panarea started at 149 ± 5 ka and was completed before 124 ka according to data from raised marine terraces (Lucchi et al., 2007). More recent chronological investigations suggest that activity on the island occurred as recently as 30 ± 2 ka (Dolfi et al., 2007). However, these U/Th ages are derived from scoria that Calanchi et al., (1992) attribute to Strombolian basaltic calc-alkaline activity from an offshore volcanic vent. Explosively produced pumices that are local are classified as andesite-dacites (Calanchi et al., 1992). Regardless of age uncertainty these local pumices are characterised in this chapter.

3.2.4 Vulcano

The oldest sub-aerial deposits on Vulcano are 120 ka, belonging to the Primordial Vulcano (Keller, 1980b). Around 50 ka, north dipping, normal faults affected the northern part of the old edifice producing caldera della Fossa (Fig. 3.4). Basaltic and shoshonitic eruptions occur during this activity (Gioncada et al., 2003). A second important volcano-tectonic phase occurred around 25 ka (Voltaggio et al., 1997).

This resulted in shoshonitic eruptions along a NNW-SSE trending fault (Spiaggia Lunga and Quadrara scoria blankets) (Fig. 3.4). The Lentia collapse concluded the formation of Caldera della Fossa, which are rhyolitic in composition. This is followed by the Tufi di Grotte dei Rossi (TGR) hydromagmatic eruptions thought to be derived from within Caldera della Fossa (De Astis et al., 1997). During this time activity at Monte Saraceno produced a scoria blanket. The most recent activity on the island produced the La Fossa cone that last erupted in 1888-1890.

3.2.5 Stromboli

Stromboli is the northern most island of the Aeolian archipelago (Fig.3.1). The island lies at an elevation of 924 m a.s.l. making up the subaerial section of a larger stratovolcano that rises 3000m above the sea floor (Giordano *et al.*, 2008). Deposits on the island are younger than 100 ka. The stratigraphy has been subdivided into seven superimposed edifices, according to major stratigraphic unconformities these include: Paleostromboli I (100-64ka; HKCA), Paleostromboli II (64-55ka; CA), Paleostromboli III (<55-35ka; HKCA to shoshonitic), Scari (35ka; shoshonitic), Vancori (<25-13ka; shoshonitic), Neostromboli (13-5ka; KS) and Stromboli (<5 ka-present; shoshonitic, HKCA) (Hornig-Kjarsgaard et al., 1993). A major topographic feature of Stromboli is the scar of a lateral sector collapse of the NE sector of the volcano, Sciara Del Fuoco (SDF; Figure 3.5) (Bertagnini and Landi, 1996).

3.2.6 Explosive Aeolian Island Activity

Explosive volcanism in the Aeolian Islands is dominated by mid to low intensity (sub-Plinian) eruptions, the largest of these eruptions producing approximately $\sim 0.5 \text{ km}^3$ (Total volume) of pyroclastic material (De Rosa et al., 2003a). Within the Aeolian Islands some of the most explosive volcanism displays eruptive sequences indicative of magmatic fragmentation, in some instances driven by magma mixing as a triggering mechanism (Calanchi et al., 1993; De Rosa et al., 2003a; Sulpizio et al., 2008). Evidence of phreatomagmatic activity is also observed (De Astis et al., 1997) and in the case of Stromboli often associated with flank failure of these volcanic islands (Bertagnini and Landi, 1996).

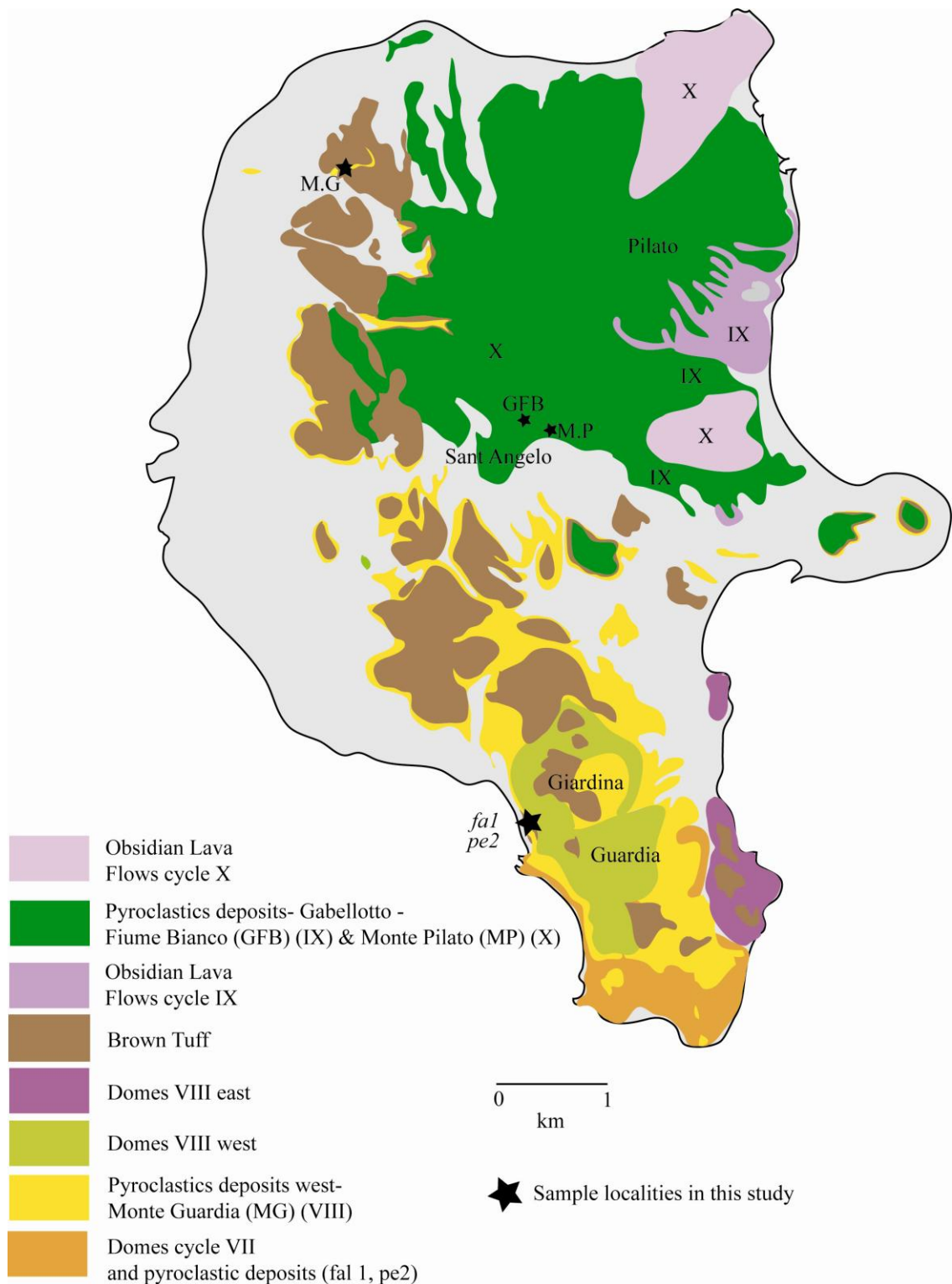


Figure 3.2: Geological map of Lipari (adapted from Gioncada et al., 2003), showing the main eruptive units produced during the last 42 ka on the island. Also shown are the sample localities of the investigated eruptions.

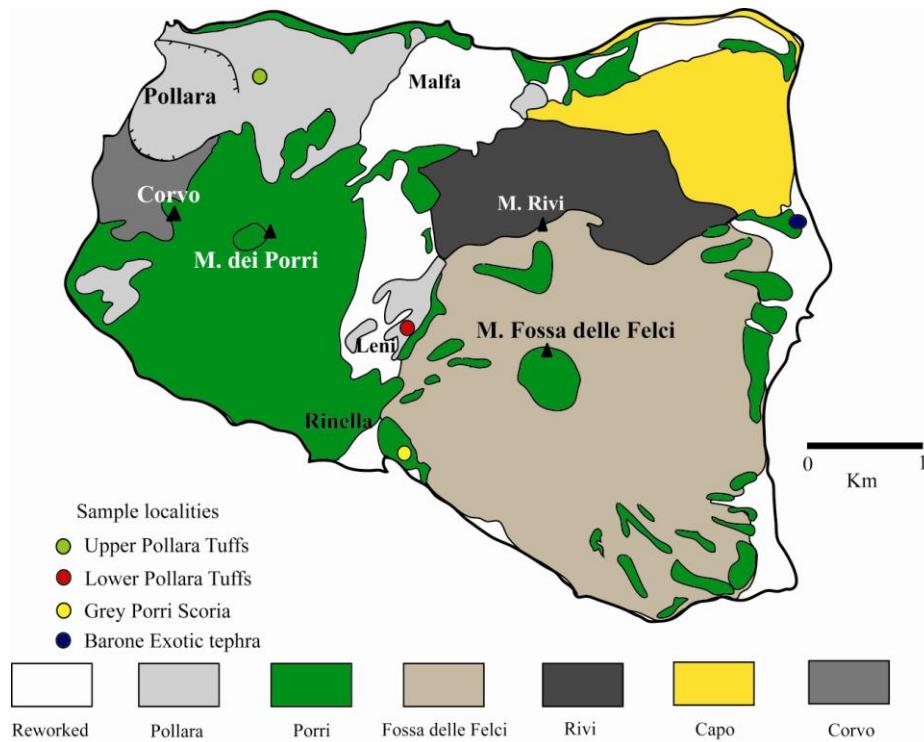


Figure 3.3: Geological map of Salina (adapted from Gertisser and Keller 2000), showing the main eruptive units spanning the 500-13 ka. Also shown are the sample localities of the eruptions investigated.

Deposits are characterised by a mixture of fall deposits from eruptive columns and flow deposits resulting from small volume, short run out pyroclastic density currents (PDC) (Sulpizio et al., 2008). Table 3.1 lists the selected significant explosive eruptions of the Aeolian Islands during the last 42 ka that have been targeted for geochemical investigation here. Published ages have been extracted from the literature and include radiocarbon ages, K/Ar ages and $^{40}\text{Ar}/^{39}\text{Ar}$ ages. Radiocarbon ages have been calibrated using OxCal 09, this calibration uses IntCal 09 (Reimer et al., 2009).

3.3. Aeolian islands Post 42 ka sampled stratigraphy

With distal tephrochronology in mind herein the focus is on stratigraphies representative of major explosive volcanism. Detailed mapping and stratigraphic investigations have greatly improved our knowledge of the overall event stratigraphy in the Aeolian Islands and were essential in the identification of the investigated deposits to be sampled (Keller, 1980a,b; Rosi, 1980; Crisci et al., 1991; Calanchi et al., 1993; De Astis et al., 1997; Lucchi et al., 2010; Tibaldi et al., 2001; Dellino et al., 2011). The following section is a brief summary of the sampled stratigraphic units that have subsequently been geochemically characterised as part of this research.

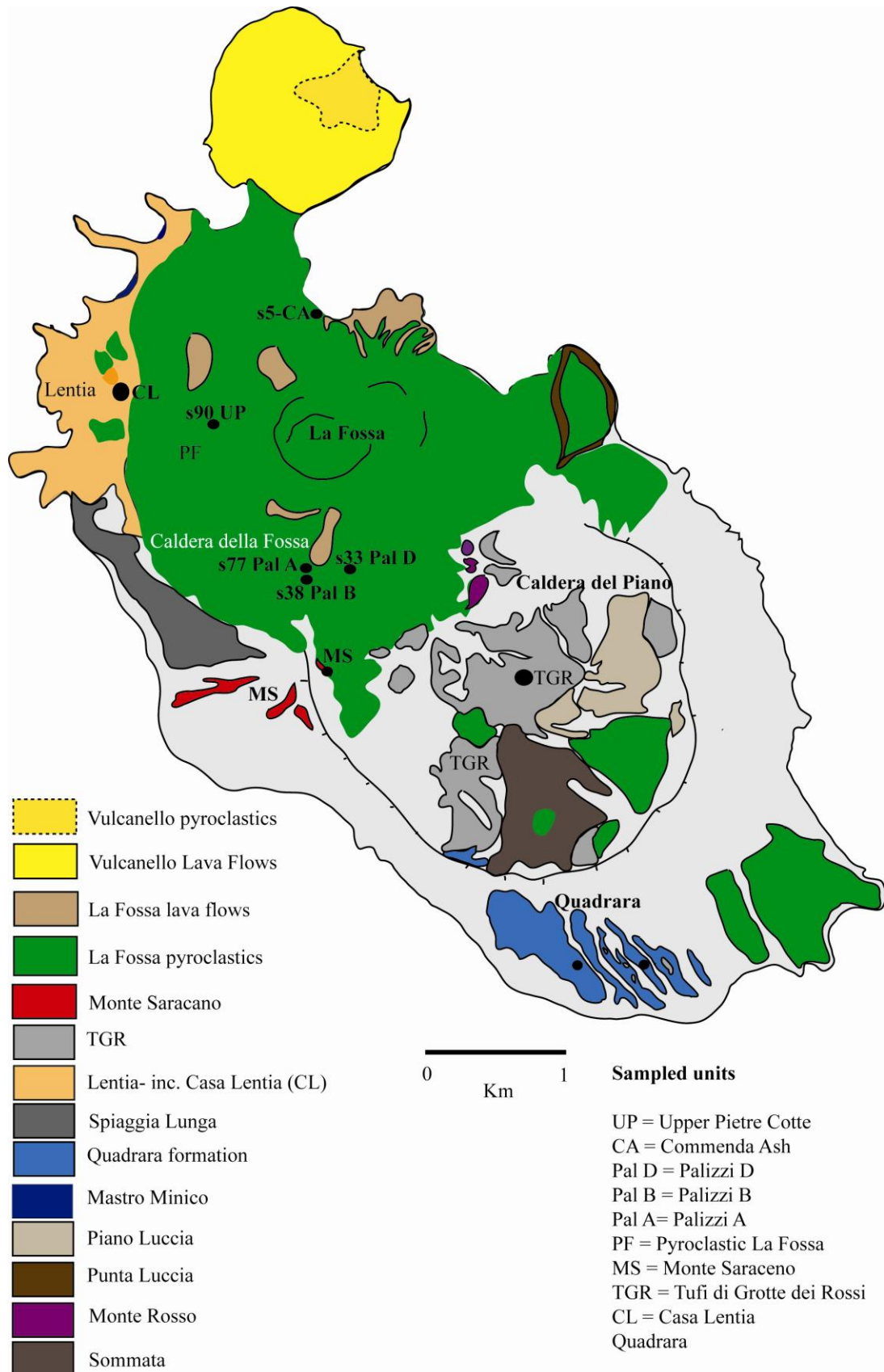


Figure 3.4: Geological map of Vulcano showing the erupted deposits produced during the last 42 ka (adapted from Gioncada et al., 2003). Also shown are the sample localities of eruptions investigated.

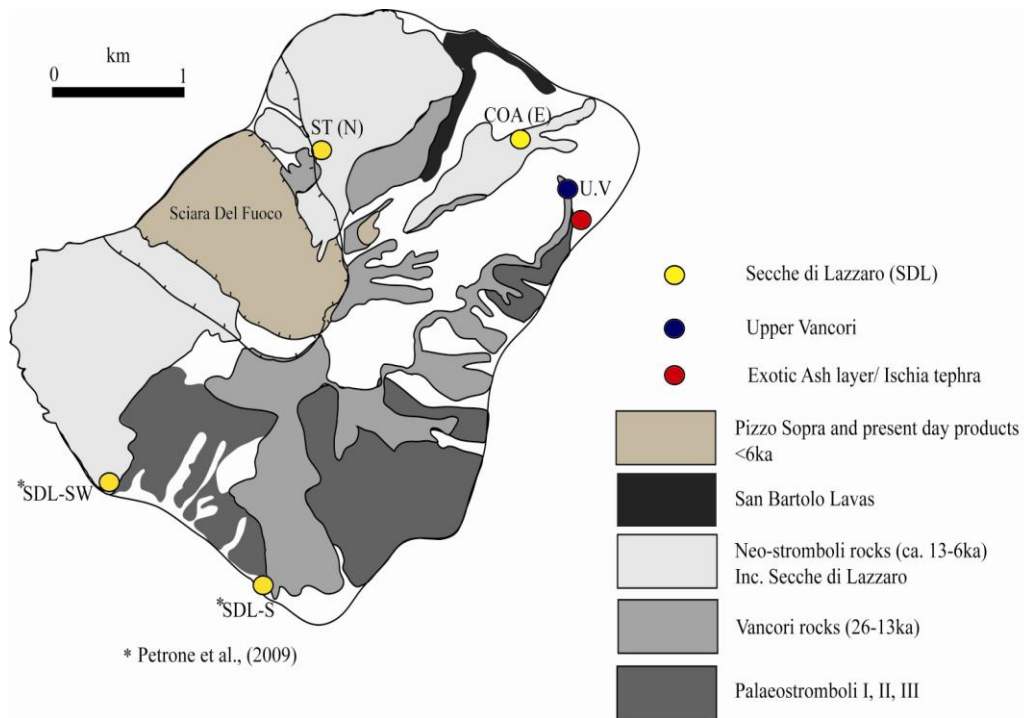


Figure 3.5: Geological map of Stromboli showing the eruptive products produced between 100 ka and present day (adapted from Hornig-Kjarsgaard et al., 1993). Also shown are the sampled localities from this investigation and also those of Petrone et al., (2009).

3.3.1 Lipari

The basal age constraint for sampling on Lipari was 42 ± 3 ka (Crisci et al., 1991) based on K/Ar determination from the lower most southern rhyolitic lava dome. This marks the onset of Lipari Epoch 4 (which encompasses eruptive cycles VII and VIII) and HKCA rhyolitic activity. Epoch 4 sees a switch from a composite volcanic centre (St. Angelo) to dome forming activity (Gioncada et al., 2003). Successive eruptions are characterised by initial explosive volcanism and subsequent effusion of superimposed viscous dome (Lucchi et al., 2010). Epoch 4 and 5 are separated by what is termed the Upper Brown Tuff (Lucchi et al., 2008), within this unit the *l2* layer has been identified on Northern Lipari, this is a pumice bed of HKCA rhyolitic activity believed to be local to Lipari, whilst its source remains unresolved it has been chronologically constrained as $>11.4 \pm 1.8$ and $< 20.5 \pm 0.7$ (Lucchi et al., 2008). Further evidence of explosive volcanism on Lipari, between Epoch 4 and 5 is identified as the Vallone Canneto Dentro formation, which also displays a high HKCA rhyolitic affinity (Lucchi et al., 2008). The onset of Epoch 5 (cycles IX and X) is related to a shift of activity to the north

eastern sector of the island, rather than eruptive style, with activity located at the Gabelotto and Pilato centres (Gioncada et al., 2003).

The southern Lipari stratigraphy is well constrained by the so called ‘Brown Tuffs’. Brown Tuffs represent ash accumulation derived from sources external to activity on Lipari (Lucchi et al., 2008). Successive brown tuff deposits separate the explosive deposits of Epoch 4 on Lipari from the younger Epoch 5 deposits. Table 3.2 summarises the pyroclastic successions from Lipari during both Epoch 4 and 5, whilst also giving details of the juvenile samples collected for analysis.

The Epoch 4 stratigraphy is best observed along the footpath leading down to spiaggia Valle Muria, south-west Lipari (Fig. 3.2). The sampled stratigraphy is shown in Figure 3.6 and details of the deposits are given in Table 3.2. Three pyroclastic units are observed interbedded between the brown tuff deposits spanning eruptive cycles VII and VIII (Fig. 3.7). Using the nomenclature of Lucchi et al. (2010) the lowermost deposit here are associated with the P. del Perciato Formation- *pe2 member* (Unit 2), these deposits represent rhythmic fall from an eruptive column and possibly subsequent surges.

Table 3.1: Over page: Major explosive eruptions targeted for juvenile geochemical analysis within the Aeolian Islands during the last 42 ka. These tephras are considered to represent potential distal tephras recorded in the distal central Mediterranean archives. Abbreviations; cpx = clinopyroxene; amp = amphibole; plag = plagioclase; bt = biotite; kf = K-feldspar; zr = zircon; ol = olivine, opx = orthopyroxene. Radiocarbon dates from the literature are calibrated using OxCal 09, this calibration uses IntCal 09 (Reimer et al., 2009). The dagger symbol represents the presence of magma mingling.

| Eruption | Source Island | Volcanic centre | Age | TAS classification (Le Bas et al., 1986) | Magma Mingling | Phenocrysts | Eruption Type | Reference |
|--|---------------|-----------------|---|---|----------------|-------------------------|-------------------------------------|---|
| P. del Perciato | Lipari | Southern Lipari | 42 ± 3 ka | Rhyolite | | cpx, kf | sub-Plinian | Crisci et al., (1981) Lucchi et al., (2010) |
| Falcone Formation | Lipari | Southern Lipari | | Trachy-rhyolite to rhyolite | | cpx, kf, zr | sub-Plinian | Lucchi et al., (2010) |
| Lower Pollara | Salina | Pollara | 27.6 ± 0.8 cal ka BP (¹⁴ C 22, 940 ± 340 yrs BP) | Basaltic andesite-Rhyolite | † | Plag, cpx, amp, ol, opx | sub-Plinian | Keller (1980) Morche (1988) Calanchi et al., (1993) |
| Monte Guardia | Lipari | Southern Lipari | 26.3 ± 0.8 cal ka BP (¹⁴ C 22, 600 ± 300 yrs BP) | Rhyolite | † | cpx, kf, zr | sub-Plinian/ Dome extrusion | De Rosa et al., (2003) |
| Quadrara | Vulcano | SW Vulcano | 21 ± 3.4 ka | Trachytic | † | bt, kf, cpx, plag | sub-Plinian | Zanella et al.(2001) |
| Upper Pollara | Salina | Pollara | 15.2 ± 0.8 cal ka BP (¹⁴ C 12,970 ± 180 yrs BP) | Dacite-Rhyolite | † | bt, cpx, amp, ol | sub-Plinian | Keller (1980b) Sulpizio et al., (2008) |
| Casa Lentia | Vulcano | La Fossa | 13 ± 3.0 ka | Trachyte-Rhyolite | | | sub-Plinian | Soligo et al., (2000) |
| Upper Vancori | Stromboli | Vancori | 13 ka | Trachyte | | cpx, plag | sub-Plinian | Cortes et al., (2005) |
| Gabellotto-Fiume bianco | Lipari | NE Lipari | 8.5 ± 0.1 cal ka BP ¹⁴ C 7770 ± 70 yrs BP | Rhyolite | | - | sub-Plinian/ Dome extrusion | Gioncada et al., (2003) Siani et al., (2004) |
| Monte Saraceno | Vulcano | Central Vulcano | 8.3 ± 1.6 Ka | Trachy-andesite | | | Violent Strombolian | Zanella et al., (2001) |
| Upper Piano Grotte dei Rossi tuffs (TGR) | Vulcano | ? | 7.7 ka | Basaltic trachy-andesite to Trachy-andesite | | cpx, plag | ? | De Astis et al., (1997) |
| Secche di Lazzaro | Stromboli | Stromboli | ~5 ka | Trachy-andesite | | cpx, plag, bt, ol | Phreatomagmatic/ sub-Plinian | Bertagnini and Landi (1996) |
| Palizzi | Vulcano | La Fossa | 2.1 ± 0.3 - 3.8 ka BP | Trachy-andesite | | plag, cpx | Violent Strombolian/ sub Plinian | Voltaggio et al., (1995) Dellino et al., (2011) |
| Monte Pilato | Lipari | Monte Pilato | 776 cal AD (¹⁴ C 1241 ± 31 yrs BP) | Rhyolite | | - | sub-Plinian/ dome extrusion | Keller (2002) Davi et al., (2010) |

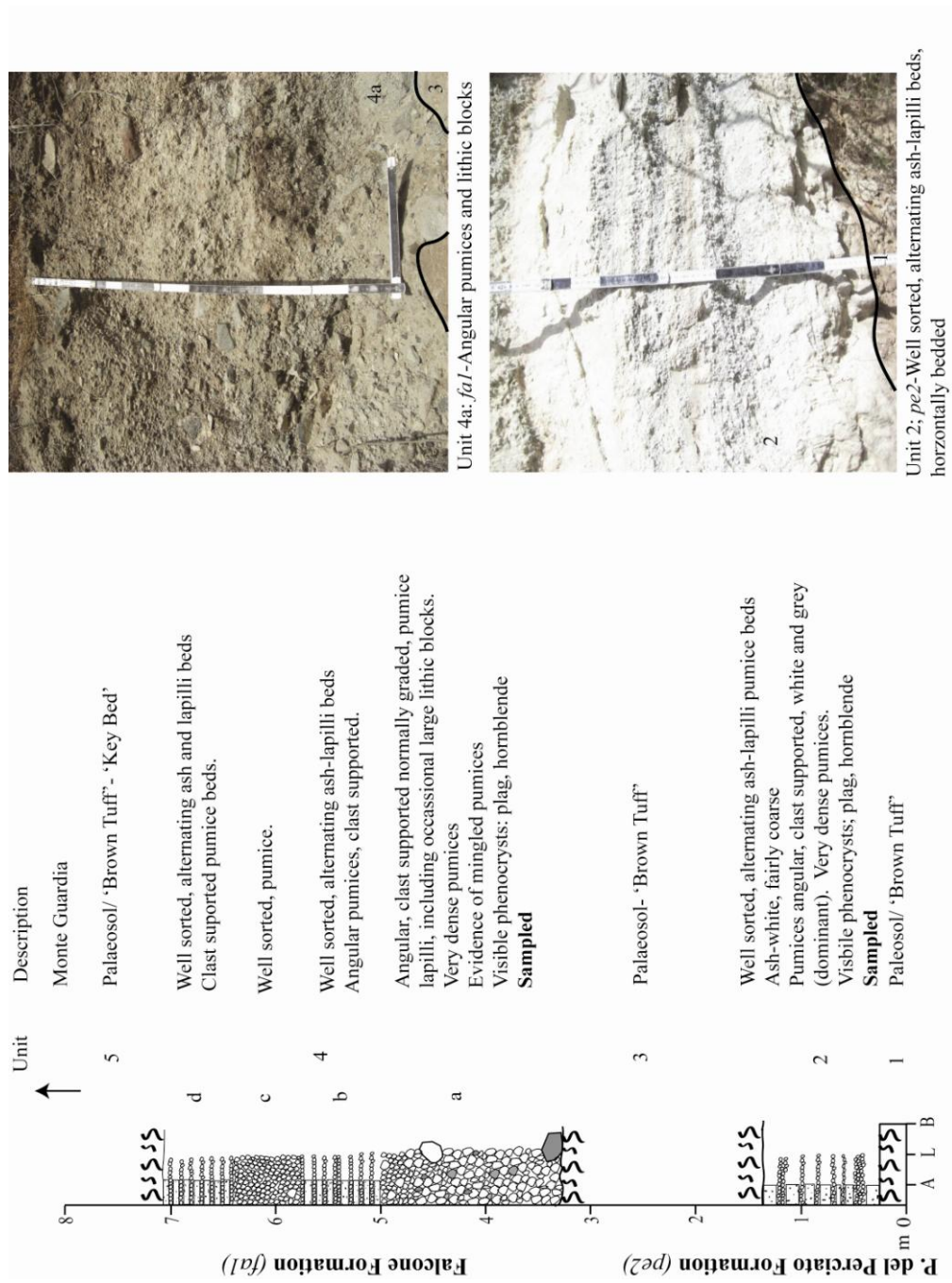


Figure 3.6: The investigated stratigraphy of the P.del Perciato (*pe2*) and Falcone (*fa1*) formations at Valle Muria, SW Lipari.

This lowermost formation has been dated to 42 ± 3 ka (Crisci et al., 1991) and is characterised by white pumice lapilli deposits. Separated from this by almost 2 meters of brown tuff is the next pyroclastic succession, the Falcone formation - *fa1* member (Unit 4), this early fall and successive surge deposits are characterised by white and grey pumices with evidence of mixing.



Figure 3.7: Complete stratigraphy of the Southern Lipari succession at Valle Muria; P.del Perciato formation (unit 2), the Falcone formation (unit 4) and capped by the Monte Guardia deposits.

The age constraints on this unit is poor, Lucchi et al., (2008) constrain it to between $> 23.5 \pm 0.9$ and 40.0 ± 2.5 ka on the basis of ages associated with the pyroclastic units above and below. The Falcone formation is capped by brown tuff and resting above this is the Monte Guardia pyroclastic succession (Fig. 3.6; 3.7).

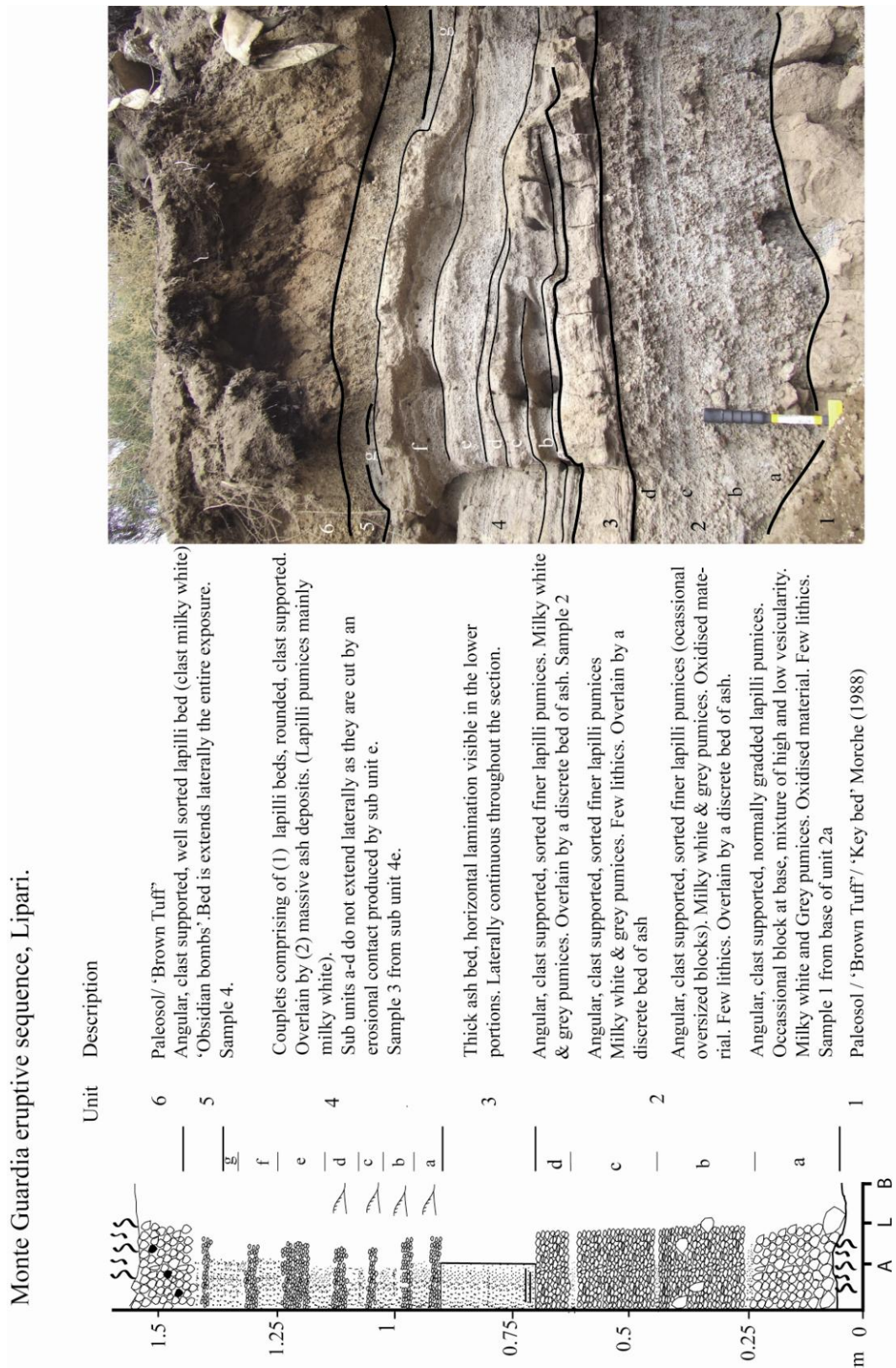


Figure 3.8: The sampled eruptive stratigraphy of fall and surge beds of the Monte Guardia, NE Lipari. The sequence is separated by a thin Palaeosol from the Lower Pollara pyroclasts from Salina.

The complete Monte Guardia eruptive sequence was sampled from north eastern Lipari (Fig. 3.8), where it stratigraphically overlies the Lower Pollara tuffs, Salina, separated by 20 cm of brown tuff (Crisci et al. 1983). The palaeosol just below the Monte Guardia succession is dated to 27.3 ± 0.8 cal ka BP (^{14}C 22.6 ± 0.3 ka BP un-calibrated; Crisci et al., (1983)) providing a maximum age. The Monte Guardia succession (Table 3.2) is comprised of opening fall deposit in which pumice lapilli were both grey and white (Units 2a-d), with evidence of magma mixing. This fall is capped by successive surge deposits containing progressively less grey pumices up section (Unit 4). The final phase of the eruption records further fall, where the grey pumices become completely absent. Milky white pumice lapilli and black obsidians make up the juvenile assemblage. Monte Guardia pyroclasts have been identified on the neighbouring islands of Salina (Lucchi et al., 2008), Vulcano (Keller 1980a; Lucchi et al., 2010) and more distally on Panarea (Lucchi et al., 2008; De Rita et al., 2008). The Monte Guardia stratigraphy was sampled near Gelso, Vulcano to provide a medial representation of the sequence to assess geochemical variability. Explosive activity in Epoch 4 finishes with M. Guardia dome activity. This followed by fall deposits associated with the Vallone Canneto Dentro dome forming extrusion (Lucchi et al., 2010). These units are interpreted as being indicative of minor explosive activity and so were not sampled.

Explosive activity of Epoch 5 is concentrated further north, the Gabellotto-Fiume Bianco (GFB) deposits of eruptive cycle IX were sampled near the summit of St. Angelo, Lipari (Fig. 3.2; Table 3.2). The most recent proximal age of this eruption is 7170 ± 720 yrs BP (Bigazzi et al., 2003). This eruption represents the initial explosive phase associated with Epoch 5. The succession contains a limited fall component (Unit 2). It is dominated by medium to thickly bedded cross stratified pumice lapilli tuffs (Fig. 3.9). These deposits are characterised by white pumices and scarce obsidian.

The most recent explosive activity on the island is associated with the Monte Pilato pumice cone; separated from the GFB deposits by a palaeosol. Field observations indicated at least two sub-phases of fall, punctuated by a small break in activity. Details of the sampled stratigraphy are given in Table 3.2. A ^{14}C age from the base of the Monte Pilato pumice sheet dates the activity to 776 ± 95 A.D (un-calibrated 1241 ± 31 yrs BP; Keller, 2002).

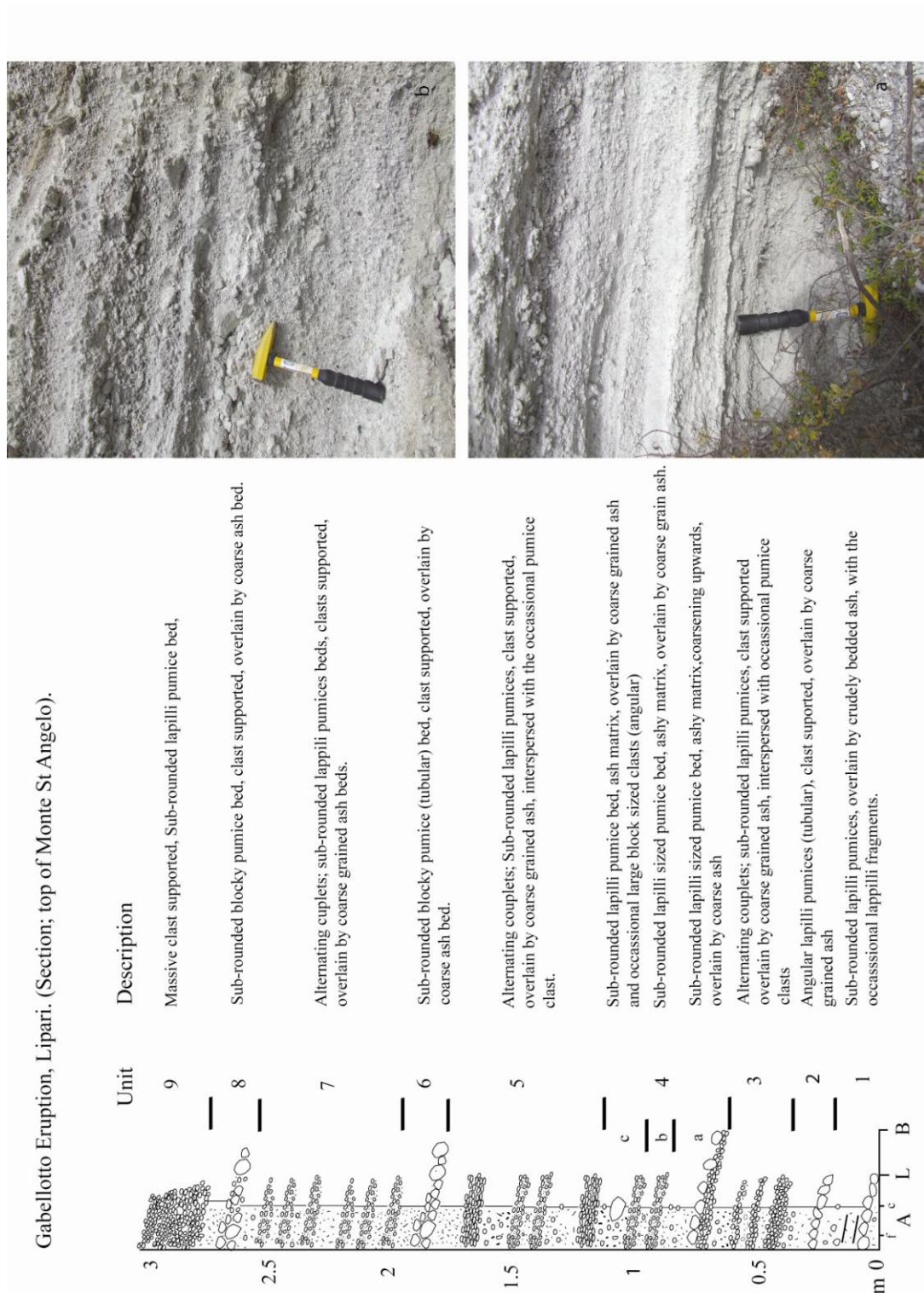


Figure 3.9: The Sampled stratigraphy of Gabellotto-Fiume Bianco from Monte Sant' Angelo. Minor fall was identified towards the base of the deposit (Table 3.2), whilst the remaining stratigraphy was dominated by surge deposits.

| Eruption | Sample Locality | Stratigraphy | Activity | Lithology and Petrology | Mixing | Dispersal | Intra-island | Sampled |
|---|--|---|---|-------------------------|--------|-----------|-------------------|---|
| EPOCH 5 Lipari | | | | | X | | | |
| Monte Pilato (M.P) Cycle X | Monte St. Angelo, Lipari N38 29'22.63 E01456'21.26 | Pyroclastic succession resting on (Unit 1) an underlying palaeosol; (Unit 2) M.P (Lower), up to 10cm thick well sorted white lapilli sized pumice bed. (Unit 3) M.P upper; (a) alternating ash (5cm), (b) lapilli sized well sorted pumice bed (5cm) and obsidian fragments; (c) capped with an ash layer (3cm). Lower pumice unit (Unit 1) is temporally separated from the upper fall (Unit 3) by evidence of biological reworking of pumices into the underlying palaeosol, only possible if this pumice bed was exposed for a period of time. | Two Sub-plinian fall episodes associated with Pilato Dome extrusion | No phenocrysts | | N, S | Stromboli Vulcano | (Unit 2) (Unit 3b) |
| Palaeosol | | Palaeosol | | | | | | |
| Gabellotto Fiume Bianco (GFB) Cycle IX | Monte St. Angelo, Lipari | 3 meter pyroclastic succession of white pumice lapilli tuffs. Minor, angular, clast supported pumice lapilli (Unit 2). Largely Medium to thickly bedded cross stratified pumice lapilli tuffs, comprised of a coarse ash matrix | (Unit 2) Small Sub-Plinian Fall contribution. (Unit 1, 3-9) dominated by thick surge deposits | No phenocrysts | | E, S | Panarea Vulcano | Unit 2 (GFB lower) white pumice lapilli; Unit 5 (GFB middle) white pumice lapilli; Unit 8 (GFB upper) white pumice lapilli |
| Palaeosol | | Upper Brown Tuff | | | | | | |
| L2 | - | Medium bedded, lithic rich, pumiceous lapilli Tuff (1-2m thick) | ? | - | | | | N.A. |
| Palaeosol | | Upper Brown Tuff | | | | | | |

Table 3.2: Part 1: Sampled proximal stratigraphy of Lipari over the last 42 ka ranging from Epoch 4 to 5. Shown are the proximal units of the P.del Perciato Formation; the Falcone formation, the Monte Guardia (MG), Gabellotto-Fiume Bianco (GFB) and Monte Pilato. K-feld = K-feldspar, plg = plagioclase; cpx = clinopyroxene; bt = biotite; amp = amphibole; Ti-mag = Titanium magnetite.

| Eruption | Sample Locality | Stratigraphy | Activity | Lithology and Petrology | Mixing | Dispersal | Intra-island | Sampled |
|--|---|--|---|--|--------|-----------|---------------------------------|--|
| Upper Brown Tuff | | | | | | | | |
| EPOCH 4 Lipari | | | | | | | | |
| Monte Guardia (MG) | NE Lipari N38 30'30.36 E14 54'59.42 | 1.5 meter pyroclastic succession rest on (Unit 1) 'Brown Tuff' which overlies the Lower Pollara Tuffs KB; (Unit 2) Four clast supported, well sorted, pumice lapilli beds capped by massive ash; both white and grey pumices are present with mixing textures; coarsest clasts in unit 2a; (Unit 3) horizontally laminated ash bed; (Unit 4) alternating couplets of rounded white pumice lapilli and ash, capped by an massive ash; (Unit 5) Clast supported, well sorted white pumice lapilli and numerous dark obsidian fragments; (Unit 6) Brown Tuff/Palaesol | (Unit 2) Early Sub-Plinian Fall, (Unit 4) surge activity dominates and the surge deposits are capped by (Unit 5) further sub-plinian fall. | White and grey pumice lapilli. White pumices are crystal poor but contain k-feld, plag, amp, bt, Ti-mag. Grey pumices contain cpx, plag and Ti-mag | X | NE, S | Stromboli Vulcano Panarea | Unit 2a , white and grey pumice lapilli; Unit 2d , white and grey pumice lapilli; Unit 4e , white pumice lapilli; Unit 5, white pumice and black obsidian |
| 20cm below MG pyroclastics are Lower Pollara Tuffs, Salina outcrop on NE Lipari | | | | | | | | |
| Falcone Formation (Cycle VII) | SW Lipari N38 27'764 E14 15 107 | The upper part of Pre-Monte Guardia succession comprises of 3.5 meter pyroclastic succession resting on (Unit 3) a 'Brown Tuff' deposit; (Unit 4) is subdivided into sub-units, access was only available to the lowermost unit (a) which comprised of a largely clast supported, angular pumice lapilli (grey and white), with a contribution of lithics and oversized bombs; (Units 4 b-d) the overlying deposits comprised of what appeared to be alternating pumice lapilli tuffs and clast supported beds. | (Unit 4a) Sub-Plinian fall, near vent given the oversized bombs, (Unit 4 b-d) the upper succession looked to include surge deposits (rhythmic pulses), capped by further fall | White and grey pumices lapilli. White pumice are crystal poor but contain plag, K-feld, amp. Grey pumices contain cpx, plag, Ti-mag. | X | E, NE | - | Unit 4a, white and grey pumice lapilli. |
| Palaesol | | | | | | | | |
| P. del Perciato Formation (Cycle VII) | SW Lipari N38 27'764 E14 15 107 | Pyroclastic succession comprises of 1 meter thick; (Unit 2) alternating horizontally bedded clast supported pumice lapilli and ash beds. | Sub-Plinian fall deposits , the fine beds indicate a rhythmic nature of activity, with a significant number of explosive pulses, dominated by white pumices. | White pumices contained plag, K-feld | | E, NE | - | (Unit 2) White milky pumice lapilli |
| EPOCH 3 Lipari | | | | | | | | |

Table 3.2: Part 2.



Monte Pilato Activity, Lipari. (Section; top of Monte St Angelo)

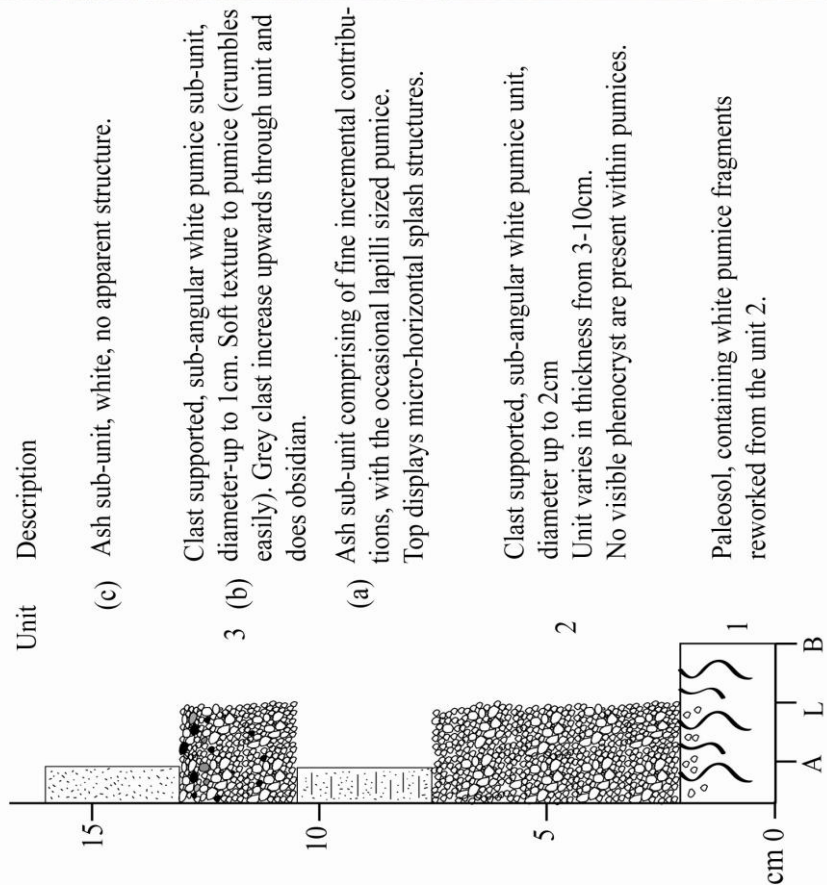


Figure 3.10: Sampled stratigraphy of the Monte Pilato eruption outcropping on Monte St. Angelo, Lipari. Two separate sub-phases to the eruption are recognised.

The Monte Pilato activity recorded on St. Angelo (Fig. 3.10) opened with a sub-Plinian fall deposit (Unit 2). These clast supported white pumice lapilli fall deposits are imbedded into the underlying palaeosol through biological reworking. This is only considered possible if the pumice bed was exposed prior to subsequent burial by the following activity (Rosi 2009 *pers comm.*). The opening phase is referred to as Monte Pilato lower, whilst the overlying ash and pumice fall (Unit 3) are reported as Monte Pilato upper. Davi et al. (2010) have highlighted that the stratigraphy of Monte Pilato is complicated with multiple sub-phases which might suggest a long lived multi-stage explosive eruption. Monte Pilato activity is identified and well constrained in the local volcanic stratigraphies of Vulcano (Lucchi et al., 2010) and Stromboli (Rosi et al., 2000).

3.3.2 Salina

Post Monte dei Porri (67-70ka) explosive activity on Salina shifted to the Pollara centre on the north western coast of the island. Activity in the last 30 ka occurred three times, starting with the lava flows of Punta del Pericato, 30 ± 3 ka (Gilliot, 1987). This was followed by two explosive eruptions from the Pollara centre (Fig. 3.3) named the Lower Pollara and the Upper Pollara tuffs (Keller, 1980b). The Lower Pollara tuff deposits were sampled both on the island of Salina near Valdichiesa and the neighbouring island of Lipari. The Valdichiesa stratigraphy (Fig. 3.11) rests on a palaeosol. This pyroclastic succession comprises opening ash fall followed by porphyritic mafic scoria fall.

The stratigraphy is interrupted by a red lithic rich horizon before a pumiceous fall deposit, comprising mingled, white and grey pumices (Fig. 3.11). Up stratigraphy the pumice fall becomes dominated by white pumices. The sequence is capped by a poorly sorted, matrix supported deposit, containing pumice lapilli and oversized lithic blocks and is interpreted as a post eruptive laharic deposits. Morche (1988) correlates Lower Pollara activity on Salina to the 'Key bed' (KB) deposits within the Lipari stratigraphy. Lower Pollara KB is well constrained by bracketing ^{14}C ages on Lipari. Morche (1988) date the base of the Lower Pollara to 27.6 ± 0.8 cal ka BP; ($22,940 \pm 340$ yrs BP uncalibrated), whilst the palaeosol overlying the Lower Pollara is dated to 26.3 ± 0.8 cal ka BP ($22,600 \pm 300$ yrs BP) by Crisci et al. (1983).

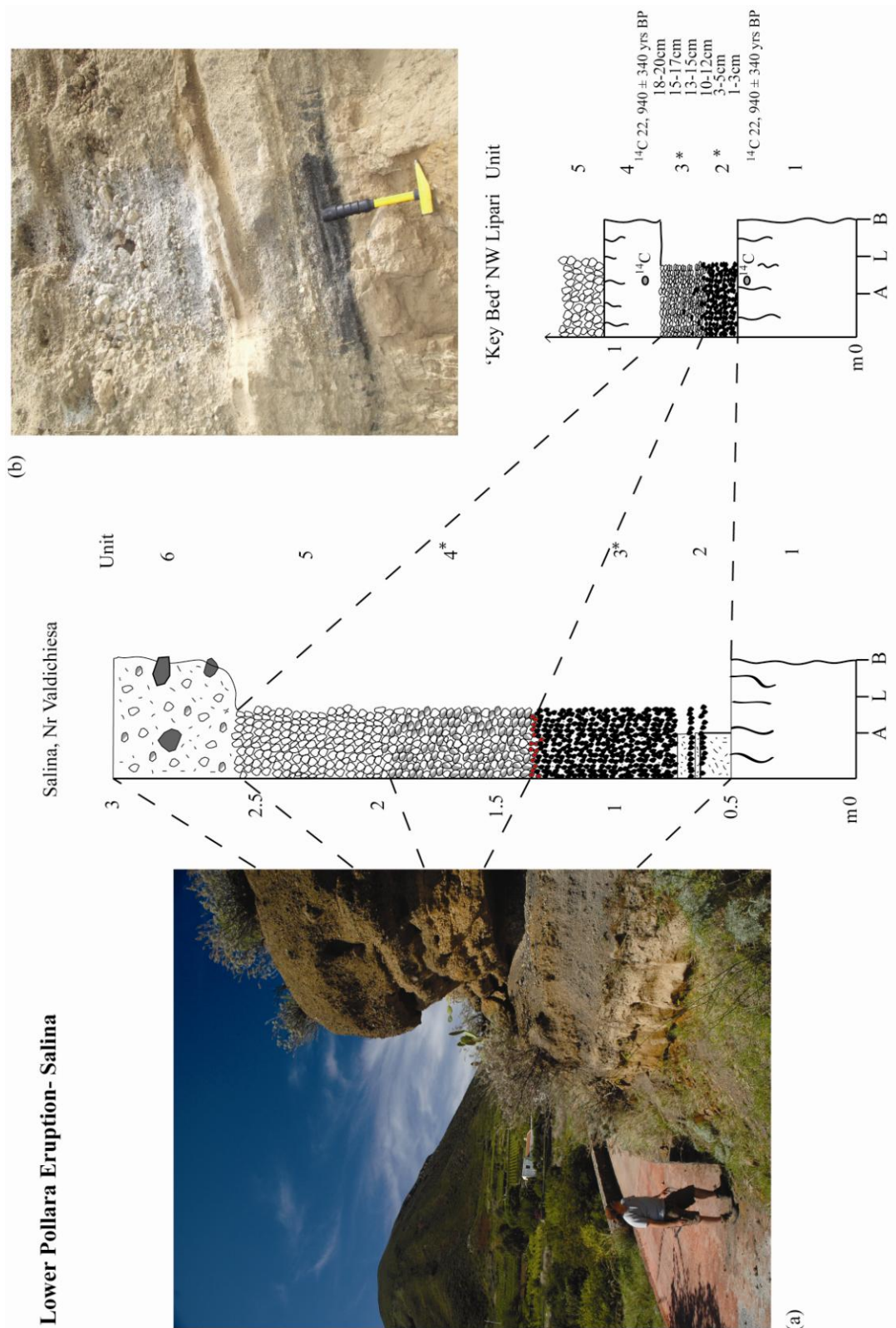


Figure 3.11: Sampled fall stratigraphy of the Lower Pollara eruption Salina at Valdichiesa and at the 'Key bed' locality on NW Lipari (Morche, 1988). (a) Valdichiesa stratigraphy; and (b) the 'Key bed' sequence separated by a thin palaeosol from the Monte Guardia deposits

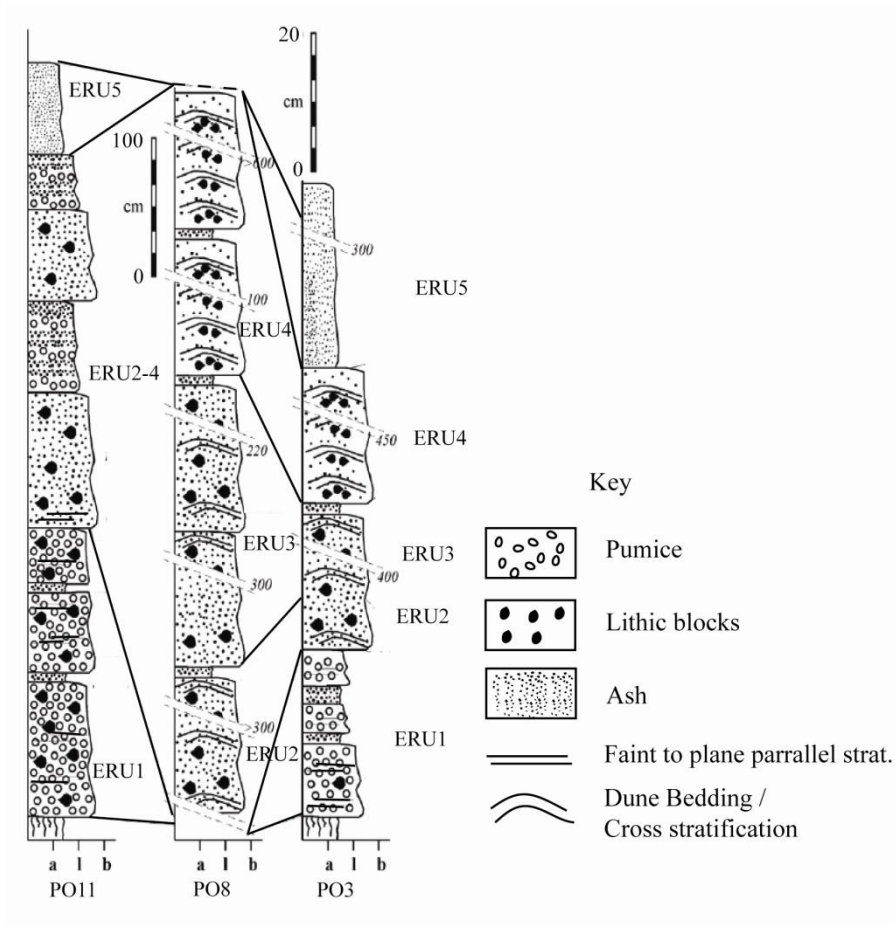


Figure 3.12: Representative Upper Pollara stratigraphy sampled, NW Salina, samples were collected from outside the Pollara crater following PO3. PO11 is inside the caldera thus the separate scale bar (Adapted from Sulpizio et al. (2008)).

This Lower Pollara KB succession (Fig. 3.11; Table 3.3) largely mirrors that of the Valdichiesa stratigraphy. Resting upon a palaeosol it is comprised of clast supported, fine grained, lapilli sized porphyritic scoria, which is capped by coarser pale white and grey pumice lapilli (Fig. 3.11). Thus both stratigraphies are characterised by a reversed eruptive sequences with mafic deposits erupted before the felsic component, this is consistent with previous observations of Calanchi et al. (1993). Distal localities indicate that the denser porphyritic scoria are likely to be less widespread given that the grain size is significantly finer relative to the pumices recorded in the KB, Lipari.

Following a period of quiescence on Salina, activity resumes on the island shortly after 15.2 ± 0.8 cal ka BP (^{14}C $12,970 \pm 180$ yrs BP; Keller, 1980b) on the basis of a C^{14} age derived from beneath the Upper Pollara sequence. Upper Pollara sampling followed the outlined and detailed stratigraphical investigations of Sulpizio et al. (2008) (Fig. 3.12), where eruptive units are defined by erosional contacts. These erosional surfaces signify pauses in the deposition of the pyroclastic deposits through the Upper Pollara stratigraphy (Sulpizio et al., 2008). The thickness of this deposit is more limited outside the Pollara crater (Fig. 3.12). A summary of the stratigraphic context of the samples analysed are given in Table 3.3. Eruptive Unit 1 (ERU1), containing dull white and grey banded pumices, provides the only evidence of fall from a sustained eruptive column during the Upper Pollara eruption. Sulpizio et al. (2008) suggest that this eruptive column was weak and fairly short lived with limited fall components capped by an almost contemporaneous dilute pyroclastic density current (PDC) deposit. The remaining four eruptive units (ERU 2-5) are attributed to PDC deposits (Sulpizio et al., 2008) summarised in Table 3.3. Juvenile glass components vary between these units. ERU 2 is dominated by dull white pumices, with only a limited grey component. ERU3 and ERU4 comprises of milky white pumices and grey pumice lapilli, with evidence of mixing/banding. ERU5 comprises almost exclusively of grey pumice lapilli. Dispersal of both Lower and Upper Pollara pyroclastic deposits are east, south-east based on isopachs (Sulpizio et al., 2008).

| Eruption | Sample Locality | Stratigraphy | Activity | Lithology and Petrology | Mixing | Sampled | |
|---------------|--|--|--|---|---|---|---|
| Upper Pollara | ERU 5 | Between Pollara crater and Malfa terrace | Poorly sorted, massive ash with sparse pumice lapilli. | PDC deposits | Grey pumices, containing plag, cpx, amp, bt. | | Grey pumices |
| | ERU 4 | Between Pollara crater and Malfa terrace | Poorly sorted, massive ash with sparse pumice lapilli. With large amounts of ballistic blocks | PDC deposits | Milky white pumices; amp, bt.; and grey pumices; plag, amp, bt. | X | Milky white pumices and grey pumices |
| | ERU 3 | Between Pollara crater and Malfa terrace | Coarsest and richest juvenile unit. (a) Poorly sorted massive ash with coarse pumices, (b) capped by crudely stratified coarse pumice and lithic lapilli | PDC deposits | Milky white pumices; amp, bt.; and grey pumices; plag, amp, bt. | X | (a) White, grey and banded pumices |
| | ERU 2 | Between Pollara crater and Malfa terrace | Poorly sorted, crudely stratified coarse pumice and lithic lapilli beds | PDC deposits | Dull white pumice are dominant, occasional grey pumice | ? | Dull white pumices |
| | ERU 1 | Between Pollara crater and Malfa terrace | (a) Clast supported lithic rich pumice and ash beds. Thickness ranges from a 1 meter to a few cm in distal localities. (b) Capped by poorly sorted, crudely stratified pumice and lithic lapilli beds | Fall from a Sustained eruptive column (Short-lived), capped by small dilute Pdc deposits. | Pumices were a dull white, dark-grey or white-grey banded pumices. Plag, amp, bt were present both loose and within the pumices | X | (a) White, grey and banded pumices |
| Lower Pollara | Valdichiesa N38 33 533 E014 49 752 | Resting on a (U 1) Palaeosol this pyroclastic succession comprises ; (U 2) grey ash massive, capped with alternating coarse lapilli scoria and ash; (U 3) partially matrix supported, inversely graded, bed of highly porphyritic scoria. Boundary between unit 3 and 4 is marked by crudely defined layer of red lithics; (U 4) largely clast supported, sorted crudely stratified pumice lapilli bed; (U5) clast supported, well sorted pumice lapilli deposits; (U 6) matrix supported ash deposit, containing lapilli and oversized lithic blocks. | Fall from a sustained eruptive column | Black porphyritic scoria , crystal rich >50% containing plag, cpx, ol, opx, amp; Grey pumices contain plag, Cpx, amp; white pumice are crystal poor containing plag amp. | X | U3 porphyritic scoria and U4 banded pumices | |
| | Lower Pollara 'Key bed' (Morche, 1988) | NE Lipari N38 30'30.36 E14 54'59.42 | Resting on (U1) a Palaeosol, this pyroclastic succession comprises of (U2) dark fine grained (2mm \emptyset) dark porphyritic scoria; (U3) grey and white pumices with white pumices, white becoming progressively more dominant up-sequence, coarsest pumices up to 2cm \emptyset ; (U4) a further Paleosol; (U5) Monte Guardia pyroclasts | Fall from a sustained eruptive column | Black porphyritic scoria , crystal rich >50% containing plag, cpx, Ol, opx, amp; Grey pumices contain plag, Cpx, amp; white pumice are crystal poor containing plag amp. | X | (U2) Three levels of porphyritic scoria 1-3, 3-5, 10-12cm and (U3) Three levels of grey and white pumices 13-15, 15-17, 18-20cm |

Table 3.3: Sampled proximal stratigraphy of explosively erupted deposits from Salina (Lower and Upper Pollara). Upper Pollara stratigraphy follows Sulpizio et al., (2008). plg = plagioclase; cpx = clinopyroxene; bt = biotite; amp = amphibole; ol = olivine.

3.3.3 Panarea

Two proximal stratigraphies were sampled on Panarea as they are interpreted as containing the most recently explosively erupted deposits on the island. Samples were collected from Punta Falcone near the centre of the island and from Palisi in the north (Fig. 3.13). The Punta Falcone succession is made up of more than 10 m of pyroclastic deposits, the source location of these deposits is poorly constrained (Lucchi et al., 2007). Pumice fall at the base, is capped by thick block and ash deposits (Fig. 3.14) with the upper portion of the stratigraphy being made up of normally graded and well sorted scoria lapilli and ash beds (Fig. 3.14). Inconsistencies exist between the chronological constraints placed on the Punta Falcone succession and in turn the timing of the final phase of explosive activity on Panarea. Lucchi et al., (2007) suggest that the Punta Falcone succession spans the third to fifth eruptive epochs recorded on the island (between ca. 127-67.5 ka). The upper basaltic scoria (Fig. 3.14) recorded in the stratigraphy are tentatively associated with fall originating from inlets east of Panarea (Calanchi et al., 1992). In keeping with these ages, interbedded within these scoria deposits is an alkaline tephra, which is correlated to the X-5 marine tephra and dated at 105 ± 2 ka (Kraml, 1997). This chronological constraint is discussed further in chapter 6. Dolfi et al., (2007) date the same scoria in the upper portion of the stratigraphy to a considerably younger 31 ± 7 ka using U/Th and attribute the alkali tephra to much younger mainland activity and the Pomici di Base eruption (Somma-Vesuvius) at ca. 22 ka.



Fig. 3.13: A map showing the sample localities on the island of Panarea.



Figure 3.14: The Punta Falcone Stratigraphy, Panarea. Pumices were sampled from the basal fall unit, thought to be representative of the last major explosive episode on the island.

Despite age uncertainties, pumices were sampled from a basal fall unit, unit 2 (Fig. 3.14), these were most certainly proximal to Panarea and would provide representative glass compositions from Panarea. These pumices are banded, containing both grey and white components. The pumice fall deposits sampled here are correlated with fall recorded at Palisi on the north of the island, these pumices were sampled for comparison (see De Rita et al., 2008).

| Eruptive unit | Sample Locality | Stratigraphy | Activity | Lithology and Petrology | Mixing | Dispersal | Intra-island | Sampled |
|--|---|---|---------------------|---|--------|-----------|----------------------------|---|
| Pietre Cotte (upper) (UP) | La Fossa caldera (Di Traglia, 2011) (Fig. 3.4) | Ash capped by a massive deposit of banded pumices; largely chaotic. Pyroclastic fall | Vulcanian | Ash and banded pumices | X | - | - | Ash and banded dark and white pumices (s90 UP) |
| Commenda Ash (CA) | | | Steam blasts | Ash | | | | Ash (s5Ca) |
| Palizzi D | | Clast supported, reverse to normally graded pumices. Pyroclastic Fall | Vulcanian | Grey pumices and black obsidian, plag and cpx | | | | Grey pumice lapilli (s33) |
| Palizzi B | | Clast supported pumices, reversely graded. Pyroclastic Fall | Vulcanian | white pumices with k-feldspar | | SE | | White pumice lapilli (s38) |
| Palizzi A | | Planar bedding and consist of massive, normally graded, black and golden ash. Pyroclastic Fall. | Violent Strombolian | Ash, including cpx and plag | | | | Black and grey ash (s77) |
| Punta Nere | | Fall deposits and thickly plane parallel and cross laminated-black tuffs | Vulcanian | Black-grey ash | | | | Not sampled |
| Upper TGR Scoria | Piano Caldera (N38 23 505; E 014 58 874) | Thin to medium bedding, grey/brown massive deposit of fine ash. Interbedded within this ash deposits was a thin bed of lapilli sized scoria. Fall deposit. | ? | | | | Upper Brown Tuffs | Scoriaceous lapilli |
| Monte Saraceno | NW rim of Piano Caldera (N23 23 196; E014 58 707) | Clast supported normally graded lapilli sized scoria. Evidence of alteration within the sampled deposit. Pyroclastic fall deposit. | Violent Strombolian | black scoria | | E | - | Scoriaceous lapilli |
| Casa Lentia | Lentia (N 38 24 940; E014 56 870) | Well sorted deposits, clast supported, bombs and lapilli, Pyroclastic Fall | Vulcanian | Black-grey pumice (plag, cpx) | | | | Grey Pumices |
| Upper TGR | Piano Caldera (N38 23 505; E 014 58 874) | Thin to medium bedding, grey/brown massive deposit of fine ash. | ? | | | | Upper Brown Tuffs | Not sampled (see De Astis et al.(1997)) |
| SW Vulcano (Change in the location of the eruptive centres) | | | | | | | | |
| Quadrara Formation | SW Vulcano: N38 22 402; E014 58 959) | Inversely graded, clast supported white pumices (up to 1 meter thick); Units 1 and 2 (Fig. 3.15) capped with dark scoriaceous deposits, sorted and evidence of welding (units 3 and 4). Pyroclastic fall deposits | sub-Plinian | Pumices contain biotite and K-feldspar. Scoria, cpx and plag. | | S? E? | Capo Milazzo (Morche 1988) | White pumices (Unit 1-2) and Scoria lapilli (Unit 3) and scoriaceous bombs (Unit 4) |

Table 3.4: The sampled stratigraphy of Vulcano includes eruptive products spanning the last 21 ka on the island, also see Todman (2012) and Di Traglia for La Fossa samples.

3.3.4 Vulcano

3.3.4.1 Pre-La Fossa

The oldest stratigraphic unit sampled on Vulcano was the Quadrara formation located on the southern flanks of the island near Gelso (Fig. 3.15). Deposits range in thickness up to 8 meters, thinning in southerly and northerly directions. The stratigraphy and the deposits are outlined in Table 3.4. The sequence opens with a pumice fall, which is inversely graded (Fig. 3.15). This pumice fall is capped by a thick scoria fall deposits (Fig. 3.15), these deposits range from lapilli to bombs and show evidence of welding. This sequence clearly indicates a change in the magmas feeding this eruption. Samples were taken throughout the stratigraphy. The deposits are dated at 21 ± 3.4 ka (De Astis et al., 1997). Casa Lentia samples were taken from the Lentia cliffs (Fig. 3.4), these bombs and lapilli were well sorted and clast supported. The deposits are dated to 13 ± 1 ka (De Rosa et al., 2003b).

Scoriaceous lapilli were sampled from the thick ash deposits associated with the TGR (Table 3.4), the outcrop investigated is documented in De Astis et al., (1997). The unit is comprised predominantly of ash and loose clinopyroxene crystals, this deposit is associated with hydromagmatic eruptions occurring within the submerged caldera della Fossa. This hydromagmatic eruptive mechanism is thought to be responsible for the Upper Brown Tuffs recorded throughout the Aeolian Islands (De Astis et al., 1997; Lucchi et al., 2008). However, debate continues with some researchers suggesting that these ash deposits represent accumulations from throughout the Aeolian Islands during a period of quiescence on Vulcano (Rosi 2009 pers comm.). The unit has been dated at 7.7 ± 1 ka BP (De Astis et al., 1997) prior to the emplacement of the Punta Nere pyroclastics 3.8 ± 2.5 ka (Soligo et al. 2000) Scoriaceous fall from Monte Saraceno pyroclastics were sampled from a locality within the Piano caldera (Fig. 3.4; Table 3.4), this unit is dated at 8.3 ± 1.6 ka (De Astis et al. 1989).

3.3.4.2 Le Fossa

The La Fossa eruptions were sampled in conjunction with the detailed stratigraphic investigations of Di Traglia (2011), the composite log of the sampled stratigraphy is given in Figure 3.16 and details of the sampled material is listed in Table 3.4.

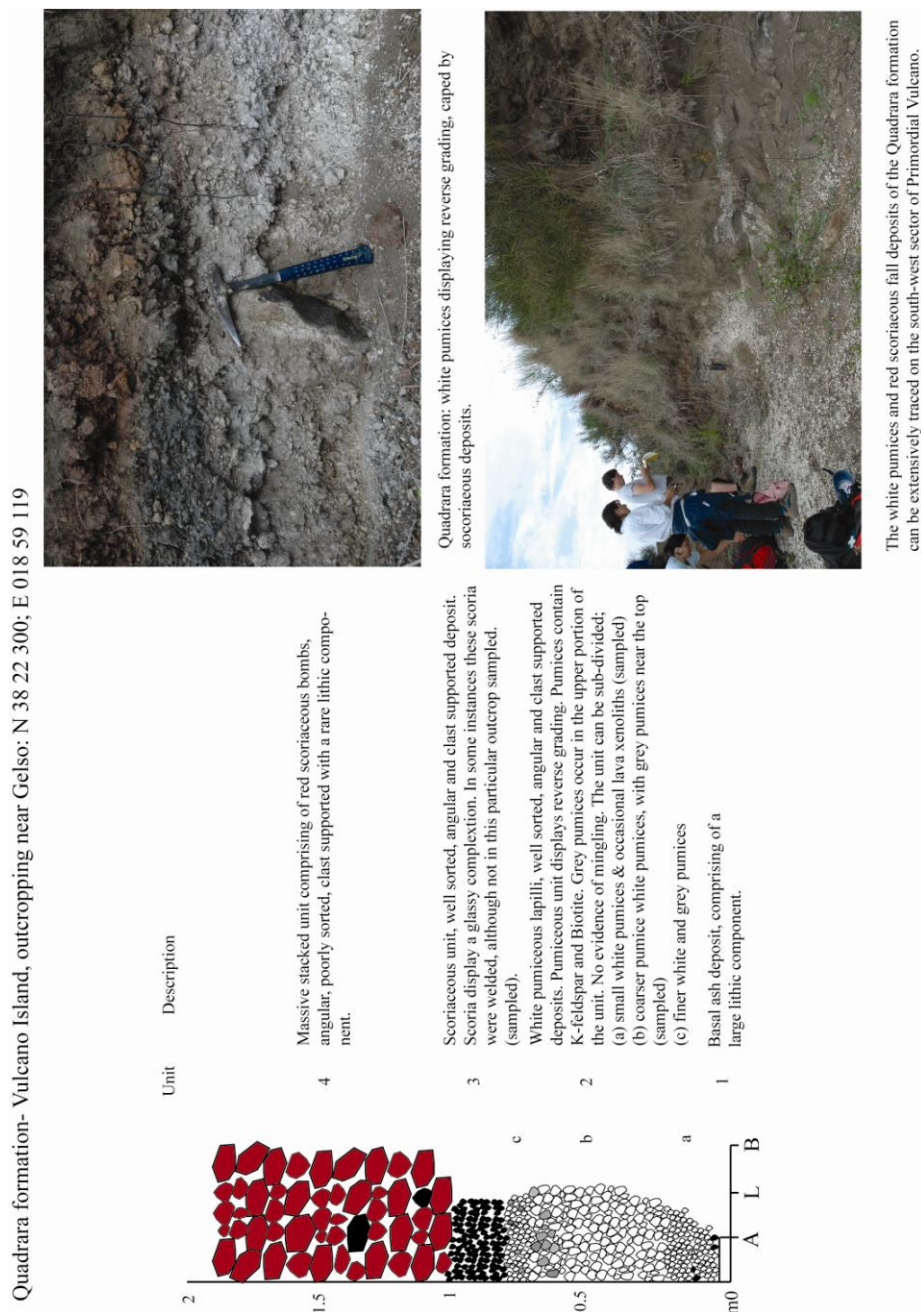


Figure 3.15: The sampled stratigraphy of the Quadrara formation outcropping on the south-western Primordial Vulcano (See Table 3.4 for details).

The La Fossa cone is thought to have been built in the last 5.5 ka (Frazzetta et al., 1983). The early Palizzi succession is comprised of decimetre thick, laminated ash layers, interpretations of these deposits are contrasting; Di Traglia (2011) interprets these ash layers as fall, whilst Dellino et al. (2011) consider these the result of dilute PDC's. The two most prominent layers in the stratigraphy relate to two lapilli pumice fall beds (Palizzi B and Palizzi D). Their fall is largely restricted to south of the La Fossa vent. The lower pumice fall bed, Palizzi B, is dated to 2.2 ± 1.3 ka (Frazzetta et al., 1983).

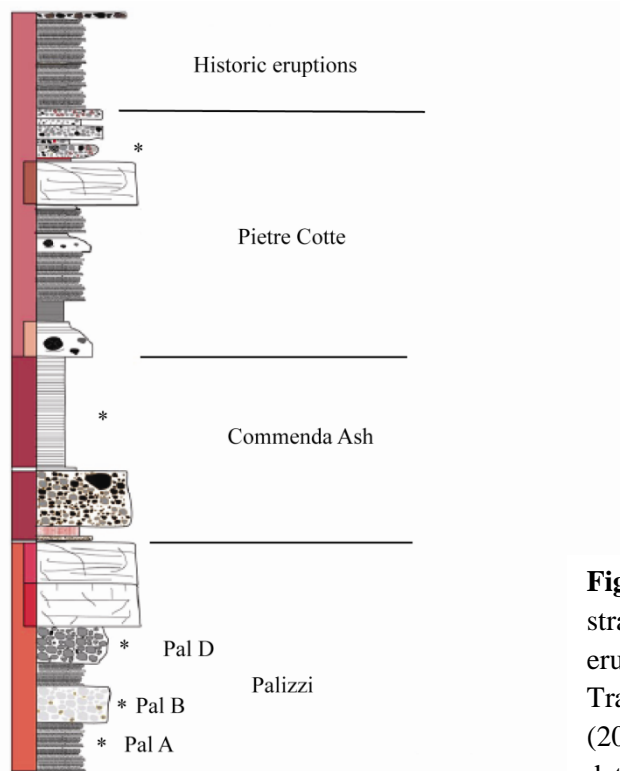


Figure 3.16: Composite stratigraphic log of the La Fossa eruptive sequence following Di Traglia (2011) and Todman (2012). See Table 3.4 for further details.

3.3.5 Stromboli:

The oldest explosive deposits investigated on Stromboli were those of the upper Vancori (~ 13 ka; Cortes et al., 2005), the sampled deposits were characterised by normally graded pumice lapilli fall, details of the sampled stratigraphy are presented in Table 3.5, the sampled locality is shown in Figure 3.5 and investigated stratigraphy is shown in Figure 3.17.

The younger phreatomagmatic pyroclastic succession of the Secche di Lazzaro (Bertagnini and Landi, 1996) was sampled at two separate localities on the island (Fig. 3.5). An outcrop on the north of the island along the Semaforo track was sampled (Fig. 3.18), whilst a second outcrop near the advanced operations centre (COA) was also investigated (Fig. 3.19). Details of both stratigraphies are described in Table 3.5. Age determinations for this eruption are not precise, an approximately 6 ka radiocarbon age from the palaeosol beneath the pyroclastic succession is referred to by Petrone et al., (2009), but precise details are not available. The Secche di Lazzaro deposits rest upon the Neo-Stromboli lavas which are dated to between 7-7.5 ka (Speranza et al., 2008). Dates from the oldest 'Recent Stromboli' activity are around 5 ka (Petrone et al., 2009), thus the age is likely to be between 7-5 ka.

| Eruption | Sample Locality | Stratigraphy | Activity | Lithology and Petrology | Dispersal | Intra-island | Sampled |
|-------------------------|---|--|--------------------------------|--|-----------|--------------|--|
| Secche di Lazzaro (SDL) | Semaforo Track (ST), Northern Stromboli N38 48'11.07; E015 12'52.65 | Pyroclastic fall, capped by reworked lahar deposits. Abundant accretionary lapilli. 2m section. Juvenile component dominated by unconsolidated massive ash (40cm-brown). The lower section contains a crude bedded layer of green/grey scoria lapilli within the ash matrix (20cm). 60cm of plane parallel bedded ash layers (green/yellow/brown). A cemented massive ash caps these laminations, whilst above is a poorly sorted massive ash deposit containing pumice lapilli and lithics (Flow unit). | Sub-plinian phreatomagmatic | Green/grey glassy vesicular scoria and pumice. Containing phenocryst, predominantly plagioclase and clinopyroxene. Occasional olivine. | NE | | Fall: Glassy green/grey scoria from 20cm thick unit near the base of stratigraphy (SDL-ST-U2). |
| | COA, Stromboli N38 48'10.81; E015 14'00.78 | A pyroclastic fall and flow succession, capped by lahar deposits. 1.3m thick succession. A thin layer of black ash deposits (0.5cm). Horizontally bedded grey ash laminations, coarse/fine grain alternations (12cm). 13cm ashy matrix supported unit containing pumices and accretionary lapilli. 2cm ash unit containing abundant pumices and accretionary lapilli (U4). Capped by a thick matrix supported, poorly sorted admix of ash, pumice and lithics (lahar). | Sub-plinian phreatomagmatic | Grey pumices are highly vesicular and display lower abundances of phenocryst including plagioclase, clinopyroxene and occasional biotite assemblage. Rare biotite occurs in these pumices. | E | | Pumices form within the lower most ash dominated units (ST-COA-U4). |
| Upper Vancori (UV) | NE Stromboli, N38 48'0334 E15 14 15.56 | A pyroclastic fall succession. Unit 1 20cm clast supported normally graded grey pumices. 15 cm massive ash (Unit 2). Unit 3 15cm of clast supported, grey pumices. Capped by a massive dark ash deposit (Neo-Stromboli). | Sub-plinian | Grey pumices are highly vesicular, containing plagioclase, clinopyroxene, Fe-Ti oxides. | E | ? | Pumices from unit 1 and 3. |

Table 3.5: The sampled stratigraphy of Stromboli includes the explosive products spanning the last 13 ka.

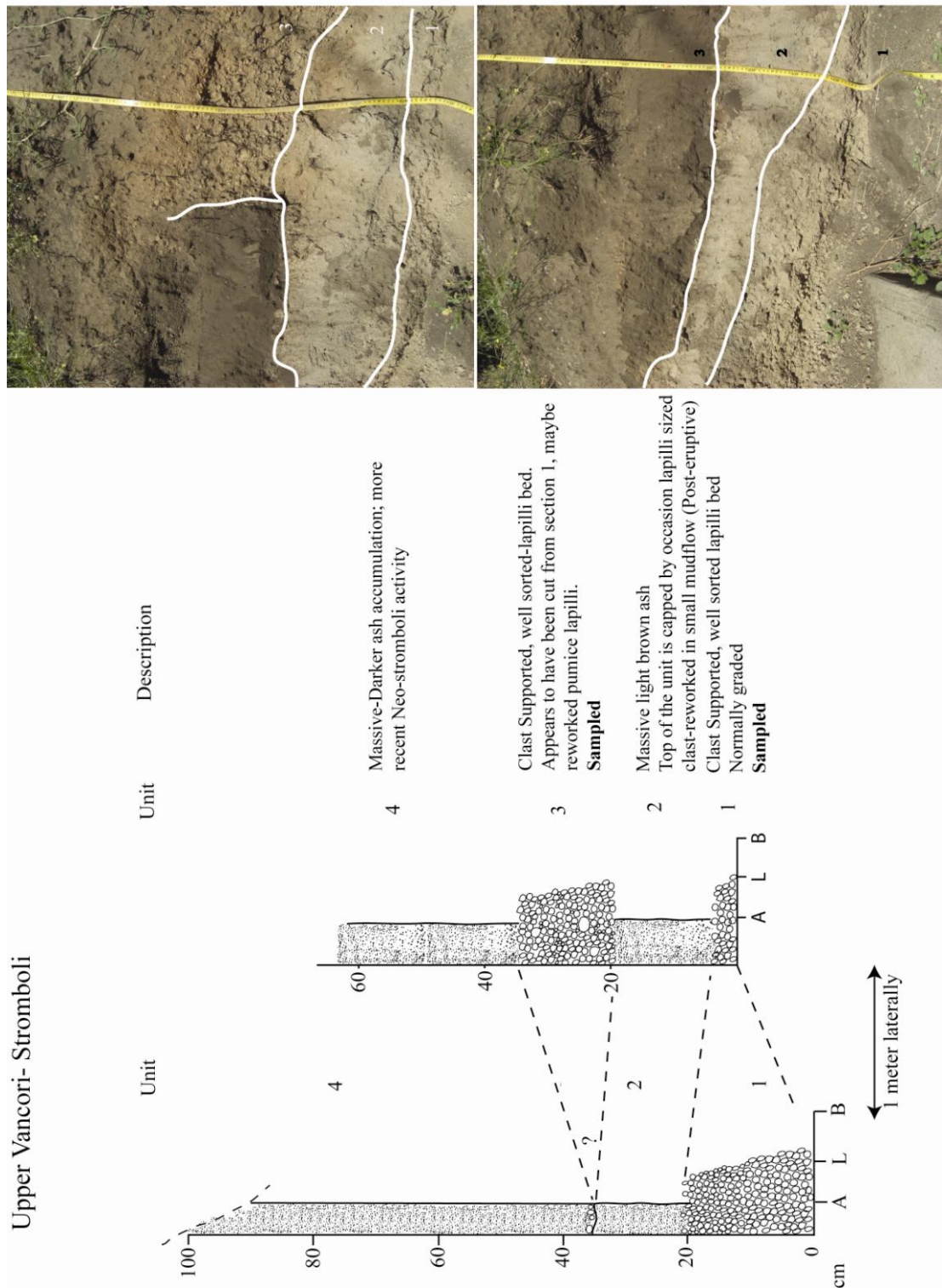


Figure 3.17: The sampled Upper Vancori stratigraphy of Stromboli (See Table 3.5 for further details).

Stromboli: Seeche di Lazzaro; Section 1: Semaforo track

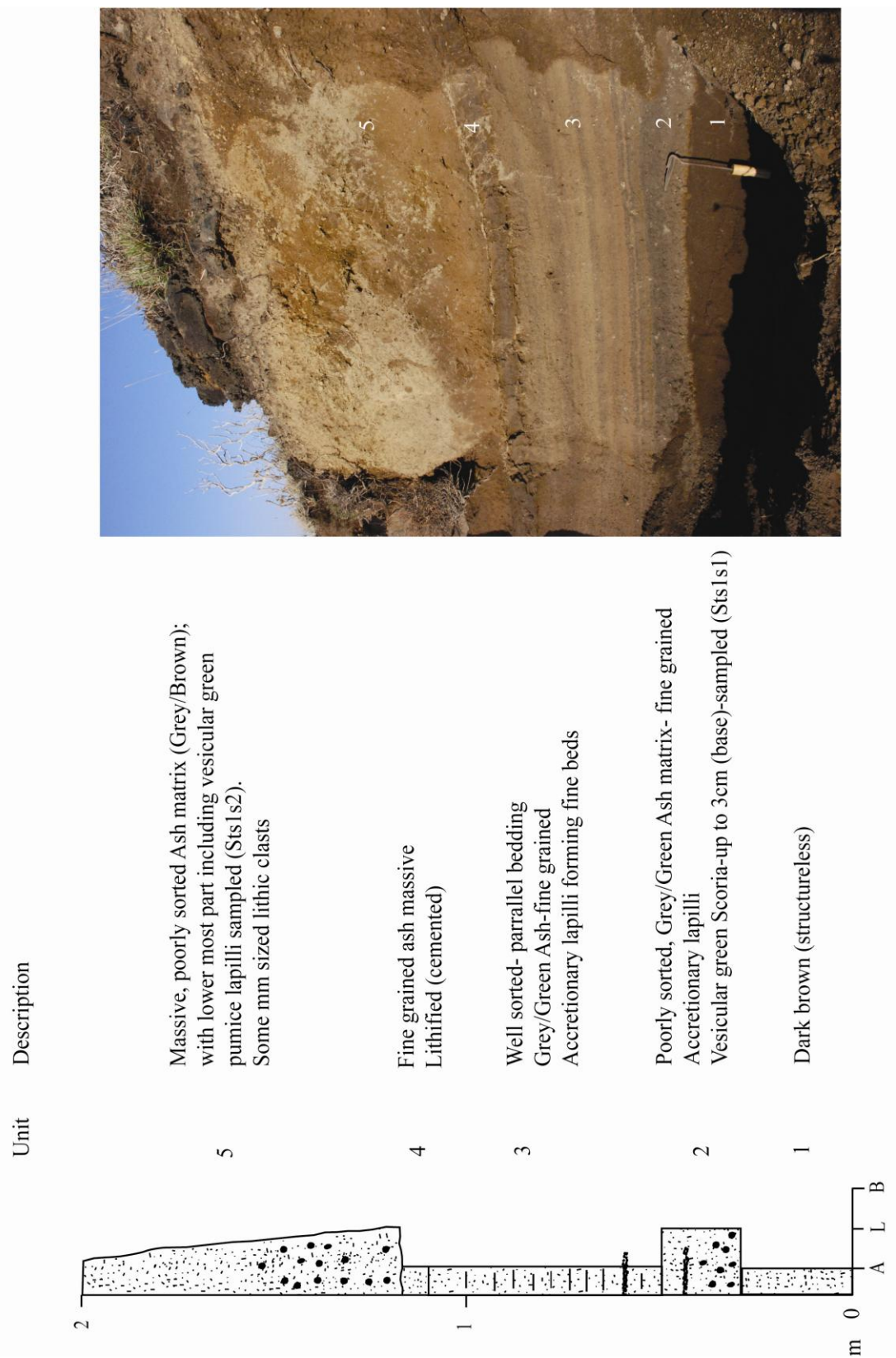
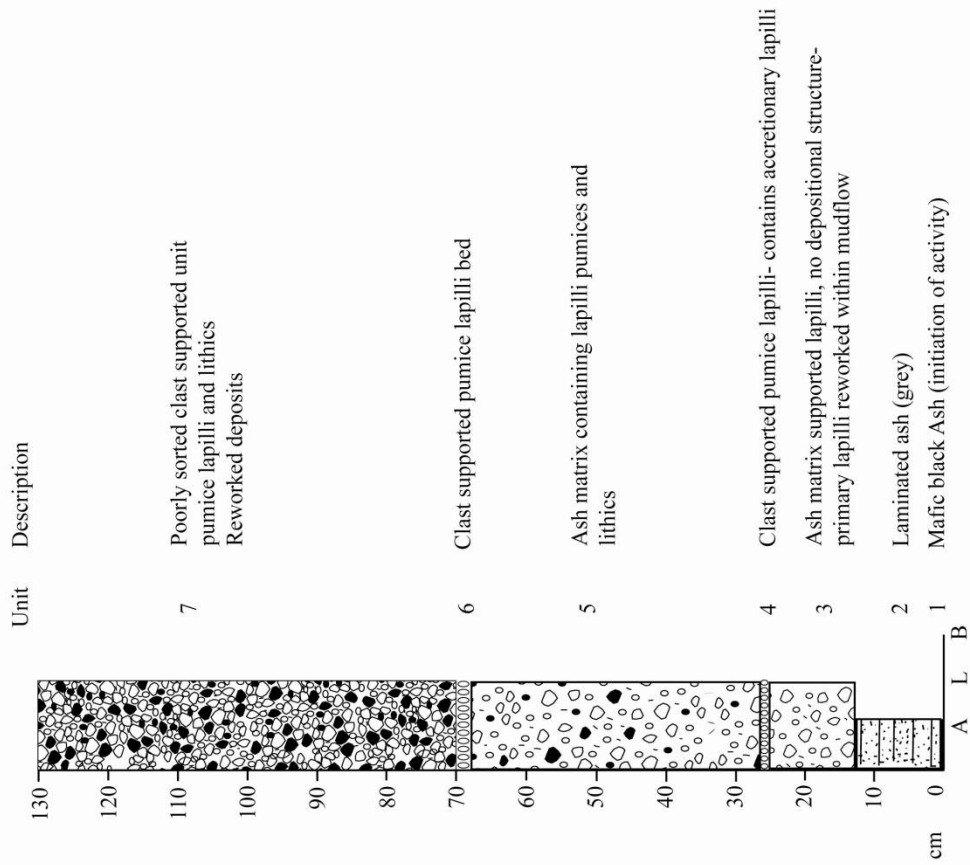
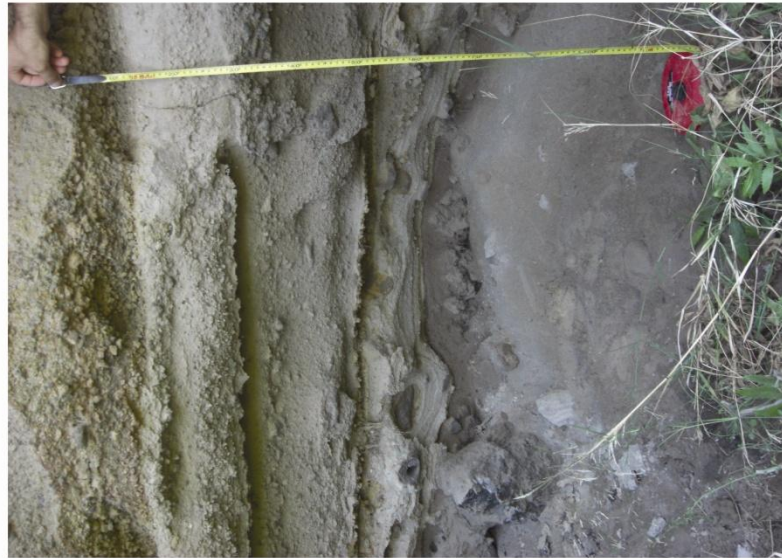


Figure 3.18: The sampled stratigraphy of the Secche di Lazzaro along the Semaforo northern Stromboli (See Table 3.5 for details).

Seeche Di Lazzaro, Stromboli- Nr COA



Above: Seven stratigraphic units of the Seeche Di Lazzaro pyroclastic unit. Units 4 and 6 are Primary lapilli fallout beds that have been sampled for geochemical analysis.

Figure 3.19: The sampled Seeche di Lazzaro stratigraphy outcropping near the Centre for advanced operations (COA) on Stromboli. (See Table 3.5 for details).

3.4. Results - Glass geochemistry

Representative major, minor and trace element data are presented in Tables 3.6-3.17. Glass compositions from the Aeolian Islands are highly variable in their major element affinities (Fig. 3.20). Calc-alkaline (CA), high potassium calc-alkaline (HKCA), shoshonitic and K-series glasses were all observed in the explosive products of the Aeolian Islands during the last 42 ka (Fig. 3.20). Glasses investigated on all islands display mantle normalised patterns that are dominated by an island arc signature, showing depletions in Nb and Ta and Ti. This is reflected in a dominant trough feature on the mantle normalised trace element diagrams (Fig. 3.21a-b).

3.4.1 Lipari

Proximal explosive deposits

Major and minor elements determined from Lipari pumices during the last 42 ka display the following variability; 67.9-76.8 wt.% SiO₂, 0.01-0.45 wt.% TiO₂, 12.1-16.6 wt.% Al₂O₃, 1-3.3 wt.% FeO; 0-0.46 wt.% MgO, 0.6-2.3 wt.% CaO, 2.8-4.6 wt. % Na₂O, 4.9-6.4 wt.% K₂O (Fig. 3.22). On the basis of glasses erupted from Lipari during this period they are classified as HKCA, ranging from trachytes to a dominant rhyolite composition (Fig. 3.20b). Trace element concentrations observed in these glasses range from 277-341 ppm Rb, 7-400 ppm Sr, 32-44 ppm Y, 114-183 ppm Zr, 29- 40ppm Nb, 3-361 ppm Ba, 31-58 ppm La, 34-55 ppm Th, 11-17 ppm U (Fig. 3.23). Glasses have pronounced anomalies at Sr, Ba and Eu most likely in response to K-feldspar fractionation (Fig. 3.21a).

3.4.1.1 Eruptive Cycle VII (P.del Perciato and Falcone Formations)

P.del Perciato formation

The basal white pumiceous deposits (unit 2) have very homogeneous major element concentrations (Table 3.6) with 76.2 ± 0.2 wt.% SiO₂, 0.1 ± 0.003 wt.% TiO₂, 12.5 ± 0.1 wt.% Al₂O₃, 1.4 ± 0.1 wt.% FeO, 0.1 ± 0.1 wt.% MgO, 0.7 ± 0.03 wt.% CaO, 3.2 ± 0.2 wt.% Na₂O, 5.7 ± 0.1 wt.% K₂O (Fig. 3.22). These glasses are classified as HKCA rhyolites (Fig. 3.20). The homogeneous nature of these pumices is also observed within the trace element concentrations, 315 ± 6 ppm Rb, 121 ± 2 ppm Zr, 34 ± 1 ppm Nb, 34 ± 1 ppm La, 39 ± 1 ppm Th (Fig. 3.23).

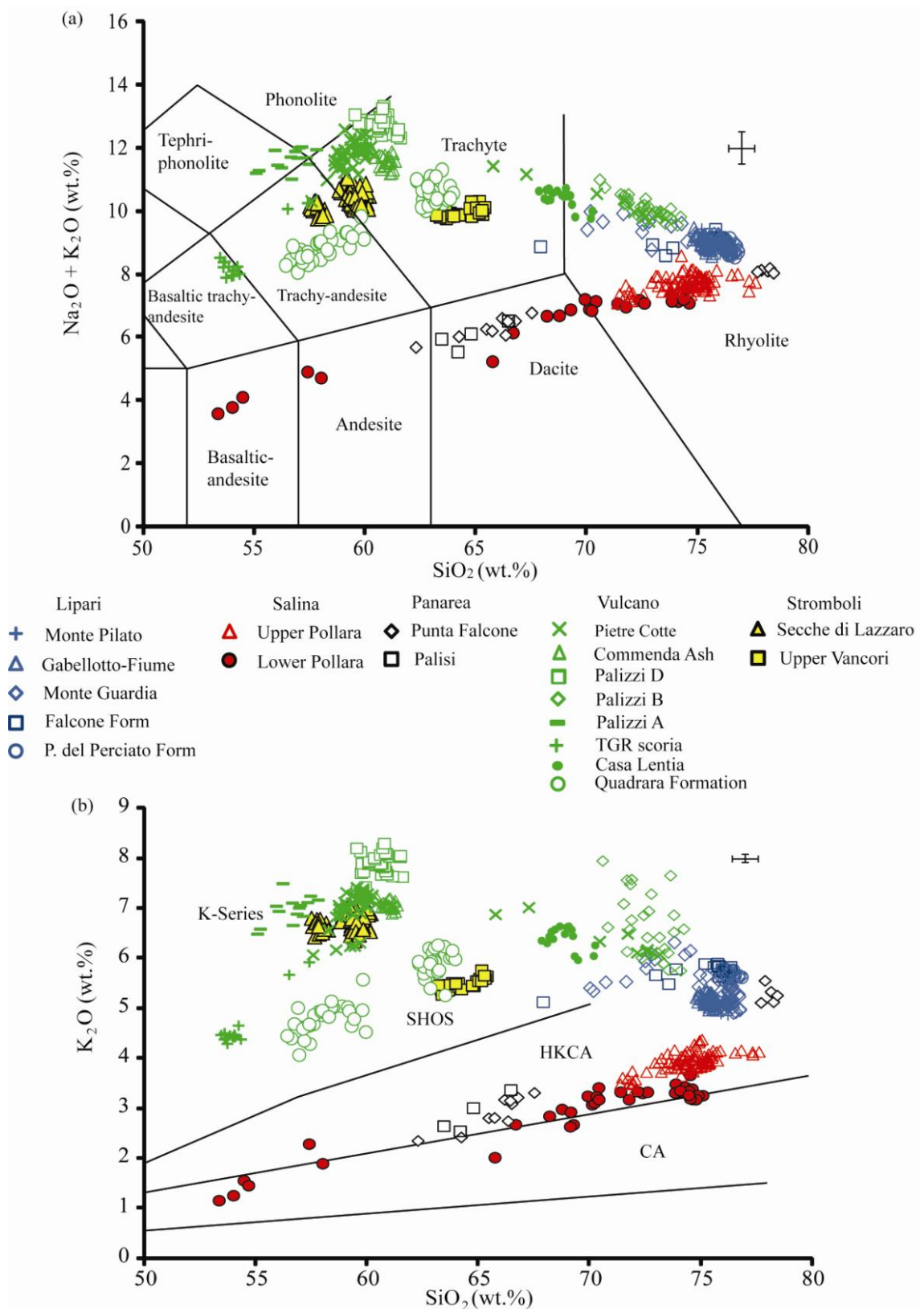


Figure 3.20: Major element variability and classification of Aeolian Islands glasses explosively produced during the last 42 ka. (a) Total alkalis diagram (Le Bas, 1986) and (b) SiO_2 vs. K_2O diagram (Peccerillo and Taylor, 1976). Errors given are 2 x standard deviation of repeat analyses of the StHs6-80G.

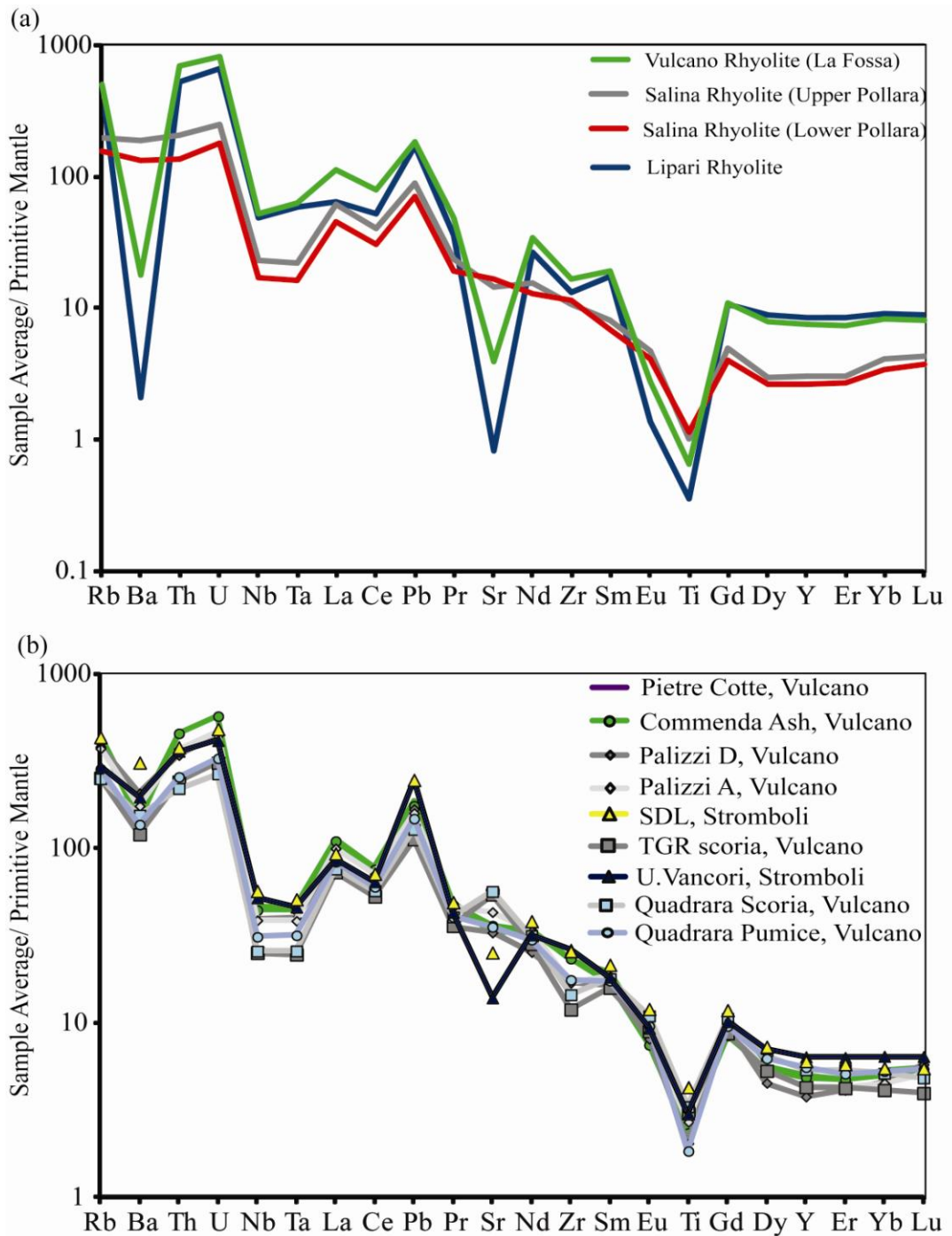


Figure 3.21: Multi-element diagrams normalised to Primitive Mantle (Sun and McDonough, 1989); (a) Average compositions of rhyolitic products of Lipari, Salina (Upper and Lower Pollara) and Vulcano (La Fossa; Palizzi B and Pietre Cotte). (b) Average compositions of explosively produced shoshonitic and K-series glasses produced on Vulcano and Stromboli.

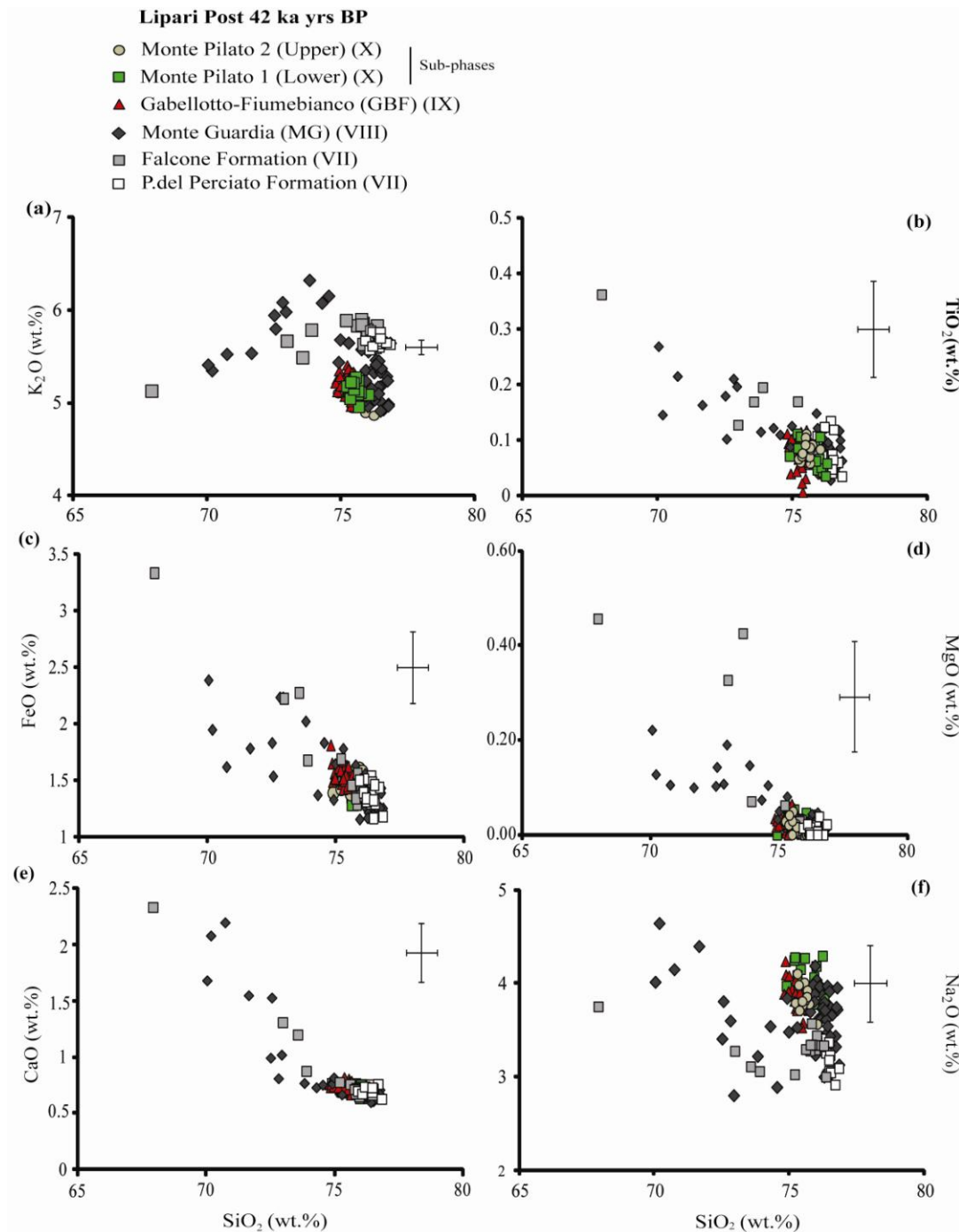


Figure 3.22: Major element bi-plots of the HKCA rhyolites produced on Lipari during the last 42 ka. Roman numerals refer to the eruptive cycles on the island following Gioncada et al., (2003). Error bars reflect two standard deviations of repeat analyses on the StHs/6-80-G standard glass.

Glasses are highly evolved ($Zr/Sr = 13.2 \pm 1$) and show LREE enrichment relative to the HREE ($Ce/Yb = 17 \pm 1$) (Fig. 3.24). Glasses display low concentrations of Sr (9.3 ± 1 ppm), Ba (3.7 ± 0.5 ppm) and a pronounced Eu anomaly ($Eu/Eu^*_N = 0.1$) (Fig. 3.21a) consistent with K-feldspar fractionation. Incompatible trace element ratios are consistent within these glasses ($Nb/Zr = 0.28 \pm 0.01$; $Nb/Th = 0.87 \pm 0.02$; $Zr/Th = 3.09$).

| Eruption Locality | P.dei Perciato formation S. Lipari n=15 | | | Falcone Formation S. Lipari n=15 | | | |
|--------------------------------------|---|--------------|---------------|--|--------------|---------------|---------------|
| | 1A pumice | 4A pumice | 15C pumice | 11C pumice | 7B pumice | 14C pumice | 15C pumice |
| Major (wt. %) | | | | | | | |
| SiO ₂ | 76.39 | 76.10 | 76.47 | 67.93 | 73.90 | 75.78 | 76.28 |
| TiO ₂ | 0.04 | 0.07 | 0.05 | 0.36 | 0.19 | 0.08 | 0.06 |
| Al ₂ O ₃ | 12.56 | 12.42 | 12.49 | 16.63 | 14.41 | 12.78 | 12.44 |
| FeOt | 1.53 | 1.51 | 1.32 | 3.33 | 1.68 | 1.34 | 1.50 |
| MnO | 0.00 | 0.06 | 0.06 | 0.08 | 0.03 | 0.09 | 0.05 |
| MgO | 0.01 | 0.01 | 0.00 | 0.46 | 0.07 | 0.03 | 0.01 |
| CaO | 0.69 | 0.69 | 0.73 | 2.33 | 0.88 | 0.72 | 0.72 |
| Na ₂ O | 3.01 | 3.36 | 3.18 | 3.75 | 3.06 | 3.34 | 3.33 |
| K ₂ O | 5.76 | 5.79 | 5.70 | 5.13 | 5.79 | 5.84 | 5.60 |
| Analytical Total | 95.66 | 94.77 | 94.97 | 96.52 | 94.93 | 94.92 | 95.34 |
| Na ₂ O + K ₂ O | 8.77 | 9.15 | 8.88 | 8.88 | 8.85 | 9.18 | 8.93 |
| K ₂ O/Na ₂ O | 1.91 | 1.72 | 1.79 | 1.37 | 1.89 | 1.75 | 1.68 |
| Trace Ppm | | | | | | | |
| Rb | 317 | 310 | 317 | | 296 | 315 | 327 |
| Sr | 9 | 8.6 | 8.4 | | 300 | 9.7 | 9.5 |
| Y | 39 | 38 | 39 | | 33.9 | 39 | 40 |
| Zr | 122 | 118 | 122 | | 130 | 122 | 118 |
| Nb | 34 | 34 | 34 | | 28.9 | 34 | 34 |
| Ba | 3.5 | 3.1 | 3.5 | | 361 | 5.1 | 3.7 |
| La | 35 | 34 | 34 | | 43 | 37 | 33 |
| Ce | 75 | 73 | 75 | | 91 | 80 | 75 |
| Pr | 8.2 | 8.2 | 8.4 | | 10.1 | 8.7 | 8.1 |
| Nd | 31 | 30 | 32 | | 43 | 35 | 33 |
| Sm | 7.2 | 6.7 | 7.6 | | 6.5 | 7.4 | 7.6 |
| Eu | 0.24 | 0.17 | 0.21 | | 0.60 | 0.19 | 0.20 |
| Gd | 6.4 | 6.9 | 5.7 | | 5.8 | 6.6 | 6.5 |
| Dy | 6.4 | 6.6 | 6.8 | | 5.4 | 6.4 | 6.6 |
| Er | 4.1 | 4.0 | 4.1 | | 3.2 | 3.9 | 4.3 |
| Yb | 4.4 | 4.3 | 4.3 | | 3.9 | 4.0 | 4.6 |
| Lu | 0.64 | 0.61 | 0.64 | | 0.55 | 0.59 | 0.71 |
| Ta | 2.2 | 2.3 | 2.2 | | 1.9 | 2.3 | 2.1 |
| Pb | 32 | 32 | 31 | | 31 | 32 | 30 |
| Th | 39 | 39 | 39 | | 34 | 39 | 38 |
| U | 13 | 13 | 13 | | 11 | 13 | 12 |

Table 3.6: Representative major, minor and trace element glass data for the pumices from the explosive deposits of cycle VII Lipari; P.del Perciato and Falcone Formations. Full data sets are available in appendix eII.

Falcone Formation

The mixed grey and white pumices of unit 4 (Fig. 3.6) have significant heterogeneity within their major and minor element concentrations (Table 3.6) ranging from 67.9-76.4 wt.% SiO₂, 1.3-3.3 wt.% FeO, 0.6-2.3 wt. % CaO, 3.0-3.8 wt.% Na₂O, 5.1-5.9 wt.%

K₂O. The glasses range from trachyte to rhyolite (Fig. 3.20). With increasing SiO₂ the following trends are observed, decreasing TiO₂, Al₂O₃, FeO, MgO, CaO, whilst Na₂O decreases until an inflection at ~ 72-74 wt. % where it increases to the values seen in the dominant white pumices (Fig. 3.22). K₂O increases with increasing SiO₂ wt. % (Fig. 3.22). Trace element concentrations reveal that these pumices are highly evolved (Zr/Sr = 11.3 ± 3.2) and are largely homogeneous with, 316 ± 9 ppm Rb, 38 ± 1 ppm Y, 121 ± 3 ppm Zr, 34 ± 2 ppm Nb, 37 ± 2 ppm La, 39 ± 1 ppm Th (Fig. 3.23). The dominant >75 wt.% SiO₂ rhyolites display low concentrations in Sr (11 ± 3 ppm), Ba (5 ± 1) and Eu (Eu/Eu*_N = 0.1). A glass composition associated with the lower silica rhyolites (< 75 wt. %) has increased Sr (300 ppm), Ba (360 ppm) and Eu (0.6 ppm), whilst also more elevated Zr (130 ppm) indicating that these elements are behaving compatibly as the glass compositions become more evolved.

3.4.1.2 Eruptive Cycle VIII

Monte Guardia

The Monte Guardia pumices reported (Table 3.7) have significant geochemical variability ranging from 70.0-76.8 wt.% SiO₂, 0.0-0.3 wt.% TiO₂, 12.1-15.9 wt.% Al₂O₃, 1.3-2.4 wt.% FeO, 0.0-0.2 wt. % MgO, 3.4-4.6 wt.% Na₂O, 4.9-6.3 wt.% K₂O (Fig. 3.22). The glasses all lie compositionally within the rhyolitic field and are HKCA (Fig. 3.20). The dominant white pumiceous deposits that are found throughout the stratigraphy (Fig. 3.8) are characterised by melt compositions with > 75 wt. % SiO₂. The grey pumices that decrease in abundance up stratigraphy are characterised by less evolved compositions with < 75wt. % SiO₂ (Fig. 3.25). The surge deposits recorded in units 4 and the final fallout of unit 5 (Fig. 3.8) are comprised solely of the most evolved components (Fig. 3.25). The following major element trends are observed throughout the entire suite, with increasing SiO₂ wt. % there is decreasing TiO₂, Al₂O₃, FeO, MgO and CaO. At 73-74 wt.% SiO₂ there is a pronounced inflection in Na₂O and K₂O, where the former increases and the later decreases (Fig. 3.22). Monte Guardia trace element concentrations have some significant variability (i.e., 114-146 ppm Zr; 30-35 ppm Nb and 34-43 ppm Th), whilst other incompatible elements are more homogenous 38 ± 1 ppm Y, 35 ± 1 ppm La, 76 ± 2 pm Ce (Fig. 3.23).

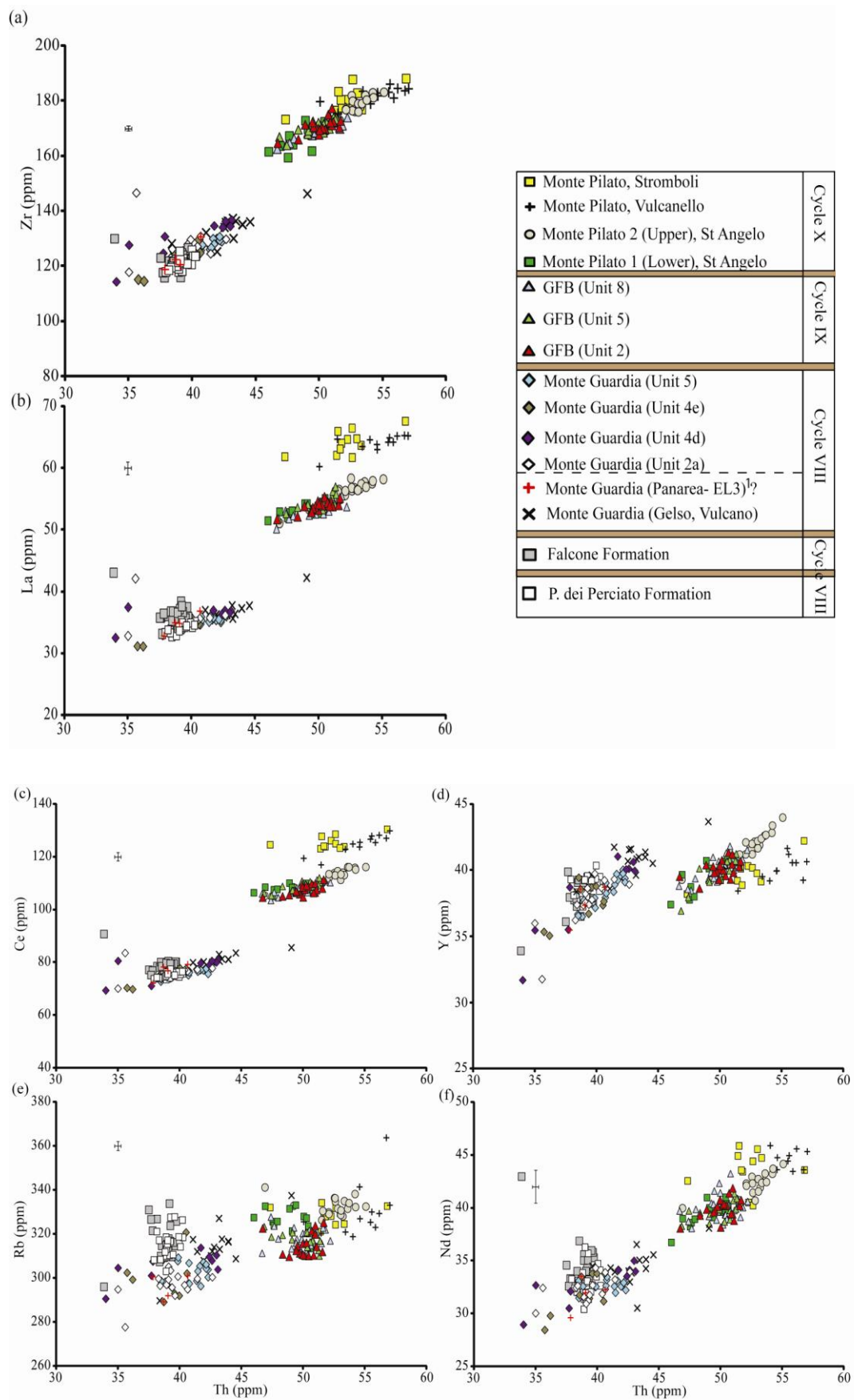


Figure 3.23: Trace element bi-plots showing the concentrations within the Lipari rhyolitic glasses erupted over the last 42 ka. Error bars given are 2 x standard deviation of repeat analyses of the StHs/80-G standard glass.

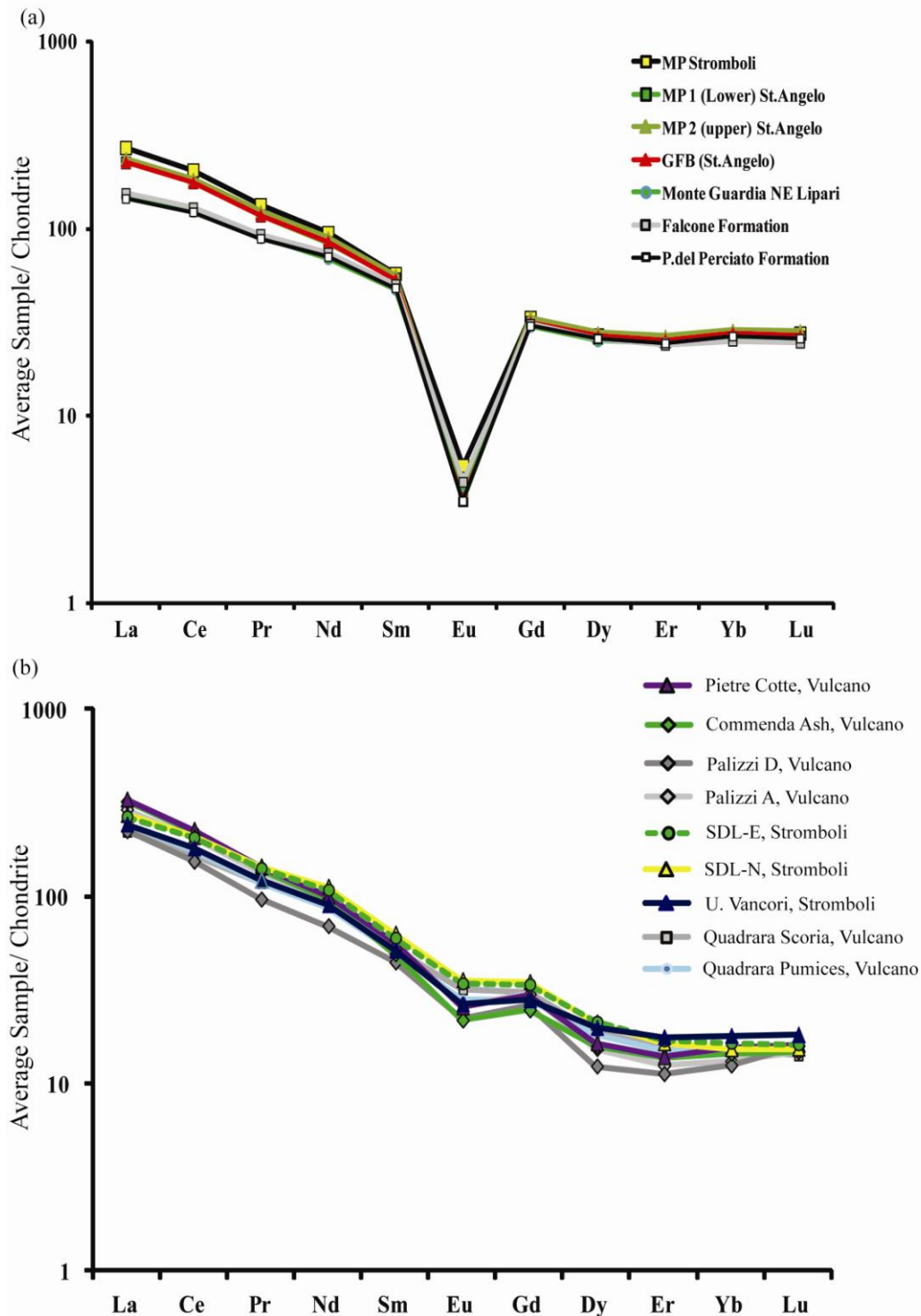


Figure 3.24: REE profiles normalised to Chondrite (Sun and McDonough, 1989); (a) REE profiles of the average glass compositions from the pumices of Lipari during the last 42 ka; (b) REE profiles of the average glass compositions of explosive erupted potassic products of Vulcano and Stromboli during the last 21 Ka.

| Eruption Locality | Monte Guardia NE, Lipari | | | | | |
|--------------------------------------|-----------------------------|--------------|--------------|-----------------|--------------|---------------|
| | Unit 2a n=15 | | | Unit 2d n=15 | | |
| Sample Material | 16D pumice | 1A pumice | 7B pumice | 7B pumice | 8B pumice | 13C pumice |
| Major (wt. %) | | | | | | |
| SiO ₂ | 72.82 | 75.29 | 76.77 | 74.98 | 72.56 | 75.96 |
| TiO ₂ | 0.21 | 0.07 | 0.10 | 0.13 | 0.10 | 0.10 |
| Al ₂ O ₃ | 14.05 | 12.83 | 12.23 | 13.18 | 14.97 | 12.68 |
| FeO _t | 2.23 | 1.78 | 1.43 | 1.64 | 1.53 | 1.43 |
| MnO | 0.09 | 0.11 | 0.09 | 0.04 | 0.03 | 0.09 |
| MgO | 0.11 | 0.08 | 0.01 | 0.05 | 0.14 | 0.02 |
| CaO | 0.81 | 0.67 | 0.66 | 0.82 | 1.53 | 0.67 |
| Na ₂ O | 3.60 | 3.53 | 3.72 | 3.48 | 3.81 | 3.23 |
| K ₂ O | 6.08 | 5.65 | 4.99 | 5.68 | 5.80 | 5.81 |
| Analytical Total | 94.99 | 94.81 | 96.29 | 95.79 | 95.88 | 95.91 |
| Na ₂ O + K ₂ O | 9.69 | 9.18 | 8.71 | 9.16 | 9.61 | 9.05 |
| K ₂ O/Na ₂ O | 1.69 | 1.60 | 1.34 | 1.63 | 1.52 | 1.80 |
| Trace ppm | | | | | | |
| Ti | 1174 | 469 | 429 | 529 | 691 | 414 |
| Rb | 278 | 295 | 296 | 291 | 305 | 307 |
| Sr | 400.1 | 15.6 | 7.6 | 94.7 | 90.8 | 7.6 |
| Y | 32 | 36 | 37 | 32 | 35 | 39 |
| Zr | 147 | 118 | 125 | 114 | 128 | 131 |
| Nb | 31 | 31 | 33 | 30 | 31 | 34 |
| Ba | 280 | 15.3 | 4.0 | 93 | 111 | 4.2 |
| La | 42 | 33 | 34 | 32 | 37 | 36 |
| Ce | 83 | 70 | 75 | 69 | 80 | 76 |
| Pr | 8.7 | 7.7 | 8.5 | 7.4 | 8.7 | 8.5 |
| Nd | 32 | 30 | 32 | 29 | 33 | 32 |
| Sm | 6.4 | 7.0 | 7.0 | 6.5 | 6.8 | 7.3 |
| Eu | 0.54 | 0.13 | 0.12 | 0.34 | 0.32 | 0.21 |
| Gd | 5.4 | 5.2 | 5.9 | 5.2 | 5.8 | 6.9 |
| Dy | 5.2 | 5.9 | 6.4 | 5.2 | 5.7 | 6.3 |
| Er | 3.4 | 3.7 | 3.9 | 3.2 | 3.6 | 3.8 |
| Yb | 3.6 | 3.8 | 4.3 | 3.5 | 3.6 | 3.8 |
| Lu | 0.56 | 0.61 | 0.60 | 0.57 | 0.57 | 0.64 |
| Ta | 1.9 | 2.0 | 2.3 | 2.1 | 2.2 | 2.2 |
| Pb | 29 | 26 | 30 | 31 | 27 | 36 |
| Th | 36 | 35 | 39 | 34 | 35 | 38 |
| U | 11 | 11 | 13 | 11 | 11 | 13 |

Table 3.7: Representative major, minor and trace element data for the pumices of the Monte Guardia eruption of Lipari. Full data set available in appendix eII.

The glasses range from moderately to highly evolved ($Zr/Sr = 0.4- 17$) and display significant LREE enrichment relative to the HREE ($Ce/Yb = 18 \pm 2$) (Fig. 3.21a). The white pumices (> 75 wt. % SiO_2) display low concentrations of Sr (8.8 ± 2 ppm), Ba (6 ± 5 ppm), Eu ($Eu/Eu^*_N = 0.1$) (Fig. 3.21). The grey pumices (< 75 wt. % SiO_2) display less elevated incompatible trace element concentrations and more elevated Sr (≤ 400 ppm), Ba (≤ 280 ppm) and Eu^*_N (≤ 0.3), Zr (≤ 146 ppm) indicating that these elements may have behaved compatibly. Incompatible trace element ratios are constant within the Monte Guardia glasses ($Nb/Th = 0.84 \pm 0.03$; $Ta/Th = 0.058 \pm 0.002$).

| Eruption Locality | Monte Guardia NE, Lipari | | | | | |
|--------------------------------------|-----------------------------|--------------|---------------|----------------|--------------|---------------|
| | Unit 4 n=15 | | | Unit 5 n=15 | | |
| Sample Material | 8B pumice | 9B pumice | 15C pumice | 1A obsidian | 8B pumice | 13C pumice |
| Major (wt. %) | | | | | | |
| SiO ₂ | 76.70 | 75.92 | 76.24 | 76.45 | 75.89 | 76.23 |
| TiO ₂ | 0.05 | 0.10 | 0.07 | 0.08 | 0.15 | 0.09 |
| Al ₂ O ₃ | 12.57 | 12.76 | 12.74 | 12.63 | 12.89 | 12.66 |
| FeO _t | 1.26 | 1.43 | 1.17 | 1.25 | 1.37 | 1.43 |
| MnO | 0.02 | 0.04 | 0.13 | 0.03 | 0.02 | 0.10 |
| MgO | 0.02 | 0.01 | 0.01 | 0.04 | 0.02 | 0.01 |
| CaO | 0.65 | 0.70 | 0.65 | 0.72 | 0.65 | 0.65 |
| Na ₂ O | 3.44 | 3.81 | 3.67 | 3.77 | 3.99 | 3.74 |
| K ₂ O | 5.29 | 5.24 | 5.33 | 5.02 | 5.02 | 5.08 |
| Analytical Total | 95.59 | 96.27 | 96.27 | 98.91 | 94.73 | 95.07 |
| Na ₂ O + K ₂ O | 8.72 | 9.05 | 9.00 | 8.79 | 9.01 | 8.82 |
| K ₂ O/Na ₂ O | 1.54 | 1.38 | 1.45 | 1.33 | 1.26 | 1.36 |
| Trace ppm | | | | | | |
| Rb | 296 | 302 | 293 | 307 | 295 | 296 |
| Sr | 7.9 | 8.4 | 9.4 | 7.8 | 7.8 | 9.2 |
| Y | 37 | 35 | 39 | 40 | 39 | 39 |
| Zr | 123 | 115 | 123 | 130 | 126 | 128 |
| Nb | 34 | 32 | 33 | 34 | 33 | 34 |
| Ba | 3.9 | 4.6 | 3.6 | 3.8 | 4.2 | 4.9 |
| La | 34 | 31 | 36 | 35 | 35 | 36 |
| Ce | 74 | 70 | 78 | 77 | 76 | 77 |
| Pr | 8.4 | 7.7 | 8.4 | 8.7 | 8.3 | 8.7 |
| Nd | 31 | 28 | 34 | 33 | 32 | 34 |
| Sm | 6.6 | 6.6 | 6.9 | 7.3 | 7.5 | 8.1 |
| Eu | < LOD | 0.27 | < LOD | 0.14 | 0.12 | < LOD |
| Gd | 6.1 | 5.8 | 6.6 | 6.0 | 5.8 | 5.5 |
| Dy | 6.2 | 5.7 | 6.8 | 6.6 | 6.7 | 6.8 |
| Er | 3.9 | 3.7 | 4.2 | 4.3 | 4.0 | 4.0 |
| Yb | 4.6 | 3.5 | 4.5 | 4.7 | 4.4 | 4.4 |
| Lu | 0.59 | 0.47 | 0.64 | 0.62 | 0.67 | 0.68 |
| Ta | 2.4 | 2.0 | 2.4 | 2.4 | 2.4 | 2.3 |
| Pb | 28 | 30 | 29 | 30 | 30 | 30 |
| Th | 39 | 36 | 40 | 42 | 41 | 42 |
| U | 13 | 12 | 13 | 13 | 13 | 13 |

Table 3.7: Continued.

3.4.1.3 Cycle IX

Gabelotto-Fiume Bianco

White pumices from units 2, 5 and 8 (Fig. 3.9) are homogeneous shown by the absence of major element variation throughout the stratigraphy with 75.3 ± 0.2 wt.% SiO₂, 13.2 ± 0.2 wt.% Al₂O₃, 1.5 ± 0.1 wt.% FeO, 0.75 ± 0.03 wt.% CaO, 3.8 ± 0.2 wt.% Na₂O, 5.2 ± 0.1 wt.% K₂O (Fig. 3.22; Table 3.8). The glasses are classified as HKCA rhyolites (Fig. 3.20). The pumices display homogeneous trace element concentrations, 316 ± 5 ppm Rb, 40 ± 1 ppm Y, 170 ± 3 ppm Zr, 37 ± 1 ppm Nb, 54 ± 1 ppm La, 108 ± 2 ppm, 50 ± 1 ppm Th (Fig. 3.23). The glasses are highly evolved (Zr/Sr = 10.8 ± 0.4) and display significant LREE enrichment relative to the HREE (Ce/Yb = 23 ± 1). The pumices display low concentrations of Sr (16 ± 1 ppm), Ba (15 ± 1 ppm), Eu (Eu/Eu*_N = 0.1). Trace element ratios within these glasses are constant (Nb/Zr = 0.22; Nb/Th = 0.74; Zr/Th = 3.5)

3.4.1.4 Cycle X

Monte Pilato

Monte Pilato sub-phase 1 (lower):

The lower fall, white pumices, of unit 2 (Fig. 3.10) are very homogeneous displaying minimal major element variation, 75.7 ± 0.4 wt.% SiO₂, 12.8 ± 0.3 wt.% Al₂O₃, 1.5 ± 0.1 wt.% FeO, 0.7 ± 0.1 wt.% CaO, 4.1 ± 0.2 wt.% Na₂O, 5.1 ± 0.1 wt.% K₂O (Fig. 3.22; Table 3.9). These glasses are classified as HKCA rhyolites (Fig. 3.8). Trace element concentrations are homogeneous 324 ± 6 ppm, 40 ± 1 ppm Y, 168 ± 5 ppm Zr, 36 ± 1 ppm Nb, 53 ± 1 ppm La, 108 ± 2 Ce, 49 ± 2 ppm Th (Fig. 3.23). The glasses are highly evolved (Zr/Sr = 10.6 ± 0.3) and display significant LREE enrichment relative to the HREE (Ce/Yb = 24 ± 1). The pumices have low concentrations of Sr (16 ± 1 ppm), Ba (15 ± 1 ppm), Eu (Eu/Eu*_N = 0.1). The glasses have constant HFSE/Th ratios (Nb/Th = 0.74; Zr/Th = 3.4).

Monte Pilato sub-phase 2 (upper):

The upper fall, white pumices, of unit 3b (Fig. 3.10) are very homogeneous displaying minimal major element variation, 75.5 ± 0.2 wt.% SiO₂, 13.1 ± 0.2 wt.% Al₂O₃, 1.5 ± 0.2 wt.% FeO, 0.8 ± 0.1 wt.% CaO, 3.9 ± 0.1 wt.% Na₂O and 5.1 ± 0.1 wt.% K₂O (Fig. 3.22). These glasses are classified as HKCA rhyolites (Fig. 3.20). Trace element concentrations are particularly homogeneous 332 ± 4 ppm, 41 ± 1 ppm Y, 177 ± 5 ppm Zr, 39 ± 1 ppm Nb, 56 ± 2 ppm La, 112 ± 3 ppm Ce, 53 ± 2 ppm Th (Fig. 3.23). The glasses are highly evolved (Zr/Sr = 10.9 ± 1) and display significant LREE enrichment relative to the HREE (Ce/Yb = 23 ± 1). The pumices display low concentrations of Sr (16 ± 1), Ba (15 ± 1), Eu (Eu/Eu*_N = 0.1). Glasses show incompatible trace element ratios that remain constant (Nb/Zr = 0.22; Nb/Th = 0.73; Zr/Th = 3.4).

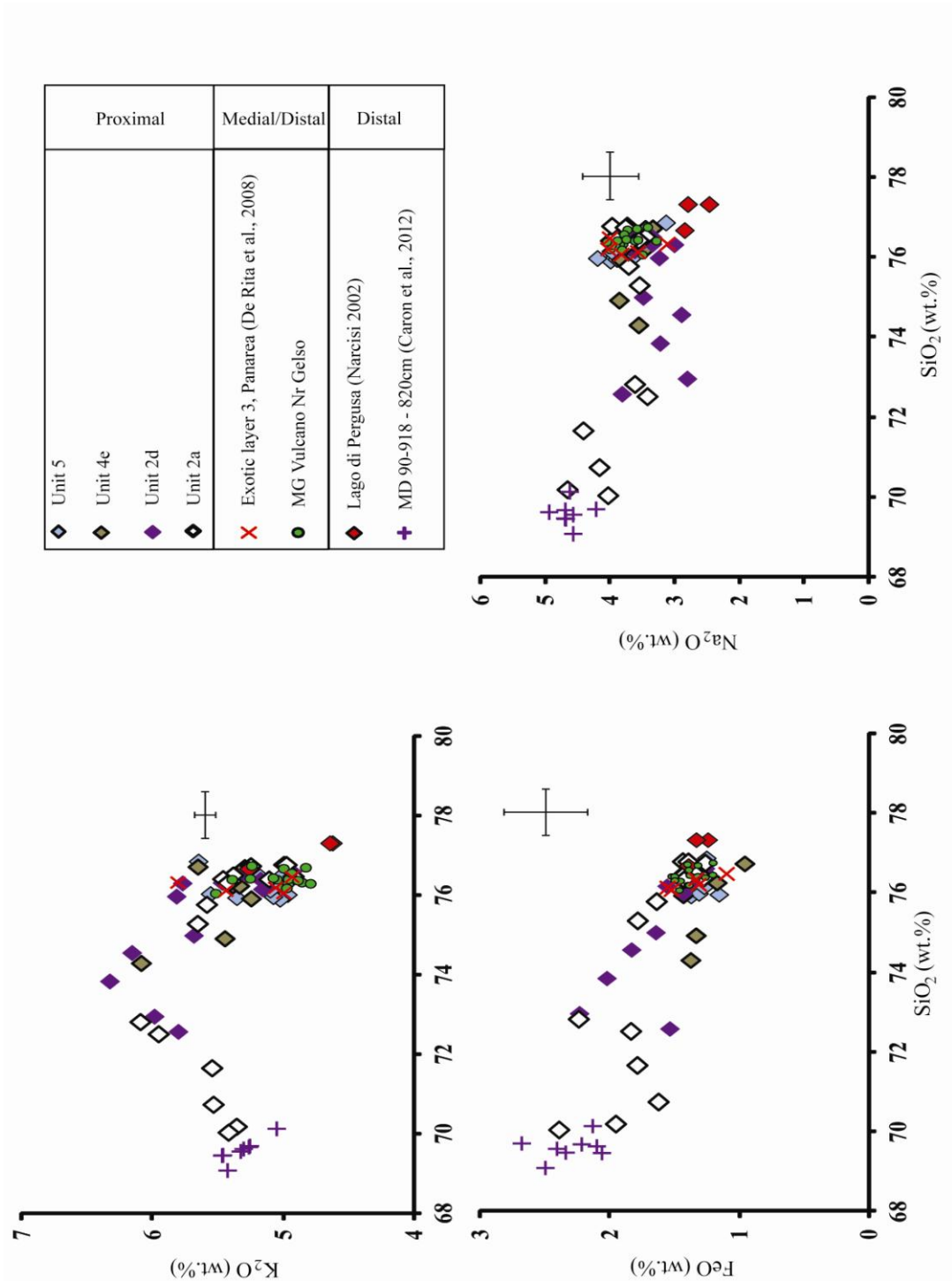


Figure 3.25: Major element bi-plots displaying the stratigraphic variability of the Monte Guardia glasses sampled from NE Lipari. Also shown are the glass compositions of MD 90 918 - 820 cm from the northern Ionian Sea (Caron et al., 2012), MG pumices from a medial distal locality on Vulcano; distal ash from Drauto (EL3; De Rita et al., 2008) Panarea and Lago di Pergusa, Sicily (Narcisi 2002). Errors given are 2 x stand deviation of repeat analyses of the StHs/6-80-G.

| Eruption Locality Unit Sample Material | Gabelotto-Fiume Bianco (GFB) Lipari, St Angelo | | | | | |
|--|---|---------------|--------------|--------------|--------------|---------------|
| | Unit 2 | | Unit 5 | | Unit 8 | |
| | 8B pumice | 11C pumice | 3A pumice | 7B pumice | 8B pumice | 11C pumice |
| Major (wt. %) | | | | | | |
| SiO ₂ | 75.38 | 75.57 | 75.18 | 75.64 | 74.80 | 75.37 |
| TiO ₂ | 0.07 | 0.07 | 0.09 | 0.06 | 0.11 | 0.08 |
| Al ₂ O ₃ | 13.28 | 12.96 | 13.37 | 13.05 | 13.37 | 13.18 |
| FeOt | 1.65 | 1.57 | 1.59 | 1.54 | 1.81 | 1.63 |
| MnO | 0.18 | 0.10 | 0.06 | 0.11 | 0.01 | 0.03 |
| MgO | 0.03 | 0.02 | 0.03 | 0.04 | 0.03 | 0.03 |
| CaO | 0.72 | 0.78 | 0.75 | 0.67 | 0.76 | 0.72 |
| Na ₂ O | 3.67 | 3.84 | 3.81 | 3.75 | 3.89 | 3.76 |
| K ₂ O | 5.01 | 5.11 | 5.12 | 5.15 | 5.21 | 5.20 |
| Analytical Total | 98.01 | 99.76 | 100.63 | 99.63 | 97.24 | 97.84 |
| Na ₂ O + K ₂ O | 8.68 | 8.94 | 8.93 | 8.90 | 9.10 | 8.96 |
| K ₂ O/Na ₂ O | 1.37 | 1.33 | 1.34 | 1.37 | 1.34 | 1.38 |
| Trace ppm | | | | | | |
| Rb | 322 | 320 | 317 | 317 | 311 | 328 |
| Sr | 16.4 | 16.3 | 16.4 | 16.5 | 14.8 | 15.4 |
| Y | 40 | 40 | 41 | 41 | 40 | 39 |
| Zr | 165 | 171 | 170 | 173 | 169 | 164 |
| Nb | 36 | 36 | 37 | 36 | 36 | 37 |
| Ba | 14.7 | 14.6 | 15.3 | 15.8 | 14.7 | 14.7 |
| La | 52 | 55 | 54 | 56 | 53 | 53 |
| Ce | 104 | 106 | 109 | 110 | 106 | 103 |
| Pr | 10.6 | 11.2 | 11.6 | 11.2 | 11.0 | 11.1 |
| Nd | 38 | 39 | 40 | 41 | 39 | 39 |
| Sm | 8.3 | 8.0 | 9.0 | 8.4 | 7.7 | 7.5 |
| Eu | 0.21 | 0.16 | 0.19 | 0.23 | 0.24 | <LOD |
| Gd | 5.9 | 6.3 | 6.5 | 6.1 | 6.2 | 6.6 |
| Dy | 6.8 | 6.8 | 7.1 | 6.8 | 7.0 | 6.5 |
| Er | 4.1 | 4.3 | 4.3 | 4.4 | 4.3 | 3.9 |
| Yb | 4.4 | 4.8 | 4.5 | 4.9 | 4.8 | 4.5 |
| Lu | 0.65 | 0.68 | 0.72 | 0.67 | 0.68 | 0.67 |
| Ta | 2.3 | 2.5 | 2.5 | 2.5 | 2.6 | 2.3 |
| Pb | 31 | 32 | 30 | 32 | 31 | 36 |
| Th | 47 | 51 | 51 | 51 | 50 | 47 |
| U | 15 | 15 | 15 | 15 | 15 | 15 |

Table 3.8: Representative major, minor and trace element glasses data for the Gabelotto-Fiume Bianco eruption of Lipari. Full data sets are available in appendix eII.

| Eruption Locality Unit | Lower M. Pilato Monte St. Angelo, Lipari | | Upper M. Pilato Lipari | | White Ash Vulcanello | Micro-pumice Stromboli |
|--------------------------------------|---|---------------|---------------------------|--------------|-------------------------|---------------------------|
| | Unit 2 n=15 | | Unit 3b n=15 | | n=15 | n=16 |
| | 7B pumice | 11C pumice | 2A pumice | 8B pumice | 10C ash | 2A pumice |
| Sample Material | | | | | | |
| Major (wt. %) | | | | | | |
| SiO ₂ | 75.41 | 76.29 | 75.30 | 75.64 | 74.96 | 74.94 |
| TiO ₂ | 0.07 | 0.06 | 0.06 | 0.07 | 0.07 | 0.04 |
| Al ₂ O ₃ | 12.97 | 12.54 | 12.93 | 13.12 | 13.04 | 13.30 |
| FeO _t | 1.55 | 1.41 | 1.61 | 1.36 | 1.75 | 1.50 |
| MnO | 0.11 | 0.06 | 0.08 | 0.08 | 0.06 | 0.13 |
| MgO | 0.05 | 0.04 | 0.02 | 0.02 | 0.03 | 0.04 |
| CaO | 0.74 | 0.74 | 0.77 | 0.75 | 0.80 | 0.73 |
| Na ₂ O | 4.15 | 3.83 | 4.11 | 3.87 | 4.29 | 4.20 |
| K ₂ O | 4.95 | 5.04 | 5.13 | 5.10 | 4.99 | 5.12 |
| Analytical Total | 96.26 | 95.05 | 99.26 | 96.45 | 97.21 | 99.24 |
| Na ₂ O + K ₂ O | 9.10 | 8.87 | 9.23 | 8.97 | 9.28 | 9.33 |
| K ₂ O/Na ₂ O | 1.19 | 1.31 | 1.25 | 1.32 | 1.16 | 1.22 |
| Trace | | | | | | |
| <i>ppm</i> | | | | | | |
| Rb | 328 | 327 | 330 | 328 | 323 | 321 |
| Sr | 16.3 | 15.6 | 16.6 | 16.9 | 17.6 | 16.9 |
| Y | 39 | 40 | 41 | 42 | 41 | 39 |
| Zr | 171 | 170 | 177 | 178 | 181 | 176 |
| Nb | 36 | 36 | 38 | 39 | 39 | 37 |
| Ba | 15.2 | 16.1 | 16.2 | 16.0 | 18.5 | 17.2 |
| La | 53 | 55 | 56 | 57 | 64 | 62 |
| Ce | 108 | 110 | 112 | 114 | 125 | 123 |
| Pr | 11.3 | 11.5 | 12.2 | 12.2 | 12.6 | 12.2 |
| Nd | 40 | 40 | 42 | 42 | 43 | 43 |
| Sm | 8.4 | 8.3 | 8.3 | 8.9 | 10.3 | 8.9 |
| Eu | 0.19 | 0.22 | 0.23 | 0.26 | 0.52 | 0.30 |
| Gd | 6.8 | 6.5 | 6.5 | 6.7 | 7.2 | 6.7 |
| Dy | 6.7 | 6.6 | 7.1 | 7.1 | 6.3 | 6.6 |
| Er | 4.0 | 4.2 | 4.5 | 4.3 | 4.2 | 4.0 |
| Yb | 4.6 | 4.7 | 5.0 | 5.2 | 4.8 | 4.8 |
| Lu | 0.67 | 0.68 | 0.68 | 0.73 | 0.74 | 0.65 |
| Ta | 2.4 | 2.6 | 2.6 | 2.7 | 2.6 | 2.3 |
| Pb | 31 | 36 | 33 | 34 | 33 | 33 |
| Th | 50 | 50 | 52 | 53 | 56 | 51 |
| U | 15 | 16 | 16 | 16 | 17 | 16 |

Table 3.9: Representative major, minor and trace element data for the Monte Pilato explosive eruption of Lipari. Full data sets are available in appendix eII.

3.4.2 Salina

3.4.2.1 Lower Pollara

Valdichiesa

Compositions range in SiO₂ from 54.7 wt.% (*whole rock*) in the crystalline scoria to 75.1 wt.% in the pumices (Table 3.10). There is SiO₂ variation between the grey pumices (69.1-72.2 wt.%) and the white pumices (74.3-75.1 wt.%). The Lower Pollara fall is silica saturated and straddles the CA/HKCA transitional boundary and appears largely bimodal; (1) basaltic-andesitic scoria and (2) dacite/rhyolite pumices with evidence of mingling (Fig. 3.20) There is a negative relationship between SiO₂ and FeO, TiO₂, Al₂O₃, CaO, MnO; whilst Na₂O and K₂O increase with SiO₂ (Fig. 3.26).

The composition of basaltic-andesitic scoria from unit 3 (Fig. 3.11) was determined by whole rock analysis (ICP-MS fusions). The porphyritic scoria were so crystalline, that the glassy areas were < 5µm and too small for meaningful LA-ICP-MS analysis. This mafic scoria displayed low levels of evolution (Zr/Sr = 0.09) with low concentrations of incompatible trace elements (Fig. 3.27).

Only the white pumices were successfully analysed from unit 4 (Fig. 3.11), due to the highly vesicular nature of the grey pumices the glassy areas were too small for meaningful LA-ICP-MS analysis. The rhyolitic, white pumices display considerably greater evolution than the scoria with Zr/Sr = 0.5 ± 0.01. Owing to low concentrations the MREE and HREE, these elements were below the limit of detection in these pumices. The one remaining pumice is LREE enriched relative to HREE (La/Yb = 19.5). Trace element concentrations in the white pumices observed at Valdichiesa show limited variation with 95-98 ppm Rb, 282-307 ppm Sr, 10-11 ppm Y, 128-142 ppm Zr, 12-14 ppm Nb, 932-1005 ppm Ba, 30-34 ppm La, 48-51 ppm Ce and 11-12 ppm Th (Fig. 3.27). HFSE/Th ratios are constant within the white pumices (Nb/Th = 1.16 ± 0.07, Zr/Th = 11.6 ± 0.8).

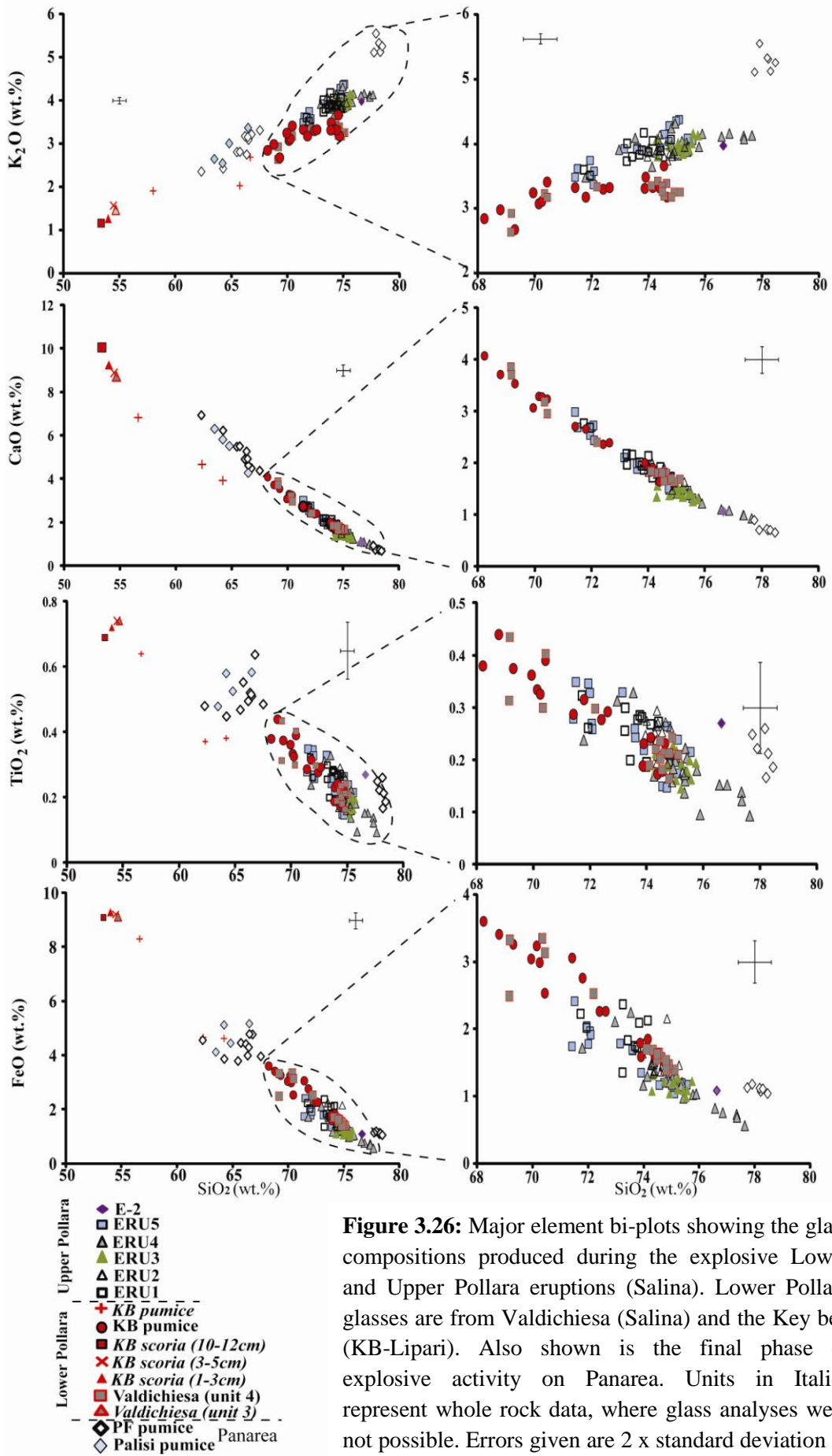


Figure 3.26: Major element bi-plots showing the glass compositions produced during the explosive Lower and Upper Pollara eruptions (Salina). Lower Pollara glasses are from Valdichiesa (Salina) and the Key bed (KB-Lipari). Also shown is the final phase of explosive activity on Panarea. Units in *Italics* represent whole rock data, where glass analyses were not possible. Errors given are 2 x standard deviation of repeat analyses of the StHs/6-80G

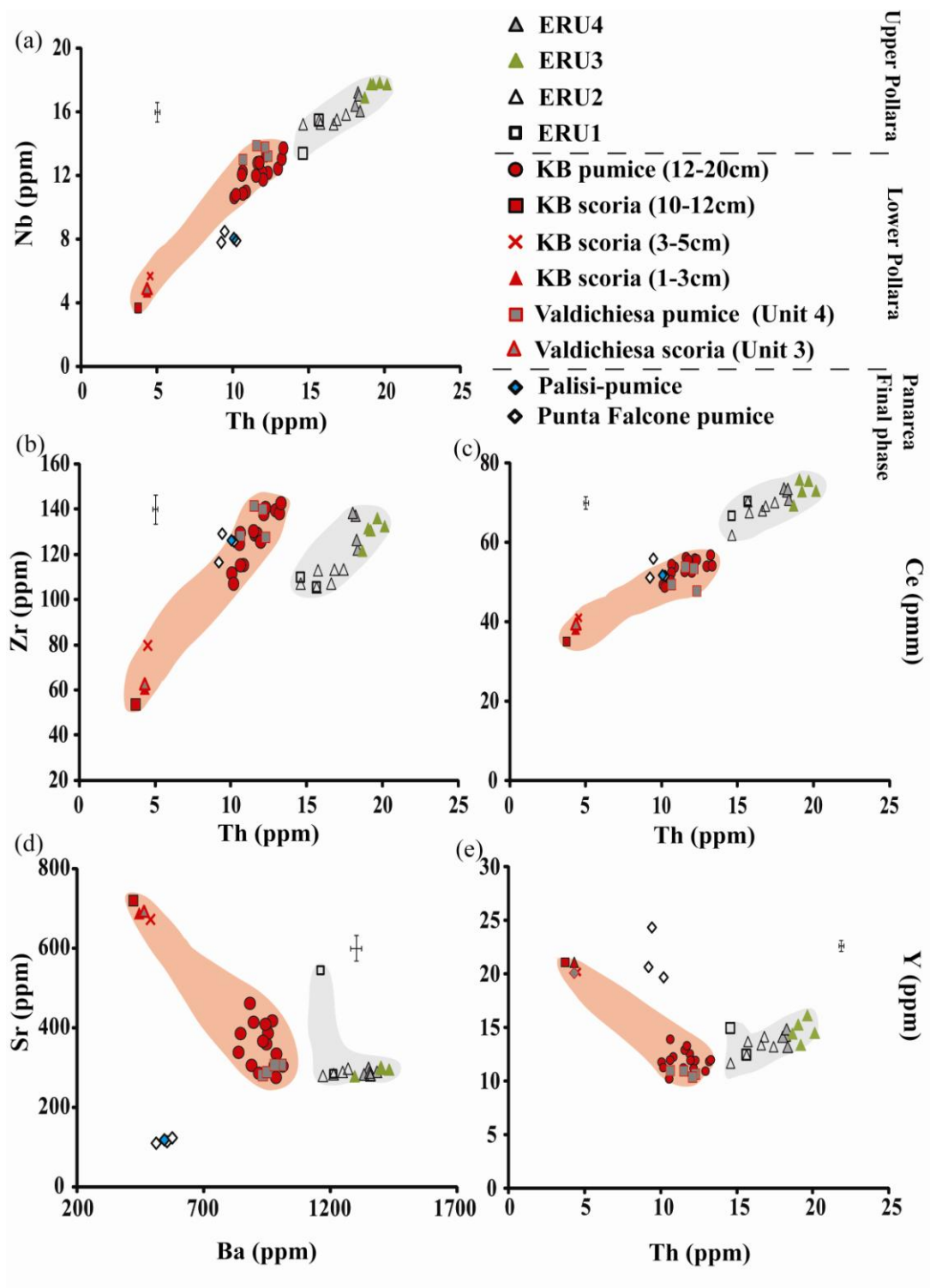


Figure 3.27: Trace element bi-plots displaying concentrations observed in the glasses of the Lower Pollara and Upper Pollara pumices, Salina, whilst those observed in the final phase of explosive activity on Panarea. Error bars given are two x standard deviation of repeat analyses of StHs/6-80G standard glass.

‘Key bed’, Lipari

Compositions range in SiO₂ from 53.4 wt.% in the crystalline scoria to 74.6 wt.% in the white pumices (Table 3.10). Grey pumices typically range in SiO₂ between 69-72 wt.%.

This LP fall is silica saturated and straddles the CA/HKCA transitional boundary and appears largely bimodal; basaltic-andesitic scoria and dacite/rhyolite pumices in which mingling is observed (Fig. 3.20). There is a negative relationship between SiO₂ and FeO, TiO₂, Al₂O₃, CaO, MnO; whilst Na₂O and K₂O increase with increasing SiO₂ (Fig. 3.26).

The basaltic-andesitic (53-54 wt.% SiO₂) scoria contained minor glass, but again in the porphyritic scoria the glass areas were too small for meaningful LA-ICP-MS analysis. Therefore trace element compositions were determined for three whole rocks samples by solution ICP-MS (1-3 cm; 5-8 cm and 10-12 cm), where systematic sampling allowed us to assess any stratigraphic heterogeneity. This mafic component displays low levels of evolution (Zr/Sr = 0.09 ± 0.02) and overall are relatively restricted in their compositional range as illustrated by 673-720 ppm Sr, 20-21 ppm Y, 54-80 ppm Zr, 3.7-5.8 ppm Nb, 421-488 ppm Ba, 21-23 ppm La and 3.7-4.6 ppm Th (Fig. 3.27). The scoria display LREE enrichment relative to the HREE (La/Yb = 9 ± 2). The upper most scoria samples taken from 10-12cm in the key bed sequence display the lowest concentrations of incompatible trace elements (Fig. 3.27).

The Lower Pollara dacitic to rhyolitic glasses (69.9-74.6 wt.% SiO₂) have significantly more evolved (Zr/Sr = 0.4 ± 0.1) compositions than the scoria (Fig. 3.27). Trace element concentrations in the pumices show some variability with 91-106 ppm Rb, 276-462 ppm Sr, 10-14 ppm Y, 107-143 ppm Zr, 10.7-13.7 ppm Nb, 836-1110 ppm Ba, 28-33 ppm La and 10-13 ppm Th (Table 3.10; Fig. 3.27). The LREE are enriched relative to the HREE (La/Yb = 19 ± 2). Within the entire Lower Pollara suite Sr decreases with fractionation (Fig. 3.27d), additionally the MREE, Y (Fig. 3.27e) and HREE display a negative relationship with increasing fractionation. Ratios of HFSE/Th remain relatively constant within the Upper Pollara pumices (Nb/Th = 1.05±0.06; Zr/Th = 11.1 ± 0.5; Ta/Th = 0.06 ± 0.01).

| Eruption Locality Unit Sample Material | Lower Pollara | | | | | | |
|--|---------------------|--------------|--------------|--------------------------|----------------------|-----------------------|----------------------|
| | Salina, Valdichiesa | | | 'Key bed', NW Lipari | | | |
| | Unit 3 | Unit 4 | | Unit 2 | Unit 3 | | |
| | <i>Scoria</i> | 2A pumice | 8B pumice | 10-12cm <i>Scoria</i> | 15-17cm-6B pumice | 18-20cm-12C pumice | 13-15cm-2A pumice |
| SiO ₂ | <i>54.69</i> | 75.10 | 74.54 | <i>53.4</i> | 70.13 | 74.38 | 74.64 |
| TiO ₂ | <i>0.74</i> | 0.21 | 0.18 | <i>0.7</i> | 0.33 | 0.17 | 0.23 |
| Al ₂ O ₃ | <i>18.10</i> | 14.00 | 14.13 | <i>18.9</i> | 15.25 | 14.60 | 14.23 |
| FeOt | <i>9.11</i> | 1.39 | 1.64 | <i>9.1</i> | 3.24 | 1.59 | 1.55 |
| MnO | <i>0.15</i> | 0.06 | 0.09 | <i>0.2</i> | 0.02 | 0.08 | 0.14 |
| MgO | <i>4.12</i> | 0.29 | 0.36 | <i>4.2</i> | 0.83 | 0.31 | 0.34 |
| CaO | <i>8.70</i> | 1.70 | 1.67 | <i>10.1</i> | 3.30 | 1.65 | 1.78 |
| Na ₂ O | <i>2.55</i> | 4.00 | 4.19 | <i>2.4</i> | 3.82 | 3.88 | 3.91 |
| K ₂ O | <i>1.46</i> | 3.26 | 3.20 | <i>1.2</i> | 3.08 | 3.32 | 3.18 |
| Analytical Total | <i>99.62</i> | 95.90 | 95.76 | <i>100</i> | 98.61 | 95.62 | 97.43 |
| Na ₂ O + K ₂ O | 4.01 | 7.26 | 7.39 | 3.59 | 6.90 | 7.21 | 7.09 |
| K ₂ O/Na ₂ O | 0.57 | 0.81 | 0.76 | 0.48 | 0.81 | 0.86 | 0.81 |
| Rb | 54 | 98 | 95 | 30 | 92 | 91 | 103 |
| Sr | 688 | 282 | 307 | 721 | 415 | 462 | 308 |
| Y | 20 | 11 | 10 | 21 | 12 | 14 | 11 |
| Zr | 62 | 128 | 140 | 54 | 115 | 115 | 138 |
| Nb | 4.7 | 13.2 | 13.8 | 3.7 | 11.0 | 10.9 | 13.3 |
| Ba | 461 | 932 | 979 | 421 | 895 | 880 | 978 |
| La | 23 | 29 | 33 | 21 | 29 | 31 | 32 |
| Ce | 39 | 48 | 54 | 35 | 54 | 55 | 56 |
| Pr | 5.1 | 4.6 | 4.8 | 5.3 | 5.7 | 5.4 | 5.3 |
| Nd | 20.7 | 16.3 | 15.2 | 21.4 | 17.0 | 17.4 | 16.2 |
| Sm | 4.7 | <LOD | <LOD | 4.9 | 4.4 | 3.8 | 3.0 |
| Eu | 1.10 | <LOD | 0.87 | 1.10 | 0.78 | 0.86 | 0.74 |
| Gd | 3.5 | <LOD | <LOD | 3.6 | 2.8 | 3.2 | 2.2 |
| Dy | 3.30 | <LOD | 2.10 | 3.30 | 2.31 | 2.24 | 1.93 |
| Er | 1.80 | <LOD | <LOD | 1.80 | 1.38 | 1.34 | 1.30 |
| Yb | 2.0 | <LOD | 1.7 | 2.0 | 1.6 | 1.8 | 1.8 |
| Lu | 0.30 | <LOD | >LOD | 0.30 | 0.31 | 0.32 | 0.32 |
| Ta | 0.20 | 0.86 | 0.82 | 0.10 | 0.64 | 0.67 | 0.67 |
| Pb | 6.5 | 10.5 | 11.9 | 5.8 | 12.2 | 11.2 | 36.5 |
| Th | 4.3 | 12.3 | 12.1 | 3.7 | 10.8 | 10.6 | 12.1 |
| U | 1.8 | 3.7 | 3.9 | 1.6 | 3.6 | 3.3 | 4.2 |

Table 3.10: Representative major, minor and trace element glass compositions for the eruptive products of the Lower Pollara eruption, Salina. Scoria data highlighted in *Italics* is based on whole rock analyses (ICP-AES/MS). Full data sets are available in appendix eII.

| Eruption Locality Unit Sample | Upper Pollara East of Pollara crater | | | | | | | | | | | | | | |
|--|---|--------|--------|--------|--------|--------|--------|--------|--------|--------|--------|--------|--------|--------|--------|
| | ERU1 | | | ERU2 | | | ERU3 | | | ERU4 | | | ERU5 | | |
| | 1A | 6B | 14C | 2A | 4A | 7B | 16D | 17D | 20D | 11C | 2A | 3A | 1A | 8B | 9B |
| Material | Pumice | Pumice | Pumice | Pumice | Pumice | Pumice | Pumice | Pumice | Pumice | Pumice | Pumice | Pumice | Pumice | Pumice | Pumice |
| SiO ₂ | 71.94 | 73.83 | 74.00 | 74.89 | 74.83 | 74.66 | 75.20 | 74.92 | 75.05 | 71.77 | 75.02 | 75.32 | 73.14 | 71.49 | 72.07 |
| TiO ₂ | 0.26 | 0.28 | 0.19 | 0.16 | 0.21 | 0.27 | 0.14 | 0.23 | 0.22 | 0.24 | 0.20 | 0.14 | 0.33 | 0.35 | 0.26 |
| Al ₂ O ₃ | 15.30 | 13.69 | 13.79 | 13.90 | 13.35 | 13.68 | 14.12 | 14.37 | 14.05 | 15.54 | 13.96 | 13.80 | 14.30 | 15.02 | 15.25 |
| FeOt | 2.02 | 2.09 | 1.71 | 1.42 | 2.16 | 1.46 | 1.10 | 1.04 | 1.23 | 1.72 | 1.27 | 1.13 | 1.79 | 2.42 | 1.92 |
| MnO | 0.15 | 0.08 | 0.10 | 0.09 | 0.09 | 0.12 | 0.11 | 0.09 | 0.11 | 0.05 | 0.07 | 0.09 | 0.02 | 0.14 | 0.04 |
| MgO | 0.43 | 0.64 | 0.36 | 0.31 | 0.23 | 0.28 | 0.24 | 0.26 | 0.26 | 0.45 | 0.28 | 0.25 | 0.35 | 0.51 | 0.60 |
| CaO | 2.69 | 1.88 | 2.14 | 1.63 | 1.49 | 1.83 | 1.36 | 1.48 | 1.42 | 2.58 | 1.49 | 1.41 | 2.12 | 2.70 | 2.45 |
| Na ₂ O | 3.71 | 3.34 | 3.83 | 3.71 | 3.79 | 3.96 | 3.87 | 3.72 | 3.74 | 4.16 | 3.87 | 3.83 | 4.02 | 3.74 | 3.82 |
| K ₂ O | 3.51 | 4.17 | 3.87 | 3.89 | 3.85 | 3.74 | 3.85 | 3.90 | 3.91 | 3.49 | 3.83 | 4.02 | 3.93 | 3.62 | 3.58 |
| Analytical Total | 97.07 | 97.21 | 96.21 | 97.80 | 96.78 | 95.99 | 94.17 | 94.02 | 94.16 | 96.35 | 95.04 | 95.50 | 94.98 | 94.39 | 95.14 |
| Na ₂ O + K ₂ O | 7.22 | 7.51 | 7.70 | 7.60 | 7.64 | 7.70 | 7.72 | 7.62 | 7.65 | 7.65 | 7.70 | 7.85 | 7.95 | 7.36 | 7.40 |
| K ₂ O/Na ₂ O | 0.95 | 1.25 | 1.01 | 1.05 | 1.02 | 0.95 | 0.99 | 1.05 | 1.05 | 0.84 | 0.99 | 1.05 | 0.98 | 0.97 | 0.94 |
| Rb | - | 93 | 127 | 125 | 132 | 121 | 133 | 134 | 135 | - | 123 | 123 | - | - | - |
| Sr | - | 544 | 284 | 281 | 280 | 290 | 303 | 296 | 298 | - | 300 | 290 | - | - | - |
| Y | - | 15 | 12 | 13 | 12 | 14 | 15 | 15 | 13 | - | 14 | 14 | - | - | - |
| Zr | - | 110 | 106 | 107 | 107 | 113 | 132 | 133 | 131 | - | 137 | 138 | - | - | - |
| Nb | - | 13.4 | 15.5 | 15.2 | 15.2 | 15.5 | 17.8 | 17.8 | 17.8 | - | 17.2 | 16.4 | - | - | - |
| Ba | - | 1160 | 1211 | 1356 | 1168 | 1246 | 1398 | 1430 | 1398 | - | 1349 | 1382 | - | - | - |
| La | - | 39 | 40 | 40 | 36 | 41 | 45 | 45 | 44 | - | 43 | 43 | - | - | - |
| Ce | - | 67 | 71 | 68 | 62 | 69 | 76 | 73 | 73 | - | 73 | 74 | - | - | - |
| Pr | - | 6.3 | 6.7 | 6.3 | 6.0 | 6.5 | 7.0 | 7.0 | 6.8 | - | 7.0 | 7.1 | - | - | - |
| Nd | - | 21.5 | 18.4 | 19.2 | 18.3 | 21.9 | 23.8 | 23.3 | 22.1 | - | 22.1 | 24.1 | - | - | - |
| Sm | - | <LOD | 4.0 | 2.9 | 4.2 | 3.7 | <LOD | <LOD | <LOD | - | 3.3 | 3.4 | - | - | - |
| Eu | - | 1.01 | 0.76 | 0.81 | <LOD | 0.79 | 0.97 | 0.75 | 0.68 | - | 0.87 | 0.83 | - | - | - |
| Gd | - | <LOD | 3.6 | 2.9 | <LOD | 3.1 | <LOD | <LOD | <LOD | - | 2.5 | 2.8 | - | - | - |
| Dy | - | 2.46 | 1.91 | 2.13 | <LOD | 2.37 | 2.19 | 1.85 | 2.50 | - | 2.15 | 2.42 | - | - | - |
| Er | - | 1.69 | 1.27 | 1.42 | <LOD | 1.51 | 1.37 | 1.54 | 1.67 | - | 1.38 | 1.48 | - | - | - |
| Yb | - | 1.9 | 1.8 | 1.8 | <LOD | 2.2 | 1.7 | 2.5 | 2.2 | - | 2.0 | 2.0 | - | - | - |
| Lu | - | <LOD | 0.32 | 0.29 | <LOD | 0.36 | <LOD | <LOD | <LOD | - | 0.32 | 0.32 | - | - | - |
| Ta | - | 0.92 | 0.87 | 0.75 | 0.85 | 0.94 | 0.97 | 1.15 | 0.89 | - | 0.96 | 1.02 | - | - | - |
| Pb | - | 13.0 | 16.9 | 15.1 | 15.5 | 42.9 | 14.4 | 16.6 | 14.6 | - | 16.4 | 15.2 | - | - | - |
| Th | - | 14.6 | 15.6 | 16.6 | 14.6 | 16.8 | 19.0 | 20.1 | 19.2 | - | 18.2 | 18.0 | - | - | - |
| U | - | 4.5 | 4.9 | 5.0 | 4.7 | 5.3 | 5.1 | 5.6 | 5.9 | - | 5.5 | 5.4 | - | - | - |

Table 3.11: Previous page: Representative major, minor and trace element glass data for the eruptive products of the Upper Pollara, Salina. Full data sets are available in appendix eII.

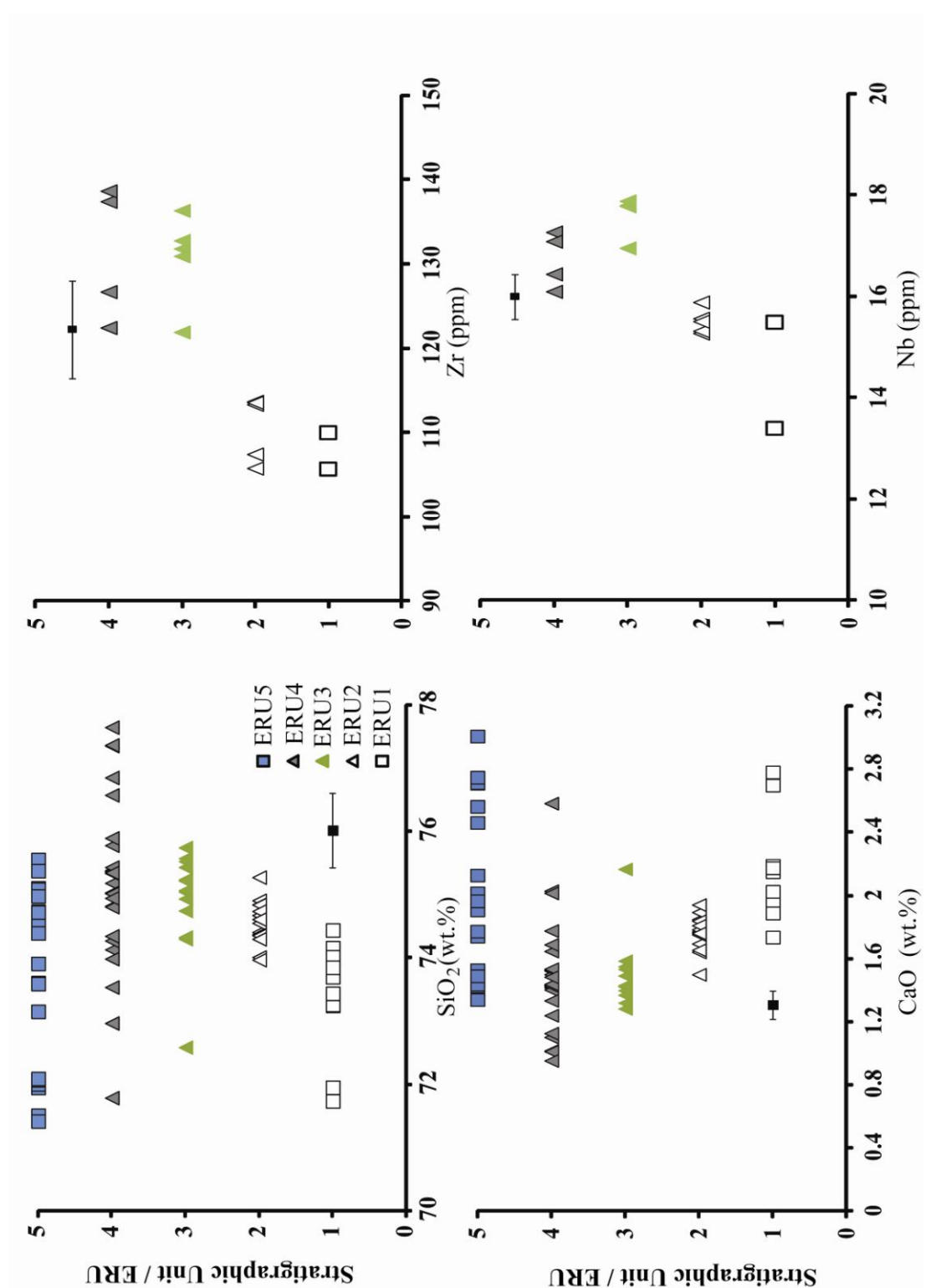


Figure 3.28: Chemostratigraphy of the Upper Pollara Tuff deposits, indicating significant stratigraphical variations in the glass geochemistry. Errors are 2 x standard deviation of repeat analyses of StHs/6-80G secondary standard.

3.4.2.2 Upper Pollara Tuffs:

The Upper Pollara tuffs display significant major element variability with 71.4-77.6 wt.% SiO₂, 0.1-0.3 wt.% TiO₂, 12.8-16.0 wt.% Al₂O₃, 0.6-2.4 wt.% FeO, 0.1-0.2 wt.% MnO, 0.1-0.6 wt.% MgO, 0.9-3.0 wt.% CaO, 3.2-4.5 wt.% Na₂O, 3.4-4.4 wt.% K₂O (Table 3.11; Fig. 3.26). These glasses are classified as HKCA rhyolites (Fig. 3.20). The following major element trends are observed in response to increasing SiO₂, K₂O increases, Na₂O is scattered but constant, whilst TiO₂, Al₂O₃, FeO, MnO, MgO, CaO all decrease (Fig. 3.26). The variability in major element concentrations is also reflected in the trace element concentrations with 93-135 ppm Rb, 279-544 ppm Sr, 12-16 ppm Y, 106-139 ppm Zr, 13-18 ppm Nb, 1160-1430 pm Ba, 36-45 ppm La, 62-76 ppm Ce, 15-20 ppm Th (Fig. 3.27). Glasses have relatively low levels of overall trace element enrichment (Zr/Sr = 0.4-0.5) (Fig. 3.21a), whilst showing significant LREE enrichment relative to the HREE (La/Yb = 21 ± 2). Trace element ratios are relatively consistent throughout the entire stratigraphy including constant ratios of HFSE/Th (Ta/Th = 0.05 ± 0.1; Nb/Th = 0.94 ± 0.04; Nb/Zr = 0.14 ± 0.01; Zr/Th = 7 ± 0.4).

Significant colour variation exists in the pumices and this appears to be related to vesicularity rather than purely compositional differences. Compositional data is dominated by white pumices from each stratigraphic unit. This is because the grey pumices have greater vesicularity and microlites and as a result LA-ICP-MS analysis was problematic. As ERU 5 is comprised exclusively of grey pumices no trace element data is available for this uppermost unit (Table 3.11).

Stratigraphic variation exists in the major element concentrations of the Upper Pollara juvenile deposits. Moving up sequence, each eruptive unit sees the introduction of more evolved glass compositions, with the exception of the final eruptive unit (ERU 5) (Fig. 3.28). Compositional variability through the sequence (Fig. 3.28) reflects the mixing and homogenising indicative of the banding observed. ERU1 glasses have the most restricted evolution of the entire sequence (SiO₂ ≤ 74.8 wt. %). The dull white pumices of ERU2 are the most homogeneous observed within the succession with 74.0-75.3 wt.% SiO₂. ERU3 contains the most contrasting pumice textures with evidence of banding, comprising highly vesicular foamy grey pumices and milky white stretched pumices, which make their first appearance in the stratigraphy. SiO₂ ranges from 72.6 wt.% (grey pumice) to 75.7 wt.% SiO₂ (milky white pumice) this variability reflects the mixing of the two textural groups. Similarly, ERU4 has more compositional

heterogeneity with 71.8-77.6 wt.% SiO₂ reflecting the mixing of the two components. ERU5 has some of the least evolved glass compositions in the Upper Pollara stratigraphy with 71.4-75.5 wt.% SiO₂. SiO₂ in the grey pumice reaches similar levels to those seen in the white components of the lower stratigraphy. This shows that pumice colour is more a function of vesicularity rather than purely compositional variability; the presence of gas rich (vesicular; grey) pumices might be indicative of the introduction of a new melt during the eruption.

Whilst the trace element analysis of the Upper Pollara succession is restricted to the white pumices, stratigraphic variability exists. The dull white pumices in the lower eruptive units (ERU1 and ERU2) display lower trace element concentrations than those observed in the milky white pumices of the upper units (ERU3 and ERU4) (Fig. 3.28). The dull white pumices in ERU1 and ERU2 have limited trace element variability but generally overlap with concentrations ranging from 15-11 ppm Y, 105-114 ppm Zr, 13-16 ppm Nb, 39-42 ppm La and 14-17 ppm Th (Fig. 3.26; 3.27). The higher concentrations observed in the milky white pumices of ERU3 and ERU4 are equally homogeneous with 122-135 ppm Rb, 279-303 ppm Sr, 13-16 ppm Y, 122-139 ppm Zr, 16-18 ppm Nb, 1294-1430 ppm Ba, 42-45 ppm La and 18-20 ppm Th (Fig. 3.27; 3.28). These elevated trace element concentrations are consistent with major element variability, where ERU3 and ERU4 pumices display some of the highest SiO₂, lowest CaO concentration and thus equate to the most evolved pumices (Fig. 3.28).

3.4.3 Panarea:

3.4.3.1 Punta Falcone Pumices

These pumices are poorly constrained temporally and are likely to be older than 42 ka, but are included for comparison with the Palisi deposits (below) and more recent activity on Salina. The pumices are banded and show a bimodal population (Fig. 20; Table 3.12) the dominant grey pumices is have a transitional CA/HKCA affinity and are dacitic (62.3-67.5 wt.% SiO₂) (Fig. 3.20). Glasses are heterogeneous at a major element level with 0.4-0.6 wt.% TiO₂, 15.3-18.5 wt.% Al₂O₃, 0.7-1.4 wt.% MgO, 4.4-6.9 wt.% and 2.4-3.3 wt.% K₂O (Fig. 3.26). The white pumice display homogenous (78.1 wt.% SiO₂; 5.3 ± 0.2 wt. % K₂O) rhyolitic compositions with a HKCA affinity (Fig. 3.20). The dacite glasses are moderately evolved (Zr/Sr = 0.3) and display LREE enrichment relative to the HREE (La/Yb = 11 ± 1). Trace element compositions are homogeneous; this may reflect limited analytical success using LA-ICP-MS due to only small areas of

glass being de-void of microlite inclusions. Trace element compositions observed in these pumices are as follows; 113 ± 17 ppm V, 115 ± 7 Rb, 397 ± 33 ppm Sr, 22 ± 3 ppm, 127 ± 7 ppm, 8.1 ± 0.4 ppm Nb, 548 ± 32 ppm Ba, 28 ± 1 ppm La and 9.6 ± 0.5 ppm Th (Fig. 3.27). The HSFE/Th ratio remain constant within these glasses with Nb/Th = 0.8 ± 0.1 , Zr/Th = 11.3 ± 1.0 . Trace element analysis was unsuccessful on the rhyolitic component.

| Eruption Locality Unit Sample Material | Panarea, Final Phase explosive Activity | | | | | | |
|---|---|--------------|---------------|---------------|------------|------------|-------------|
| | Punta Falcone | | | | Palisi | | |
| | Unit 2 2A | Unit 2 6B | Unit 2 14C | Unit 2 16D | base 1A | base 2A | base 13C |
| | pumice | pumice | pumice | pumice | pumice | pumice | pumice |
| SiO ₂ | 65.48 | 64.25 | 67.53 | 78.17 | 66.47 | 64.79 | 63.46 |
| TiO ₂ | 0.47 | 0.45 | 0.48 | 0.26 | 0.58 | 0.53 | 0.48 |
| Al ₂ O ₃ | 17.51 | 18.15 | 16.11 | 11.38 | 14.94 | 16.96 | 17.90 |
| FeOt | 3.78 | 3.85 | 3.95 | 1.12 | 5.17 | 4.45 | 4.12 |
| MnO | 0.11 | 0.09 | 0.11 | 0.03 | 0.12 | 0.21 | 0.16 |
| MgO | 0.92 | 0.96 | 0.67 | 0.18 | 1.47 | 0.99 | 1.62 |
| CaO | 5.47 | 6.21 | 4.37 | 0.74 | 4.28 | 5.52 | 6.31 |
| Na ₂ O | 3.46 | 3.60 | 3.47 | 2.78 | 3.16 | 3.11 | 3.30 |
| K ₂ O | 2.81 | 2.42 | 3.31 | 5.34 | 3.37 | 3.01 | 2.65 |
| Analytical Total | 97.91 | 97.00 | 96.11 | 95.15 | 94.46 | 96.61 | 97.02 |
| Na ₂ O + K ₂ O | 6.27 | 6.03 | 6.78 | 8.12 | 6.53 | 6.12 | 5.95 |
| K ₂ O/Na ₂ O | 0.81 | 0.67 | 0.95 | 1.92 | 1.07 | 0.97 | 0.80 |
| Trace Ppm | | | | | | | |
| Rb | 113 | 110 | 123 | - | - | 118 | - |
| Sr | 423 | 408 | 359 | - | - | 341 | - |
| Y | 20 | 21 | 24 | - | - | 22 | - |
| Zr | 126 | 116 | 129 | - | - | 126 | - |
| Nb | 7.9 | 7.8 | 8.5 | - | - | 8.0 | - |
| Ba | 555 | 512 | 576 | - | - | 544 | - |
| La | 28 | 27 | 29 | - | - | 26 | - |
| Ce | 52 | 51 | 56 | - | - | 52 | - |
| Pr | 5.7 | 5.6 | 6.0 | - | - | 5.7 | - |
| Nd | 21 | 21 | 25 | - | - | 22 | - |
| Sm | 4.2 | 4.0 | 4.6 | - | - | 4.1 | - |
| Eu | 1.0 | 1.0 | 0.9 | - | - | 1.0 | - |
| Gd | 4.0 | 3.6 | 4.3 | - | - | 4.0 | - |
| Dy | 3.9 | 3.8 | 4.0 | - | - | 3.8 | - |
| Er | 1.9 | 2.3 | 2.5 | - | - | 2.6 | - |
| Yb | 2.7 | 2.2 | 2.5 | - | - | 2.4 | - |
| Lu | 0.36 | 0.40 | 0.41 | - | - | 0.44 | - |
| Ta | 0.55 | 0.54 | 0.51 | - | - | 0.54 | - |
| Pb | 13.5 | 12.7 | 14.1 | - | - | 15.2 | - |
| Th | 10.2 | 9.2 | 9.4 | - | - | 10.0 | - |
| U | 3.1 | 3.2 | 3.3 | - | - | 3.2 | - |

Table 3.12: Representative major, minor and trace element glass data for the most recently explosive erupted pumices outcropping on the Island of Panarea. Full data are given in appendix eII.

3.4.3.2 Palisi Pumices

Grey fall pumices from Palisi are CA dacites (Fig. 3.20) with fairly heterogeneous glass compositions with 63.5-66.5 wt.% SiO₂ (Fig. 3.26). Using increasing silica as a fractionation index Al₂O₃, MgO, CaO decrease; whilst FeO, Na₂O and TiO₂ remain fairly constant and K₂O increases. LA-ICP-MS of these pumices was problematic due to the highly vesicular nature of the glasses; areas available to analyse at a 20 µm spot size

were very limited. Consequently, the Palisi pumices are represented by only one trace element data point. This glass is moderately evolved ($Zr/Sr = 0.4$) and displays LREE enrichment relative to the HREE ($La/Yb = 11$). Trace element concentrations for this pumice are shown in Figure 3.27. HFSE/Th for this pumices are $Nb/Th = 0.8$; $Zr/Th = 11.0$.

3.4.4 Vulcano

The explosive deposits produced on Vulcano during the last 42 ka BP are particularly diverse, ranging from basaltic trachy-andesite through to rhyolite. Glasses display either a (1) K-series or; (2) Shoshonitic affinity (Fig. 3.20):

(1) K-series glasses display significant heterogeneity with 55.1-61.6 wt.% SiO_2 , 0.4-0.7 wt.% TiO_2 , 16.55-19.44 wt.% Al_2O_3 , 3.57-7.26 wt.% FeO , 0.9-2.5 wt.% SiO_2 , 1.98-5.36 wt.% CaO , 3.9-5.6 wt.% Na_2O , 6.2-8.3 wt.% K_2O (Fig. 3.20).

(2) The shoshonitic glasses display significant heterogeneity with 53.5-74.2 wt.% SiO_2 , 0.1-0.8 wt.% TiO_2 , 13.1-19.0 wt.% Al_2O_3 , 1.8-9.2 wt.% FeO , 0.1-4.2 wt.% MgO , 0.7-8.0 wt.% CaO , 2.2-4.5 wt.% Na_2O and 4.3-8.0 wt. % K_2O (Fig. 3.20).

3.4.4.1 Quadrara Formation:

Representative major minor and trace element glass data for the Quadrara formation are given in Table 3.13. The Quadrara formation displays clear stratigraphic variation with opening pumices capped by a scoria blanket and this is reflected in the glass geochemistry. Compositional heterogeneity observed within this eruptive sequence ranges from 56.4-64.0 wt.% SiO_2 ; whilst 4.1-6.3 wt.% K_2O defines a shoshonitic affinity (Fig. 3.20). The Quadrara Formation is geochemically bimodal (Fig. 3.29; 3.30); basal white pumices are characterised by significantly more evolved compositions than the overlying scoriaceous deposits. The pumices have ≥ 62 wt.% SiO_2 (trachytic), whilst the scoriaceous deposits have glasses typically with ≤ 60 wt.% SiO_2 (trachy-andesites), with only some glasses falling at the more evolved end-member (Fig. 3.30). With increasing SiO_2 as a fractionation index we observed the following patterns; decreasing TiO_2 , Al_2O_3 , FeO , MnO , MgO , CaO ; whilst increasing Na_2O and K_2O (Fig. 3.30).

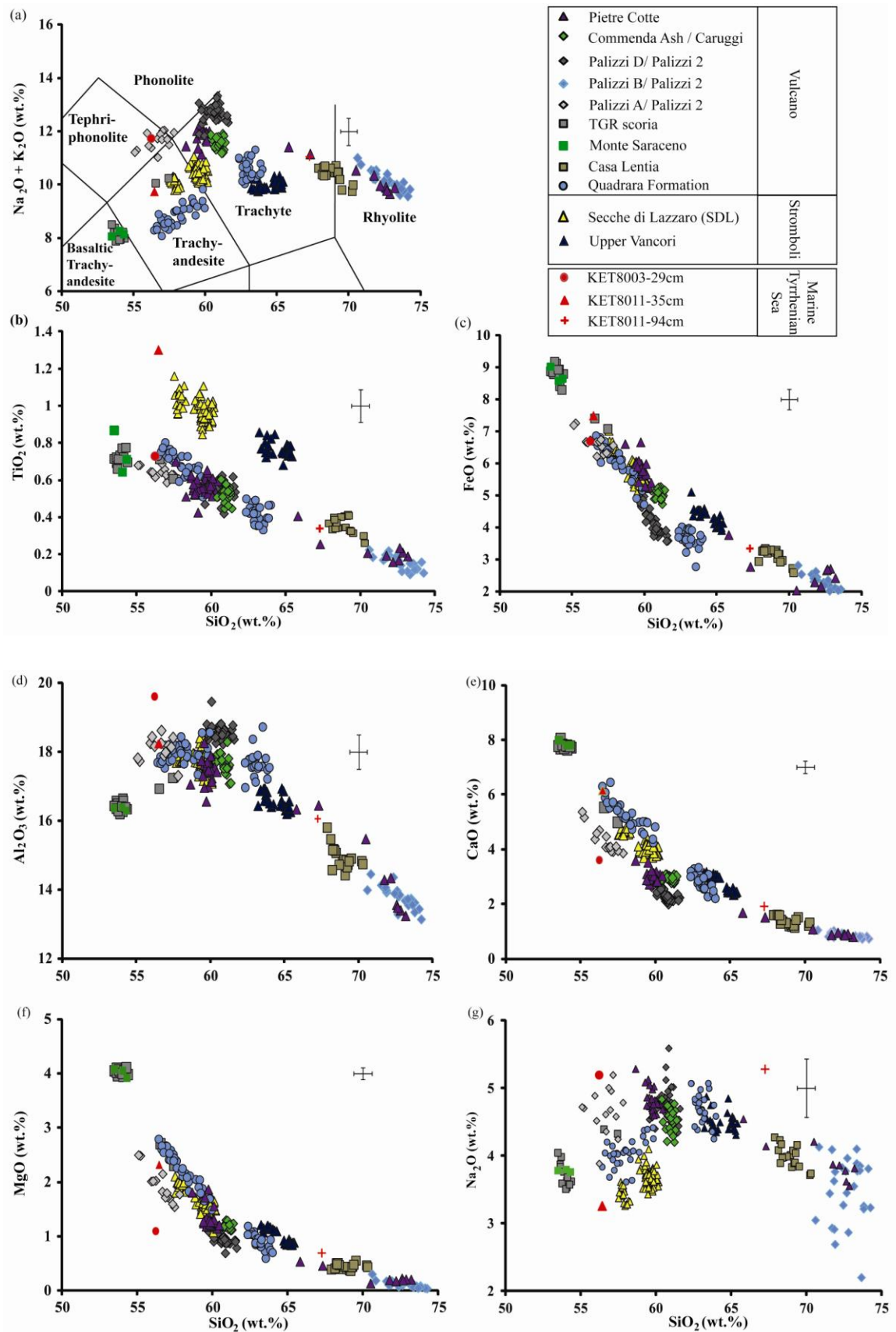


Figure 3.29: Major element bi-plots showing the chemical variability and overlap of the erupted glasses produced explosively on Vulcano and Stromboli during the last 21 ka.

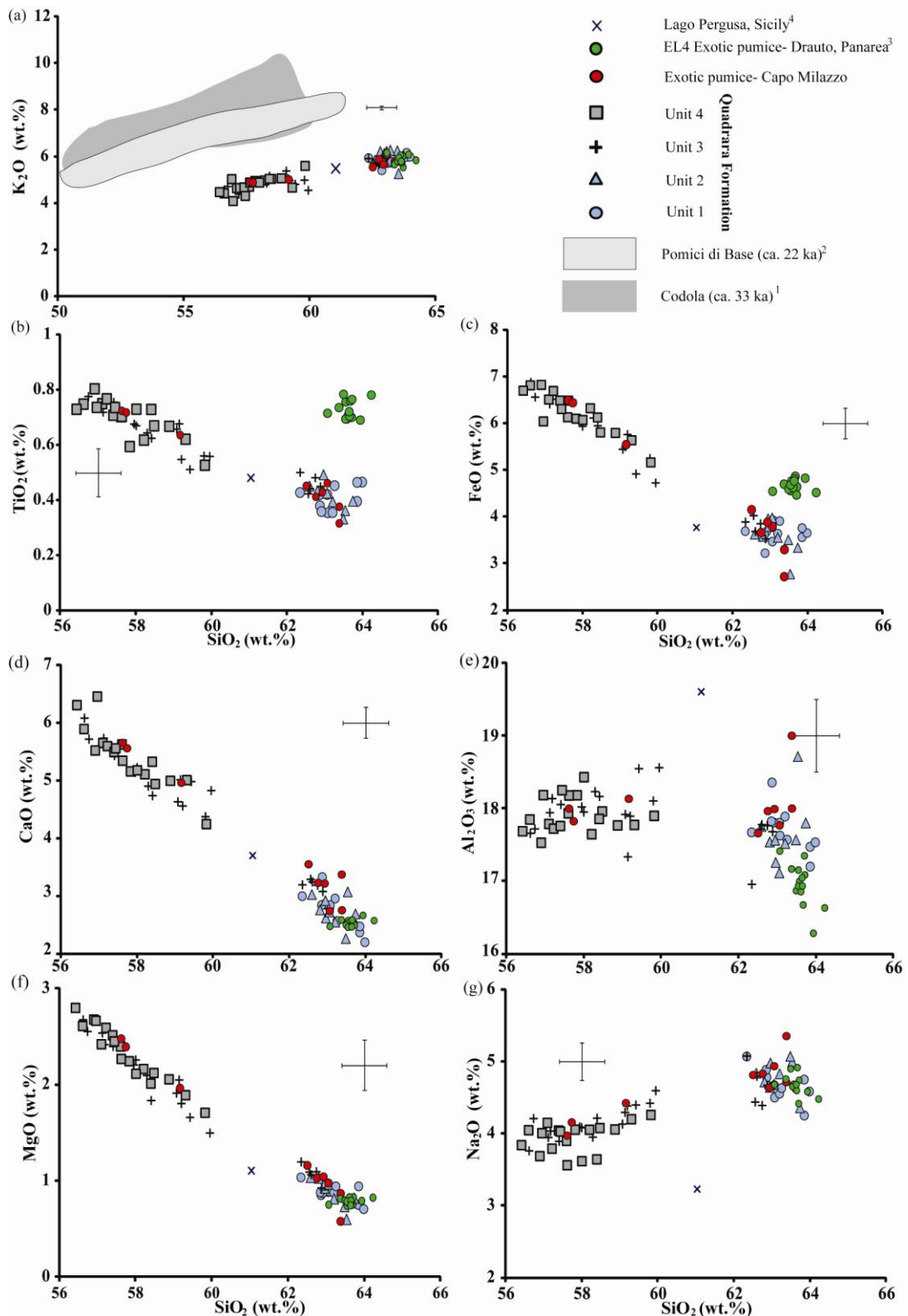


Figure 3.30: Major element bi-plots displaying the glass compositions of the Quadrara formation explosively erupted on Vulcano. Also given are the glass compositions of pumices found outcropping at Capo Milazzo (Sicily) and Drauto, Panarea (EL4; De Rita et al., 2008). Finally an average glass composition from a distal tephra layer recorded at Pergusa on Sicily (Narcisi et al., 2002).

| Eruption Locality Unit | Quadrara SW Vulcano | | | | | | | |
|--------------------------------------|------------------------|--------------|---------------|---------------|--------------|--------------|---------------|---------------|
| | 1 | | 2 | | 3 | | 4 | |
| | 3A pumice | 7B pumice | 17D pumice | 19D pumice | 3A Scoria | 5A Scoria | 11C Scoria | 13C Scoria |
| Major(wt. %) | | | | | | | | |
| SiO ₂ | 63.05 | 62.90 | 62.95 | 63.05 | 58.00 | 57.19 | 59.82 | 57.23 |
| TiO ₂ | 0.42 | 0.36 | 0.49 | 0.43 | 0.67 | 0.75 | 0.53 | 0.77 |
| Al ₂ O ₃ | 17.81 | 17.81 | 17.26 | 17.12 | 17.95 | 18.13 | 17.90 | 17.72 |
| FeOt | 3.48 | 3.69 | 3.79 | 3.98 | 5.94 | 6.51 | 5.16 | 6.69 |
| MnO | 0.18 | 0.20 | 0.12 | 0.19 | 0.11 | 0.13 | 0.15 | 0.20 |
| MgO | 0.88 | 0.87 | 0.92 | 0.97 | 2.25 | 2.41 | 1.70 | 2.59 |
| CaO | 2.80 | 2.86 | 2.62 | 2.73 | 5.22 | 5.67 | 4.24 | 5.59 |
| Na ₂ O | 4.68 | 4.66 | 4.98 | 4.69 | 4.08 | 4.04 | 4.26 | 3.79 |
| K ₂ O | 5.96 | 5.94 | 6.12 | 6.21 | 4.96 | 4.36 | 5.58 | 4.63 |
| Analytical Total | 98.30 | 97.82 | 98.13 | 95.86 | 98.70 | 99.15 | 98.52 | 98.54 |
| Na ₂ O + K ₂ O | 10.64 | 10.60 | 11.11 | 10.90 | 9.04 | 8.40 | 9.84 | 8.42 |
| K ₂ O/Na ₂ O | 1.28 | 1.27 | 1.23 | 1.32 | 1.22 | 1.08 | 1.31 | 1.22 |
| Trace ppm | | | | | | | | |
| V | 54 | 48 | 50 | 38 | - | - | - | - |
| Rb | 190 | 175 | 201 | 184 | 165 | 154 | 164 | 161 |
| Sr | 839 | 811 | 900 | 826 | 1173 | 1182 | 1246 | 1220 |
| Y | 27 | 26 | 27 | 23 | 25 | 25 | 25 | 23 |
| Zr | 205 | 194 | 213 | 192 | 168 | 155 | 165 | 162 |
| Nb | 23 | 22 | 24 | 22 | 19 | 18 | 18 | 18 |
| Ba | 995 | 949 | 1064 | 1259 | 1061 | 1074 | 1113 | 1079 |
| La | 62 | 54 | 63 | 58 | 54 | 52 | 53 | 52 |
| Ce | 113 | 105 | 114 | 102 | 101 | 101 | 105 | 101 |
| Pr | 11.6 | 10.9 | 12.0 | 10.6 | 11.5 | 10.4 | 11.4 | 11.0 |
| Nd | 46 | 35 | 45 | 41 | 43 | 44 | 44 | 44 |
| Sm | 8.5 | 6.9 | 8.5 | 6.8 | 7.9 | 8.2 | 8.0 | 7.9 |
| Eu | 1.7 | 1.5 | 1.8 | 1.9 | 1.7 | 1.9 | 1.8 | 1.7 |
| Gd | 6.0 | 5.6 | 6.7 | 4.7 | 6.0 | 6.7 | 5.9 | 6.3 |
| Dy | 5.0 | 4.5 | 4.9 | 4.2 | 4.8 | 4.8 | 5.1 | 5.0 |
| Er | 2.4 | 2.2 | 2.7 | 2.3 | 2.6 | 2.5 | 2.6 | 2.5 |
| Yb | 2.8 | 2.5 | 2.6 | 2.7 | 2.5 | 2.6 | 3.0 | 2.5 |
| Lu | 0.40 | 0.35 | 0.37 | 0.39 | 0.37 | 0.37 | 0.33 | 0.33 |
| Ta | 1.3 | 1.4 | 1.2 | 1.3 | 1.1 | 1.0 | 1.2 | 0.9 |
| Pb | 28.8 | 27.8 | 29.5 | 28.3 | 23.3 | 24.6 | 24.0 | 22.3 |
| Th | 23.4 | 21.6 | 23.9 | 22.5 | 18.9 | 18.0 | 19.3 | 18.6 |
| U | 7.5 | 7.3 | 6.8 | 6.6 | 5.3 | 5.6 | 5.4 | 5.5 |

Table 3.13: Representative major, minor and trace element glass data for the explosively erupted Quadrara formation. Full data sets are available in appendix eII.

This major element variability is illustrated in the range of trace element concentrations within the entire formation of 147-201 ppm Rb, 523-1304 ppm Sr, 21-28 ppm Y, 150-213 ppm Zr, 18-24 ppm Nb, 733-1259 ppm Ba and 17-24 ppm Th (Fig. 3.31; 3.33). The glasses display LREE enrichment relative to the HREE ($La/Yb = 21 \pm 2$) (Fig. 3.24b) and relatively constant ratios of HFSE/Th ($Nb/Th = 1.0 \pm 0.05$; $Zr/Th = 8.8 \pm 0.36$). The reversely graded trachytic white pumices (unit 1 and 2) display significant compositional variability demonstrated by the following range in major and minor element compositions; 62.3-64.0 wt.% SiO₂, 2.8-4.0 wt.% FeO, 2.2-3.3 wt.% CaO, 4.3-5.1 wt.% Na₂O, 5.3-6.3 wt.% K₂O (Fig. 3.29). Glasses display moderate levels of fractionation ($Zr/Sr = 0.2-0.4$) and show LREE enrichment relative to the HREE ($La/Yb = 21 \pm 1$) (Fig. 3.24b).

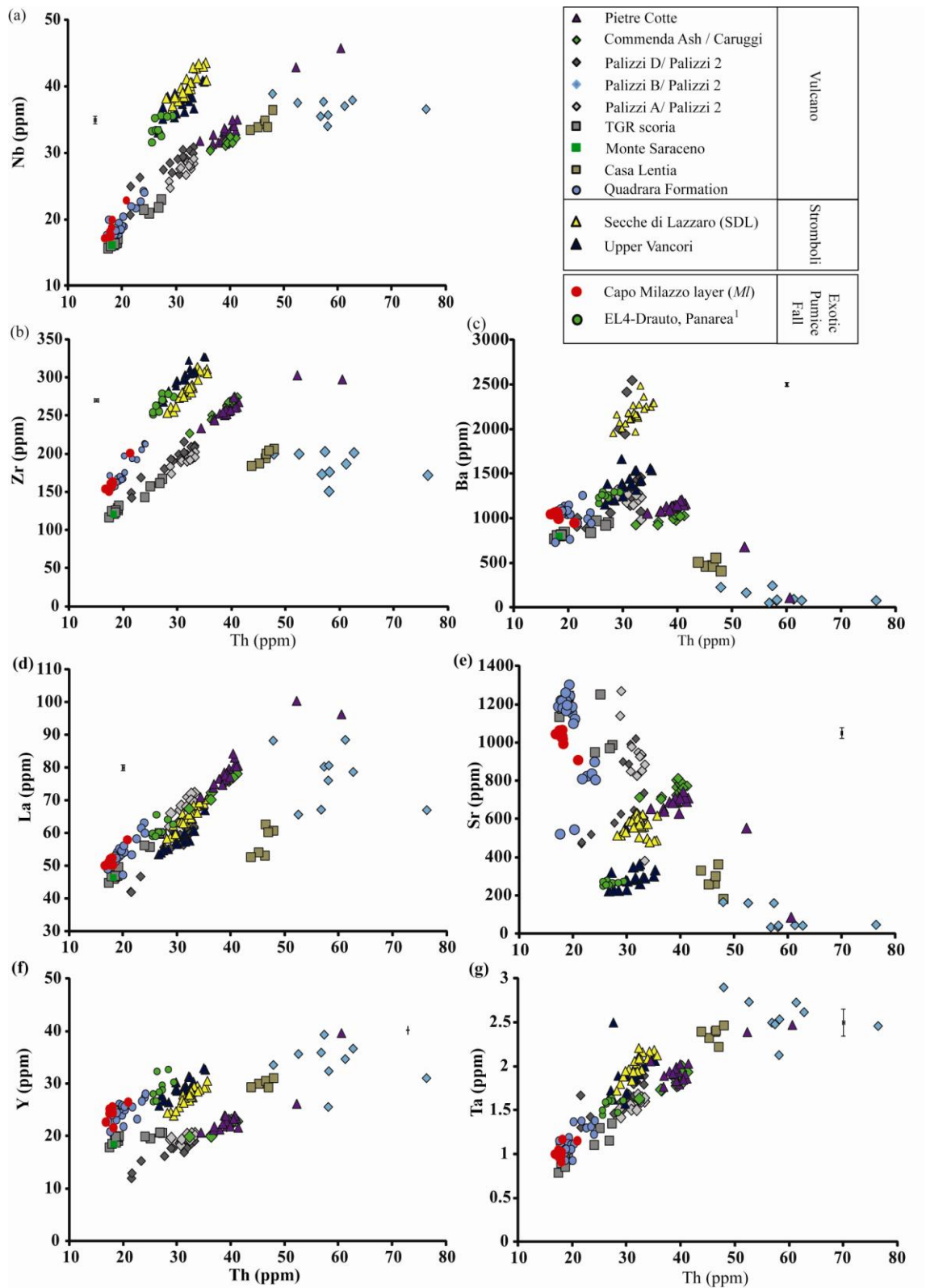


Figure 3.31: Trace element bi-plots displaying the glass compositions of tephras explosively produced on Vulcano and Stromboli during the last 21 ka. Errors given are 2 x standard deviations of repeat analyses of the StHs/6-80G secondary standard.

Trace element concentrations within these glasses display significant variability with the following ranges 161-201 ppm Rb, 523-900 ppm Sr, 21-28 ppm Y, 171-213 ppm Zr, 20-24 ppm Nb, 732-1259 ppm Ba, 50-63 ppm La and 18-24 ppm Th (Fig. 3.32). HFSE/Th ratios remain constant within these pumices ($\text{Nb/Th} = 1.00 \pm 0.03$, $\text{Zr/Th} = 8.8 \pm 0.2$) apart from two pumices which display lower concentrations of Sr (523-546 ppm) and Ba (733-767 ppm) and subtly more elevated ratios of HFSE/Th ($\text{Nb/Th} = 1.08$; $\text{Zr/Th} = 9.8$) (Fig. 3.32).

The scoria deposits of units 3 are the most heterogeneous; with major element composition that are comparable with the trachytic white pumices below, but also contain the less evolved end-member present in the Quadrara formation (> 60 wt.%). The least evolved components show significant chemical variability with 56.4-60.0 wt.% SiO_2 , 0.5-0.8 wt.% TiO_2 , 3.7-6.9 wt.% FeO , 3.2-6.5 wt.% CaO , 3.6-4.6 wt.% Na_2O , 4.1-5.6 wt.% K_2O (Fig. 3.30). Glasses are significantly less evolved than the white pumices below ($\text{Zr/Sr} = 0.12$ - 0.15) and display LREE enrichment relative to the HREE ($\text{La/Yb} = 21 \pm 2$) (Fig. 3.24b). Glass display significant trace element variability with the following ranges in concentrations; 147-165 ppm Rb, 1101-1304 ppm Sr, 22-26 ppm Y, 150-175 ppm Zr, 18-20 ppm Nb, 1045-1150 ppm Ba, 47-55 ppm La and 17-20 ppm Th (Fig. 3.32). HFSE/Th ratios remain constant in these glasses ($\text{Nb/Th} = 0.98 \pm 0.03$, $\text{Zr/Th} = 8.7 \pm 0.2$; Fig. 3.32).

3.4.4.2 Casa Lentia

Representative major, minor and trace element data for the fall deposits identified on the Monte Lentia cliff, Vulcano are given in Table 3.14. Glasses have variable compositions (67.9-70.2 wt.% SiO_2 ; 5.7-6.6 wt.% K_2O) and are classified as shoshonitic ranging from trachyte to rhyolite in composition (Fig. 3.20). Increasing SiO_2 as a fractionation index shows a negative relationship with TiO_2 , FeO , MgO , CaO and Na_2O . MnO remains constant with increasing SiO_2 , whilst K_2O increases until an inflection at ca. 69.4 wt.% SiO_2 where it decreases. Glasses are moderately evolved ($\text{Zr/Sr} = 0.6$ - 1.1) and display LREE enrichment over the HREE ($\text{La/Yb} = 16 \pm 2$). Trace element concentrations observed in the glasses are fairly homogeneous with 309 ± 10 ppm Rb, 30 ± 1 ppm Y, 196 ± 9 ppm Zr, 35 ± 1 ppm Nb and 46 ± 2 ppm Th (Fig. 3.31). Sr and Ba display negative relationships with increasing fractionation and show some of the most significant variation (183-364 ppm Sr and 410-556 ppm Ba). HFSE/Th ratios are constant within these glasses ($\text{Nb/Th} = 0.75 \pm 0.02$; $\text{Zr/Th} = 4.3 \pm 0.08$) (Fig. 3.31).

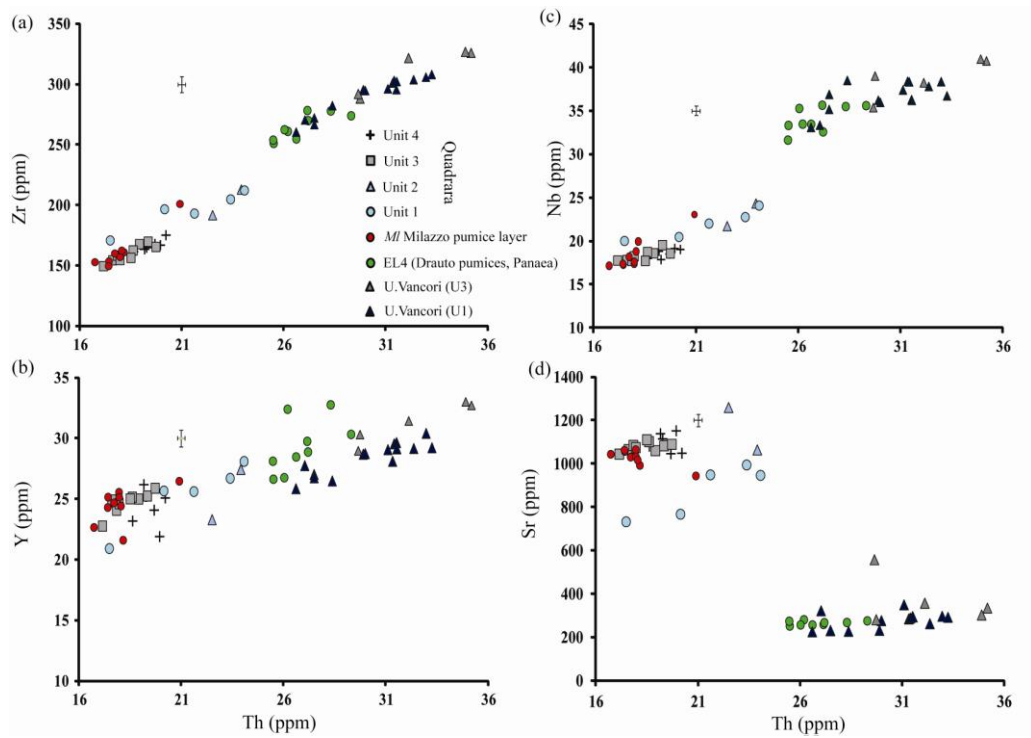


Figure 3.32: Trace element bi-plots displaying glass compositions of the Quadrara formation, Vulcano and the Upper Vancori pumices, Stromboli. Glass composition of pumices outcropping on Capo Milazzo (*Ml*), Sicily and at Drauto (EL4), Panarea are given.

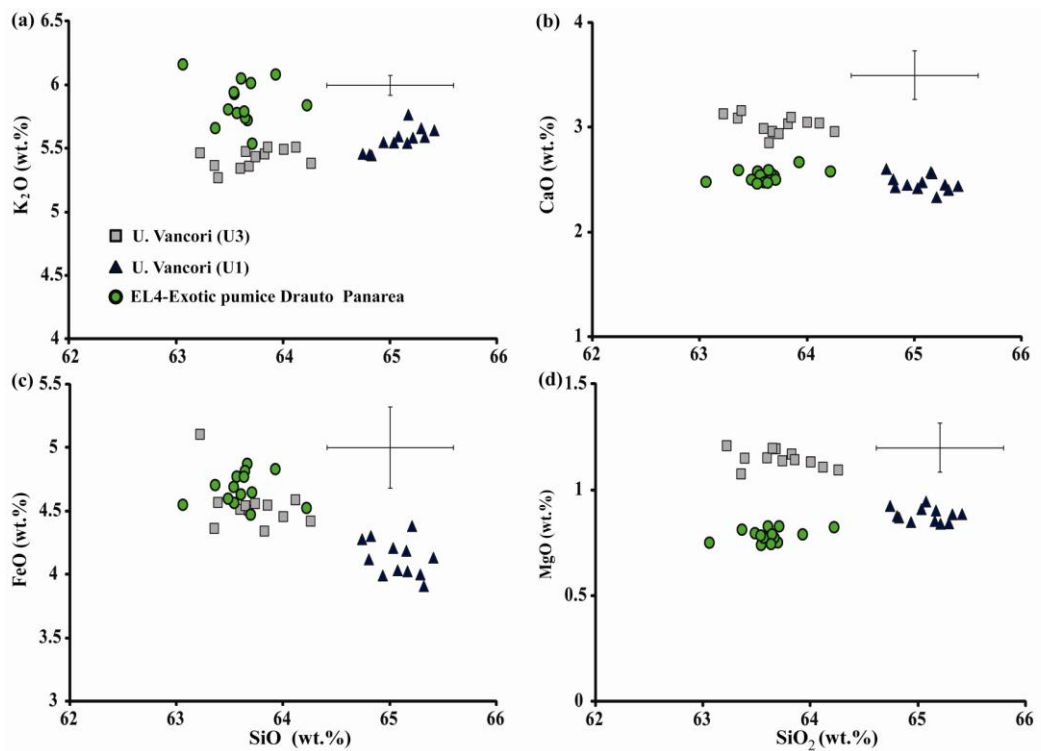


Figure 3.33: Major element bi-plots displaying glass concentrations of trachytic pumices erupted during the Upper Vancori eruption, Stromboli. Also shown are glass compositions of the pumice fall bed recorded at Drauto (EL4), Panarea.

3.4.4.3 Monte Saraceno:

Representative major, minor and trace element data for the scoria blanket sampled on the rim of the Piano caldera, Vulcano are given in Table 3.14. The deposits sampled appeared altered with pitting of the glass surfaces. Consequently, glass characterisation was restricted and only offers a brief insight into the melt compositions produced during this activity.

| Eruption Locality Sample Material | Casa Lentia Lentia | | TGR ? Scoria Piano Caldera | | M. Saraceno Rim of Piano Caldera | |
|--|-----------------------|--------------|-------------------------------|---------------|-------------------------------------|--------------|
| | 1A pumice | 3A pumice | 5A Scoria | 12B Scoria | 1A Scoria | 6B Scoria |
| Major (wt. %) | | | | | | |
| SiO ₂ | 70.22 | 68.93 | 54.37 | 57.44 | 54.31 | 53.48 |
| TiO ₂ | 0.30 | 0.41 | 0.70 | 0.61 | 0.71 | 0.87 |
| Al ₂ O ₃ | 14.82 | 14.80 | 16.33 | 17.23 | 16.29 | 16.36 |
| FeO _t | 2.72 | 3.29 | 8.80 | 7.08 | 8.65 | 9.03 |
| MnO | 0.12 | 0.05 | 0.10 | 0.09 | 0.15 | 0.12 |
| MgO | 0.47 | 0.40 | 3.98 | 2.31 | 3.92 | 4.08 |
| CaO | 1.21 | 1.19 | 7.72 | 4.98 | 7.81 | 7.99 |
| Na ₂ O | 3.72 | 4.01 | 3.63 | 4.33 | 3.77 | 3.79 |
| K ₂ O | 6.04 | 6.48 | 4.37 | 5.91 | 4.38 | 4.28 |
| Analytical Total | 99.00 | 99.02 | 98.37 | 98.79 | 98.42 | 98.32 |
| Na ₂ O + K ₂ O | 9.76 | 10.50 | 8.00 | 10.25 | 8.15 | 8.07 |
| K ₂ O/Na ₂ O | 1.62 | 1.61 | 1.21 | 1.37 | 1.16 | 1.13 |
| Trace ppm | | | | | | |
| V | | | | | | |
| Rb | 305 | 318 | 143 | 201 | 149 | - |
| Sr | 264 | 302 | 1136 | 972 | 1172 | - |
| Y | 30 | 31 | 18 | 21 | 19 | - |
| Zr | 194 | 200 | 117 | 162 | 121 | - |
| Nb | 34 | 35 | 16 | 22 | 16 | - |
| Ba | 472 | 463 | 772 | 925 | 802 | - |
| La | 53 | 63 | 45 | 60 | 47 | - |
| Ce | 102 | 120 | 84 | 107 | 88 | - |
| Pr | 10.4 | 12.4 | 8.5 | 11.1 | 9.6 | - |
| Nd | 38 | 43 | 33 | 42 | 35 | - |
| Sm | 7.1 | 7.7 | 7.1 | 7.7 | 7.3 | - |
| Eu | 0.5 | 0.8 | 1.4 | 1.5 | 1.4 | - |
| Gd | 5.0 | 6.5 | 4.6 | 5.4 | 5.2 | - |
| Dy | 4.9 | 5.5 | 3.3 | 4.6 | 3.6 | - |
| Er | 3.3 | 3.5 | 1.9 | 2.1 | 1.8 | - |
| Yb | 3.8 | 3.4 | 1.8 | 2.5 | 1.8 | - |
| Lu | 0.46 | 0.51 | 0.28 | 0.33 | 0.28 | - |
| Ta | 2.4 | 2.4 | 0.8 | 1.2 | 0.9 | - |
| Pb | 30.2 | 33.8 | 18.9 | 25.2 | 18.6 | - |
| Th | 46.3 | 46.4 | 17.4 | 26.7 | 18.2 | - |
| U | 14.1 | 14.0 | 5.4 | 8.1 | 5.8 | - |

Table 3.14: Representative major, minor and trace element data form explosively erupted glasses produced during the Casa Lentia, TGR and Monte Saraceno eruptions. Full data sets are available in appendix eII.

Due to limited analyses glass compositions were homogeneous with 53.9 ± 0.4 wt.% SiO₂, 0.7 ± 0.1 wt.% TiO₂; 16.3 ± 0.1 wt.% Al₂O₃, 8.8 ± 0.2 wt.% FeO, 4.0 ± 0.1 wt. % MgO, 7.9 ± 0.1 wt.% CaO, 3.8 ± 0.1 wt. % Na₂O and 4.4 ± 0.1 wt.% K₂O (Fig. 3.29). These glasses are classified as basaltic-trachy-andesites and show a high K-series affinity (Fig. 3.20). A single trace element analysis reveal that the glasses are poorly

evolved ($Zr/Sr = 0.10$) and show LREE enrichment relative to the HREE ($La/Yb = 25$). Trace element concentrations are given in Table 3.14.

3.4.4.4 TGR scoria

Representative major, minor and trace elements of the scoria are given in Table 3.14. Glass compositions of the scoria are high-K silica and range from basaltic trachyandesite to trachyte (Fig. 3.20). Major and minor element are variable with 53.5-57.4 wt.% SiO_2 , 8.1-5.0 wt.% CaO and 4.3-5.9 wt.% K_2O (Fig. 3.29). Using increasing SiO_2 as a fractionation index, major and minor elements respond with increasing Al_2O_3 , Na_2O and K_2O ; decreasing TiO_2 , FeO (Fig. 3.16), MnO , MgO and CaO . Glasses are poorly evolved ($Zr/Sr = 0.1 \pm 0.02$) but with the variability of trachy-andesites to the trachytes trace element concentrations display significant variability as shown by 143-209 ppm Rb, 117-167 ppm Zr, 16-23 ppm Nb, 45-60 ppm La and 17-27 ppm Th (Fig. 3.31). The primitive mantle normalised diagram (Fig. 3.21b) illustrates LREE enriched relative to the HREE ($La/Yb = 25 \pm 2$). Increasing fractionation sees a reduction in Sr concentrations (950-1253 ppm Sr), whilst Ba continues to increase (772-1253 ppm Ba). Incompatible elements have a positive linear relationship (Fig. 3.31) and show constant ratios of HFSE/Th (Fig. 3.31).

3.4.4.5 La Fossa

Explosive deposits from La Fossa activity are given in Todman (2012) and incorporated into this data set for comparisons with other Vulcano and Aeolian Island deposits. The Palizzi deposits reported herein correspond to the Palizzi 2 succession of Dellino et al. (2011). Full geochemical descriptions of these tephra are outlined in Todman (2012), below is a brief summary of the chemical features of these eruptive units. Representative data for these eruptions are given in Table 3.15; whilst full data can be found in the appendix in Todman (2012).

Palizzi A; Glasses display compositions that are transitional between tephri-phonolite, trachy-andesite and phonolite (Fig. 3.20, 3.29). Glasses display only moderate levels of trace element enrichment ($Zr/Sr = 0.2 \pm 0.03$) (Fig. 3.21b) and are relatively homogeneous.

Palizzi B; These pumice fall deposits are rhyolitic in composition (70.6-74.2 wt.% SiO₂) and have a shoshonitic affinity (5.8-8.0 wt.% K₂O) (Fig. 3.20). These glasses are highly evolved (Zr/Sr = 1.2-4.9; Eu/Eu*_N = 0.2) and display LREE enrichment relative to the HFSE (La/Yb = 18-28) (Fig. 3.21a)

Palizzi D; This pumice fall deposit is trachytic in composition (60.6 ± 0.6 wt.% SiO₂) and glasses display a high-K-affinity (7.9 ± 0.2 wt.% K₂O) (Fig. 3.16). Glasses are moderately evolved (Zr/Sr = 0.2-0.4) and display LREE enrichment relative to the HREE (La/Yb = 16-30) (Fig. 3.21b, 3.24b).

| Eruption | Palizzi A | Palizzi B | Palizzi D | Commenda Ash | Pietre Cotte | |
|--------------------------------------|-------------|--------------|-----------------|--------------|--------------|------------|
| Locality | | | | | | |
| | S77-tot.5.1 | GRVULC46.3.1 | S33,90-110.3.g2 | CA5.1 | AT1.w.2.2 | S90ca.7.i1 |
| Sample Material | scoria | pumice | pumice | ash | pumice | pumice |
| Major (wt. %) | | | | | | |
| SiO ₂ | 56.66 | 73.15 | 60.08 | 61.21 | 71.75 | 59.72 |
| TiO ₂ | 0.64 | 0.11 | 0.59 | 0.56 | 0.19 | 0.60 |
| Al ₂ O ₃ | 18.24 | 13.68 | 18.72 | 17.55 | 14.28 | 17.52 |
| FeOt | 6.68 | 2.12 | 4.43 | 4.73 | 2.29 | 5.91 |
| MnO | 0.15 | 0.09 | 0.14 | 0.16 | 0.07 | 0.18 |
| MgO | 1.83 | 0.10 | 1.05 | 1.11 | 0.20 | 1.18 |
| CaO | 4.08 | 0.78 | 2.43 | 2.78 | 0.87 | 2.96 |
| Na ₂ O | 4.62 | 3.55 | 4.82 | 4.77 | 3.87 | 4.61 |
| K ₂ O | 7.11 | 6.42 | 7.92 | 7.13 | 6.48 | 7.32 |
| Analytical Total | 97.62 | 95.20 | 99.37 | 98.28 | 97.23 | 98.05 |
| Na ₂ O + K ₂ O | 11.73 | 9.98 | 12.74 | 11.90 | 10.35 | 11.93 |
| K ₂ O/Na ₂ O | 1.54 | 1.81 | 1.64 | 1.49 | 1.67 | 1.59 |
| Trace | | | | | | |
| ppm | | | | | | |
| V | | | | | | |
| Rb | 234 | 281 | 247 | 263 | 414 | 264 |
| Sr | 851 | 161 | 889 | 768 | 87 | 655 |
| Y | 18 | 39 | 19 | 22 | 40 | 21 |
| Zr | 189 | 203 | 199 | 264 | 297 | 233 |
| Nb | 28 | 38 | 29 | 31 | 46 | 32 |
| Ba | 1178 | 245 | 1949 | 1020 | 111 | 1059 |
| La | 67 | 80 | 64 | 76 | 96 | 71 |
| Ce | 122 | 149 | 108 | 137 | 179 | 130 |
| Pr | 12.4 | 14.7 | 10.8 | 13.3 | 17.4 | 12.3 |
| Nd | 43 | 52 | 37 | 45 | 62 | 43 |
| Sm | 7.6 | 9.3 | 6.6 | 7.7 | 9.8 | 8.5 |
| Eu | 1.6 | 0.6 | 1.3 | 1.3 | 0.5 | 1.4 |
| Gd | 5.4 | 6.6 | 5.9 | 5.2 | 7.3 | 5.9 |
| Dy | 3.7 | 6.5 | 3.5 | 4.1 | 6.2 | 3.7 |
| Er | 1.9 | 4.0 | 2.0 | 2.3 | 4.0 | 2.3 |
| Yb | 2.2 | 4.6 | 2.3 | 2.4 | 4.3 | 2.4 |
| Lu | 0.38 | 0.64 | 0.40 | 0.36 | 0.65 | 0.38 |
| Ta | 1.6 | 2.5 | 1.7 | 1.8 | 2.5 | 2.1 |
| Pb | 30.6 | 33.4 | 33.9 | 35.3 | 33.5 | 32.4 |
| Th | 30.6 | 57.3 | 30.3 | 39.2 | 60.5 | 34.4 |
| U | 10.0 | 16.1 | 10.4 | 12.2 | 19.8 | 10.9 |

Table 3.15: Representative major, minor and trace element glass data for glasses explosively produced by La Fossa, Vulcano during the last 5.5 ka. Full data can be found in Todman (2012). Data presented here is for comparisons with older Vulcano glasses and other Aeolian Island activity.

Commenda Ash; The varicoloured Commenda ash, also termed the Caruggi by Dellino et al., (2011) contains K-series trachytic glasses (61.0 ± 0.3 wt.% SiO_2 and 7.1 ± 0.1 wt.% K_2O) (Fig. 3.20; 3.29). Glasses are moderately evolved ($\text{Zr}/\text{Sr} = 0.3\text{-}0.4$) and display LREE enrichment relative to the HREE ($\text{La}/\text{Yb} = 31 \pm 2$) (Fig. 3.24b).

Pietre Cotte; Banded pumices from the upper Pietre Cotte are bimodal, comprising homogeneous K-series trachytes (59.3 ± 0.6 wt.% SiO_2 , 6.2 ± 0.1 wt.% K_2O) and trachytic-rhyolitic glasses ($65.8\text{-}73.2$ wt.% SiO_2 , $6.1\text{-}7.0$ wt.% K_2O) (Fig. 3.20). Trace element analysis of the white trachytic to rhyolitic glasses reveal moderate to highly evolved composition ($\text{Zr}/\text{Sr} = 0.5\text{-}3.4$) and glasses display significant LREE enrichment relative to the HREE ($\text{La}/\text{Yb} = 23\text{-}36$) (Fig. 3.21b). Upper Pietre Cotte ash contains K-series trachyte glasses (59.8 wt.% SiO_2 , $6.9\text{-}7.4$ wt.% K_2O) (Fig. 3.20). Glasses display moderate levels of evolution ($\text{Zr}/\text{Sr} = 0.4$) and LREE enrichment relative to the HREE ($\text{La}/\text{Yb} = 30 \pm 2$).

3.4.5 Stromboli

3.4.5.1 Upper Vancori

The Upper Vancori glasses are trachytes ($63.2\text{-}65.4$ wt.% SiO_2) and display a shoshonitic affinity ($5.3\text{-}5.8$ wt.% K_2O) (Fig. 3.20; Table 3.16). The lower most pumices (unit 1) are homogenous displaying $64.7\text{-}65.4$ wt.% SiO_2 , $3.9\text{-}4.4$ wt.% FeO , $0.8\text{-}0.9$ wt.% MgO , $2.3\text{-}2.6$ wt.% CaO , $4.3\text{-}4.9$ wt.% Na_2O and $5.4\text{-}5.8$ wt.% K_2O (Fig. 3.29). Trace element concentrations in the lower pumices are moderately evolved ($\text{Zr}/\text{Sr} = 1.1 \pm 0.1$) and display LREE enrichment relative to the HREE ($\text{La}/\text{Yb} = 18.9 \pm 1.3$) (Fig. 3.21b). Trace element concentrations are particularly homogeneous with 21 ± 1 ppm V, 182 ± 8 ppm Rb, 274 ± 73 ppm Sr, 29 ± 2 ppm Y, 296 ± 19 ppm Zr, 37 ± 2 ppm Nb, 1381 ± 132 ppm Ba, 59 ± 2 La and 30 ± 3 ppm Th (Fig. 3.31, 3.32). HFSE/Th ratios are constant within these glasses ($\text{Nb}/\text{Th} = 1.22 \pm 0.07$; $\text{Zr}/\text{Th} = 9.7 \pm 0.2$).

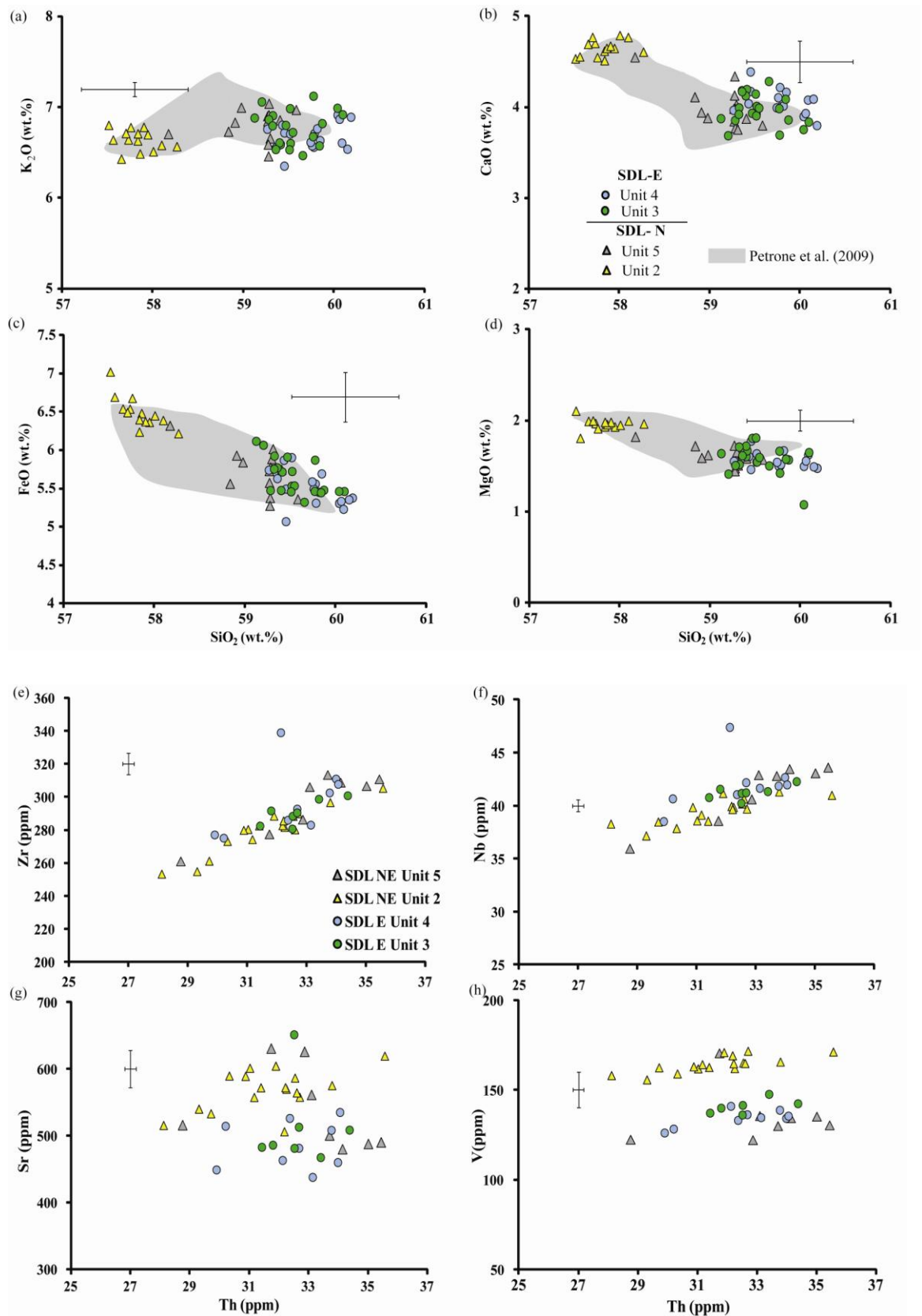


Figure 3.34: Secche di Lazzaro, Stromboli glass compositions (a-d) major element concentrations; (e-h) trace element concentrations. Demonstrating the stratigraphic variation at SDL-N locality. (See Fig.3.5; Table 3.5).

The upper most pumices (unit 3) are of equally homogeneous compositions with 63.2-64.3 wt.% SiO₂, 4.2-5.1 wt.% FeO, 1.1-1.2 wt.% MgO, 2.9-3.2 wt.% CaO, 4.4-4.9 wt.% Na₂O and 5.3-5.5 wt.% K₂O (Fig. 3.29; Table 3.16). The trace element compositions are again homogeneous within these pumices shown by 49 ± 3 ppm V, 197 ± 8 ppm Rb, 366 ± 111 ppm Sr, 31 ± 2 ppm Y, 311 ± 19 ppm Zr, 1541 ± 97 ppm Ba, 65 ± 4 ppm La and 32 ± 3 ppm Th (Fig. 3.31; 3.32). HFSE/Th ratios are constant (Nb/Th = 1.21 ± 0.06 ; Zr/Th = 9.7 ± 0.3).

| Eruption Locality Unit Sample Material | Upper Vancori Eastern Stromboli | | | | | |
|--|------------------------------------|-------------------|---------------|--------------|-------------------|---------------|
| | 1A pumice | 1 7B pumice | 10B pumice | 1A pumice | 3 6B pumice | 14C pumice |
| Major (wt. %) | | | | | | |
| SiO ₂ | 65.21 | 64.80 | 65.41 | 63.59 | 63.68 | 63.22 |
| TiO ₂ | 0.79 | 0.75 | 0.73 | 0.80 | 0.72 | 0.86 |
| Al ₂ O ₃ | 16.32 | 16.57 | 16.25 | 16.92 | 16.93 | 16.42 |
| FeOt | 4.39 | 4.12 | 4.14 | 4.52 | 4.51 | 5.11 |
| MnO | 0.13 | 0.07 | 0.02 | 0.14 | 0.22 | 0.16 |
| MgO | 0.84 | 0.88 | 0.89 | 1.15 | 1.20 | 1.21 |
| CaO | 2.34 | 2.51 | 2.44 | 3.00 | 2.97 | 3.14 |
| Na ₂ O | 4.40 | 4.85 | 4.48 | 4.53 | 4.41 | 4.41 |
| K ₂ O | 5.59 | 5.45 | 5.64 | 5.35 | 5.36 | 5.47 |
| Analytical Total | 99.37 | 99.51 | 98.98 | 98.38 | 97.97 | 96.81 |
| Na ₂ O + K ₂ O | 9.98 | 10.31 | 10.13 | 9.87 | 9.77 | 9.88 |
| K ₂ O/Na ₂ O | 1.27 | 1.12 | 1.26 | 1.18 | 1.22 | 1.24 |
| Trace ppm | | | | | | |
| V | 21 | 21 | 19 | 48 | 52 | 45 |
| Rb | 180 | 183 | 180 | 200 | 199 | 183 |
| Sr | 349 | 297 | 230 | 281 | 334 | 557 |
| Y | 29 | 30 | 27 | 30 | 33 | 29 |
| Zr | 297 | 306 | 273 | 289 | 326 | 292 |
| Nb | 37 | 38 | 35 | 39 | 41 | 35 |
| Ba | 1446 | 1418 | 1235 | 1396 | 1541 | 1667 |
| La | 59 | 61 | 55 | 60 | 67 | 61 |
| Ce | 99 | 111 | 113 | 113 | 129 | 115 |
| Pr | 11.3 | 11.9 | 11.2 | 11.6 | 13.6 | 11.9 |
| Nd | 42 | 44 | 41 | 42 | 53 | 42 |
| Sm | 7.4 | 8.3 | 6.8 | 9.4 | 8.8 | 7.5 |
| Eu | 1.8 | 1.7 | 1.4 | 1.6 | 1.8 | 1.8 |
| Gd | 6.4 | 5.9 | 4.8 | 6.6 | 8.1 | 7.6 |
| Dy | 4.9 | 5.4 | 5.1 | 5.4 | 6.5 | 5.4 |
| Er | 2.9 | 3.1 | 2.6 | 3.1 | 3.7 | 2.8 |
| Yb | 3.2 | 3.3 | 2.9 | 3.2 | 3.8 | 3.1 |
| Lu | 0.47 | 0.53 | 0.41 | 0.49 | 0.55 | 0.46 |
| Ta | 1.9 | 2.0 | 1.6 | 1.7 | 2.1 | 1.6 |
| Pb | 33.8 | 34.0 | 37.0 | 49.6 | 44.0 | 35.7 |
| Th | 31.1 | 33.0 | 27.5 | 29.7 | 35.2 | 29.6 |
| U | 8.6 | 8.9 | 8.0 | 8.7 | 9.7 | 8.3 |

Table 3.16: Representative major, minor and trace element glass data for the explosive deposits of the Upper Vancori eruption, Stromboli. Full data sets are available in appendix eII.

3.4.5.2 Secche di Lazzaro (SDL):

Semaforo Track (ST), Northern Stromboli

SDL glasses from vesicular green scoria in unit 2 on the Semaforo Track (Fig. 3.18), northern Stromboli, are K-series trachy-andesites (57.5-58.3 wt.% SiO₂, 6.4-6.8 wt.% K₂O) (Fig. 3.20, 3.29; Table 3.17)). The glasses in this unit are homogeneous with only the following variability 1.0-1.2 wt.% TiO₂, 6.2-7.0 wt.% FeO, 1.8-2.1 wt.% MgO, 4.5-4.8 wt.% CaO, 3.3-3.6 wt.% Na₂O (Fig. 3.34). The glasses are moderately evolved (Zr/Sr = 0.5) with LREE enrichment relative to the HREE (La/Yb = 25 ± 1). Trace element concentrations within the glasses are equally homogeneous with 164 ± 5 ppm V, 275 ± 8 ppm Rb, 568 ± 31 ppm Sr, 27 ± 2 ppm Y, 280 ± 14 ppm Zr, 40 ± 1 ppm Nb, 2125 ± 88 ppm Ba, 64 ± 3 La, 32 ± 2 ppm Th (Fig. 3.34e-h). HFSE/Th ratios remain constant within these glasses (Nb/Th = 1.25 ± 0.04, Zr/Th = 8.9 ± 0.2).

Towards the top of the sequence, unit 5 contains predominantly light grey pumices. These pumices range from K-series trachy-andesites to trachytes (58.2-59.6 wt.% SiO₂, 6.5-7.0 wt.% K₂O) (Fig. 3.34; Table 3.17). Glasses display more major element variation with 0.8-1.1 wt.% TiO₂, 17.5-18.4 wt.% Al₂O₃, 5.3-6.3 wt.% FeO, 1.4-1.8 wt.% MgO, 3.8-4.6 wt.% CaO, 3.3-4.0 wt.% Na₂O (Fig. 3.21). The glasses are moderately evolved (Zr/Sr = 0.6) and display LREE enrichment relative to the HREE (La/Yb = 23 ± 2). Trace element concentrations within these glasses are homogeneous reflected by 135 ± 14 ppm V, 277 ± 16 ppm Rb, 536 ± 58 ppm Sr, 28 ± 2 ppm Y, 296 ± 18 ppm Zr, 41 ± 3 ppm Nb, 2298 ± 90 ppm Ba, 67 ± 4 ppm La and 33 ± 2 ppm Th (Fig. 3.34e-h). HFSE/Th ratios are constant within these glasses (Nb/Th = 1.3 ± 0.03, Zr/Th = 9.0 ± 0.2).

Advanced Operative Centre (COA)

Grey pumices in unit 3 are K-series trachytes (59.1-60.1 wt.% SiO₂, 6.5-7.1 wt.% K₂O). The glasses are homogeneous with 0.8-1.1 wt.% TiO₂, 17.1-18.4 wt.% Al₂O₃, 5.3-6.1 wt.% FeO, 1.1-1.8 wt.% MgO, 3.7-4.3 wt.% CaO and 3.4-4.0 wt.% Na₂O (Fig. 3.21; Table 3.17). The glasses are moderately evolved (Zr/Sr = 0.6) and have LREE enrichment relative to the HREE (La/Yb = 23 ± 1). The glasses are particularly homogeneous with 141 ± 4 ppm V, 276 ± 9 ppm Rb, 513 ± 69 ppm Sr, 28 ± 1 ppm Y, 291 ± 8 ppm Zr, 41 ± 1 ppm Nb, 2196 ± 100 ppm Ba, 64 ± 2 ppm La and 33 ± 1 ppm Th (Fig. 3.34). HFSE/Th ratios are constant within these glasses (Nb/Th = 1.3 ± 0.1; Zr/Th = 9.2 ± 0.6, 0.07).

Grey pumices sampled in unit 4 are again K-series trachytes (59.1-60.2 wt.% SiO₂, 6.4-7.1 wt.% K₂O). The glasses are homogeneous with 0.9-1.1 wt.% TiO₂, 17.1-18.4 wt.% Al₂O₃, 5.1-6.1 wt.% FeO, 1.1-1.8 wt.% MgO, 3.7-4.4 wt.% CaO, 3.4-4.1 wt.% Na₂O (Fig. 3.34a-d; Table 3.17). The glasses are moderately evolved (Zr/Sr = 0.6) and display LREE enrichment relative to the HREE (La/Yb = 23 ± 2). Trace element concentrations are equally homogeneous with 134 ± 5 ppm V, 276 ± 8 ppm Rb, 486 ± 36 ppm Sr, 27 ± 2 ppm Y, 297 ± 20 ppm Zr, 42 ± 2 ppm Nb, 2132 ± 132 ppm Ba, 63 ± 6 ppm La and 32 ± 2 ppm Th (Fig. 3.34e-h). HFSE/Th ratios are constant within these glasses with Nb/Th = 1.3 ± 0.1, Zr/Th = 9.2 ± 0.6).

| Eruption Locality Unit Sample Material | Secche di Lazzaro | | | | | | | |
|--|-----------------------|---------------|--------------|--------------|--------------|--------------|---------------|---------------|
| | Semaforo track SDL-NE | | | | COA SDL-E | | | |
| | 2 | | 5 | | 3 | | 4 | |
| | 4A scoria | 14C scoria | 2A pumice | 5A pumice | 3A pumice | 5A pumice | 12C pumice | 15C pumice |
| Major (wt. %) | | | | | | | | |
| SiO ₂ | 57.65 | 58.01 | 59.28 | 58.98 | 59.87 | 59.36 | 59.27 | 59.78 |
| TiO ₂ | 1.01 | 1.05 | 0.99 | 1.00 | 0.89 | 0.97 | 0.98 | 0.96 |
| Al ₂ O ₃ | 17.83 | 17.71 | 17.61 | 17.70 | 17.58 | 17.66 | 17.72 | 17.73 |
| FeO _t | 6.54 | 6.45 | 5.78 | 5.84 | 5.48 | 5.77 | 5.74 | 5.56 |
| MnO | 0.23 | 0.24 | 0.07 | 0.15 | 0.14 | 0.18 | 0.15 | 0.19 |
| MgO | 1.99 | 1.95 | 1.60 | 1.62 | 1.57 | 1.62 | 1.56 | 1.51 |
| CaO | 4.69 | 4.79 | 3.77 | 3.88 | 3.86 | 4.17 | 3.97 | 4.22 |
| Na ₂ O | 3.62 | 3.28 | 3.85 | 3.83 | 3.78 | 3.72 | 3.85 | 3.48 |
| K ₂ O | 6.44 | 6.52 | 7.04 | 7.00 | 6.83 | 6.54 | 6.76 | 6.57 |
| Analytical Total | 99.19 | 98.89 | 98.88 | 98.69 | 98.02 | 98.14 | 98.45 | 98.40 |
| Na ₂ O + K ₂ O | 10.05 | 9.80 | 10.89 | 10.83 | 10.60 | 10.26 | 10.62 | 10.04 |
| K ₂ O/Na ₂ O | 1.78 | 1.99 | 1.83 | 1.83 | 1.81 | 1.76 | 1.75 | 1.89 |
| Trace ppm | | | | | | | | |
| V | 163 | 166 | 130 | 131 | 136 | 142 | 133 | 139 |
| Rb | 280 | 270 | 291 | 289 | 259 | 274 | 270 | 276 |
| Sr | 533 | 575 | 500 | 490 | 651 | 481 | 526 | 508 |
| Y | 25 | 29 | 30 | 29 | 27 | 27 | 27 | 28 |
| Zr | 261 | 297 | 314 | 311 | 281 | 289 | 286 | 303 |
| Nb | 38 | 41 | 43 | 44 | 40 | 41 | 41 | 42 |
| Ba | 2011 | 2228 | 2367 | 2307 | 2327 | 2194 | 2302 | 2282 |
| La | 60 | 66 | 68 | 70 | 63 | 65 | 64 | 65 |
| Ce | 122 | 131 | 133 | 133 | 124 | 128 | 124 | 132 |
| Pr | 12.8 | 14.1 | 13.9 | 14.4 | 13.2 | 13.9 | 13.4 | 13.9 |
| Nd | 48 | 55 | 54 | 56 | 50 | 51 | 50 | 51 |
| Sm | 9.6 | 9.8 | 10.4 | 9.8 | 9.1 | 8.9 | 9.1 | 9.3 |
| Eu | 1.9 | 2.2 | 2.1 | 2.1 | 2.1 | 2.0 | 2.1 | 2.0 |
| Gd | 6.6 | 7.4 | 7.8 | 7.8 | 7.0 | 6.7 | 6.6 | 7.0 |
| Dy | 5.2 | 5.6 | 5.0 | 5.8 | 5.0 | 5.1 | 5.2 | 5.7 |
| Er | 2.6 | 3.0 | 3.1 | 3.1 | 2.9 | 2.8 | 2.9 | 2.9 |
| Yb | 2.4 | 2.6 | 3.0 | 3.0 | 2.9 | 2.7 | 2.9 | 3.1 |
| Lu | 0.39 | 0.39 | 0.49 | 0.46 | 0.44 | 0.42 | 0.43 | 0.39 |
| Ta | 1.9 | 2.1 | 2.1 | 2.1 | 2.0 | 2.3 | 2.1 | 2.3 |
| Pb | 48.3 | 42.2 | 43.9 | 48.9 | 41.1 | 41.6 | 42.4 | 40.9 |
| Th | 29.7 | 33.8 | 33.7 | 35.4 | 32.5 | 32.5 | 32.4 | 33.8 |
| U | 9.5 | 10.3 | 10.6 | 10.6 | 10.0 | 10.5 | 10.1 | 10.5 |

Table 3.17: Representative major, minor and trace element glass data from the explosive products of the Secche di Lazzaro eruption, Stromboli. Full data sets are available in appendix eII.

3.5 Discussion: Tephrochronological implications

3.5.1 Lipari proximal explosive deposits

During the last 42 ka Lipari has produced HKCA trachytes to high-SiO₂ rhyolite glass compositions (i.e., 67.9-76.8 wt.% SiO₂ and 4.9-6.4 wt.% K₂O (Fig. 3.20)). The high SiO₂ rhyolites are dominant during this period (i.e., 74-76 wt. %). Consequently, distinguishing distal tephra sourcing from Lipari from other Aeolian Island sources is fairly straight forward, particularly given that their incompatible trace element profiles are distinctive, dominated by dramatic anomalies at Ba, Sr and Eu (Fig. 3.21). However, Lipari products erupted during the last 42 ka show very little major element compositional variability through time (Fig. 3.22). This feature has been noted previously based on whole rock analyses of the deposits (Gioncada et al., 2003). Statistical distance tests comparing the glass compositions of the Lipari explosive deposits erupted during the last 42 ka (Table 3.18) demonstrate that these products are largely indistinguishable at a multi-element level. Explosive volcanic activity on Lipari is a classic example of near identical glass (i.e., magmas) being produced by a single volcanic centre over significant period of time (42 ka). This is highly problematic for distal tephrochronology. Proximal geochemical signatures for the main explosive eruptions during the last 42 ka are used to identify any diagnostic features that can help to distinguish these deposits.

3.5.1.1 Cycle VII- P.del Perciato and Falcone Formations

The oldest explosive HKCA products of Lipari and cycle VII, the P.del Perciato (*pe2 member*) is dated to 42 ± 3 ka (Crisci et al., 1981), these explosive deposits are particularly homogeneous rhyolitic white pumices (Fig. 3.20). These older explosive deposits are separated by a brown tuff accumulation from the younger cycle VII Falcone formation (Fig. 3.7). The main distinguishing feature between glass chemistry of these two deposits is the compositional variability observed in the glasses of the Falcone formation, with trachytic to rhyolitic compositions (Fig. 3.20; 3.22). At a trace element level the two deposits are statistically indistinguishable ($D^2 = 0.3$; Table 3.18). Concentrations of Ba, Sr and Eu are equally low in the P. del Perciato and Falcone rhyolites, a response to K-feldspar fractionation (Table 3.6). The Falcone glasses do present subtly more elevated La (Fig. 3.23b) and Ce (Fig. 3.23c) concentrations than those seen in the older P.del Perciato formation pumices. Overall the most evolved (> 75 wt.% SiO₂) glasses are characterised by limited ranges in incompatible trace element

concentrations. A single analysis of the least evolved trachytic end-member of the Falcone formation reveals higher LREE and Zr concentrations, a feature highlighted by Gioncada et al. (2003) based on their WR analyses of the less evolved products of Lipari during the last 42 ka. The presence of the less evolved compositions in the Falcone formation is not only a diagnostic feature of this older Lipari explosive volcanism, but provides insights into the less evolved melt compositions produced at Lipari and indicates that the elements mentioned might to a degree be behaving compatibly.

The Falcone formation presents clear evidence of magma mixing, with the presence of two glass components, a trachy-rhyolite and a rhyolite. It is plausible that the injection of a less evolved magma into a high level rhyolite body triggered explosive activity, envisaging a similar scenario to more recent activity on the island (De Rosa et al., 2003a).

The oldest confirmed Lipari HKCA rhyolitic tephra layer in the Tyrrhenian Sea marine record (KET8003) is reported by Paterne et al., (1988) and is termed the E-11. It is stratigraphically just above the Campanian Ignimbrite (Y-5/C-13) and is dated to 37.7 ka (Paterne et al., 1988). A similar scenario is observed in the southern Adriatic marine core SA-03-11, where again a HKCA rhyolitic tephra is observed just above the Y-5 (Matthews 2012 *pers comm.*). The P.del Perciato formation is dated at 42 ± 3 ka (Crisci et al., 1991) and as such predates the wide spread Campanian Ignimbrite (39.28 ± 0.11 ka BP; De Vivo et al., 2001). Consequently, the HKCA rhyolitic P.del Perciato formation is less likely to be the proximal correlative of the E-11, although, proximal and distal ages do just overlap with error. Given proximal stratigraphic super position, the younger Falcone formation may present a better correlative for the E-11 tephra since the brown tuff separating the Falcone and P.dei Perciato Formations must represent a period of local quiescence on Lipari (Fig. 3.7). Whilst determining detailed geochemistry for the distal E-11 ash might provide a useful insight into precise proximal-distal links, geochemically separating these two older rhyolitic eruptions of Lipari is difficult and dependant on geochemical variability being recorded distally (above). The use of these eruptions as distal stratigraphic markers is not precluded by their indistinguishable glass chemistries, since their position relative to the Campanian Ignimbrite provides a stratigraphic constraint.

| Deposit | M.P Stromboli | M.P Vulcanello | M. Pilato 2 | M. Pilato 1 | Gabellotto-Fiume | M. Guardia | Falcone Form | P.del Perciato |
|------------------|----------------------------------|----------------|-------------|-------------|------------------|------------|--------------|----------------|
| | Trace elements D2 values; f = 10 | | | | | | | |
| M.P Stromboli | 0.0 | 0.2 | 8.8 | 21.1 | 28.2 | 5.6 | 305.8 | 2.4 |
| M.P Vulcanello | 0.5 | 0.0 | 3.6 | 9.7 | 11.3 | 5.6 | 117.3 | 2.4 |
| M. Pilato 2 | 3.7 | 3.8 | 0.0 | 6.9 | 14.2 | 4.4 | 228.6 | 1.9 |
| M. Pilato 1 | 4.0 | 4.1 | 1.4 | 0.0 | 3.0 | 2.9 | 149.5 | 1.3 |
| Gabellotto-Fiume | 1.3 | 1.4 | 1.4 | 3.4 | 0.0 | 2.9 | 206.3 | 1.4 |
| M. Guardia | 0.3 | 0.3 | 0.1 | 0.4 | 0.1 | 0.0 | 0.4 | 0.1 |
| Falcone Form | 0.7 | 0.6 | 0.7 | 1.1 | 0.5 | 0.2 | 0.0 | 0.3 |
| P. del Perciato | 59.0 | 46.0 | 30.2 | 13.8 | 36.1 | 1.3 | 1.6 | 0.0 |
| | Major elements D2 values; f = 8 | | | | | | | |

(a)

| | | |
|-----------------------------|------------------------|--|
| <i>p</i> (confidence limit) | $D^2_{critical}, f=8$ | |
| 0.995 | 1.344 | < 0.5 % probability that the two samples are compositionally different if D^2 is less than 1.344 |
| 0.990 | 1.646 | < 1% probability that the two samples are compositionally different if D^2 is less than 1.646 |
| 0.950 | 2.733 | < 5% probability that the two samples are compositionally different if D^2 is less than 2.733 |
| 0.050 | 15.507 | >95% probability that the two samples are compositionally different if D^2 is greater than 15.507 |
| 0.010 | 20.090 | >99% probability that the two samples are compositionally different if D^2 is greater than 20.090 |
| <i>p</i> (confidence limit) | $D^2_{critical}, f=10$ | |
| 0.995 | 2.156 | < 0.5 % probability that the two samples are compositionally different if D^2 is less than 2.156 |
| 0.990 | 2.558 | < 1% probability that the two samples are compositionally different if D^2 is less than 2.558 |
| 0.950 | 3.940 | < 5% probability that the two samples are compositionally different if D^2 is less than 3.940 |
| 0.050 | 18.307 | > 95% probability that the two samples are compositionally different if D^2 is greater than 18.307 |
| 0.010 | 23.209 | > 99% probability that the two samples are compositionally different if D^2 is greater than 23.209 |

(b)

Table 3.18: (a) Statistical distance values (D^2) matrix based on major, minor and trace element compositions of the explosive products associated with Lipari during the last 42 ka. (b) The *p* (confidence limits) values and the $D^2_{critical}$ values for the statistical distance, where $f = 8$ (major and minor elements) and $f = 10$ (trace elements).

3.5.1.2 Cycle VII- Monte Guardia

Stratigraphically the Falcone formation (*fal member*) is separated from more recent Monte Guardia (Cycle VIII) explosive activity by further brown tuff deposits (Fig. 3.7) and more significantly a palaeosol (Lucchi et al., 2010) indicative of a significant period of quiescence on the island. Monte Guardia has a maximum age of 26.3 ± 0.8 cal yrs BP (^{14}C 22, 600 ± 300 ; Crisci et al., 1983). This period of quiescence is important given the overall geochemical similarity observed between the glasses of the Monte Guardia and previous Falcone formation at both a major, minor ($D^2 = 0.3$) and trace ($D^2 = 0.4$) element level (Table 3.18).

Glasses from the basal Monte Guardia (MG) fall units display the most compositional variability reflecting the mixing of the grey and white pumices. These glasses display similar compositional variability to the Falcone formation stratigraphically below. The basal fall, unit 2a, displays the least evolved glass compositions observed in the entire sequence. At ca. 74 wt.% SiO_2 the K_2O contents reach the highest values produced on Lipari during the last 42 ka, whilst an inflection to lower K_2O contents at higher SiO_2 are a response to K-feldspar fractionation (Fig. 3.22a). The least evolved component is never exclusively present within the sampled Monte Guardia stratigraphy (Fig. 3.25). The full compositional variability of the eruption is seen throughout the fall deposits of unit 2 (Fig. 3.25). Within the surge deposits (unit 4), the white pumices and obsidian dominate the juveniles; these have the most evolved glass compositions with the lowest K_2O contents (Fig. 3.25). The chemostratigraphy (Fig. 3.25) for Monte Guardia supports the previous interpretations that the eruption represents the tapping a zoned magma system (De Rosa et al., 2003a). The fractionated magmas are inverted in the eruptive sequence, with the least evolved component only present in the earliest phase of the eruption (Fig. 3.25). Glasses investigated here are restricted to the rhyolitic compositional field; and the lowest SiO_2 compositions identified by De Rosa et al. (2003a) are not reproduced in this study.

Distinguishing the Monte Guardia (MG) glasses from the older P.del Perciato and Falcone formation glasses at a multi-element level is not statistically valid (Table 3.18). However diagnostic geochemical features are identified using major and trace element bi-plots;

(1) The least evolved MG glasses display higher K_2O than the Falcone formation glasses (Fig. 3.22a);

(2) The most evolved MG glasses (> 75 wt.% SiO_2) extend to much lower K_2O and higher Na_2O concentrations than the P.del Perciato and Falcone formation glasses (Fig. 3.22a,f).

(3) MG glasses have a much wider range in incompatible trace element concentrations, particularly well illustrated by the range in Th (Fig 3.23).

(4) Linked to lower K_2O in the MG glasses and K-feldspar fractionation, the MG glasses display lower Rb concentrations at a given Th than the P.del Perciato and Falcone formations (Fig. 23e).

3.5.1.3 Cycle IX- Gabelotto-Fiume Bianco

Following the Monte Guardia eruption (Cycle VIII Lipari) it is broadly considered that proximally there was a period of quiescence on Lipari before the onset of cycle IX activity and the movement of activity NE towards the Gabelotto centre. Lucchi et al. (2010) recognised small localised deposits associated with the Canneto dentro formation and also the *l2* layer both showing HKCA rhyolitic compositions stratigraphically between the Monte Guardia eruption and the Gabelotto-Fiume Bianco. These deposits are poorly constrained temporally between ~ 26.3 cal ka BP and ~ 8.5 cal ka BP, using ages from underlying Monte Guardia and the overlying Gabelotto-Fiume bianco eruptions. The proximal Gabelotto-Fiume Bianco (GFB) is dated to 7170 ± 720 yrs BP (Bigazzi et al., 2003), although the most widely accepted age is 8730–8400 cal yrs BP (^{14}C 7770 ± 70 yrs BP) based on its correlation to the E-1 marine tephra in the early Holocene Sapropel 1 sediments of the southern Adriatic (Siani et al., 2004). The GFB deposits are dominated by surge deposits (Fig. 3.9) and these homogeneous HKCA rhyolites display no stratigraphic geochemical variability (Fig 3.22).

GFB rhyolitic glasses are easily distinguished from the most evolved MG glasses given their consistently lower SiO_2 contents, whilst not presenting evidence of a less evolved mixing component (Fig. 3.22). Where SiO_2 concentrations do overlap with MG glasses the MG glasses have more elevated K_2O (Fig. 3.22a). Trace element distinctions are more precise, the GFB rhyolites display significantly more elevated concentrations of LREE, Zr and Th than the earlier rhyolitic activity on the island (Fig. 3.23).

3.5.1.4 Cycle X- Monte Pilato

HKCA rhyolitic GFB activity on Lipari is separated from the most recent explosive HKCA rhyolitic activity at Monte Pilato 776 cal AD (^{14}C 1241 \pm 31 yrs BP; Keller (2002)) by a palaeosol. Monte Pilato activity erupts glasses that are largely indistinguishable from the Gabellotto-Fiume Bianco (GFB) at a major element level (Table 3.18).

Two sub-phases of explosive Monte Pilato activity were recognised at M. St Angelo, Lipari (Fig. 3.10) and geochemically this is reflected in stratigraphic variation in the Monte Pilato fall. Monte Pilato 1 lower (MP1) fall comprises higher SiO_2 group than the Monte Pilato 2 upper (MP2) pumices. At a trace element level, MP1 lower pumices show lower incompatible trace element concentrations than the MP2 upper pumices. Trace element compositions in the MP1 lower pumices and the GFB glasses are indistinguishable ($D^2 = 3$). Any geochemical distinction between the GFB pumices and the MP1 lower pumices is only possible through identification of subtly elevated silica in MP 1 glasses, which is problematic given the associated errors with SiO_2 (Fig. 3.22). The MP2 upper glasses display identical SiO_2 to the older GFB glasses and are indistinguishable at a major element level ($D^2 = 1.4$). However these MP2 glasses can be distinguished from those of the GFB. They display more elevated incompatible trace element concentrations than the GFB glasses (Fig. 3.23) and this reflected in greater statistical distance, $D^2 = 14.2$ (Table 3.18). Overall the geochemical variability observed within the entire Monte Pilato eruptive sequence is far greater than that seen in the GFB stratigraphy. Incompatible trace element concentrations in the Monte Pilato glasses extend to significantly higher concentrations than the GFB.

In summary;

- (1) The most recent rhyolitic activity on Lipari, the Gabellotto-Fiume Bianco and Monte Pilato can be distinguished from older southern Lipari explosive cycles VII and VIII on the basis of more elevated LREE, Zr and Th concentrations (Fig. 3.23).
- (2) Monte Pilato can be distinguished from Gabellotto-Fiume bianco where glasses extend to higher incompatible trace element concentrations than those seen in the more homogeneous Gabellotto-Fiume Bianco.

3.5.1.5 Distal Lipari deposits in the Aeolian Islands and the central Mediterranean

Given the explosive origin and highly evolved compositions of the Lipari rhyolites ($\text{SiO}_2 > 70$ wt.%; $\text{Zr}/\text{Sr} = > 10$) it is unsurprising that these deposits outcrop externally elsewhere in the Aeolian Islands (Keller 1980b, Morche, 1988, Lucchi et al., 2008; 2010). Some of these occurrences are examined. Where stratigraphically well-constrained these deposits provide further data for individual eruptions helping to constrain the ash dispersal axes, important for proximal distal links. Where mid-distal deposits in the Aeolian Islands are stratigraphically less well constrained they provide a test bed for proximal geochemical data sets.

| Deposit Locality | Monte Guardia Nr Gelso, Vulcano | | | Monte Guardia Drauto Panarea | | EL4 | | Milazzo pumice Capo Milazzo | |
|--|------------------------------------|---------------|--------------|---------------------------------|------------|--------------|--------------|--------------------------------|---------------|
| | pumice 2A | pumice 11C | pumice 6B | Ash 15C | Ash 10B | pumice 2A | pumice 5A | pumice 18D | pumice 20D |
| Sample Material | | | | | | | | | |
| Major (wt. %) | | | | | | | | | |
| SiO_2 | 76.17 | 76.36 | 76.27 | 76.33 | 76.19 | 63.70 | 63.36 | 57.74 | 62.50 |
| TiO_2 | 0.07 | 0.03 | 0.14 | 0.07 | 0.04 | 0.70 | 0.74 | 0.72 | 0.45 |
| Al_2O_3 | 12.75 | 12.72 | 12.55 | 12.65 | 12.68 | 17.35 | 17.17 | 17.83 | 17.66 |
| FeOt | 1.39 | 1.26 | 1.45 | 1.33 | 1.31 | 4.47 | 4.71 | 6.45 | 4.16 |
| MnO | 0.12 | 0.03 | 0.08 | 0.02 | 0.01 | 0.05 | 0.20 | 0.27 | 0.15 |
| MgO | 0.01 | 0.03 | 0.00 | 0.69 | 0.02 | 0.75 | 0.81 | 2.39 | 1.16 |
| CaO | 0.70 | 0.64 | 0.63 | 0.01 | 0.68 | 2.54 | 2.59 | 5.56 | 3.56 |
| Na_2O | 3.81 | 4.04 | 3.91 | 3.10 | 4.01 | 4.42 | 4.76 | 4.16 | 4.82 |
| K_2O | 4.97 | 4.89 | 4.96 | 5.80 | 5.05 | 6.01 | 5.66 | 4.89 | 5.55 |
| Analytical Total | 94.31 | 94.86 | 95.09 | 95.81 | 97.84 | 99.76 | 98.71 | 98.27 | 95.84 |
| $\text{Na}_2\text{O} + \text{K}_2\text{O}$ | 8.78 | 8.93 | 8.87 | 8.90 | 9.06 | 10.44 | 10.42 | 9.05 | 10.36 |
| $\text{K}_2\text{O}/\text{Na}_2\text{O}$ | 1.30 | 1.21 | 1.27 | 1.87 | 1.26 | 1.36 | 1.19 | 1.17 | 1.15 |
| Trace ppm | | | | | | | | | |
| V | - | - | - | - | - | 12.5 | 13.4 | - | - |
| Rb | 337 | 313 | 316 | 292 | 300 | 160 | 156 | 155 | 197 |
| Sr | 9.9 | 8.9 | 8.3 | 9.1 | 7.5 | 252 | 276 | 1200 | 872 |
| Y | 44 | 41 | 41 | 37 | 35 | 27 | 30 | 24 | 26 |
| Zr | 146 | 130 | 135 | 120 | 119 | 252 | 274 | 163 | 201 |
| Nb | 37 | 36 | 36 | 33 | 34 | 33 | 36 | 19 | 23 |
| Ba | 5.1 | 4.2 | 4.0 | 4.3 | 4.0 | 1170 | 1296 | 1018 | 944 |
| La | 42 | 36 | 37 | 35 | 33 | 59 | 63 | 52 | 57 |
| Ce | 85 | 80 | 81 | 77 | 72 | 110 | 121 | 100 | 109 |
| Pr | 10.0 | 9.3 | 9.2 | 8.9 | 8.2 | 11.4 | 12.5 | 10.6 | 11.4 |
| Nd | 38 | 30 | 35 | 32 | 30 | 39 | 47 | 41 | 44 |
| Sm | 7.9 | 8.5 | 8.0 | 7.3 | 7.3 | 6.8 | 9.4 | 7.4 | 7.3 |
| Eu | >LOD | 0.3 | 0.2 | < LOD | < LOD | 1.5 | 1.5 | 1.8 | 1.7 |
| Gd | 8.6 | 6.4 | 6.1 | 6.3 | 6.6 | 6.3 | 6.5 | 5.6 | 5.9 |
| Dy | 8.7 | 7.0 | 7.0 | 6.3 | 6.0 | 4.4 | 5.3 | 5.1 | 4.1 |
| Er | 5.1 | 4.3 | 4.3 | 4.1 | 3.9 | 2.9 | 3.1 | 2.6 | 2.2 |
| Yb | 5.6 | 4.6 | 4.5 | 4.3 | 3.8 | 2.7 | 3.1 | 2.4 | 2.6 |
| Lu | 0.83 | 0.73 | 0.70 | 0.63 | 0.58 | 0.47 | 0.51 | 0.40 | 0.39 |
| Ta | 2.7 | 2.4 | 2.6 | 2.5 | 2.0 | 1.4 | 1.6 | 1.0 | 1.2 |
| Pb | 31.3 | 31.0 | 32.1 | 29.5 | 31.9 | 29.8 | 37.6 | 25.2 | 29.0 |
| Th | 49.1 | 43.3 | 44.0 | 39.1 | 37.9 | 25.5 | 29.3 | 18.0 | 20.9 |
| U | 15.4 | 13.3 | 13.7 | 12.5 | 12.5 | 6.7 | 7.4 | 5.2 | 6.0 |

Table 3.19: Representative major, minor and trace element glass data for selected tephra ‘external’ to the island that they were sampled upon. Including Monte Guardia outcropping on

Vulcano and Panarea, an unknown pumice fall on Panarea (EL4; see De Rita et al., 2008) and pumices sampled from Capo Milazzo, Sicily.

Monte Guardia (MG) deposits outcrop near Gelso, on Vulcano were examined as a medial-distal equivalent (Lucchi et al., 2008; 2010) (Fig. 3.35). Juvenile pumices are sampled from basal fall deposits and were dominated by milky white pumices, obsidian and lithics. The poorly sorted units stratigraphically above were interpreted as either surge deposits or reworked lahar deposits. Representative glass data are presented in Table 3.19. Glasses match the most evolved compositions of the MG proximal sequence, dominated by the > 75wt.% SiO₂ rhyolitic glasses (Fig. 3.25). Major element compositions are largely indistinguishable from the MG proximal deposits and display the diagnostic variability in K₂O at a given silica wt.% (Fig. 3.25; 3.36). Major elements compositions observed on Vulcano are most consistent with the upper fall deposits sampled on Lipari (unit 5) where $D^2 = 0.8$. This is due to the absence of the lower silica rhyolites from Vulcano deposits. Trace element compositions of these mid-distal glasses provide a useful test of the suitability of the proximal data presented herein to determine precise provenance (Fig. 3.23). MG glasses sampled on Vulcano display elevated incompatible trace element compositions relative to the older formations of P.del Perciato and Falcone (Fig. 3.23, 3.37). They are consistent with the most fractionated glasses produced during the MG proximal sequence, geochemical correlation is best illustrated by Rb which is higher in the older rhyolitic glasses (Fig. 3.37c). Importantly these medial glasses display lower LREE, Zr and Th concentrations than those observed in the more recent GFB and Monte Pilato activities (Fig. 3.23; 3.37). These medial deposits confirm the southwards dispersal of the most fractionated glasses of the Monte Guardia eruption.

North east of Lipari, De Rita et al. (2008) and Lucchi et al., 2008 identify the presence of white rhyolitic ash within the Drauto stratigraphy of Panarea (Fig. 3.13). Ash was sampled from beneath the more prominent pumice bed (EL4) in their reported stratigraphy; here this ash is termed EL3 consistent with De Rita et al. (2008). Again the ash is restricted to the highly evolved rhyolitic pumices compositions of the Monte Guardia sequence (>75wt.% SiO₂) and shows the variable K₂O observed proximally (Fig. 3.36). Importantly K₂O extends to lower concentrations than those observed in the older HKCA rhyolitic activity of Lipari (P.del Perciato and Falcone formations). Incompatible trace elements lie within the MG compositional field, but for most elements overlap with the older Lipari rhyolitic deposits (Fig. 3.37).

Monte Guardia Eruptive deposits: sampled on the Island of Vulcano (N38 22 244; E014 59 632)

| Unit | Description |
|------|--|
| 10 | Massive dark ash |
| 9 | Clast supported, angular, white pumice lapilli. |
| 8 | Massive, poorly sorted, ashy matrix. Contains white pumices and lithics similar to the units below |
| 7 | Clast supported, sorted angular, white pumice lapilli. |
| 6 | Massive, poorly sorted, ashy matrix. Contains white pumices and lithics similar to the units below |
| 5 | Alternating ash and white sorted pumice beds containing lithics |
| 4 | Massive, white ash (oxidised ash at along the upper contact) |
| 3 | Discrete clast support, angular pumice lapilli bed, containing lithics and obsidian. |
| 2 | Massive, white/grey ash |
| 1 | Poorly sorted, ashy matrix supported massive. clast ranging from lapilli to occasional blocks |

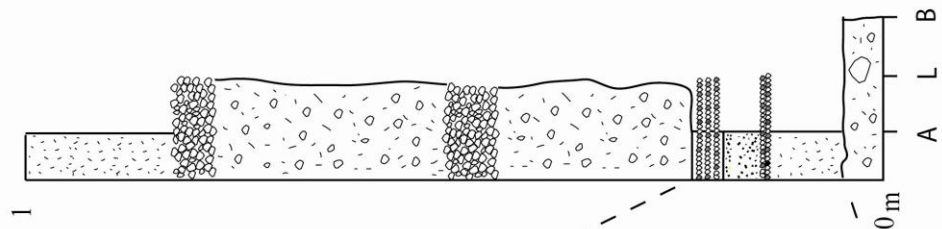


Figure 3.35: Monte Guardia fall deposits and surges deposits outcropping on the south western slopes of Vulcano, near Gelso.

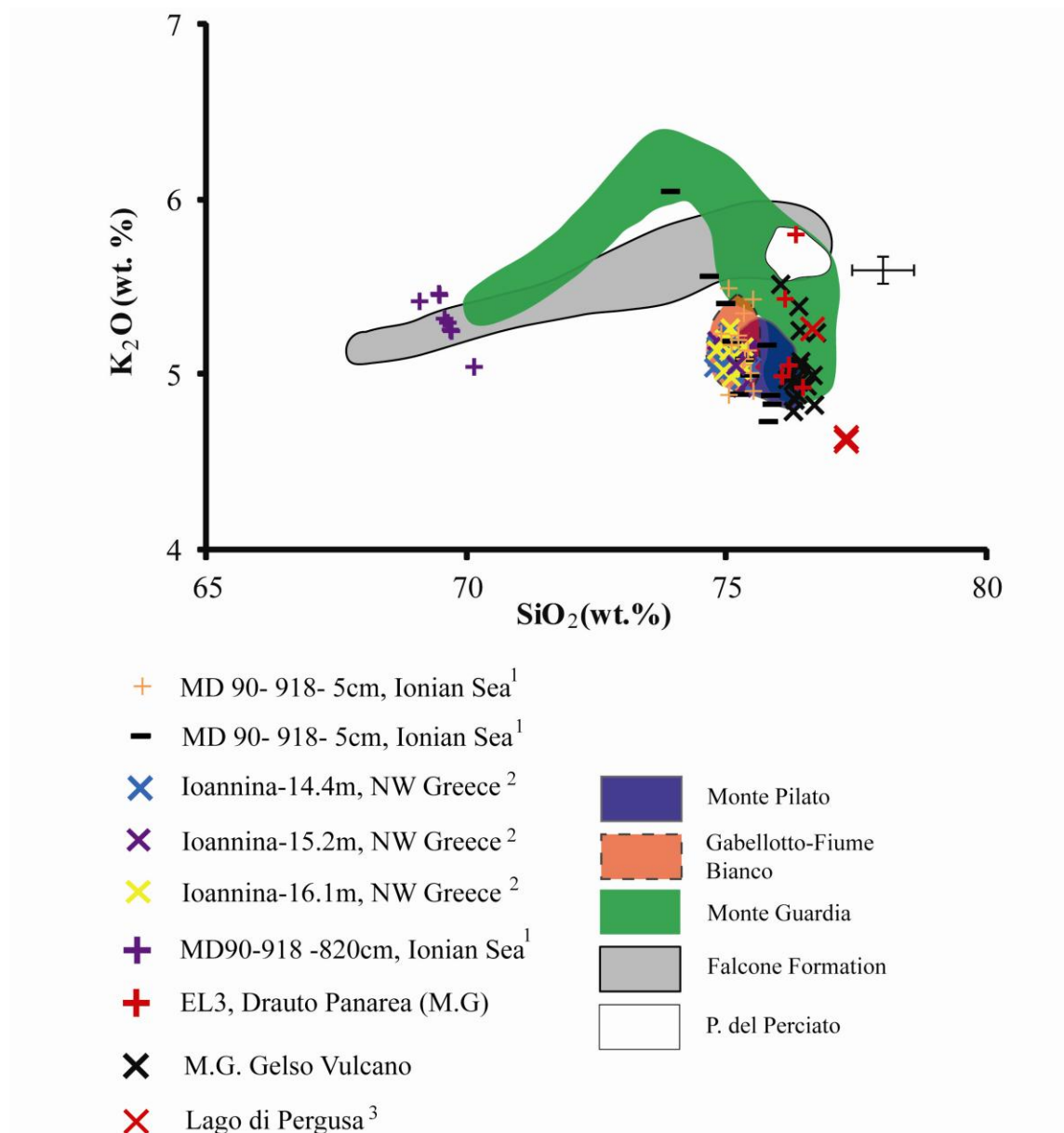


Figure 3.36: SiO₂ vs. K₂O diagram displaying the medial and distal HKCA rhyolitic tephras associated with explosive Lipari activity during the last 42 ka compared with proximal data presented herein. Included are distal ash and pumice layers previously attributed to explosive activity on the island of Lipari. (1) ash layers from the Northern Ionian Sea; Caron et al., (2012); (2) cryptotephra layers recorded in Lake Ioannina, NW Greece (T. Jones 2012 *pers comm.*). (3) Monte Guardia ash recorded in Lago di Pergusa (Narcisi, 2002).

However, lower Rb concentrations in these glasses confirm that the ash dispersal is related to the MG formation (Fig. 3.37c). This demonstrates the advantage of determining diagnostic trace element features for distinguishing compositionally similar tephra. Geochemical data thus confirms both north eastward and southern dispersals of most evolved Monte Guardia glasses within the Aeolian Islands.

More distally MG has been identified by Narcisi (2002) on Sicily in Lago di Pergusa. Average compositions of 'T3' tephra are available and they display slightly higher SiO₂ than the proximal data (Fig. 3.36). Most elements are consistent with the proximal data of the MG, K₂O extends to lower concentrations than observed proximally, but this is consistent with a trend towards lower K₂O values with increasing silica (Fig. 3.36). The chronology at Lago Pergusa is slightly complicated by some age reversals in the radiocarbon chronology. However, Narcisi (2002) places this rhyolitic ash dispersal at between 23.3- 25.9 cal ka BP (based on two ¹⁴C determinations; 20820 ± 375 yrs BP and 20090 ± 260 yrs BP). These ages are in accordance with the maximum age derived from beneath the proximal MG succession (26.3 ± 0.8 cal ka BP; ¹⁴C 22, 600 ± 300; Crisci et al., 1983). Combined chronology and major element data would support a correlation to Monte Guardia activity and reinforce the observed southern dispersal. Monte Guardia is not extensively reported in the marine archives, Paterne et al. (1988) identify an Aeolian Island rhyolite at 260 cm in KET8003, north east of Salina. Although this marine tephra is dated to 27.6 ka, the absence of geochemical data makes it difficult to assess whether this tephra relates to rhyolitic activity representing eruptions from Salina (i.e., Lower Pollara) or Lipari (i.e. Monte Guardia) both of which offer chronologically suitable rhyolitic eruptions.

Caron et al. (2012) have more recently reported the Monte Guardia (MG) eruption in the northern Ionian Sea core MD 90-918 at a depth of 820 cm. The layer is radiocarbon dated and the marine reservoir offset corrected to between 19260-19467 cal yrs BP (¹⁴C 16610 ± 70 yrs BP). Major element data from this marine tephra are compared to the proximal Lipari data present herein. The trachy-rhyolitic glasses are most similar to the least evolved rhyolitic glasses produced on Lipari during the last 42 ka. However correlation specifically to MG activity is problematic for the following reasons;

(1) MD 90-918 820 cm trachy-rhyolitic glasses are less evolved than the least evolved glasses presented proximally in the MG sequence (ca.70 wt.% SiO₂), in contrast,

medial-distal dispersals to Vulcano and Panarea of MG are exclusively dominated by the most evolved rhyolitic components (Fig. 3.25).

(2) Caron et al. (2012) suggest that the absence of the most evolved components of the MG eruption, which dominates the medial-distal deposits within the Aeolian Islands, is the result of differing dispersal axes during the eruption. However, within the proximal stratigraphy of Monte Guardia (Fig. 3.25) the least evolved glasses are never exclusive and are always found mixed with the most evolved pumices (Fig. 3.25). Only the white most evolved pumices become exclusive during the latter stages of the eruption.

(3) Chronology is problematic, Caron et al. (2012) suggest that the distal age of MD 90-918 820cm is in agreement with proximal ages of the MG. However, Caron et al. (2012) present proximal ages of MG as calibrated, when in fact the age is uncalibrated. The calibrated age of 19260-19467 cal yrs BP for the tephra at 820 cm is significantly younger than the calibrated proximal age range for the MG deposits. The age of 26.3 ± 0.8 cal ka BP (^{14}C $22,600 \pm 300$; Crisci et al., 1983) is derived from just beneath the MG deposits and can be considered slightly younger, but close to the true age of the MG. Whilst a less precise age from above the MG deposits, presenting a minimum age for the eruption of 24.3 ± 1.8 cal ka BP (^{14}C $20,300 \pm 0.7$; Crisci et al., 1983).

This evidence would suggest that rather than a correlation to Monte Guardia, MD 90-918 820 cm may present a new distal marker tephra that is chronologically constrained to between the MG and GFB eruptions on Lipari. However its precise proximal links to Lipari remain unresolved, its trachy-rhyolitic melt composition is more consistent with a provenance from the southern domes of Lipari. This presents evidence for ash dispersal from southern Lipari that post dates the MG eruption. Indicating that either the recognised proximal units between MG and GFB are under estimated regards their potential to disperse ash or proximal equivalents have not been studied. Minor fallout deposits of HKCA rhyolitic compositions are identified in conjunction with the Monte Giardina and Punta di Costa formations on the southern sector of the island (Lucchi et al., 2010) and possibly presented future targets for proximal investigations.

The Gabellotto-Fiume Bianco (GFB) outcrops on Vulcano (Keller, 1980a; De Astis et al., 2006) and Panarea (Lucchi et al., 2008). Beyond the Aeolian Islands, as mentioned above GFB is related to the E-1 marine tephra, located in the early Holocene sapropel sediments (Paterne et al., 1988; Siani et al., 2004; Caron et al., 2012). More distally, three HKCA rhyolitic cryptotephra layers have been recognised in the lacustrine

sediments of Lake Ioannina, NW Greece (T. Jones 2012 *pers comm.*). These cryptotephra layers were recovered from sediments at 14.4 m, 15.2 m and 16.1 m, respectively, and a radiocarbon age model for the core has been developed using experimental dating of n-alkanes (T. Jones 2012 *pers comm.*). The upper most tephra (14.4 m) lies in the early Holocene sediments and is dated to 7.5 cal ka BP. The next tephra at 15.2 m is dated to 13.5 cal ka BP and the lower most tephra 16.06 m is dated to 18.3 cal ka BP. All three tephras display the homogeneous major element compositions identical to the GFB (Fig. 3.36) and are distinct from the older southern Lipari activity (Monte Guardia, Falcone formation and P.del Perciato formation). Due to the size fraction of this distal ash, trace element characterisation of only the upper and lower layer was possible (T. Jones 2012 *pers comm.*). Whilst incompatible trace element concentrations in the glasses are scattered, shards overlap the compositions of the GFB, demonstrating the more elevated LREE, Zr and Th (to some extent) than the older MG, Falcone and P.del Perciato formations (Fig. 3.37). The distal stratigraphy of Ioannina presents three geochemically indistinguishable tephras. The tephra in the early Holocene can be correlated to GFB based on stratigraphy allowing an age of 8730–8400 cal yrs BP to be imported. The 7.5 cal ka BP age derived for the Ioannina tephra at 14.4 m is not too dissimilar from the widely accepted age of the GFB (~8.5 ka), suggesting that the experimental radiocarbon chronology offers a reasonable relative age proxy for the remaining two older rhyolitic tephra layers. One is late-glacial in age (13.5 cal ka BP) and the oldest tephra is close to the last glacial maximum (18.3 cal ka BP).

Monte Pilato ash was sampled from within the stratigraphy of Vulcanello, Vulcano and as micro-pumices on Stromboli from beneath the onset of present day activity (Rosi et al., 2000). These HKCA rhyolitic glasses (Table 3.9; Table 3.18) display major element compositions that are indistinguishable from the GFB and MP2 upper glasses. For most incompatible elements, concentrations overlap with those observed in the pumices of the GFB and the Monte Pilato 2 (MP2), demonstrating the difficulties in separating the two eruptions on Lipari. However, Monte Pilato glasses sampled mid-distally on Vulcano and Stromboli display higher concentrations in LREE (La, Ce, Pr and Nd) than the glasses of both GFB and Monte Pilato sampled at Monte St Angelo, Lipari (Fig. 3.23). Whole rock data from the proximal stratigraphy of Lami, Monte Pilato (Davi et al., 2011) reveal that pumices display variable concentrations of LREE as identified here in mid-distal localities.

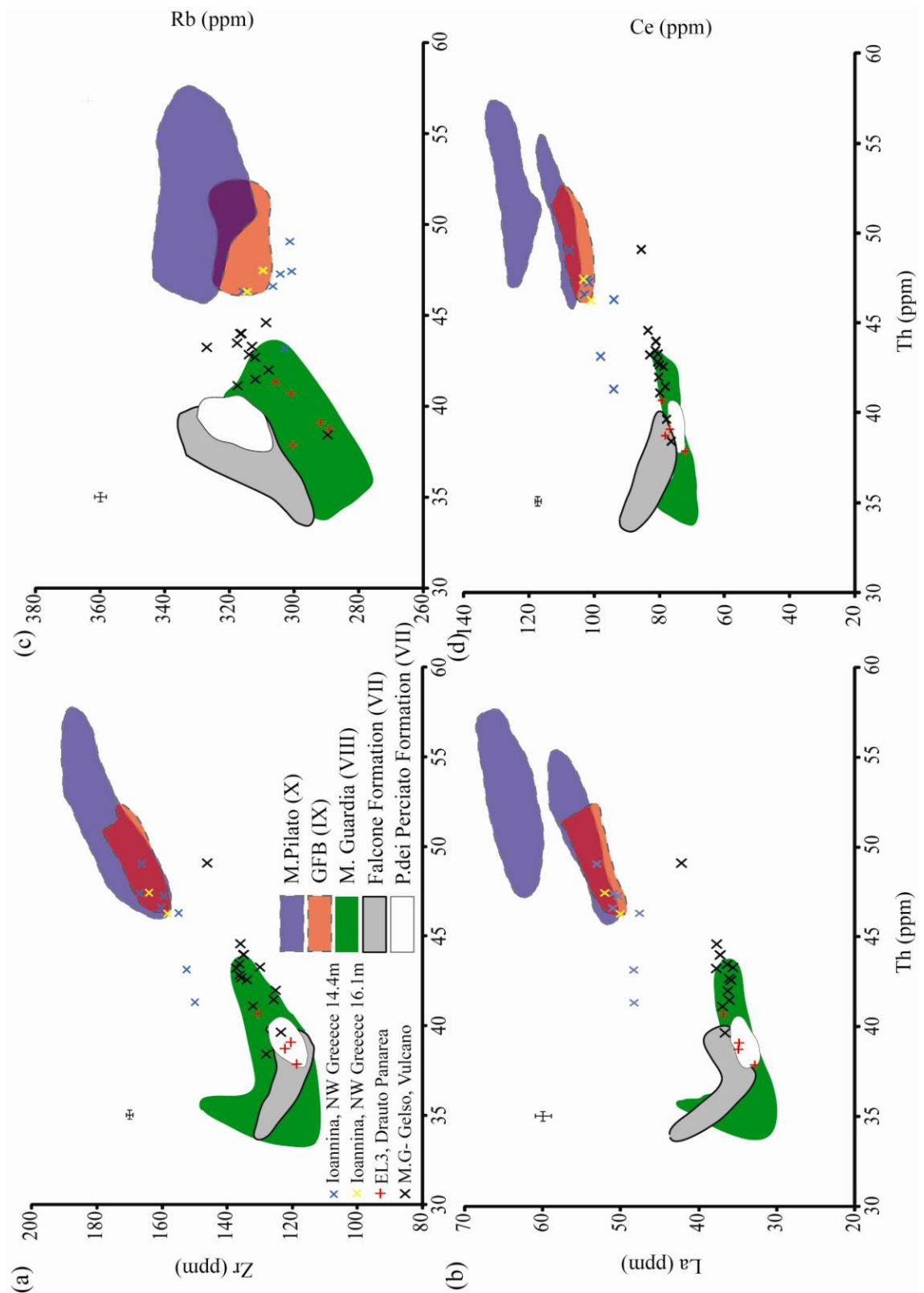


Figure 3.37: Diagnostic trace element bi-plots for distinguishing the products of Lipari during the last 42 ka. Shown are medial and distal ash and pumices associated with activity on the island of Lipari. Including cryptotephra layers recorded in Lake Ioannina, NW Greece (T. Jones 2012 *pers comm.*). Ash and pumices from Panarea and Vulcano respectively. Compositional fields are proximal data reported and Roman numeral refers to the eruptive cycle.

These stratigraphically well constrained occurrences of Monte Pilato activity recorded within the Aeolian Islands present further evidence for greater trace element geochemical diversity during this eruption than the previous Gabelotto-Fiume bianco. Glasses erupted during the Monte Pilato eruption have two discrete LREE groups;

(1) La = 56 ppm; Ce = 112 ppm; Pr = 11.8 ppm and Nd = 42 ppm;

(2) La = 64 ppm; Ce = 125 ppm; Pr = 12.7 ppm and Nd = 44 ppm (Fig. 3.23bc; 3.37b, d)

Higher Th and LREE in these Monte Pilato glasses confirm a temporal increase in these elements concentrations with successive major explosive eruptions on the Island (Fig. 3.23), a feature also recognised by whole rock investigations (Gioncada et al., 2003).

3.5.1.6 Lipari summary

Major element glass compositions produced over the last 42 ka at Lipari are dominated by HKCA rhyolites showing limited major element variability. K₂O shows the most diagnostic variation (Fig. 3.22a). Trace element can be used more effectively to distinguish the glass explosively produced during the main investigated eruptive cycles occurring on Lipari during the last 42 ka.

Importantly there is a trend towards higher Th and LREE concentrations in the glasses through time. Th plotted against the LREE, Rb and Y appears to be the most diagnostic means to geochemically separate the HKCA Lipari rhyolites. Temporal evolution in the trace element glass compositions produced on Lipari enable separation of the main eruptive cycles (VII, VIII, IX and X). However, distally evidence exists for more numerous eruptions sourcing from the island. These tephtras are not always geochemically distinguishable using the trace element analysis as demonstrated by tephtras recorded in Lake Ioannina, north-west Greece (Fig. 3.37).

The implications are twofold;

1. Repeated glass geochemistries indistinguishable at a major, minor and trace element levels sourcing from Lipari are recorded distally. This is problematic for distal tephtra correlations and highlights the importance of stratigraphic/bio-stratigraphic control when using these tephtra layers as chronological/stratigraphic markers.

2. The appearance of more numerous distal Lipari HKCA rhyolites might indicate that the less prominent eruptive units on the islands have the potential to present widespread tephra markers.

3.5.2 Salina proximal explosive deposits:

Within the last 30 ± 3 ka (Gertisser and Keller, 2000) explosive activity has been focused at the Pollara centre on the NW of the island. Two explosive eruptions; the Lower Pollara tuff and the Upper Pollara eruptions are characterised and discussed here;

3.5.2.1 Lower Pollara

As previously reported by Calanchi et al. (1993) the Lower Pollara (LP), dated between 27.6 ± 0.8 cal ka BP (Morche 1988) and 26.3 ± 0.8 cal ka BP (Crisci et al., 1983), represents a reversed compositional sequence, i.e., mafic scoria fall is capped by felsic pumice fall. The LP deposits sampled at Valdichiesa, Salina display compositions that are transitional along the CA-HKCA boundary. WR analyses of the mafic scoria in the lower portion of the stratigraphy reveal a basaltic andesite composition consistent with previous reports (Calanchi et al., 1993). The sequence is then interrupted by an oxidised lithic rich layer which is interpreted as indicating vent widening just prior to the switch to the eruption of the more felsic rich end-members (Fig. 3.11). The pumices are heterogeneous (69.1-75.1 wt.% SiO₂), with glass composition in the pumices ranging from dacites to rhyolites (Fig. 3.20). Trace element concentrations in the pumices are far more evolved than the scoria (Fig. 3.26). Previously published data for the Lower Pollara pumices are based on WR data (Calanchi et al., 1993). It should be emphasised that WR pumice analysis performed herein are clearly not comparable with, or representative of, the glass compositions and as such are not suitable for distal tephra correlations (Fig. 3.26). The bi-modality of the Lower Pollara erupted end-members is concealed within WR data, WR analysis of the pumices containing phenocrysts produce more mafic compositions, which shows an erroneous compositional continuity from basaltic andesite straight through to rhyolite (Calanchi et al., 1993). However, glass compositions of the LP pumices are significantly more evolved demonstrating a clear compositional gap between the basaltic scoria and the silicic pumice end-members (dacite-rhyolites) (Fig. 3.26).

The major element variability in the glass compositions of the Valdichiesa outcrop is mirrored in the 'Key bed' stratigraphy outcropping on NE Lipari which was previously

correlated to LP (Morche, 1988). The WR analyses of the basaltic andesitic scoria are similar between the two localities (Fig. 3.26) and pumices have a similar range in SiO₂ (69.0-74.6 wt. %) with indistinguishable glass compositions ($D^2 = 0.75$) at a 99.5 % confidence limit. Incompatible trace element concentrations observed between the proximal and medial locality on Lipari reveal that the two stratigraphies are indistinguishable ($D^2 = 2.5$). Glasses have consistent levels of trace element enrichment including LREE enrichment relative to HREE. An interesting feature of the Lower Pollara glasses is that they display a slight trough in the middle to heavy REE profile (Fig. 3.21a). This could be related to the fractionating phases within these pumices.

3.5.2.2 Upper Pollara

The upper Pollara pumices are heterogeneous HKCA rhyolites probably due to mixing of two evolved melt compositions, demonstrated by a wide ranging SiO₂ with 71.4-77.6 wt.%. Banding (white and grey pumice) reflects both compositional variability and textural differences. There is stratigraphic heterogeneity within the Upper Pollara deposits; white/grey pumice pairs in ERU1-4 show a progressive introduction of more evolved compositions (Fig. 3.28). White pumices in the Upper Pollara stratigraphy display trace element variability, the most silicic glasses in ERU1 and ERU2 display lower incompatible trace element concentrations than the most silicic glasses of ERU3 and ER4 (Fig. 3.28). Sulpizio et al. (2008) suggest that the emplacement of the Upper Pollara pyroclasts was a prolonged eruptive episode, with the eruptive units representing separate pulsating PDC deposits separated by erosional unconformities. The subtle incompatible trace element enrichment of the stratigraphically higher pumices might reflect replenishment and high-level fractionation facilitated by temporal gaps in activity.

3.5.2.3 Distinguishing Pollara activity, Salina

Distinguishing between the products of the Upper and Lower Pollara eruptions in distal localities is straightforward with good stratigraphic control, due to the temporal gap between the two eruptions. However in situations where the stratigraphy is more complex (i.e. continental successions, archaeological contexts) geochemical distinctions are required.

| | Lower Pollara Pumices | Upper Pollara Pumices |
|-----------------------------------|----------------------------------|----------------------------------|
| SiO₂ (wt.%) | 69.1 -75.1 | 71.4-77.6 |
| K₂O (wt.%) | 2.3-3.7 | 3.4-4.4 |
| Ba (ppm) | 836-1010 | 1430-1660 |
| Zr/Th | 11.1 ± 0.5 | 6.9 ± 0.4 |
| Nb/Zr | 0.10 ± 0.004 | 0.13 ± 0.1 |

Table 3.20: Diagnostics used to distinguish the Upper and Lower Pollara glasses distally.

The most obvious distinguishing feature of the Lower Pollara is the presence of the mafic scoria emplaced during an opening phase of the eruption. However, in the medial locality of the Lipari ‘Key bed’, the scoria component is much finer than the overlying pumices this density separation more distally suggests that the dispersal of the mafic component is likely to be far more restricted. From a tephrochronological perspective it is likely that more fractionated pumice compositions will be found distally and their diagnostic features are most important (Table 3.20).

The Lower and Upper Pollara pumices have overlapping major element concentrations and share a similar evolutionary path (Fig. 3.26) with the Upper Pollara glasses extending to higher SiO₂, resulting in lower TiO₂, FeO, CaO and MgO (Fig. 3.26). The pumices of the two eruptions display similar levels of heterogeneity. However the range in the Upper Pollara pumices is towards slightly more elevated SiO₂ (Fig. 3.28). Mantle normalised trace element profiles for the two sets of pumices are similar, with Upper Pollara glasses displaying overall greater levels of trace element enrichment (Fig. 3.21a). Both the Pollara glasses display a slight trough in the MREE and HREE (Dy, Y, Er). It would appear that this is a petrological feature of the Salina rhyolites, as it is not observed in the Lipari rhyolites which display a flat MREE/HREE profile (Fig. 3.21). Whilst pumice compositions produced during the two eruptions do overlap (Fig. 3.26), the incompatible trace element concentrations in the Upper Pollara are largely more elevated. Petrogenetic differences between the two melts mean they can be easily differentiated (Table 3.20).

3.5.2.4 Distal Salina deposits in the central Mediterranean

Distally Paterno et al. (1988) reported the E-2 as the Upper Pollara tephra in KET8003 north-west of Salina (Fig. 3.1). The average composition does not precisely overlap the proximal data presented herein on all major elements, but it does lie at the most evolved end-member of the Upper Pollara range (Fig. 3.26) indicating a possible association with the more evolved ERU 3 and 4. It is difficult to assess whether the high-SiO₂ products of the Upper Pollara are preferentially dispersed to distal locations based on a single average value. Due to limited fall reported within the Upper Pollara stratigraphy (Sulpizio et al., 2008) the ash identified in KET8003 (NW of Salina) could be instead dominated by co-ignimbritic ash associated with the PDC deposits which dominate the stratigraphy. Furthermore the location of the Pollara centre on the NW sector of the island might lead to interpretation that the ash layer represents a turbidite deposit reflecting Upper Pollara PDC entering the marine environment.

3.5.3 Panarea proximal explosive deposits

Whilst the age of final phase of explosive activity on Panarea is poorly constrained, geochemical data from the dacite pumices at Punta Falcone and Palisi are indistinguishable ($D^2 = 0.7$). This geochemical similarity is confirmed by trace element concentrations in the glasses (Fig. 3.26). Geochemical evidence supports the previous stratigraphic correlations between the two stratigraphies on the island (Dolfi et al., 2007). The Panarea dacite glasses can be easily distinguished from the Pollara explosive deposits due to their lower degrees of evolution, reflected in lower SiO₂, K₂O, Na₂O and higher CaO, FeO, Al₂O₃, MgO, TiO₂ (Fig. 3.20; 3.25). Where SiO₂ overlaps with the Lower Pollara glasses the Panarea dacite pumices trend towards more elevated K₂O concentrations than the Salina glasses (Fig. 3.25a). At a trace element level, the Panarea pumices share similar less enriched incompatible trace element concentrations, consistent with the Salina glasses, rather than the more elevated concentrations of Lipari. Panarea dacite glasses are easily distinguished from Salina glasses based on significantly lower Sr and Ba concentrations (Fig. 3.26d). The rhyolitic component mingled with the Punta Falcone dacite glasses, indicate that the most evolved products of Panarea show a HKCA affinity (Fig. 3.20), with significantly more elevated alkalis than those observed in the Pollara rhyolitic glasses (Fig. 3.20).

3.5.4 Lipari-Salina rhyolitic activity

Distal tephras are typically dominated by the most evolved glass compositions produced during explosive eruptions. Rhyolitic end-members from Salina and Lipari display some overlap in major element concentrations particularly when the error is considered. Petrological differences mean that Lipari rhyolites consistently display more elevated K_2O than the products of Salina (Fig. 3.20), whilst the Salina glasses display more elevated CaO.

Trace elements are particularly diagnostic, the Lipari rhyolites display dramatically more elevated incompatible trace element concentrations than those observed in the Salina rhyolites (Fig. 3.21a). Lipari rhyolites are heavily depleted in Ba, Sr and Eu in response to K-feldspar removal (Fig. 3.21a). K-feldspar is not present in the Salina rhyolitic glasses and consequently Ba remains incompatible showing no decrease in concentrations (Fig. 3.21a), this supports whole rock interpretations (Donato et al., 2006). As mentioned above Salina rhyolitic glasses display a slight trough in their MREE/HREE profiles (Fig. 3.21a), this depletion is reinforced by Y behaving compatibly and decreasing within Th in the Lower Pollara glasses (Fig. 3.27e).

3.5.5 Vulcano proximal explosive deposits

Vulcano glasses display the most geochemical diversity explosively erupted by a single Aeolian island during the investigated time frame of the last 21 ± 3.4 ka (Fig. 3.20). The explosive deposits investigated range from basaltic-trachy andesites to rhyolites (Fig. 3.20). Glasses show a temporal progression towards higher K_2O compositions. Glass compositions move from shoshonitic series in the oldest deposits investigated (ca. 21 ka) to high-K series compositions associated with La Fossa in the last 5 ka. Activity on the island in the last 5 ka is dominated by the more felsic products (trachytes and rhyolites) (Fig. 3.29). Compositional variability of the glasses produced on Vulcano is consistent with the variability observed in the whole rock products of the island (De Astis et al., 1997; Del Moro et al., 1998; De Astis et al., 2000). This variability is attributed to changes in the different magma ponding depths beneath Vulcano and has been confirmed by fluid inclusion studies (Zanon et al., 2003).

3.5.5.1 Quadrara Formation

The oldest investigated products are associated with the explosively emplaced Quadrara formation (21 ± 3.4 ka) and they display a shoshonitic affinity consistent with the older series deposits on the island (De Astis et al. 1997) (Fig. 3.20). Glasses are heterogeneous, comprising of scoriaceous trachy-andesites and biotite/K-feldspar bearing trachytes (Fig. 3.29). The trachytic pumices are distinctive in their composition and mineralogy and do not appear to be reported elsewhere on the island. The less evolved trachy-andesitic scoria is unlikely to be unique given the presence of other thick scoriaceous deposits beneath the Quadrara formation (i.e. Spaggia Lunga Formation; 24 ± 5 Ka; Soligo et al., (2000)).

The inversely graded pumices at Quadrara (Fig. 3.15) are indicative of a fall from a sustained column with increasing energy. Whilst the vent location remains unknown, Lucchi et al. (2008) suggest SW Vulcano as the most likely source of origin, but an off shore location cannot be ruled out. The absence of Quadrara pumices further north on the island might suggest either a south-ward dispersal of fall or that deposits elsewhere on the island are not exposed due to burial by more recent activity. Given the geochemical variability through the stratigraphy with the most evolved products (trachytes) emitted first followed by the least evolved components, it might be possible to infer tapping of a compositionally stratified magma chamber (Fig. 3.30). The trachytic pumices are likely to be the product of fractional crystallisation of a trachy-andesite parent magma. However, major element variations clearly demonstrate two discrete melt compositions (Fig. 3.30), their trace element analysis reveals that they display overlapping incompatible trace element concentrations (Fig. 3.32). Despite overlapping trace element concentrations, clear major element differences would indicate they are likely to represent two separate melts rather than compositional zoning (Fig. 3.32). It is proposed that the injection of the basaltic-andesite melt into the high-level trachytic magma batch was the likely trigger. Explosive activity is facilitated by the marked difference in temperature and volatiles between mafic and felsic melts (Sparks et al., 1977; Huppert et al., 1982; Turner et al., 1983). Interestingly Ba and Sr concentrations in the basaltic-andesite component remain constant whilst those in the trachytic glasses appear to follow a different evolutionary path (Fig. 3.32). The injection of a less evolved melt into a higher level magma system is consistent with Zanon et al. (2003) who suggest that there are multiple magma ponding depths beneath Vulcano.

3.5.5.2 Casa Lentia

Casa Lentia activity around 13 ± 1 ka (Soligo et al., 2000) presents evidence of the trachy-rhyolitic compositions. This composition is fairly unique to Lentia at this time and is compositionally most similar to the trachy-rhyolites of the Pietre Cotte ($D^2 = 1.94$). However, these eruptions are temporally very distinct where the Pietre Cotte is constrained to historic times and younger than 1260-1470 cal AD based on radiocarbon dates from the underlying Commenda Ash (Todman 2012). Furthermore Pietre Cotte glasses can be easily distinguished based on their trace element concentrations where the two trachy-rhyolitic analyses display more elevated Th, Nb, Zr and La (Fig. 3.31). With an age of 13 ± 1 ka (De Rosa et al., 2003b) Casa Lentia explosive products offer a distinct marker for late-glacial activity on the island.

3.5.5.3 TGR scoria and Monte Saraceno

Prior to the onset of La Fossa cone formation on the island of Vulcano activity is associated with the Tufi Grotte dei Rossi Tuffs (7.7 ka; De Astis et al., 1997). These tuffs are attributed to phreatomagmatic activity within the present day La Fossa caldera (De Astis et al., 1997). These comprise of thick ash deposit and these tephra are thought to be widespread throughout the Aeolian Islands. Within the accumulation profiles throughout the Aeolian island these deposits are believed to be associated with the 'upper brown Tuffs' (De Astis et al., 1997; Lucchi et al., 2008). Within the Piano caldera, Vulcano, a thin scoriaceous lapilli bed interbedded within these deposits was identified at the locality VL201 from De Astis et al. (1997). Glasses reveal a basaltic trachy-andesitic composition ranging to trachy-andesites (Fig. 3.29) and these glasses are compositionally identical to the Monte Saraceno scoria blanket ($D^2 = 0.3$) (Fig. 3.29). Consequently, they are likely to represent Monte Saraceno activity at 8.3 ± 1.6 ka (De Astis et al., 1989) rather than the explosive phreatomagmatic activity of the Tufi Grotte dei Rossi. The scoria glass compositions are important as they reveal the more basic melts compositions explosively produced on the island during the last 21 ka, providing an important proxy for mafic ash dispersals that may have been erupted at Vulcano.

Attribution of the lapilli bed recorded with Tufi dei Rossi deposits to Monte Saraceno mean that the glasses of the Tufi dei Rossi are not characterised here. De Astis et al. (1997) presented major element glass analysis of ash from the upper VL201 sequence above the lapilli layer reported here. These average glass compositions reveal high-K

trachy-andesite to trachyte compositions, with 57.9-60.65 wt.% SiO₂; 0.65-0.69 wt.% TiO₂ and 6.9 K₂O, which is consistent with more recent La Fossa compositions outlined below. Lucchi et al., (2008) suggest that these glass compositions are consistent with the Punta Nere activity on Vulcano.

3.5.5.4 La Fossa

The formation of La Fossa is constrained to within the last 5.5 ka (Frazzetta et al., 1983), activity during this period is punctuated by explosive and effusive activity (Frazzetta et al., 1983; Dellino et al., 2011). The stratigraphy was outlined by Di Traglia (2011) and Dellino et al. (2011). Using explosively erupted glasses from La Fossa (Todman, 2012) and the pre-La Fossa activities presented here, glasses fall into two broad compositional groups (Fig. 3.29);

(1) Tephri-phonolites/trachytes

(2) trachy-rhyolites.

Explosive activity largely alternates between the two compositional end-members (e.g. Todman 2012). The high-K glass compositions are broadly similar at a major element level and characteristic of Vulcano (Fig. 3.20). The glasses can be separated on the basis of their major element chemistries, although this is not always statistically valid (Table 3.21). Trace element concentrations within the glasses produced during the La Fossa explosive activity are not unique to individual eruptions (Fig. 3.31). However they do differ temporally between the older Palizzi cycle and the younger Commenda/Pietre Cotte cycles (Fig. 3.31) and offer an important relative age control. For instance the older Palizzi tephri-phonolite/trachyte glasses display overlapping trace element concentrations (i.e. Palizzi A and Palizzi D), whilst the younger high-K trachytic (Commenda/Pietre Cotte) glasses display more elevated trace element concentrations again overlapping one another (Fig. 3.31).

Palizzi A glass compositions represent the least evolved melts explosively erupted by La Fossa. Todman (2012) demonstrated that compositions are consistent with those produced on nearby Vulcanello. These glasses are important in that they provide the most likely proxy for pre-La Fossa activity, which is reinforced by the limited statistical distance between ($D^2 = 3.5$) the Palizzi A glass compositions and those of the upper brown tuff (TGR) (De Astis et al. (1997). Major element geochemistry reveals that the oldest Palizzi A glass compositions can be easily distinguished from the Palizzi D

trachytes ($D^2 = 52.8$; Table 3.21). Palizzi A, tephri-phonolite glasses display lower SiO_2 (55.1-57.8 wt.%), K_2O ; higher TiO_2 FeO and CaO than the Palizzi D trachytic pumice fall (Fig 3.29). As outlined above the trace element concentrations between these two Palizzi deposits are indistinguishable ($D^2 = 1.04$). Interestingly the darker glasses presented by De Astis et al. (1997) for the upper brown tuff (TGR) are very comparable to the Palizzi D compositions ($D^2 = 2.1$).

Palizzi A and D are separated by a compositionally distinct Palizzi B rhyolitic eruption; this pumice fall is compositionally unique within the Palizzi succession. These rhyolitic glasses represent the most evolved compositions produced by La Fossa given their elevated SiO_2 (Fig. 3.29), Th (Fig. 3.31) and more pronounced europium anomaly ($\text{Eu}/\text{Eu}^*_\text{N} = 0.2$) (Fig. 3.21a). Incompatible trace elements displays significant variability within the Palizzi B glasses symptomatic of a highly evolved melts.

Distinguishing the post-Palizzi products of La Fossa is more problematic. Major element differences are limited between the Commenda ash/Caruggi and the trachytic components of the Pietre Cotte. The Commenda ash only displays slightly elevated SiO_2 ; lower TiO_2 , FeO and consequently they are not statistically different (Table 3.21). As mentioned above following the Palizzi activity the levels of trace element enrichment become more elevated within all the products where the Commenda Ash and Pietre Cotte high-K trachytes are indistinguishable (Fig. 3.21b; 30).

Unique to the Pietre Cotte cycle however is the presence of mingling, where the high-K trachytic (dark glass) component is mingled with a white pumice of rhyolitic composition, seen in the banded pumices (Fig. 3.30). Major element concentrations of these trachy-rhyolitic pumices are very similar to the glass compositions of the older Palizzi B eruption. Palizzi B rhyolites display significantly more K_2O variability (Fig. 3.20b) than the Pietre Cotte rhyolites. $D^2 = 1.4$ (Table 3.21) and reflects their overall similarity. Importantly at a trace element level these two rhyolitic melts can be distinguished by subtle variations. Pietre Cotte rhyolitic glasses display higher Nb, Zr and more elevated LREE concentrations (Fig. 3.31). Interestingly the banded pumices of the Pietre Cotte are the only example in the La Fossa stratigraphy where the two compositional groups interact directly. This is probably the result of the deeper less evolved melt intruding into the shallower trachy-rhyolitic magma batch triggering this explosive episode.

| Eruption | Pietre Cotte Upper (Tra) | Pietre Cotte (R) | Commenda Ash (T) | Palizzi D (T) | Palizzi B (R) | Pal A (T-P) |
|--------------------------|--------------------------|------------------|------------------|---------------|---------------|-------------|
| Pietre Cotte Upper (Tra) | | | | | | |
| Pietre Cotte (R) | 61.34 | | | | | |
| Commenda Ash (T) | 10.65 | 51.16 | | | | |
| Pal D (T) | 17.57 | 53.45 | 12.73 | | | |
| Pal B (R) | 327.06 | 1.40 | 321.88 | 280.53 | | |
| Pal A (TP) | 26.58 | 94.33 | 61.62 | 52.80 | 389.17 | |

(a)

| p (confidence limit) | D^2 critical, $f=8$ | |
|------------------------|-----------------------|--|
| 0.995 | 1.344 | < 0.5 % probability that the two samples are compositionally different if D^2 is less than 1.344 |
| 0.990 | 1.646 | < 1% probability that the two samples are compositionally different if D^2 is less than 1.646 |
| 0.950 | 2.733 | < 5% probability that the two samples are compositionally different if D^2 is less than 2.733 |
| 0.050 | 15.507 | > 95% probability that the two samples are compositionally different if D^2 is greater than 15.507 |
| 0.010 | 20.090 | > 99% probability that the two samples are compositionally different if D^2 is greater than 20.090 |

(b)

Table 3.21: (a) Statistical distance values (D^2) matrix for the explosive deposits of La Fossa, Vulcano produced during the last 5.5 ka. (b) The p (confidence limits) values and the D^2 critical values for the statistical distance test where $f = 8$ (major and minor elements).

The transition from shoshonitic compositions (i.e. Quadrara) to High-K compositions (i.e. La Fossa) is marked by a distinct switch in the source characteristics of the melts. The older Quadrara deposits display more elevated Zr/Th and Y/Th ratios compared with the younger La Fossa deposits (Fig. 3.31). This transition present a relative age tool for distinguish unknown Vulcano tephra distally.

Explosive deposits produced on Vulcano clearly demonstrate significant geochemical variability at a major element level which is the most diagnostic tool for distinguishing the eruptive products, particularly when considering the tephri-phonolite and trachyte compositions. Trace element concentrations can be indistinguishable between some eruptions within the same eruptive cycle. Trachy-rhyolitic glasses produced on Vulcano can be distinguished at a trace element level where variability probably reflects greater sensitivity to high level fractionation (Fig. 3.31).

In summary compositionally indistinguishable magmas (i.e. glasses) are repeatedly erupted over time. For instance the Upper brown tuff glass compositions (De Astis et al., 1997) are consistent with both Palizzi A and D compositions. From a distal tephrochronology perspective this means that Pre-La Fossa activity may be erroneously correlated with more recent activity or vice versa, highlighting the importance of stratigraphic control when determining proximal distal tephra correlations.

3.5.6 Stromboli proximal explosive deposits

Two major explosive episodes are recognised in the proximal stratigraphy of Stromboli during the last 13 ka; (1) Upper Vancori pumices (ca. 13 ka) and (2) Secche di Lazzaro (ca. 5 ka). Glass compositions of the two deposits are very distinct and reflect a compositional switch in the magmas feeding Stromboli (Tommasini et al., 2007).

3.5.6.1 Upper Vancori

The Upper Vancori products display a shoshonitic affinity and are trachytic in composition (Fig. 3.20). The fall pumices display stratigraphic heterogeneity, with two discrete glass compositions observed in the sequence. The lower pumices (unit 1) display more elevated SiO₂ and K₂O, with lower FeO, MgO and CaO than the upper pumices (unit 3) (Fig. 3.33). Based on major element concentrations the two fall deposits can be statistically distinguished at a 99.5 % confidence limit ($D^2_{\text{critical}} = 21.955$) using major elements where $D^2 = 27.7$.

Interestingly the incompatible trace element concentrations are not reflective of major element variations (Fig. 3.33). Both the lower and higher SiO₂ group have elevated incompatible trace elements and are essentially indistinguishable (Fig. 3.32). HFSE ratios to Th are consistent indicating that the two sets of pumices derived from a common source (Fig. 3.31). The only trace element to enable distinction between the two pumice deposits is the V (Fig. 3.38d), given its compatible behaviour concentrations are lower in the higher SiO₂ unit 1 lower pumices.

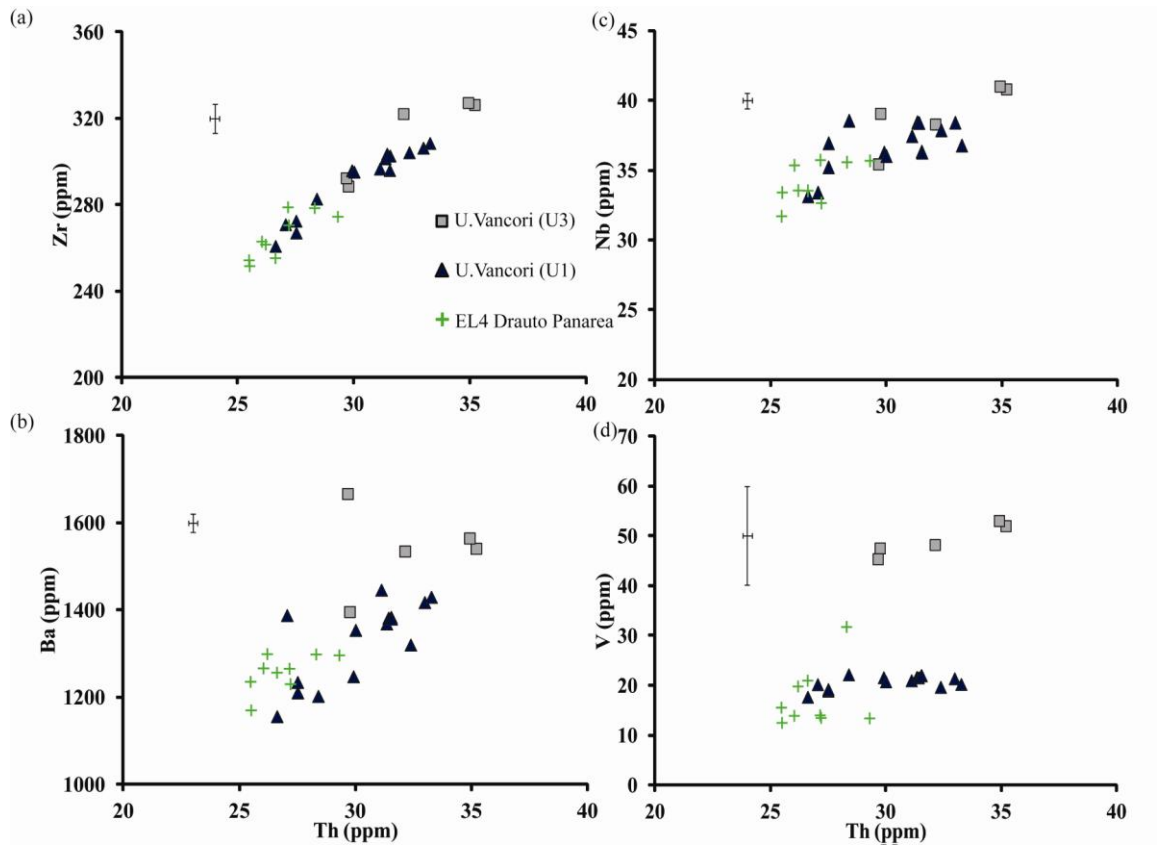


Figure 3.38: Trace element bi-plots displaying the Upper Vancori pumices, Stromboli. Shown also are the glass compositions of the EL4 pumices at Drauto, Panarea.

As shown by data presented here, Cortes et al. (2005) also recognise a progression to lower SiO₂ and higher MgO, CaO compositions with increasing stratigraphic height in the upper Vancori sequence using WR samples. Cortes et al. (2005) propose that closed system conditions allowed for high level fractional crystallisation of clinopyroxene and plagioclase to generate a trachytic melt composition (Unit 1). Following significant period of repose on Stromboli a Sciara collapse triggered the rise of a new basaltic magma which entered the trachytic melt, triggering the eruption. The stratigraphically

higher pumices of unit 3 might be the product of further mixing of a new basaltic magma and the residual trachytic melts thus explaining the lower SiO₂, higher MgO and CaO. This possibly indicates a temporal gap in the explosive product recorded in this Upper Vancori stratigraphy. Cortes et al. (2005) suggest that the arrival of new basaltic melts marks the introduction of Neo-Stromboli compositions at Stromboli.

3.5.6.2 Secche di Lazzaro

The Neostromboli period 13-6 ka terminates with the phreatomagmatic activity Secche di Lazzaro. As with the Upper Vancori this explosive episode is linked to a collapse of Sciara del Fuoco (Bertagnini and Landi, 1996; Porreca et al., 2006; Giordano et al. 2008 and Petrone et al., 2009). Bertagnini and Landi (1996) suggest that the collapse enabled water to enter the conduit triggering phreatomagmatic activity; accretionary lapilli abundant in both stratigraphies are contributed to this interpretation. Sections from along the Semaforo track (Northern Stromboli; SDL-N) and near the Centre for Advanced operations (COA; Eastern Stromboli; SDL-E) were sampled for geochemical analysis (See Fig. 3.5). Major element glass data is also available from other localities on the south of island including the type locality at Secche di Lazzaro (Petrone et al., 2009).

Secche di Lazzaro (SDL) phreatomagmatic deposits are characterised by the switch from shoshonitic activity (Vancori) to K-series activity (Neo-Stromboli). SDL glasses range from trachy-andesite to trachyte at different localities (Fig. 3.29). Table 3.22 presents the statistical distance values of all the glasses characterised here and incorporates those from other localities (Petrone et al. 2009).

At the SDL-N locality major element data reveals two discrete glass compositions within the stratigraphy. The darker green scoria fall of unit 2 can be distinguished from the grey pumices in the stratigraphically higher unit 5 on the basis of lower SiO₂, higher MgO, FeO and most dominantly CaO (Table 3.20). Indeed the unit 5 displays a single glass analysis that belongs to the lower SiO₂ group from unit 2. These two components are largely indistinguishable based on their trace element compositions (Table 3.20); with consistent HFSE/Th elements ratios (Fig. 3.34e).

At SDL-E only the most evolved higher SiO₂ glasses (trachytic) are observed in the thin fall beds of grey pumice at the base of the stratigraphy. The two pumice beds of U3 and U4 display major element compositions that are consistent with the upper portion of the

SDL-N stratigraphy (Table 3.20). Again incompatible trace element concentrations within the glasses of SDL-E are indistinguishable stratigraphically (Fig. 3.34e-h), but also are indistinguishable from the lower SiO₂ (trachy-andesitic) glass of SDL-N. V concentrations offer the only diagnostic feature at a trace element level between the trachy-andesite and trachyte glass populations. Given its compatible behaviour V has lower concentrations in the higher silica trachytic glasses (Fig. 3.34h).

Integrating the data from the SDL localities (Petrone et al., 2009) reveals that overall there is general agreement between the two data sets (Fig. 3.34a-d), this would indicate that the two localities investigated herein are fully representative of the compositional variability produced during this explosive phase on Stromboli. Interestingly if we focus more specifically on the southern localities reported by Petrone et al., (2009), at Secche di Lazzaro (type site) the glasses from the lower most portion of the stratigraphy UA (Giordano et al., 2008) have lower SiO₂ (trachy-andesitic) similar to the glasses at the base of the SDL-N locality investigated herein ($D^2 = 2.3$; Table 3.22). WR trace element variations between northern and southern SDL deposits observed by Petrone et al., (2009) are inconsistent with glass data herein, this would indicate that WR analyses are compromised by the variable proportions of phenocryst observed within the glassy matrix of the Secche di Lazzaro products.

Geochemical data here reveals two compositionally and statistically discrete major element glass compositions in the stratigraphy of the SDL explosive activity. From a distal tephrochronological perspective recognition of both these end-members is important as dispersal of these respective products appears to be variable across the island. Petrone et al., (2009) suggest that the two similar but ultimately different compositions reflect discrete and separate melts that resided in closed system conditions in the high level plumbing system of Stromboli. Collapse of the Sciara del Fuoco caused rapid decompression of the high level system and enabled water to enter the conduit (Bertagnini and Landi, 1996; Porreca et al., 2006 Giordano et al. 2008) triggering the explosive eruption of compositions that had previously been erupted effusively on the island.

| Sample | SDL-S-UB | SDL-SW-UA | SDL-E-U4 | SDL-E- U3 | SDL-N-U5 | SDL-N-U2 |
|---|----------|-----------|----------|-----------|----------|----------|
| Trace elements D ² values; <i>f</i> = 11 | | | | | | |
| SDL-S-UB (297)* | 0.0 | - | - | - | - | - |
| SDL-SW-UA (291)* | 3.5 | 0.0 | - | - | - | - |
| SDL-E-U4 | 5.7 | 5.7 | 0.0 | 0.6 | 1.7 | 1.5 |
| SDL-E- U3 | 4.5 | 30.9 | 0.2 | 0.0 | 3.7 | 1.1 |
| SDL-N-U5 | 2.1 | 19.2 | 2.0 | 1.1 | 0.0 | 6.1 |
| SDL-N-U2 | 4.9 | 2.3 | 37.7 | 34.8 | 22.2 | 0.0 |
| Major element D ² values; <i>f</i> = 8 | | | | | | |

(a)

| | | |
|-----------------------------|---------------------------------------|---|
| <i>p</i> (confidence limit) | D ² critical, <i>f</i> =8 | |
| 0.995 | 1.344 | < 0.5 % probability that the two samples are compositionally different if D ² is less than 1.344 |
| 0.990 | 1.646 | < 1% probability that the two samples are compositionally different if D ² is less than 1.646 |
| 0.950 | 2.733 | < 5% probability that the two samples are compositionally different if D ² is less than 2.733 |
| 0.050 | 15.507 | > 95% probability that the two samples are compositionally different if D ² is greater than 15.507 |
| 0.010 | 20.090 | > 99% probability that the two samples are compositionally different if D ² is greater than 20.090 |
| <i>p</i> (confidence limit) | D ² critical, <i>f</i> =11 | |
| 0.995 | 2.603 | < 0.5 % probability that the two samples are compositionally different if D ² is less than 2.155 |
| 0.990 | 3.053 | < 1% probability that the two samples are compositionally different if D ² is less than 2.558 |
| 0.950 | 4.575 | < 5% probability that the two samples are compositionally different if D ² is less than 3.940 |
| 0.050 | 24.725 | > 95% probability that the two samples are compositionally different if D ² is greater than 18.307 |
| 0.010 | 26.757 | > 99% probability that the two samples are compositionally different if D ² is greater than 23.209 |

(b)

Table 3.22: (a) Statistical distance values (D²) matrix for the explosive deposits of Secche di Lazzaro, Stromboli produced during the last 5.5 ka. (b) The *p* (confidence limits) values and the D² critical values for the statistical distance test where *f* = 8 (major and minor elements).

Petrone et al. (2009) infer that the presence of these two separate magma bodies feeding the SDL phreatomagmatic event might be interpreted as two separate explosive events in time and space. The temporal relationship between different successions and the two glass components is complex. Evidence of the trachy-andesite exclusively in the lower successions of both the SDL type locality (Petrone et al., 2009) and SDL-N might indicate this batch was erupted first. However, there is no evidence of these compositions in the basal deposits of the SDL-E which is exclusively trachytic. This clearly highlights the spatial complexities of these deposits. Porreca et al., (2006) recognised different emplacement temperatures associated with the different SDL PDC and provide evidence for two eruptive events. Determining the temporal relationship of the two explosive events is overshadowed by uncertainties in the dating of the entire SDL explosive succession which is still poorly constrained.

3.5.7 Distinguishing Vulcano and Stromboli glasses, a distal tool

Explosive activity at Vulcano and Stromboli during the last 21 ka has explosively produced magma compositions overlapping in their major element chemistry (Fig. 3.29). Both are dominated by a switch from shoshonitic to high-K series glasses. Incompatible trace element concentrations for glasses produced at Vulcano and Stromboli are similar, including indistinguishable levels of LREE enrichment (Fig. 3.24b). Consequently, from a distal tephrostratigraphy perspective it is important to consider the geochemical features of the two islands together and to identify diagnostic features.

Fortunately differences in the petrogenetic processes operating beneath the two islands are reflected in the glass chemistries of proximal deposits. Consequently, these diagnostic features can be used to assign volcanic provenance to distal tephtras even in the absence of known proximal counterparts. The key features are summarised below;

Major and minor elements

(1) K-series glasses at a similar SiO₂ wt.% produced at Vulcano display significantly higher Na₂O (Fig. 3.29g) and significantly lower TiO₂ than the glasses of Stromboli (Secche di Lazzaro) (Fig. 3.29b).

(2) The shoshonitic glasses at a similar SiO₂ wt.% produced at Vulcano (Quadrara) display higher Al₂O₃ and lower FeO than the glasses of Stromboli (U.Vancori) (Fig. 3.29).

Trace elements

(1) HFSE/Th ratios are significantly different between the glass compositions of the two islands;

- Nb/Th is the most diagnostic ratio - Stromboli glasses displaying more elevated values (Fig. 3.31a).
- Zr/Th ratios change with time in the glasses produced on Vulcano between the Shoshonitic glasses and the K-series glasses (Fig. 3.31b).
- K-series activity (La Fossa) display Zr/Th values that are dramatically lower than those seen in Neo-Stromboli glasses (SDL) (Fig. 31b). *Pre La Fossa*: The older shoshonitic series glasses (Quadrara) display more elevated ratios than those seen in the shoshonitic glasses of the Upper Vancori Stromboli.

(2) Neo-Stromboli SDL glasses predominantly display more elevated Ba and Pb concentrations than glasses erupted La Fossa glasses on Vulcano.

(3) K-series glasses on Vulcano at La Fossa display consistently lower Y concentrations than the glasses of SDL, Stromboli, as shown by lower Y/Th (Fig. 3.31e).

(4) Shoshonitic trachytes produced on Vulcano are restricted to lower Th concentrations than those on Stromboli (U. Vancori).

3.5.7.1 Medial-distal Vulcano and Stromboli deposits

Diagnostic features are tested on medial-distal tephra in the Aeolian Islands in an attempt to assess/refine their provenance solutions. A pumice fall bed at Drauto, Panarea contain grey cm size lapilli (Fig. 3.39). Lucchi et al. (2008) propose a local origin from inlets east of Panarea. The glasses are trachytic and exotic/external when compared with the CA activity on Panarea (Fig. 3.20). Representative glass analyses for the pumices are presented in Table 3.19; the layer was termed 'EL4' by De Rita et al. (2008) and was tentatively correlated to pumice fall from the Quadrara formation, Vulcano (21 ka).



Figure 3.39: ‘Exotic’ lapilli pumice fall recorded at Drauto (EL4), Panarea, consistent with the layer reported by De Rita et al., (2008).

| Sample | Exotic Layer 4 | Upper Vancori U3 | Upper Vancori U1 | Quadrara Pumice |
|------------------------------|----------------------------------|------------------|------------------|-----------------|
| | Trace elements D2 values; f = 10 | | | |
| Exotic Layer 4 (EL4) Panarea | 0.0 | 15.2 | 1.0 | 22.8 |
| Upper Vancori U3 | 6.5 | 0.0 | 4.8 | 25.9 |
| Upper Vancori U1 | 29.6 | 27.7 | 0.0 | 19.0 |
| Quadrara Pumice | 9.5 | 13.5 | 30.3 | 0.0 |
| | Major elements D2 values; f = 8 | | | |

(a)

| p (confidence limit) | $D^2_{critical}, f=8$ | |
|------------------------|-----------------------|--|
| 0.995 | 1.344 | < 0.5 % probability that the two samples are compositionally different if D^2 is less than 1.344. |
| 0.990 | 1.646 | < 1% probability that the two samples are compositionally different if D^2 is less than 1.646. |
| 0.950 | 2.733 | < 5% probability that the two samples are compositionally different if D^2 is less than 2.733. |
| 0.050 | 15.507 | > 95% probability that the two samples are compositionally different if D^2 is greater than 15.507 |
| 0.010 | 20.090 | > 99% probability that the two samples are compositionally different if D^2 is greater than 20.090 |

| p (confidence limit) | $D^2_{critical}, f=10$ | |
|------------------------|------------------------|--|
| 0.995 | 2.156 | < 0.5 % probability that the two samples are compositionally different if D^2 is less than 2.155 |
| 0.990 | 2.558 | < 1% probability that the two samples are compositionally different if D^2 is less than 2.558 |
| 0.950 | 3.940 | < 5% probability that the two samples are compositionally different if D^2 is less than 3.940 |
| 0.050 | 18.307 | > 95% probability that the two samples are compositionally different if D^2 is greater than 18.307 |
| 0.010 | 23.209 | >99% probability that the two samples are compositionally different if D^2 is greater than 23.209 |

(b)

Table 3.23: (a) Statistical distance values (D^2) matrix for the explosive deposits of the Upper Vancori, Stromboli (13 ka); the Quadrara pumices (21 ka), Vulcano and the EL4 pumices, Drauto, Panarea. (b) The p (confidence limits) values and the D^2 critical values for the statistical distance test where $f = 8$ (major and minor elements).

The trachytic glasses display a relatively homogenous population with 63.1-64.2 wt.% SiO₂, 0.7-0.8 wt.% TiO₂ and 5.5-6.2 wt.% K₂O. Major element compositions of the glasses outcropping on Panarea are statistically indistinguishable from either the upper Vancori unit 3 ($D^2 = 6.5$) and Quadrara ($D^2 = 9.5$) trachytic glasses. Interestingly the distal pumices display TiO₂ more consistent with Stromboli activity, whilst the K₂O is subtly more elevated and consistent with Vulcano. Consequently major element compositions are inconclusive in determining a provenance of this pumice bed.

EL4 pumices display HFSE/Th ratios (Nb/Th = 1.3 ± 0.05 ; Zr/Th = 9.9 ± 0.3) consistent with an origin from Stromboli (Fig. 3.31a-b). Trace element concentrations of these pumices at a multi-element level are clearly very similar to those produced proximally during the Upper Vancori period (Table 3.23). Given the discrepancies between the EL4 major element concentrations and the Upper Vancori a precise proximal-distal link is not possible in this instance. Trace element geochemistry of these shoshonitic glasses suggests that this fall may be related to a south-western dispersal of pumice lapilli during the Upper Vancori, explosive activity. It may present evidence for another subtly discrete magma composition that has not yet been characterised on the island. The published correlation to the fall from the Quadrara explosive activity is cannot be confirmed (De Rita et al., 2008).

To the south of the Aeolian Islands a diffuse pumice lapilli bed was identified in the accumulation profile of Capo di Milazzo, Sicily. Pumices were bi-modal with a trachy-andesite to trachytic composition with major elements ranging from 57.6-63.4 wt.% SiO₂, 2.7-6.5 wt.% FeO, 2.7-5.7 wt.% CaO and 4.9-6.1 wt.% K₂O. Representative data is given in Table 3.19. The major element glass composition corresponded to the two end-members of the Quadrara formation on Vulcano (Fig. 3.30). Trace element concentrations re-affirm this correlation with identical HFSE/Th ratios (Nb/Th = 1.0 ± 0.04 ; Zr/Th = 8.9 ± 0.2) (Fig. 3.31a- b). A single trace element analysis of the lighter (trachytic) pumice at Capo Milazzo reveals the similarity with the basal pumices of Quadrara formation (Fig. 3.32). Elevated Th and lower Sr concentrations in this glass are indicative of proximally reported lighter Quadrara pumices (Fig. 3.32d). This provides strong evidence for a south-ward dispersal of the explosive Quadrara formation on Vulcano.

Narcisi (2002) reports a trachy-andesitic to trachytic tephra layer from Lago di Pergusa, central Sicily that displays indistinguishable major element concentrations to the

Quadrara proximal data presented herein ($D^2 = 6.6$). Unfortunately only an average value is given and it lies between the two proximal end-members (Fig. 3.30). However major element bi-plots confirm that this average is derived from data points that correspond with both proximal end-members. Chronological and stratigraphical problems with correlations to the Quadrara formation, Vulcano meant that Narcisi (2002) suggested a more distal origin for the ash layer. A source on the Italian mainland was proposed and in particular the (i.e., Pomici di Base, Vesuvius). Figure 3.30a clearly illustrates that both Pomici di Base and Codola glasses of Vesuvius have significantly more elevated K_2O than is present in the Lago di Pergusa tephra and the Aeolian island trachytic glasses. Consequently Vesuvius seems an unlikely source for this tephra.

The Quadrara formation correlation to Lago di Pergusa was rejected by Narcisi (2002) given that the distal tephra lies stratigraphically beneath a tephra correlated to the Monte Guardia activity, Lipari. Proximal stratigraphic investigations place the Quadrara formation above the Monte Guardia (Lucchi et al., 2008). The two deposits are never present in the same stratigraphy on Vulcano. The Quadrara formation is dated at 21.3 ± 3.4 ka and is younger than the Monte Guardia activity (ca. 26.3 cal ka BP) supporting the stratigraphic interpretations of Lucchi et al. (2008). However the Quadrara age is far from precise given the errors reported. There is no proximal evidence of evolved trachytic glass compositions stratigraphically beneath the Quadrara formation. However the absence of exposed products does not preclude similar compositions being erupted. The origin of the Quadrara type ash at Lago di Pergusa remains unresolved and may require reinvestigation of the proximal stratigraphy, SW Vulcano.

3.5.7.2 Distal marine tephtras

Three tephra layers from the Tyrrhenian Sea marine cores (Paterne et al., 1988) display compositions comparable to glass explosively produced on Vulcano and Stromboli, only average glass compositions are presented (Paterne et al., 1988). Below are re-evaluations of these distal tephtras in light of the new proximal data herein.

KET8011-94cm is trachytic in composition and is dated at 11.9 ka. It is geochemically similar to the trachy-rhyolitic deposits of Casa Lentia and the Pietre Cotte, Vulcano (Fig. 3.29). Considering its stratigraphic position and age the Lentia complex is a sensible solution (Paterne et al., 1988). The locality of KET8011 north-east of Stromboli might provide evidence for a north-east dispersal during this activity. KET8011-35cm represents high-K activity and is dated to 5.7 ka (Paterne et al., 1988),

at a similar SiO₂ wt.% the distal tephra displays more elevated TiO₂ than the products of Vulcano. This tephra lies on the evolutionary trend of the Stromboli glasses (Fig. 3.29), whilst displaying lower Na₂O than is typical of the Vulcano glasses (Fig. 3.29). Consequently proximal data would suggest a provenance from Stromboli. The glass data does not overlap with the Secche di Lazzaro (SDL) deposits, the elevated TiO₂ and the age of the tephra (5.7 ka) would support correlation to the phreatomagmatic eruption of the SDL. KET8003-0cm is tephri-phonolitic and dated to 1.7 ka. This tephri-phonolite is comparable to the oldest Palizzi A (La Fossa) and to Vulcanello (Todman, 2012). Given their similar total alkalis and their lower TiO₂ at a given SiO₂ these distal glasses may have derived from Vulcano (Fig. 3.29). These three tephras from Tyrrhenian Sea marine cores require a re-investigation given the comprehensive glass database for Stromboli and Vulcano.

3.6 Conclusions:

1. Glass geochemistry from the major explosive episodes in the Aeolian Islands indicates dramatic variability consistent with previous whole rock investigations.
2. Similar major elements compositions produced at separate volcanic centres can be easily distinguished based on differing petrological processes in operation reflected in the trace element geochemistry of the glasses, essential for determining provenance of unknown distal tephras sourcing from the Aeolian Islands.
3. Vulcano specific geochemical variability maybe best defined by major, minor element diagnostic features (i.e., Vulcano and Stromboli), whilst in other instances trace elements variations are imperative to reliably distinguishing proximal units (i.e., Lipari).
4. The integration of major, minor and trace element glass geochemistry offers an essential diagnostic tool for defining and refining proximal-distal correlations.
5. Where repeated major, minor and trace element geochemistries are produced from a single volcanic centre, stratigraphy has a crucial role to play in determining age and provenance of distal tephras (i.e., P.del Perciato and Falcone formations, Lipari).
6. Stratigraphic compositional variability is evident in many of the eruptive sequences of Aeolian island eruptions, this has two important implications;
 - This variation may reflect polybaric storage and mixing of compositionally discrete melts with explosive eruptions being triggered during replenishment.

- From a tephrochronological perspective this investigation highlights the importance of grain-specific analyses to capture the full stratigraphic geochemical variability of an eruption, essential for proximal-distal correlations.

7. Mid-distal outcrops on the neighbouring islands offer a test bed for proximal-distal matching. Proximal data has been used to verify the southern and north-eastern dispersal of the Monte Guardia eruption (Lipari). Pumice fall on Panarea previously linked to the Quadrara formation (Vulcano) is refuted, these pumices have a greater trace element affinity to the neighbouring island of Stromboli. The distal fall from the Quadrara formation confirms a south-eastern dispersal with pumices outcropping 25 km away on Capo Milazzo (Sicily).

8. Proximal data herein indicate that several published interpretations of distal marine, lacustrine and continental tephra might require re-investigation.

Chapter 4: Marine-continental tephra correlations: volcanic glass geochemistry from the Marsili Basin and the Aeolian Islands, Southern Tyrrhenian Sea, Italy.

This chapter is adapted from a paper that was published in the Journal of Volcanology and Geothermal Research in June 2012. The paper's text and figures were produced by the candidate. The original standalone version can be found in the appendix I.

Abstract

Major, minor and trace element analysis of volcanic glass in proximal and distal tephra (<2mm) deposits underpins tephrochronology. This approach has been tested in the Aeolian Islands and the Tyrrhenian Sea using juvenile clasts in pyroclastic fall and flow deposits. Geochemical data are used to link marine tephra in the Marsili Basin (core TIR2000-C01) to explosive eruptions of (i) Lipari (Monte Pilato; 776 cal AD); (ii) Vulcano; (iii) Campi Flegrei (Soccavo 1; 11915-12721 cal yrs BP). Whether a polymictic coarse grained volcanoclastic turbidite in the Marsili Basin originated from collapse on Salina remains unresolved because multi-elemental analysis raises doubt about the published correlation to the Pollara region.

It is evident that correlation of proximal continental and distal marine tephra, at a high level of confidence, requires a full complement of major, minor and trace element data. In conjunction with considerations of the mineralogy and morphology of juvenile deposits these data help define petrological lineages such that precise provenance can be established. Whilst a precise proximal-distal match must be based on identical major, minor and trace element concentrations it is clear that resurgent activity from a single volcano can produce magmas with identical compositions. In such cases stratigraphic relationships must complement any geochemical study. Occasionally proximal stratigraphies may be unrepresentative of the complete eruptive history because of a lack of exposure due to burial by more recent effusive and explosive activity, or sector collapse which can remove vital stratigraphy particularly on volcanic islands.

4.1 Introduction

Presented in this chapter is major, minor and trace element glass data for five tephra layers from the marine core TIR2000-C01 from the Marsili basin in the Tyrrhenian Sea. The proximity of this core to the explosive activity on the Aeolian Islands presents a test-bed for continental proximal-marine distal correlations. Initial investigations on this same Marsili basin core (Di Roberto et al., 2008) identified three primary tephra that were correlated to eruptions from the Aeolian Islands (i.e., Lower Pollara; Salina and Gabelotto-Fiume Bianco; Lipari) and Vesuvius (AP1-3). Additionally two monogenetic (single composition) turbidites were also correlated to volcanic sources, all on the basis of major element data (EDAX).

To date tephrochronology has largely been based on matching stratigraphies, phenocryst mineralogy and texture underpinned by major and minor element glass geochemistry. This chapter illustrates the benefits of grain-specific major, minor and trace element analysis of glasses as a diagnostic tool in tephrochronology. The following aspects of proximal distal correlations will be addressed:

- a) Does major element data (Wavelength Dispersive Electron Micro Probe Analysis-EMPA) provide the same provenance solutions as trace element data (Laser Ablation Inductively Coupled Plasma Mass Spectrometry; LA-ICP-MS)?
- b) Do exposed proximal deposits record the same geochemical variability as the distal equivalents?
- c) To what extent do monogenetic and polygenetic turbidites in the marine environment provide tephrochronological information?

4.2 Marsili Basin core (TIR2000-C01)

The Tyrrhenian Sea is a backarc basin formed during the convergence of the European and African plates (Lucchi and Kidd, 1998). The Marsili Basin core (TIR2000-C01; Fig. 4.1) was recovered from a site 27 km ENE of the main channel mouth of the Stromboli Valley and about 20 km ESE from the summit of the Marsili Volcano (Fig. 4.1). The Stromboli Valley channels unconsolidated volcanoclastic material from the flanks of the Eastern Aeolian Islands (Lucchi and Kidd, 1998).

core from nearby (Paterne et al., 1988) Markings are as follows; Aeolian islands; A, Alicudi; F, Filicudi; S, Salina; L, Lipari; V, Vulcano; P, Panarea; St, Stromboli. Seamounts; Si, Sisifo; Eo, Eolo; En, Enarete; La, Lametini, M, Marsili.

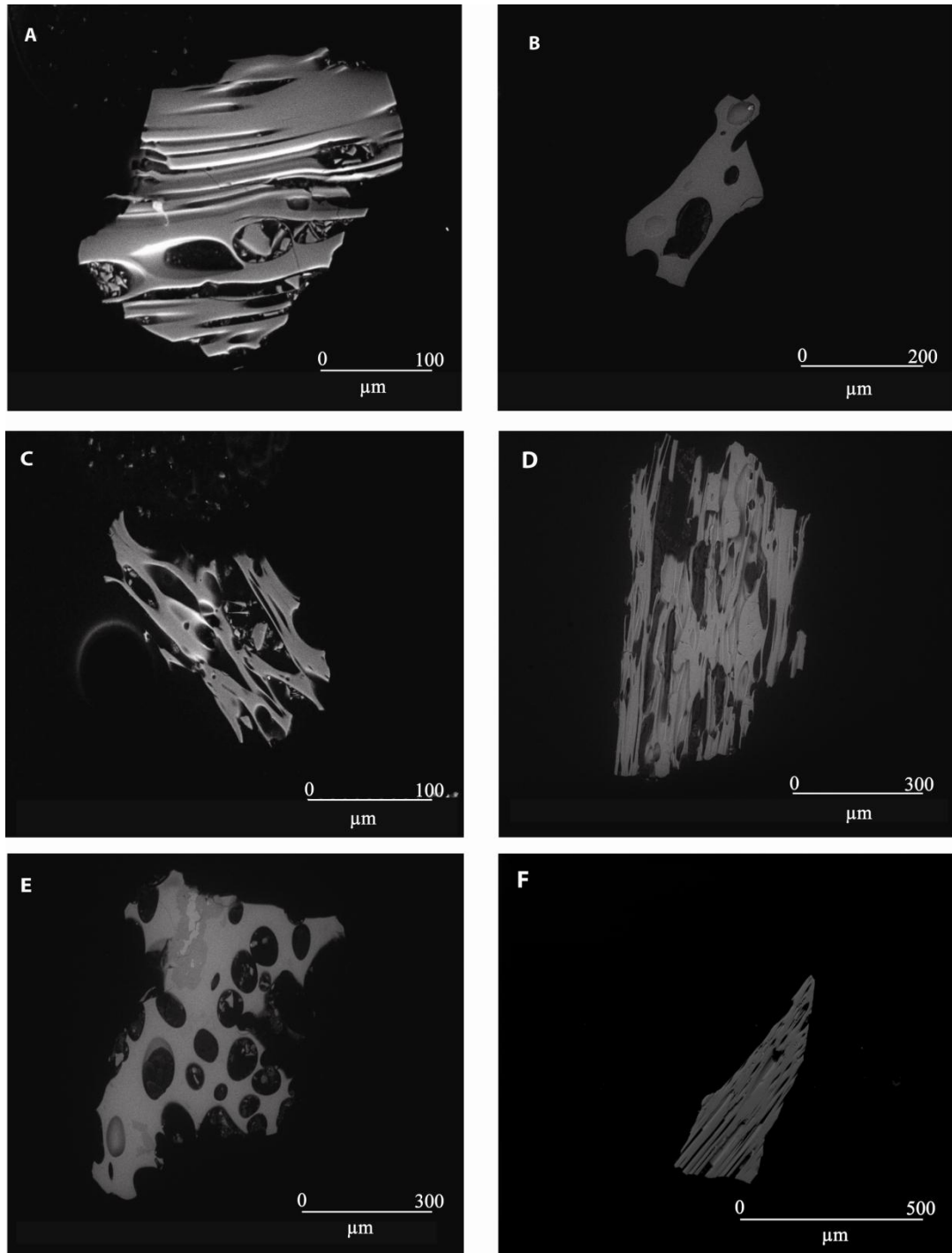


Figure 4.2: SEM images of Marsili Basin (TIR2000-C01) tephras; (A) TIR2000-7; (B) TIR2000-50; (C) TIR2000-93; (D) TIR2000-398-Component 1; (E) TIR2000-398-Component 2; (F) TIR2000-417.

The Marsili Basin core was recovered during the TIR2000 cruise using 1.5 tonne gravity corer at a water depth of about 3200m on a small topographic high that rises about 100 m from the sea floor in the eastern sector of the basin (Di Roberto et al., 2008). The core is 4.8 m long (Fig. 4.1) and further details on the core are given in Di Roberto et al. (2008).

Investigated samples were taken from five layers, two were primary tephra fall and three were turbidites. Primary tephra were identified on the basis of their contact with the underlying sediments. Primary tephra displayed planar contacts with the underlying sediments and there were no erosive features. In an attempt to constrain the chronology of the marine core we have bracketed the core by analysing tephra layers at the top and the base of TIR2000-C01 (Fig. 4.1). The samples were dried and sieved between 63-125 μm , 125-250 μm and 250-500 μm . Analysis was conducted on all size fractions to insure all chemical heterogeneity was observed. However data presented here are from the largest available size fraction, as long as the glass populations were consistent within the different fractions. Individual glass shards were hand-picked under a light microscope and mounted in Struers Epofix epoxy resin.

4.3 Results

4.3.1 TIR2000-C01 (Marsili Basin)

TIR2000-C01 tephra often contained background shard populations. This is common within marine archives with such close proximity to active volcanoes (e.g., Siani et al., 2004). Here we focus on the geochemistry of the dominant shard populations, which we consider reflective of volcanic related events in time and space. Shard populations which make up $\leq 15\%$ of the bulk are considered “background” and are not discussed herein.

The Marsili Basin is surrounded by subduction derived explosive and effusive volcanism from both the Aeolian Islands and the Italian mainland. Primitive mantle normalised patterns for all tephra recorded in the Marsili basin core were consistent with this tectonic setting, displaying enrichment in the large ion lithophile elements (LILE; Rb, Th, U), relative to the high field strength elements (i.e., HFSE; Nb, Ta and Zr).

| TIR2000-C01 Depth (cm) Shards Material Sample Major (wt. %) | TIR2000-7 | | | TIR2000-50 | | | TIR2000-93 | | |
|--|-----------|-------|-------|------------|-------|-------|------------|-------|-------|
| | n=32 | | | n=38 | | | n=32 | | |
| | Glass | Glass | Glass | Glass | Glass | Glass | Glass | Glass | Glass |
| | 42D | 1A | 26C | 4A | 11A | 22B | 21C | 22C | 7A |
| SiO ₂ | 75.14 | 75.59 | 75.29 | 56.46 | 56.93 | 57.8 | 57.79 | 58.61 | 59.11 |
| TiO ₂ | 0.08 | 0.10 | 0.04 | 0.66 | 0.80 | 0.70 | 0.48 | 0.48 | 0.52 |
| Al ₂ O ₃ | 13.28 | 12.85 | 13.25 | 17.45 | 18.11 | 17.05 | 19.18 | 19.26 | 18.92 |
| FeOt | 1.48 | 1.41 | 1.53 | 6.8 | 6.23 | 6.65 | 4.56 | 4.06 | 3.83 |
| MnO | 0.00 | 0.09 | 0.13 | 0.12 | 0.16 | 0.09 | 0.13 | 0.16 | 0.19 |
| MgO | 0.04 | 0.04 | 0.03 | 2.41 | 2.15 | 2.23 | 1.07 | 0.88 | 0.72 |
| CaO | 0.78 | 0.74 | 0.74 | 4.93 | 4.26 | 4.64 | 3.64 | 3.45 | 3.20 |
| Na ₂ O | 3.85 | 3.64 | 3.8 | 4.52 | 4.55 | 4.47 | 3.73 | 3.71 | 3.82 |
| K ₂ O | 5.35 | 5.54 | 5.2 | 6.65 | 6.81 | 6.38 | 9.43 | 9.39 | 9.68 |
| Analytical Total | 94.90 | 94.46 | 98.68 | 97.20 | 98.28 | 97.83 | 97.47 | 94.30 | 98.53 |
| D.I. | 93.7 | 94.2 | 93.2 | 69.1 | 71.4 | 70.4 | 78.0 | 79.3 | 81.6 |
| Na ₂ O + K ₂ O | 9.20 | 9.18 | 9 | 11.17 | 11.36 | 10.85 | 13.15 | 13.1 | 13.5 |
| K ₂ O/Na ₂ O | 1.39 | 1.52 | 1.37 | 1.47 | 1.49 | 1.43 | 2.53 | 2.53 | 2.53 |
| Trace ppm | | | | | | | | | |
| Ti | 493 | 439 | 495 | 4208 | 4148 | 4002 | 3167 | 2963 | 2959 |
| Rb | 339 | 328 | 351 | 231 | 236 | 230 | 385 | 387 | 395 |
| Sr | 30.4 | 16.8 | 17.9 | 1235 | 1152 | 1095 | 940 | 950 | 910 |
| Y | 38.1 | 42 | 40.6 | 19.8 | 19.1 | 20.8 | 26.5 | 26.4 | 26.2 |
| Zr | 167 | 177 | 182 | 180 | 194 | 179 | 274 | 288 | 295 |
| Nb | 37.0 | 38.0 | 38.7 | 25.5 | 26.2 | 25.8 | 46.2 | 48.3 | 47.7 |
| Ba | 19.5 | 16 | 18.6 | 1241 | 1249 | 1143 | 1946 | 2010 | 1891 |
| La | 53.7 | 56.7 | 66.2 | 66 | 68.9 | 65.9 | 66.2 | 70.8 | 70.7 |
| Ce | 105 | 113 | 128 | 120 | 122 | 122 | 130 | 133 | 134 |
| Pr | 10.8 | 11.4 | 12.7 | 12.6 | 12.1 | 12.6 | 14.4 | 14.2 | 14.2 |
| Nd | 39.0 | 42.6 | 43.8 | 44.6 | 46.9 | 46.9 | 52.2 | 54.5 | 54.0 |
| Sm | 8.0 | 7.9 | 8.3 | 8.4 | 7.9 | 7.2 | 10.3 | 9.3 | 9.6 |
| Eu | 0.2 | 0.2 | 0.2 | 1.7 | 1.7 | 1.5 | 2.2 | 2.5 | 2.3 |
| Gd | 6.4 | 7.2 | 6.4 | 5.5 | 5.5 | 5.6 | 6.7 | 6.4 | 7.3 |
| Dy | 6.6 | 7.2 | 7.2 | 4.1 | 3.8 | 3.9 | 5.2 | 5.0 | 5.2 |
| Er | 4.3 | 4.2 | 4.3 | 1.9 | 2.0 | 2.1 | 2.7 | 2.4 | 2.4 |
| Yb | 4.6 | 4.8 | 4.8 | 1.9 | 2.0 | 2.2 | 2.5 | 2.6 | 2.4 |
| Lu | 0.68 | 0.71 | 0.70 | 0.30 | 0.31 | 0.28 | 0.36 | 0.37 | 0.33 |
| Ta | 2.71 | 2.68 | 2.4 | 1.4 | 1.44 | 1.34 | 2.17 | 2.23 | 2.38 |
| Pb | 33.2 | 32.9 | 32.3 | 29.6 | 30.2 | 27.7 | 55.8 | 58.2 | 60.7 |
| Th | 48.6 | 53 | 54.4 | 28.8 | 29.4 | 29.8 | 26.2 | 26.4 | 28.7 |
| U | 16.4 | 16.2 | 16.9 | 9.0 | 9.3 | 9.4 | 9.6 | 9.4 | 10.3 |

Table 4.1: Representative grain-specific major (EPMA) and trace (LA-ICP-MS) element data for the distal Marsili Basin tephtras (Full data given in Appendix eIII).

| TIR2000-C01 Depth (cm) Shards Material Sample Major (wt. %) | TIR2000- 398cm Component 1 | | | TIR2000- 398cm Component 2 | | | TIR2000- 417 cm | | | |
|--|-------------------------------|-------|--------|-------------------------------|-------|-------|--------------------|-------|-------|-------|
| | <i>n=47</i> | | | <i>n=19</i> | | | <i>n=79</i> | | | |
| | Glass | Glass | Glass | Glass | Glass | Glass | Glass | Glass | Glass | Glass |
| | 8A | 23B | 37D | 28C | 12A | 5A | 15B | 21B | 11A | 37E |
| SiO ₂ | 55.01 | 62.57 | 71.6 | 52.76 | 55.51 | 57.15 | 52.37 | 58.43 | 66.83 | 70.59 |
| TiO ₂ | 1.31 | 1.22 | 0.60 | 1.32 | 1.23 | 1.25 | 1.01 | 1.17 | 0.71 | 0.63 |
| Al ₂ O ₃ | 14.42 | 14.44 | 13.98 | 15.25 | 16.7 | 14.78 | 15.73 | 15.09 | 15.42 | 14.17 |
| FeO _t | 11.66 | 8.07 | 3.43 | 11.46 | 9.58 | 10.64 | 9.55 | 8.99 | 4.62 | 2.87 |
| MnO | 0.24 | 0.13 | 0.13 | 0.11 | 0.2 | 0.17 | 0.11 | 0.28 | 0.10 | 0.14 |
| MgO | 4.15 | 2.23 | 0.56 | 4.48 | 3.09 | 3.19 | 6.10 | 3.15 | 1.26 | 0.75 |
| CaO | 8.23 | 5.31 | 2.28 | 9.19 | 8.08 | 6.92 | 11.25 | 6.73 | 3.41 | 2.25 |
| Na ₂ O | 3.01 | 3.41 | 4.06 | 3.22 | 3.58 | 3.10 | 2.44 | 3.37 | 4.02 | 4.59 |
| K ₂ O | 1.96 | 2.63 | 3.37 | 2.23 | 2.03 | 2.80 | 1.43 | 2.79 | 3.63 | 4.02 |
| Analytical Total | 98.37 | 97.47 | 92.35 | 98.71 | 97.85 | 98.96 | 99.06 | 98.23 | 94.83 | 97.35 |
| D.I. | 38.7 | 58.6 | 81.4 | 40.4 | 43.6 | 47.0 | 29.1 | 50.5 | 73.2 | 84.2 |
| Na ₂ O + K ₂ O | 4.97 | 6.04 | 7.43 | 5.45 | 5.61 | 5.90 | 3.87 | 6.16 | 7.64 | 8.61 |
| K ₂ O/Na ₂ O | 0.65 | 0.77 | 0.83 | 0.69 | 0.57 | 0.90 | 0.59 | 0.83 | 0.9 | 0.88 |
| Trace ppm | | | | | | | | | | |
| Ti | 7668 | 6830 | 3422 | 8276 | 8595 | 7004 | 6209 | 5126 | 4857 | 3752 |
| Rb | 59.73 | 84.59 | 110.52 | 75.48 | 75.92 | 78.72 | 38.64 | 64.56 | 106 | 122 |
| Sr | 587 | 344 | 291 | 646 | 459 | 547 | 487 | 476 | 320 | 243 |
| Y | 28.4 | 29.7 | 34.4 | 31.1 | 30.5 | 26.6 | 19.2 | 23.8 | 32.8 | 34.9 |
| Zr | 101 | 142 | 179 | 155 | 149 | 110 | 82 | 143 | 253 | 293 |
| Nb | 7.9 | 8.8 | 10.9 | 18.1 | 14.3 | 8.6 | 10.3 | 19.1 | 32.2 | 36.6 |
| Ba | 472 | 538 | 690 | 678 | 608 | 592 | 484 | 761 | 1144 | 1253 |
| La | 27.8 | 25.3 | 34.7 | 54.8 | 39.9 | 34.3 | 24.5 | 38.3 | 58 | 61.2 |
| Ce | 57.5 | 51.5 | 70.4 | 106 | 81.2 | 69.9 | 51.1 | 76.8 | 112 | 117 |
| Pr | 6.8 | 6.1 | 8.0 | 11.7 | 9.2 | 7.6 | 5.8 | 7.9 | 12.1 | 11.9 |
| Nd | 30.1 | 25.5 | 32.6 | 47.5 | 38.9 | 31.1 | 23.8 | 32.1 | 43.2 | 44.9 |
| Sm | 6.1 | 5.5 | 6.9 | 8.7 | 7.5 | 6.9 | 5.6 | 5.8 | 8.4 | 8.8 |
| Eu | 1.7 | 1.3 | 1.5 | 2.2 | 2.0 | 1.7 | 1.4 | 1.5 | 1.7 | 1.6 |
| Gd | 5.3 | 5.4 | 5.9 | 7.1 | 6.4 | 5.7 | 5.0 | 5.5 | 6.7 | 6.4 |
| Dy | 5.4 | 5.4 | 6.2 | 6.4 | 6.2 | 4.9 | 4.2 | 4.6 | 6.0 | 6.3 |
| Er | 3.0 | 3.4 | 3.9 | 3.4 | 3.3 | 2.9 | 2.2 | 2.6 | 3.5 | 3.6 |
| Yb | 3.0 | 3.4 | 3.9 | 3.1 | 3.0 | 2.7 | 1.9 | 2.4 | 3.3 | 4.0 |
| Lu | 0.43 | 0.53 | 0.59 | 0.45 | 0.47 | 0.44 | 0.30 | 0.35 | 0.54 | 0.57 |
| Ta | 0.41 | 0.57 | 0.68 | 0.87 | 0.79 | 0.51 | 0.52 | 0.93 | 1.61 | 1.87 |
| Pb | 10 | 13.6 | 17.0 | 15.9 | 13.8 | 12.2 | 11.2 | 17.3 | 22.2 | 23.1 |
| Th | 5.3 | 6.9 | 10.1 | 15.7 | 11.3 | 7.7 | 7.0 | 12.9 | 20.5 | 22.6 |
| U | 1.9 | 2.2 | 3.1 | 4.2 | 3.7 | 2.5 | 1.7 | 3.7 | 5.5 | 6 |

Table 4.1: Continued.

| Tephra | TIR-7cm | M. Pilato | TIR-IV-50cm | Palizzi A | SDL | Upper TGR | TIR-IV-93cm | Soccavo 1 | TIR-I-38cm (1) | (2) | TIR-I-57cm | Lower Pollara |
|-----------|-----------|-----------|-------------|-----------|-----------|------------------|-------------|---------------|----------------|---------------|------------|---------------|
| Sampled | M.B | Lipari | M.B | Vulcano | Stromboli | Vulcano | M.B | Campi Flegrei | M.B | M.B | M.B | Salina |
| Chemistry | R | R | T.A | T.A / P | T.A | Bas.Tr.And - T.A | P | P | Bas.And - R | Bas.And - T.A | Bas.And- R | Bas.And - R |
| Nb/Zr | 0.20-0.22 | 0.21-0.23 | 0.13-0.14 | 0.14-0.15 | 0.13-0.15 | 0.13-0.15 | 0.16-0.18 | 0.15-0.17 | 0.06-0.08 | 0.11-0.12 | 0.11-0.16 | 0.07-0.10 |
| Ti/Zr | 2.4-3 | 2.4-2.7 | 20.9-25.3 | 16.8-22.0 | 19.7-22.4 | 22.9-33.0 | 9.7-15.4 | 9.01-11.86 | 89.9-19.1 | 51.2-53.5 | 12.3-81.3 | 8.0-77.9 |
| Ti/Y | 10.5-13.1 | 10.1-11.5 | 170-227 | 164-193 | 198-234 | 183-217 | 113-168 | 76.3-124.9 | 123-281 | 265-270 | 77.4-365.4 | 2.1-94.8 |
| Ta/Th | 0.04-0.05 | 0.05 | 0.04-0.06 | 0.04-0.05 | 0.06-0.07 | 0.04-0.05 | 0.08-0.10 | 0.08-0.10 | 0.06-0.08 | 0.05-0.06 | 0.06-0.08 | 0.04-0.07 |
| Nb/Th | 0.7-0.8 | 0.7-0.8 | 0.8-0.9 | 0.8-0.9 | 1.2-1.5 | 0.8-0.9 | 1.7-2.0 | 1.5-1.8 | 1.0-1.5 | 1.2-1.5 | 1.4-2.3 | 1.0-1.3 |
| Zr/Th | 3.3-3.5 | 3.3-3.5 | 5.9-6.6 | 5.9-6.4 | 8.6-10.6 | 6.8-6.9 | 10.1-11.7 | 7.2-12 | 14.4-21.5 | 9.9-13.5 | 9.9-15.0 | 10.5-17.8 |
| Nd/Nb | 1-1.2 | 1.6-1.1 | 1.7-1.9 | 1.6-1.8 | 1.2-1.4 | 1.8-2.3 | 1.01-1.16 | 0.83-1.16 | 2.72-3.99 | 2.33-2.64 | 0.98-2.22 | 1.2-5.8 |
| Zr/Sr | 10-11 | 0.02 | 0.1-0.2 | 0.2-0.5 | 0.5-0.7 | 0.1-0.2 | 0.8-0.9 | 0.6-0.90 | 0.1-0.7 | 0.2-0.3 | 0.2-1.7 | 0.1-0.5 |
| La/Yb | 11-15 | 11-13 | 25-38 | 27-34 | 23-27 | 24-29 | 26-32 | | 6.9-12.9 | 11-19 | 10-23 | 5.8-21 |
| La/Sm | 6.7-8.0 | 6.1-7.2 | 7.4-10.0 | 7.5-9.6 | 6.2-7.2 | 6.2-8.3 | 6.4-8.3 | 4.9-8.7 | 4.0-5.7 | 5.1-6.6 | 4.4-9.4 | 4.3-16.3 |
| Ce/Yb | 23-31 | 23-26 | 46-69 | 49-64 | 45-56 | 43-54 | 50-63 | 28-62 | 14-29 | 25-37 | 21-44 | 11-36 |
| Eu/Eu* | 0.06-0.10 | 0.06-0.11 | 0.7 | 0.58-0.75 | 0.7-0.8 | 0.68-0.80 | 0.64-0.95 | 0.6-1.3 | 0.7-0.9 | 0.8-0.9 | 0.5-0.9 | 0.6--2.7 |

Table 4.2: Trace element ratios for the distal tephra investigated in TIR2000-C01 and their potential correlatives sourcing from the Aeolian Islands and Campi Flegrei. **R** = Rhyolite; **T.A** = Trachy-andesite; **B.as.And** = Basaltic andesite; **P** = Phonolite; **Tr.And** = Trachy-andesite.

The tephra display a “trough” or negative anomaly at Nb and Ta, whilst also displaying a negative anomaly at Ti (Fig. 4.4; 4.6; 4.8; 4.10; 4.11). Representative major, minor and trace element data for distal tephra are given in Table 4.1 and diagnostic ratios in Table 4.2. Full geochemical data sets for distal marine tephra are given in appendix eIII

4.3.2 TIR2000-7 (7 cm below sea floor (b.s.f.))

The upper most tephra layer in the Marsili Basin core is TIR2000-7cm which was previously correlated to Monte Pilato explosive activity on Lipari (Di Roberto et al., 2008). The tephra comprised of an uneven basal contact with the underlying sediments and was interpreted as deriving from a turbidity current (Di Roberto et al., 2008). Two shard populations can be identified macroscopically; the dominant is represented by angular, moderately vesicular shards, with tubular vesicles that extend the length of the shard (Fig. 4.2). The layer comprised of loose crystals of plagioclase and clinopyroxene, in addition to some minor lava and bioclasts fragments.

The major element analysis defines a dominant (~ 85%) population of shards with a high silica composition. This rhyolitic population is homogeneous and displays a HKCA compositional affinity (Fig. 4.3a) with 74.5-75.5 wt.% SiO₂ and 5.1-5.5 wt.% K₂O (Table 4.1). Due to the dominance of the homogeneous HKCA rhyolitic shards within this layer it is interpreted as being representative of a significant event in time and space (i.e., volcanic eruption/collapse).

TIR2000-7 rhyolitic glasses are highly evolved ($Zr/Sr = 10.2 \pm 0.7$) (Fig. 4.4a) and homogeneous with 313-351 ppm Rb, 49-55 ppm Th; 171-185 ppm Zr and 38-40 ppm Nb (Table 4.1). The most significant heterogeneity is observed within the LREE elements (La = 54-64 ppm; Ce = 108-128 ppm). Primitive mantle normalised (Fig. 4.4a) profiles reveal LREE enrichment over the HREE ($La/Yb = 13 \pm 2$) and that the glasses are depleted in Sr, Ba and Eu (16-20 ppm Sr, 16-21 ppm Ba, $Eu/Eu^*_N = 0.8 \pm 0.01$) relative to the incompatible elements (Fig. 4.4a, Table 4.2). Incompatible trace elements display constant inter-element positive relationships (Fig. 4.5) and constant HFSE/Th ratios (Table 4.2).

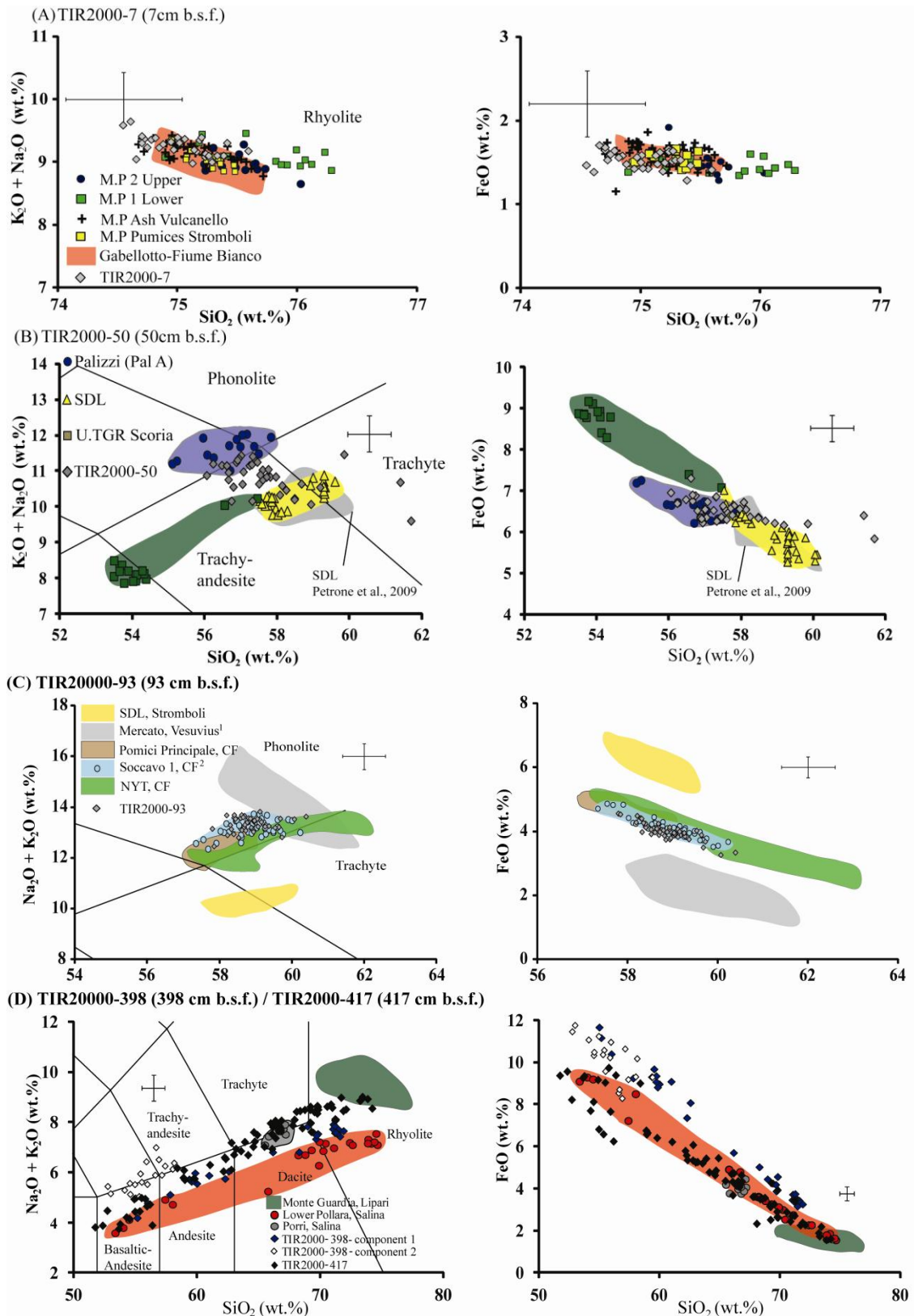


Figure 4.3: TAS (Le Bas et al., 1986) and SiO₂ vs. FeO diagrams of the Marsili basin tephras and possible proximal counterparts. (A) TIR2000-7, Lower Monte Pilato and Upper Monte Pilato (Monte St. Angelo Lipari), white Ash, Vulcanello (Vulcano) and white Lapilli (Stromboli). (B) TIR2000-50; Pal A (Vulcano); Secche di Lazzaro (Stromboli); Upper TGR

(Vulcano). SDL water-free data from Petrone et al. (2009) for comparison (C) TIR2000-93, Secche di Lazzaro (Stromboli), Mercato (Vesuvius); Pomici Principali (CF); Soccavo 1 (CF); Neapolitan Yellow Tuff (NYT; CF). (D) TIR2000-398, component 1 and component 2; TIR2000-417; Monte Guardia (Lipari); Lower Pollara (Salina); Monte dei Porri (Salina). Errors given are 2 x standard deviation based on reproducibility of MPI-DING StHs6/80 analyses. ⁽¹⁾ Wulf et al. (2004). ⁽²⁾ Smith et al. (2011).

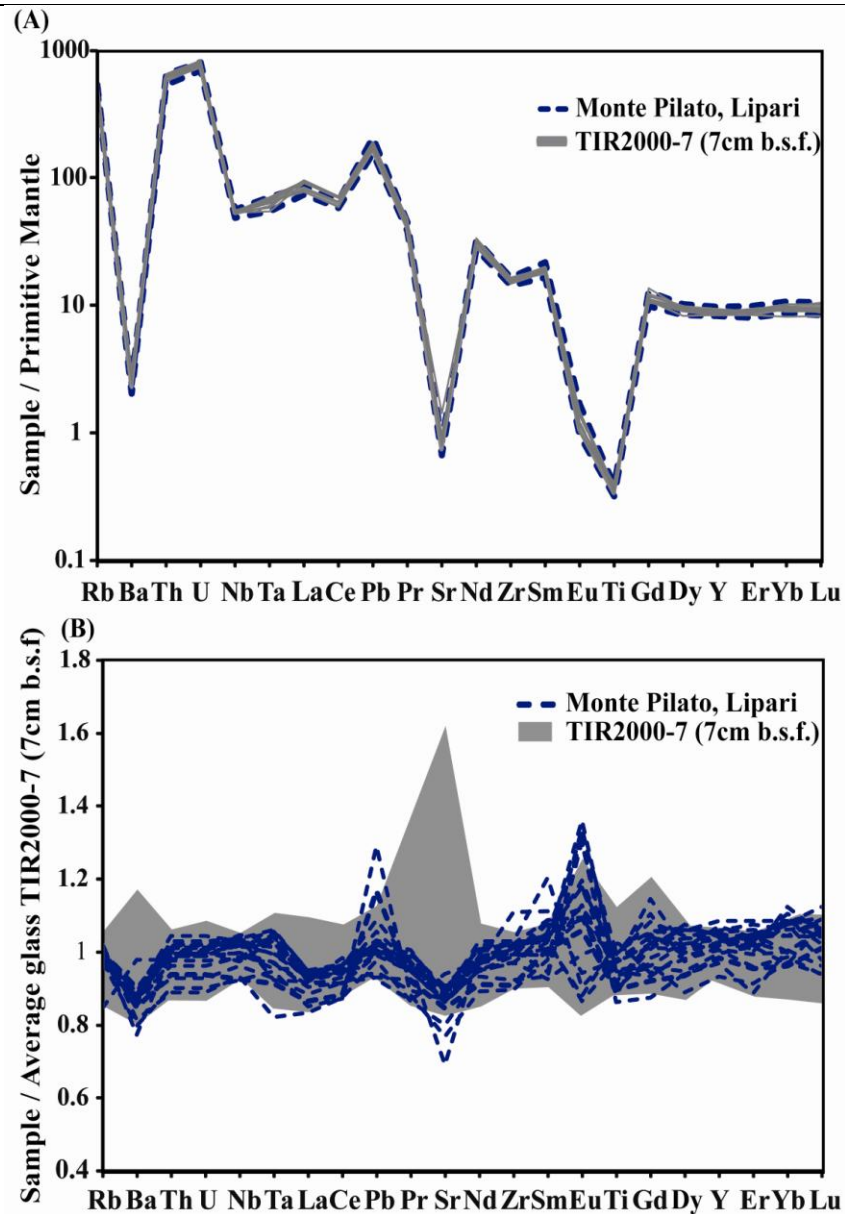


Figure 4.4: TIR2000-7 cm (7cm b.s.f.); Monte Pilato, Lipari; White ash, Vulcanello trace element plots. (A) Sample average and average ± 2 x standard deviation of the data set normalised to Primitive mantle compositions (Sun and McDonough, 1989). (B) Monte Pilato and distal TIR2000-7 glass compositions normalised to the average composition of the distal tephra (TIR2000-7).

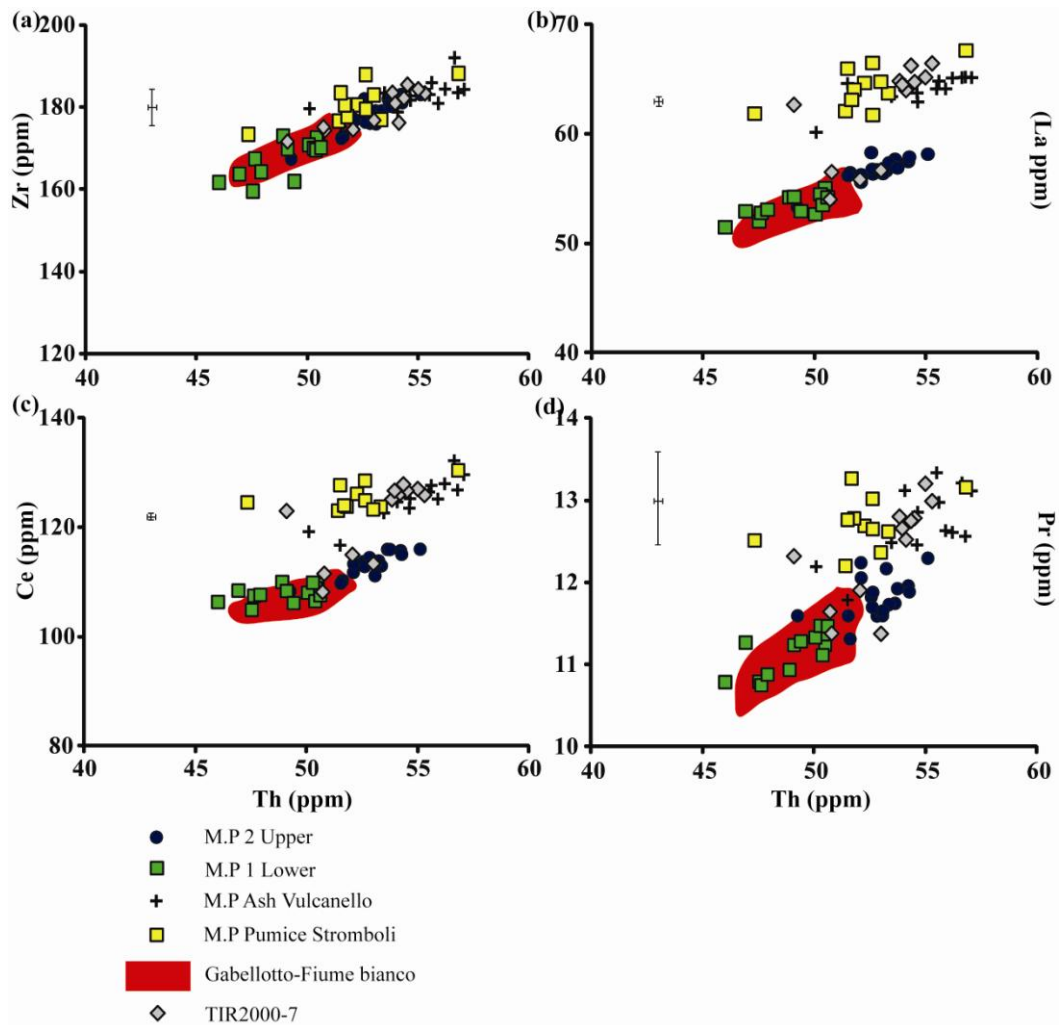


Figure 4.5: Incompatible trace element bi-plots comparing TIR2000-7, Monte Pilato Lower and Upper, a white Ash layer from Vulcanello stratigraphy, Vulcano and micro-pumices outcropping on Stromboli. Also given is the compositional field of the Gabbellotto-Fiume Bianco. Errors given are 2 x standard deviation based on reproducibility of MPI-DING StHs6/80 analyses.

4.3.3 TIR2000- 50 (50 cm b.s.f.)

Di Roberto et al. (2008) correlated this tephra to the Secche di Lazzaro eruption and associated flank collapse of Stromboli. This tephra layer displays a bimodal population, with one dominant population of light/dark brown blocky/Y shaped vesicular shards (Fig. 4.2b), and a second smaller population of clear stretched tubular shards. The tephra contains loose crystals of plagioclase and clinopyroxene. The tephra showed an uneven contact with the underlying sediments and is interpreted as a turbidite (Di Roberto et al., 2008).

Major element analysis confirms the morphological observations, indentifying two shard populations (Fig. 4.3b). The dominant shard population (~90%) is silica undersaturated, displaying a fairly homogeneous trachy-andesite composition (Fig. 4.3b), with 56.0-59.8 wt.% SiO₂ and 5.9-7.1 wt.% K₂O (Table 4.1). The dominance of this shard population is taken to represent an individual event in time and space. Increasing SiO₂ concentrations see a decrease in K₂O, Na₂O (Fig. 4.7), FeO (Fig. 4.3b), TiO₂ (Fig. 4.7), MgO, CaO, whilst Al₂O₃ and MnO remain largely constant.

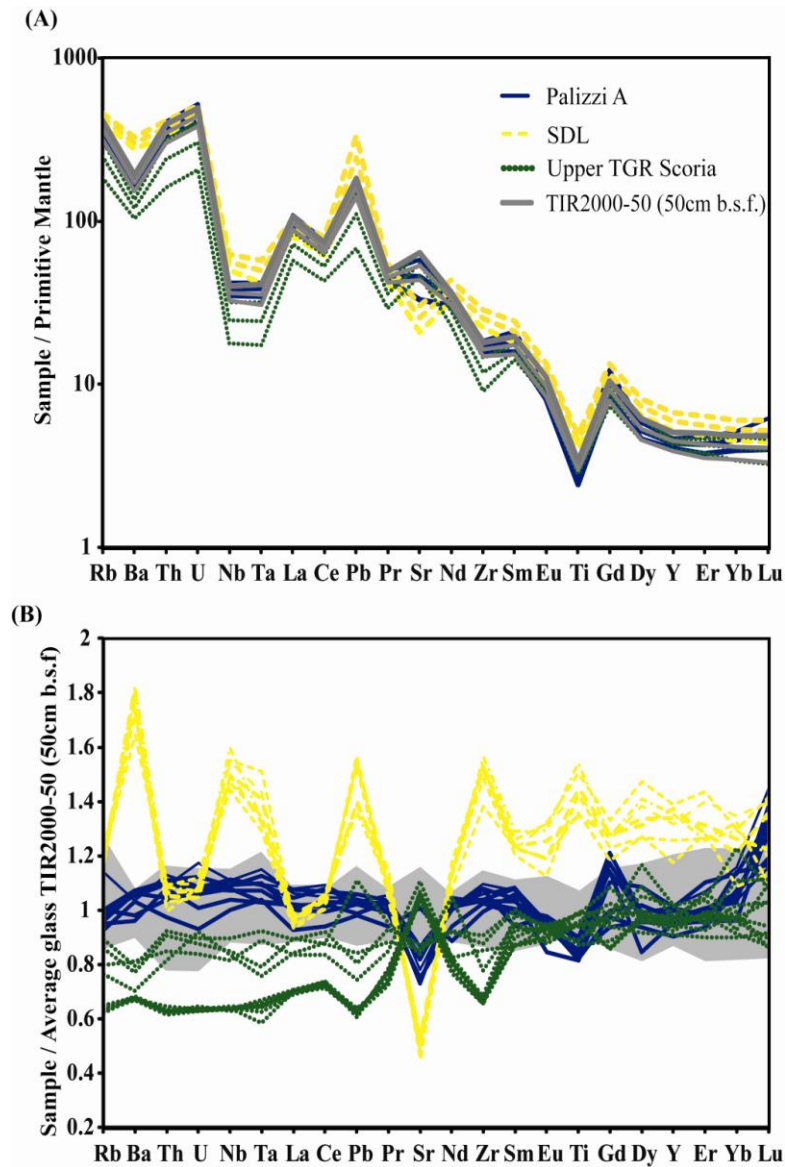


Figure 4.6: TIR2000-50 (50cm b.s.f.), Palizzi (Vulcano), Secche di Lazzaro (Stromboli) and the Upper TGR (Vulcano) trace element plots. **(A)** Sample averages and average ± 2 x standard deviations of glass data set normalised to Primitive mantle compositions (Sun and McDonough, 1989). **(B)** Proximal Pal A, Secche di Lazzaro, Upper TGR scoria and distal TIR2000-50 glass compositions normalised to the average composition of the distal tephra (TIR2000-50).

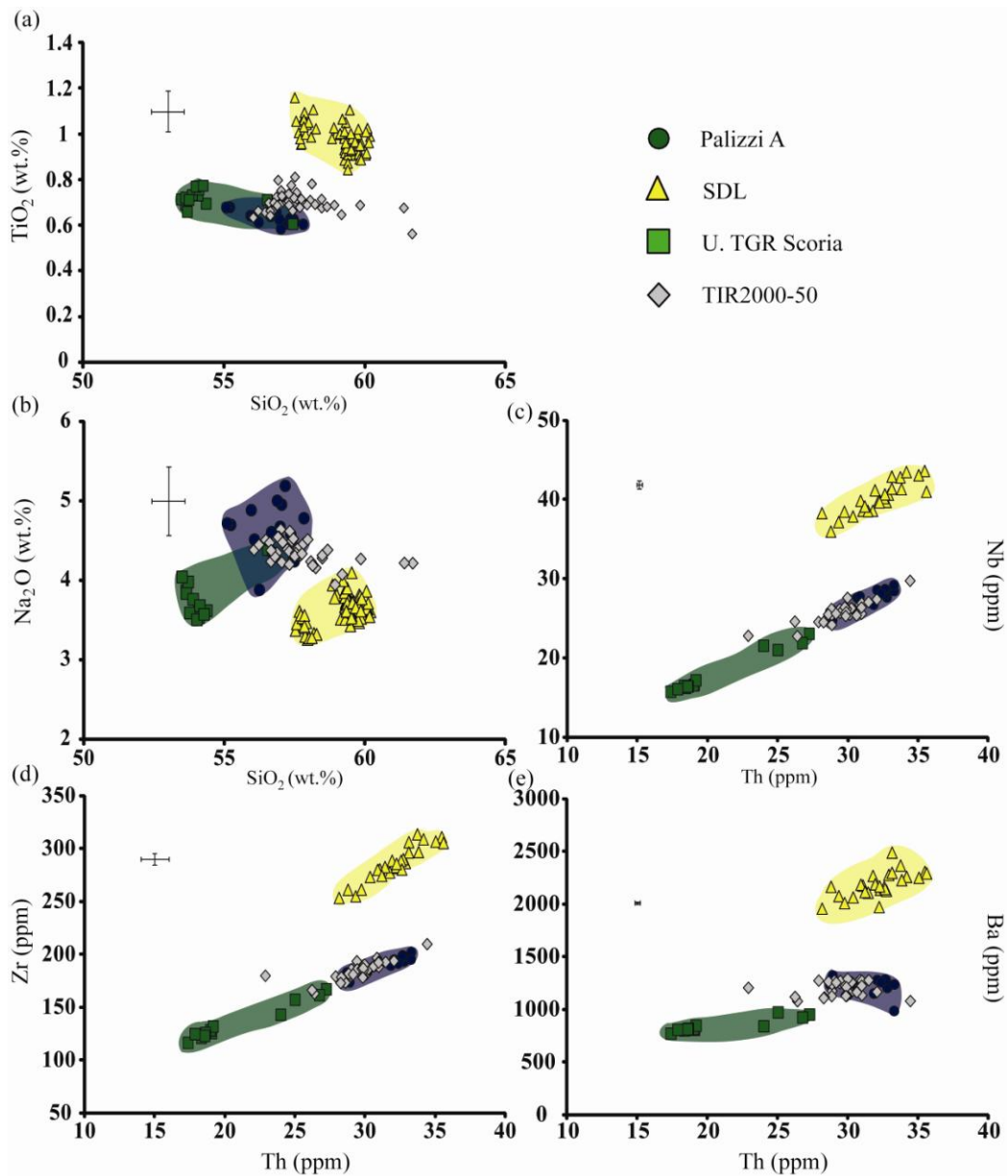


Figure 4.7: Major and trace element bi-plots comparing the TIR2000-50 distal tephra with proximal Secche di Lazzaro (Stromboli), Palizzi A and TGR scoria (Vulcano). Errors given are 2 x standard deviation based on reproducibility of MPI-DING StHs6/80 analyses.

Glasses display moderate levels of evolution ($Zr/Sr = 0.2 \pm 0.02$) (Fig. 4.6) and are largely homogeneous with 201-297 ppm Rb, 163-216 ppm Zr, 23-32 ppm Nb, 59-72 ppm La and 23-37 ppm Th (Fig. 4.7c-e; Table 4.1). Strontium and Ba display the most significant variability (715-1307 ppm Sr; 1051-1292 ppm Ba), where Sr behaves compatibly. Primitive mantle normalised glasses display significant LREE enrichment relative to the HREE ($La/Yb = 32 \pm 3$) and incompatible trace elements display tight positive linear relationships (Fig. 4.7c-d), with constant ratios of HFSE/Th (Table 4.2).

4.3.4 TIR2000- 93 (93 cm b.s.f.)

This tephra layer is considered a primary fall tephra due to its planar contact with the underlying sediments in the Marsili Basin core (Di Roberto et al., 2008). The fall tephra was correlated by Di Roberto et al. (2008) to cycle IX explosive activity, Lipari. The tephra layer is comprised of clear/light brown tephra. Shards range from highly vesicular to poorly vesiculated and blocky. Where vesicles coalesce, shards display a tubular morphology (Fig. 4.2c). Previous work by Di Roberto et al. (2008) had exhausted the > 250 μm component on this fall tephra, therefore analysis concentrated on the 125-250 μm and 63-125 μm components.

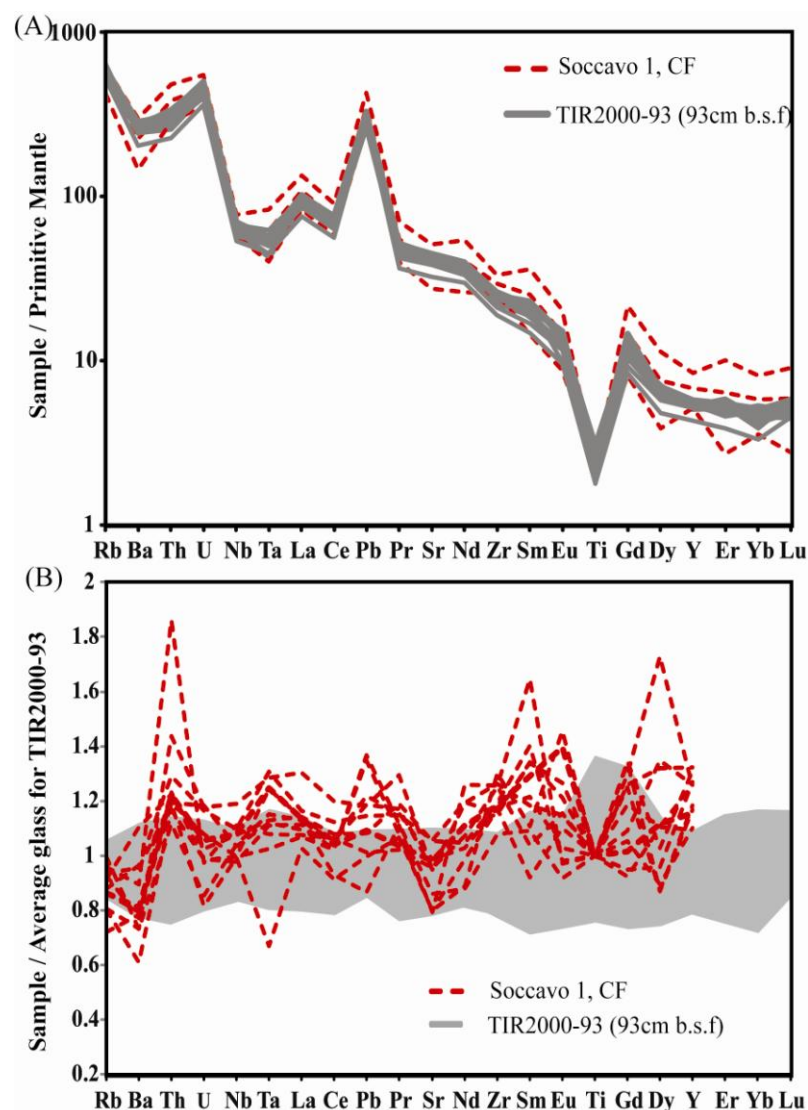


Figure 4.8: TIR2000-93 (93cm b.s.f) and Soccavo 1 (Campi Flegrei) trace element plots. **(A)** Sample average and average ± 2 x standard deviations of the data set normalised to Primitive mantle compositions (Sun and McDonough, 1989). **(B)** Soccavo 1 normalised to the average composition of the distal tephra (TIR2000-93).

TIR2000-93 comprises of compositionally homogeneous phonolitic shards (Fig. 4.3c) with 57.8-60.4 wt.% SiO₂ and high-K (9.2-10.2 wt.% K₂O). There is a negative relationship between SiO₂ and FeO, CaO, MgO and TiO₂. K₂O increases with increasing SiO₂, until a slight inflection at ~59 wt.% SiO₂, whilst Al₂O₃, MnO and Na₂O remain constant. Glasses display moderate levels of evolution (Zr/Sr = 0.3 ± 0.02) (Fig. 4.8a), significant variability is observed in the range of trace element concentrations with 327-404 ppm Rb, 20-27 ppm Y, 19-29 ppm Th, 212-295 ppm Zr, 38-49 ppm Nb and 52-71 ppm La. Ba and Sr display the most significant heterogeneity (1413-2010ppm Ba, 686-950ppm Sr) both increasing with fractionation. Glasses display significant LREE enrichment relative to the HREE (La/Yb = 29 ± 2) and glasses display constant ratios of HFSE to Th (Table 4.2).

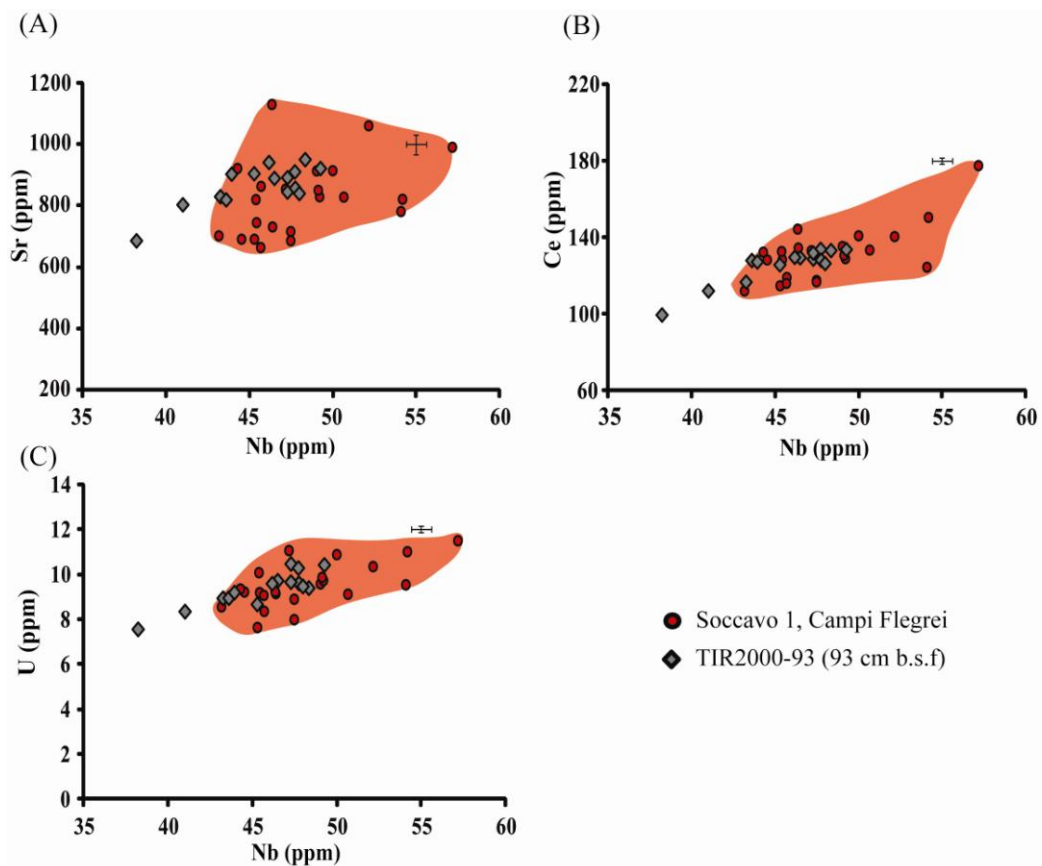


Figure 4.9: Trace element bi-plots comparing TIR2000-93 distal tephra with proximal flow deposits of the Soccavo 1 eruption, Campi Flegrei (Smith et al., 2011). Errors given are 2 x standard deviation based on reproducibility of MPI-DING StHs6/80 analyses.

4.3.5 TIR2000-398 (398 cm b.s.f.); Coarse Grained Volcaniclastic Turbidite (CGVT):

A stratified volcaniclastic polygenetic turbidite deposit occurs at 398 cm below the sea floor (Di Roberto et al., 2008). It is a 10cm thick unit with an erosional lower contact (Fig. 4.1), it comprises three types of glass (Fig. 4.2) as outlined by Di Roberto et al. (2008);

- (1) honey coloured, poorly vesicular, porphyritic scoria glass shards;
- (2) grey moderately vesicular pumices;
- (3) colourless, highly vesicular, nearly aphyric pumice fragments.

In addition the unit contains loose crystals of clinopyroxene and lithics (e.g., quartz rich sediments, metamorphic basement). Di Roberto et al. (2008) suggested that this layer comprises partly of Lower Pollara tephra and results from a sector collapse of the Island of Salina, an event that post dated the eruption.

Analysis was conducted at intervals through the deposit, to confirm that all geochemical heterogeneity was observed. All levels were consistent with the presented sample TIR2000-398. The total alkali silica diagram (Fig. 4.3d) demonstrates that glasses within this deposit contain two magmatic suites (Table 4.1). Firstly, a calc-alkaline/HKCA transitional suite spanning from basaltic-andesite to rhyolite where the following range in major element chemistry is observed, 55-71.9 wt.% SiO₂, 0.5-1.3 wt.% TiO₂, 3.2-11.7 wt.% FeO, 2.2-8.7 wt.% CaO, 2.7-4.6 wt.% Na₂O and 1.5-3.6 wt.% K₂O. Secondly, High-K basaltic-andesites trending towards trachy-andesite, these glasses are less heterogeneous, 52.8-58.1 wt.% SiO₂, 1.1-1.5 wt.% TiO₂, 8.3-11.8 wt.% FeO, 5.8- 9.2 wt.% CaO, 2.9-3.7 wt.% Na₂O and 1.9-3.4 wt.% K₂O (Table 4.1). Increasing SiO₂ reflecting increasing fractionation results in; increasing K₂O and Na₂O; decreasing TiO₂, FeO (Fig. 4.3d), CaO Al₂O₃, MgO and MnO. Trace element data reinforces the presence of two geochemically distinct volcanic suites within this turbidite (Fig. 4.12). The Nb vs. Zr plot clearly defines the two separate suites (Fig. 4.12b) and this is confirmed by incompatible trace element ratios (Nb/Zr; Zr/Th; Table 4.2).

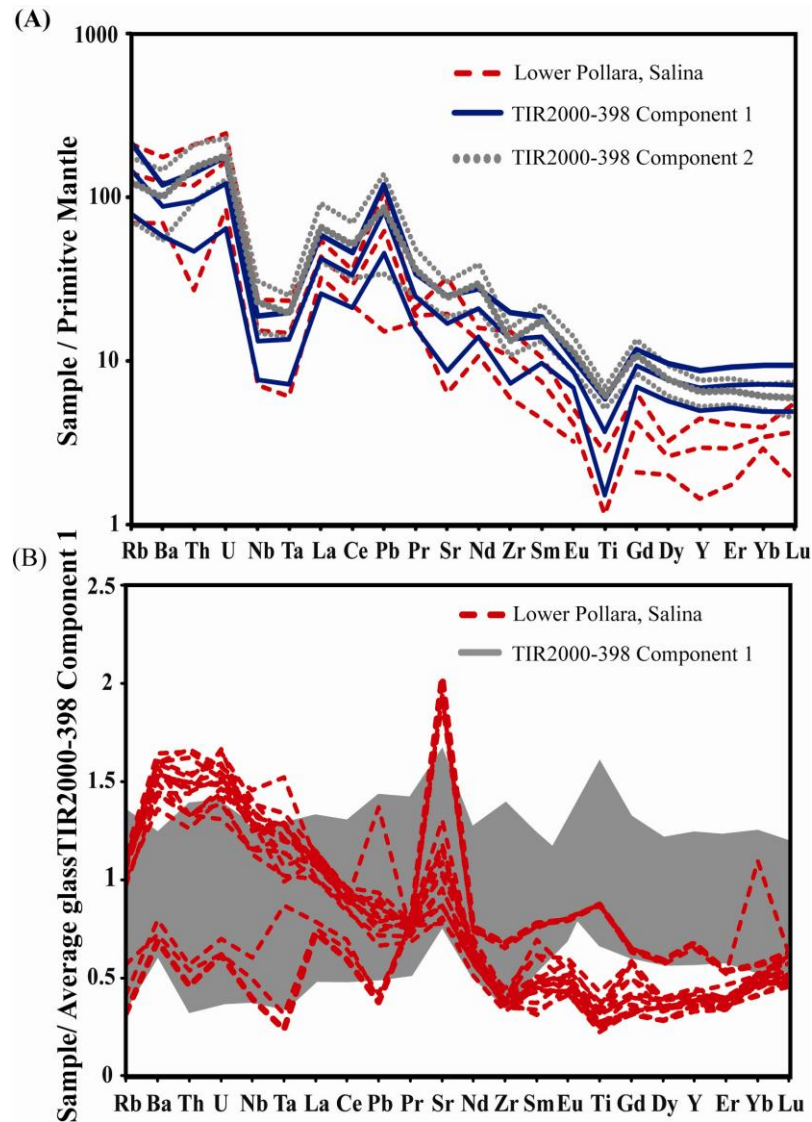


Figure 4.10: (A) TIR2000-398 and Lower Pollara; sample average and average ± 2 x standard deviations of the data set normalised to primitive mantle compositions (Sun and McDonough, 1989). (B) Lower Pollara compositions normalised to the average composition of the distal tephra (TIR2000-398 component 1).

The two compositionally distinct types are as follows:

(1) CA/HKCA suite (component 1) - Compositional heterogeneity is reflected in the trace element concentrations observed in this suite of tephra (Table 4.1) with the following ranges: 36-125 ppm Rb, 18-38 ppm Y, 55-208 ppm Zr, 3.6-11.8 ppm Nb, 14-38 ppm La and 2.6-11 ppm Th. The basaltic-andesites are poorly evolved ($Zr/Sr = 0.1$) whilst glasses become more evolved towards the rhyolitic end-member ($Zr/Sr = 0.5-0.7$) (Fig. 4.10a). Throughout this suite the LREE are enriched relative to the HREE ($La/Yb = 8.4 \pm 1.5$). Strontium concentrations decrease strongly (267-589 ppm Sr) with

increasing fractionation as demonstrated by increasing Nb (Fig. 4.12). Other incompatible elements display positive linear correlations (Fig. 4.12) and relatively constant incompatible trace element ratios (Table 4.2).

(2) High-K basaltic andesites (component 2) - The High-K basaltic glasses are moderately evolved ($Zr/Sr = 0.3 \pm 0.03$) (Fig. 4.10a) and relative to component 1 glasses, the trace element concentrations are homogeneous as indicated by 59-116 ppm Rb, 24-34 ppm Y, 120-167 ppm Zr, 12-20 ppm Nb, 30-35 ppm La and 9-16 ppm Th (Table 4.1). These glasses appear to display comparable levels of trace element enrichment (Fig. 4.10a) to the rhyolitic glasses of component 1 despite their lower silica concentrations. This is reflected by their greater levels of LREE enrichment relative to the HREE ($La/Yb = 15 \pm 3$). Within this suite both Sr and Ba (442-638 ppm Sr and 491-1019 ppm Ba) increase with increasing fractionation (Fig. 4.12).

4.3.6 TIR2000-417 (417 cm b.s.f.)

This tephra layer is the lowermost visible fallout layer within TIR2000-C01 (417cm b.s.f.) and was correlated to fall from the Lower Pollara eruption, Salina by Di Roberto et al. (2008). Shard morphologies indicate two populations, (1) greyish, low to moderately vesicular shards; (2) abundant colourless, highly vesicular shards (Fig. 4.2f). Major and trace element data are given in Table 4.1. The glass analyses within this distal tephra display a wide compositional range from a mafic end-member (i.e. basaltic andesite on the CA/HKCA boundary) to a felsic end-member (i.e. rhyolite with HKCA affinity) (Fig. 4.3d). TIR2000-417 glasses are heterogeneous with the following major and minor element variability, 51.8-74.2 wt.% SiO_2 , 0.3-1.2 wt.% TiO_2 , 1.5-9.7 wt.% FeO, 1.1-11.4 wt.% CaO, 2.4-4.9 wt.% Na_2O and 1.2-5.2 wt.% K_2O (Table 4.1). With increasing silica there is an increase in K_2O , Na_2O ; decreasing TiO_2 , FeO (Fig. 4.3d), CaO, Al_2O_3 , MgO and MnO. At ~ 72 wt.% SiO_2 an inflection is observed with a switch to decreasing Na_2O .

Glasses within this suite range in terms of evolution between the basaltic-andesites ($Zr/Sr = 0.2$) and the rhyolitic ($Zr/Sr = 1.7$) components (Fig. 4.11a). This is illustrated in the range of the trace element concentrations from 36-193ppm Rb, 16-43ppm Y, 82-320ppm Zr, 10-39ppm Nb, 25-68ppm La and 6.8-30ppm Th (Fig. 4.12). The suite displays consistent levels of LREE enrichment relative to the HREE ($La/Yb = 16 \pm 2$). Sr (184-628 ppm) decreases with increasing fractionation, whilst Ba (404-1438 ppm)

continues to increase throughout the suite (Fig. 4.12). Incompatible trace element concentrations display positive linear relationships demonstrated by Nb vs Rb, Y, Zr and La (Fig. 4.12).

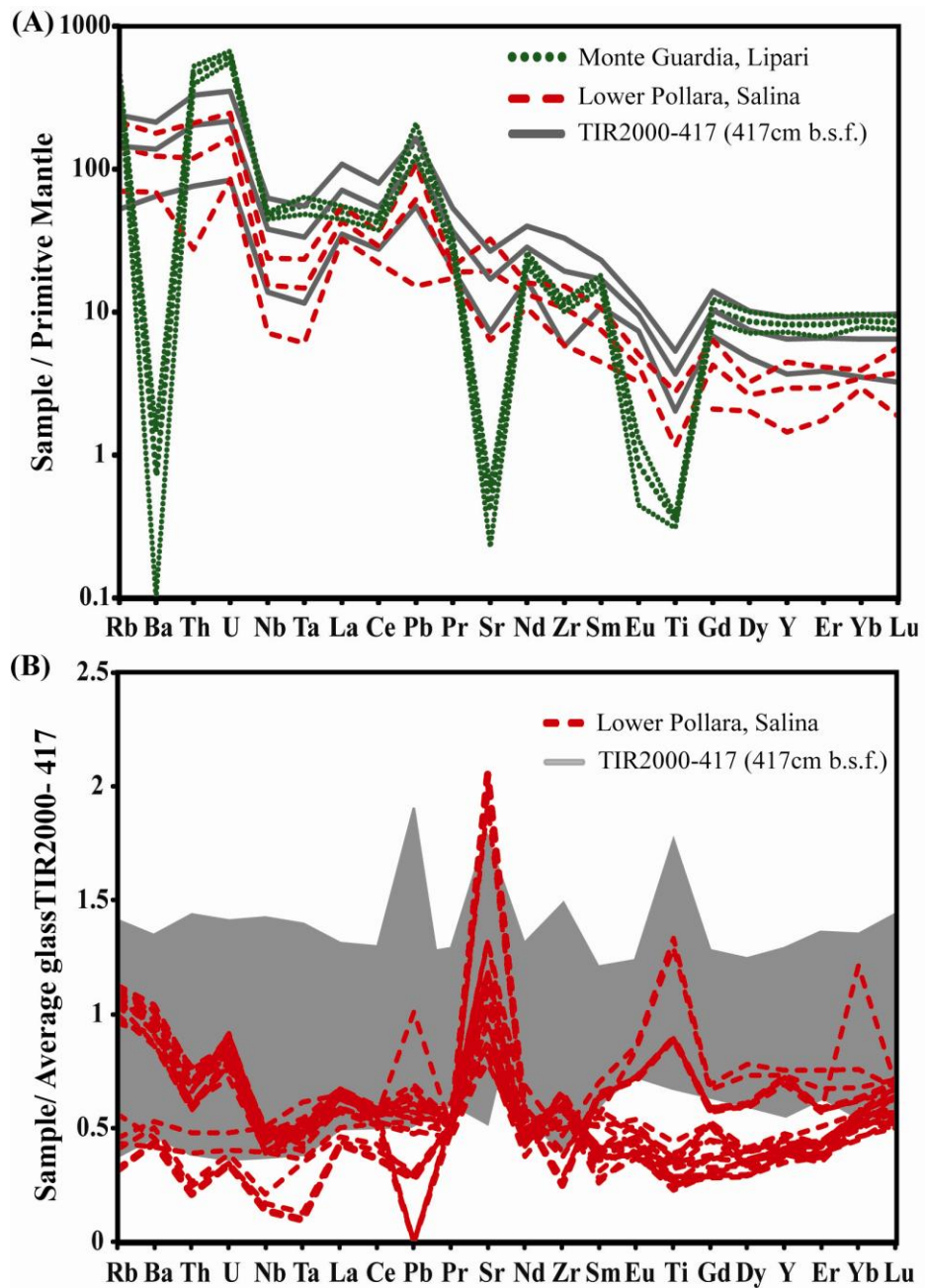


Figure 4.11: (A) TIR2000-417 and Lower Pollara; sample average and average ± 2 x standard deviations of the data set normalised to primitive mantle compositions (Sun and McDonough, 1989). (B) Lower Pollara compositions normalised to the average composition of the distal tephra (TIR2000-417).

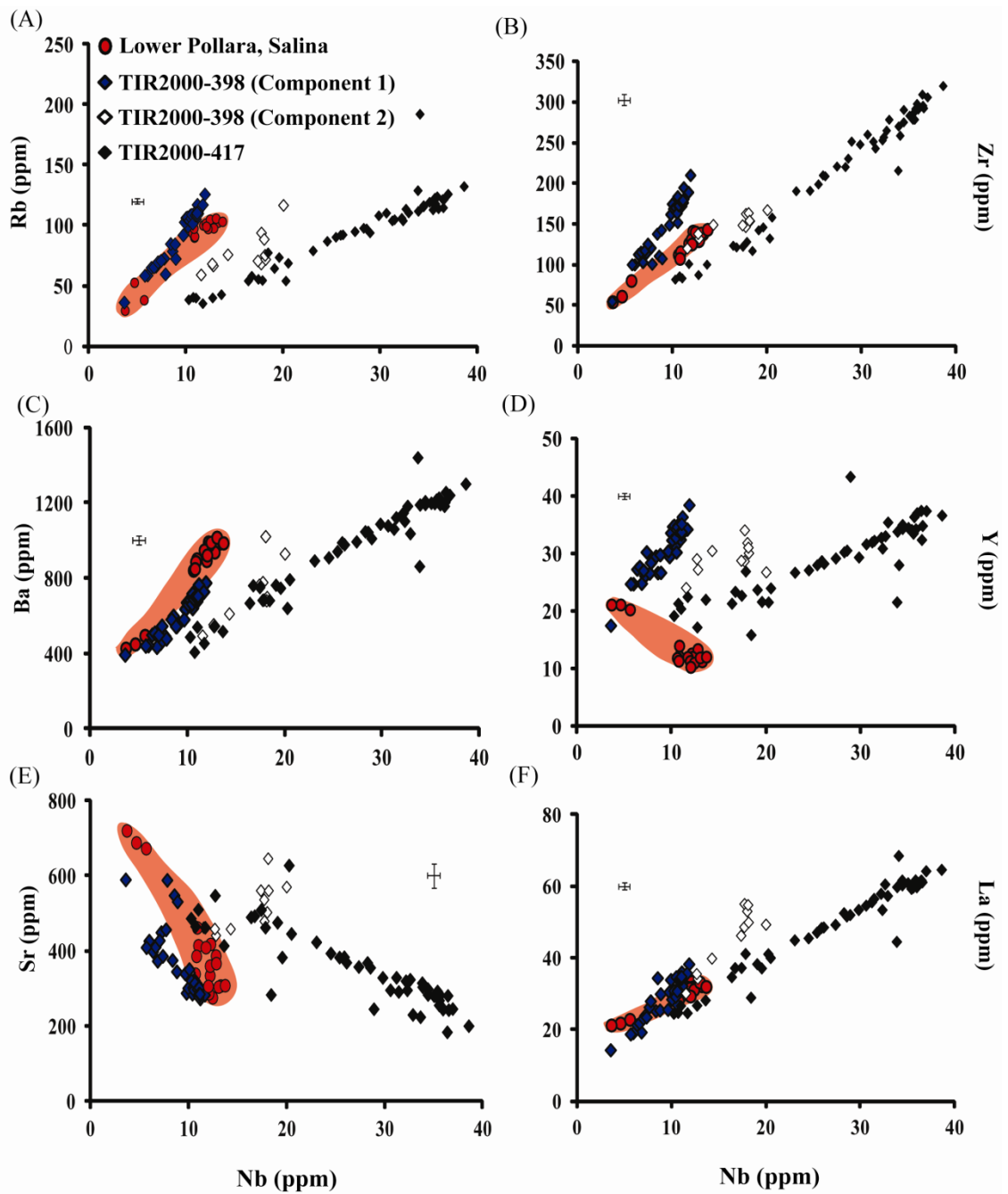


Figure 4.12: Trace element bi-plots: Distal tephras TIR2000-398 (398cm b.s.f.); TIR2000-417 (417cm b.s.f.) and proximal explosive deposits of the Lower Pollara, Salina. Errors given are 2 x standard deviation based on reproducibility of MPI-DING StHs6/80 analyses.

4.4 Discussion

4.4.1 Proximal-distal correlations/Tephrochronology

The basis of tephrochronology is an accurate assessment of the source of a particular tephra layer such that time can be accurately assigned to that layer. Chapter three presented detailed glass geochemical data for the major explosive eruptions occurring within the Aeolian Islands during the last 42 ka. The investigated eruptions are detailed in Table 3.1. Below five marine tephra layers previously assigned provenance solutions on the basis of SEM-EDS data (Di Roberto et al., 2008) are re-evaluated, using a multi-elemental approach, in light of this new proximal glass data.

4.4.1.1 TIR2000-7 (7 cm b.s.f.)/Lipari 776 cal AD

This tephra was previously correlated with the medieval eruption of Monte Pilato (MP, Lipari) (Di Roberto et al., 2008) based on the tephra's position at the top of the core and its HKCA rhyolitic affinity. Major and minor element glass compositions in this tephra are indistinguishable from the glasses produced during the Monte Pilato and Gabelotto-Fiume Bianco (GFB) eruptions (Fig. 4.3a). TIR2000-7 glasses have the characteristic mantle normalised pattern associated with Lipari rhyolites, where depletions are observed in Ba, Sr and Eu (Fig. 4.4a; Chapter 3). Trace element concentrations in the distal tephra enable precise attribution to the Monte Pilato eruption (Fig. 4.4b), owing to more elevated concentrations than those seen in the homogeneous, older, Gabelotto-Fiume Bianco (Fig. 4.5; Table 3.8). Investigations of proximal Monte Pilato fall glasses both on Lipari and in medial-distal stratigraphies within the Aeolian Islands revealed that this activity is more heterogeneous than the previous explosive episode, GFB (Chapter 3). Two groups of LREE concentrations were identified in the Monte Pilato glasses (Chapter 3; Table 3.9). The glasses recorded from the volcanic stratigraphies of Vulcanello and Stromboli displayed more elevated LREE than the fall recorded more proximally on Lipari at Monte Sant' Angelo (Fig. 4.5). The monogenetic turbidite TIR2000-7 has glasses corresponding to both the LREE groups which is a diagnostic feature of the Monte Pilato activity. Subtle variations within the geochemistry of Monte Pilato glasses observed proximally and distally may support the interpretations of Davi et al. (2011), who suggest Monte Pilato was made up of numerous closely spaced explosive phases. Consequently the small temporal gaps in the activity from MP may result in the subtle compositional variations seen in the glasses.

It seems plausible that ash fall from the multi-phase Monte Pilato explosive activity mantles the seafloor and would be readily available to be remobilised by a turbidity current. The turbidity current is likely to result from a PDC entering the marine environment or a partial collapse of the Monte Pilato cone. The result is a tephra deposit (TIR2000-7) that is geochemically representative of the entire prolonged Monte Pilato explosive activity.

Ash layers attributed to the Monte Pilato activity are identified in other marine cores from the southern Tyrrhenian Sea (Keller and Leiber, 1974; Paterne et al., 1988). Keller and Leiber (1974) identify a HKCA rhyolitic ash layer at the base of a 4 meter core from the central Marsili basin. Paterne et al. (1988) report a rhyolitic tephra in the uppermost centimetre of the marine core KET8003, located north-west of Salina (Fig. 4.1). Significant discrepancies in the depths of the Monte Pilato tephra are likely to represent the highly variable depositional environments in the southern Tyrrhenian Sea. Paterne et al. (1988) suggest that the rhyolite in KET8003 is fall from Monte Pilato. KET8003 is located sufficiently north west of Lipari and might avoid dominant turbidite inputs that are predominantly fed via the Stromboli canyon to the Marsili basin (Gamberi and Marani, 2007). The rhyolitic tephra identified by Keller and Leiber (1974) in the Marsili basin is likely to represent the contemporaneous input of a turbidite and fall as recorded in TIR2000-C01. At the temporal resolution of marine archives the Monte Pilato activity provides an important regional tephrochronological marker in the southern Tyrrhenian Sea, multiple closely spaced eruptive episodes are likely to represent composites in the marine record. In the context of intra-island stratigraphic correlations it has been demonstrated that identification of subtle trace element variations are important for robustly correlating individual stratigraphies. The Monte Pilato has more recently been recognised beyond the southern Tyrrhenian Sea region, Caron et al., (2012) have identified a HKCA rhyolitic tephra in the 2-5 cm sediments of MD90-918 in the northern Ionian Sea. This extends the known dispersal of the Monte Pilato eruption further east and confirms it as a widespread distal tephra sourcing from the Aeolian Islands.

4.4.1.2 TIR2000- 50 (50 cm b.s.f.)/K-series activity of Stromboli/Vulcano

Whilst originally correlated with the Secche di Lazzaro (SDL; Stromboli; ~5 ka BP) (Di Roberto et al., 2008), the high-K composition of TIR2000-50 tephra requires comparison with the products of Stromboli and Vulcano (Fig. 4.3b; Chapter 3). Similarities exist between the marine tephra and SDL (~ 5 ka BP), Stromboli (Fig. 4.3b) including some major element compositional overlap, whilst also showing similarities in physical characteristics of the glasses. Both SDL juvenile glasses and the distal tephra display a high K-series signature and are characterised by blocky-Y shaped shards typical of phreatomagmatic activity. This appears to underpin the original correlation made by Di Roberto et al. (2008). However, some discrepancies are observed between the distal tephra and the SDL glasses, specifically the distal tephra have lower TiO₂ wt.% and higher Na₂O wt.% than the SDL proximal glasses (Fig. 4.7a-b).

Normalising the trace element concentrations of the proximal Secche di Lazzaro (SDL) glasses to the average composition of the distal TIR2000-50 glasses reveals significant differences between the two populations (Fig. 4.6b). SDL glasses display more elevated concentrations in Ba, Nb, Ta, Pb, Sr, Zr, the MREE and HREE (Fig. 4.6b). These discrepancies are most pronounced within Ba, Nb, Ta, Zr, Y (Fig. 4.7c-e). HFSE/Th ratios indicate the distal tephra derive from a different magmatic source to Stromboli (Table 4.2). Based on trace element data presented herein, the correlation of TIR2000-50 and Secche di Lazzaro eruption, Stromboli cannot be verified and so assigning the SDL age of 5 ka to the Marsili basin core is questionable. In the absence of other significant proximally defined K-series explosive eruptions from Stromboli activity on Vulcano is considered as an alternative. Two explosive deposits on the island displaying high-K compositions are considered here, the scoria within Upper TGR (7.7 ± 1 ka BP; De Astis et al., 1997) and the younger Palizzi A activity dated 2.1 ± 0.3 ka BP (Voltaggio et al., 1995) (Fig. 4.3b). The scoria from the TGR unit is largely less evolved than the distal tephra. However, the most evolved glasses display similar major elements (Fig. 4.3b; 4.7a-b). Glasses from this particular sub-unit do not provide a precise correlation on the basis of major elements. The Palizzi A scoriaceous deposits are compositionally similar in major element chemistry to the distal tephra (Fig. 4.3b; 4.7a-c). However, glasses display slightly higher total alkalis, a function of more elevated K₂O (Fig. 4.3b), whilst TiO₂ is much more comparable with the distal glasses

(Fig. 4.7). Statistical distance calculated between the marine tephra and both proximal Palizzi A and SDL glasses show greater distance between the SDL and the marine tephra ($D^2 = 5.2$) than the Palizzi A ($D^2 = 2.5$). Discrepancies identified between the distal glasses and Palizzi A are probably the result of slightly elevated K_2O (Fig. 4.3b). In summary neither proximal Vulcano units provide a precise correlation at a major element level.

Palizzi A glasses normalised to the distal tephra indicate at a multi-element level that this tephra is far more comparable than the Stromboli deposits (Fig. 4.6b). The HFSE (Nb, Ta, Zr) and Ba concentrations of TIR2000-50 are more comparable to those observed in the Vulcano glasses (Fig. 4.7). Ratios of the HFSE to Th confirm Vulcano as a more likely source for this distal ash (Table 4.2). Multi-element data suggest that the distal tephra is derived from Vulcano rather than its previous attribution to Stromboli (Di Roberto et al., 2008).

Proximal-distal correlation to an eruptive phase on Vulcano is difficult. Subtle major element discrepancies coupled with the stratigraphic position of this marine tephra (TIR2000-50), some 20cm below the Vesuvian layer TIR2000-30 cm, correlated to AP1-3 (2.7-3.6 ka BP; ^{14}C 2710 \pm 60 yrs BP to ^{14}C 3,200 \pm 65 yrs BP) (Andronico et al., 1995; Rolandi et al., 1998; Di Roberto et al., 2008), invalidate correlation to Palizzi A given proximal age constraints (2.1 \pm 0.3 ka BP; Voltaggio et al., 1995). As such the TIR2000-50cm tephra is likely to originate from pre-Palizzi activities on the island of Vulcano. Given the blocky morphology of the distal tephra (Fig. 4.2) it is probable that this tephra was produced by phreatomagmatic activity on the island. Paterne et al. (1988) presented tephras from the Tyrrhenian Sea geochemically similar to this trachy-andesitic activity of TIR2000-50 (Chapter 3), indicating tephras of this geochemical affinity are not uncommon and are dispersed in the southern Tyrrhenian Sea region. At present TIR2000-50 glass compositions indicate a provenance from the Vulcano magmatic system, but a precise proximal equivalent is not available currently. It would seem sensible to suggest that this layer was produced prior to the formation of the La Fossa cone, with perhaps more recent intra-caldera activity of La Fossa removing vital proximal information.

4.4.1.3 TIR2000-93 (93 cm b.s.f.)/Campi Flegrei 11915-12721 cal yrs BP

Geochemical characterisation of this distal fall tephra demonstrates homogeneous, silica undersaturated, K-series phonolitic glass compositions (Fig. 4.3c). This differs significantly from Di Roberto et al. (2008) who reported HKCA rhyolitic shards matching the narrow composition of cycle IX Lipari. This allowed for comparison to proximal equivalents at the Vallone Canneto dentro and Gabellotto-Fiume Bianco centres on the island (Gioncada et al., 2003). The former is poorly constrained in age, but is significantly older than the later which is dated distally in the Adriatic to 8547 ± 74 cal yrs BP (^{14}C 7770 ± 70 yrs BP; Siani et al., 2004 and reference therein). Di Roberto et al. (2008) analyses were conducted on the $>250\mu\text{m}$ size fraction, the coarsest grain size in the > 1 cm thick fall deposit. The HKCA rhyolitic shards made up 90% of this size fraction, with the remaining shards displaying tephra-phonolitic compositions (Di Roberto et al., 2008).

This study aimed to validate the provenance of this fall tephra, investigating the smaller grain size fractions (250-125/125-63 μm) in the absence of remaining $> 250\mu\text{m}$ shards. The identification of 100% homogeneous, phonolitic glasses in the finer size fraction of TIR2000-93 confirms that this fall tephra comprises mixed provenance recording fall events from two contemporaneous but compositionally distinct (rhyolitic and phonolitic) explosive events.

Total alkalis, in particular K_2O values (> 9 wt.%) in these phonolites are more elevated than the most fractionated K-series glasses sourcing from the Aeolian islands (i.e., Vulcano; $\sim 7\text{-}8$ wt.% K_2O). Consequently, volcanic source regions further to the north-east on mainland Italy at Somma-Vesuvius and Campi Flegrei are considered. Specifically, early Holocene and Late-glacial proximal activities at Vesuvius-Campi Flegrei (<14 ka) were considered given the presence of cycle IX HKCA Lipari rhyolites intermixed with the phonolite and its stratigraphic position beneath the Monte Pilato (776 cal AD) in TIR2000-C01. Zanchetta et al. (2011) recognise that the phonolitic Mercato eruption of Vesuvius, 7750-8550 cal yrs BP (^{14}C 7770 ± 40 yrs; Zanchetta et al., 2011), occurs distally in the Ionian Sea at a similar stratigraphic position to the early Holocene rhyolitic Gabellotto-Fiume Bianco/E-1 within sapropel 1. TIR2000-93cm was compared to glass data associated with the Mercato eruption (Wulf et al., 2004), but the Mercato tephras displayed considerable differences, most noticeably lower FeO and

MgO and higher Na₂O (Fig. 4.3c). Consequently, Vesuvius is rejected as a possible source for the marine tephra.

At Campi Flegrei the caldera forming eruptions of the Neapolitan Yellow Tuff (NYT) dated to 15.6 ± 0.8 ka BP (Deino et al., 2004) and the Pomici Principali (PP), 11.97-12.39 cal ka BP (¹⁴C 10 320 yrs BP) (De Vito et al., 1999) are two of the largest magnitude eruptions during the last 30 ka BP. NYT was rejected on the basis that these glasses displayed far greater compositional variation (56-62 wt.% SiO₂; Fig. 4.3c) than the distal tephra and at overlapping SiO₂, the distal tephra displays higher Al₂O₃, K₂O; lower TiO₂, CaO, MgO and comparable FeO, MnO and Na₂O. PP glasses are similar to TIR2000-93, but can be separated from the distal tephra because they show lower SiO₂, K₂O and higher CaO.

The geochemistry of the TIR2000-93 phonolites is more consistent with Campi Flegrei activity during post NYT, Epoch 1 activity at between ~ 15 -10.6 ka BP (Smith et al., 2011). Glasses precisely match the Pre-Pomici Principale phreatomagmatic eruptions of Soccavo 1 that occurred between 11915-12721 cal yrs BP according to calibrated ¹⁴C chronology (Smith et al., 2011). This eruption represents the second largest eruption of Epoch 1 (0.5 km³) (Smith et al., 2011). Conveniently the major and minor elements of Soccavo 1 surge deposits (Fig. 4.3c) are unique to Epoch 1 (Smith et al., 2011). Soccavo 1 trace elements concentrations normalised to TIR2000-93 (Fig. 4.8b) and bi-plots (Fig. 4.9a-c) confirm the geochemical correlation.

The attribution of the phonolitic component to Soccavo 1 (11915-12721 cal yrs BP) makes correlation of the rhyolitic component (Di Roberto et al., 2008) to the Gabellotto-Fiume Bianco/E-1 (8547 \pm 74 cal yrs BP) problematic given the age discrepancies. Distally the Gabellotto-Fiume Bianco/E-1 tephra is constrained to sapropel 1 sediments (Siani et al., 2004; Zanchetta et al., 2011), but the Marsili Basin core offers no such bio-stratigraphy which makes constraining the early Holocene of the core problematic. Zanchetta et al. (2011) recognise that the identification of the Gabellotto-Fiume Bianco/E-1 is problematic if it is not supported by a stratigraphic or chronological framework. The occurrence of compositionally similar rhyolites is common in the successions of the Tyrrhenian and Ionian Sea. Thus, given the unique diagnostic composition of the Soccavo 1 eruption and its constraints within Epoch 1 it presents a more reliable chronological marker than the Lipari rhyolites in this instance.

The alternative attribution of the rhyolitic glass component to Gabellotto-Fiume Bianco/E-1 (8547 ± 74 cal yrs BP) in the Marsili core would chronologically constrain the contemporaneously deposited phonolitic component to a period of volcanic quiescence at Campi Flegrei between Epoch 2 and 3. The calibrated ^{14}C chronostratigraphy at Campi Flegrei presents a period of quiescence between ~ 9.1 and 5.5 ka BP (Smith et al., 2011; Isaia et al., 2012). Instead it is proposed that the rhyolitic ash component remains attributed to cycle IX activity on Lipari (Di Roberto et al., 2008), but relates to pre-Gabellotto-Fiume Bianco explosive activity, tentatively attributed to the older Vallone Canneto Dentro deposits reported on the island (Lucchi et al., 2008).

Currently, tephra from Soccavo 1 eruption has a N to NE dispersal axis. Given the absence of intra-caldera deposits and the proximity of Campi Flegrei caldera to the Tyrrhenian Sea an assessment of other dispersals axes may be problematic. This proximal-distal correlation represents the first record of the Soccavo 1 eruption being recorded outside the immediate Campi Flegrei region and enables a southerly dispersal axis to be inferred. The distal occurrence of Soccavo 1, in the southern Tyrrhenian Sea may require a revision of estimated magma volumes for this eruption.

Compositional variations observed between the different ash size fractions of the distal fall layer TIR2000-93 have important implications for distal tephrochronological investigations. The coarsest ash component of TIR2000-93 ($> 250 \mu\text{m}$) derived from a more proximal source on Lipari (Di Roberto et al., 2008), whilst the finer ash ($< 250 \mu\text{m}$) reported here sourced more distally from Campi Flegrei. Geochemical characterisation of the different size fractions is imperative to ensure tephrochronological information is not lost.

4.4.1.4 TIR2000-398 (398 cm b.s.f.)/CA/HKCA activity, Aeolian Islands

Geochemical analysis of the glasses within the coarse grained volcanoclastic turbidite (CGVT) indicates that it is comprised of two volcanic suites, (1) CA/HKCA transitional glasses; and (2) High K basaltic andesites (Fig. 4.3d) illustrated best by the trace element bi-plots (Fig. 4.12).

(1) CA/HKCA transitional glasses (Component 1): The wide ranging compositional variation ($55.2\text{--}71.9$ wt.% SiO_2) observed in CA/HKCA glasses (Fig. 4.3d) coupled with particularly low K_2O (Table 4.1) values immediately confirm Salina as the most likely provenance of these tephra. Salina and the Pollara centre are recognised as

displaying the most typical of calc-alkaline island arc products, displaying the lowest K_2O values in the Aeolian Island arc (Keller, 1980b). The tephra fall stratigraphy of the Lower Pollara (LP) contains juvenile clasts with a wide geochemical range from basaltic-andesite to rhyolite. The observed depositional sequence and geochemical analysis (Fig. 4.3d) of the fallout from this sub-plinian eruption, with mafic scoria followed by felsic pumices, support previous interpretations that a felsic melt entered a mafic magma body triggering the eruption (Calanchi et al., 1993). The CA/HKCA component of the distal tephra displays similar major element chemistry to the LP fall deposits and critically is characterised by low K_2O glasses (Fig. 4.3d). However, some subtle variations in the glass chemistry exist. The compositional range of the distal glasses is more restricted than LP, with the proximal glasses displaying more elevated SiO_2 than those observed in the distal tephra. At overlapping SiO_2 values Al_2O_3 , MgO , MnO , CaO , Na_2O and K_2O are very comparable, whilst the distal glasses display slightly elevated TiO_2 and FeO (Fig. 4.3d). Overlapping major element chemistries certainly provide justification for previous correlations to the LP eruption (Di Roberto et al., 2008). Additionally the distal glasses and the LP glasses share a similar incompatible trace element pattern, displaying wide overlapping degrees of enrichment (Fig. 4.10a). Both LP and distal glasses display increasing Ba with increasing differentiation (Fig. 4.12c) and no pronounced Eu depletion (Fig. 4.10a) confirming the absence of K-feldspar fractionation. At a multi-element level normalising the LP proximal deposits to the distal glasses reveals some critical variations. LP glasses display slightly elevated Ba, Th, U and most noticeably lower middle and heavy REE concentrations (Fig. 4.10b). With such compositionally diverse tephtras, trace element bi-plots (Fig. 4.12) illustrate both similarities and difference between the LP fall and transitional CA/HKCA distal tephra. Rb, Nb Sr, La concentrations are similar and overlap in the distal tephra and LP glasses (Fig. 4.12), however Zr is more elevated in the LP glasses. Nb/Zr ratios should remain constant during fractionation and therefore subtle variations reflect differences in magmatic source compositions or degrees of melting (Table 4.2). Y concentrations in the LP glasses are considerably lower and decreasing with fractionation (Fig. 4.12d). The lower concentration of middle and heavy REE in the LP glasses could be associated with the removal of hornblendes, dominant within the felsic Salina products. Gertisser and Keller (2000) also suggest that amphiboles in the older Salina dacites were responsible for MREE depletions. Multi-elemental data do not confirm that the CA/HKCA component of the distal tephra

contain Lower Pollara (LP) pyroclasts. Some similarities in trace element compositions exist but ultimately REE profiles differ significantly.

(2) High-K basaltic-andesites (Component 2): These glasses are believed to be representative of pre-Pollara activity on Salina (Di Roberto et al., 2008). Elevated K_2O is consistent with magma of earlier activity from Salina and Monte dei Porri (Fig. 4.3d). Low TiO_2 concentrations (~ 0.4 wt.%) in Porri glasses confirm similarity to more recent Pollara activity on Salina and consequently they dramatically differ from those of component 2 ($TiO_2 = > 1$ wt.%) of the CGVT (Appendix eIII).

The absence of a robust correlation between the trace element compositions of the glasses within the CGVT and activity on Salina, in particular Lower Pollara (LP), raises broader volcanological implications. As previously suggested the CGVT is attributed to a major volcanic collapse (Di Roberto et al., 2008). In which case, considering the dominance of fractionated pumices this deposit is considered related to an explosive volcanic event. Salina offered a logical provenance solution based on some similarities in major element chemistry, in the type of lithics (quartz-bearing shale fragments and thermometamorphic rounded basement fragments), but crucially physical parameters. Salina displays evidence of a young collapse scar (Pollara) and a clear submarine passage for material to travel to the Marsili basin. If the CGVT does not originate from Salina, then it provides important evidence of a major collapse/explosive eruption not yet recognised on land. Briefly considered are other CA volcanic centres in the arc with the necessary pathways for material to enter the Marsili basin. Panarea shares a largely similar CA affinity to Salina, although analyses of dacite pumices suggest SiO_2 is restricted to 66 wt.% (Calanchi et al., 2002; Lucchi et al., 2008). Evidence for caldera collapse during the evolution of Panarea is suggested by Gabbianelli et al. (1993), whilst other researchers suggest instabilities from the western flank of Panarea (Favilli et al., 2005; Cimarelli et al., 2008). With explosive activity on Panarea associated with dome collapse (Cimarelli et al., 2008). Presently geochemical evidence casts doubt on the origin of the CGVT, despite strong volcanological evidence suggesting provenance from Salina. At present the origin of the CGVT remains unresolved.

4.4.1.5 TIR2000-417 (417 cm b.s.f)/HKCA of the Aeolian Island activity

These tephras display a wide degree of differentiation (52.4-74.2 wt.% SiO_2) which is mirrored by wide ranging incompatible trace element concentrations (Fig. 4.3d; Fig.

4.12). Constant incompatible trace element ratios within the TIR2000-417 confirm a single magmatic source (Table 4.2). The tight inter-element ratios within the distal tephra is consistent with magma mixing, which is typical of the explosive products of the Aeolian islands, including Salina (Calanchi et al., 1993) and Lipari (De Rosa et al., 2003) (Fig. 4.12). The wide range in major element compositions justifies initial correlations with the Lower Pollara, eruption of Salina (Di Roberto et al., 2008). However, these distal glasses display slightly more elevated K_2O than the proximal Lower Pollara glasses, illustrated by overall higher total alkalis (Fig. 4.3d). Levels of trace element enrichment are greater in this distal tephra compared with the Lower Pollara deposits (Fig. 4.11). This is best illustrated by variations in Nb (Fig. 4.12), at a multi-element level, trace element concentrations in the most fractionated distal glasses far exceed those seen in the most fractionated Lower Pollara glasses (Fig. 4.11b). Multi-element data presented herein suggest that the previous correlation to fall from the Lower Pollara eruption is invalid (Di Roberto et al., 2008).

The CA/HKCA affinity of this marine tephra merely confirms its origin from this island arc setting, rather than any of the volcanic centers to the north-east on the Italian mainland (e.g., Campi Flegrei, Vesuvius). Recognised eruptions producing glass compositions with a HKCA affinity are dominant in the volcanostratigraphy of Lipari, as demonstrated by the Monte Pilato glasses. The Monte Guardia eruption of Lipari with an age slightly younger than 26.3 ± 0.8 cal ka BP (^{14}C 22, 600 \pm 300 yrs BP; Crisci et al., 1983) is chronologically suitable for consideration, however, as with all HKCA explosive volcanism at Lipari, these products are easily dismissed as a potential source of TIR2000-417 fall on the basis that rhyolitic glasses from Monte Guardia are characterised by low Ba, Sr, Eu concentrations (Fig. 4.11a).

The absence of K-feldspar related trace element anomalies within the highly fractionated Lower Pollara rhyolites and those of the distal tephra TIR2000-417 indicate that they are the product of a similar magmatic system, one that differs from that of Lipari. Ba and Sr concentrations are decoupled in both the TIR2000-417 and Lower Pollara glasses. Strontium concentrations decrease with increasing degrees of fractionation (Fig. 4.12e), whilst Ba is highly incompatible (Fig. 4.12c) and rhyolitic shards in the distal tephra have high Ba up to 1200 ppm. Both the proximal Lower Pollara and the distal tephra are produced by magmatic systems in which conditions prevented the crystallisation of K-feldspar, a phase typical of highly silicic rhyolites.

Similar observations were made by Donato et al. (2006) who highlighted that high water content may have been responsible for preventing the crystallisation of K-feldspar within the younger Upper Pollara pyroclasts. Trace element data present here indicate that a similar control is likely for both the Lower Pollara glasses (H_2O ~3-4 wt.%) and the distal tephra TIR2000-417 (H_2O 3-4 wt.%).

As outlined above Panarea pumices are geochemically similar to that of Salina, with the lower levels of trace element enrichment and consequently do not offer a potential solution to the provenance of TIR2000-417. The western part of the Aeolian arc offers a potential source of provenance; ages of final phase activity on Alicudi are poorly constrained. On the neighboring island of Filicudi two exotic fall deposits have been attributed to possible explosive activity on Alicudi (Lucchi et al., 2008). Most recent activity on Alicudi (Villari, 1980, Peccerillo and Wu, 1992), based on whole rock analysis, indicates andesitic products with incompatible trace element concentrations that differ from those of Salina. Alicudi deposits display more elevated K_2O than those of Salina, whilst showing HFSE ($\text{Nb} > 20\text{ppm}$ at 55-59 wt.% SiO_2), LREE ($\text{La} > 50\text{ppm}$; $\text{Ce} > 85\text{ppm}$) and HREE concentrations equal or greater than those seen in the more evolved Lower Pollara rhyolites of Salina (Villari, 1980; Peccerillo and Wu, 1992). Although this is based on whole rock data that is not appropriate for precise tephra correlation due to the occurrence of phenocrysts and possibly lithics, it does offer an insight into Alicudi compositions which would appear to be in better agreement with the glasses of TIR2000-417. Final phase activity on Alicudi is tentatively suggested as a potential source of this tephra.

A final consideration concerning the provenance of this marine tephra and other previously unresolved tephras in TIR2000-C01 is the possibility of submerged volcanic edifices that may have been sub-aerial during lower Mediterranean sea levels during the last glacial (Lambeck and Bard, 2000). The Aeolian island volcanoes represent only the sub-aerial portion of significantly larger volcanic structures, for instance approximately 2/3 of Stromboli is submerged (Rosi et al., 2000). Activity from volcanic edifices below sea level in the Aeolian Islands arc may provide the sources of proximally unrecognised geochemical signatures in the glasses. However, this remains problematic given the absence of such tephras from within the accumulation profiles recorded on the Aeolians Islands during the last glacial period (i.e. Lucchi et al., 2008). Currently the origin of TIR2000-417 remains unresolved; the presence of fall in the Marsili Basin provides

evidence of a major explosive event not presently recognised on-land in Aeolian Islands.

4.4.2 Implications for tephra correlations

This study highlights the necessity, of wherever possible, to supplement major element analysis with trace element analysis of distal glasses, in order to precisely validate tephra marine-continental (distal-proximal) correlations. In some instances major and minor element data may suggest a reliable match between proximal and distal tephras (i.e. TIR2000-417 - Lower Pollara). However, through the examination of a full suite of trace elements, it is evident that these major element correlations do not necessarily provide robust proximal-distal matches.

This is not a new problem for distal tephrochronology. It is well recognised that many magmatic systems systematically over time produce distally dispersed tephras with very similar (often indistinguishable) major element chemistries, for example Katla, Iceland (Haflidason et al., 2000; Hall and Pilcher, 2002; Davies et al., 2004), Mount St Helens (Busacca et al., 1992), Toba caldera (Smith et al., 2011b) and the Campanian province (Wulf et al., 2004; Smith et al., 2011a). Consequently, correlations based solely on major element data given the associated errors and limited variability between temporally distinct erupted deposits can be erroneous. In the absence of good stratigraphic control, trace element concentrations of distal tephras are essential in defining reliable proximal-distal correlations.

This chapter has highlighted that highly evolved tephras recorded distally in the Marsili basin are not yet recognised in the proximal deposits on the Aeolian Islands. Volcanic islands are prone to multiple flank failures (Pasquare et al., 1993; Kokelaar and Romagnoli, 1995; Masson et al., 2006; Tibaldi, 2001; Di Roberto et al., 2010; de Alteriis et al., 2010), where vital proximal information is lost during subsequent volcanic and seismic activity, manifested in the marine environment as polygenetic turbidites with complex mix tephra compositions (Di Roberto et al., 2010). Determining the complete eruptive history of volcanic islands can be difficult owing to the following factors; small on-land volume of deposits; their limited lateral extent and burial and erosion of underlying deposits by more recent activity (Gertisser et al., 2010; Tamburrino et al., 2012). Limited Aeolian Island fall tephras are reported in the

southern Tyrrhenian Sea (Paterne et al., 1988; McCoy and Cornell, 1990) for the reason articulated in Paterne et al. (1988);

(1) Despite the explosive nature of volcanic activity at these volcanic centres, the quantity of erupted material was volumetrically much lower than for the Campanian centres;

(2) Prevailing westerly winds prevented the widespread northward dispersal of Aeolian island tephra;

(3) The orientation of dispersal axes from short-lived eruptions may be an issue.

More recently Aeolian Island tephra are reported distally in the southern Adriatic (Siani et al., 2004) and Ionian Seas (Clift and Blusztajn, 1999) and continentally on Sicily. Examples include distally occurring tephra from Salina (Grey Porri Tuff; Keller, pers comm.), Lipari (Monte Guardia and Gabelotto-Fiume Bianco; Narcisi, 2002; Siani et al., 2004; Lucchi et al., 2008) and Vulcano (Quadrara; Morche, 1988). This would suggest that despite lower magma volumes, these eruptions can be dispersed long distances (>600 km; Clift and Blusztajn, 1999). Additionally more recent detailed field investigations suggest that some of the explosive Aeolian island eruptions are prolonged (Sulpizio et al., 2008; Davi et al., 2010). Thus it seems most likely that the prevailing westerlies are the dominant control on ash dispersals from the Aeolian Islands.

4.4.3 Primary tephra Vs. Turbidites

Three primary fall tephra have been identified within the TIR2000-C01 core, TIR2000-30 (30 cm b.s.f.); TIR2000-93 (93 cm b.s.f.) and TIR2000-417 (417 cm b.s.f.). Fall tephra are infrequent in the Tyrrhenian Sea (see above). It is widely accepted that Tyrrhenian Sea stratigraphies are complicated by the presence of turbidites (McCoy and Cornell, 1990; Calanchi et al., 1994; De Ateris et al., 2010) and the Marsili basin core is no exception. The basin is directly linked to the Aeolian Islands and the Italian mainland by a series of submarine canyons (Gamberi and Marani, 2007). These canyons act as conduits for volcanoclastic debris produced by pyroclastic flow, flank failures and sector collapse on the sub-aerial volcanoes. Stacked sequences of turbidites as seen in TIR2000-C01 are not always related to collapse, they can be related to the erosion and remobilisation of volcanic detritus related to instabilities and seismic activity.

Monogenetic turbidites must be considered carefully, where there is a clear dominance of a single chemical affinity that can be reliably correlated to proximal source this is considered as representing a 'syn-volcanic' event (i.e., TIR2000-7 (7 cm b.s.f)). Consequently, these deposits present an event marker with tephrostratigraphic significance (Di Roberto et al., 2008). Monogenetic turbidites may result from the collapse of a rhyolitic dome and/or the formation of hot or cold pyroclastic (block and ash) flows and detached surges which can enter the marine environment (Schneider et al., 2001). They may also represent the remobilization of primary tephra fall, where ash mantling the sea floor is available to be entrained by turbidity currents.

Polymictic turbidites usually have no chronostratigraphic meaning. These tephras represent the remobilization of volcanic material following a gravitational collapse, seismically induced failure or a major erosive event. Such material may have originated within (1) the sub-aerial volcano-stratigraphies; (2) submarine deposits surrounding the sub-aerial part of the volcano; or (3) a mixture of both. The high frequency of polygenetic tephra within the Marsili basin core is likely to reflect that of volcano-sedimentary processes (mass wasting and erosional processes) that are very dominant within this active back arc basin (Di Roberto et al., 2008).

4.4.4 Chronological implications for the Marsili basin core:

Two chronological points can be fixed within the upper portion of the TIR2000-C01 stratigraphy, the Monte Pilato eruption of Lipari at 7 cm b.s.f (776 cal AD) and the Soccavo 1 eruption, Campi Flegrei, at 93 cm b.s.f (11915-12721 cal yrs BP). A third chronological constraint is derived from the previous attribution of TIR2000-30 (30 cm b.s.f) to the AP1-3 eruptions of Vesuvius (between 2.7-3.6 cal ka BP) (Di Roberto et al., 2008). Although this tephra does not offer a precise chronological tie point it provides an age range. Given the limited number of fixed chronological points within the Marsili basin core a simple linear age-depth relationship for the upper portion of the core is determined. Given the numerous turbidite inputs linear age models are problematic (see Lowe et al., 2007) and sedimentation rates must be considered only as rough estimates. Between present day and the Monte Pilato eruption a sedimentation rate of 6.36 cm ka^{-1} is observed. This is a period of lower volcanoclastic input and perhaps indicative of a less volcanoclastic dominated sedimentation within the Tyrrhenian Sea. Between Monte Pilato and the Soccavo 1 tephra layer sedimentation rates increased to 7.72 cm ka^{-1} . The AP1-3 Vesuvius activity at 30 cm (Di Roberto et al., 2008) is in keeping with the age-

depth relationship reported. Given the sedimentation rates between Monte Pilato and Soccavo 1, TIR2000-50 (50 cm b.s.f) has an approximate age of 6.6 ka BP. Reaffirming that despite similarities with the Palizzi A major, minor and trace element data, the proximal deposits on Vulcano are too young to be the proximal counterpart of TIR2000-50. This confirms that repeated geochemistries are produced from the Vulcano magmatic system through time.

The absence of a reliable tephra marker beneath Soccavo 1 becomes problematic for assessing both the chronology and sedimentation rates in the lower core. The absence in the Marsili core of the two prominent visible marine tephra markers the Y-3 and Y-5, at 30-31 ka BP (Zanchetta et al., 2008) and 39 ka BP (De Vivo et al., 2001) respectively, which are reported extensively in southern Tyrrhenian Sea cores (Paterne et al., 1988), would indicate that the basal age of the Marsili core is younger than 30-31 ka BP. This indicates that sedimentation has increased beneath Soccavo 1, this is supported by the high frequency volcanoclastic turbidite inputs (Fig. 4.1). This could be related to a greater number of near instantaneous volcanoclastic sediment input events within this time period, such as flank collapse or sub-marine failures of material on the continental shelf. Additionally, lower sea levels during the last glacial (Lambeck and Bard, 2000), meaning sub-aerial volcanic edifices in the Aeolian islands were larger thus offering greater potential for erosion/collapse which would provide increased quantities of volcanoclastic material to become delivered into the Marsili basin.

4.5. Conclusions

(1) Proximal continental-distal marine tephra correlations are more reliable when based on an integration of major, minor and trace element glass data (EMPA and LA-ICP-MS).

(2) Correlations based solely on major elements given the associated errors, can in some cases be misleading and result in incorrect attribution of age-markers to marine archives. The addition of trace element data, with smaller errors, offers more diagnostic geochemical information essential for fingerprinting tephras.

(3) Characterisation of the geochemistry of proximal deposits must include juvenile deposits of all eruptive phases to ensure reliable proximal-distal matches. Examples are provided of proximal-distal correlations to both proximal fall and flow deposits.

(4) Flank failure and sector collapse can remove proximal stratigraphies especially on volcanic islands such that the remaining proximal suites are not fully representative of all the eruptive events/geochemistries identified distally.

(5) The Marsili Basin is dominated by turbidites. Monogenetic turbidites can be used as tephrostratigraphic markers of syn-eruptive activity within the island arc marine setting. Polygenetic turbidites offer very little tephrochronological meaning.

(6) Only limited tephra fall is reported north in the Marsili Basin from Aeolian Island volcanism, suggesting that fall footprints are dispersed in a south south-easterly direction. Hence the paucity of Aeolian tephra in the Tyrrhenian Sea and their greater abundance on neighbouring islands to the south, Sicily and in Ionian Sea marine cores. Dispersal is mainly controlled by prevailing circulation patterns in the Mediterranean which are westerly during most of the year.

Chapter 5: Ionian Sea Marine Core (M25-4/12)

Abstract

Primary fall tephras recorded from major Aeolian Islands explosive eruptions were found to be limited in their northward dispersal with only few examples in the Marsili basin core (Chapter 4). Herein sediments from the Ionian Sea core M25/4-12 were examined to assess whether Ionian Sea marine archives might contain a cryptotephra record of Aeolian island explosive activity and provide new chronological constraints for the core. The provenance of two visible layers in the core Y-3 and Y-5 is assessed using additional trace element characterisation.

Two explosive eruptions from the Aeolian Islands (early Holocene to 40 ka) are present in the core, indicating that there is potential to improve the chronology of the Ionian archives using cryptotephra analysis. HKCA rhyolitic shards dispersed by the Gabelotto-Fiume Bianco (GFB) eruption of Lipari are identified within sapropel 1 (28cm b.s.f) in the early Holocene sediments of Ionian Sea core M25/4-12 providing a new age marker of 8730–8400 yrs BP cal (7770 ± 70 yrs BP uncalibrated).

Trace element data confirm that the VRa proximal deposits of Tufi Biancastri are not the proximal equivalent of the Y-3 tephra marker recorded in the Ionian Sea. Whilst the precise proximal source of the Y-3 tephra remains unresolved, the diagnostic geochemical characteristics reported from the type locality (M25/4-12) should be used as the preferred criteria for the assignment of Y-3 correlations. Trace element data are presented that verifies the correlation of the Ionian Sea Y-5 tephra to the Campanian Ignimbrite (Kraml, 1997). Geochemical data here confirm that this distal tephra can be attributed to the first Plinian episode of the eruption, a feature consistent with other ultra distal occurrences of the Campanian Ignimbrite.

5. 1 Introduction

Primary fall tephra from major Aeolian Islands explosive eruptions were found to be rather limited in their northward dispersal with few examples in the Marsili Basin core (Chapter 4). The eastward dispersal of tephra from the Aeolian Islands is assessed; sediments from an Ionian Sea marine core (M25/4-12; Fig. 5.1) are examined with the following aims;

- (1) To establish whether the Ionian Sea marine archives contain tephra from the Aeolian Islands.
- (2) To improve the chronology of the Ionian Sea core M25/4-12, furnishing it with additional cryptotephra (non-visible) chronological markers.
- (3) Assess the provenance solutions of visible tephra layers using additional trace element characterisation.

The Ionian Sea core contains numerous visible tephra layers, which were assigned provenance predominantly from the Campanian region and to a lesser extent the Roman provenance, Etna and Pantelleria (Keller et al., 1978). The visible tephrostratigraphy provides a chronological framework that enabled a targeted investigation of sediments overlapping in time with last 40 ka of explosive volcanism on the Aeolian Islands. Visible tephra layers, Y-5, Y-3 and sapropel stratigraphy are used to establish a temporal framework for the upper portion of the core. Y-5 is assigned to the Campanian Ignimbrite (CI) eruption (Keller et al., 1978; Kraml, 1997), which is $^{40}\text{Ar}/^{39}\text{Ar}$ dated at 39.28 ± 0.11 ka BP (De Vivo et al., 2001). This provides the lowermost boundary for this investigation and is correlated to distal tephra from the Tyrrhenian, Adriatic and Ionian Seas (Paterne et al., 1988; Thunell et al., 1979; Vezzoli, 1991). Y-5/CI has also been identified within numerous terrestrial records including Lago Grande di Monticchio (LGdM) tephra TM-18 (Wulf et al., 2004) and has been reported as far afield as the Russian plains (Pyle et al., 2006). Consequently the CI represents the most widespread late Quaternary tephra horizon (Zanchetta et al., 2008).

Keller et al., (1978) was first to report the most recent last glacial visible trachytic tephra layer in the Ionian Sea, termed the Y-3, with a source attributed to explosive activity within Campi Flegrei. This eruption coincides with a period of significant environmental change during the last glacial. Y-3 occurs at the transition between

marine isotope stage 2/3 or Heinrich event 3 and hence offers enormous potential to assess leads and/or lags in environmental change (Zanchetta et al., 2008). Zanchetta et al., (2008) review the presence of Y-3 tephra in other archives across the central Mediterranean and emphasise its widespread dispersal throughout the region as far as the Balkans (Wagner et al., 2008). Considerable discrepancies exist in the age of this distal tephra, largely as the precise proximal counterpart remains unresolved and ages are thus imported from distal archives. Interpolation of the Mediterranean Sapropel chronology allowed Kraml (1997) to assign an age of 25.3 ± 3 ka yrs B.P to this tephra in the Ionian Sea. Wulf et al., (2004) correlated LGdM tephra, TM-15 a 29cm thick, predominantly co-ignimbritic ash to the Y-3 tephra, providing the first terrestrial record and age of this eruption. The early varve chronology of LGdM suggested an age of 23,930 yrs BP, but more recently this was revised to 27,256 yrs B.P (Wulf et al., 2006). Importantly at LGdM TM-15 falls in a decline in the tree pollen spectra related to a climatic transition linked with Heinrich event 3. A maximum age of $30,493 \pm 303$ cal yrs B.P ($25,570 \pm 110$ ^{14}C yrs B.P) using IntCal 09 (Reimer et al., 2009) is derived from a foraminifera ^{14}C age from 3 cm beneath the Y-3 layer in Salerno Gulf cores (Munno and Petrosino, 2004). Y-3 data from the Ionian Sea presents an opportunity to assess proximal links and re-access distal to distal correlations.

Herein we present grain specific major minor and trace element data to verify the provenance solutions of the Y-5 and Y-3 (Keller et al., 1978; Kraml, 1997), whilst attempting to complement the existing visible tephrostratigraphy with additional cryptotephra markers horizons.

5.2 Site

M25/4-12 is a type site for tephrochronology in the Ionian Sea (Keller et al., 1978), distal tephra reported across the central Mediterranean are correlated to its visible tephrostratigraphy. M25/4-12 is located on the Calabrian rise, in the Ionian Sea (Fig. 5.1), east of Sicily (N37 57, 98 E18, 11, 04). Water depth is 2473 meters and the total core length is 12.40 meters. The core is located 450 km SE of the Campanian Volcanic Zone (CVZ), 280km east of Mount Etna, 290 km east of the Aeolian islands and is over 650 km NW of Santorini and the Aegean volcanic centres.

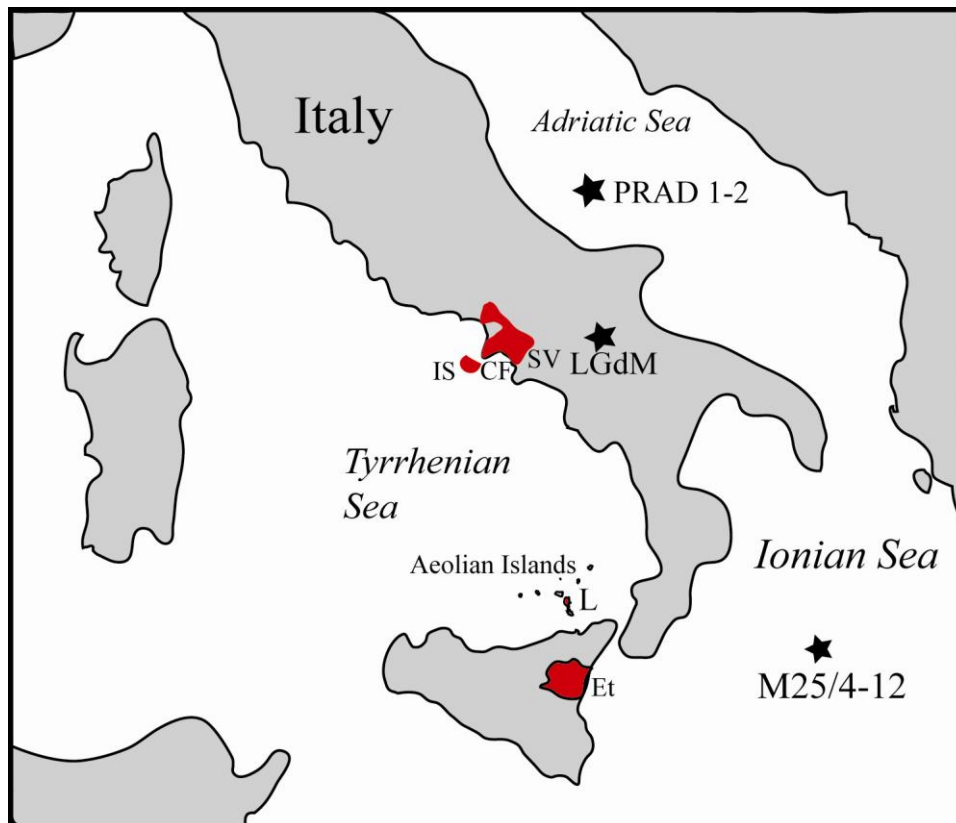


Figure 5.1: Location of the investigated marine core M25/4-12 in the Ionian Sea, also shown is the location of Lago Grande di Monticchio (LGdM) and the PRAD 1-2. (L=Lipari; CF= Campi Flegrei; SV = Somma-Vesuvius; IS = Ischia; Et = Mount Etna).

5.3 Methodology

For visible tephra samples of both the Y-3 and Y-5 tephra layers were separated, washed in distilled in water, picked under a light microscope and mounted in epoxy resin, shards were then sectioned and polished.

For cryptotephra in the sediments of M25/4-12 continuous 5cm scans ($5 \times 1 \text{cm}^3$) were taken from the top of sapropel 1 to the Y-5 tephra, as described by Keller et al. (1978). All samples were dried and weighed to allow for the calculation of tephra glass shards concentrations per gram of dry sediment (shards/g). Samples were then processed using the cryptotephra extraction technique (Blockley et al., 2005). Shard concentrations were counted under a high powered microscope to identify tephra layers. On identification of cryptotephra the 5 cm scan was re-sampled at a continuous 1cm^3 resolution, repeating the processing outlined above. Once 1cm resolution peaks in shard concentrations were identified, new samples were processed for geochemistry. Shards were picked from

distilled water using a microscopic needle, mounted in resin and sectioned for geochemical analysis.

5.4 Results

5.4.1 Stratigraphy and Visible tephra layers

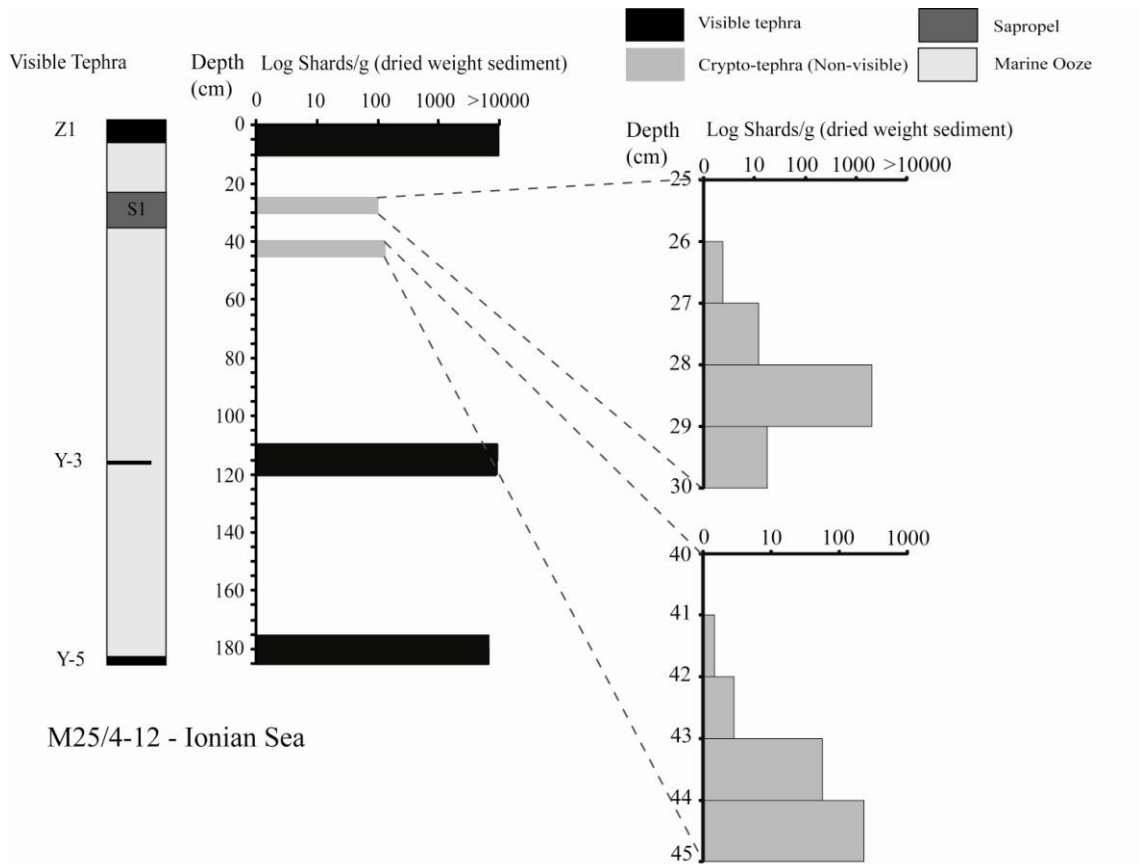


Figure 5.2: Tephrostratigraphy of the investigated upper 180cm of the Ionian Sea marine core M25/4-12

Detailed litho-stratigraphy and oxygen isotope stratigraphy of M25/4-12 was outlined by Keller et al., (1978) and Kraml, (1997). The relevant stratigraphy and markers relevant to this investigation are shown in Figure 5.2 and include;

- (1) Sapropel 1, organic rich layer; between 24-36cm below sea floor (b.s.f);
- (2) Y-3: The 1 cm thick Y-3 tephra layer occurs between 117.5-118.5cm b.s.f. Y-3 shards were all dominated by clear glasses. Shards sampled displayed typically two shard morphologies, those that were angular and blocky with limited vesicularity and

then those that are highly vesiculated (Fig. 5.3). Shards from this layer were typically between 100-200 μm in length (Fig. 5.3).

(3) Y-5: The 2.5cm thick tephra layer occurs between 184-186.5 cm b.s.f. Y-5 shards were dominated by clear glasses with occasional brown shards. Shards were highly vesicular and elongate (Fig. 5.3). Shards sampled were typically greater than 300 μm on the long axis (Fig. 5.3).

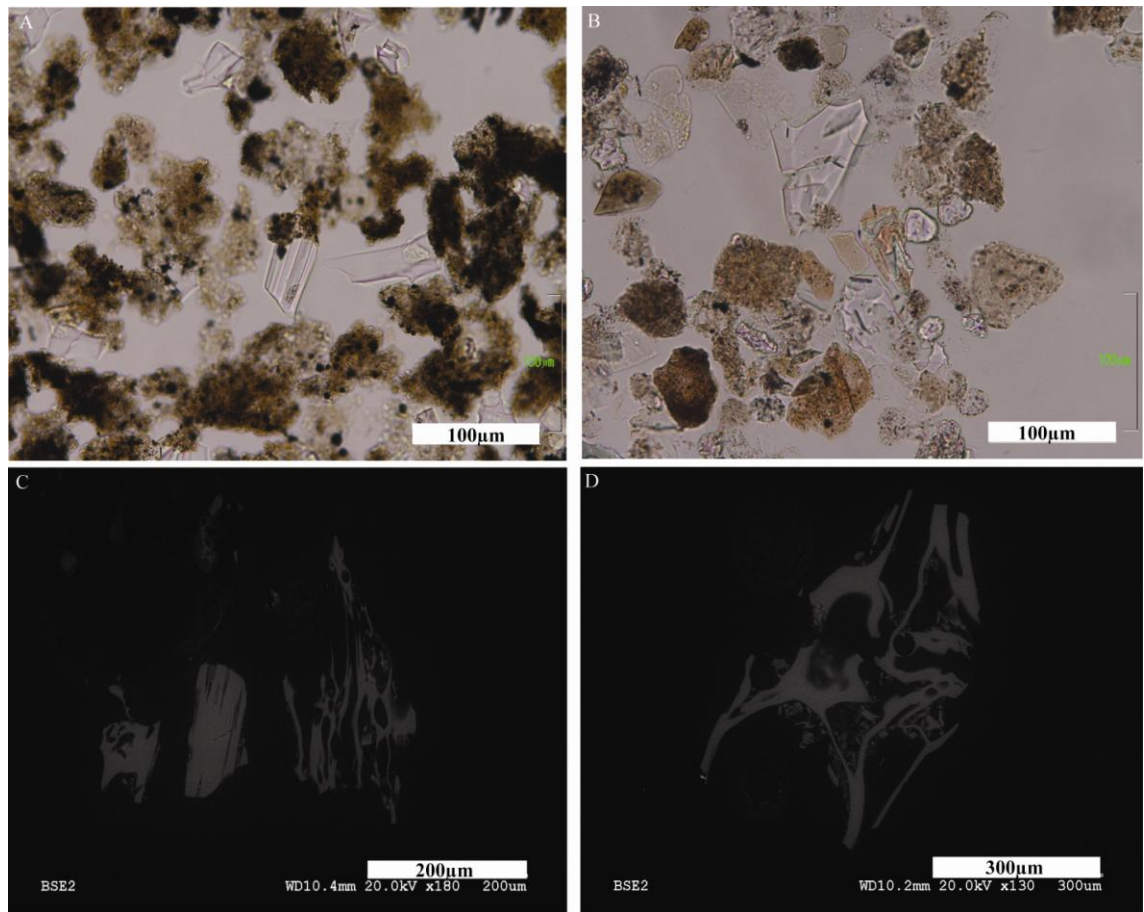


Figure 5.3: Shards extracted from the four investigated tephra layers. (a) M25/4-12_28cm, small stretched highly vesicular shards; (b) M25/4-12_44cm, larger angular and blocky shards; (c) M25/4-12_118.5cm b.s.f. Y-3, two distinct shard morphologies, right, highly stretched vesicular shards, left, less vesicular and more blocky shard; (d) M25/4-12_184.5cm b.s.f. Y-5, particularly large (> 300 μm) and highly vesicular.

5.4.2 Cryptotephra layers

Two discrete cryptotephra layers have been identified on the basis of their peaks in shard concentrations (Fig. 5.2). Layers are named according to their depth in the M25/4-12 core (in cm). The upper most cryptotephra (M25/4-12_28) is located at 28 cm b.s.f. and lies within the sapropel 1 sediments. A second peak in tephra shard concentrations M25/4-12_44 was identified at a depth of 44 cm b.s.f. Shards concentrations were most abundant in M25/4-12_28, with a precise peak of 2037 shards/dried gram of sediment. M25/4-12_44cm displayed much lower shard concentrations, with 234 shards/dried gram of sediment. This tephra is more diffuse with a less pronounced peak in glass shard concentrations. The physical characteristic of the tephra shards appear to differ between the two cryptotephra layers, the upper most layer (28cm b.s.f) is characterised by smaller (typically < 80um), tubular shards (Fig. 5.3). The lowermost layer is characterised by larger (typically > 80um), blocky shards (Fig. 5.3). These shards display high abundances of microcrysts within the glasses.

5.4.3 Geochemistry:

Representative major, minor and trace element geochemistry for the four tephra layers are given in Table 5.1 and full geochemical data sets are available in appendix eIV. Diagnostic trace element ratios for the tephtras, potential proximal source volcanic and other distal equivalents are given in Table 5.2.

M25/4-12_28cm b.s.f

Glasses are homogeneous with 75.37 ± 0.11 wt. % SiO_2 ($n=11$) and are classified as rhyolitic (Fig. 5.4). These rhyolites contain typically 5 wt. % K_2O making them HKCA in composition. Glasses are highly evolved, $\text{Zr}/\text{Sr} = 10.7 \pm 0.3$, the homogeneous rhyolitic shards ($\text{Rb} = 313 \pm 4$ ppm; $\text{Th} = 49 \pm 1$ ppm; $\text{Zr} = 174 \pm 2$ ppm; $\text{Nb} = 37 \pm 1$ ppm; $\text{La} = 55 \pm 0.4$ ppm) display relative enrichment in the LIL elements relative to the HFSE (Fig. 5.5a), with a strong depletion in Ti ($\text{Ti}/\text{Gd}_N = 0.03-0.05$).

| Sample Shard | M25/4-12_28cm | M25/4-12_44cm | M25/4-12_118.5cm- Y-3 | | M25/4-12_184.5cm- Y-5 | | |
|--------------------------------|----------------------|---------------|-----------------------|-------|-----------------------|-------|-------|
| | 12A | 17A | 31C | 18B | 36C | 49D | 47D |
| EPMA | (wt. % oxide) | | | | | | |
| SiO ₂ | 75.24 | 75.91 | 60.53 | 62.23 | 61.12 | 61.07 | 62.09 |
| TiO ₂ | 0.07 | 0.09 | 0.40 | 0.34 | 0.46 | 0.42 | 0.34 |
| Al ₂ O ₃ | 13.27 | 12.98 | 18.35 | 17.82 | 18.63 | 18.68 | 18.36 |
| FeOt | 1.42 | 1.32 | 3.77 | 2.77 | 2.97 | 2.97 | 2.72 |
| MnO | 0.08 | 0.01 | 0.11 | 0.10 | 0.24 | 0.21 | 0.14 |
| MgO | 0.04 | 0.04 | 0.83 | 0.35 | 0.31 | 0.33 | 0.47 |
| CaO | 0.70 | 0.64 | 2.63 | 2.28 | 1.70 | 1.84 | 2.13 |
| Na ₂ O | 4.19 | 3.98 | 2.98 | 4.50 | 6.60 | 6.46 | 4.57 |
| K ₂ O | 4.99 | 5.03 | 9.96 | 8.75 | 7.07 | 7.18 | 8.72 |
| P ₂ O ₅ | - | - | 0.14 | 0.05 | - | - | - |
| Cl | - | - | 0.30 | 0.81 | 0.90 | 0.85 | 0.45 |
| Total | 95.57 | 94.25 | 95.26 | 98.59 | 99.38 | 99.19 | 98.41 |
| LA-ICP-MS | (ppm) | | | | | | |
| V | <LOD | <LOD | 68.87 | 29.79 | 14.10 | 15.38 | 32.19 |
| Rb | 316 | 322 | 268 | 344 | 448 | 466 | 307 |
| Sr | 17 | 13 | 597 | 138 | 25 | 21 | 139 |
| Y | 41 | 42 | 19 | 31 | 55 | 56 | 25 |
| Zr | 178 | 169 | 172 | 370 | 645 | 668 | 256 |
| Nb | 38 | 37 | 30 | 53 | 118 | 122 | 42 |
| Ba | 15 | 12 | 801 | 24 | 21 | 15 | 45 |
| La | 55 | 50 | 43 | 71 | 126 | 128 | 60 |
| Ce | 108 | 102 | 79 | 134 | 237 | 245 | 113 |
| Pr | 12 | 11 | 8 | 14 | 23 | 25 | 12 |
| Nd | 40 | 39 | 31 | 49 | 84 | 86 | 44 |
| Sm | 7.5 | 7.2 | 6.1 | 8.3 | 14.0 | 15.6 | 7.6 |
| Eu | < LOD | 0.2 | 1.9 | 1.6 | 1.3 | 1.5 | 1.8 |
| Gd | 7.2 | 6.5 | 4.5 | 6.0 | 10.3 | 11.4 | 5.7 |
| Dy | 6.7 | 7.0 | 3.6 | 5.6 | 9.7 | 9.9 | 4.6 |
| Er | 4.4 | 4.3 | 1.8 | 3.1 | 5.5 | 5.7 | 2.7 |
| Yb | 4.6 | 4.8 | 1.7 | 3.3 | 5.5 | 5.5 | 2.5 |
| Lu | 0.7 | 0.7 | 0.3 | 0.5 | 0.8 | 0.8 | 0.4 |
| Ta | 2.6 | 2.7 | 1.5 | 2.7 | 5.7 | 5.6 | 2.2 |
| Pb | 33 | 32 | 37 | 60 | 67 | 65 | 44 |
| Th | 50 | 50 | 13 | 31 | 51 | 53 | 20 |
| U | 15 | 15 | 4.4 | 10 | 18 | 18 | 6.7 |
| <i>Ratio</i> | | | | | | | |
| Zr/Sr | 10.5 | 12.7 | 0.3 | 2.7 | 26.1 | 32.6 | 1.8 |
| Nb/Zr | 0.21 | 0.22 | 0.17 | 0.14 | 0.18 | 0.18 | 0.17 |
| La/Yb | 12.1 | 10.4 | 24.4 | 21.5 | 23.1 | 23.1 | 23.6 |
| Nb/Th | 0.8 | 0.7 | 2.2 | 1.7 | 2.3 | 2.3 | 2.1 |

Table 5.1: Representative major, minor and trace element data from investigated marine tephras in the Ionian Sea core (M25/4-12). Full data set are given in appendix eIV.

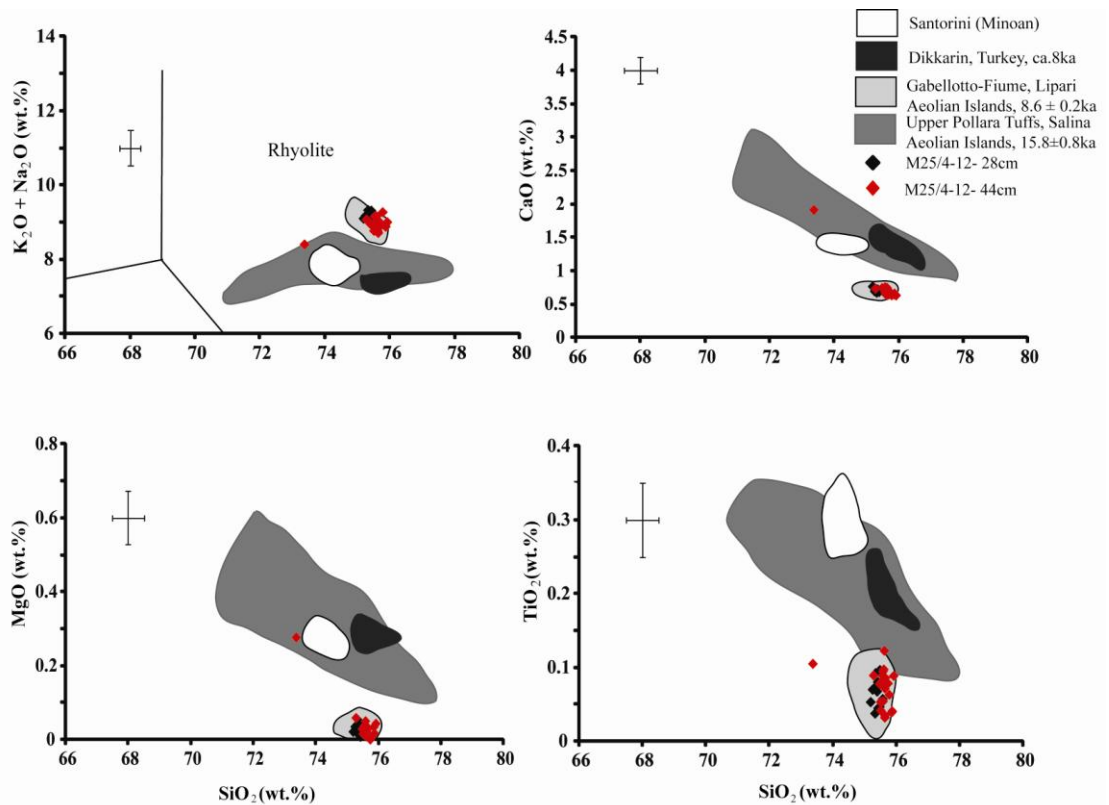


Figure 5.4: Major element glass chemistry of M25/4-12_28cm and M25/4-12_44cm cryptotephra layers recorded in the Ionian Sea. (TAS classification after Le Bas et al., 1986).

Glasses display LREE enrichment relative to the HREE ($La/Yb = 11.9 \pm 1.2$) and are heavily depleted in Sr, Ba and Eu ($Sr = 16.2 \pm 0.5\text{ppm}$; $Ba = 15.5 \pm 0.8\text{ppm}$; $Eu/Eu^*_N = 0.14$) relative to incompatible elements (Fig. 5.5a). Incompatible trace elements display positive linear relationships ($Nb/Zr = 0.21\text{-}0.23$; $Ta/Th = 0.05\text{-}0.06$).

M25/4-12_44 cm b.s.f.

Glass shards in this layer display slightly more major element variability than the overlying tephra (Fig. 5.4). Silica concentrations range from 73.4 - 75.9 wt. % ($n=21$) and are classified as rhyolitic. The glasses are characterised by typically 5 wt. % K_2O making them HKCA in composition. Glasses are highly evolved, up $Zr/Sr = 12.04 \pm 0.9$, displaying strong depletions in Ti ($Ti/Gd_N = 0.03\text{-}0.04$). Glasses display LREE enrichment relative to the HREE ($La/Yb = 10.3 \pm 0.7$), whilst pronounced depletions in Sr, Ba and Eu are observed ($Sr = 13.1 \pm 0.6\text{ ppm}$; $Ba = 13.7 \pm 7\text{ ppm}$; $Eu/Eu^*_N = 0.14$) (Fig. 5.5a). Incompatible trace elements display tight positive linear relationships supported incompatible trace element ratios ($Nb/Zr = 0.21\text{-}0.23$; $Ta/Th = 0.05\text{-}0.06$).

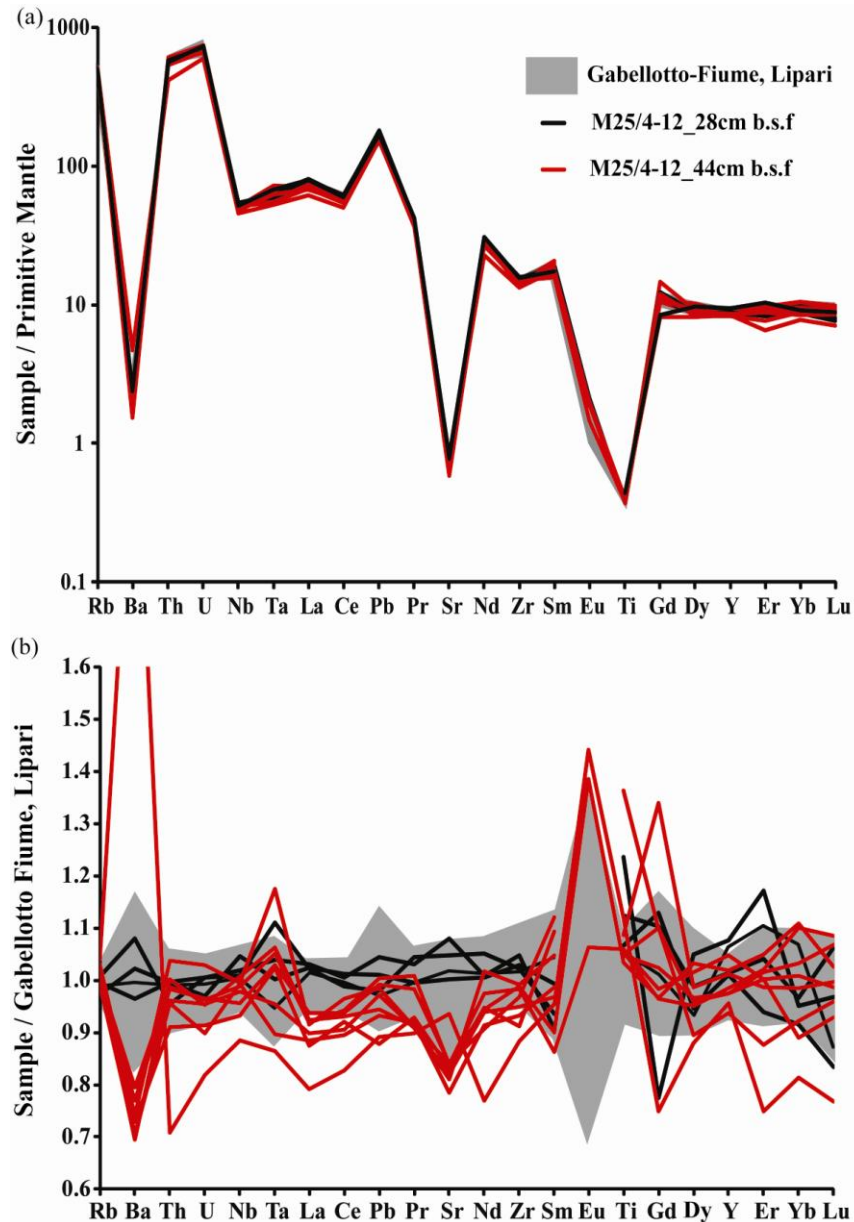


Figure 5.5: (A) Distal cryptotephra normalised to Primitive Mantle (Sun and McDonough, 1989) (B) Cryptotephra normalised to the glass compositions from proximal surge deposits of the Gabelotto-Fiume bianco, Lipari.

M25/4-12_118.5 cm b.s.f. - Y-3

Silica concentrations range from 60.0-62.8 wt. % ($n=32$). These silica undersaturated glasses display variable FeO_t (2.7 -3.8 wt. %) and CaO (2-2.8 wt. %) and high K₂O > Na₂O (K₂O = 8.2-10.4 wt. %). Glass shards in this tephra horizon range from phonotachytic to trachytic compositions (Fig. 5.6). Increasing SiO₂ as a fractionation index

shows the following major and minor element variations, decreasing Al₂O₃, FeO, MgO, CaO, K₂O, P₂O₅; whilst increasing Na₂O, Cl; and constant TiO₂ and MnO. Glass compositions largely cluster at both ends of the SiO₂ variation observed here, with some glass compositions lying between the two end members. Trace elements concentrations reflect this bimodality at the two ends of the SiO₂ variation. A small number of shards lie compositionally between the two end-members ($n=4$) outlined below.

The higher silica (> 62 wt. %), trachytes ($n=7$) show high levels of trace element enrichment levels (Zr/Sr = 2.46 ± 0.6) and are largely homogeneous (Rb = 343 ± 7 ppm; Th = 30 ± 3 ppm; Zr = 356 ± 32 ppm; Nb = 53 ± 3 ; La = 53 ± 3 ppm). Glasses display significant concentrations of V (32 ± 4 ppm) given the levels of enrichment. These shards show depletions in Sr and Ba (Sr = 131-265ppm; Ba = 23-211ppm) relative to the enrichment in other LILE and HFSE trace elements (Fig. 5.5). Shards display LREE enrichment relative to HREE (La/Yb = 22.6 ± 1.2) and pronounced Eu depletions (Eu/Eu*_N = 0.5-0.9). Incompatible trace element ratios are consistent within these shards (Nb/Zr = 0.15 ± 0.01 ; Nb/Th 1.8 ± 0.1 ; Zr/Th = 12 ± 0.3).

The lower silica (< 62 wt. %), phonolitic-trachytic shards ($n=7$) display lower levels of trace element enrichment (Zr/Sr = 0.32 ± 0.01), concentrations are largely homogeneous (Rb = 272 ± 4 ppm; Th = 14 ± 1 ppm; Zr = 183 ± 8 ppm; Nb = 29 ± 1 ppm; La 44 ± 1 ppm). Greater enrichment of LREE relative to the HREE (La/Yb = 25 ± 1) is apparent in these glasses. The phonolitic-trachytic shards show more elevated concentrations of V, Sr, Ba and Eu (V = 64 ± 4 ; Sr = 530-638ppm; Ba = 667-845ppm; Eu/Eu*_N = 1.06 ± 0.09) than the higher silica shards (Fig. 5.7a). Consequently V, Ba, Sr (Fig. 5.8) and Eu behave compatibly with increasing fractionation, whilst the remaining trace elements behave incompatibly (Fig. 5.8). Incompatible trace element ratios in this end member glasses are internally consistent, but are more elevated than those in the most silica rich glasses shown in Table 5.2 (Nb/Th = 2.1 ± 0.1).

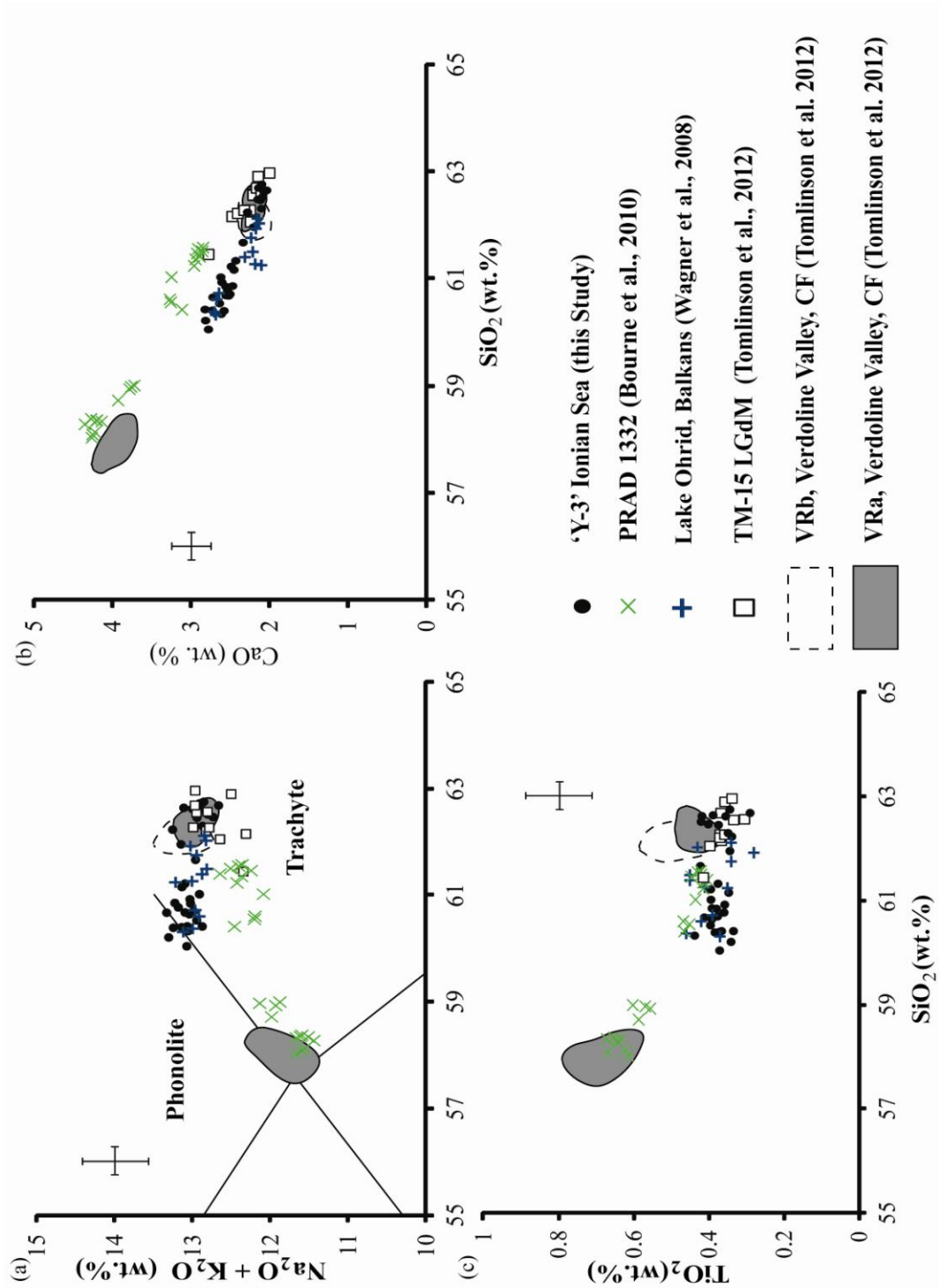


Figure 5.6: Major element bi-plots displaying major element concentrations of the ‘Y-3’ tephra layer M25/4-12_118.cm b.s.f compared to the proximal Tufi Biancastri, Campanian deposits recorded in the Verdoline Valley, VRa and VRb units (Tomlinson et al., 2012b) and also other previously interpreted distal equivalents of the ‘Y-3’ tephra; TM-15 (LGdM) (Wulf et al., 2004; 2008; Tomlinson et al., 2010b); PRAD 1332 (Bourne et al., 2011) and a layer from Lake Ohrid, in the Balkans (Wagner et al. 2008). (TAS classification; after Le Bas et al., 1986). Errors given are 2 x standard deviation of repeated analyses of the StHs6/80G secondary standard.

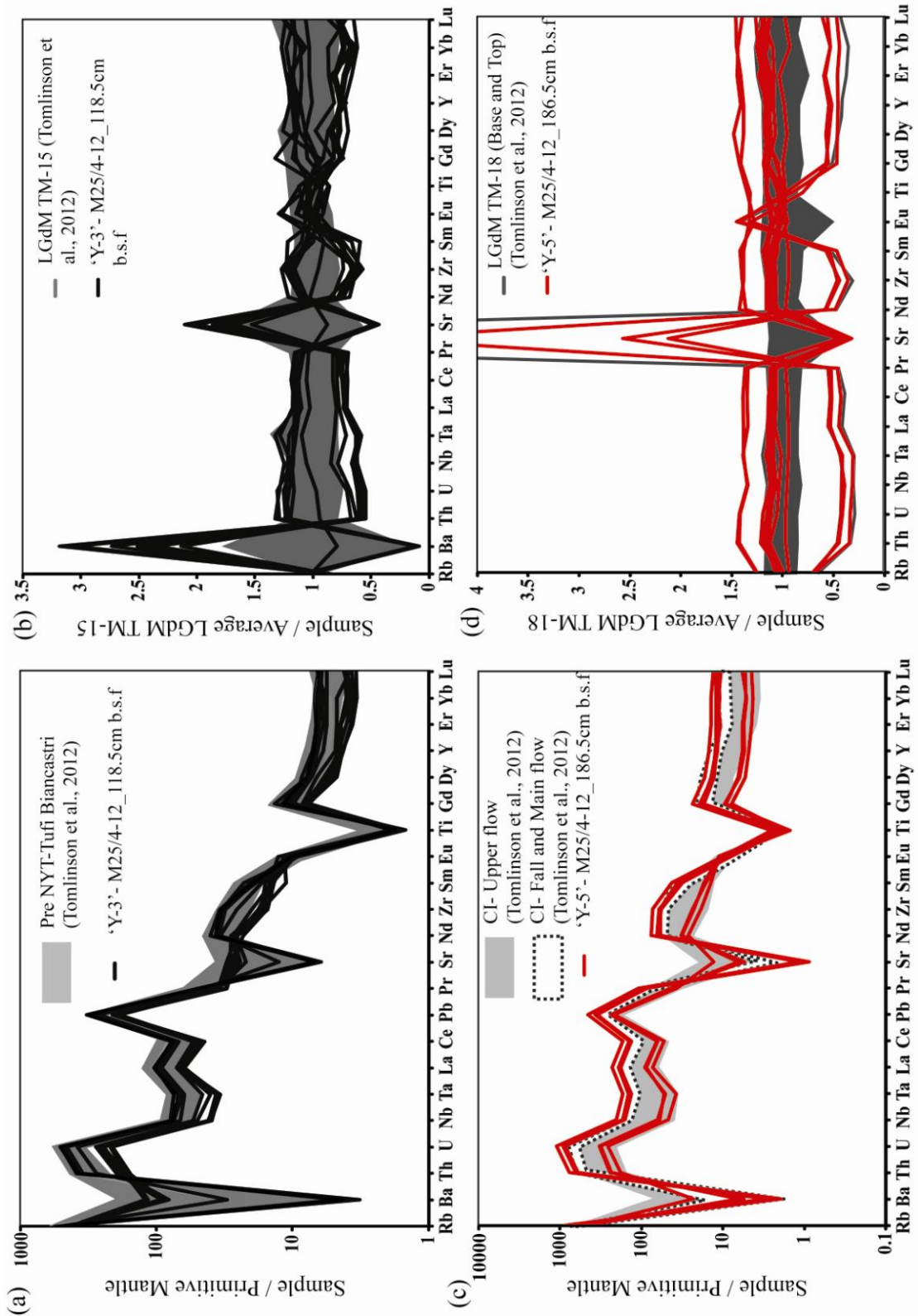


Figure 5.7: (a) Y-3 Ionian Sea glasses and Tufi Biancastri proximal glasses normalised to primitive mantle (Sun and McDonough, 1989); (b) Y-3 glasses normalised to LGdM TM-15 glasses; (c) Y-5 Ionian Sea glasses and CI glasses normalised to primitive mantle; (d) Y-5 Ionian Sea glasses normalised to LGdM TM-18 glass compositions.

M25/4-12_186.5 cm b.s.f. 'Y-5'

Shards in this tephra layer predominantly display a Phonolitic composition, lying upon the phonolite-trachyte boundary, whilst a small population of trachytic shards are observed (Fig. 5.9). The phonolites demonstrate a very homogeneous population ($n=42$), with 61.2 ± 0.3 wt. % SiO_2 ; 1.7 ± 0.1 wt. % CaO ; 2.9 ± 0.1 wt. % FeO . The smaller population ($n=5$) of trachytic shards have slightly elevated SiO_2 displaying higher concentrations of CaO , MgO , K_2O and lower Na_2O (Fig. 5.9).

The main phonolitic population are highly evolved, displaying significant overall trace element enrichment ($n=21$; $\text{Zr/Sr} = 33 \pm 2.9$) (Fig. 5.7a) and are largely homogeneous ($\text{Rb} = 461 \pm 34$ ppm; $\text{Th} = 54 \pm 4$ ppm; $\text{Nb} = 122 \pm 9$ ppm; $\text{La} = 130 \pm 9$ ppm). These glasses show low concentrations of Ba , Sr , Eu ($\text{Ba} = 16 \pm 4$ ppm; $\text{Sr} = 20 \pm 3$ ppm; $\text{Eu} = 1.4 \pm 0.1$ ppm) relative to the enrichment seen in other trace elements (Fig. 5.6). Incompatible trace element ratios are particularly tight in the phonolites (Table 5.2) ($\text{Th/Nb} = 2.3 \pm 0.05$).

The trachytic shard population ($n=3$) is characterised by low to moderate levels of evolution ($\text{Zr/Sr} = 1.6 \pm 0.8$) (Fig. 5.7c), with less elevated concentrations of incompatible trace elements ($\text{Rb} = 302 \pm 4$ ppm; $\text{Th} = 6 \pm 0.8$ ppm; $\text{Zr} = 242 \pm 33$ ppm; $\text{Nb} = 40 \pm 6$ ppm; $\text{La} = 57 \pm 6$ ppm). The trachytic glasses display more elevated Ba , Sr , Eu concentrations than phonolites. Strontium, Ba and Eu behave compatibly within this minority shard population (Fig 5.10). The phonolitic shards comprise of consistently lower concentrations (typically $\text{Sr} < 30$ ppm; $\text{Ba} < 30$ ppm; $\text{Eu} < 1.7$ ppm) regardless of increasing fractionation shown (Fig. 5.10). Trace element ratios in the trachytic glasses are constant (Table 5.2; $\text{Nb/Th} = 2.2 \pm 0.04$) and are slightly lower than those in the phonolites.

5.5 Discussion - Tephra correlations

5.5.1 M25/4-12_28cm & M25/4-12_44cm b.s.f

Both tephra layers display an almost indistinguishable HKCA rhyolitic glass chemistry ($D^2 = 0.4$), consequently the two tephtras will be discussed together in the context of potential provenance. Their major element rhyolitic composition with high K_2O and subsequently high total alkalis (Fig.5.4) suggests a provenance from Lipari, Aeolian Islands. Other Mediterranean rhyolitic magma producing volcanic systems (Pantelleria,

Santorini, Salina), can be excluded on the basis of lower K₂O and noticeably more elevated MgO, CaO, TiO₂, FeO (Fig. 5.4). Both tephra layers display an island arc signature (i.e. Nb, Ta, Ti depletions) comparable with that of the Lipari rhyolites (Fig. 5.5a). The chemistry of both rhyolitic tephtras is strongly influenced by the fractionation of K-feldspar, evident in the loss of Ba, Sr and Eu typical of Lipari rhyolites.

Although the trace element concentrations observed in both the distal tephra layers are very similar (Fig 5.5a,b), they do show subtle variations. Most noticeably the lower most rhyolitic tephra layer (44cm b.s.f) displays lower concentrations of La, Ce than the upper rhyolitic layer (Fig. 5.5b). Where $D^2 = 7.01$ between the trace element compositions of the two distal tephtras, it is not possible to statistically distinguish them at a 95% confidence interval ($D^2_{\text{calculated}} = < 18.307$). However the D^2 value is not particularly low confirming some differences exist between the two tephtras.

Eruption of homogeneous rhyolites is typical of Lipari, with the last four eruptive cycles (< 42 ka) showing very little compositional variation, typically restricted to Sr, Ba, Zr, La, Ce and Th (Chapter 3). Therefore stratigraphic controls are vital for unravelling distal equivalents of Lipari rhyolites and attributing age.

Since the upper rhyolitic tephra (28cm b.s.f), is stratigraphically located within sapropel 1, (Early Holocene), we consider the early Holocene eruption of Gabelotto-Fiume bianco (GFB) on Lipari. Proximal deposits on the Lipari display limited fall deposits. Instead they are dominated by thick surge beds (Chapter 3) which are thickest in Vallone del Gabelotto and comprise of white pumices that flow from west to east. Contemporaneous tephra are reported in the volcanic stratigraphies of the nearby Vulcano (Lucchi et al., 2008), Panarea (Lucchi et al., 2007) and Stromboli (Di Roberto 2012 *pers comm.*). This tephra is associated with widespread dispersal in the central Mediterranean with contemporaneous rhyolitic tephtras reported in marine archives from; (a) Tyrrhenian Sea, E-1 (Paterne et al., 1988; Di Roberto et al., 2008); (b) Adriatic Sea (Siani et al., 2004) and more recently (c) the Ionian Sea (Zanchetta et al.2011; Caron et al. in prep). Importantly in both the Adriatic and Ionian Sea archives the occurrence of the tephra is within Sapropel 1 (Siani et al., 2004; Zanchetta et al., 2011; Caron et al., 2012).

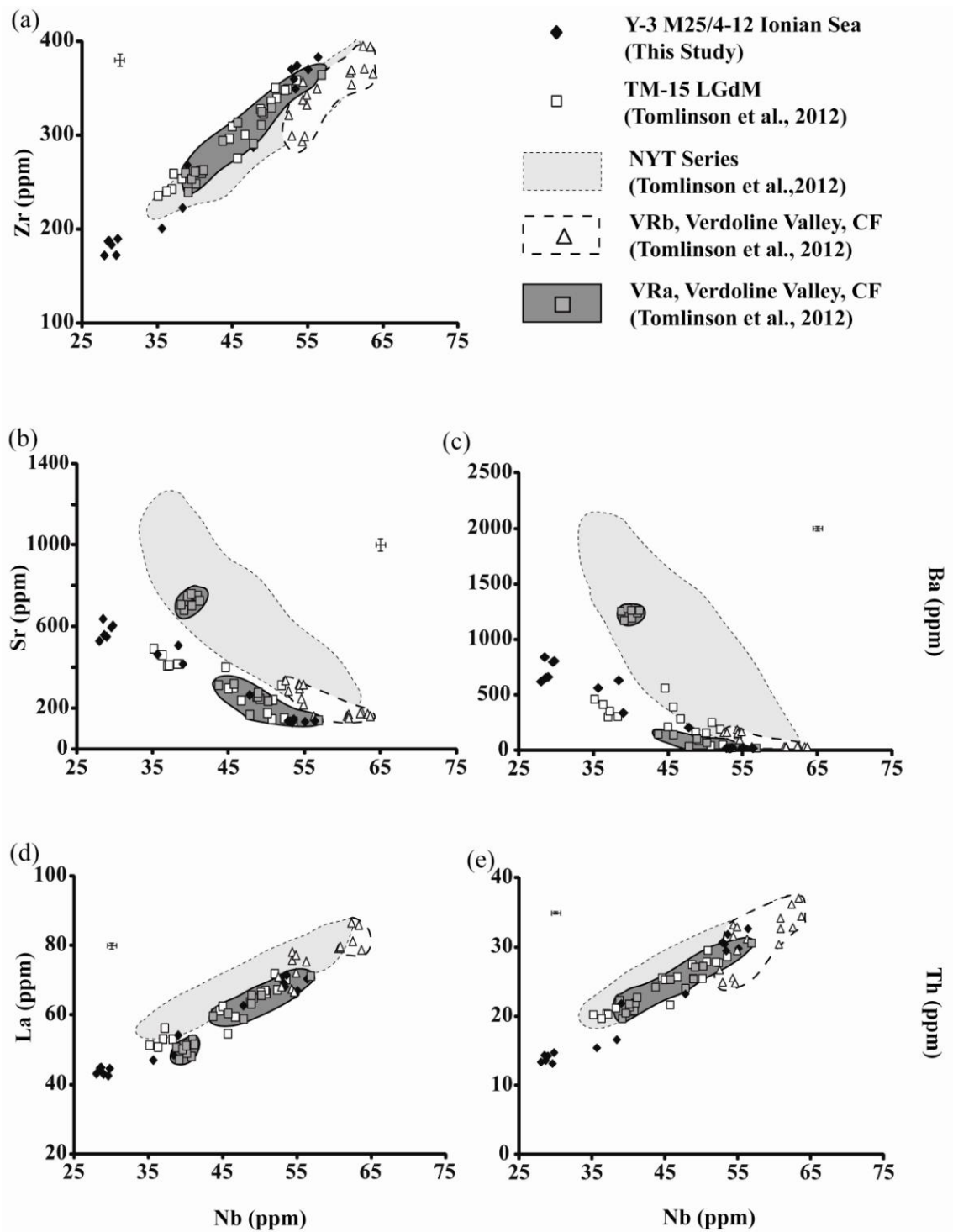


Figure 5.8: Trace element bi-plots displaying the concentrations within the ‘Y-3’ tephra layer M25/4-12_118.5 cm b.s.f compared to the proximal Tufi Biancastri Campanian deposits recorded in the Verdoline Valley, VRa and VRb units (Tomlinson et al., 2012b), whilst also the NYT series data (Tomlinson et al. 2012b) and also the previously interpreted distal equivalent of the ‘Y-3’ tephra; LGdM TM-15 reported in Lago di Monticchio (Wulf et al., 2004; 2008; Tomlinson et al., 2010b). Errors given are 2 x standard deviation of repeat analyses of the StHs6/80G secondary standard.

| Sample | M25/4-12_118.5- Y-3 | | VRa | | VRb | TM-15 |
|---------------------------|----------------------------|-----------------|---------------------------|---------------------------|------------------------|-----------------------------|
| Locality | Ionian Sea (This Study) | | Verdoline Valley | | Verdoline Valley | LGdM |
| TAS classification | Phonolite-trachyte | Trachyte | Phonolite-trachyte | Trachyte | Trachyte | Trachyte |
| | (This Study) | | Tomlinson et al. (2012b) | | | |
| FeO/CaO | 1.3 ± 0.1 | 1.3 ± 0.1 | 1.3 ± 0.1 | 1.3 ± 1 | 1.2 ± 1 | 1.3 ± 1 |
| Nb/Th | 2.1 ± 0.1 | 1.8 ± 0.1 | 1.9 ± 0.1 | 1.9 ± 0.1 | 1.9 ± 0.3 | 1.8 ± 0.1 |
| Zr/Th | 13.1 ± 0.4 | 12.0 ± 0.3 | 12.0 ± 0.4 | 12.2 ± 0.3 | 11.2 ± 1.1 | 12.2 ± 0.5 |
| Ta/Th | 0.10 ± 0.01 | 0.09 ± 0.01 | 0.09 ± 0.003 | 0.09 ± 0.01 | 0.09 ± 0.01 | 0.09 ± 0.01 |
| Nb/Zr | 0.16 ± 0.01 | 0.15 ± 0.01 | 0.16 ± 0.004 | 0.15 ± 0.01 | 0.17 ± 0.01 | 0.15 ± 0.01 |
| Y/Th | 1.43 ± 0.04 | 1.03 ± 0.1 | 1.15 ± 0.04 | 1.06 ± 0.1 | 1.01 ± 0.1 | 1.09 ± 0.1 |
| Sample | M25/4-12_186.5- Y-5 | | C.I. (Fall) | C.I (Main flows) | C.I. Upper Flow | TM-18 (Base and Top) |
| Locality | Ionian Sea (This Study) | | Voscone & Aquafidia | Mondragone | Mondragone | LGdM |
| TAS classification | Phonolite | Trachyte | Phonolite-Trachyte | Phonolite-Trachyte | Trachyte | Phonolite-Trachyte |
| | (This Study) | | Tomlinson et al., (2012b) | | | |
| FeO/CaO | 1.7 ± 0.1 | 1.3 ± 0.1 | 1.6 ± 0.2 | 1.8 ± 0.1 | 1.3-2.2 | 1.7 ± 0.1 |
| Nb/Th | 2.2 ± 0.1 | 2.2 ± 0.04 | 2.4 ± 0.1 | 2.4 ± 0.2 | 2.1-2.5 | 2.4 ± 0.1 |
| Zr/Th | 12.5 ± 0.2 | 13.0 ± 0.3 | 13.4 ± 0.6 | 12.7 ± 0.6 | 11.8-13.4 | 12.9 ± 0.4 |
| Ta/Th | 0.11 ± 0.003 | 0.10 ± 0.004 | 0.11 ± 0.004 | 0.11 ± 0.01 | 0.16-0.19 | 0.11 ± 0.01 |
| Nb/Zr | 0.18 ± 0.002 | 0.17 ± 0.002 | 0.18 ± 0.01 | 0.19 ± 0.01 | 0.10-1.13 | 0.19 ± 0.01 |
| Y/Th | 1.04 ± 0.03 | 1.31 ± 0.1 | 1.04 ± 0.1 | 1.06 ± 0.06 | 1.0-1.5 | 1.08 ± 0.1 |

Table 5.2: Y-3 and Y-5 elemental ratios allowing comparison to proximal Tufi Biancastri and Campanian Ignimbrite deposits (Tomlinson et al., 2012b). Also shown are corresponding Lago Grande di Monticchio (LGdM) tephra layers.

Whilst major and trace element data confirm the similarity of both the Ionian Sea distal tephra to the Gabelotto-Fiume bianco rhyolitic eruption (Fig. 5.4, 5a, b), the younger rhyolitic tephra (28cm) correlates better with the GFB proximal deposits (Fig. 5.5b), particularly in the LREE concentrations (La & Ce). This is reflected statistically by the lower statistical distance values ($D^2 = 1.68$), compared to the older 44cm b.s.f tephra ($D^2 = 3.79$).

Based on geochemical evidence and crucially its stratigraphic position in sapropel 1, this rhyolitic tephra can be confidently assigned to the GFB proximal deposits and the E-1 marine tephra. Zanchetta et al., (2011) suggest the best age for the E-1 tephra is 7770 ± 70 yrs BP (8730–8400 cal yrs BP); based on corrected ^{14}C ages from the Adriatic (Siani et al., 2001, 2004). This distal age is in reasonable accordance with the most recent proximal age of $7,170 \pm 720$ yrs B.P derived for the GFB based on fission track dating (Bigazzi et al., 2003). Therefore an age of 8730-8400 yrs B.P cal is assigned to the 28 cm b.s.f tephra in M25/4-12.

The identification of the GFB within this Ionian Sea marine core stratigraphy has important implications. The tephra provides an additional well constrained age for M25/4-12. It provides further evidence that this eruption was a widely dispersed tephra marker within the central Mediterranean. Given its stratigraphic position relative to Sapropel 1 it is important for the synchronisation of palaeoenvironmental records from the Tyrrhenian, Adriatic and Ionian Seas. This is particularly important as in the higher resolution archives (MD 909 17; Adriatic) GFB/E-1, occurs at the onset of Sapropel interruption between S1a and S1b. This interruption is tentatively associated with the 8.2 ka cooling event (Zanchetta et al., 2011) and thus offers new potential to constrain the timing of this environmental event in this Ionian Sea core.

Proximal stratigraphies on Lipari indicate a period of quiescence between the major explosive HKCA eruptions of Monte Guardia 27.3 ± 0.8 ka BP cal (22.6 ± 0.3 ka BP un-calibrated; Morche, 1988) and the GFB. Given the depth of the lower HKCA rhyolitic tephra (44cm b.s.f) and the age of Monte Guardia activity, it would require a dramatic change in sedimentation rate, not supported by the depth and age associated with the Y-5 tephra (discussed below).

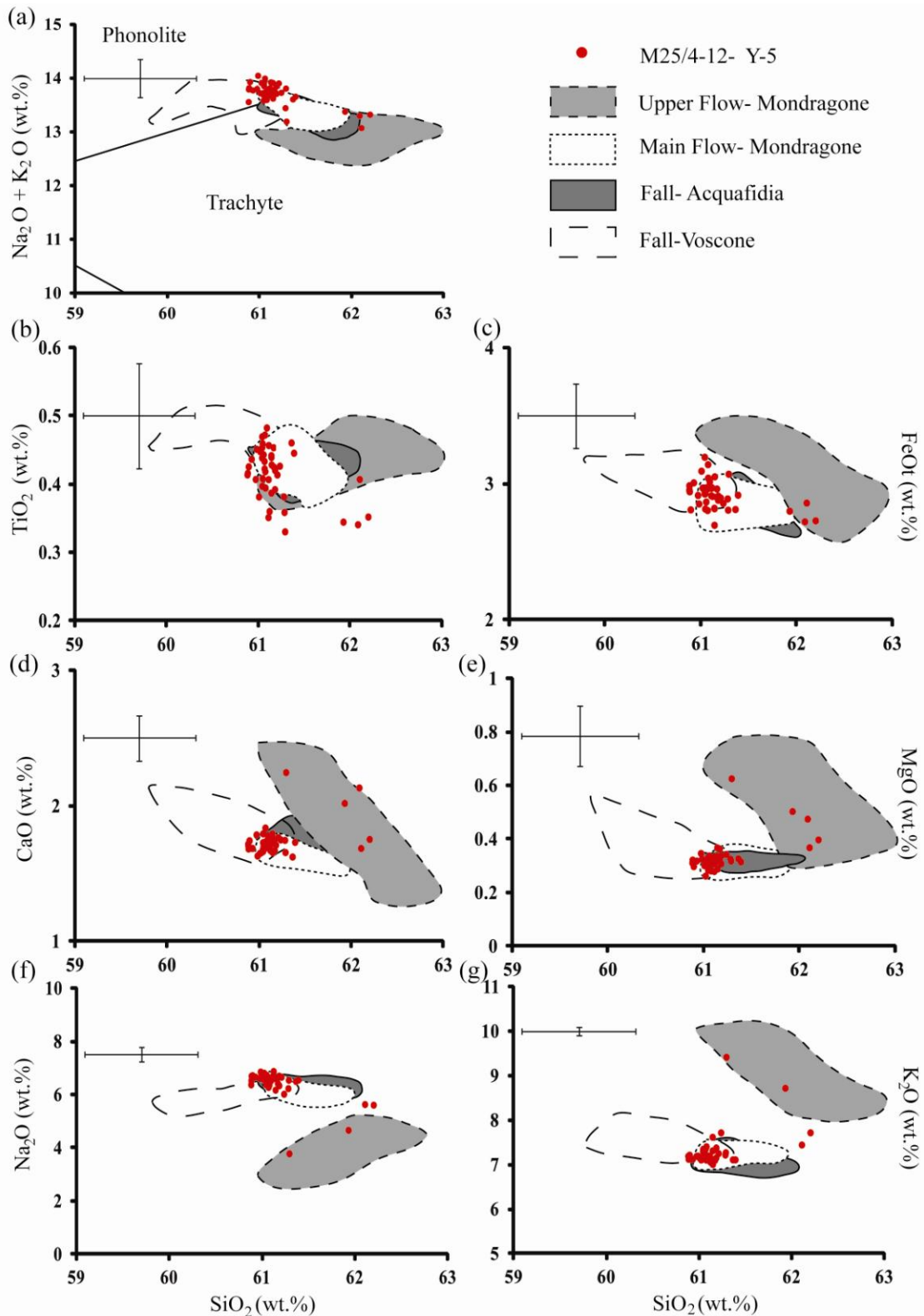


Figure 5.9: Major and minor element bi-plots displaying the concentrations of the ‘Y-5’ tephra layer M25/4-12_186.5cm b.s.f. compared to the proximal deposits of the Campanian Ignimbrite; including First Plinian deposits recorded at Aquifidia. (TAS classification; after Le Bas et al., 1986). Errors given are 2 x standard deviation of repeat analyses of the StHs6/80G secondary standard.

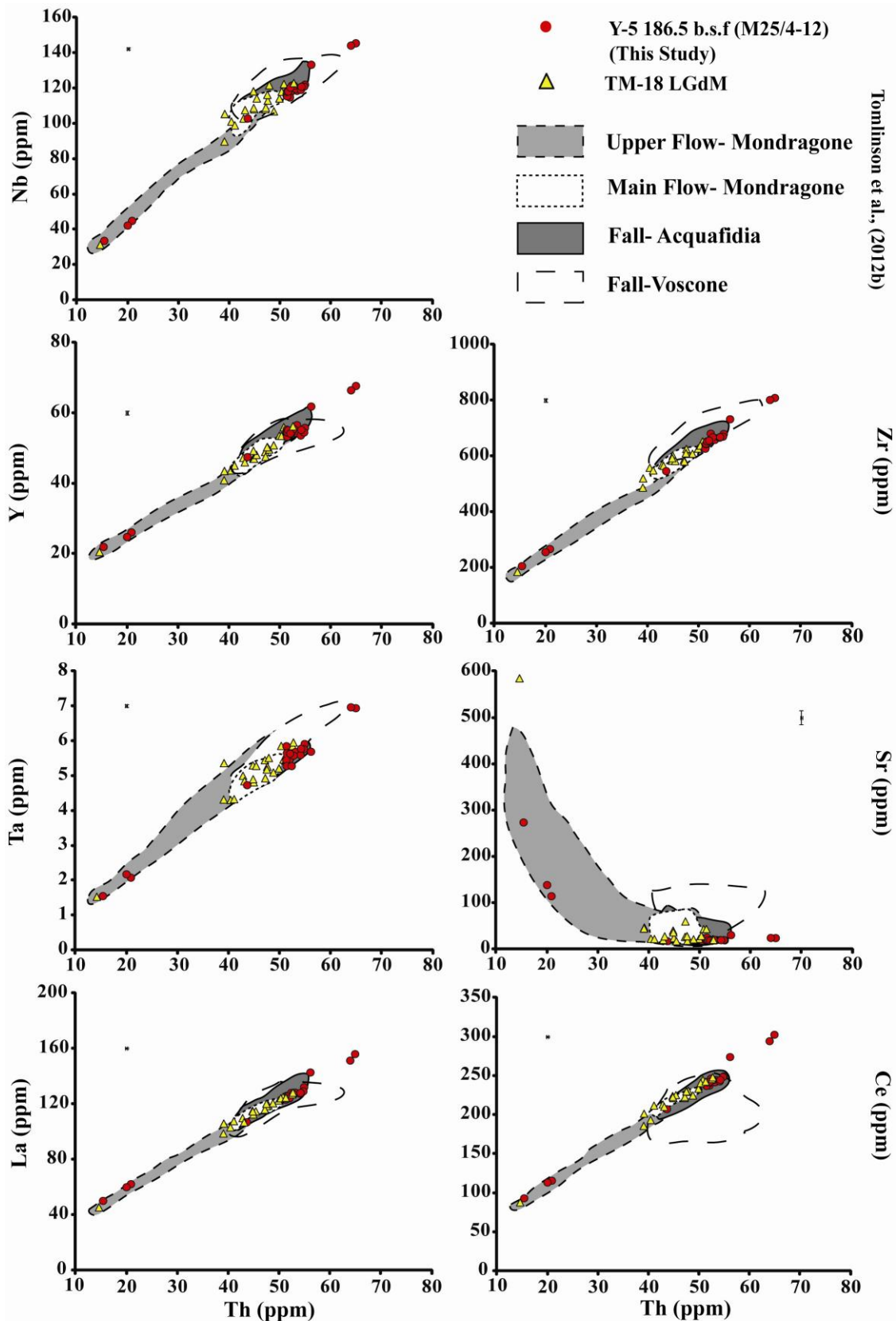


Figure 5.10: Trace element bi-plots displaying concentrations of the ‘Y-5’ tephra layer M25/4-12_184cm b.s.f. compared to the proximal deposits of the Campanian Ignimbrite (Tomlinson et al., 2012b). Errors given are 2 x standard deviation of repeat analyses of the StHs6/80G secondary standard.

Furthermore, as discussed in chapter 3, Monte Guardia rhyolites can be separated from the younger Gabellotto-Fiume bianco glasses on the basis of subtle trace element variations (i.e., lower Th, Zr, La, Ce concentrations). Based on the depth of the Y-1 (Biancavilla) in neighbouring Ionian Sea cores (M25/4-13 and M25/4-11) and the depth of this tephra in M25/4-12 (44cm b.s.f) it would indicate that the layer represents an eruption younger than Y-1 (ca.16-18 ka; Chapter 7). According to the $\delta^{18}\text{O}$ (*G.ruber*) curve of M25/4-12 (Negri et al., 1999) this tephra at 44cm b.s.f lies in the transition to lower $\delta^{18}\text{O}$ values indicative of climatic warming in the early Holocene, thus it is likely to present the distal evidence of an explosive HKCA rhyolitic eruption from the Aeolian Islands in the Late-glacial period.

Interestingly, a tephra from the Marsili basin, Tyrrhenian Sea was previously attributed to the Gabellotto-Fiume Bianco (Di Roberto et al., 2008) (Chapter 4). This tephra layer was shown to be of mixed provenance, containing HKCA rhyolites (Di Roberto et al., 2008) and the smaller size fraction phonolites. Albert et al., (2012) correlate these phonolites to the Soccavo 1 eruption, Campi Flegrei (ca. 12 ka). Since the age of this eruption is older than the previously reported Gabellotto-Fiume bianco occurrences it is proposed that the mixed tephra layer in the Marsili basin (TIR2000-IV-93cm b.s.f) is equivalent to the older tephra recorded in the M25/4-12 (44cm b.s.f). It should be noted that the Marsili basin core does not provide the same stratigraphic control as the Ionian Sea core due to the absence of sapropel formation. Furthermore this older rhyolitic tephra recorded in the Ionian Sea sediments may relate to the HKCA rhyolite ash recorded in Lake Ioannina (NW Greece) at 15.2 m, provisionally dated at 13.5 cal ka BP (T. Jones 2012; pers comm.) (Chapter 3).

Evidence of an older (44cm b.s.f) HKCA rhyolitic eruption largely compositionally indistinguishable from the Gabellotto-Fiume Bianco/E-1(28cm b.s.f) in sediments beneath the Sapropel 1 emphasises the importance of stratigraphic control when assigning provenance to HKCA rhyolites from Lipari and importing or exporting age. It also raises issues regarding the precise proximal origin of this older distal rhyolitic tephra. No major explosive eruptions have been reported on Lipari between the GFB and the Monte Guardia explosive eruption. However, more recently Lucchi et al., (2010) have recognised HKCA rhyolitic pumiceous fallout units, pyroclastic breccias and additionally tuff layers (surge beds) in the lower part of the Vallone Caneto Dentro formation, Lipari. This unit outcrops just to the south of the Vallone de Gabellotto and

predates the Gabellotto-Fiume bianco formation (Lucchi et al. 2010). However, it is not regarded as more than a small localised explosive eruption (De Rosa pers comm.). One could argue the presence of a distal marker indicative of explosive volcanism almost 300 km from source prior to the Gabellotto-Fiume bianco activity, might suggest that the full extent of explosive activity in this north-eastern sector of Lipari may not have been fully recognised proximally. This is likely to be exacerbated by (a) resurgent dome formation concealing earlier deposits (i.e. Gabellotto and Pilato eruptive centres); (b) collapse of proximal deposits into the Tyrrhenian Sea; (c) erosion of limited on-land proximal deposits. A final consideration regarding a proximal source on Lipari is that the Gabellotto-Fiume bianco episode was not a single eruptive pulse. Recent studies suggest that some explosive eruptions occurring on the Aeolian Islands are punctuated by periods of quiescence, including the Upper Pollara, Salina and Monte Pilato, Lipari (Sulpizio et al., 2008; Davi et al., 2010). However there is no significant evidence of a hiatus in the deposition of the proximal deposits of Gabellotto-Fiume bianco reported in Chapter 3.

Finally, an alternative less likely scenario is that the Ionian sea tephra M25/4-12_44cm b.s.f derives from another volcanic source within the Aeolian Islands, a source that produced HKCA rhyolites with an near identical to those produced by Lipari. The Lentia domes, Vulcano, are probably the best equivalent as they are considered part of the same volcanic complex as Lipari (Gioncada et al., 2005) The Lentia collapse, Vulcano occurred between 13-15 ka (Soligo et al., 2000). However, compositions reported by Gioncada et al., (2005) indicate slightly less differentiated compositions than observed in the pumices of Lipari rhyolites. Pumices display ca. 73 wt. % SiO₂ and crucially have only limited evidence of K-feldspars micro-crysts (Gioncada et al., 2005) indicating that trace element compositions of the glass would not be as significantly depleted in Ba, Sr and Eu concentrations as the distal tephra M25/4-12_44cm b.s.f. However without a detail glass study of these proximal deposits it is difficult to fully assess a potential correlation of this tephra to the Lentia dome collapse.

A precise provenance solution for the older rhyolitic eruption (44cm b.s.f) consequently remains unresolved. It does however provide evidence for a previously unreported explosive eruption originating from Lipari in the late-glacial period that must post date the Monte Guardia eruption and pre-date the Gabellotto-Fiume bianco eruption.

The presence of at least two eruptions originating from the Aeolian Islands in the upper 1.8 m of the Ionian Sea core (M25/4-12), demonstrates that the sub-Plinian eruptions typical of an arc magmatic setting are of significant magnitude to disperse tephras up to 300 km. Thus these tephras can provide important chronostratigraphic markers in marine archives beyond the Tyrrhenian Sea. The dominantly westerly winds across the central Mediterranean would disperse tephras to the east from the Aeolian Islands towards the Ionian Sea as indicated by previous investigations of Ionian Sea sediments (Keller et al., 1978; Clift and Blusztajn, 1999; Caron et al., 2012).

The identification of these two cryptotephra layers also highlights the potential for further investigations of the remaining marine sediments of M25/4-12 to determine a more robust eruptive history of explosive Aeolian Island volcanism. Proximal records becomes more complicated with age due to burial of older deposits by more recent activities, whilst the Tyrrhenian sea records are complicated by reworking and turbidity currents due to proximity to active volcanism.

5.5.2 M25/4-12_118.5 b.s.f ‘Y-3’

Major element data presented here re-affirms the previous identification that the Y-3 tephra is phono-trachytic to trachytic in composition deriving from Campi Flegrei (Keller et al. 1978). Shards display $K_2O \gg Na_2O$ which is characteristic of Campi Flegrei. Niobium and Th concentrations ratios in the most evolved glasses confirm that the Y-3 tephra is associated with the NYT/Pre-NYT series of erupted deposits from the Campi Flegrei caldera (Fig. 5.11). These values being typically lower than observed in the older Campanian Ignimbrite series (39 ka). V concentrations (Table 5.1) are relatively high indicative of the NYT/Pre NYT series compositions (Tomlinson et al., 2012b) within the Tufi Biancastri deposits. Mantle normalised diagram (Figure 5.7a) illustrates that the most evolved Y-3 glasses overlap with the Pre-NYT glasses, whilst the least enriched glasses (phono-trachytes) are less enriched than anything characterised by Tomlinson et al., (2012b). Other HSE to Th ratios observed in the Y-3 glasses are slightly more elevated than those observed in Pre-NYT proximal deposits (Tomlinson et al., 2012b), but values remain typically lower than the Campanian ignimbrite series, particularly in the most silica-rich glasses (Table 5.2).

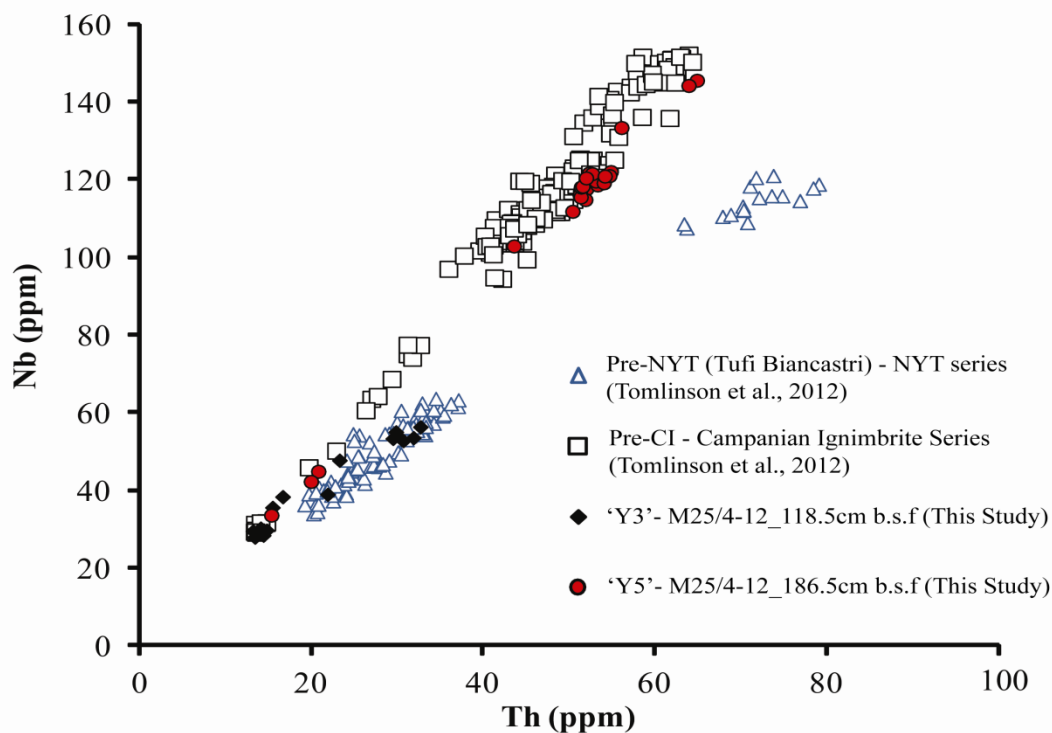


Figure 5.11: Th vs. Nb diagram showing the M25/4-12_118.5cm b.s.f – Y-3 and M25/4-12_186.5cm b.s.f- Y-5 shards concentrations from the Ionian Sea core tephra layers, the plot clearly defines the origin of the two Campanian tephras from the separate magmatic series. The evolved Y-3 shards clearly associated with the younger Pre-NYT (Tufi Biancastri) - NYT magmas, whilst the Y-5 clearly lies within the Pre CI and Campanian Ignimbrite series.

We can assess the precise proximal source of the Y-3 tephra in the context of proximal Tufi Biancastri deposits given; (a) the stratigraphic position of this tephra layer above the Y-5/Campanian Ignimbrite (discussed below), (b) its interpolated age (25.3 ± 0.3 ka yrs BP) (Kraml, 1997) and (c) a greater affinity of its trachytic glasses to the NYT/Pre NYT chemistries. Tufi Biancastri represents the products of numerous eruptions recognised by Orsi et al., (1996) that pre-date the NYT eruption (ca. 14 ka) and post date the Campanian Ignimbrite (ca. 39 ka).

The Y-3 is considered a precise stratigraphic marker across the central Mediterranean, however its proximal counterpart and consequently age are not clearly defined (Zanchetta et al., 2008). Consequently exporting proximal ages to distal archives is complicated. Sulpizio et al., (2003) and Di Vito et al., (2008) suggest that the white pumiceous SMP1-e eruptive unit ($30,670 \pm 230$ yrs B.P cal) recorded on the Sorrentina peninsular is a medial-distal equivalent of the distal Y-3 tephra layer. Di Vito et al., (2008) correlated SMP1-e to the proximal Campi Flegrei intra-caldera deposits, unit

VRa, located in the Verdoline Valley (Orsi et al., 1996). The VRa unit is $^{40}\text{Ar}/^{39}\text{Ar}$ dated to $30,000 \pm 200$ yrs B.P. (Pappalardo et al., 1999). The sequence comprises of basal, rounded white pumice lapilli beds associated with surges, capped by clast supported angular pumice lapilli fall bed comprised on both white and grey pumices (Orsi et al., 1996).

The evidence used to support the correlation of VRa/SMP1-e proximal deposits to the distal Y-3 tephras included the following similarities; (1) stratigraphic position (stratigraphically closer to the CI than the NYT); (2) chemistry; white/clear K-trachytic pumiceous glasses; (3) mineral assemblage (sanidine, biotite) and; (4) proximal ages derived largely correspond to the distal Y-3 ages (Sulpizio et al., 2003; Zanchetta et al., 2008).

The correlation of unknown trachytic tephras to the Y-3 and adopting associated ages is equally problematic for the following reasons; (1) proximally the Tufi Biancastri stratigraphy is made up of numerous eruptions post CI (Orsi et al., 1996); (2) the trachytic glass components of these Tufi Biancastri deposits are at both a major and trace element level are indistinguishable (i.e. VRa, VRb, PRa) shown in Table 5.3; the consequence of (3) very similar mineral assemblages (typically k-feldspar, clinopyroxene, plagioclase and biotite); (4) given the errors associated with distally derived tephras it is possible that numerous eruptions are potentially masked within this boarder time period. Presented here is the first full major, minor and trace element characterisation of the Y-3 from the type site in the Ionian Sea. These geochemical data are used to validate proximal-distal correlations;

5.5.2.1 Proximal Tufi Biancastri and distal Y-3 Ionian Sea correlation

Both the proximal VRa (Fig. 5.6) deposits (Tomlinson et al., 2012b) and the distal Ionian Sea Y-3 tephra (Fig. 5.6) display compositional bi-modality, with both phonotrachytic and trachytic components. Consequently when considering them as correlatives, using statistical distance test (Perkins, 1995), both end-members are considered independently (Table 5.3). At a major element level it becomes apparent that the most fractionated, trachytic end-members of the distal Ionian Sea Y-3 shards (M25/4-12) are geochemically indistinguishable from the evolved trachytic component of the bimodal VRa ($D^2 = 1.69$) (Fig. 5.6). However as identified by Tomlinson et al., (2012b) these temporally distinct, Tufi Biancastri trachytic eruptions are not easily

distinguished. As a result the VRa trachytes are also indistinguishable from the stratigraphically younger VRb ($D^2 = 3.64$) and PRa ($D^2 = 1.19$) eruptions (Table 5.3), highlighting the issues of repeat magma compositions through time within individual volcanic systems. Trace element concentrations in the most fractionated, trachytic, distal Y-3 Ionian Sea glasses correspond to the trachytes of the VRa ($D^2 = 2.99$) (Fig. 5.8), re-affirming major element observations (Fig. 5.8). Although again the trachytic distal Y-3 glasses are also indistinguishable from the younger VRb eruption ($D^2 = 1.79$).

The phono-trachytic component of the bimodal VRa proximal tephra and distal Y-3 Ionian Sea tephra layer differ on major element concentrations. Y-3 phono-trachytes display higher SiO_2 , K_2O ; lower TiO_2 , FeO_t , CaO , MgO , Na_2O than the phono-trachytic component of the VRa (Fig. 5.6). At a 99.5 % confidence limit the phono-trachytic shards of VRa are statistically different to the phono-trachytic shards of the distal Y-3 (Table 5.3; $D^2 = 99.06$). However on the basis of major element concentrations one might suggest that the least evolved phono-trachytic component of the Y-3 represents a missing proximal component of the VRa and that they lie upon an evolutionary trend between the bi-modal VRa end-members as argued by Di Vito et al. (2008).

Trace element bi-plots (Fig. 5.8) reveal that a correlation between the Y-3 Ionian Sea tephra and the proposed proximal counterpart is not possible. The trace element variability of the VRa deposits between the two end-members is more restricted than that of the distal Y-3 (Fig. 5.8). Crucially the lower silica, phono-trachytic glasses observed in the VRa unit, display greater incompatible trace element enrichment than the higher silica phono-trachytic component of Y-3 tephra layer (Fig. 5.8).

| Sample | | TM-15 (Tra) | Y-3 (M25/4-12) (Pho/Tra) | Y-3 (M25/4-12) (Tra) | PRa (Tra) | VRb (Tra) | VRa (Pho/Tra) | VRa (Tra) |
|--|---------------|----------------|-----------------------------|-------------------------|--------------|--------------|------------------|--------------|
| Distal | TM-15 | 0.00 | 38.05 | 3.39 | 0.92 | 7.55 | 145.20 | 1.57 |
| | Y-3 (Pho/Tra) | 17.80 | 0.00 | 156.85 | 143.48 | 119.78 | 106.65 | 138.23 |
| | Y-3 (Tra) | 3.74 | 51.55 | 0.00 | 7.54 | 1.79 | 670.24 | 2.99 |
| Tufi Biancastrì Stratigraphic order | Pra | 4.65 | 42.09 | 2.64 | 0.00 | 1.31 | 881.53 | 1.76 |
| | VRb (Tra) | 7.55 | 49.25 | 7.22 | 1.15 | 0.00 | 515.44 | 0.49 |
| | VRa (Pho/Tra) | 143.16 | 99.06 | 375.01 | 301.36 | 378.09 | 0.00 | 695.01 |
| | VRa (Tra) | 2.24 | 34.95 | 1.69 | 1.19 | 3.64 | 284.56 | 0.00 |

(a)

| p (confidence limit) | D^2 critical, $f=8$ | |
|------------------------|------------------------|--|
| 0.995 | 1.344 | < 0.5 % probability that the two samples are compositionally different if D^2 is less than 1.344 |
| 0.990 | 1.646 | < 1% probability that the two samples are compositionally different if D^2 is less than 1.646 |
| 0.950 | 2.733 | < 5% probability that the two samples are compositionally different if D^2 is less than 2.733 |
| 0.050 | 15.507 | > 95% probability that the two samples are compositionally different if D^2 is greater than 15.507 |
| 0.010 | 20.090 | > 99% probability that the two samples are compositionally different if D^2 is greater than 20.090 |
| p (confidence limit) | D^2 critical, $f=10$ | |
| 0.995 | 2.156 | < 0.5 % probability that the two samples are compositionally different if D^2 is less than 2.155 |
| 0.990 | 2.558 | < 1% probability that the two samples are compositionally different if D^2 is less than 2.558 |
| 0.950 | 3.940 | < 5% probability that the two samples are compositionally different if D^2 is less than 3.940 |
| 0.050 | 18.307 | > 95% probability that the two samples are compositionally different if D^2 is greater than 18.307 |
| 0.010 | 23.209 | > 99% probability that the two samples are compositionally different if D^2 is greater than 23.209 |

(b)

Table 5.3: (a) Statistical distance values (D^2) matrix based on major, minor and trace element compositions of the Ionian Sea distal Y-3 tephra, in light blue the major and minor element values, whilst in grey the trace element values. Compared to proximal to proximal Tufi-Biancastrì deposits (VRa, VRb and PRa) and the distal tephra TM-15 recorded in LGdM; Tra = Trachytic and Pho/Tra = Phono-trachytic (b) The p (confidence limits) values and the D^2 critical values for the statistical distance, where $f = 8$ (Major and minor elements). and $f=10$ (trace elements).

Problems with this proximal-distal correlation are best illustrated by the Sr and Ba verses Nb diagrams (Fig. 5.8), where the phono-trachytic glasses of VRa display far more elevated Sr and Ba concentrations than the phono-trachytic component of the Y-3 tephra layer. The D^2 value between the two phono-trachytic populations confirm that they are statistically different at a 99.5% confidence limit (Table 5.3; $D^2 = 106.65$). The phono-trachytic glasses from the VRa proximal deposits and the distal Ionian Sea Y-3 tephra are then compositionally distinct. Trace element concentrations observed in the phono-trachytic distal Ionian Sea Y-3 glasses are not consistent with the currently available NYT/Tufi-Biancastri series data (Fig. 5.8; Tomlinson et al., 2012b). This is confirmed by more elevated incompatible trace element ratios in this component of the distal Y-3 (Table 5.2; Nb/Th, Zr/Th, Ta/Th) than the VRa glasses. Instead the VRa glasses despite their bimodality, display constant incompatible element ratios (Table 5.2) between the phono-trachytic and trachytic end-members. These are consistent with the younger VRb deposits (Table 5.2). Instead the phono-trachytic distal Y-3 glasses display concentrations and ratios arguably more akin to those seen in the older Campanian Ignimbrite Upper flow (Table 5.2).

The compositional variability of the VRa distinguishes this unit from the other trachytic Tufi Biancastri eruptions (Sulpizio et al., 2003; De Vito et al., 2008). However, as outlined above the phono-trachytic glass component of the distal Y-3 displays diagnostic characteristics that differ from the proximal VRa phono-trachytic glasses. Consequently the distal Ionian Sea Y-3 tephra (M25/4-12) is not the distal product of the VRa, Tufi Biancastri eruption. The absence of a presently identified proximal stratigraphy displaying a phono-trachytic component matching the Y-3 means that proximal age cannot be exported distally.

5.5.2.2 Distal-distal Y-3 correlations

Major and trace element glass compositions of the distal Y-3 Ionian sea ash layer are now used to assess the integrity of the distal-distal correlations. As outlined previously the Lago Grande di Monticchio (LGdM) TM-15 tephra layer is assigned to the Y-3 (Wulf et al., 2004). At a major element level, the trachytic TM-15 glasses are indistinguishable from the trachytic components of the distal Ionian Sea Y-3 tephra layer ($D^2 = 3.74$) (Fig. 5.6), but also similar to the trachytic proximal Tufi Biancastri

deposits; VRa ($D^2 = 2.24$); VRb ($D^2 = 7.55$). It is this greater similarity to the VRa unit, supported by stratigraphy, lithology and mineralogy that is previously used to support correlation of TM-15 (Di Vito et al. 2008; Zanchetta et al., 2008; Tomlinson et al., 2012b). Trace element concentrations in the trachytic TM-15 glasses re-affirm the similarity to the most evolved, trachytic glasses of the distal Y-3 (Fig. 5.7b) ($D^2 = 3.39$) and again with proximal Tufi Biancastri trachytes, VRa ($D^2 = 1.57$); VRb ($D^2 = 1.69$) (Table 5.3).

Given the diagnostic importance of the least evolved, phono-trachytic end-members, it is unfortunate that TM-15 does not offer such a component (Fig. 5.6, 5.8). Tephra recorded in distal archives being dominated by the most fractionated glasses is common; for instance the Vedde Ash, dispersed across much of Northern Europe, typically only contains the rhyolitic end-member rather than the basaltic component observed at source (Lane et al., 2012). In the case of TM-15, Tomlinson et al., (2012b) argue that the absence of the VRa bimodality does not preclude a proximal-distal correlation, instead suggesting that changes in eruptive dynamics and/or wind direction may mean that only the early most fractionated deposits were recorded distally in LGdM.

Despite the absence of a diagnostic phono-trachytic glass population within the TM-15, trace element concentrations observed reveal the most compelling evidence to support the correlation of TM-15 to the distal Ionian Sea Y-3. The fractionation trend observed within the glasses of TM-15 clearly indicates a relationship with least evolved end-member of the distal Y-3 glasses rather than the VRa proximal deposits (Fig. 5.8). The least enriched TM-15 glasses correspond to the Y-3 glasses that compositionally lie between phono-trachytic and trachytic end-members (Fig. 5.8). Strontium and Ba concentrations in the TM-15 glasses trend with Y-3 glasses rather than towards the more elevated compositions seen in the VRa glasses (Fig. 5.8). Consequently, the evolutionary trends shown in the trace element concentrations of TM-15 validate correlation with the Ionian Sea Y-3 re-affirming the proposed correlation by Wulf et al., (2004). As a result of the trace element comparison of TM-15 to the Ionian Sea Y-3 tephra, it becomes evident that TM-15 is the equivalent of the Y-3, but is not related to the VRa.

Bourne et al., (2010) correlate the PRAD 1332 cm in the Adriatic to the Y-3/TM-15. However, Figure 5.6 illustrates that PRAD 1332 is not a robust correlative for the Y-3 Ionian Sea/ TM-15. PRAD 1332 cm glasses display a bi-modality with a greater similarity to the VRa proximal deposits and the phono-trachytic end-member (Tomlinson et al. 2012b). However the trachytic glasses do not offer a precise match. PRAD 1332 is stratigraphically located near the MIS 2/3 transition and may represent a distal occurrence of the VRa rather than the Y-3. Another proposed distal ‘Y-3’ tephra layer is presented from Lake Ohrid in the Balkans, major element glass data (Fig. 5.6) (Wagner et al. 2008) clearly illustrates that this tephra displays the same range from phono-trachytic to trachytic glass compositions as the Ionian Sea Y-3 layer providing a strong major element correlation.

5.5.2.3 Implications

The rejection of the VRa - Y-3 links does not preclude the proposed correlation between SMP1-e and the Y-3 tephra (Sulpizio et al. 2003); this remains untested at a trace element level. However, it appears that conclusive links can only be determined by establishing which least evolved end-member (phono-trachytic component) is present or if not, which evolutionary trend can be identified within the SMP1-e glasses.

Clearly resurgent activity within the Campi Flegrei caldera complicates proximal-distal links and prevents the determination of a complete eruptive history proximally. Grain-specific trace element characterisation of distal tephra layers with clear stratigraphic superposition may offer an opportunity to unravel the frequency of the different explosive events during the Tufi Biancastri period. Given that they represent different eruptions, the identification and superposition of the VRa and Y-3 tephtras within the same distal stratigraphy would provide clarity. With the Y-3 tephra lying at a critical environmental transition in the oxygen isotope curve, it is imperative that proximal ages are not incorrectly exported to distal localities. It is equally imperative that when synchronising environmental archives across the central Mediterranean, proposed ‘Y-3’ correlatives are validated using the diagnostic compositional features identified within the Y-3 tephra from the type site. Without this validation there is potential for distal equivalents of the chemically and temporally similar Tufi Biancastri eruptions (i.e. VRa and VRb) being incorrectly assigned to the Y-3 tephra. Consequently this might prevent

the accurate synchronisation of palaeoenvironmental records. For instance the PRAD 1332 tephra (Bourne et al. 2010) should not be used to synchronise this Adriatic core with the Ionian Sea core Y-3 (M25/4-12). Where the diagnostic features of the Y-3 are met then distal archives can be robustly synchronised (i.e. LGdM TM-15 - Y-3 (M25/4-12)).

5.5.3 M25/4-12_186.5 b.s.f - ‘Y-5’

Major element glass data presented here in Figure 5.9 unequivocally overlaps the Campanian Ignimbrite (CI) glass data set (Tomlinson et al., 2012b). This re-affirms previous major and minor element correlations of this prominent Ionian Sea tephra marker to the CI eruption (Keller et al., 1978; Kraml 1997).

The homogeneous phonolitic shard population of the Y-5 reported here overlaps the compositions of the early fallout recorded at Aquafidia and fall from Voscone, whilst also the composition of the main ignimbrite flows (Lower and Intermediate) recorded at Mondragone (Fig. 5.9). The smaller population of trachytic shards reported in this Ionian Sea Y-5 layer overlap with the compositions of the Upper flow. This unit is compositionally distinct from the other CI units, characterised by higher CaO, MgO, K₂O and lower FeO_t and Na₂O (Fig. 5.9).

The phonolitic component of the Y-5 Ionian Sea tephra is assessed in relation to the geochemically similar fall and flow deposits. Proximal glass compositions illustrate at a major element level there is very little compositional variability between the Plinian fall and main flow (Co-ignimbrite) components of the CI (Fig. 5.9). The exception is the fall recorded at Voscone that displays slightly more variability ranging to lower silica concentrations (Fig. 5.9). Statistical distance values in Table 5.4 indicate that the Y-5 Ionian sea tephra are particularly similar to the early fall at Aquafidia and the main flows at Mondragone, given a less than 5% probability that they are different. Given the absence of less evolved compositions reported in the Voscone fall, the D^2 values is higher (Table 5.4).

| Locality | Y-5 Ionian Sea (This Study) | Mondragone (Main Flow) | Voscone (Fall) | Aquafidia (Fall) (Fall) | TM-18 (Base) | TM-18 (Top) | LC21 (Aegean) | Kozarnika (Bulgaria) |
|-----------------------------|--------------------------------|----------------------------|-------------------|----------------------------|-----------------|----------------|------------------|-------------------------|
| Y-5 Ionian Sea (This Study) | 0.00 | | | | | | | |
| Main Flow (Mondragone) | 1.48 | 0.00 | | | | | | |
| Voscone (Fall) | 4.98 | 4.94 | 0.00 | | | | | |
| Aquafidia (Fall) | 2.68 | 1.05 | 6.46 | 0.00 | | | | |
| TM-18 (Base) | 1.33 | 1.33 | 7.20 | 2.04 | 0.00 | | | |
| TM-18 (Top) | 2.68 | 1.88 | 6.13 | 3.07 | 0.70 | 0.00 | | |
| LC21 (Aegean) | 2.72 | 3.43 | 7.26 | 4.20 | 1.34 | 1.15 | 0.00 | |
| Kozarnika (Bulgaria) | 1.34 | 0.67 | 3.80 | 0.64 | 0.39 | 0.42 | 1.13 | 0.00 |

(a)

| p (confidence limit) | D^2 critical, $f=8$ | |
|------------------------|-----------------------|--|
| 0.995 | 1.344 | < 0.5 % probability that the two samples are compositionally different if D^2 is less than 1.344 |
| 0.990 | 1.646 | < 1% probability that the two samples are compositionally different if D^2 is less than 1.646 |
| 0.950 | 2.733 | < 5% probability that the two samples are compositionally different if D^2 is less than 2.733 |
| 0.050 | 15.507 | > 95% probability that the two samples are compositionally different if D^2 is greater than 15.507 |
| 0.010 | 20.090 | > 99% probability that the two samples are compositionally different if D^2 is greater than 20.090 |

(b)

Table 5.4: (a) Statistical distance values (D^2) matrix based on major and minor element compositions of the Y-5 Phonolitic-trachytic tephra (Ionian Sea). Compared to proximal Campanian Ignimbrite (fall and Main flows; Tomlinson et al., 2012b) and distal layers attributed to the Campanian Ignimbrite (TM-18 LGdM; Tomlinson et al., 2012b; Kozarnika, Lane et al., in prep; LC21, Satow et al., in prep). Shaded grey are values where less than 5% probability that the two samples are compositionally different. (b) The p (confidence limits) values and the D^2 critical values for the statistical distance, where $f = 8$ (Major and minor elements).

| Locality <i>f</i> = 10 | Y-5 Ionian Sea (This Study) | Mondragone (Main Flow) | Voscone (Fall) | Aquafidia (Fall) (Fall) | TM-18 (Base) | TM-18 (Top) | LC21 (Aegean) | Kozarnika (Bulgaria) |
|-----------------------------|--------------------------------|----------------------------|-------------------|----------------------------|-----------------|----------------|------------------|-------------------------|
| Y-5 Ionian Sea (This Study) | 0.00 | | | | | | | |
| Main Flow (Mondragone) | 5.14 | 0.00 | | | | | | |
| Voscone (Fall) | 1.05 | 3.88 | 0.00 | | | | | |
| Aquafidia (Fall) | 0.32 | 8.44 | 1.01 | 0.00 | | | | |
| TM-18 (Base) | 3.12 | 0.97 | 2.26 | 3.48 | 0.00 | | | |
| TM-18 (Top) | 2.78 | 1.07 | 2.89 | 4.66 | 1.88 | 0.00 | | |
| LC21 (Aegean) | 0.48 | 5.10 | 1.75 | 0.44 | 2.97 | 2.55 | 0.00 | |
| Kozarnika (Bulgaria) | 0.03 | 9.37 | 1.39 | 0.74 | 4.15 | 4.75 | 0.91 | 0.00 |

(a)

| <i>p</i> (confidence limit) | $D^2_{\text{critical}}, f=10$ | |
|-----------------------------|-------------------------------|--|
| 0.995 | 2.156 | < 0.5 % probability that the two samples are compositionally different if D^2 is less than 2.155 |
| 0.990 | 2.558 | < 1% probability that the two samples are compositionally different if D^2 is less than 2.558 |
| 0.950 | 3.940 | < 5% probability that the two samples are compositionally different if D^2 is less than 3.940 |
| 0.050 | 18.307 | > 95% probability that the two samples are compositionally different if D^2 is greater than 18.307 |
| 0.010 | 23.209 | > 99% probability that the two samples are compositionally different if D^2 is greater than 23.209 |

(b)

Table 5.5: Statistical distance values (D^2) based on trace element compositions of the Y-5 Phonolitic tephra shards (Ionian Sea). Compared to proximal Campanian Ignimbrite (Fall and Main flows; Tomlinson et al., 2012b) and distal layers attributed to the Campanian Ignimbrite (TM-18 LGdM, Tomlinson et al., 2012b; Kozarnika, Lane et al., in prep; LC21, Satow et al., in prep). Values shaded in grey and in bold represent where the probability of the two samples being different is less than 0.5%, (b) The p (confidence limits) and the D^2_{critical} values for the statistical distance test where $f = 10$ (trace elements).

Table 5.4 demonstrates the very strong major element correlation of Y-5 Ionian Sea glasses to other distally reported CI glasses elsewhere including LGdM (TM-18 base and top), Kozanrika Cave, Bulgaria (Lowe et al., 2012) and from LC21 a marine core in the Aegean (Lowe et al., 2012). All with D^2 value indicating less than a 5% probability that they are different to the Y-5 Ionian Sea glasses.

The trace element compositions of the phonolitic shards are largely homogenous; compositions lie firmly within the compositional field of the CI fall reported at Aquafidia and Voscone (Fig. 5.10). Two shards display enrichment beyond the range of any proximal glasses reported by Tomlinson et al. (2012b). The levels of trace enrichment observed in the Y-5 reported here are largely beyond the range observed in the flow units from Mondragone (Fig. 5.9). Flow deposits and associated Co-ignimbrite ash display compositions that are more restricted within the overall compositional field of the CI fall. Evidence suggests that the Y-5 reported here is the result of the First Plinian phase of the CI eruption rather than subsequent co-ignimbrite ash dispersals. Y-5 Ionian Sea glass do overlap the TM-18 glasses from Lago Grande di Monticchio (LGdM), however resided at the more fractionated end of this range observed in this distal tephra (Fig. 5.7d). This evidence confirms distal-distal correlations and affirms the potential of the CI to synchronise environmental archives. Figure 5.10 illustrates that the TM-18 glasses are more heterogeneous, but are more restricted in their levels of overall enrichment similar to the Mondragone lower and intermediate flows.

Furthermore in an attempt to precisely correlate distal Y-5 phonolitic component to a specific eruptive phase, statistical distance values are presented based on the more sensitive trace element concentrations, D^2 values are given in Table 5.5. D^2 values in bold and grey represent where the probability of the two samples being different is less than 0.5%. Y-5 Ionian Sea glasses shows greater difference from the Mondragone flow compositions ($D^2 = 5.14$) than Aquafidia fall ($D^2 = 0.32$). Voscone fall remain statistically similar ($D^2 = 1.05$) based on trace element concentrations, however combining both major, minor (Table 5.5) and trace element observations, Y-5 glasses here do not present a precise correlation, particularly in the absence of lower silica glasses in the distal tephra. Mondragone main flow glasses (lower and intermediate) and TM-18 glasses appear to correspond well, given their D^2 values (Base; $D^2 = 1.07$; Top = $D^2 = 0.97$).

Statistical treatment of the glass data available support observations seen in Figure 5.9, demonstrating that the Y-5 Ionian Sea tephra layer is more likely to have derived from the first Plinian column of the Campanian Ignimbrite eruption recorded at Aquafidia. The similarity between trace element glass population observed as those at Kozarnika ($D^2 = 0.03$) and in LC21 ($D^2 = 0.48$) in these ultra distal localities is staggering and provides further support that the major dispersal of CI ash is the result of the first Plinian column (Table 5.5). Whilst trace element concentrations recorded in the TM-18 glasses (Tomlinson et al., 2012b) appears to contain a significant co-ignimbritic ash component associated with the highly buoyant pyroclastic density currents (Civetta et al., 1997) of the Mondragone flow units. This re-affirms the interpretation of Wulf et al., (2004), where the upper portion of TM-18 is attributed to the finer grain material associated with a co-ignimbrite ash.

The minority population of trachytic shards ($n=3$) observed within the Y-5 Ionian Sea display trace element concentrations with low levels of enrichment (Fig. 5.7c, 5.10) that are consistent with the Upper flow recorded at Mondragone (Fig. 5.10). The presence of compositions exclusive to the Upper flow, a less energetic eruptive phase, of low volume and high viscosity magma (Civetta et al., 1997) over 450 km from source recorded in M25/4-12 is intriguing. It additionally supports the limited evidence presented by Tomlinson et al., (2012b) that this component is distally recognised at LGdM (a single shard). The trachytic magma associated with the upper flow is considered an isotopically distinct recharge of the CI chamber (Arienzo et al., 2011) perhaps the trigger of the CI eruption. Two possible implications can be drawn from the discovery of this melt composition distally in the Y-5 Ionian Sea tephra layer; (1) this eruptive phase was more energetic than previously interpreted with an associated co-ignimbritic ash dispersal; or (2) highly efficient mixing processes facilitate small amounts of the trachytic composition to be erupted distally as part of the First Plinian phase of the CI recorded distally, whilst the majority of this component is erupted during the latter phase of the CI eruption.

5.6 Conclusions

1. Two explosive eruptions from the Aeolian Island eruptions (early Holocene to 40ka) are present in the core, indicating that there is potential to improve the chronology of the

Ionian archives using cryptotephra analysis. It does however seem unlikely that Ionian Sea archives will provide a detailed record of eruptive history in the Aeolian Islands.

2. HKCA rhyolitic shards dispersed by the Gabelotto-Fiume bianco (GFB) eruption of Lipari are identified within the Sapropel 1 (28 cm b.s.f) in the early Holocene sediments of Ionian Sea core M25/4-12 providing a new age marker of 8730–8400 cal yrs BP (7770 ± 70 yrs BP uncalibrated).

3. An older HKCA rhyolitic tephra layer with nearly identical compositions to GFB has been detected. This is the first reported distal occurrence of a significant pre-GFB and post Monte Guardia eruption from Lipari in the Ionian Sea.

4. Trace element data here confirm the VRa eruption is not the proximal counterpart of the Y-3 tephra layer recorded in the Ionian Sea. Consequently proximal ages associated with the VRa should not be used for dating distal sequences. With currently no known proximal counterpart the Y-3 does not present a precise tephrochronological marker.

5. The absence of a proximal equivalent for the Y-3 confirms that the post CI-pre-NYT Tufi Biancastri stratigraphy is not yet fully defined.

6. Whilst the proximal source of the Y-3 tephra remains unresolved, the diagnostic geochemical characteristics reported from the type locality (M25/4-12) should be used as the preferred criteria for the assignment of Y-3 correlations.

7. Where the diagnostic criteria of the Y-3 reported are satisfied, then this tephra can provide a precise stratigraphic marker across the central Mediterranean.

8. Trace element data from distal Ionian Sea Y-3 tephra shards confirm correlation to the Lago Grande Monticchio tephra layer TM-15.

9. The Y-5 layer Ionian Sea tephra layers correlation to the Campanian Ignimbrite (Kraml, 1997) has been validated using new proximal glass data from the multiple eruptive phases (Tomlinson et al., 2012b).

10. Geochemical data reveal that southern dispersal of Campanian Ignimbrite ash from the CVZ to the Ionian Sea was part of the First Plinian phase (i.e., buoyant column, fall), given that the levels of trace element enrichment in the phonolitic glasses exceed those observed in the glasses from the ignimbrite deposits (i.e., collapsed column; flows

and fall). Correlations based on statistical distance indicate that ultra distal CI occurrences are all linked to the early most fractionated Plinian episode.

11. A minor trachytic glass component representative of the chemically distinct viscous upper Flow is reported distally in the Y-5 Ionian Sea layer, supporting its distal occurrence in Lago Grande di Monticchio.

Chapter 6: External ash layers recorded in the volcanic stratigraphies of the Aeolian Islands: implications for Mediterranean Ash dispersals.

Abstract

External ash layers originating predominately from the Italian mainland are identified in the proximal stratigraphies of the Aeolian Islands. These primary fall deposits form important stratigraphic markers and where correlated with dated tephtras, either proximally or distally, they provide useful chronological markers. In this chapter, three external tephtra layers outcropping in the Aeolian Islands are geochemically characterised using major, minor and trace element grain-specific data in order to test whether a multi-elemental approach can confirm or refute published correlations and attribution of age to these layers. Furthermore this presents an opportunity to integrate these ash fall episodes within the known dispersal of equivalent marine, lacustrine and continental tephtra layers recorded in archives throughout the central Mediterranean.

The 'Ischia layer' or Y-7 recorded throughout the Aeolian Islands was sampled on Stromboli. Multi-elemental glass data reveal that this tephtra is related to the MEGT caldera forming eruption of Ischia. This eruption is geochemically distinguishable from other more homogeneous Ischia tephtras. Geochemical data herein confirms links to a series of distal equivalents including TM-19 at Lago Grande di Monticchio (LGdM) and marine tephtras (Y-7 Ionian Sea; PRAD 1870 cm central Adriatic; SA03-03-685 cm southern Adriatic) confirming this as a geochemical distinguishable, well dated, widespread central Mediterranean tephtra marker.

The remaining two external tephtra layers are thought to have been deposited in MIS 5. A pink ash layer recorded on Panarea (Punta Falcone) remains unresolved. Previous correlations to the X-5 marine tephtra are refuted based on geochemical data presented herein. Whilst examining links with the X-5 and other MIS 5 High alkali ratio tephtras it became apparent that significant complexities exist regarding the use of these tephtra as tephrostratigraphic markers owing to temporally distinct eruptions with overlapping major element chemistries. A low alkali ratio tephtra recorded at Barone, Salina, represents the southern dispersal of the LGdM tephtra TM-27 (108.3 ka BP), the geochemical bimodality of this tephtra offers greater confidence in distal-distal correlations of these tephtras. This ash dispersal is linked to numerous archives in the central Mediterranean presenting an important and widespread tephrostratigraphical marker.

6.1 Introduction

Numerous external ash layers originating predominantly from the Italian mainland have been recognised in the proximal stratigraphies of the Aeolian Islands (Keller, 1980; Morche 1988; Kraml, 1997; Lucchi et al., 2008). These primary fall layers are important stratigraphic markers and where they can be correlated with dated proximal deposits they provide chronological markers. Salina has the most detailed record of major eruptions from the Campanian region (Keller 1980; Morche 1988; Lucchi et al. 2008). Ash dispersals recorded on the islands are continental equivalents of some of the most widespread marine tephra layers identified in the central Mediterranean region. Identification and correlation of these external ash layers is based on lithology, stratigraphy, glass chemistry and phenocryst assemblages.

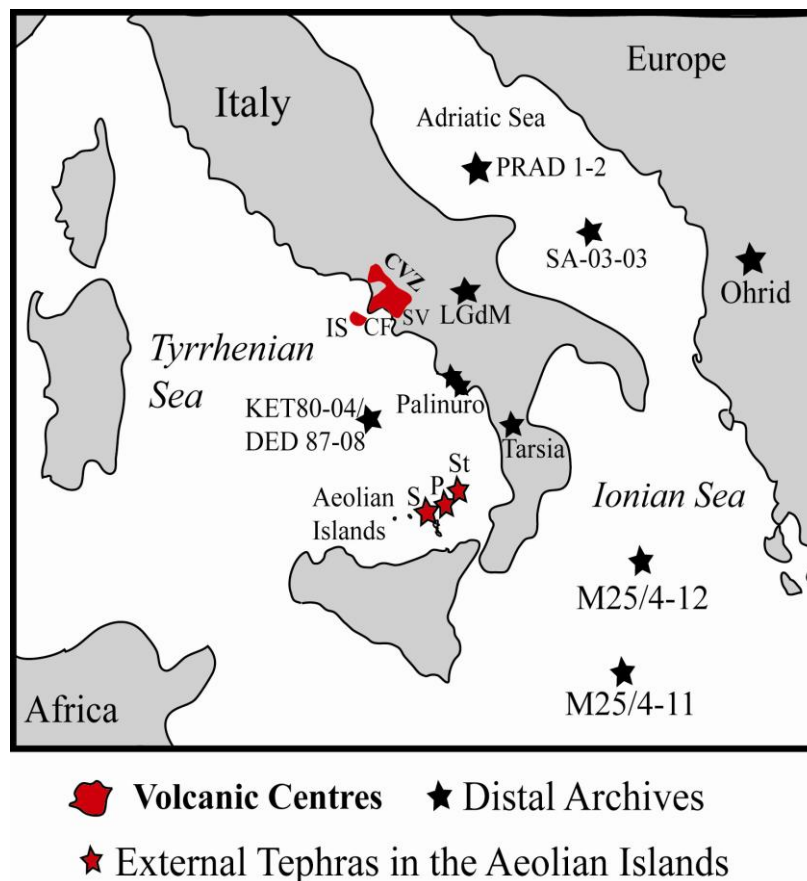


Figure 6.1: A map showing the location of distal archives and volcanic centres referred to in this chapter. CVZ = Campanian Volcanic zone; IS = Ischia; CF = Campi Flegrei; SV = Somma-Vesuvius; S = Salina; P = Panarea; St = Stromboli.

Major, minor and trace element grain-specific glass data for three external ash layers outcropping in the Aeolian Islands are presented with two main aims;

(1) To test whether trace element grain-specific glass data can confirm or refute published correlations and attributed age constraints.

(2) To verify ash dispersal in the central Mediterranean integrating the Aeolian Island records and proposed equivalents in marine, lacustrine and continental archives found elsewhere (Fig. 6.1).

The second aim is important in the context of Mediterranean tephrostratigraphy. These tephras represent explosive volcanic eruptions producing widespread dispersals of ash and it is these tephrostratigraphic markers that are used in order to assess the “lead and/or lags” in environmental change recorded in the archives across the central Mediterranean. Thus it is vital to characterise these tephras using all available information including new multi-elemental glass data. Furthermore where distal tephras are dated (i.e. $^{40}\text{Ar}/^{39}\text{Ar}$), precise correlations enable age constraints to become imported from one distal archive to another.

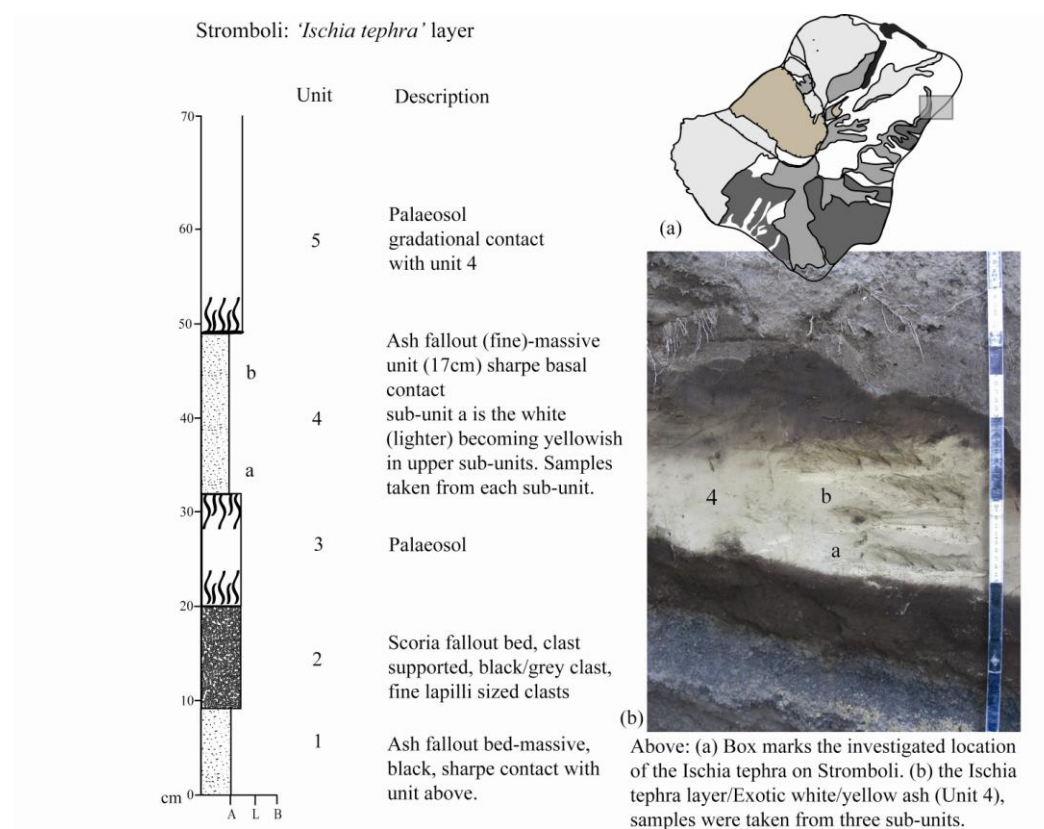


Figure 6.2: 'Ischia tephra' layer outcropping on Stromboli, samples were taken from the top and base of the layer.

6.2 'Ischia tephra' layer

The 'Ischia tephra' layer was first recognised on the Island of Salina (SAL VI; Keller 1980; Morche 1988) and outcrops also occur on Filicudi, Lipari, Panarea and Stromboli (Morche 1988; Lucchi et al., 2008). Glass data are presented from the 'Ischia tephra', Stromboli (Fig. 6.2), where it forms a thick (17 cm) yellow ash deposit. It has been correlated to the Y-7 marine tephra marker (Morche, 1988; Kraml; 1997) in the Ionian Sea (Keller et al., 1978). The Y-7 has been attributed to the Unita Monte Sant' Angelo (U.M.S.A), Ischia island (Wulf et al., 2008). Rosi et al. (1988) previously interpreted this proximal unit as the earliest phase of the Monte Epomeo Green Tuff (MEGT), Ischia.

The MEGT is associated with caldera subsidence across all or part of the Island (Vezzoli 1988, Brown et al., 2008). It is recognised as the largest volcanic event to occur between ~75-50 ka, producing at least two intra-caldera ignimbrite flow units (55 ka; Vezzoli 1988; Brown et al., 2008).

Brown et al., (2008) revised the Ischia stratigraphy between ~ 75-50 ka and proposed some important reinterpretations. Unita Monte Sant' Angelo (i.e. Sant' Angelo tephra) is interpreted as a pre-MEGT deposits (Fig. 6.3). The identification of subsequent pre-MEGT eruptive units and palaeosols suggests that the Sant' Angelo tephra records a temporally separate eruption prior to the caldera forming MEGT (Fig. 6.3). The Sant' Angelo tephra, restricted to the south of the island, resides on a palaeosol formed on top of a lava dome (100 ka; Gillot et al., 1982) which provides the only chronological constraint. Furthermore a post-MEGT stratigraphy is defined and significant portions of the extra-caldera MEGT stratigraphy (Vezzoli 1988; Rosi et al. 1988) are recognised as temporally separate eruptions, based on lithological differences and their intercalation with palaeosols (Fig. 6.3; Brown et al., 2008). The upper portions of the extra-caldera deposits (Vezzoli, 1988; Rossi et al., 1988) are redefined as the Schiappone tephra (Fig. 6.3; Brown et al., 2008). Radiometric ages for this redefined deposits clustered ~ 50 ka (Vezzoli 1988), in contrast to the stratigraphically lower intra-caldera MEGT deposits where ages are ~ 56 ka (Vezzoli 1988; Brown et al., 2008).

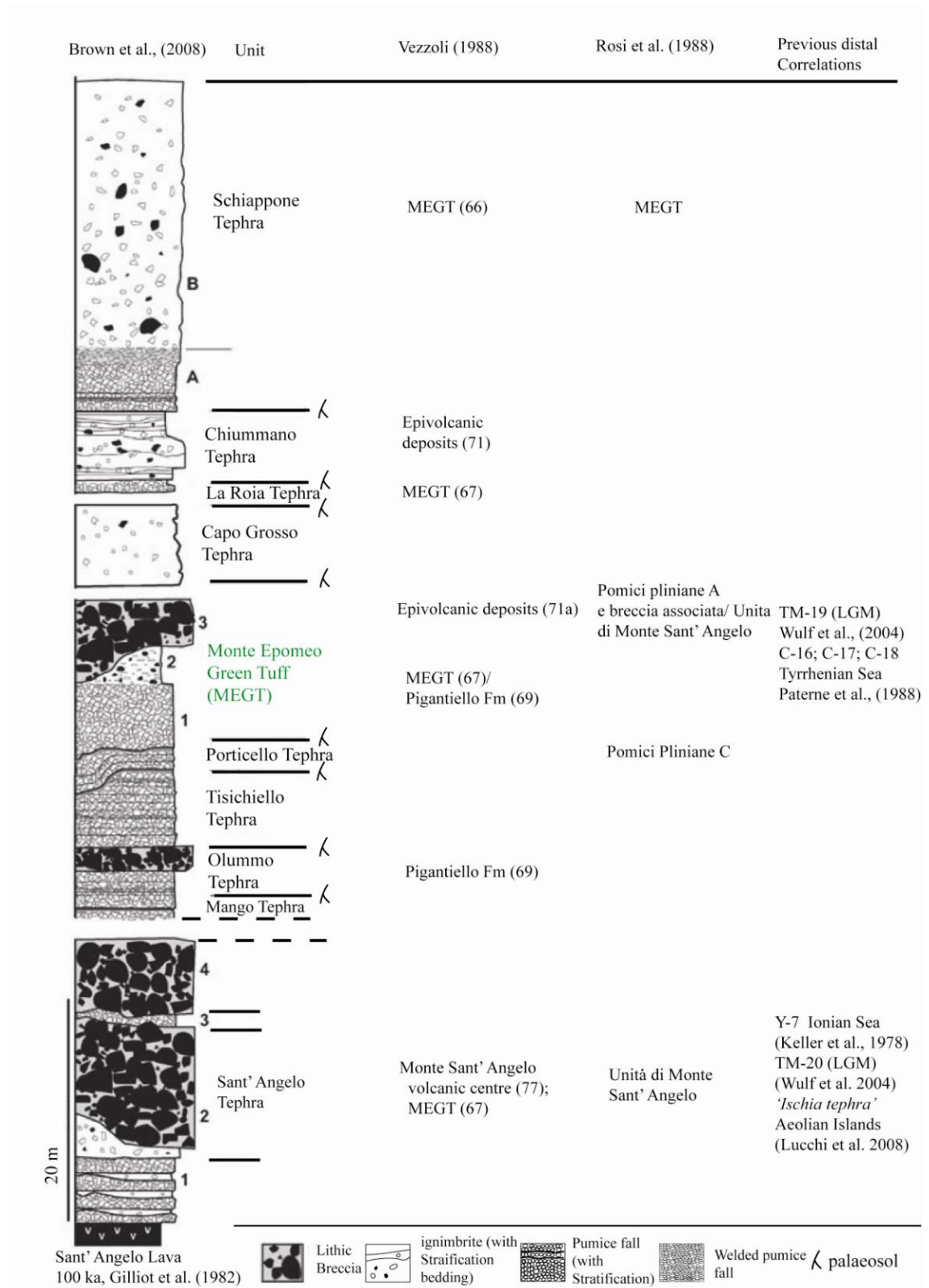


Figure 6.3: A composite succession of the volcanic deposits erupted between 100-50 ka on Ischia adapted from Brown et al., (2008). Gaps in the stratigraphy indicate uncertainties in the stratigraphic position due to incomplete exposure. Also shown are links with previously proposed stratigraphies (Vezzoli 1988; Rosi et al., 1988) and the previously determined proximal-distal correlations.

| Tephra | Depth (cm) | Varve Age (yrs BP) | ⁴⁰ Ar/ ³⁹ Ar Ka yrs BP | Thickness (mm) | Max grain size | Colour | Phenocrysts | Lithics |
|--|------------|--------------------|--|-------------------|----------------|-------------|--------------------------|----------------|
| <i>'Ischia tephra'</i> layer Stromboli | - | - | - | 170 | 400 | Beige | Kf, bt, plg, cpx, ac, ti | V ¹ |
| Y-7 Ionian Sea | - | - | 56 ± 4 ⁽¹⁾ | - | 300 | Beige | Kf, bt, plg, cpx, ac, ti | V ¹ |
| Lago Grande di Monticchio | | | | | | | | |
| TM-19 | 3831.0 | 60060 | 55 ± 2 ⁽²⁾ | 332 | 1100 | Beige-green | Kf, bt, cpx, plg | V ² |
| TM-20 | 3923.8 | 61370 | - | 6 | 200 | Beige | Kf, bt, plg, cpx, ac, ti | V ² |
| TM-20-1b | 4067.6 | 64140 | - | 8 | 300 | Beige | Kf, bt, cpx, plg, ap | V |
| TM-20-1c | 4104.7 | 64470 | - | 3 | 230 | Grey-brown | Kf, bt, cpx, ap, ac | V |
| PRAD 1-2 (C. Adriatic) | 1870 | - | - | Diffuse over 1000 | - | Clear | - | - ³ |
| SA03-03 (S. Adriatic) | 685 | - | - | Diffuse over 1500 | - | Clear | - | - ³ |

Table 6.1: Investigated Ischia tephtras currently attributed to MEGT or Sant' Angelo tephra (U.M.S.A) proximal tephtras; included depth, age, thickness and physical parameters of these distal tephtras. Kf =K-feldspar, bt = biotite, plg = plagioclase, cpx = clinopyroxene, ac = acmite, ti = ti-oxides. References; ¹ Kraml (1997); ² Wulf et al., (2004); ³ Bourne (2012).

The Y-7 has been dated distally in the Ionian Sea using sanidine phenocrysts (56 ± 4 ka; Kraml, 1997). The Y-7 is reported in Lago Grande di Monticchio (LGdM) as TM-20 (Fig. 6.4; Wulf et al., 2004), TM-20-1b and TM-20-1c (Wulf 2012 *pers comm.*). These three LGdM tephra layers are temporally separated in the high resolution lacustrine record and varve ages are reported in Table 6.1. Overlying the ‘youngest’ TM-20 layers is the prominent 32.2 cm thick tephra TM-19 (Fig. 6.4). This tephra is attributed to the co-ignimbritic fall from the MEGT (~ 56 ka; Vezzoli, 1988) caldera forming eruption (Wulf et al., 2004). At LGdM TM-19 has been $^{40}\text{Ar}/^{39}\text{Ar}$ dated as 55 ± 2 ka using single grain analysis of sanidine, whilst a varve age of 60,060 years BP is reported (Wulf et al., submitted). Distal marine tephras correlated to the MEGT eruption are reported in the Tyrrhenian Sea (C-16, C-17, C-18) (Paterne et al., 1988) and the Adriatic (PRAD 1870 cm) (Bourne et al., 2010). These tephras are of crucial importance given that distally they lie close to the transition between marine isotope stages 3 and 4 (MIS 3/4).

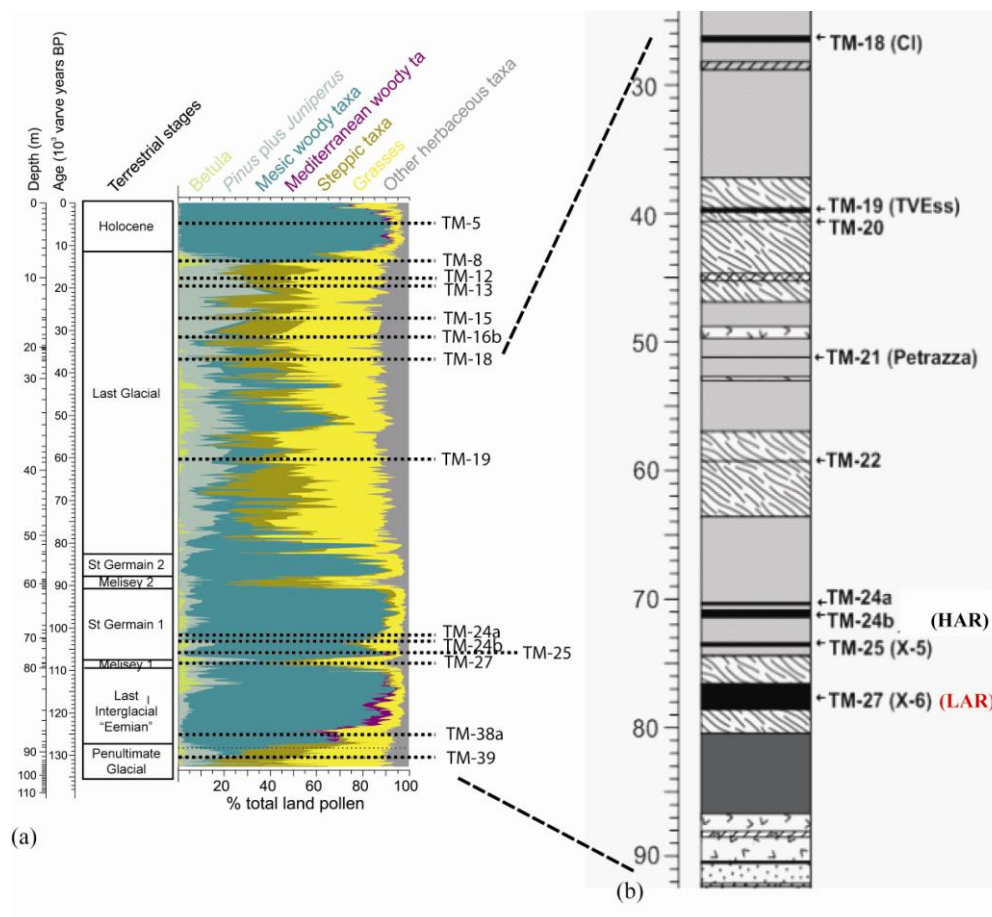


Figure 6.4: (a) Lago Grande di Monticchio tephrostratigraphy (Wulf et al, 2004) and pollen stratigraphy (after Brauer et al. 2007; adapted from Bourne 2012). (b) The pre- Campanian Ignimbrite (TM-18) tephrostratigraphy (Wulf et al., submitted).

In the Tyrrhenian and Adriatic Seas (Fig. 6.5) the distal MEGT equivalents lie stratigraphically above the marine isotope 3/4 transition. Y-7, attributed to the Unita Monte Sant' Angelo (U.M.S.A) or Sant' Angelo tephra (pre-MEGT) appears to reside slightly stratigraphically lower at the transitions (Keller et al., 1978). It is important to establish whether the potentially variable stratigraphic/environmental positions of these distal Ischia type tephras are indeed the result of different temporally distinct eruptions or alternatively whether they reflect a single major ash dispersal. With the latter implying a variable response of proxy records to climate forcing across the Mediterranean basins.

Published major element glass compositions for the Y-7 tephra layer (Keller et al., 1978) and distal MEGT equivalents (Paterne et al., 1988; Wulf et al., 2004; Bourne et al., 2010) appear indistinguishable particularly in the absence of grain specific glass data. Both the *Ischia tephra* layer and the Y-7 marine tephra display all the mineral phases typical of trachytic melts from Ischia (Table 6.1). In addition they include the accessory phases acmite and titanite which are not presently reported in MEGT distal layers (Table 6.1). Keller et al. (1978) termed the Y-7 the 'acmite-trachyte' whilst also recognising that this mineral phase is identified in the U.S.M.A/Sant' Angelo tephra (Keller et al., 1978). The presence of acmite and titanite, in the Y-7 tephra and the pre-MEGT Sant' Angelo eruption, currently provides the most compelling evidence for this correlation, rather than with the younger MEGT caldera forming eruption.

Complexities exist because resurgent activity on Ischia involves magmas with similar whole rock major element chemistries between ca. 100-55 ka (Poli et al 1987; Brown et al., 2008). Major and trace element geochemistry may be able to resolve different magma batches and thus refine proximal-distal correlations. Distal tephras are compared to proximal glasses according to the recently re-defined stratigraphy (Brown et al., 2008).

6.2.1 Samples

Representative proximal deposits were sampled according to the recently revised stratigraphy (Fig. 6.3) of Brown et al. (2008). Pumice were taken as representative of juvenile material. Grain-specific major, minor and trace element glass data was generated for comparisons with distal tephras. The '*Ischia tephra*' layer was sampled on Stromboli (Fig. 6.2) and the Y-7 tephra from the Ionian Sea (M25/4-11) type locality of Keller et al., (1978).

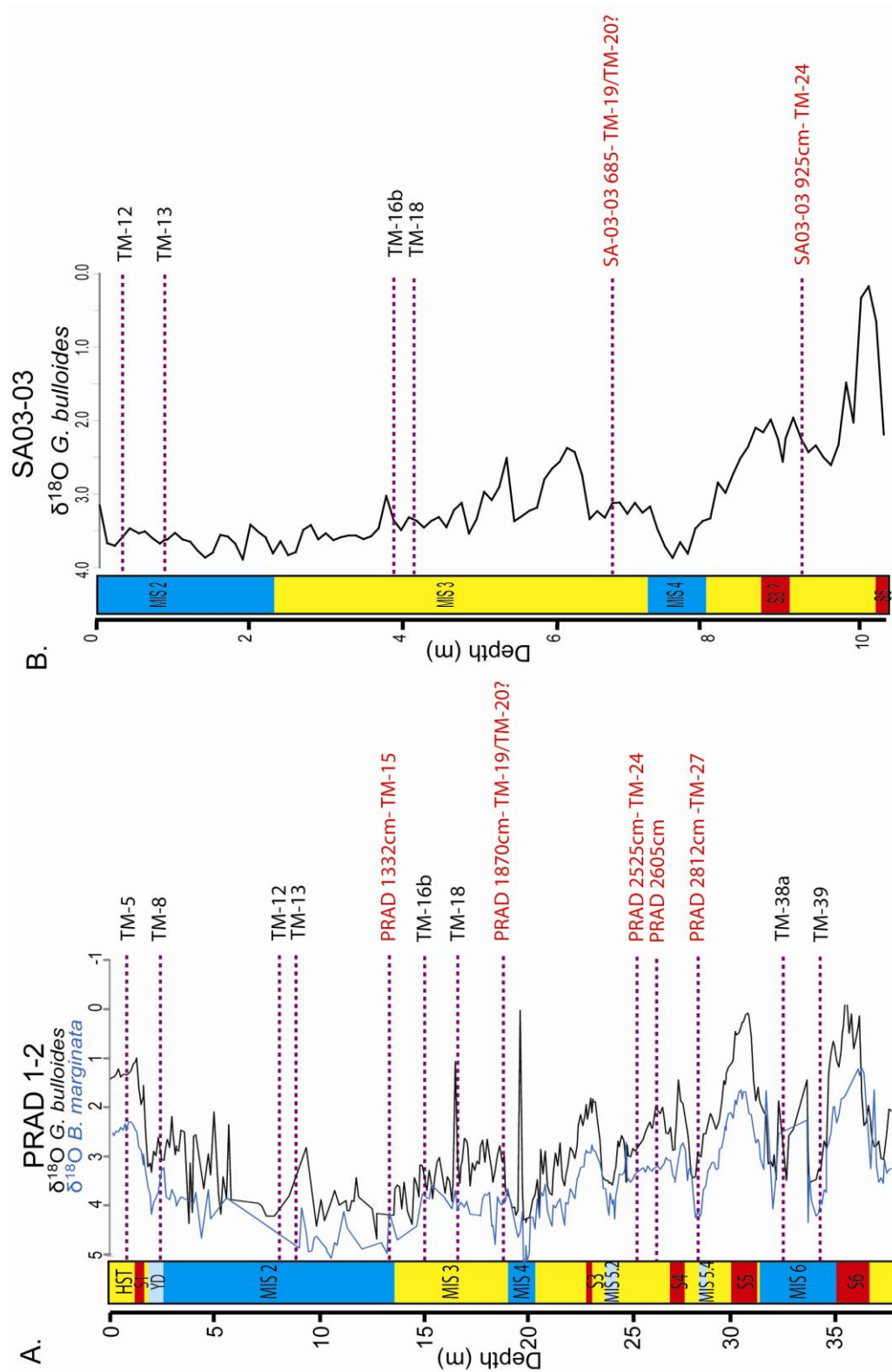


Figure 6.5: The tephrostratigraphy and isotope curves of Central Adriatic marine cores PRAD 1-2 and SA03-03 (Bourne 2012). Highlighted in red are the tephras revisited in this study and their existing correlations within the Lago Grande Monticchio archive (Bourne 2012). Note: only confidently assigned tephra correlations were kept in this illustration for clarity (Adapted from Bourne, 2012).

Relevant Ischia tephras Lago Grande di Monticchio (TM-19, TM-20, TM-20-1b, TM-20-1c) are investigated and chronological information is presented in Table 6.1. MIS 3/4 last-glacial Ischia tephras layers were investigated from Adriatic marine cores; PRAD 1-2 and SA03-03 (Fig. 6.5). Individual shards from loose glass separates were hand-picked under a microscope and mounted in resin blocks, sectioned and polished. Details of all distal tephras investigated are given in Table 6.1; shards were typically stretched and highly vesicular with the exception of the more blocky TM-20 and TM-20-1c layers at LGdM (Fig. 6.6).

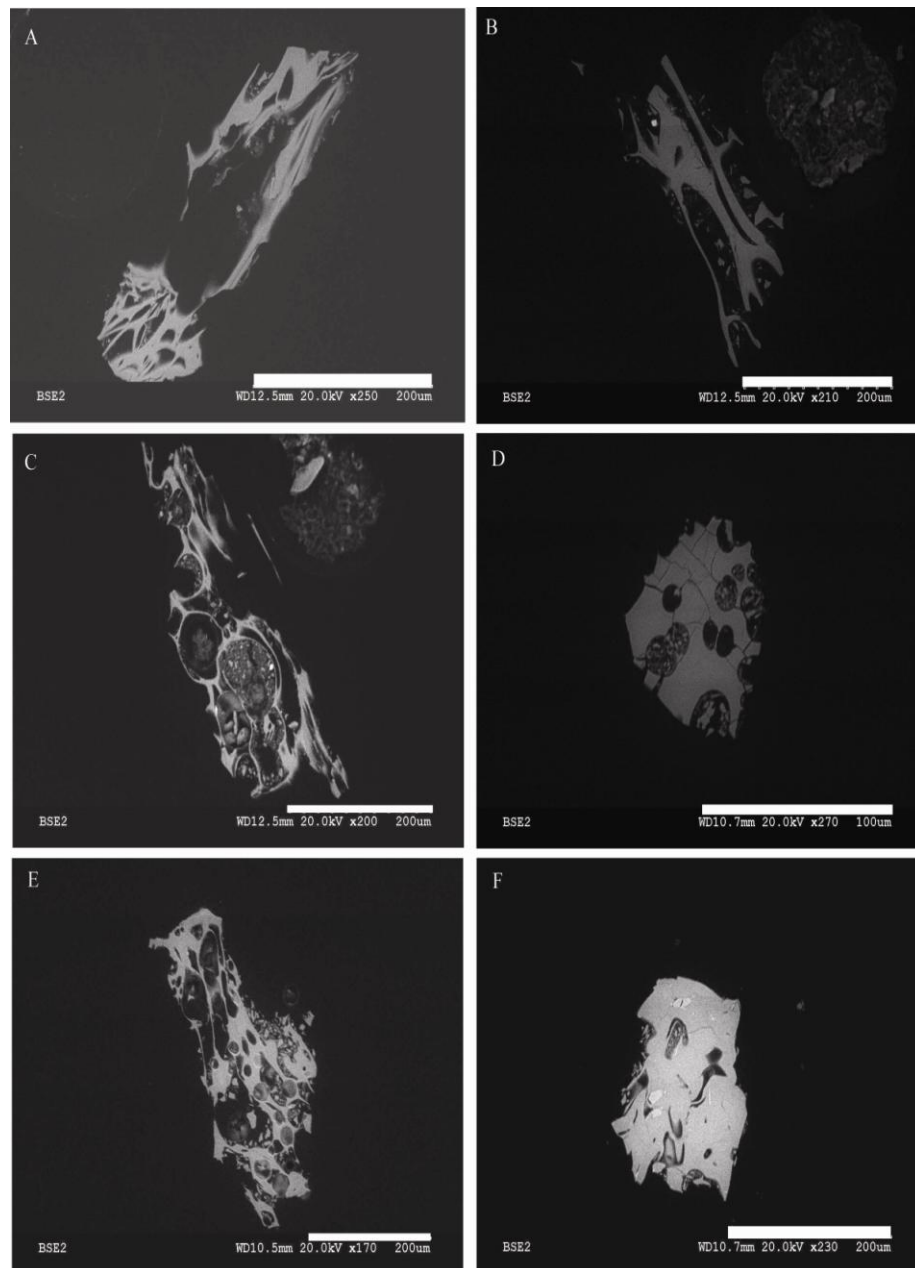


Figure 6.6: SEM images of investigated tephras. (A) Ischia tephra layer Stromboli; (B) Y7 tephra Ionian Sea (M25/4-11); (C) LGM TM-19; (D) LGM TM-20; (E) LGM TM-20-1b; (F) LGM TM20-1c. White scale bar represents 200 μm.

| Unit ID Sample ID Material | Sant' Angelo Tephra | | | | | | | Olummo Tephra | Tisichiello Tephra | Porticello Tephra | | | | |
|------------------------------------|---------------------|-------|-------|----------|-------|-------|----------------|---------------|--------------------|-------------------|---------|-------|-------|-------|
| | Fall | | | Flow | | | <i>Breccia</i> | Fall | Fall | Fall | | | | |
| | OIS 0326 | | | OIS 0330 | | | <i>OIS0332</i> | OIS0302 | OIS0315 | OIS0316 | OIS0320 | | | |
| | 2A | 6A | 19D | 1A | 2A | 3A | <i>W/R</i> | 4A | 6B | 2A | 8B | 9B | 4A | 7B |
| | glass | glass | glass | glass | glass | glass | <i>W/R</i> | glass | glass | glass | glass | glass | glass | glass |
| SiO ₂ | 61.33 | 61.60 | 62.04 | 61.85 | 61.40 | 61.75 | <i>61.98</i> | 60.87 | 60.85 | 61.84 | 61.38 | 61.68 | 62.27 | 61.77 |
| TiO ₂ | 0.59 | 0.64 | 0.63 | 0.56 | 0.65 | 0.56 | <i>0.56</i> | 0.56 | 0.61 | 0.59 | 0.53 | 0.61 | 0.58 | 0.59 |
| Al ₂ O ₃ | 18.71 | 18.74 | 18.79 | 18.45 | 18.61 | 18.44 | <i>18.60</i> | 18.57 | 18.77 | 18.74 | 18.37 | 18.37 | 18.58 | 18.63 |
| FeOt | 2.69 | 2.59 | 2.47 | 2.72 | 2.50 | 2.68 | <i>3.51</i> | 2.82 | 2.80 | 2.74 | 2.53 | 3.01 | 2.55 | 2.71 |
| MnO | 0.25 | 0.33 | 0.27 | 0.20 | 0.29 | 0.26 | <i>0.31</i> | 0.37 | 0.32 | 0.15 | 0.25 | 0.29 | 0.23 | 0.25 |
| MgO | 0.34 | 0.35 | 0.36 | 0.35 | 0.30 | 0.36 | <i>0.35</i> | 0.27 | 0.28 | 0.31 | 0.34 | 0.35 | 0.29 | 0.31 |
| CaO | 1.17 | 1.22 | 1.13 | 1.09 | 1.18 | 1.09 | <i>1.03</i> | 0.95 | 1.02 | 1.15 | 1.49 | 1.08 | 1.11 | 1.04 |
| Na ₂ O | 7.70 | 7.26 | 7.25 | 7.67 | 8.04 | 7.91 | <i>7.87</i> | 8.56 | 8.49 | 7.09 | 7.53 | 7.34 | 7.17 | 7.54 |
| K ₂ O | 6.56 | 6.55 | 6.43 | 6.39 | 6.26 | 6.16 | <i>6.52</i> | 6.15 | 6.00 | 6.64 | 6.54 | 6.41 | 6.44 | 6.40 |
| P ₂ O ₅ | 0.09 | 0.07 | 0.04 | 0.02 | 0.05 | 0.09 | <i>0.03</i> | 0.06 | 0.09 | 0.07 | 0.35 | 0.04 | 0.09 | 0.07 |
| Cl | 0.57 | 0.65 | 0.60 | 0.71 | 0.73 | 0.71 | - | 0.82 | 0.77 | 0.68 | 0.70 | 0.83 | 0.70 | 0.68 |
| Total | 96.79 | 94.83 | 96.55 | 97.07 | 93.52 | 96.10 | <i>100.77</i> | 98.78 | 96.81 | 98.08 | 96.49 | 96.63 | 96.58 | 96.49 |
| K ₂ O+Na ₂ O | 14.3 | 13.8 | 13.7 | 14.1 | 14.3 | 14.1 | <i>14.4</i> | 14.7 | 14.5 | 13.7 | 14.1 | 13.7 | 13.6 | 13.9 |
| K ₂ O/Na ₂ O | 0.9 | 0.9 | 0.9 | 0.8 | 0.8 | 0.8 | <i>0.8</i> | 0.7 | 0.7 | 0.9 | 0.9 | 0.9 | 0.9 | 0.8 |
| spot size (um) | 25 | 25 | 25 | 25 | 25 | 25 | - | 20 | 20 | 20 | 20 | 20 | 20 | 20 |
| Rb (ppm) | 472 | 492 | 462 | 527 | 542 | 532 | <i>553</i> | 589 | 602 | 450 | 463 | 468 | 407 | 466 |
| Sr | 10.6 | 9.7 | 10.9 | 2.1 | 5.0 | 3.1 | <i>4.8</i> | 2.9 | 2.4 | 17.1 | 5.0 | 3.5 | 5.5 | 4.0 |
| Y | 69 | 70 | 67 | 60 | 70 | 70 | <i>105</i> | 89 | 95 | 61 | 66 | 65 | 67 | 62 |
| Zr | 872 | 900 | 807 | 660 | 762 | 762 | <i>1167</i> | 1081 | 1116 | 591 | 700 | 649 | 666 | 616 |
| Nb | 127 | 130 | 128 | 113 | 122 | 125 | <i>157</i> | 162 | 167 | 102 | 114 | 105 | 112 | 105 |
| Ba | 6.6 | 6.3 | 6.9 | 2.6 | 3.8 | 3.2 | <i>2.2</i> | 4.5 | 3.5 | 23.4 | 6.4 | 3.9 | 5.2 | 3.8 |
| La | 163 | 166 | 162 | 138 | 157 | 156 | <i>216</i> | 205 | 212 | 133 | 140 | 138 | 142 | 133 |
| Ce | 318 | 320 | 305 | 259 | 302 | 298 | <i>416</i> | 376 | 393 | 253 | 284 | 275 | 285 | 273 |
| Pr | 31 | 33 | 29 | 26 | 32 | 30 | <i>40</i> | 37 | 40 | 27 | 28 | 29 | 29 | 28 |
| Nd | 109 | 108 | 102 | 85 | 99 | 105 | <i>139</i> | 122 | 125 | 91 | 102 | 100 | 102 | 101 |
| Sm | 15.5 | 16.9 | 16.9 | 15.7 | 18.8 | 17.4 | <i>22.0</i> | 19.3 | 20.9 | 16.7 | 21.5 | 18.2 | 19.0 | 18.9 |
| Eu | 1.30 | 1.18 | 1.22 | 0.78 | 1.02 | 0.94 | <i>1.06</i> | 0.97 | 1.09 | 1.27 | 1.21 | 1.11 | 1.28 | 1.03 |
| Gd | 13.8 | 13.1 | 12.3 | 9.9 | 13.6 | 12.2 | <i>17.7</i> | 13.9 | 15.2 | 11.8 | 13.9 | 13.8 | 14.3 | 13.3 |
| Dy | 12.5 | 11.8 | 11.1 | 9.7 | 11.9 | 11.7 | <i>15.7</i> | 15.3 | 14.7 | 10.9 | 12.5 | 12.2 | 11.9 | 10.9 |
| Er | 7.6 | 7.5 | 7.0 | 5.6 | 6.7 | 6.8 | <i>9.7</i> | 9.2 | 9.7 | 6.5 | 6.9 | 6.9 | 6.5 | 6.3 |
| Yb | 7.7 | 7.0 | 7.2 | 6.4 | 8.0 | 7.3 | <i>10.7</i> | 9.3 | 10.9 | 6.8 | 6.8 | 6.9 | 7.0 | 6.2 |
| Lu | 1.30 | 1.22 | 1.17 | 0.92 | 1.14 | 1.07 | <i>1.57</i> | 1.44 | 1.49 | 0.91 | 1.04 | 0.94 | 0.97 | 0.96 |
| Ta | 6.0 | 6.2 | 5.7 | 5.0 | 6.0 | 5.5 | <i>7.5</i> | 6.6 | 6.9 | 5.2 | 5.5 | 5.3 | 5.4 | 5.0 |
| Th | 62.7 | 63.0 | 60.2 | 44.3 | 52.2 | 52.1 | <i>84.8</i> | 78.9 | 82.6 | 40.9 | 46.4 | 43.0 | 46.4 | 43.1 |
| U | 18.5 | 18.8 | 17.5 | 14.6 | 16.7 | 16.1 | <i>19.2</i> | 24.0 | 24.4 | 13.2 | 13.9 | 13.5 | 13.4 | 13.2 |

Table 6.2: Representative major, minor and trace element glass data from the juvenile fall and flow deposits explosively erupted on Ischia between ca. 100-50 ka. Analyses given in Italics are whole rock data including new analyses of the Sant Angelo lag breccia, XRF data for the LMEGT is taken from Brown et al., (2008).

| Unit ID | MEGT | | | | | | Schiappone | |
|------------------------------------|------------------|------------------|-------------|------------------|------------------|---|------------------|------------------|
| | Fall OIS 0333 | Fall OIS 0321 | | Fall OIS 0319 | Fall OIS 0325 | Flow LMEGT <i>Brown et al.2008)</i> | Fall SC-03151 | Fall SC-03151 |
| Sample ID Material | 1A glass | 1A glass | 2A glass | 7 glass | 1 glass | W/R | 1 glass | 2 glass |
| SiO ₂ | 61.87 | 61.99 | 62.15 | 62.92 | 62.31 | 62.19 | 62.03 | 62.40 |
| TiO ₂ | 0.57 | 0.47 | 0.55 | 0.50 | 0.57 | 0.51 | 0.50 | 0.48 |
| Al ₂ O ₃ | 18.68 | 18.56 | 18.45 | 18.20 | 18.40 | 18.55 | 18.42 | 18.51 |
| FeOt | 2.74 | 2.71 | 2.45 | 2.39 | 2.72 | 2.65 | 2.40 | 2.20 |
| MnO | 0.26 | 0.30 | 0.24 | 0.13 | 0.27 | 0.10 | 0.18 | 0.18 |
| MgO | 0.26 | 0.22 | 0.25 | 0.48 | 0.29 | 0.36 | 0.30 | 0.31 |
| CaO | 0.91 | 0.94 | 1.03 | 1.36 | 0.74 | 1.18 | 1.40 | 1.35 |
| Na ₂ O | 7.81 | 7.92 | 7.67 | 6.11 | 7.11 | 5.44 | 6.78 | 6.31 |
| K ₂ O | 6.08 | 6.16 | 6.38 | 7.58 | 7.03 | 7.90 | 7.39 | 7.68 |
| P ₂ O ₅ | 0.03 | 0.00 | 0.03 | 0.05 | 0.07 | 0.08 | 0.07 | 0.04 |
| Cl | 0.80 | 0.74 | 0.81 | 0.28 | 0.50 | - | 0.53 | 0.55 |
| Total | 96.48 | 95.00 | 94.55 | 94.39 | 98.70 | 99.78 | 94.27 | 95.76 |
| K ₂ O+Na ₂ O | 13.9 | 14.1 | 14.0 | 13.7 | 14.1 | 13.3 | 14.2 | 14.0 |
| K ₂ O/Na ₂ O | 0.8 | 0.8 | 0.8 | 1.2 | 1.0 | 1.5 | 1.1 | 1.2 |
| spot size (um) | 25 | 25 | 25 | 25 | - | - | - | - |
| Rb (ppm) | 352 | 513 | 538 | 279 | - | 267 | 332 | 319 |
| Sr | 4.4 | 1.5 | 1.8 | 23.5 | - | 85.7 | 20.6 | 27.2 |
| Y | 58 | 63 | 66 | 29 | - | 41 | 37 | 34 |
| Zr | 679 | 764 | 801 | 240 | - | 376 | 368 | 326 |
| Nb | 114 | 121 | 123 | 46 | - | 51 | 60 | 53 |
| Ba | 3.5 | 2.3 | 2.3 | 20.6 | - | 54.0 | 10.3 | 21.8 |
| La | 138 | 142 | 151 | 68 | - | 88 | 79 | 74 |
| Ce | 266 | 273 | 284 | 133 | - | 175 | 157 | 142 |
| Pr | 26 | 28 | 27 | 14 | - | - | 17 | 15 |
| Nd | 86 | 89 | 94 | 51 | - | 69 | 58 | 55 |
| Sm | 15.4 | 16.8 | 15.2 | 10.3 | - | 12.3 | 9.9 | 9.6 |
| Eu | 0.78 | 0.82 | 0.74 | 1.36 | - | 1.33 | 1.41 | 1.42 |
| Gd | 11.5 | 10.8 | 10.2 | <LOD | - | - | 9.1 | 7.1 |
| Dy | 10.3 | 10.7 | 11.9 | 5.8 | - | 7.6 | 7.0 | 6.3 |
| Er | 6.2 | 7.1 | 6.8 | 3.0 | - | - | 3.9 | 3.5 |
| Yb | 6.4 | 6.7 | 7.0 | 2.9 | - | 3.8 | 4.2 | 3.3 |
| Lu | 0.98 | 1.04 | 1.10 | <LOD | - | 0.56 | 0.58 | 0.51 |
| Ta | 5.3 | 5.1 | 5.6 | 2.2 | - | 3.3 | 3.2 | 2.8 |
| Th | 49.1 | 49.9 | 54.1 | 16.4 | - | 22.4 | 22.6 | 21.4 |
| U | 15.8 | 16.1 | 16.0 | 5.7 | - | 16.7 | 7.8 | 6.6 |

Table 6.2: Continued. Full glass data sets are available in appendix eV.

6.2.2 Results

6.2.2.1 Proximal Ischia

Representative juvenile glasses (pumice) for the proximal deposits erupted between 100-50 ka on Ischia are reported in Table 6.2 and full geochemical data are presented in Electronic Appendix V. Ischia glasses range from phonolitic to trachytic displaying more elevated total alkalis (i.e. 'peralkalic') than the other Neapolitan volcanic centres at overlapping SiO₂ wt.% (Campi Flegrei and Somma-Vesuvius) (Fig. 6.7a). This is most obvious with the higher Na₂O in the Ischia glasses (Fig. 6.7b). The phonolitic end-members on Ischia have Na₂O > K₂O in direct contrast to Campi Flegrei and Somma-Vesuvius where K₂O >> Na₂O (Rosi and Sbrana, 1988). MEGT deposits and stratigraphic units above the MEGT sees the introduction of glasses with K₂O > Na₂O (Fig. 6.8) on Ischia (56-50 ka). In addition total alkalis in these glasses typically remain more elevated than the other Neapolitan centres (Fig. 6.7a) and CaO extend to lower values (Fig. 6.7c).

Mantle normalised trace element signatures of all the Ischia proximal deposits are characterised by depletions in the HFSE element relative to the LILE, with a characteristic trough at Nb, Ta (Fig. 6.9b). Coupled with Ti depletions (Fig. 6.9b), these features reflect the subduction derived source feeding Ischia. The glasses also display pronounced depletions in Ba, Sr and Eu in response to the fractionation of K-feldspar a dominant phase in the pumices sampled on the island. The MEGT glasses display the most significant variability of the proximal suite (Fig. 6.9b).

6.2.2.2 '*Ischia tephra*' layer, Stromboli

Major element glass compositions display some significant compositional variability (61.4-62.93 wt.% SiO₂; 1-1.5 wt.% CaO) and elevated alkalis defining a range from phonolitic to trachytic compositions (Fig. 6.9a). Glasses with Na₂O > K₂O and K₂O ≥ Na₂O are reported (Fig. 6.10a) and it is noteworthy that lower Na₂O is typically restricted to the higher SiO₂ glasses (Fig. 6.10c). Trace element concentrations indicate highly evolved melt compositions (Zr/Sr = 32-245) with significant LREE enrichment (La/Yb = 21 ± 1) (Fig. 6.9b). Glasses have heterogeneous trace element geochemistry (Fig. 6.10d-f).

| Shard I.D | 'Ischia Tephra' layer Stromboli | | | | Y7 | | | | TM-19 | | | | TM-20 | | |
|------------------------------------|---------------------------------|-------|-------|-------|---------------------|-------|-------|-------|-------|-------|-------|-------|-------|-------|-------|
| | Base | | Top | | M25/4-11 Ionian Sea | | | | LGdM | | | | LGdM | | |
| | 2A | 18B | 23C | 27C | 21C | 23C | 28C | 1A | 14B | 20B | 19B | 25B | 3A | 44D | 48D |
| SiO ₂ | 61.84 | 62.01 | 61.42 | 62.67 | 61.59 | 62.32 | 62.39 | 62.93 | 62.05 | 61.75 | 62.96 | 62.64 | 62.05 | 61.31 | 61.74 |
| TiO ₂ | 0.57 | 0.56 | 0.48 | 0.51 | 0.56 | 0.65 | 0.55 | 0.41 | 0.57 | 0.59 | 0.54 | 0.56 | 0.62 | 0.51 | 0.58 |
| Al ₂ O ₃ | 18.19 | 18.47 | 18.46 | 18.42 | 18.80 | 18.33 | 18.78 | 18.68 | 18.48 | 18.44 | 18.46 | 18.26 | 18.62 | 18.30 | 18.64 |
| FeO | 2.60 | 2.67 | 2.74 | 2.53 | 2.35 | 2.65 | 2.58 | 2.39 | 2.69 | 2.62 | 2.42 | 2.45 | 2.61 | 2.59 | 2.63 |
| MnO | 0.32 | 0.23 | 0.30 | 0.22 | 0.26 | 0.21 | 0.20 | 0.13 | 0.22 | 0.23 | 0.16 | 0.21 | 0.28 | 0.27 | 0.28 |
| MgO | 0.26 | 0.27 | 0.33 | 0.36 | 0.25 | 0.31 | 0.43 | 0.47 | 0.33 | 0.30 | 0.41 | 0.42 | 0.29 | 0.33 | 0.32 |
| CaO | 1.05 | 1.00 | 1.03 | 1.15 | 0.94 | 1.09 | 1.32 | 1.46 | 1.12 | 1.12 | 1.26 | 1.30 | 1.08 | 1.00 | 1.05 |
| Na ₂ O | 8.38 | 7.94 | 8.22 | 6.57 | 8.37 | 7.19 | 6.73 | 5.60 | 7.57 | 7.86 | 6.90 | 6.84 | 7.37 | 7.69 | 7.59 |
| K ₂ O | 6.05 | 6.09 | 6.19 | 6.99 | 6.01 | 6.47 | 6.44 | 7.41 | 6.14 | 6.27 | 6.36 | 6.66 | 6.32 | 6.84 | 6.36 |
| P ₂ O ₅ | 0.01 | 0.01 | 0.04 | 0.04 | 0.05 | 0.05 | 0.08 | 0.11 | 0.05 | 0.05 | 0.09 | 0.08 | 0.05 | 0.04 | 0.07 |
| Cl | 0.74 | 0.76 | 0.81 | 0.54 | 0.82 | 0.72 | 0.49 | 0.41 | 0.78 | 0.75 | 0.45 | 0.57 | 0.71 | 1.12 | 0.75 |
| Total | 98.14 | 95.21 | 97.54 | 95.11 | 96.69 | 95.08 | 95.99 | 99.09 | 96.14 | 98.08 | 97.09 | 95.97 | 94.89 | 96.20 | 99.39 |
| K ₂ O+Na ₂ O | 14.43 | 14.02 | 14.41 | 13.56 | 14.37 | 13.66 | 13.17 | 13.01 | 13.71 | 14.13 | 13.27 | 13.51 | 13.69 | 14.53 | 13.95 |
| K ₂ O/Na ₂ O | 0.7 | 0.8 | 0.8 | 1.1 | 0.7 | 0.9 | 1.0 | 1.3 | 0.8 | 0.8 | 0.9 | 1.0 | 0.9 | 0.9 | 0.8 |
| Spot size | 25 | 25 | 25 | 25 | 25 | 25 | 25 | 25 | 20 | 20 | 20 | 20 | 20 | 20 | 20 |
| ppm | | | | | | | | | | | | | | | |
| Rb | 503 | 466 | 534 | 335 | 512 | 453 | 334 | 261 | 489 | 424 | 368 | 287 | 477 | 310 | 479 |
| Sr | 5.5 | 4.5 | 3.3 | 11.9 | 2.8 | 3.5 | 8.6 | 31.7 | 4.2 | 3.8 | 8.6 | 15.6 | 4.1 | 14.9 | 3.7 |
| Y | 66 | 64 | 68 | 42 | 68 | 66 | 43 | 29 | 66 | 67 | 41 | 30 | 64 | 63 | 64 |
| Zr | 723 | 633 | 806 | 380 | 803 | 646 | 376 | 227 | 766 | 645 | 378 | 258 | 655 | 654 | 675 |
| Nb | 117 | 108 | 125 | 65 | 127 | 110 | 66 | 41 | 119 | 110 | 63 | 46 | 110 | 106 | 112 |
| Ba | 6.1 | 5.8 | 4.6 | 13.4 | 3.7 | 4.3 | 7.4 | 24.8 | 11.7 | 11.0 | 8.2 | 10.8 | 4.8 | 25.9 | 3.5 |
| La | 146 | 134 | 154 | 91 | 155 | 141 | 91 | 66 | 145 | 129 | 88 | 68 | 138 | 136 | 137 |
| Ce | 284 | 272 | 293 | 169 | 293 | 278 | 180 | 124 | 282 | 258 | 180 | 136 | 266 | 261 | 271 |
| Pr | 29 | 28 | 29 | 20 | 29 | 28 | 19 | 13 | 29 | 28 | 19 | 14 | 28 | 26 | 27 |
| Nd | 97 | 101 | 102 | 67 | 96 | 104 | 75 | 48 | 99 | 102 | 70 | 55 | 99 | 94 | 100 |
| Sm | 17.0 | 17.4 | 18.6 | 10.9 | 16.5 | 17.7 | 11.9 | 8.6 | 16.7 | 20.3 | 13.7 | 10.6 | 16.8 | 17.4 | 18.3 |
| Eu | 1.04 | 0.94 | 0.85 | 1.03 | 0.75 | 1.14 | 1.23 | 1.48 | 0.91 | 0.94 | 1.36 | 1.31 | 1.03 | 1.10 | 1.02 |
| Gd | 11.8 | 12.2 | 12.9 | 8.4 | 12.4 | 15.2 | 9.5 | 6.7 | 13.4 | 12.4 | 9.8 | 6.7 | 12.4 | 11.8 | 13.1 |
| Dy | 11.9 | 11.7 | 12.0 | 7.5 | 11.4 | 12.5 | 8.5 | 6.2 | 12.1 | 11.8 | 7.3 | 6.4 | 12.2 | 10.7 | 11.8 |
| Er | 6.7 | 6.7 | 6.9 | 3.9 | 7.0 | 6.8 | 4.0 | 2.9 | 6.6 | 6.2 | 4.2 | 3.2 | 6.8 | 6.6 | 7.4 |
| Yb | 7.5 | 6.7 | 7.6 | 3.8 | 7.2 | 6.7 | 4.9 | 2.9 | 7.7 | 5.4 | 3.6 | 3.0 | 6.9 | 6.5 | 6.5 |
| Lu | 1.01 | 1.00 | 1.17 | 0.57 | 1.14 | 0.96 | 0.60 | 0.44 | 1.00 | 0.93 | 0.46 | 0.42 | 1.05 | 1.01 | 1.01 |
| Ta | 5.1 | 5.4 | 5.5 | 2.8 | 5.7 | 5.7 | 3.6 | 2.3 | 5.3 | 5.3 | 3.3 | 2.5 | 5.5 | 5.3 | 5.6 |
| Th | 49 | 43 | 53 | 23 | 53 | 43 | 25 | 16 | 51 | 37 | 23 | 18 | 46 | 45 | 46 |
| U | 15.2 | 13.4 | 15.8 | 7.0 | 16.2 | 13.5 | 7.8 | 4.9 | 15.4 | 11.6 | 7.2 | 5.4 | 14.1 | 13.6 | 14.5 |

Table 6.3: Representative major, minor and trace element glass analyses of shards from distal tephra layers including the 'Ischia tephra' layer Stromboli, the Y-7 tephra Ionian Sea, Lago Grande di Monticchio layers (LGdM); TM-19, TM-20, TM-20-1b, TM-20-1c and Central Adriatic marine tephra PRAD 1-2 1870 cm and SA0303- 685cm. Major element data for the Ischia type tephra in central Adriatic cores are presented in Bourne (2012). Full data sets are presented in appendix eV.

| I.D | TM-20-1b LGdM | | | TM-20-1c LGdM | | | 1870 cm PRAD 1-2 C. Adriatic Bourne et al. (2010) | | | | 865 cm SA03-03 C. Adriatic Bourne (2012) | | |
|------------------------------------|------------------|-------|-------|------------------|-------|-------|---|------|------|------|--|------|------|
| | 11B | 27C | 39D | 8A | 9A | 19C | 6 | 4 | 5 | 4 | 2 | 5 | 10 |
| SiO ₂ | 62.14 | 61.95 | 61.87 | 61.96 | 62.08 | 61.81 | | | | | | | |
| TiO ₂ | 0.57 | 0.56 | 0.58 | 0.61 | 0.63 | 0.56 | | | | | | | |
| Al ₂ O ₃ | 18.63 | 18.41 | 18.44 | 18.41 | 18.40 | 18.57 | | | | | | | |
| FeO | 2.58 | 2.70 | 2.81 | 2.56 | 2.61 | 2.71 | | | | | | | |
| MnO | 0.36 | 0.29 | 0.23 | 0.23 | 0.28 | 0.29 | | | | | | | |
| MgO | 0.30 | 0.31 | 0.31 | 0.29 | 0.32 | 0.28 | | | | | | | |
| CaO | 1.07 | 1.10 | 1.08 | 1.11 | 1.10 | 1.08 | | | | | | | |
| Na ₂ O | 7.26 | 7.48 | 7.39 | 7.55 | 7.58 | 7.54 | | | | | | | |
| K ₂ O | 6.37 | 6.38 | 6.53 | 6.59 | 6.29 | 6.46 | | | | | | | |
| P ₂ O ₅ | 0.04 | 0.06 | 0.08 | 0.04 | 0.03 | 0.04 | | | | | | | |
| Cl | 0.69 | 0.76 | 0.68 | 0.63 | 0.68 | 0.66 | | | | | | | |
| Total | 99.28 | 99.21 | 99.22 | 99.83 | 99.19 | 98.32 | | | | | | | |
| K ₂ O+Na ₂ O | 13.63 | 13.86 | 13.92 | 14.14 | 13.88 | 14.00 | | | | | | | |
| K ₂ O/Na ₂ O | 0.9 | 0.9 | 0.9 | 0.9 | 0.8 | 0.9 | | | | | | | |
| Spot size (µm) | 20.0 | 20.0 | 20.0 | 20.0 | 20.0 | 20.0 | | | | | | | |
| Rb (ppm) | 458 | 450 | 468 | 456 | 542 | 446 | 432 | 416 | 376 | 272 | 530 | 479 | 373 |
| Sr | 3.2 | 4.0 | 3.2 | 3.0 | 2.4 | 2.7 | 49.8 | 4.8 | 5.9 | 18.3 | 2.6 | 3.8 | 5.9 |
| Y | 64 | 62 | 62 | 65 | 64 | 63 | 48 | 65 | 51 | 31 | 75 | 70 | 49 |
| Zr | 623 | 623 | 635 | 610 | 604 | 634 | 604 | 576 | 434 | 247 | 824 | 715 | 415 |
| Nb | 108 | 103 | 104 | 107 | 108 | 106 | 112 | 100 | 74 | 42 | 125 | 116 | 71 |
| Ba | 3.8 | 4.5 | 4.0 | 3.7 | 3.3 | 3.6 | 5.2 | 5.0 | 5.0 | 12.9 | 3.7 | 3.5 | 5.4 |
| La | 135 | 129 | 132 | 134 | 133 | 132 | 120 | 127 | 103 | 67 | 159 | 144 | 104 |
| Ce | 274 | 259 | 269 | 271 | 268 | 264 | 228 | 268 | 215 | 133 | 302 | 293 | 202 |
| Pr | 27 | 26 | 28 | 28 | 27 | 27 | 23 | 28 | 21 | 15 | 31 | 31 | 22 |
| Nd | 102 | 92 | 101 | 96 | 96 | 99 | 80 | 107 | 85 | 55 | 111 | 114 | 80 |
| Sm | 18.1 | 16.0 | 16.9 | 16.8 | 17.9 | 18.7 | 14.7 | 21.1 | 18.1 | 9.7 | 15.8 | 18.6 | 13.7 |
| Eu | 1.19 | 1.03 | 1.08 | 1.16 | 1.05 | 1.07 | 1.86 | 1.29 | 1.27 | 1.40 | 0.98 | 1.14 | 1.23 |
| Gd | 13.4 | 13.3 | 12.6 | 12.0 | 11.6 | 13.7 | 9.8 | 13.9 | 10.3 | 6.9 | 13.4 | 15.0 | 10.4 |
| Dy | 11.8 | 10.7 | 11.9 | 11.7 | 11.9 | 11.8 | 9.0 | 12.9 | 9.9 | 6.4 | 12.4 | 13.2 | 9.2 |
| Er | 6.8 | 6.2 | 6.3 | 6.5 | 6.3 | 6.6 | 4.8 | 6.6 | 4.9 | 3.0 | 7.3 | 7.1 | 4.6 |
| Yb | 6.3 | 6.6 | 6.3 | 6.5 | 6.9 | 6.0 | 5.0 | 6.3 | 3.8 | 3.2 | 7.4 | 7.4 | 4.3 |
| Lu | 0.94 | 0.87 | 0.99 | 0.98 | 0.92 | 0.96 | 0.73 | 0.95 | 0.76 | 0.41 | 1.11 | 1.09 | 0.80 |
| Ta | 5.4 | 5.2 | 5.4 | 5.0 | 5.2 | 5.3 | 5.3 | 5.7 | 4.3 | 2.2 | 5.3 | 5.9 | 3.4 |
| Th | 42 | 41 | 43 | 43 | 42 | 43 | 52 | 38 | 29 | 17 | 51 | 47 | 28 |
| U | 13.2 | 13.0 | 14.1 | 12.7 | 12.9 | 13.4 | 16.3 | 11.5 | 9.1 | 5.0 | 16.2 | 14.5 | 8.1 |

Table 6.3: Continued.

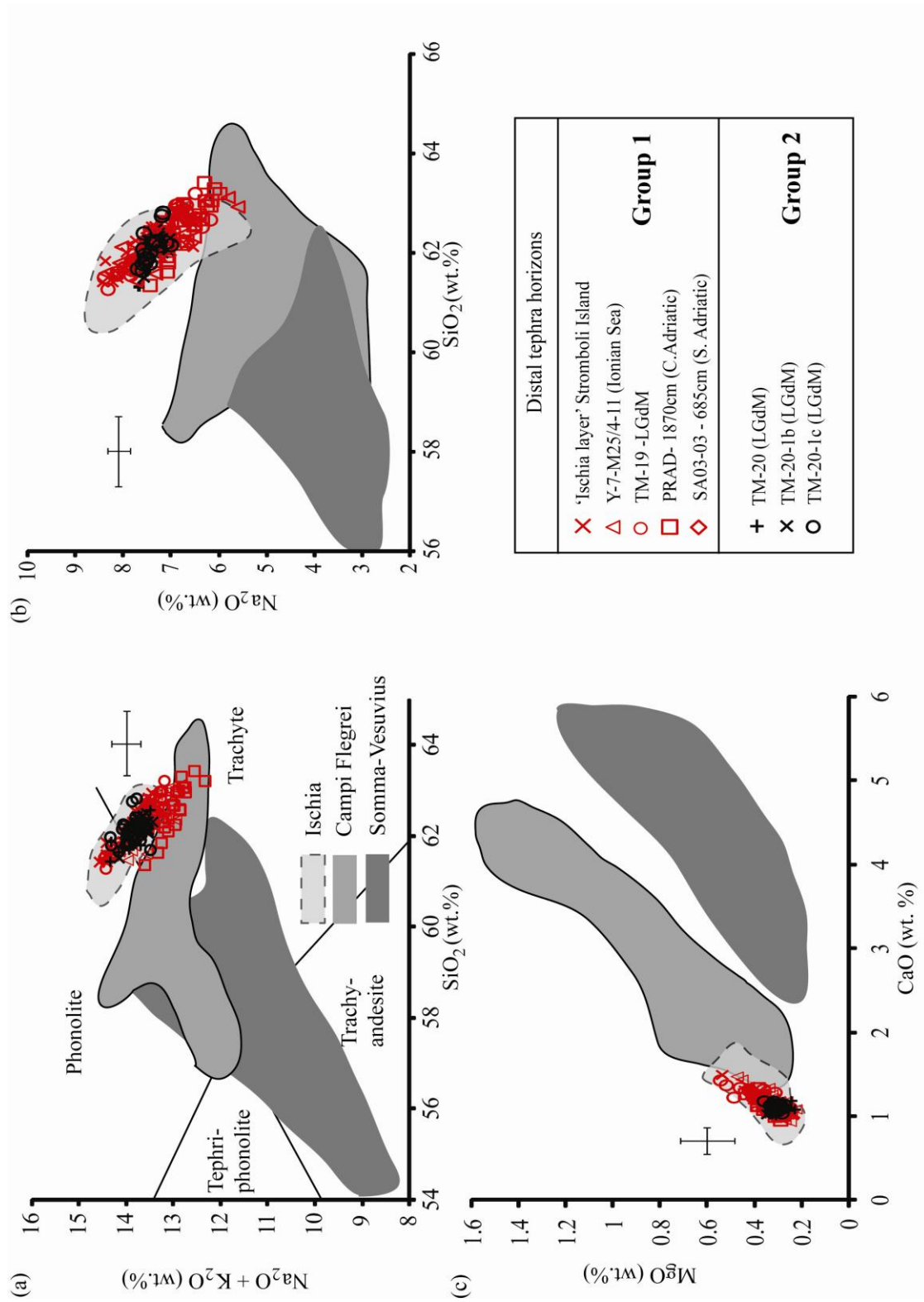


Figure 6.7: Major element bi-plots displaying the glass compositions of the 'Ischia tephra' layer Stromboli, Y-7 tephra, Ionian Sea (M25/4-11), Lago Grande di Monticchio tephtras TM-19, TM-20, TM-20-1b, TM-20-1c and the Adriatic tephtras PRAD 1-2 1870cm and SA03-03 685cm. Also shown are the glass compositional fields of Ischia Island (ca.100-50 ka; includes

the Sant' Angelo , Olummo, Tisichiello, Porticello, MEGT and Schiappone tephra); Campi Flegrei (ca. 60-12 ka; Pre-Campanian Ignimbrite tephra, Campanian Ignimbrite, VRb, VRa, PRa, Neapolitan Yellow Tuff, Pomici Principale; Tomlinson et al., 2012b) and Somma-Vesuvius (ca. 33-12 ka Codola, Pomici di Base, Verdoline; unpublished data).

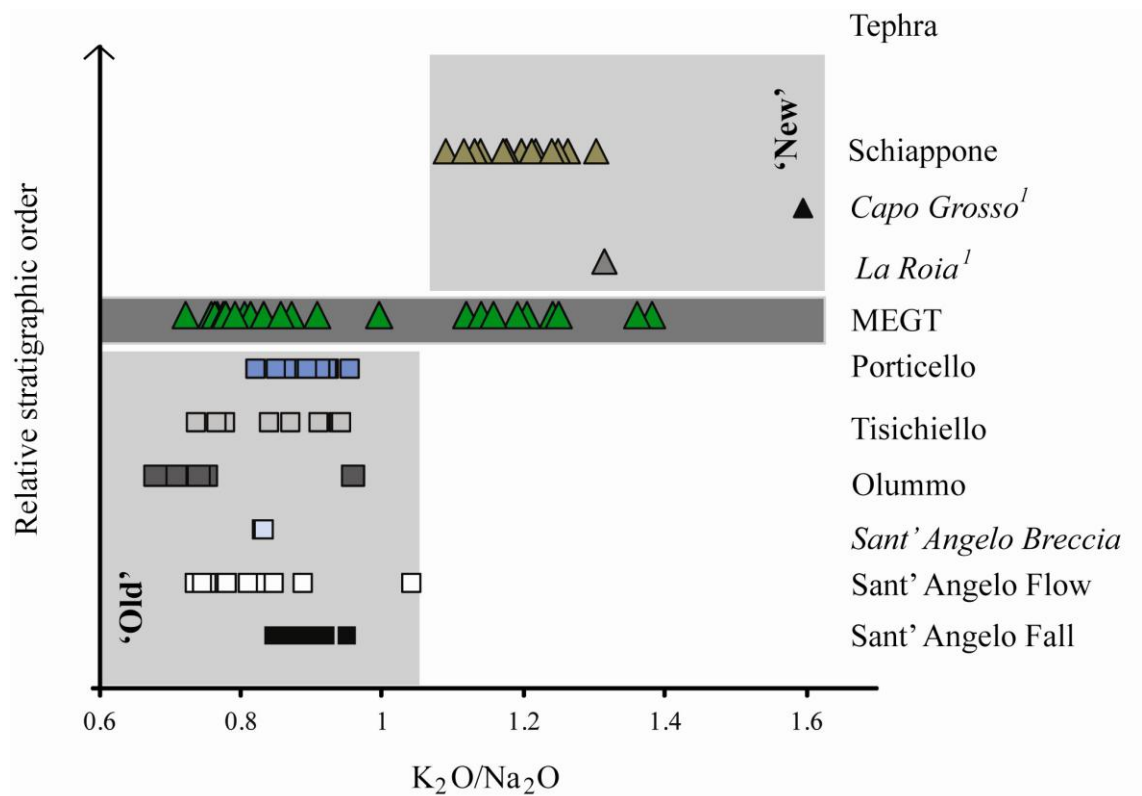


Figure 6.8: K_2O/N_2O through the Ischia stratigraphy between ca.100-50 ka. Stratigraphic units presented in italic are based on whole rock data. ⁽¹⁾ Data from Brown et al., (2008).

The glasses display significant depletions in Ba, Sr and Eu relative to other incompatible trace elements indicative of K-feldspar fractionation (4-23 ppm Ba, 3-14 ppm Sr, $Eu/Eu^*_N = 0.2$) (Fig. 6.10b). HFSE ratios to Th are constant within the glasses ($Nb/Th = 2.52 \pm 0.14$; $Zr/Th = 15.1 \pm 0.6$; $Ta/Th = 0.12 \pm 0.01$) (Fig. 6.10e).

The remaining distal tephra have been separated into two compositional groups based on major and trace element geochemical similarities, the 'Ischia tephra' layer Stromboli compositionally falls within group 1. Full geochemical descriptions of the individual distal tephra are given in Appendix II.

6.2.2.3 Group 1

Group 1 comprises the 'Ischia tephra' layer Stromboli, TM-19 in Lago Grande di Monticchio (LGdM) and the following marine tephra, Y-7 tephra, Ionian Sea (M25/4-

11), PRAD 1870 cm and SA03-03 685 cm. These tephras display major element variability ranging from phonolitic to trachytic glass compositions (Fig. 6.9a), glasses display significant ranges in CaO and MgO (Fig. 6.10b). Glasses with both $\text{Na}_2\text{O} > \text{K}_2\text{O}$ and $\text{K}_2\text{O} \geq \text{Na}_2\text{O}$ are reported in these tephra layers (Fig. 6.10a) and lower Na_2O is observed in the higher SiO_2 glasses (Fig. 6.10c). Trace element concentrations indicate highly evolved melts ranging from $\text{Zr}/\text{Sr} = 7\text{-}385$. These distal tephra layers display particularly heterogeneous trace element geochemistry (Fig. 6.10d-f; Table 6.3). Similarly to the '*Ischia tephra*' layer these distal glasses show comparable LREE enrichment ($\text{La}/\text{Yb} = 21.7 \pm 1.9$) and display significant depletions in Sr, Ba and Eu indicative of feldspar fractionation (Fig. 6.9b; Table 6.3). These tephras are all characterised by constant and consistent HFSE/Th ratios (Table 6.3).

6.2.2.3 Group 2

Group 2 comprises three investigated tephra layer from LGdM; TM-20; TM-20-1b and TM-20-1c, these layers are grouped because they comprise exclusively of phonolitic to trachytic glasses (Fig. 6.9a) where $\text{Na}_2\text{O} > \text{K}_2\text{O}$ and are more restricted (Fig. 6.10a). Major element glass compositions are far more homogeneous than the group 1 tephras, displaying more limited variation in CaO and MgO (Fig 6.10b). Trace element compositions are homogenous in contrast to group 1 tephras (Fig. 6.10d-f). Levels of evolution are more restricted in these tephras with $\text{Zr}/\text{Sr} = 44\text{-}255$. Glasses display significant LREE enrichment ($\text{La}/\text{Yb} = 20.5 \pm 1.1$) and display tight ratios of HFSE elements to Th (Table 6.3). Observed concentrations of Ba (< 15 ppm), Sr (< 15 ppm) and Eu (< 1.2 ppm) are low relative to other incompatible trace elements (Table 6.3).

6.2.3 Discussion

6.2.3.1 Diagnostic glass geochemistry between 100-50 ka within the Ischia deposits

In order to assess the provenance of distal tephras it is important to identify some of the key diagnostic features of the proximal succession erupted between 100-50 ka on the island of Ischia. Recognising such features is crucial to determining the precise provenance solutions for the distal tephras.

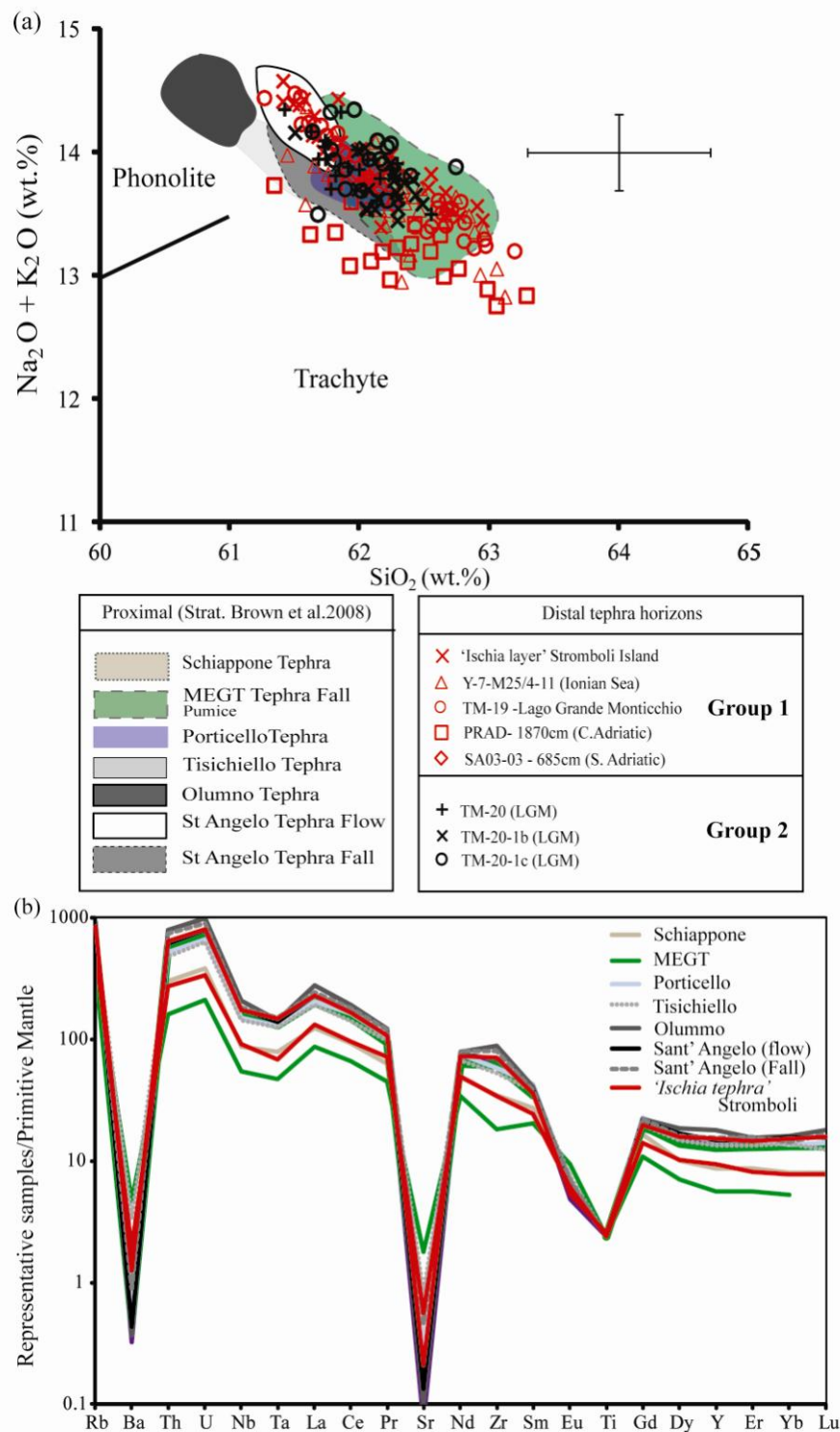


Figure 6.9: (a) TAS classification diagram displaying the 'Ischia tephra' Stromboli, whilst other distal tephras associated with explosive volcanism on Ischia between 75-55 ka. Including the four layers recorded at Lago Grande Monticchio, the Y-7 tephra from the Ionian Sea and PRAD 1870 cm Central Adriatic (Bourne 2012). Ischia compositional fields are given for the proximal glass deposits characterised following the stratigraphy of Brown et al. (2008). (b) Representative proximal glasses and the 'Ischia tephra' layer normalised to Primitive Mantle (Sun and McDonough, 1989).

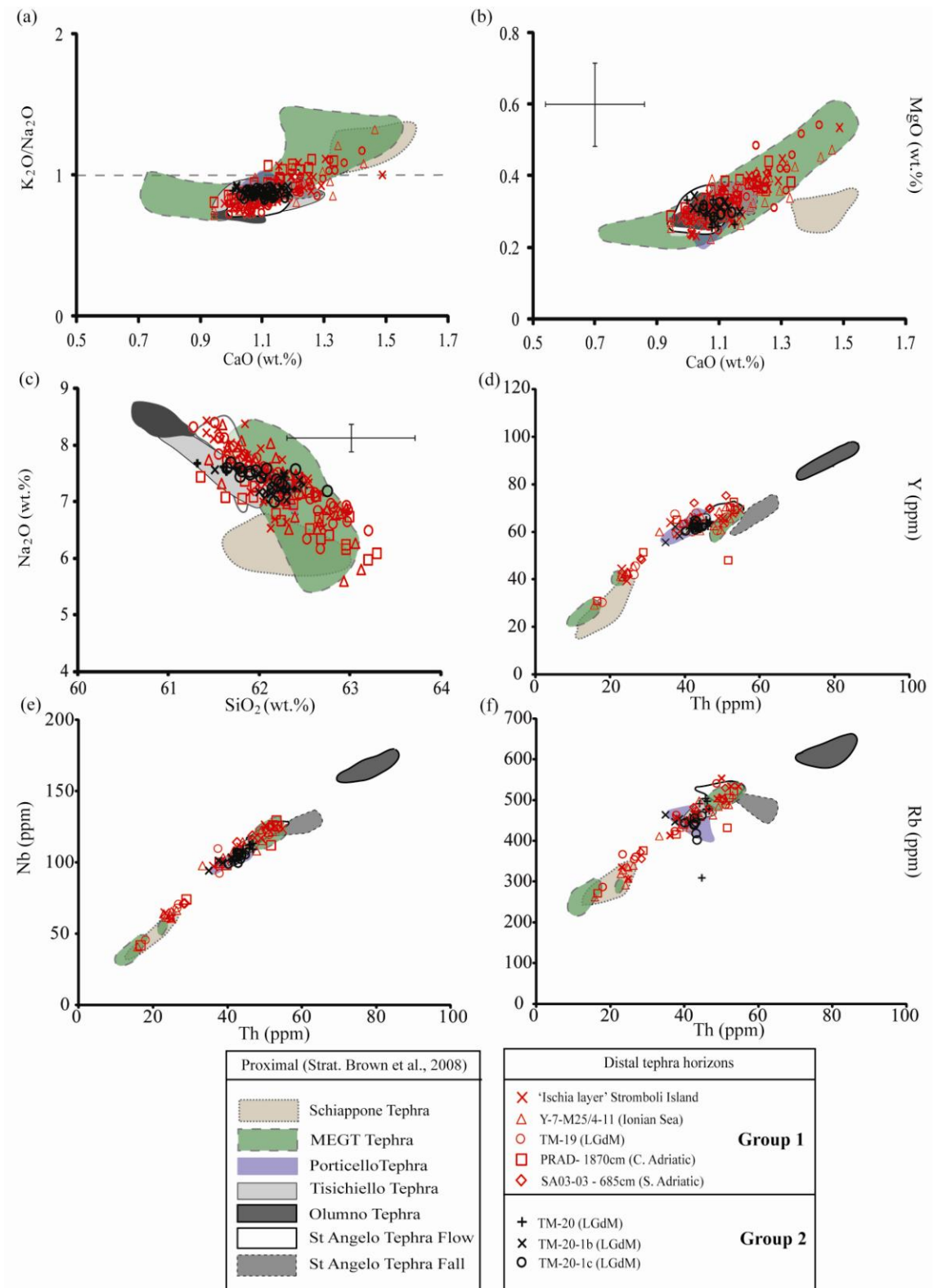


Figure 6.10: Major and trace element bi-plots displaying the 'Ischia tephra', whilst other distal tephras attributed to explosive volcanism on the island of Ischia between 75-55 ka. Also given are the compositional fields of proximal glasses of Ischia. Errors for trace element plots (d-f) are smaller than data symbols presented.

(i) Pre-MEGT (100-56 ka)

The pre-MEGT succession comprising the Sant' Angelo, Olummo, Tisichiello and Porticello tephra (Brown et al., 2008) are all phono-trachytic glasses, where $\text{Na}_2\text{O} > \text{K}_2\text{O}$ dominates (Fig. 6.8, 6.9a, 6.10a). Thus the exclusivity of $\text{Na}_2\text{O} > \text{K}_2\text{O}$ is the diagnostic of these Pre-MEGT glasses with $\text{Na}_2\text{O} > 7$ wt.% (Fig. 6.10c). These glasses are very difficult to distinguish at a major element level (Fig. 6.9a; 6.10a-c). The Olummo tephra presents an exception, it can be distinguished from the other Pre-MEGT tephra given that these phonolitic glasses comprise of the lower SiO_2 (Fig. 6.9a) and higher Na_2O (> 8 wt.%; Fig. 6.10a,c).

Trace element concentrations in these pre-MEGT tephra enable some further distinctions. Again the Olummo tephra can be easily distinguished on the basis of significantly more elevated incompatible trace element concentrations (Fig. 6.10d-f). The Sant' Angelo tephra presents the most significant variability of all the pre-MEGT eruptions (Fig. 6.10d-f).

Sant' Angelo fall is clearly distinguishable from the other Pre-MEGT tephra, with the exception of Olummo tephra, it displays most elevated incompatible trace element concentrations in the remaining pre-MEGT glasses (Fig. 6.9b; 6.10d-f). Yttrium in the Sant' Angelo fall tephra is lower at overlapping Th concentrations with other pre-MEGT tephra (Fig. 6.10d), whilst Rb extends to lower values with increasing Th (Fig. 6.10f).

The associated ignimbrite deposits of the Sant' Angelo tephra displays lower incompatible trace element concentrations than the fall deposits (Fig. 6.9b; 6.10d-f). With the exception of a single analysis these Sant' Angelo ignimbrite deposits show more elevated incompatible trace element compositions than the sub-Plinian pre-MEGT Tisichiello and Porticello tephra. In the Sant' Angelo ignimbrite glasses Rb concentrations are more elevated at overlapping Th than those of the Tisichiello and Porticello tephra (Fig. 6.10f). These two sub-Plinian deposits display homogeneous and overlapping trace element compositions that are the least evolved of the pre-MEGT deposits (Fig. 6.10d-f).

(ii) MEGT (ca. 56 ka; Vezzoli 1988)

The MEGT eruption involves the most geochemically diverse magmas erupted on Ischia between 100-50 ka. The lowermost extra-caldera pumice fall (i.e. the opening

stages of the MEGT eruption; (Brown et al., (2008)), comprises phono-trachytic (Fig. 6.8) pumiceous glasses with $\text{Na}_2\text{O} > \text{K}_2\text{O}$, consistent with the pre-MEGT deposits (OIS0333; OIS0321; Table 6.2). In contrast higher in the stratigraphy the extra-caldera pumices switch to exclusively trachytic (Fig. 6.8) glass compositions with $\text{K}_2\text{O} \geq \text{Na}_2\text{O}$ (OIS0325; OIS0319; Table 6.2). This feature is also observed within the Lower MEGT (LMEGT) intra-caldera co-ignimbrite ash deposits (Brown et al., 2008) (Table 6.2). Accordingly Na_2O values are lower within the subtly higher SiO_2 glasses of the upper extra-caldera MEGT deposits and the LMEGT intra-caldera glasses (Table 6.2). Consequently the glass compositions erupted during the entire MEGT suite displays the most variation in Na_2O , extending to lower values than observed in any of the pre-MEGT eruptions (Fig. 6.10c). Whilst changes in alkalis are a particularly useful indicator of MEGT, CaO and MgO also display significant and diagnostic variability when distinguishing MEGT deposits from pre-MEGT deposits (Fig. 6.10b). CaO and MgO extend to more elevated concentrations in MEGT glasses (Fig. 6.10b). Major element data indicate a switch in magma composition beneath Ischia prior to and during the MEGT eruption, where an injection of a new magma may have triggered the MEGT eruption. This major element variability is reflected in the trace element concentration of the MEGT glasses. The most evolved phono-trachytic glasses with $\text{Na}_2\text{O} > \text{K}_2\text{O}$ show concentrations consistent with the older Sant' Angelo ignimbrite deposits (Fig. 6.10d-f), whilst glasses with $\text{K}_2\text{O} > \text{Na}_2\text{O}$ display less elevated incompatible trace element concentrations (i.e. 15-20 ppm Th; Fig. 6.10d-f). The LMEGT bulk glass analyses presented by Brown et al., (2008) provides a further separate and distinct less evolved component (~ 22 ppm Th; Fig. 6.10d-f) adding to the MEGT trace element variability.

(iii) Post-MEGT (55-50 ka)

The MEGT deposits mark the introduction of magmas with $\text{K}_2\text{O} \geq \text{Na}_2\text{O}$. This geochemical feature persists in the post-MEGT stratigraphy (Fig. 6.8) according to whole rock geochemical data from the overlying *Capo Grosso* and *La Roia* tephra (Brown et al., 2008) and glass data from the voluminous Schiappone tephra. Glass data support the stratigraphic separation of the Schiappone tephra from the MEGT deposits (Fig. 6.3; Brown et al. 2008), given that Schiappone glasses display significantly more elevated CaO at a similar MgO to the MEGT glasses (Fig. 6.10b). The proposed temporal gap of ~ 6 ka between the emplacement of MEGT and the Schiappone tephra (Brown et al., 2008) is marked by another compositionally discrete magma. The

Schiappone magma displays lower concentration of incompatible trace elements, consistent with the least enriched glasses introduced during the MEGT eruption (Fig. 6.10d-f).

In summary, whilst significant geochemical overlaps exists within the magmas explosively erupted between 100-50 ka on Ischia, the MEGT tephtras can be distinguished from the pre-MEGT tephtras on the basis of greater alkali variability (Fig. 6.8), extension to higher CaO and MgO values (Fig. 6.10b) and a far greater range in incompatible trace element concentrations (Fig. 6.10d-f).

6.2.3.1 Proximal-distal correlations:

The origin of the distal '*Ischia tephra*' layer on Stromboli is discussed in the context of this major, minor and trace element data. Since geochemically distinct sub-populations exist within the distal tephtras, a statistical approach was considered meaningless as it assumes normally distributed populations. Thus either similarity coefficients or statistical distance tests would generate 'averages' which are unrepresentative of real glass/magma compositions present.

The '*Ischia tephra*' layer within group 1 is discussed separately as it formed the initial focus of this study.

'Ischia tephra' layer Stromboli

There can be little doubt that the '*Ischia tephra*' layer derives from explosive activity on Ischia, because the glasses display lower CaO and higher Na₂O at a similar SiO₂ wt.% than the glasses produced at either Campi Flegrei and Vesuvius (Fig. 6.7). This is consistent with previous interpretations (Keller 1980; Morche 1988 and Lucchi et al. 2008). These phonolitic to trachytic glasses overlap the fall and flow deposits of the pre-MEGT eruptions (Sant' Angelo; Tisichiello and Porticello tephtras) and MEGT itself (Fig. 6.9a). They can be distinguished from the pre-MEGT Olummo tephra or the post-MEGT Schiappone tephra (Fig. 6.9a; 6.10a-c).

The '*Ischia tephra*' layer has major element variability that is important in linking it to precise proximal deposits on Ischia. Two major element components can be identified; (1) phono-trachytic glasses where Na₂O > K₂O (K₂O/Na₂O = 0.7-0.9) and; (2) trachytic glasses where K₂O ≥ Na₂O (K₂O/Na₂O = 0.95-1.11) (Fig. 6.9a; 6.10a).

The higher SiO₂ trachytic glass components display significantly lower Na₂O than the trachy-phonolitic glasses and extend to higher CaO and MgO values (Fig. 6.10b-c). The presence of both these components is consistent with the diagnostic features of the proximal MEGT glasses (Fig. 6.10b-c). Although the phono-trachytic component of this ash layer is consistent with the Sant' Angelo tephra (Fall and Flow), the additional major element variability is not observed in the Sant' Angelo tephra (Fig. 6.10a-c). Major element glass data indicate that the greater variability observed in the MEGT proximal sequence offers a more satisfactory proximal solution for the '*Ischia tephra*' layer than the Sant' Angelo tephra (Morche 1988; Lucchi et al., 2008),

Trace element analyses from shards in the '*Ischia tephra*' layer, Stromboli, reveal significant variability (i.e. 23-55 ppm Th) (Fig. 6.10d-f). Trace element concentrations observed in the '*Ischia tephra*' shards broadly form separate clusters (Fig. 6.10d-f). The most enriched glasses (49-55 ppm Th) are associated with the phono-trachytic glasses, where Na₂O > K₂O. These glass compositions overlap the trace element compositions of the Sant' Angelo flow deposits and the earliest extra-caldera Plinian pumice fall of the MEGT eruption.

Only this cluster of trace element compositions overlap the field of the Sant' Angelo tephra. The '*Ischia tephra*' layer does not record shards with the greater levels of trace element enrichment that are observed within the acmite bearing basal Plinian fall pumices of the Sant' Angelo tephra (Fig. 6.9b; 6.10d-f). Where Th concentrations in the distal tephra do overlap with the Sant' Angelo fall pumices (a single analyses), the distal tephra observes more elevated Y and Rb consistent with the MEGT (Fig. 6.10d; f).

The proximal data enable us to confidently rule out the Sant' Angelo Plinian fall as the source of the '*Ischia tephra*' layer on Stromboli (Fig. 6.10d; f). Whilst the trace element geochemistry indicates that the '*Ischia tephra*' partially overlaps the ignimbritic component of the Sant' Angelo tephra (Fig. 6.10d-f), significant compositional variability exists in this distal ash layer that is not present within the Sant' Angelo tephra. The only other stratigraphic component of the Sant' Angelo tephra to be considered is the monomict lag breccias that cap the fall and flow deposits (Fig. 6.3). These deposits display even more elevated incompatible trace element concentrations (Table 6.2) than in the underlying pumices and do not present a comparable geochemical variability comparable to the distal tephra. This breccia is interpreted as a localised block and ash flow resulting from dome collapse, that may have mark the end of the Sant' Angelo eruption (Brown et al., 2008).

A second cluster of less enriched glasses (33-43 ppm Th) are identified within the '*Ischia tephra*' layer (Fig. 6.10d-f). They overlap with the compositions of the sub-Plinian phono-trachytic Porticello and Tisichiello tephras (Fig. 6.10d-f). Neither the investigated Sant' Angelo or MEGT tephras have these trace element concentrations.

Finally the least evolved glasses (23-25 ppm Th) observed in the '*Ischia tephra*' layer appear to correspond to a bulk ash sample of the LMEGT intra-caldera ignimbritic deposits (Fig. 6.9d; Brown et al., 2008). These distal shards are characterised by $K_2O \geq Na_2O$ and are derived from the upper sample of the '*Ischia tephra*' layer.

The trace element variability in the glass geochemistry of the '*Ischia tephra*' layer Stromboli indicates either;

- (1) Composite ash fall recording multiple explosive eruptions from the Ischia (pre-MEGT/MEGT composite); or
- (2) Ash fall from a single eruption, a eruption that taps the discrete and differentiated magmas residing beneath Ischia. Consequently encompassing much of the variability in melt compositions observed at Ischia during this period of explosive volcanism.

The former is unlikely, because on Ischia palaeosols are interbedded within the pre-MEGT deposits (Brown et al., 2008), whilst there is no evidence of temporal gaps in the deposition of the '*Ischia tephra*' layer on Stromboli (Fig. 6.2). The latter seems more plausible, trace element variability in the glasses produced within the pre-MEGT succession (i.e., Sant' Angelo, Olummo, Tisichiello and Porticello tephras) indicates the presence of subtly discrete melt compositions beneath Ischia (Fig. 6.10d-f). Whilst the MEGT eruption appears to encompass much of this variability and more, including the introduction of new melt compositions where $K_2O \geq Na_2O$, CaO and MgO extend to higher values and incompatible trace element concentrations are lower.

Given the major and trace element glass variability observed in the '*Ischia tephra*' layer, Stromboli, it would seem the MEGT proximal variability offers the most compelling correlation. However the presence of acmite in the distal layer and its absence in the MEGT deposits remains an unresolved issue. The distal '*Ischia tephra*' contains some shards with compositions that are not currently represented in the MEGT glass data, but this could be a sampling bias. Sampling of MEGT deposits focused on extra-caldera juvenile pumices, yet much of the intra-caldera deposits are characterised by altered ash (Brown et al. 2008). Whilst bulk glass analyses broadly correspond with

a trace element cluster within the Ischia tephra layer (~ 22 ppm Th), the full trace element variability of these deposits remains uncharacterised at a grain-specific level. Overall the geochemical diversity that is currently presented for the MEGT is far greater than that of any single pre-MEGT eruptions. This variability is possibly related to caldera formation (Vezzoli, 1988; Rossi et al., 1988), with the partial destruction of the magma chamber (Brown et al., (2008) enabling the tapping of discrete melts.

6.2.3.2 Further proximal-distal tephrocorrelations and implications

Group 1

The remaining distal tephra layers, Group 1, are also correlated with the MEGT eruption based on their major and trace element glass geochemistry. Consequently TM-19 (Lago Grande di Monticchio) and marine tephra the Y-7 (Ionian Sea), PRAD 1870cm and SA03-03 685cm (Adriatic) are all considered the distal equivalent of the caldera forming MEGT eruption. They all display the diagnostic features unique to the MEGT eruption on Ischia (~ 56 ka; Vezzoli). These include wider ranging phonotrichytic compositions (Fig. 6.9a) where alkali ratios are more variable, with both $\text{Na}_2\text{O} > \text{K}_2\text{O}$ and $\text{K}_2\text{O} \geq \text{Na}_2\text{O}$ glasses (Fig. 6.10a), reflecting a negative relationship between increasing SiO_2 and Na_2O (Fig. 6.10c). Furthermore all these tephra display glasses extending to higher CaO and MgO values (Fig. 6.10b). These distal tephra layers show wider ranges in incompatible trace element concentrations than any of the other pre-MEGT deposits and are more consistent with the range observed in the MEGT (Fig. 6.10d-f). TM-19, Y-7 and PRAD 1870 display the most significant range in incompatible trace elements concentrations of all the distal tephra layers investigated, glasses with lower Na_2O display the least evolved glass compositions consistent with the MEGT suite (Fig. 6.10d-f; Table 6.3).

Major and trace element glass data presented herein (Fig. 6.9; 6.10) reinforce the previously proposed distal link between the '*Ischia tephra*' layer on Stromboli and the Y-7 marine tephra (Morche 1988; Gillot and Keller, 1993; Kraml 1997; Lucchi et al. 2008). This confirms that they represent a contemporaneous southern ash dispersal from Ischia. Previously both were related to the Sant' Angelo tephra, a correlation strongly influenced by the presence of acmite in both the distal tephra deposits (Table 6.1), a phase only recognised in the Sant' Angelo tephra. Comparing the two distal tephra to proximal glass data sets presents a different interpretation to their proximal counterpart. Sant' Angelo glasses do not display the compositional variability observed in the distal

tephras particularly noticeable is the absence of the higher CaO and MgO values observed in the two distal tephra deposits. At a trace element level only the ignimbritic components of the Sant' Angelo tephra offers any form of correlative, yet this only satisfies a single component of the Y-7 glasses. A significant portion of the Y-7 glasses remain unrepresented by the Sant' Angelo tephra. Indeed the Y-7 tephra does not display the elevated incompatible trace element concentrations observed in the thick Sant' Angelo fall tephra or the monomict lag breccia (Table 6.2). Furthermore the distal tephra does not display diagnostic Y and Rb concentrations of the Sant' Angelo Plinian fall (Fig. 6.10d, f).

In summary proximal glasses with less enriched trace element compositions are not observed in the Sant' Angelo stratigraphy, including the Plinian fall, flow and subsequent dome collapse (Fig. 6.10d-f; Table 6.2). Therefore the Sant' Angelo tephra is unlikely to be the proximal equivalent of the Y-7 marine tephra based on glass data presented. As discussed above, MEGT offers a better glass correlation to the Ischia layer and by extension the Y-7.

Mid-distal tephras from Lago Grande di Monticchio (LGdM) were investigated in an attempt to refine the provenance solutions of the distal Ischia tephras produced between ca. 55-65 ka ($^{40}\text{Ar}/^{39}\text{Ar}$ and varve chronology). All the distal tephras investigated at LGdM originated from Ischia (Fig. 6.4) (see Wulf et al., 2004). Given its attribution to group 1, TM-19 is confirmed as a distal correlative of the MEGT caldera forming eruption. Major and trace element glass data confirm the previous correlation of TM-19 to the MEGT eruption (Wulf et al., 2004). Wulf et al., (2004) had correlated TM-19 to the MEGT (ca. 56 ka; Vezzoli 1988) based on its Ischia type major element glass chemistry, its prominent thickness in the (32 cm), mineral assemblage and a comparable age determinations for TM-19 (55 ± 2 ka; $^{40}\text{Ar}/^{39}\text{Ar}$). The precise major and trace element glass correlations between MEGT and TM-19 glasses nicely complement these other parameters. The $^{40}\text{Ar}/^{39}\text{Ar}$ age constraints of this distal tephra correspond well with the cluster of proximal age determinations for the intra-caldera MEGT deposits ca. 56 ka (Vezzoli 1988; Brown et al. 2008). The MEGT represents the largest volcanic event recorded on Ischia (Vezzoli 1988, Rosi et al. 1988; Brown et al. 2008) and this is consistent with TM-19 representing the thickest Ischia tephra at LGdM. Interestingly TM-19 does not contain acmite (Wulf et al., 2004) yet its glass chemistry is identical to the distal layers that do, Y-7 and the '*Ischia tephra*' layer Stromboli.

Further east from Ischia, in the Adriatic, Bourne (2012) attributed PRAD 1870 cm and SA03-03 685 cm tephra layers (Fig. 6.5) to either TM-19 or TM-20 layers solely on the basis of the major element chemistry of the glasses. Multivariate statistical analysis of major element glass compositions was used to constrain correlations with the LGdM layers. However, this approach was unable to distinguish between TM-19 or TM-20 correlatives (Bourne 2012). This is of course problematic if you want to precisely synchronise these archives. New proximal glass compositions allow the correlation of PRAD 1-2 1870 cm and SA03-03 685cm to MEGT (Fig. 6.10a-c). Trace element data from PRAD 1-2 mirrors precisely the wide trace element variability of the Y-7 and TM-19 tephra (Fig. 6.10d-f), reinforcing these strong distal-distal links.

Group 2

This group comprises of the three phono-trachytic LGdM (TM-20; TM-20-1b and TM-20-1c) that are derived from Ischia (Fig. 6.9a; 6.10). These tephra are recorded stratigraphically below TM-19/MEGT at LGdM. TM-20 is 1310 varve years older than TM-19 (55 ± 2 ka) in LGdM, whilst TM20-1b is 2770 varve years older than TM-20 and TM-20-1c is 330 varve years older than TM-20-1b (Table 6.1). The high resolution LGdM record indicates that these thinner tephra represent temporally separate pre-MEGT eruptions (Table 6.1). These tephra display more homogeneous glass compositions than the Group 1 tephra at both a major and trace element level (Fig. 6.10). They comprise exclusively of glasses where $\text{Na}_2\text{O} > \text{K}_2\text{O}$ ($\text{K}_2\text{O}/\text{Na}_2\text{O} = 0.86\text{--}0.94$; Fig. 6.10a, c), whilst CaO and MgO do not extend to the elevated values of the group 1 tephra (Fig. 6.10b). These features are consistent with the pre-MEGT glasses outlined above. The more homogenous trace element concentrations observed in these glasses lie firmly within the compositional fields of the inter-Plinian Tisichiello and Porticello tephra (Fig. 6.10d-f).

TM-20 was previously attributed to the Y-7 tephra (56 ± 4 ka; Kraml, 1997) and the proximal Sant' Angelo tephra (Wulf et al., 2004), although Y-7 is here reinterpreted as MEGT/TM-19. Links to the Sant' Angelo eruption are problematic. Whilst major elements compositions are similar, at a trace element level the TM-20 glasses only overlap with the very least evolved glasses of the Sant' Angelo ignimbritic deposits (Fig. 6.10d-f). They do not display any of the more dominant elevated compositions seen in this flow component of the Sant' Angelo tephra, or the underlying fall deposits (Fig. 6.10d-f). If this tephra were to relate to the Sant' Angelo tephra it is hard to

envisage why only such a very restricted geochemical overlap would occur, given the overall variability of Sant' Angelo tephra.

Given the confirmed correlation of TM-19 to MEGT, these tephras are stratigraphically and chronologically constrained to older activity. As highlighted above the phono-trachytic group 2 tephras (TM-20; TM-20-1b and TM-20-1c) which display exclusively phono-trachytic glasses with $\text{Na}_2\text{O} \gg \text{K}_2\text{O}$ appear to fall exclusively within the more restricted trace element compositional ranges of the inter-Plinian eruptions recorded as the Tisichiello and Porticello tephras (Fig. 6.10d-f). Given that the TM-20 layers only represent thin tephra layers (Table 6.1) it seems plausible that these tephra layers recorded in LGdM provide a distal record of the sub-Plinian activities on Ischia prior to the caldera forming MEGT eruption (Porticello, Tisichiello).

A 20-25 cm palaeosol exists between the MEGT caldera forming deposits and the underlying Porticello formation (Brown et al., 2008). Proximal-distal correlations tentatively suggested that this is representative of 1310 varve years (i.e. between TM-19 and TM-20 in LGdM). Other palaeosols exist between the stratigraphically lower inter-Plinian eruptions and might correspond to temporal gaps recorded between the older TM-20, TM-20-1b and TM-20-1c layers in LGdM (Table 6.1).

Other distal correlatives:

South-west of Ischia in the Tyrrhenian Sea the story is more complex, Paterne et al., (1988) attribute multiple layers (C-16, C-17, C-18) to the 'Green Tuff Series' or MEGT spanning 50-60 ka. Average glass data are not directly comparable, due to different operating parameters. However, the ash layers are considered 'peralkaline' in composition, where predominantly $\text{Na}_2\text{O} \geq \text{K}_2\text{O}$ (Paterne et al., 1988) and this is consistent with the Ischia tephra data presented herein. Based on new proximal data presented here there is potential to try and refine and validate the distal tephras from Ischia recorded in the Tyrrhenian Sea.

6.2.3.3 Tephrochronological implications

Grain-specific major, minor and trace element proximal and distal glass data might require revisions of some existing proximal-distal correlations associated with explosive volcanism on Ischia between 100-50 ka. The diagnostic feature of the MEGT eruption is its heterogeneity with both of the following glass compositions present (Fig. 6.8);

(1) Pre-MEGT: Phono-trachytic glasses where $\text{Na}_2\text{O} > \text{K}_2\text{O}$ and with elevated concentration of incompatible trace elements are consistent with Pre-MEGT activities (Sant' Angelo flow, Tisichiello and Porticello tephtras);

(2) Trachytic glasses with lower Na_2O ($\text{K}_2\text{O} \geq \text{Na}_2\text{O}$), whilst extending to higher CaO and MgO values. Trace element concentrations in these glasses are less elevated and more consistent with the Post-MEGT glasses (i.e. Schiappone).

Consequently distal tephra layers that contain both components can be confidently attributed to the MEGT eruption dated to ca. 56 ka (Vezzoli, 1988) or the medial-distal TM-19 ($^{40}\text{Ar}/^{39}\text{Ar}$; 55 ± 2 ka yrs BP) at LGdM. Consequently the more precise age of 55 ± 2 ka can be imported into the stratigraphy of Stromboli. Glass data herein show that the Y-7 is geochemically identical to TM-19, Y-7 is dated to 56 ± 4 ka yrs BP (Kraml, 1997), these two ages lie firmly within analytical error and support the geochemical links between the two distal tephtras.

Beyond the range of radiocarbon dating, these $^{40}\text{Ar}/^{39}\text{Ar}$ ages present an important chronological marker in the central Mediterranean archives. By refining proximal-distal links between the MEGT glass compositions and the '*Ischia tephra*' layer Stromboli and the Y-7 tephra Ionian Sea it might be possible to extend the known dispersal of this eruption further south, making it one of the most widespread Central Mediterranean tephtras (Fig. 6.11) during the last 100 ka. Furthermore this would increase the known dispersal of the MEGT eruption to over 600 km from source.

TM-20 Ischia tephra layers recorded at LGdM are more homogeneous at a major and trace element level than the other distal tephtras reported and are consistent with the pre-MEGT inter-Plinian eruptions; their thicknesses at LGdM might suggest less widespread dispersals. Correlating distal tephtras to these older sub-Plinian eruptions is more challenging, given that their more restrict compositions fall within the compositional range of the MEGT. Whilst the presence of additional MEGT variability might enable correlations, the absence of this variability does not preclude correlation to the MEGT. These inter-Plinian tephtras demonstrate the problems of repeat geochemistries being produced from a single volcanic centre. In these instances where only the more restrict compositions are identified distally then it might be suggested that the distal tephtra offers only an approximate time bracket associated with this Pre-MEGT/MEGT activities (ca. 53-60 ka). However within some archives, particularly

archaeological sites such a time bracket might offer the most reliable age constraint achievable.

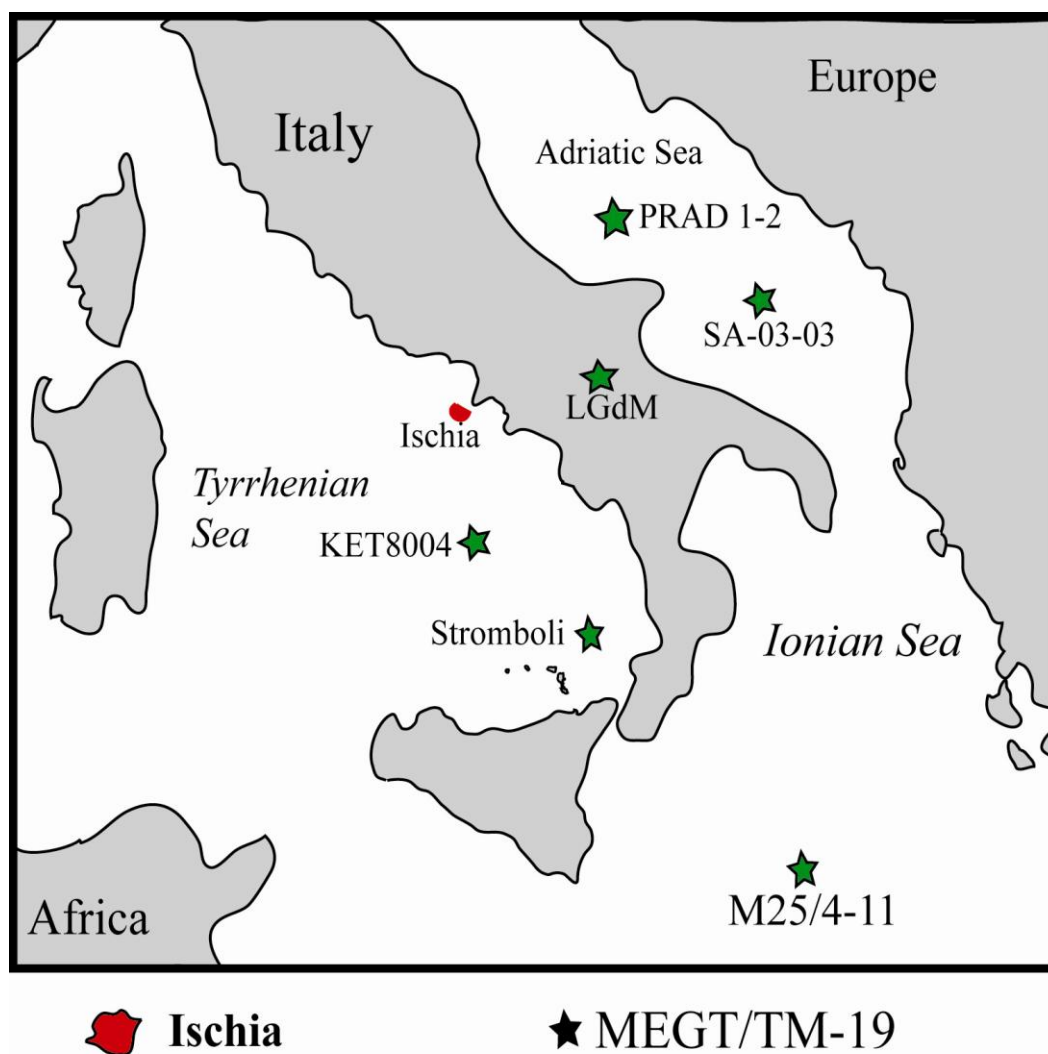


Figure 6.11: A map showing the proposed distribution of distal tephras attributed to the MEGT eruption of Ischia or the medial-distal TM-19 within the central Mediterranean region.

Sant' Angelo tephra

Major and trace element links between these TM-20 layers and the inter-Plinian proximal deposits (Tisichiello and Porticello tephras) on Ischia indicate that the Sant' Angelo tephra may represent even an older explosive event. The only age constraint for this eruption is the 100 ka Sant' Angelo lava dome (Gillot et al. 1982) on which the Sant' Angelo tephra rests, separated by a palaeosol (Brown et al. 2008). At LGdM Ischia type tephras occur between *ca.* 71-69 ka varve years and display $\text{Na}_2\text{O} > \text{K}_2\text{O}$

phono-trachytic compositions consistent with the pre-MEGT glasses including the Sant' Angelo tephra (Wulf 2012 *pers comm.*). As demonstrated above, the Sant' Angelo fall displays a unique and diagnostic trace element signature (section pre-MEGT 100-56 ka; Fig. 6.10d-f). A trace element investigation of these older LGdM Ischia type tephras may enable a precise correlation and provide a more robust chronological constraints for the Sant' Angelo tephra.

Correlating the Y-7 marine tephra to the MEGT eruption and TM-19, means that the Sant' Angelo eruption might not represent as widespread a distal marker as previously thought. Brown et al., (2008) tentatively suggested that the absence of Sant' Angelo elsewhere on the island, might indicate that it was erupted from a small volcanic centre resulting in a minor amount of localised explosive activity. Only through proximal dating of the pyroclastic deposits on Ischia or correlations with LGdM may further light be shed onto the timing of this eruption.

Crucially where the full diagnostic variability of the MEGT eruption is identified in distal tephra layers, it then becomes a powerful tool for the synchronisation of archives across the central Mediterranean region. Precise links between LGdM TM-19 and central Adriatic PRAD 1870 cm can facilitate precise assessment of marine-continental responses to environmental change during the onset of MIS 3. Links between the Ionian Sea Y-7 and the central Adriatic PRAD core can enable further assessment of leads and lags between the different Mediterranean marine basins during this important environmental transition that lies beyond the range of radiocarbon dating.

6.2.4 Summary

- 1.** Major and trace element glass data indicate that the '*Ischia tephra*' layer Stromboli, the Y-7, PRAD 1870, SA03-03 685 and TM-19 are all distal equivalents of the MEGT caldera forming eruption, Ischia.
- 2.** Limited overall major element variability exists within proximal tephra produced prior to the MEGT (100-56 ka).
- 3.** Phono-trachytic glasses with $\text{Na}_2\text{O} > \text{K}_2\text{O}$ dominate the Pre-MEGT explosive eruptions (Fig. 6.8).
- 4.** MEGT tephras display more major, minor and trace element variability than any of the Pre-MEGT explosive eruptions on Ischia (Fig. 6.8; 6.9a; 6.10) due to the introduction of new magma compositions.

5. Whilst comprising partly of Pre-MEGT compositions, the MEGT erupted deposits display an additional component of trachytic glasses with lower Na₂O (Fig. 6.10c) and higher CaO and MgO (Fig. 6.10c).
6. MEGT glasses display significant trace element heterogeneity in accordance with the major element variability observed (Fig. 6.9b, 6.10d-f).
7. Identification of MEGT geochemical variability in distal tephra layers provides the potential to synchronise distal archives across the central Mediterranean basin (Fig. 6.11).

6.3 MIS 5 external tephras outcropping in the Aeolian Islands:

It is often difficult to assign precise provenance to tephras produced prior to MIS 3/4 due to poorly preserved proximal volcanostratigraphy (Di Vito et al., 2008). This is particularly relevant at volcanic centres such as Campi Flegrei, where large caldera collapses (i.e. Campanian Ignimbrite and Neapolitan Yellow Tuff) produced thick pyroclastic successions at source which have buried the older volcanic deposits (Orsi et al. 1996). The best preserved exposures of these older large volume eruptions are in medial-distal localities within colluvial or alluvial deposits (Di Vito et al. 1998; Zanchetta et al., 2004; Di Vito et al., 2008).

Age constraints for these older eruptions can be derived from medial-distal localities, but age can only be exported to other archives if precise correlations are established (i.e., stratigraphy, mineralogy and glass chemistry). Older tephras believed to have originated from the Campanian volcanic zone are best preserved and hence dated, in marine and lacustrine successions (Keller et al., 1978; Paterne et al., 1988; 2008; Kraml 1997; Wulf et al., 2004; 2008; submitted). Approaches include $^{40}\text{Ar}/^{39}\text{Ar}$ dating of K-rich phenocrysts (Kraml 1997) and varve counting of annually laminated lake sediments (i.e. Lago Grande di Monticchio; Wulf et al., 2004; Wulf et al., submitted). Thus in the absence of proximal equivalents it becomes imperative that distal tephras are correlated to well characterised distal tephrostratigraphies with well constrained ages (i.e. deep sea archives; varved lakes).

Two external ash layers on the Aeolian Islands, represent major ash dispersals and have been correlated to the prominent MIS 5 marine tephra layers, the X-5 and X-6 (Morche 1988; Lucchi et al., 2008). These marine tephras were first recognised by Keller et al., (1978) in their type locality, within the Ionian Sea. Based on stratigraphic correlations on the respective Aeolian Islands, both tephras are interpreted as occurring between the high sea level, palaeoshorelines I (MIS 5e) and II (MIS 5c) (Lucchi et al., 2008). This is consistent with the stratigraphic positions of the marine tephras in sediments from MIS 5. Sanidines phenocrysts within the X-5 marine tephra were $^{40}\text{Ar}/^{39}\text{Ar}$ dated at 105 ± 2 ka (Kraml 1997); whilst X-6 has an interpolated age of ca. 108-110 ka (Keller et al., 1978; Kraml, 1997; Keller and Kraml 2004; Wulf et al. Submitted).

| Tephra | GPS | Depth (cm) | Stratigraphic context | Varve Age (yrs BP) | Thickness (mm) | Colour | Phenocrysts | Lithics | Ref |
|---------------------------|------------------------------|------------|--------------------------------------|--------------------|----------------|-------------------|---------------------------|---------|-------|
| Aeolian Islands | | | | | | | | | |
| Panarea Pink Ash | 38° 38.271'N 15° 4.216'E | - | Between MIS 5e and MIS 5c shorelines | - | 100 | pink | Kf, plg, cpx | - | 1,2 |
| Barone tephra/Salina I | 38° 34.320'N 14° 52.260'E | - | Between MIS 5e and MIS 5c shorelines | - | 300 | grey | Kf, cpx, bt, amp | V | 2,3 |
| LGdM | | | | | | | | | |
| TM-24a | | 6929.7 | Within Early St Germain | 101,800 | 70 | Pink-brown | plg, cpx, bt, Kf | V | 4,5,6 |
| TM-24b | | 7019.8 | Within Early St Germain | 102,800 | 97 | Pale brown | plg, kf, cpx, bt | V | 4,5,6 |
| TM-25 | | 7411 | Within Early St Germain | 105, 480 | 113 | clear-light brown | Kf, plg, bt, amp, cpx, ol | V | 4,5,6 |
| TM-27 | | 7885 | Within Melisey I (MIS-5.4?) | 108, 330 | 2000 | clear-light brown | Kf, bt, plag. Cpx, amp | V | 4,5,6 |
| Palinuro (Cilento) | | | | | | | | | |
| LeS1 (319) | 40° 3.660'N 15° 16.893'E | - | Stratigraphic level Post MIS 5e | - | 500 | clear | Kf, cpx, plg, bt | V | 7,8 |
| LeS2 (293-294) | 40° 3.341'N 15° 17.011'E | - | Stratigraphic level Post MIS 5e | - | 1000 | light brown | Kf, cpx, bt, amp | V | 7,8 |
| Crati Valley | | | | | | | | | |
| Tarsia | 39, 36.819'N 16° 16.493'E | - | Stratigraphic level Post MIS 5e | - | 800 | clear-light brown | Kf, cpx, bt, amp | V | 9 |
| C. Adriatic | | | | | | | | | |
| PRAD 1-2 | | 2525 | Between MIS 5.4 and MIS 5.2 | - | 100 | clear | - | - | 10 |
| PRAD 1-2 (C. Adriatic) | | 2605 | Between MIS 5.4 and MIS 5.3 | - | 150 diffuse | clear | - | - | 11 |
| PRAD 1-2 (C. Adriatic) | | 2812 | Within MIS 5.4 | - | 500 | clear | - | - | 11 |
| S. Adriatic | | | | | | | | | |
| SA03-03 | | 925 | MIS 5 | - | 150 diffuse | clear | - | - | 11 |

Table 6.4: Details of 'External' MIS 5 tephra layer investigated in the Aeolian Island. Also shown are prominent tephtras investigated for comparative purposes; these include visible tephtra layers from Lago Grande di Monticchio (LGdM), pyroclastic deposits outcropping at Le Saline, Palinuro and at Tarsia in the Crati Valley (Calabria). Finally thick visible tephtras layers from two Adriatic marine cores were investigated. For localities see Figure 6.1. Kf = K-feldspar; plg = plagioclase; cpx = clinopyroxene; bt = biotite; amp = amphibole; ol = olivine. This data build upon the previous investigations of; (1) Lucchi et al. (2007); (2) Lucchi et al. (2008); (3) Keller et al. (1980); (4) Wulf et al. (2004); (5) Brauer et al. (2007); (6) Wulf et al. (submitted); (7) Lirer et al. (1967); (8) Marciano et al. (2008); (9) Carobene et al. (2006); (10) Bourne et al. (2010); (11) Bourne (2012).

'X-5' is identified in the accumulation profiles of Salina (Morche 1988; Kraml 1997 and Lucchi et al., 2008) and Panarea (Lucchi et al., 2007; Lucchi et al., 2008). On Panarea the same tephra deposit, a 10-15 cm thick layer of pink ash outcropping at Punta Falcone (Fig. 6.12), has also been correlated by De Rita et al. (2008) to significantly younger activity on Somma-Vesuvius and more specifically to Pomice di Base eruption (ca. 22 cal yrs BP; Santacrose et al., 2008). At Barone, north-east Salina, Keller (1980) first recognised an alkali-trachytic tephra layer interbedded within palaeo-alluvial deposits (Fig. 6.13). Keller (1980) correlated it to the 'Palinuro layer', Salerno, on the basis of similarities in composition and mineralogy with the pyroclastic succession reported by Lirer et al. (1967) (Fig. 6.13; Table 6.4). Both the Palinuro and Barone tephras were interpreted as trachytic Campanian activity (Lirer et al., 1967; Keller 1980). More recent investigations of the Palinuro tephra have interpreted it as the continental equivalent of the X-6 marine tephra (Marciano et al., 2008).

These two external tephras on Panarea and Salina are investigated using a grain-specific multi-element approach to assess previously proposed correlations. Without detailed geochemical data for the X-5 and X-6, comparisons here are restricted to major elements. In addition prominent tephra deposits recorded in MIS 5 depositional settings from a series of archives in the central Mediterranean are also considered (Fig. 6.1).

6.3.1 Samples:

The Panarea Pink Ash (PPA) layer from Punta Falcone, Panarea (Fig. 6.12) and the Barone tephra, Salina (Fig. 6.13) were sampled, washed and sieved. Shards were analysed for major, minor and trace element compositions (Table 6.5). Other prominent tephras erupted during MIS 5 that are investigated are shown in Table 6.4 with localities shown in Figure 6.1. Thick pyroclastic deposits recorded in colluvial sediments at two localities near Le Saline, Palinuro (Cilento) on the Italian mainland were sampled. A further continental deposit at Tarsia, within the Crati Valley was investigated (Northern Calabria; Fig. 6.13). All three of these deposits are interpreted as stratigraphically outcropping above the MIS 5e terrace (Carobene et al., 2006; Marciano et al., 2008). Visible MIS 5 marine tephras from the central (PRAD1-2) and southern (SA03-03) Adriatic marine cores were also analysed for trace element concentrations to complement existing major element analysis (Bourne et al., 2010; Bourne 2012).

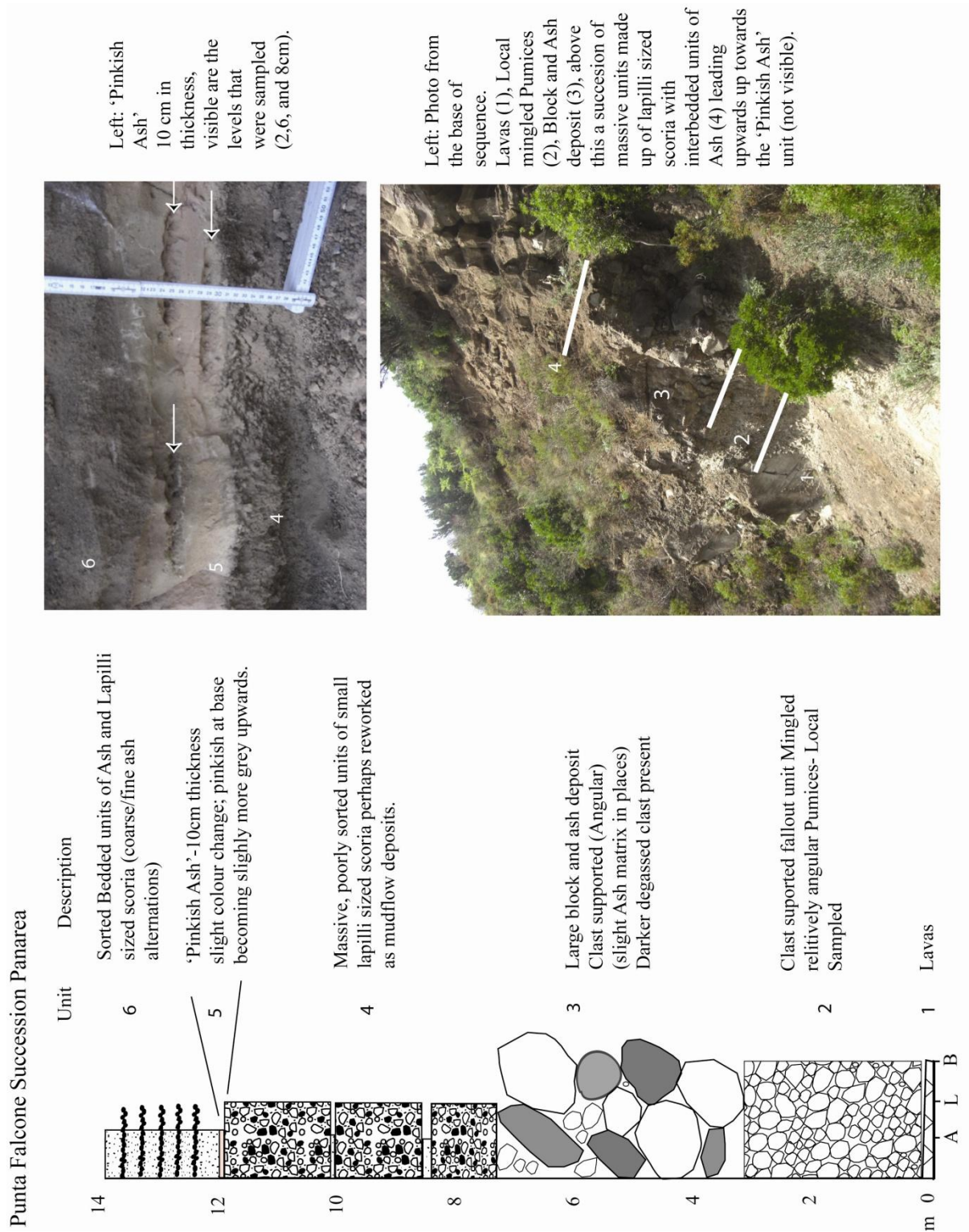
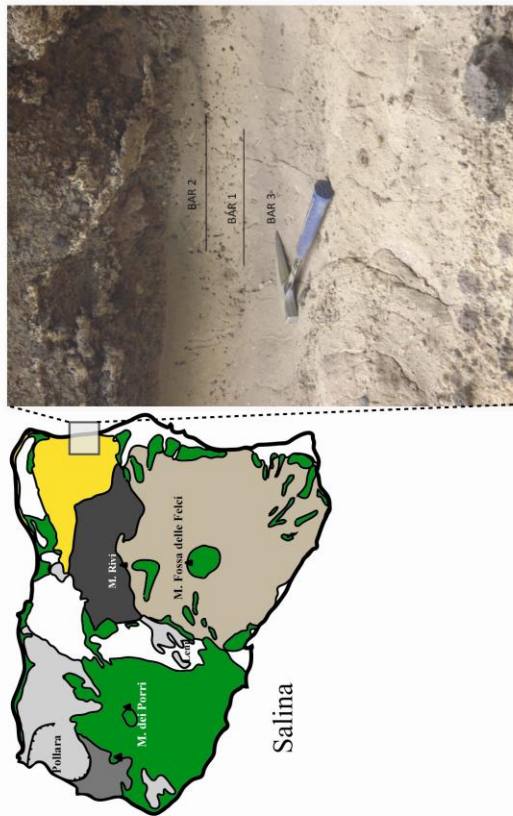
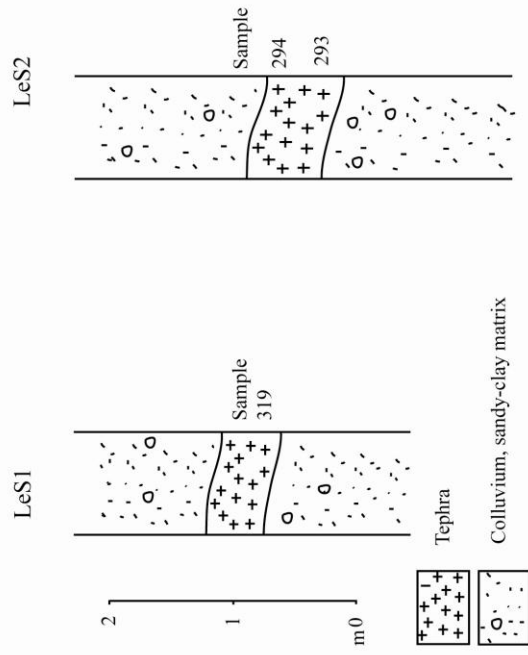


Figure 6.12: Top right insert, the 10-15cm thick, Panarea Pink ash (PPA) and its stratigraphic position within the Punta Falcone stratigraphy.

(a) Barone tephra/ Salina I (Salina)



(b) Le Saline, Palinuro (Salerno)



(c) Tarsia, Crati Valley (N. Calabria)

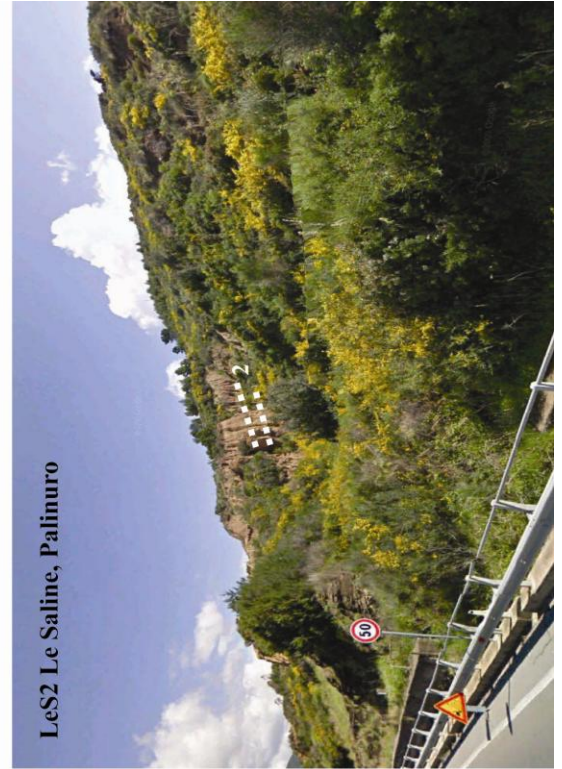
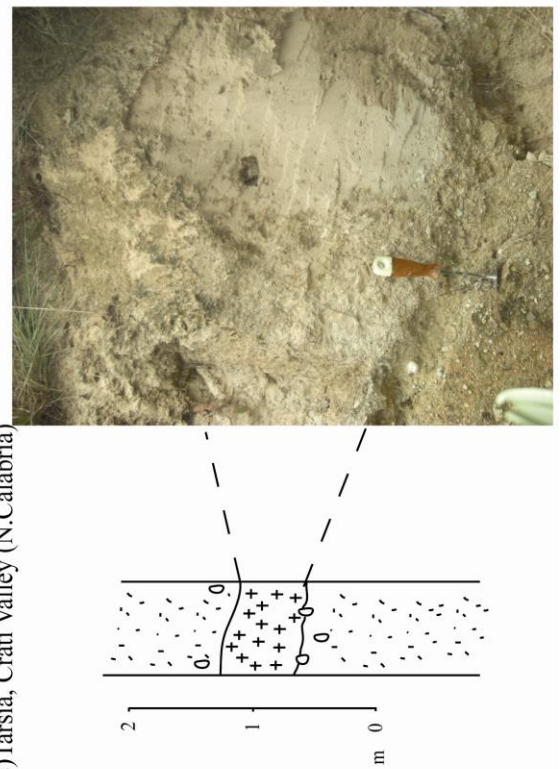


Figure 6.13: Investigated continental outcrops where MIS 5 tephras were sampled; (a) Barone tephra (Salina Island); (b) Le Saline Palinuro (Cilento) and (c) Tarsia, Crati Valley (Northern Calabria).

| | Panarea - Pink Ash (PPA) | | | | Barone tephra/ Salina I | | | Palinuro (Cilento) | | | Palinuro (Cilento) | | | Tarsia (Crati Valley, Calabria) | | | |
|--------------------------------------|--------------------------|-------|-------|-------|-------------------------|-------|-------|--------------------|-----------|-----------|--------------------|-----------|-----------|---------------------------------|-------|-------|-------|
| | Base | | Top | | 10B | 16C | 11C | LeS1 | | | LeS2 | | | Base | | Top | |
| Shard I.D | 6A | 17B | 19B | 31C | | | | 11B (319) | 15B (319) | 36D (319) | 26D (293) | 24D (293) | 13B (294) | 1A | 9A | 1A | 7A |
| SiO ₂ | 59.75 | 60.19 | 53.95 | 57.37 | 63.21 | 62.88 | 62.42 | 61.12 | 61.54 | 61.50 | 61.82 | 61.35 | 61.72 | 62.19 | 62.24 | 62.17 | 62.07 |
| TiO ₂ | 0.43 | 0.48 | 0.99 | 0.72 | 0.40 | 0.53 | 0.48 | 0.40 | 0.45 | 0.35 | 0.49 | 0.55 | 0.50 | 0.52 | 0.54 | 0.51 | 0.53 |
| Al ₂ O ₃ | 19.69 | 19.43 | 18.92 | 19.11 | 19.14 | 18.53 | 18.60 | 18.80 | 18.71 | 18.88 | 18.51 | 18.60 | 18.57 | 18.09 | 18.57 | 18.71 | 18.38 |
| FeO | 2.90 | 3.04 | 6.64 | 4.48 | 3.02 | 3.02 | 3.33 | 3.28 | 3.15 | 3.07 | 3.16 | 3.00 | 3.07 | 3.33 | 3.03 | 2.99 | 2.94 |
| MnO | 0.18 | 0.17 | 0.16 | 0.18 | 0.22 | 0.35 | 0.32 | 0.13 | 0.16 | 0.17 | 0.38 | 0.40 | 0.33 | 0.28 | 0.29 | 0.40 | 0.37 |
| MgO | 0.36 | 0.36 | 2.36 | 1.30 | 0.53 | 0.28 | 0.29 | 0.63 | 0.60 | 0.54 | 0.26 | 0.30 | 0.32 | 0.24 | 0.30 | 0.30 | 0.27 |
| CaO | 2.09 | 2.07 | 6.44 | 4.05 | 1.90 | 1.69 | 1.74 | 2.34 | 2.41 | 2.47 | 1.68 | 1.72 | 1.76 | 1.65 | 1.72 | 1.65 | 1.63 |
| Na ₂ O | 6.13 | 5.29 | 3.65 | 4.54 | 5.13 | 7.01 | 7.20 | 4.12 | 3.79 | 4.00 | 7.18 | 7.65 | 7.02 | 7.37 | 6.77 | 6.72 | 7.12 |
| K ₂ O | 8.48 | 8.98 | 6.89 | 8.24 | 8.51 | 6.75 | 6.93 | 9.18 | 9.19 | 9.02 | 6.53 | 6.43 | 6.71 | 6.32 | 6.54 | 6.55 | 6.70 |
| Analytical Total | 94.75 | 97.45 | 96.74 | 94.27 | 94.90 | 93.93 | 94.18 | 95.15 | 96.01 | 95.96 | 96.99 | 96.37 | 93.41 | 96.33 | 93.19 | 94.09 | 95.59 |
| K ₂ O + Na ₂ O | 14.61 | 14.26 | 10.54 | 12.78 | 13.64 | 13.76 | 14.13 | 13.31 | 12.98 | 13.02 | 13.71 | 14.08 | 13.73 | 13.69 | 13.31 | 13.28 | 13.82 |
| K ₂ O/Na ₂ O | 1.38 | 1.70 | 1.89 | 1.81 | 1.66 | 0.96 | 0.96 | 2.23 | 2.42 | 2.26 | 0.91 | 0.84 | 0.96 | 0.86 | 0.97 | 0.97 | 0.94 |
| ppm | 25µm | 25µm | 25µm | 25µm | 34µm | 34µm | 34µm | 34µm | 34µm | 25µm | 34µm | 34µm | 34µm | 20µm | 20µm | 20µm | 20µm |
| Rb | 337 | 358 | 203 | 246 | 307 | 537 | 544 | 286 | 288 | 287 | 551 | 460 | 525 | 554 | 523 | 519 | 522 |
| Sr | 312 | 122 | 1218 | 1100 | 56 | 2 | 12 | 564 | 640 | 716 | 2.6 | 11.2 | 2.7 | 3.2 | 3.6 | 2.6 | 6.1 |
| Y | 33 | 46 | 33 | 34 | 41 | 106 | 110 | 28 | 30 | 30 | 106 | 90 | 103 | 115 | 103 | 102 | 98 |
| Zr | 414 | 572 | 278 | 319 | 382 | 1226 | 1211 | 276 | 287 | 284 | 1232 | 1057 | 1130 | 1245 | 1100 | 1147 | 1099 |
| Nb | 80 | 107 | 51 | 60 | 68 | 207 | 208 | 49 | 48 | 48 | 210 | 187 | 198 | 225.0 | 198 | 194 | 184 |
| Ba | 431 | 13.7 | 1553 | 1246 | 6.7 | 3.6 | 23.1 | 703 | 851 | 949 | 3 | 16 | 3 | 2.8 | 2.5 | 3.0 | 28.6 |
| La | 104 | 148 | 84 | 98 | 109 | 261 | 266 | 72.1 | 75.2 | 81.7 | 272 | 230 | 264 | 290 | 256 | 264 | 239 |
| Ce | 201 | 273 | 171 | 201 | 208 | 508 | 541 | 139.0 | 142.0 | 150.9 | 537.1 | 460.3 | 510.1 | 559 | 504 | 506 | 471 |
| Pr | 21 | 29 | 19 | 22 | 22 | 53 | 51 | 14.5 | 14.7 | 15.1 | 54.4 | 45.0 | 51.3 | 55 | 49 | 50 | 47 |
| Nd | 75 | 95 | 71 | 71 | 79 | 170 | 174 | 52 | 53 | 61 | 174 | 155 | 176 | 193 | 174 | 179 | 171 |
| Sm | 11.0 | 15.1 | 14.1 | 15.2 | 14.1 | 27.3 | 32.5 | 8.7 | 9.5 | 9.0 | 29.0 | 25.6 | 29.9 | 33.4 | 34.3 | 27.8 | 24.5 |
| Eu | 1.7 | 2.5 | 3.2 | 3.4 | 2.3 | 1.6 | 1.5 | 2.1 | 2.3 | 2.4 | 1.6 | 1.5 | 1.8 | 1.8 | 1.78 | 1.91 | 1.64 |
| Gd | 7.7 | 12.2 | 10.8 | 12.0 | 9.6 | 21.7 | 22.2 | 7.4 | 6.3 | 6.6 | 20.6 | 19.3 | 21.4 | 23 | 21.8 | 19.9 | 20.4 |
| Dy | 6.5 | 9.6 | 7.1 | 7.8 | 8.2 | 18.6 | 19.0 | 5.4 | 5.8 | 5.6 | 19.0 | 16.7 | 18.5 | 21.1 | 19 | 19 | 17 |
| Er | 3.9 | 4.5 | 3.1 | 3.3 | 4.1 | 10.8 | 10.5 | 3 | 3 | 3 | 10.7 | 9.7 | 10.2 | 12.0 | 10.5 | 10.0 | 9.2 |
| Yb | 3.2 | 4.6 | 2.4 | 3.0 | 3.7 | 10.3 | 10.6 | 2.6 | 2.9 | 3.2 | 11 | 10 | 11 | 12.3 | 10.4 | 10.8 | 9.8 |
| Lu | 0.50 | 0.68 | 0.36 | 0.41 | 0.54 | 1.59 | 1.56 | 0.35 | 0.42 | 0.44 | 1.52 | 1.27 | 1.62 | 1.58 | 1.45 | 1.60 | 1.46 |
| Ta | 3.5 | 4.7 | 2.2 | 2.9 | 3.1 | 8.9 | 9.0 | 2.3 | 2.3 | 2.6 | 9.9 | 8.2 | 9.1 | 10.0 | 9.2 | 9.0 | 8.6 |
| Th | 36 | 55 | 22 | 31 | 32 | 99 | 99 | 21 | 23 | 22 | 102 | 87 | 97 | 113 | 98 | 96 | 89 |
| U | 11.2 | 17.4 | 6.8 | 8.8 | 9.6 | 31 | 31 | 6.6 | 6.6 | 7.4 | 32 | 28 | 29 | 35 | 29 | 29 | 29 |
| Nb/Th | 2.2 | 1.9 | 2.3 | 2.0 | 2.1 | 2.1 | 2.1 | 2.3 | 2.1 | 2.2 | 2.1 | 2.2 | 2.0 | 2.0 | 2.0 | 2.0 | 2.1 |
| Zr/Th | 11.5 | 10.4 | 12.4 | 10.4 | 12.0 | 12.4 | 12.3 | 12.9 | 12.7 | 12.9 | 12.1 | 12.2 | 11.7 | 11.0 | 11.2 | 12.0 | 12.3 |
| Ta/Th | 0.10 | 0.09 | 0.10 | 0.10 | 0.10 | 0.09 | 0.09 | 0.11 | 0.10 | 0.12 | 0.10 | 0.09 | 0.09 | 0.09 | 0.09 | 0.09 | 0.10 |

Table 6.5: Previous page: Representative major, minor and trace element analyses for glasses from the 'External' tephra recorded in the Aeolian Islands; the Panarea Pink Ash (PPA) and the Barone tephra, Salina. Also presented are analyses from colluvial sequences on the Italian mainland at both Le Saline, Palinuro and Tarsia in the Crati Valley (Calabria). Full data given in appendix eV.

6.3.2 Results

Representative glass analyses of the investigated tephra layers are given in Table 6.5 and 6.6 and full geochemical data for the investigated tephra are presented in Appendix eV.

6.3.2.1 Panarea Pink Ash (PPA), Punta Falcone

The Panarea pink ash (PPA) deposit outcropping at Punta Falcone (Fig. 6.12) forms a particularly heterogeneous tephra layer (54-60 wt.% SiO₂, 0.2-3.6 wt.% MgO and 1.9-7.0 wt.% CaO; Table 6.5). Using increasing SiO₂ as a fractionation index, TiO₂, FeO (Fig. 6.16), MgO, CaO (Fig. 6.16) all decrease, whilst Al₂O₃ increases. Na₂O remains constant up to 58 wt.% SiO₂ and then increases sharply in the higher SiO₂ glasses (58-60 wt.%) (Fig. 6.15b). K₂O increases to its most elevated concentrations at 59.3 wt.% SiO₂, where there is an inflection to lower values at 60 wt.% SiO₂. Given the SiO₂ variation and the high alkalis concentrations these glasses range from tephri-phonolite to phonolitic compositions (Fig. 6.14). Glasses display variable alkali ratios with 1.1-2.8 (K₂O/Na₂O) (Fig. 6.15a). The least evolved glasses occur at the top of the ash layer (Table 6.5). Significant incompatible trace element heterogeneity exists in this tephra population (Fig. 6.17; Table 6.5). The glasses range from moderately evolved (tephri-phonolites) to highly evolved (phonolites) with Zr/Sr = 0.3-6.0 and have LREE enrichment relative to the HREE (La/Yb = 31-37). Sr (101-1218 ppm) and Ba (10-1553 ppm) behave compatibly decreasing to their lowest concentrations in the most evolved glasses (Fig. 6.17d). Incompatible trace element ratios are constant within these glasses (Nb/Th = 2.1 ± 0.2; Zr/Th = 11 ± 1 (Fig. 6.17a); Ta/Th = 0.09 ± 0.01).

6.3.2.2 Barone tephra layer (Salina I), Salina

The Barone glasses are variable (61.5-63.2 wt.% SiO₂) with the most variation in the alkalis (Na₂O = 5.1-7.4 wt.% and K₂O = 6.5-8.5 wt.%). Consequently, the glasses range from phonolite to trachyte in composition (Fig. 6.14). This variability is reflected in alkali ratios, 0.9-1.7 (K₂O/Na₂O) (Fig. 6.15a). The glasses have a major element bi-

modality; the dominant population have $\text{Na}_2\text{O} \geq \text{K}_2\text{O}$. Whilst a smaller population has glasses displaying $\text{K}_2\text{O} > \text{Na}_2\text{O}$ these are associated with higher MgO concentrations (> 0.4 wt. %) (Fig. 6.18). Incompatible trace element concentrations in the glasses are also bi-modal (Fig.6.19a-d; Table 6.5). This variation between the end-members is reflected in the range of evolution observed ($\text{Zr}/\text{Sr} = 3.5$ to 554). The glasses display LREE enrichment relative to the HREE ($\text{La}/\text{Yb} = 25 \pm 2$) and Ba and Sr are depleted in these glasses due to K-feldspar removal. Incompatible trace element ratios are constant between the two end-members of the Barone tephra ($\text{Nb}/\text{Th} = 2.1 \pm 0.1$; $\text{Zr}/\text{Th} = 12.1 \pm 0.3$; Fig. 18a,d).

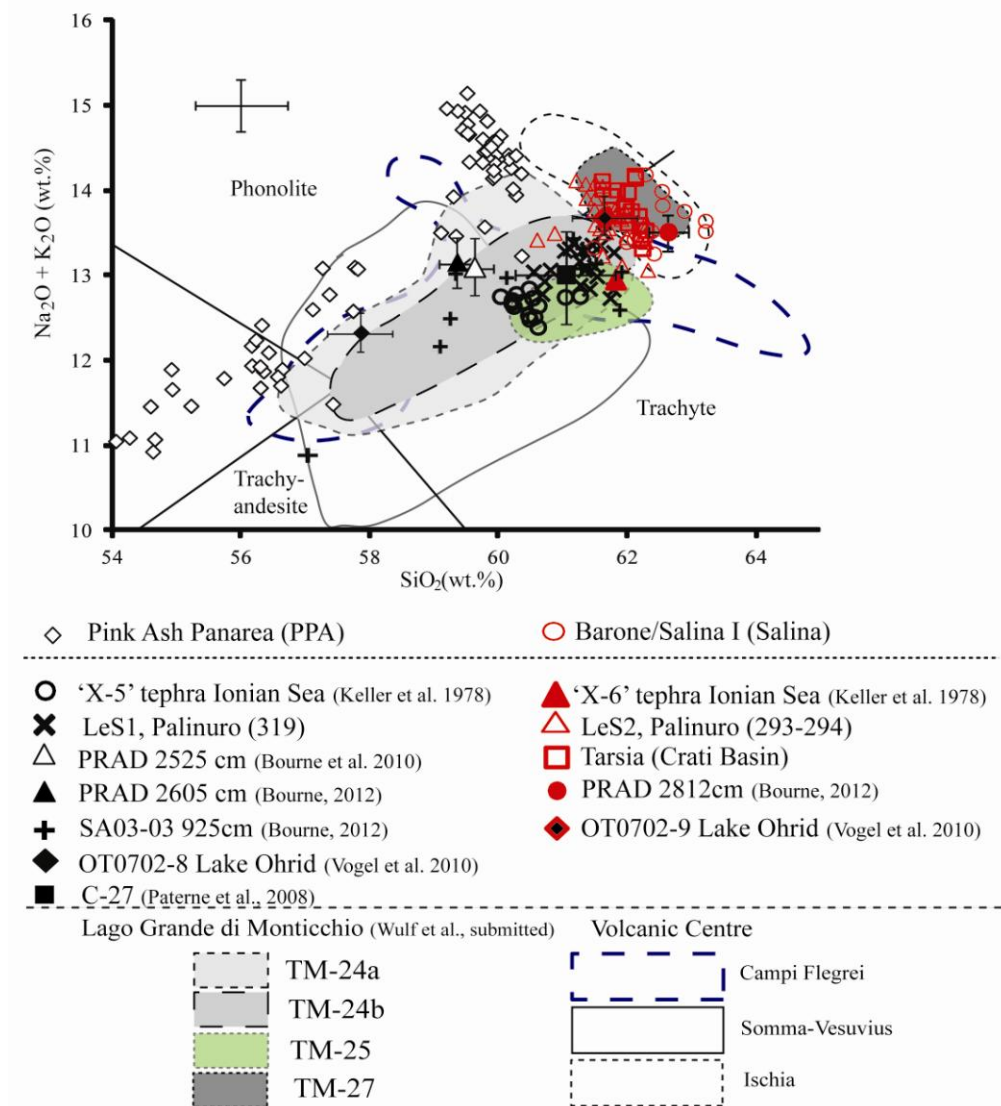


Figure 6.14: TAS diagram showing the Panarea pink ash (PPA) and the Barone tephra (Salina). Also shown are glass data from other MIS 5 tephra recorded at Le Saline, (Palinuro) and Tarsia, Crati valley (Calabria) on the Italian mainland. Compositional fields are based on glass data from Tomlinson et al., 2012b; Tomlinson et al., unpublished. (TAS classification; Le Bas et al., 1986).

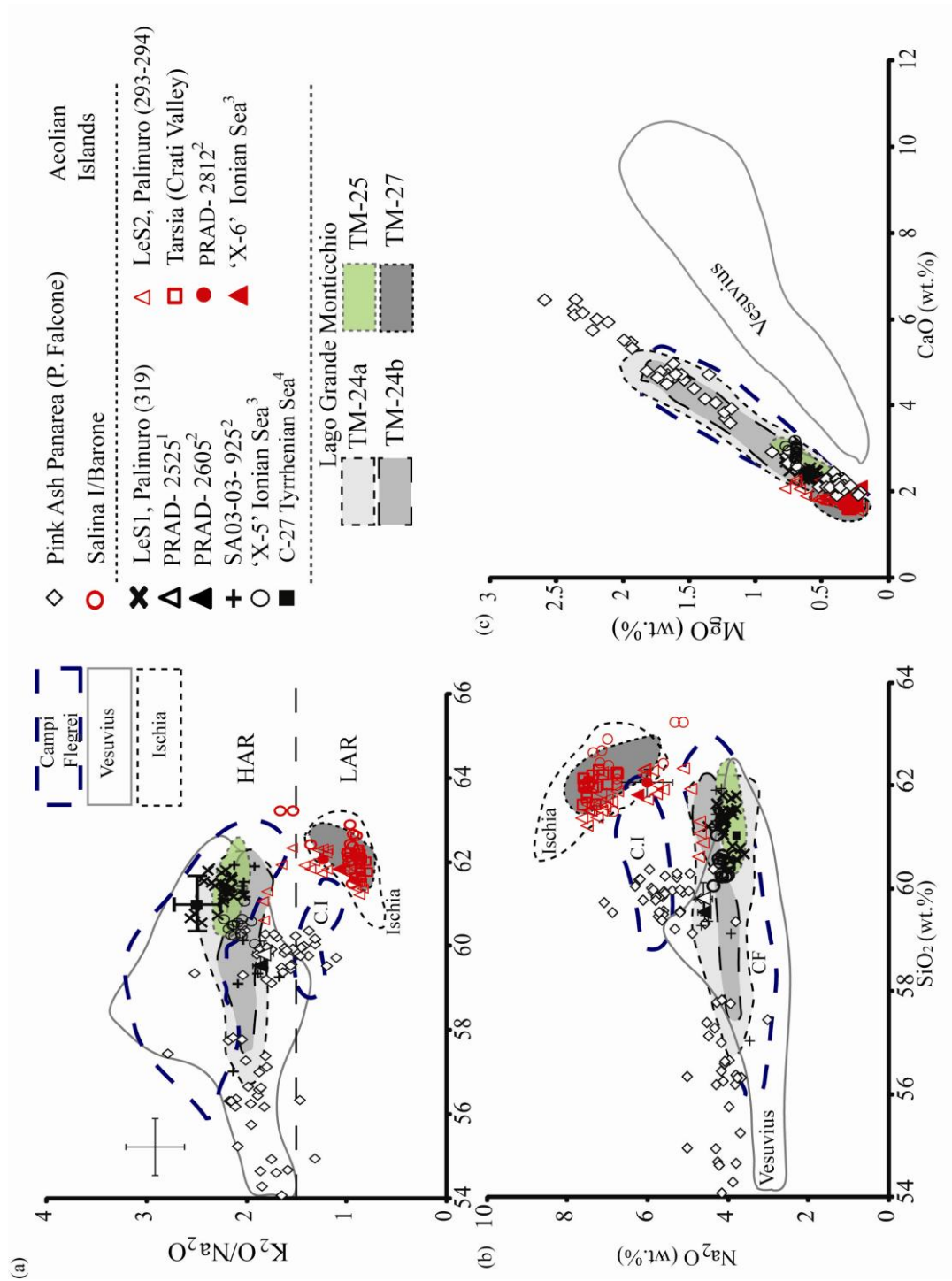


Figure 6.15: Major element bi-plot showing the Panarea pink ash (PPA) and the Barone tephra/Salina I (Salina). Also shown are glass data from other MIS 5 tephras recorded at Le Saline (Palinuro) and Tarsia, Crati Valley (Northern Calabria) on the Italian mainland. Additionally given are the compositional fields of prominent MIS 5 tephras Lago Grande di Monticchio (Wulf et al. Submitted) Also shown are the compositional fields of proximal glasses from the Neapolitan volcanic centres (Tomlinson et al., 2012b; Tomlinson in prep). (1) Bourne et al. (2010); (2) Bourne (2012); (3) Keller et al. (1978); (4) Paterne et al. (2008).

6.3.2.3 Italian Mainland

Le Saline 1, Palinuro (319):

The Le Saline Locality 1 (LeS1) glasses (sample 319) are homogeneous (61.3 ± 0.3 SiO₂ wt.%; 2.5 ± 0.2 CaO wt.%). These K-trachytic glasses show K₂O \gg Na₂O (K₂O/Na₂O = 2.0-2.8) (Fig. 6.15) and display moderate levels of enrichment of incompatible trace elements (Zr/Sr = 0.5 ± 0.1). Overall these glasses are homogeneous (Fig. 6.17; Table 6.5) and have significant LREE enrichment relative to the HREE (La/Yb = 26 ± 3). Sr and Ba behave compatibly (Fig. 6.17d), but concentrations are high for such evolved trachytic compositions (Sr = 523-715ppm; Ba = 532-1428 ppm). Incompatible trace element ratios are consistent within the LeS1 glass population (Nb/Th = 2.2 ± 0.2 ; Zr/Th = 12.7 ± 0.5).

Le Saline 2, Palinuro (293-294):

At the Le Saline locality 2 (LeS2) glasses (samples 293 and 294) show limited variation in most major elements (61.2 - 62.3 wt.% SiO₂, 1.53 - 1.88 wt.% CaO), whilst the most significant variation is observed in the alkalis (K₂O = 6.4 - 8.2 wt.% and Na₂O = 4.0 - 7.7 wt.%). These glasses straddle the phono-trachyte boundary (Fig. 6.14). Glass data indicate that discrete glass populations are present within the tephra deposit. This is best illustrated by the alkali ratios and MgO, which clearly demonstrate two distinct populations, a lower alkali ratio, low MgO group and a higher alkali ratio, high MgO group (Fig. 6.18). Incompatible trace element concentrations within these glasses display significant heterogeneity forming bi-modal populations (Fig. 6.19). This is reflected in the range of evolution observed in these glasses (Zr/Sr = 10 to 472). Glasses display LREE enrichment relative to the HREE (La/Yb = 27 ± 3) and consistent HFSE/Th ratios (Nb/Th = 2.1 ± 0.1 ; Zr/Th = 11.91 ± 0.5).

Tarsia, Crati Valley (Northern Calabria)

The Tarsia tephra have homogeneous glass compositions with 62.0 ± 0.2 wt.% SiO₂; 1.7 ± 0.1 wt.% CaO. Glasses have elevated alkali contents (Na₂O = 7.2 ± 0.3 wt.%; K₂O = 6.5 ± 0.1 wt.%) with Na₂O > K₂O (Fig. 6.15a; Table 6.5). These glasses range from phonolitic to trachytic compositions (Fig. 6.14). Trace element concentrations in these phono-trachytic glasses are highly evolved (Zr/Sr = 96-438) and homogeneous (i.e., Th = 97 ± 7 ppm; Zr = 1131 ± 68 ppm) whilst also displaying LREE enrichment relative to the HREE (La/Yb = 25 ± 1). Concentrations of Sr and Ba are consistently low in these

glasses ($\text{Sr} = 5.2 \pm 3\text{ppm}$; 3.5 ± 1) indicative of K-feldspar fractionation, a phase present in these deposits. HFSE/Th ratios in these glasses are constant ($\text{Nb/Th} = 2.05 \pm 0.03$; $\text{Zr/Th} = 11.6 \pm 0.5$).

6.3.2.4 Central Adriatic: PRAD 1-2

PRAD 2525 cm and 2605 cm; Major element data for the two tephra layer, PRAD 2525 cm and 2605 cm (Fig. 6.5) are presented in Bourne (2012). Glasses from these two layers form two homogenous and overlapping phono-trachytic glass populations (Fig. 6.14), where $\text{K}_2\text{O}/\text{Na}_2\text{O} = 1.5\text{-}2.0$ (Fig. 6.15a). Compositional fields are presented in Figure 6.16. These phono-trachytic glasses display moderate levels of enrichment ($\text{Zr/Sr} = 0.5 \pm 0.1$). Trace element data are presented here for PRAD 2525 and 2605cm (Table 6.6). Both tephtras display overlapping homogenous glass populations (Fig. 6.17). Sr and Ba concentration remain elevated within these glasses ($\text{Sr} = 652 \pm 56$ and $\text{Ba} = 1131 \pm 92$). HFSE/Th ratios are constant ($\text{Nb/Th} = 1.9 \pm 0.1$; $\text{Zr/Th} = 10.7 \pm 0.3$).

PRAD 2812cm; Major element glass data for PRAD 2812cm (Fig. 6.5) is presented in Bourne (2012). These glasses are classified as trachytes (Fig. 6.14) and show a bimodal population where both $\text{Na}_2\text{O} > \text{K}_2\text{O}$ and $\text{K}_2\text{O} > \text{Na}_2\text{O}$ shards are present (Fig. 6.18). Trace element glass data for this tephra layer confirms a bi-modal population (Fig. 6.19; Table 6.6). Consequently, the glasses display wide ranging levels of evolution ($\text{Zr/Sr} = 11\text{-}454$). The HFSE/Th ratios between the two end-members are constant ($\text{Nb/Th} = 2.1 \pm 0.1$; $\text{Zr/Th} = 12.0 \pm 0.3$).

6.3.2.5 SA03-03 Southern Adriatic

SA03-03 925cm: Major element data for SA03-03 925 cm (Fig. 6.5) is presented in Bourne (2012), glasses from this tephra extend from phonolite to trachyte, where $\text{K}_2\text{O}/\text{Na}_2\text{O} = 1.7\text{-}2.1$ (Fig. 6.15a). Compositional fields are presented in Figure 6.16. Trace element data for this SA03-03 925 cm tephra are presented in Table 6.6. These glasses display moderate levels of trace element enrichment ($\text{Zr/Sr} = 0.5 \pm 0.1$) and display some trace element variability (Fig. 6.17). Ba (Fig. 6.17d) and Sr display the most significant variation due to their compatibility (114-1373 ppm Ba and 268-857 ppm Sr). HFSE/Th are constant within these glasses ($\text{Nb/Th} = 2.1 \pm 0.1$; $\text{Zr/Th} = 11.7 \pm 0.3$).

| Core Depth | PRAD 1-2 (Central Adriatic) | | | | | | | | | | | | SA03-03 (Southern Adriatic) | | |
|-----------------|-----------------------------|-------------|-------------|-------------|-------------|-------------|-------------|-------------|-------------|-------------|-------------|-------------|-----------------------------|-------------|-------------|
| | 2525 cm | | | | | | 2605 cm | | | 2812 cm | | | 925 cm | | |
| | Base | | | Top | | | | | | | | | | | |
| Sample Shard ID | RH0078 | RH0078 | RH0078 | RH0075 | RH0075 | RH0075 | RH0122 | RH0122 | RH0122 | RH0074 | RH0074 | RH0074 | RH0617 | RH0617 | RH0617 |
| | 1 | 6 | 13 | 1 | 2 | 7 | 1 | 2 | 3 | 3 | 4 | 5 | 2 | 3 | 4 |
| Rb (ppm) | 318 | 323 | 338 | 316 | 313 | 311 | 336 | 322 | 312 | 373 | 373 | 553 | 283 | 292 | 298 |
| Sr | 712 | 617 | 615 | 611 | 653 | 669 | 602 | 693 | 692 | 19.1 | 23.9 | 2.6 | 723 | 749 | 720 |
| Y | 28 | 30 | 30 | 27 | 27 | 29 | 30 | 29 | 30 | 54 | 52 | 103 | 29 | 30 | 30 |
| Zr | 332 | 342 | 336 | 322 | 312 | 326 | 329 | 329 | 335 | 546 | 506 | 1162 | 301 | 298 | 314 |
| Nb | 60 | 59 | 60 | 58 | 55 | 59 | 59 | 60 | 60 | 96 | 91 | 198 | 57 | 52 | 54 |
| Ba | 1213 | 1007 | 1100 | 1067 | 1128 | 1169 | 1031 | 1203 | 1189 | 3.0 | 3.8 | 2.5 | 1110 | 1075 | 1073 |
| La | 82 | 82 | 81 | 78 | 76 | 77 | 78 | 80 | 81 | 140 | 132 | 255 | 79 | 77 | 81 |
| Ce | 152 | 154 | 151 | 143 | 137 | 146 | 146 | 149 | 149 | 270 | 257 | 502 | 152 | 148 | 155 |
| Pr | 14.7 | 15.2 | 15.2 | 14.6 | 13.9 | 14.5 | 14.3 | 15.3 | 14.4 | 28.4 | 26.8 | 49.5 | 14.9 | 15.2 | 15.2 |
| Nd | 50 | 53 | 52 | 52 | 50 | 53 | 52 | 53 | 55 | 101 | 92 | 167 | 56 | 53 | 58 |
| Sm | 9.8 | 9.8 | 10.2 | 7.6 | 8.0 | 10.3 | 8.5 | 9.0 | 10.3 | 16.7 | 14.4 | 29.1 | 8.4 | 8.0 | 9.8 |
| Eu | 1.9 | 1.9 | 1.9 | 1.8 | 1.9 | 1.8 | 2.0 | 2.0 | 2.0 | 2.2 | 2.2 | 1.7 | 2.0 | 2.2 | 2.1 |
| Gd | 6.7 | 6.5 | 6.6 | 7.0 | 6.3 | 7.2 | 6.2 | 6.5 | 6.8 | 13.5 | 10.7 | 22.1 | 6.5 | 7.1 | 6.8 |
| Dy | 5.6 | 5.8 | 5.5 | 5.8 | 4.9 | 5.6 | 5.5 | 5.7 | 5.8 | 9.5 | 9.4 | 18.7 | 5.5 | 5.6 | 5.6 |
| Er | 2.9 | 2.9 | 2.7 | 3.1 | 2.6 | 3.1 | 2.9 | 2.9 | 3.0 | 5.4 | 5.2 | 11.0 | 2.9 | 2.8 | 3.2 |
| Yb | 3.1 | 2.9 | 2.9 | 2.9 | 2.9 | 3.1 | 2.7 | 2.9 | 3.0 | 4.9 | 4.8 | 10.7 | 2.5 | 2.6 | 3.0 |
| Lu | 0.44 | 0.46 | 0.41 | 0.46 | 0.45 | 0.43 | 0.41 | 0.47 | 0.43 | 0.81 | 0.72 | 1.54 | 0.41 | 0.43 | 0.47 |
| Ta | 2.7 | 3.0 | 3.0 | 3.1 | 2.7 | 2.6 | 2.7 | 2.8 | 2.8 | 4.4 | 4.2 | 8.7 | 2.7 | 2.5 | 2.3 |
| Th | 31 | 32 | 31 | 30 | 29 | 31 | 31 | 31 | 32 | 46 | 43 | 94 | 26 | 24 | 27 |
| U | 10.2 | 10.4 | 10.2 | 10.0 | 9.4 | 9.9 | 10.1 | 9.6 | 10.6 | 14.6 | 13.1 | 30.2 | 8.4 | 7.8 | 8.2 |
| <i>Nb/Th</i> | <i>1.9</i> | <i>1.9</i> | <i>1.9</i> | <i>1.9</i> | <i>1.9</i> | <i>1.9</i> | <i>1.9</i> | <i>1.9</i> | <i>1.9</i> | <i>2.1</i> | <i>2.1</i> | <i>2.1</i> | <i>2.2</i> | <i>2.1</i> | <i>2.0</i> |
| <i>Zr/Th</i> | <i>10.8</i> | <i>10.7</i> | <i>10.8</i> | <i>10.6</i> | <i>10.9</i> | <i>10.4</i> | <i>10.7</i> | <i>10.6</i> | <i>10.6</i> | <i>11.8</i> | <i>11.9</i> | <i>12.3</i> | <i>11.5</i> | <i>12.2</i> | <i>11.7</i> |
| <i>Ta/Th</i> | <i>0.09</i> | <i>0.10</i> | <i>0.09</i> | <i>0.10</i> | <i>0.09</i> | <i>0.08</i> | <i>0.09</i> | <i>0.09</i> | <i>0.09</i> | <i>0.10</i> | <i>0.10</i> | <i>0.09</i> | <i>0.10</i> | <i>0.10</i> | <i>0.09</i> |

Table 6.6: Representative trace element glass analyses from MIS 5 tephra layers recorded in PRAD 1-2 (central Adriatic) and SA03-03 (southern Adriatic).

| | TM-24a | | | | | | TM-24b | | | | TM-25 | | | | TM-27 | | | | |
|--------------------------------------|--------------------------------------|------------|------------|------------|------------|--------------|--------------------------------------|------------|------------|------------|--------------------------|-------|-------|-------|--------------------------------------|-----------|-----------|------------|------------|
| | Wulf et al., (submitted), This study | | | | | | Wulf et al., (submitted), This study | | | | Wulf et al., (submitted) | | | | Wulf et al., (Submitted), This Study | | | | |
| | O352 1 | O352 13 | O352 22 | O353 19 | O353 21 | O353 0353 | O354 31 | O354 40 | O354 55 | O354 51 | | | | | O355 18 | O355 3 | O355 1 | O355 23 | O355 29 |
| SiO ₂ | 58.76 | 58.36 | 62.09 | 60.02 | 60.31 | 60.99 | 57.60 | 61.03 | 61.24 | 61.55 | 60.43 | 61.15 | 61.83 | 62.40 | 62.21 | 62.74 | 61.97 | 61.91 | 61.86 |
| TiO ₂ | 0.52 | 0.52 | 0.37 | 0.47 | 0.40 | 0.38 | 0.54 | 0.41 | 0.36 | 0.33 | 0.49 | 0.51 | 0.40 | 0.38 | 0.39 | 0.43 | 0.47 | 0.49 | 0.56 |
| Al ₂ O ₃ | 18.05 | 18.70 | 18.06 | 18.65 | 18.44 | 18.90 | 18.57 | 18.75 | 18.43 | 18.73 | 18.53 | 18.40 | 18.66 | 18.95 | 18.03 | 17.60 | 18.09 | 17.53 | 18.21 |
| FeO | 4.94 | 4.69 | 2.95 | 3.83 | 3.67 | 3.14 | 5.44 | 3.29 | 3.50 | 3.10 | 3.98 | 3.73 | 3.35 | 2.88 | 3.01 | 3.04 | 3.32 | 3.40 | 3.12 |
| MnO | 0.15 | 0.14 | 0.20 | 0.15 | 0.16 | 0.26 | 0.12 | 0.15 | 0.10 | 0.10 | 0.13 | 0.15 | 0.09 | 0.13 | 0.21 | 0.23 | 0.38 | 0.34 | 0.42 |
| MgO | 1.41 | 1.27 | 0.56 | 0.80 | 0.70 | 0.58 | 1.73 | 0.66 | 0.75 | 0.55 | 0.82 | 0.81 | 0.56 | 0.44 | 0.45 | 0.42 | 0.28 | 0.22 | 0.25 |
| CaO | 4.23 | 4.01 | 2.51 | 3.09 | 2.73 | 2.79 | 4.61 | 2.54 | 2.77 | 2.49 | 3.03 | 2.96 | 2.44 | 2.17 | 1.94 | 1.80 | 1.67 | 1.72 | 1.71 |
| Na ₂ O | 4.11 | 4.11 | 4.37 | 4.03 | 4.60 | 4.02 | 3.80 | 4.46 | 4.38 | 4.36 | 3.87 | 3.73 | 3.98 | 4.10 | 6.15 | 5.99 | 7.55 | 7.96 | 7.47 |
| K ₂ O | 7.85 | 8.21 | 8.89 | 8.96 | 8.98 | 8.94 | 7.59 | 8.72 | 8.48 | 8.80 | 8.71 | 8.55 | 8.69 | 8.56 | 7.61 | 7.76 | 6.27 | 6.44 | 6.41 |
| Total | 96.41 | 95.78 | 94.75 | 93.80 | 98.18 | 96.20 | 97.23 | 97.26 | 94.20 | 95.32 | 97.37 | 94.01 | 95.77 | 95.46 | 97.02 | 94.92 | 95.24 | 93.12 | 97.70 |
| K ₂ O + Na ₂ O | 11.95 | 12.31 | 13.26 | 12.99 | 13.58 | 12.96 | 11.39 | 13.18 | 12.86 | 13.16 | 12.58 | 12.29 | 12.67 | 12.65 | 13.76 | 13.75 | 13.82 | 14.40 | 13.88 |
| K ₂ O/Na ₂ O | 1.91 | 2.00 | 2.03 | 2.22 | 1.95 | 2.22 | 2.00 | 1.95 | 1.94 | 2.02 | 2.25 | 2.29 | 2.18 | 2.09 | 1.24 | 1.30 | 0.83 | 0.81 | 0.86 |
| Rb (ppm) | 270 | 283 | 297 | 307 | 319 | 298 | 262 | 308 | 315 | 290 | | | | | 321 | 352 | 539 | 522 | 507 |
| Sr | 903 | 836 | 708 | 751 | 737 | 871 | 971 | 725 | 781 | 748 | | | | | 37.5 | 24.1 | 2.0 | 2.3 | 2.7 |
| Y | 31 | 31 | 30 | 33 | 31 | 31 | 28 | 30 | 30 | 31 | | | | | 44 | 51 | 105 | 103 | 100 |
| Zr | 286 | 298 | 314 | 326 | 342 | 335 | 248 | 317 | 322 | 340 | | | | | 413 | 507 | 1210 | 1143 | 1103 |
| Nb | 47 | 53 | 56 | 55 | 59 | 60 | 43 | 54 | 53 | 55 | | | | | 72 | 88 | 208 | 199 | 190 |
| Ba | 1162 | 1250 | 1100 | 1302 | 1306 | 1458 | 1757 | 1111 | 1124 | 1107 | | | | | 4.3 | 3.7 | 4.8 | 3.6 | 3.5 |
| La | 80 | 79 | 82 | 79 | 83 | 84 | 72 | 82 | 81 | 86 | | | | | 114 | 135 | 270 | 256 | 247 |
| Ce | 152 | 151 | 153 | 151 | 156 | 157 | 137 | 154 | 153 | 158 | | | | | 221 | 259 | 525 | 490 | 489 |
| Pr | 15.3 | 15.6 | 16.2 | 15.3 | 16.0 | 15.4 | 14.7 | 15.9 | 16.2 | 15.8 | | | | | 22.9 | 26.1 | 53.0 | 50.8 | 48.0 |
| Nd | 56 | 53 | 56 | 58 | 54 | 56 | 53 | 54 | 56 | 58 | | | | | 79 | 93 | 179 | 165 | 164 |
| Sm | 10.3 | 9.5 | 9.5 | 10.1 | 8.5 | 10.2 | 9.9 | 9.7 | 10.3 | 10.3 | | | | | 13.3 | 16.2 | 30.2 | 28.3 | 28.1 |
| Eu | 2.4 | 2.2 | 2.1 | 2.2 | 2.1 | 2.2 | 2.5 | 2.2 | 2.0 | 2.3 | | | | | 2.1 | 2.3 | 1.6 | 1.6 | 1.7 |
| Gd | 8.7 | 7.2 | 6.8 | 8.1 | 7.3 | 6.7 | 7.4 | 7.0 | 6.9 | 8.3 | | | | | 10.0 | 11.1 | 22.4 | 19.5 | 20.0 |
| Dy | 6.2 | 5.8 | 5.7 | 6.3 | 5.6 | 6.2 | 5.5 | 5.9 | 5.5 | 6.1 | | | | | 8.5 | 10.0 | 19.1 | 18.0 | 18.0 |
| Er | 3.0 | 3.0 | 3.0 | 3.2 | 3.1 | 3.1 | 2.7 | 3.0 | 2.8 | 3.1 | | | | | 4.2 | 5.1 | 10.6 | 9.8 | 9.9 |
| Yb | 2.9 | 2.9 | 3.2 | 3.0 | 3.1 | 3.2 | 2.7 | 2.9 | 2.6 | 3.2 | | | | | 4.4 | 5.2 | 11.0 | 10.0 | 9.7 |
| Lu | 0.42 | 0.42 | 0.40 | 0.45 | 0.47 | 0.46 | 0.37 | 0.43 | 0.41 | 0.39 | | | | | 0.63 | 0.74 | 1.59 | 1.47 | 1.46 |
| Ta | 2.5 | 2.5 | 2.4 | 2.4 | 2.5 | 2.5 | 1.9 | 2.5 | 2.4 | 2.4 | | | | | 3.4 | 4.0 | 9.3 | 8.4 | 8.3 |
| Th | 24 | 27 | 27 | 27 | 29 | 29 | 20 | 26 | 25 | 27 | | | | | 34 | 42 | 99 | 93 | 90 |
| U | 7.8 | 8.7 | 8.7 | 8.8 | 9.6 | 9.3 | 6.0 | 8.5 | 8.1 | 8.9 | | | | | 10.5 | 13.0 | 31 | 29 | 28 |
| Nb/Th | 1.9 | 2.0 | 2.1 | 2.0 | 2.0 | 2.1 | 2.2 | 2.1 | 2.1 | 2.0 | | | | | 2.1 | 2.1 | 2.1 | 2.2 | 2.1 |
| Zr/Th | 11.7 | 11.2 | 11.6 | 11.9 | 11.6 | 11.6 | 12.7 | 12.2 | 12.7 | 12.5 | | | | | 12.0 | 12.1 | 12.2 | 12.3 | 12.3 |
| Ta/Th | 0.10 | 0.09 | 0.09 | 0.09 | 0.09 | 0.08 | 0.10 | 0.10 | 0.10 | 0.09 | | | | | 0.10 | 0.10 | 0.09 | 0.09 | 0.09 |

Table 6.7: Representative major, minor and trace element glass analyses from prominent MIS 5 tephtras recorded at Lago Grande di Monticchio. Representative data is given for TM-24a; TM-24b, TM-25 and TM-27 tephtras (Wulf et al., submitted; C. Satow *pers comm.*).

6.3.3 Discussion

Stratigraphically the Panarea Pink Ash (PPA) and the Barone tephtra are believed to be constrained to MIS 5 (Lucchi et al., 2008). These external tephtras recorded in the Aeolian Islands are considered within the context of other prominent MIS 5 distal tephtra either reported here or previously published in the literature. Figure 6.15a demonstrates that all the prominent MIS 5 tephtras considered as potential correlatives for these two external tephtra layers outcropping in the Aeolian Islands can be categorised based on their alkali ratios (Table 6.8). This diagnostic characteristic has also been previously recognised and utilised by Paterne et al. (2008) for distinguishing trachytic tephtras recorded in the central Mediterranean region. Tephtras with alkalis ratios >1.5 are classified as High Alkali Ratio (HAR) glasses and those dominated by < 1.5 are Low Alkali Ratio (LAR) glasses (Table 6.8).

| Alkali Ratio | Investigated samples (This study) | Referenced tephtras |
|--------------|---|---|
| HAR | Le Saline 1 (LeS1), | X-5 ¹ , TM-25 ² , C-27 ³ TM-24b ² , TM-24a ² , SA-03-03-925cm ⁴ ; PRAD 2605cm ⁴ ; PRAD 2525cm ⁵ ; OT0702-8 ⁶ |
| LAR | Le Saline 2 (LeS2), Tarsia Crati Valley | X-6 ¹ ; TM-27 ² ; PRAD 2812cm ² ; OT0702-9 ⁶ |

Table 6.8: Alkali ratio grouping of prominent MIS 5 tephtras investigated herein and those previously referenced in the central Mediterranean region. Groupings are based on alkalis ratio, with > 1.5 = High Alkali Ratio tephtras and < 1.5 = Low Alkali ratios. For tephtra localities see Figure 6.1. References: ¹ Keller et al. (1978); ² Wulf et al. (submitted); ³ Paterne et al. (2008); ⁴ Bourne (2012); ⁵ Bourne et al. (2010); ⁶ Vogel et al. (2008).

(i) Panarea Pink Ash (PPA), Punta Falcone

Owing to their transitional alkali ratios, the tephri-phonolitic to phonolite PPA glasses cannot be categorised as either a HAR or LAR tephra. This tephra has previously been correlated to the X-5 marine tephra (Lucchi et al. 2008), which is classified within the HAR tephra group, therefore comparisons are made between the PPA and the prominent MIS 5 HAR tephras using major, minor and trace element data to fully assess this correlation (Table 6.8). Further to discrepancies in the alkali ratio, such a correlation is problematic for the following reasons;

- (1) The PPA is dominated by a phonolitic end-member, which has significantly more elevated total alkalis (Fig. 6.14).
- (2) At overlapping SiO₂, the PPA glasses have lower FeO (Fig. 6.16b), MgO, CaO (Fig. 6.16a) and more elevated Na₂O (Fig. 6.15b).
- (3) Incompatible trace elements are significantly more elevated (Fig.6.17) in the PPA glasses.
- (4) Ba and Sr extend to significantly lower concentrations in the evolved end-members (Fig. 6.17d).

The correlation between this PPA and the X-5 marine tephra is rejected based on multi-element data. As such, the X-5 age of 105 ± 2 ka (Kraml, 1997) cannot be imported into the Punta Falcone stratigraphy, Panarea. None of the other prominent MIS 5 tephras investigated (Table 6.4) offer a strong correlative for the tephri-phonolite to phonolite tephra recorded on Panarea (Fig. 6.14-6.16).

With the PPA unrelated to the prominent MIS 5 tephras presented above, an alternative scenario proposed by Di Rita et al. (2008) suggests that this tephra is significantly younger and related the Pomici di Base eruption of Somma-Vesuvius. Although the PPA is dominated by phonolitic glass compositions (Fig. 6.14) characteristic of Somma-Vesuvius (Santacroce et al., 2008), these distal glasses have lower CaO (at a given MgO) than the glasses from the Verdoline, Pomici di Base and Codola eruptions of Somma-Vesuvius (Fig. 6.15c). Consequently, Somma-Vesuvius can be confidently ruled out as the provenance solution for this distal tephra. The CaO/MgO bi-plot (Fig. 6.15c) suggests that the compositions are more consistent with magmas from Campi Flegrei, while the age of the tephra remains unresolved. Only as more distal central Mediterranean tephras become characterised will there be a greater opportunity to identify and chronologically constrain the PPA.

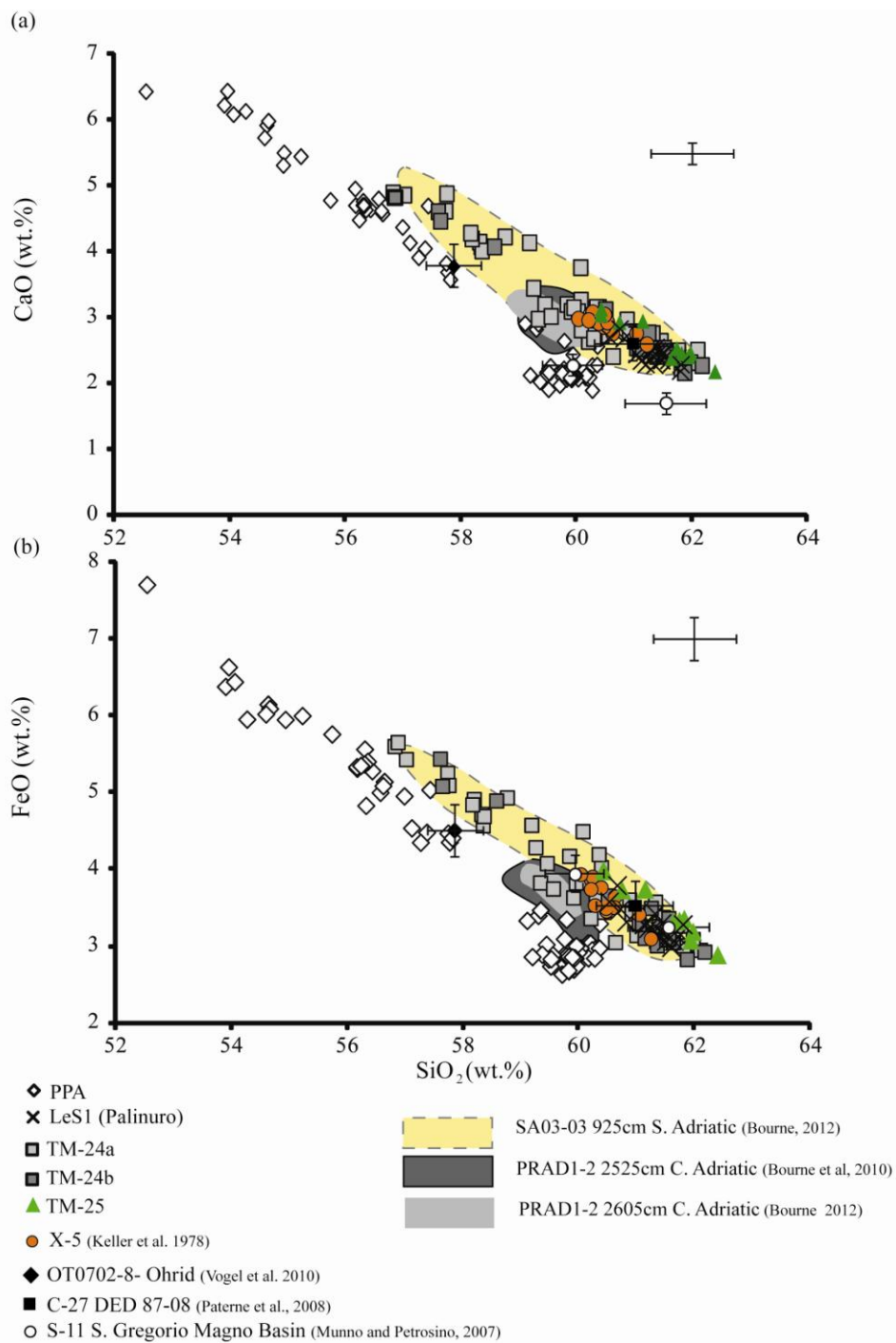


Figure 6.16: Major element bi-plots showing the Panarea pink ash (PPA). Also given are the glass compositions from prominent HAR ratio MIS 5 tephra layers (See Table 6.8).

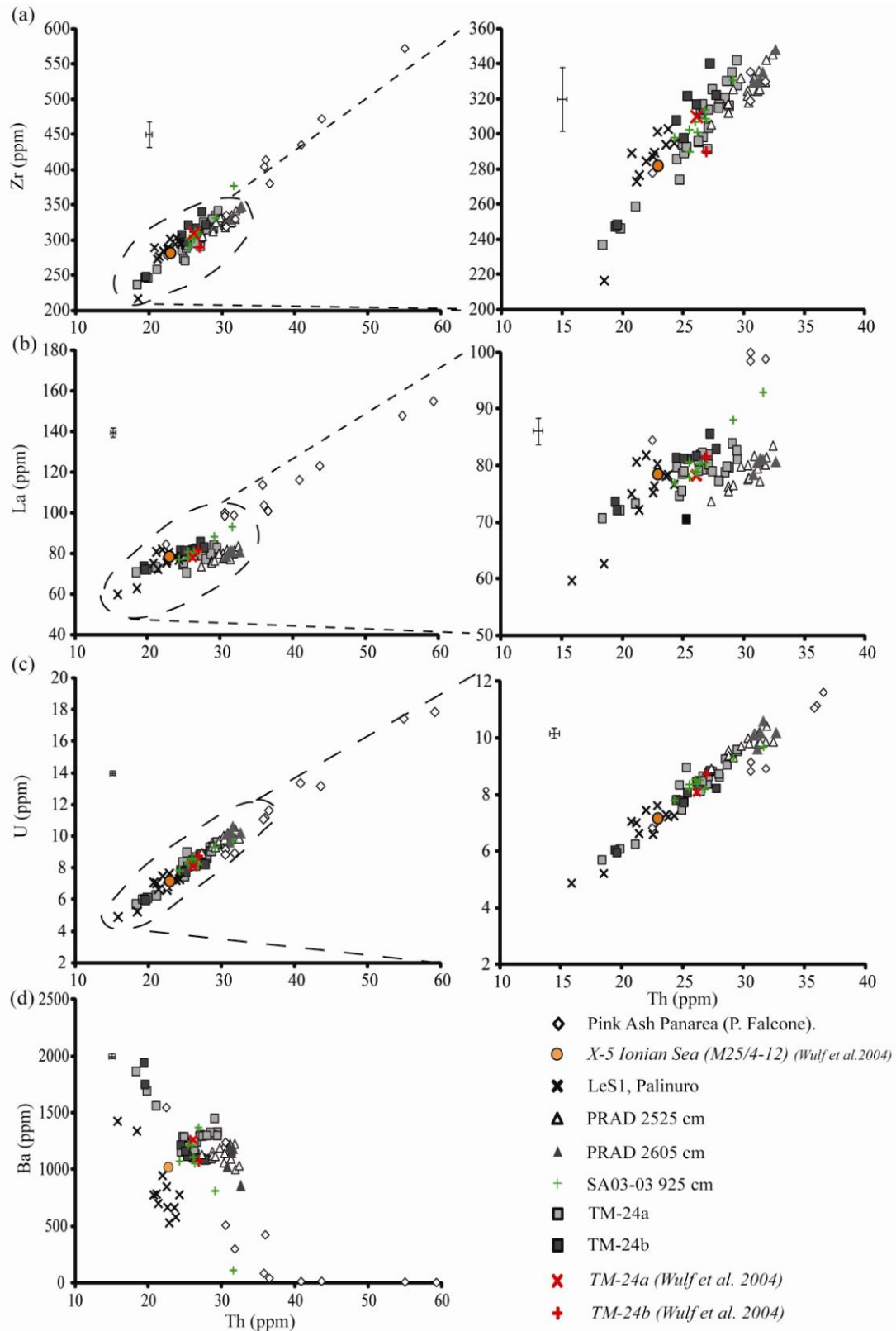


Figure 6.17 Trace element bi-plots showing glasses from the Panarea Pink ash (PPA) deposit. Also given are the glass compositions from prominent HAR ratio MIS 5 tephra layers (See Table 6.8). Also included is a single analysis of the X-5 marine tephra is based on a bulk glass analyses (Wulf et al., 2004).

(ii) MIS 5 HAR tephtras

While considering the potential correlation of the PPA to the MIS 5 HAR tephtras, new trace element data offers an opportunity to assess some of the previously correlated tephtras within the group. Many of the prominent MIS 5 tephtras within the HAR group have been associated with the X-5 marine tephtra due to their shared stratigraphic context within MIS 5 and their high alkali affinity (Table 6.8). These include temporally similar tephtras recorded at Lago Grande di Monticchio (LGdM). Representative data for these tephtras are presented in Table 6.7. At LGdM Wulf et al., (submitted) correlate TM-25 (105.5 ka BP) to the X-5 and C-27 marine tephtras, all three tephtras are characterised by homogeneous K-trachytic glasses (Fig. 6.14). However, initially the X-5 was assigned to two overlying and temporally distinct tephtras, TM-24a (101.8 ka BP) and TM-24b (102.8 ka BP) in the LGdM record (Wulf et al., 2004) (Fig. 6.4). These two tephtras are far more heterogeneous than the TM-25/X-5/C-27 tephtras (Fig. 6.14), whilst the latter do fall within the wider compositional fields of TM-24a/TM-24b (Fig. 6.14-6.15). Chronologically, TM-25 (105.5 ka) is more consistent with the age of the X-5 marine tephtra (105 ± 2 ka; Kraml 1997). This period in the LGdM record presents evidence of three separate large magnitude eruptions (Fig. 6.4), with overlapping major element chemistries (Fig. 6.14) spanning ca. 5 ka period. This highlights the difficulty of synchronising distal archives using these HAR tephtras during MIS 5.

At Le Saline (LeS), Palinuro, south of the Campanian volcanic zone, volcanoclastic deposits sourcing from the Campanian region were identified by Lirer et al., (1967). Morche (1988) linked the Palinuro tephtra, interbedded within colluvial sediments, to the X-6 marine tephtra. Grams (1999) identified two pyroclastic levels at Palinuro, suggesting both X-5 and X-6 were present. More recently, Marciano et al. (2008) interpreted these deposited as post MIS 5e and suggested links with the X-6 marine tephtra. Alkali ratios confirm that the two outcrops investigated in this study contain ash deposits from different eruptions (Fig. 6.15a; Table 6.8). LeS1 glasses display a HAR affinity, whilst the LeS2 glasses display a LAR affinity and are discussed below.

Le Saline 1

The HAR LeS1 glasses present an opportunity to try and correlate this deposit, which constitutes a large volcanic eruption emplaced within MIS 5, with other prominent HAR MIS 5 tephtras. The LeS1 homogeneous K-trachytic glasses are consistent with the major element compositions of TM-25, the X-5 and C-27 marine tephtras (Fig. 6.14-6.16). Consequently,

LeS1 glasses also overlap the trachytic end-members of TM-24a and TM-24b, but do not present their extended geochemical range (Fig. 6.14-6.16).

Trace element analyses confirm that the LeS1 glasses broadly fall within the compositional range of the two indistinguishable TM-24 layers (Fig. 6.17). However, their incompatible trace element concentrations do not correspond with the dominant component, concentrations are lower than those in the most evolved end-members of the TM-24 layers (Fig. 6.17). Indeed, the LeS1 glasses can be separated from the TM-24 layers, where Ba and Sr are offset on separate evolutionary trends extending to lower concentrations (Fig. 6.17d). Currently based on a bulk glass analysis it is difficult to determine whether the X-5 trace element composition is associated with the LeS1 glasses or the TM-24 layers (Fig. 6.17d). Grain-specific trace element analyses of the TM-25/X-5 tephra are essential to determine whether they too are geochemically distinct from the TM-24 layers and more comparable with the LeS1 tephra. This would make TM-25/X-5 a geochemically distinct marker imperative to synchronise distal archives with greater confidence. Failure to distinguish TM-25/X-5 from the TM-24 layers at trace element level would further compound the difficulties of using these tephra layers for the synchronisation of distal archives.

A precise correlative of the LeS1 tephra cannot be determined at a trace element level, however, excluding correlation with the TM-24 layers does leave the TM-25 layer at LGdM as the most likely candidate, given that both these distal HAR tephra deposits represent large magnitude eruptions in MIS 5 with corresponding major element compositions.

As mentioned above, prior to re-interpretation at LGdM record (Wulf et al., submitted), TM-24a and TM-24b were considered the equivalents of the X-5 (Wulf et al., 2004). As such these geochemically heterogeneous tephra at LGdM were used as a basis for distal-distal tephra correlations. Correlations with the TM-24 layers meant subsequent links to the X-5 marine marker were determined by association, contributing to seemingly erroneous X-5 correlations (i.e., Bourne et al., 2010; Vogel et al., 2010). Indeed, the homogenous phonolitic tephra PRAD 2525 cm and OT0702-8 were attributed to the X-5 marine tephra on the basis that their compositions fall firmly within the compositional range of the two TM-24 layers (Bourne et al., 2010; Vogel et al., 2010).

PRAD1-2 (2525cm and 2605cm)

Bourne et al. (2010) correlated the Adriatic MIS 5 visible tephra PRAD 2525 cm (Fig. 6.5) to TM-24a/TM-24b and (by extension, c.f. Wulf et al., 2004) to the X-5 tephra, importing the 105 ± 2 ka X-5 age (Kraml, 1997).

Major element data (Bourne, 2012) presented for this layer and the underlying non-visible PRAD 2605 cm layer have phonolitic glass chemistries that are indistinguishable from one another (Fig. 6.14-6.16). These homogeneous glass populations fall within the compositional fields of TM-24a/TM-24b, thus supporting previous correlations (Fig. 6.14-6.16). Trace element analyses reveal that concentrations in these two PRAD1-2 tephras are homogeneous and indistinguishable (Fig. 6.17). However, they are offset from the more heterogeneous TM-24a and TM-24b LGdM layers to more elevated incompatible trace element concentrations (Fig. 6.17), Zr/Th ratios are significantly lower in the PRAD 2525 and 2605cm layers than the LGdM TM-24 layers (Fig.16a-b; Table 6.6; 6.7). Trace element data presented herein suggest neither of the PRAD layers are correlatives of the LGdM TM-24 layers.

Major element compositions in the PRAD tephras do not appear to overlap the TM-25/X-5 tephras (Fig. 6.14-6.15). Incompatible trace element concentrations observed in these two PRAD layers are far more elevated than those observed in the bulk glass analyses of the X-5 marine tephra (Fig. 6.17a-c) (Wulf et al., 2004). Consequently, the X-5 age (105 ± 2 ka) should not be imported to PRAD 2525 cm. This is further supported by stratigraphic inconsistencies, in the Ionian Sea cores; X-5 appears to reside at the base of Sapropel 4 (Keller et al., 1978), whilst PRAD 2525 and 2605 layers are significantly higher in the MIS 5 sediments (Fig. 6.5) (Bourne 2012). It seems PRAD 2525 cm and 2605 cm might represent younger MIS 5 explosive events.

Broad similarities in glass chemistry might indicate that these two distal MIS 5 PRAD tephras derive from the same volcanic source that produced the TM24/25 tephras at LGdM (Wulf et al., submitted). However, differences in trace element glass chemistry might present evidence of further temporally separate, unrecognised explosive events.

SA03-03 925 cm

The southern Adriatic visible MIS 5 tephra SA03-03 925 cm was attributed by Bourne (2012) to the TM-24a/TM24-b tephtras and by association, to the X-5 marine tephra. The age of the X-5 tephra was imported into the SA03-03 stratigraphy. Major element variability in this tephra layer is consistent with the TM-24a/TM-24b tephtras (Fig. 6.14-6.16) and this is substantiated by corresponding incompatible trace element concentrations (Fig. 6.17). SA03-03 925 cm glasses have trace element concentrations that are significantly more elevated than the X-5 bulk glass analysis (Fig. 6.17). The previous correlation with TM-24a and TM-24b is confirmed by trace element analyses. However, since the link between TM-24a/TM-24b and X-5 is no longer considered valid (Wulf et al., submitted), the X-5 age should not be imported to this tephra. Instead, a varve age bracketing the two indistinguishable TM-24a and TM-24b layers is preferable (ca 101.8-102.8 ka BP; Table 6.4) (Wulf et al., submitted) for this tephra.

OT0702-8 Lake Ohrid (Vogel et al., 2010)

This phonolitic tephra in Lake Ohrid is significantly different from the homogeneous K-trachytic LeS1, TM-25 and X-5 tephtras (Fig. 6.14). Therefore X-5 age constraints should not be imported to this layer. The tephra does fall within the compositional range of the TM-24 layers at LGdM, further trace element analysis might help resolve its association with these TM-24 layers or to other HAR MIS 5 tephtras.

In summary data presented from the HAR group illustrates the complexity of precisely correlating these tephtras erupted during MIS 5 owing to the following factors; (1) multiple large magnitude events; (2) with overlapping major element glass chemistries; (3) and incomplete trace element data sets mean that the potential to fully decipher some of these eruptions cannot be fully recognised.

(iii) MIS 5 LAR tephtras

Wulf et al., (submitted) correlate the LAR tephra TM-27 to the X-6 (Keller et al., 1978) and C-31 (Paterne et al., 2008) marine tephtras based on major element analyses; additionally, Bourne (2012) links PRAD 2812 cm to TM-27. TM-27 is the thickest tephra in the LGdM record (Table 6.4; Fig. 6.4), it is located within the terrestrial Melisey II cold interval, which is importantly associated with stadial conditions (MIS 5d) (Brauer et al. 2007). Indeed, Paterne et al. (2008) and Bourne (2010) identify the C-31 and PRAD 2812cm respectively in

MIS 5d stadial conditions, highlighting them as important tephrostratigraphic markers (Fig. 6.5). X-6 has been more recently recognised in the lacustrine deposits of Lake Ohrid (Caron et al., 2010; Vogel et al., 2010) and within colluvial deposits at Le Saline, Palinuro (Morche 1988; Marciano et al., 2008). TM-27 is an important stratigraphic marker at LGdM due to its thickness and because it is geochemically distinguishable from the overlying HAR tephras (TM-24/25) (Fig. 6.15a) (Wulf et al., submitted). In the absence of detailed available data for the X-6 LAR tephras presented herein are compared to TM-27 at LGdM.

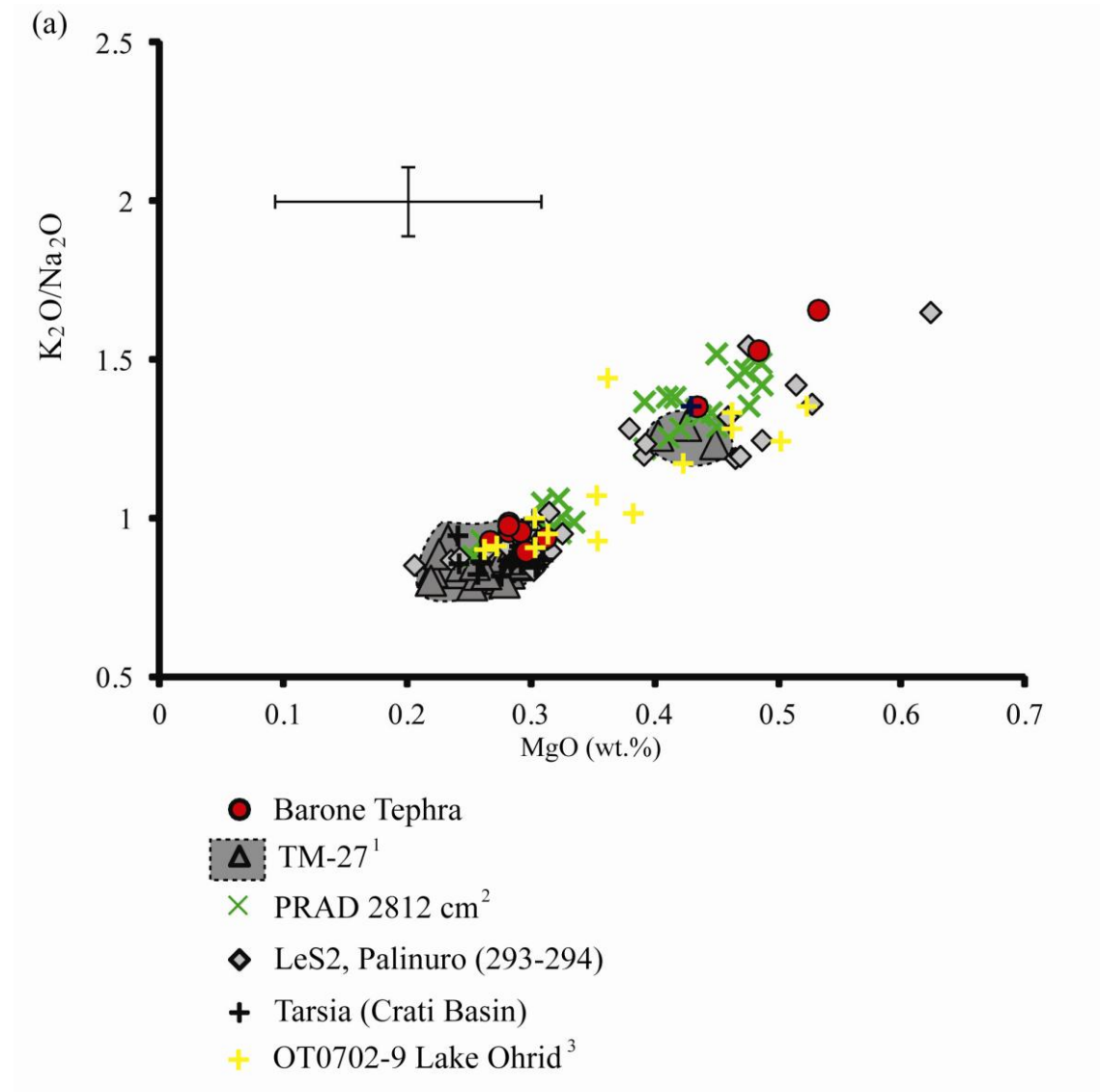


Figure 6.18: Alkali ratios versus MgO showing the Barone tephra/Salina I and other prominent LAR tephras recorded during MIS 5. ⁽¹⁾ TM-27 from Lago Grande di Monticchio (Wulf et al., submitted); LeS2 Palinuro (Cilento); Tarsia Crati valley (Northern Calabria); ⁽²⁾ PRAD 2812 cm (Bourne, 2012) and ⁽³⁾ OT0702-9, Lake Ohrid (Vogel et al., 2010).

The 30 cm thick Barone tephra/Salina I, Salina Island, and Le Saline (LeS2) from the second volcaniclastic deposit sampled near Palinuro, straddle the phonolitic to trachytic classification boundary (Fig. 6.14). Both tephras have major and trace element bimodality that is also displayed in PRAD 2812 cm marine tephra and is consistent with the LGdM tephra TM-27.

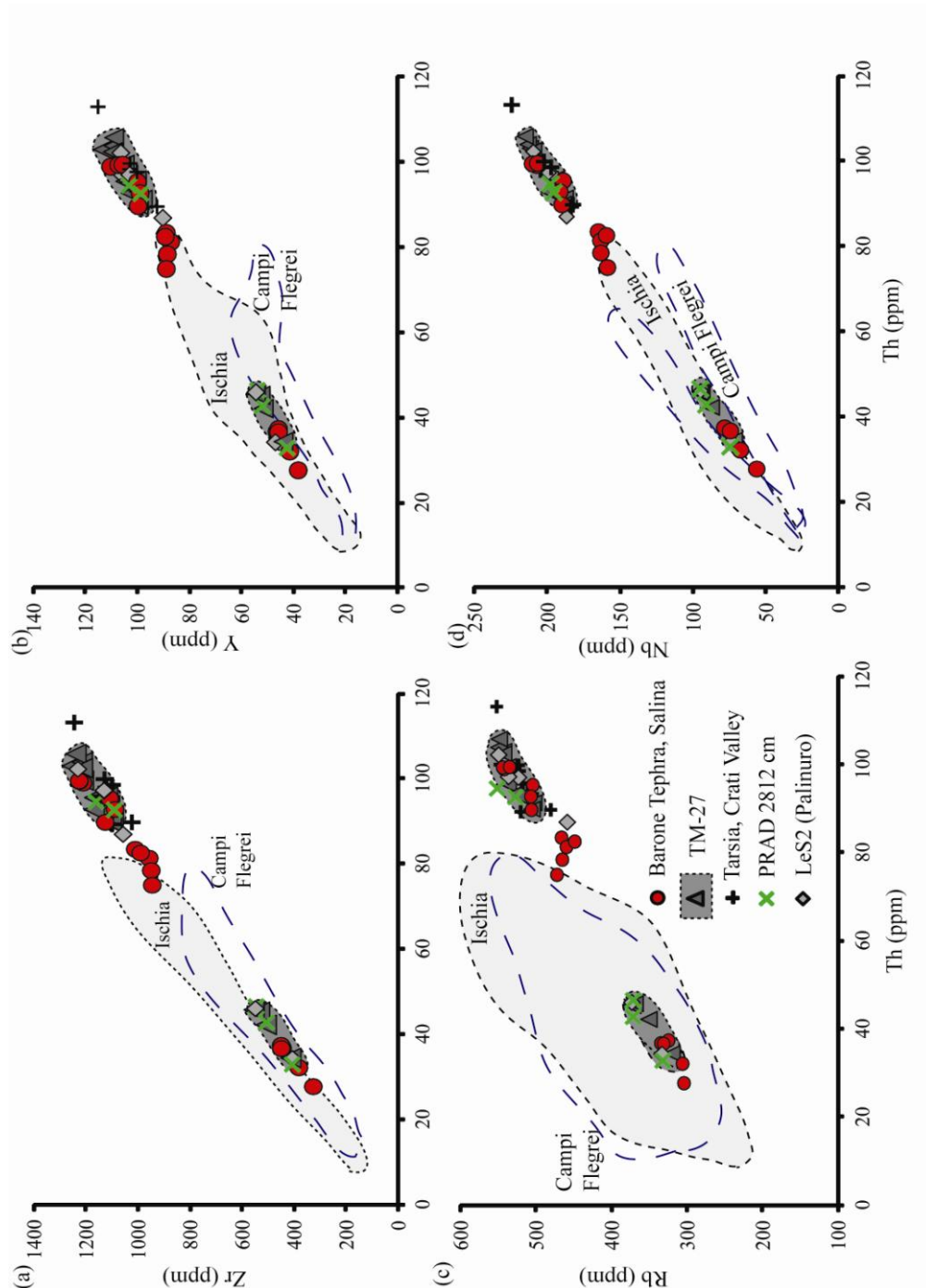


Figure 6.19: Trace element bi-plots showing concentrations observed in the Barone tephra. Also shown are prominent LAR tephras identified in MIS 5 (See Table 6.8). Compositional field for Campi Flegrei based on Tomlinson et al., (2012b) and Ischia (unpublished data/Chapter 6.2).

All these tephra deposits have indistinguishable major, minor and trace element glass compositions, including incompatible trace element ratios (Fig. 6.18; 6.19; Tables 6.5, 6.6, 6.7). This link enables age from LGdM to be exported to these distal stratigraphies (108.3 ka BP; Wulf et al., submitted), but importantly builds upon the known dispersal of this tephra. The X-6 clearly has a shared LAR affinity, its visible thickness in the Ionian Sea marine record constitutes an equally large magnitude eruption, but without grain-specific major, minor and trace element data it is not yet possible to confirm the diagnostic bi-modality present in the other LAR tephras. The X-6 identified at Lake Ohrid (Vogel et al., 2012) displays the same major element variability as the LAR tephras presented above (Fig. 6.18). This, despite a lack of trace elements confirmation, would indicate that lake Ohrid tephra is related to the TM-27 tephra at LGdM.

At Tarsia, within the Crati Valley 200 km south-east of the Campanian volcanic zone, an 80 cm thick phono-trachytic tephra deposit is characterised. Whilst the glasses do not have the same major and trace element bi-modality as TM-27, the glasses clearly correspond to the dominant component of TM-27 (Fig. 6.14) where $\text{Na}_2\text{O} > \text{K}_2\text{O}$ (Fig. 6.15a; 6.18). Trace element concentrations are also consistent with the more evolved end-member of TM-27. Previous interpretations that this pyroclastic deposit represents younger explosive activity (42-25 ka; Carobene et al. 2006) from the Campanian region thus appear unlikely. Trace element concentrations in these glasses are more elevated than any tephras proximally characterised in the Neapolitan region in the proposed time frame (Fig. 6.19). Further to similarities in major and trace element glass data, the Tarsia deposit contains amphibole which is largely unique to these LAR tephras (Table 6.4). Given the thickness of the deposits, the geochemical data and the mineral assemblage, it is proposed that the Tarsia tephra relates to TM-27.

In summary glass data presented here from Barone (Salina), LeS2 (Palinuro), Tarsia (Crati Valley, Calabria), PRAD 1-2 Adriatic (Bourne 2012) and published data from Lake Ohrid (Vogel et al. 2010) clearly demonstrate the potential to confidently link archives to TM-27 at LGdM (Fig. 6.20). Major and trace element bi-modality provides an important diagnostic feature of this tephra and presents greater confidence in determining distal-distal correlations (Fig. 6.18; 6.19).

Provenance

According to the TAS classification (Fig. 6.14) the LAR tephras all fall within the compositional field of glasses produced at Ischia (14-100 ka; Tomlinson et al., in prep) with the exception of the LAR X-6 due to overall lower total alkalis, possibly related to different analytical conditions. Alkalis concentrations are consistent with a derivation from Ischia, where glasses are dominated by $\text{Na}_2\text{O} > \text{K}_2\text{O}$, whilst also displaying some glasses with $\text{K}_2\text{O} > \text{Na}_2\text{O}$ (Fig. 6.15a-b). Finally the Ischia deposits produced between 55-100 ka have more elevated incompatible trace element concentrations than the Campanian deposits (12-59 ka) (Fig. 6.19). The even higher concentrations observed in the Barone/TM-27 glasses might be more consistent with older, uncharacterised Ischia activity. However, in the absence of proximal evidence these interpretations remain tentative.

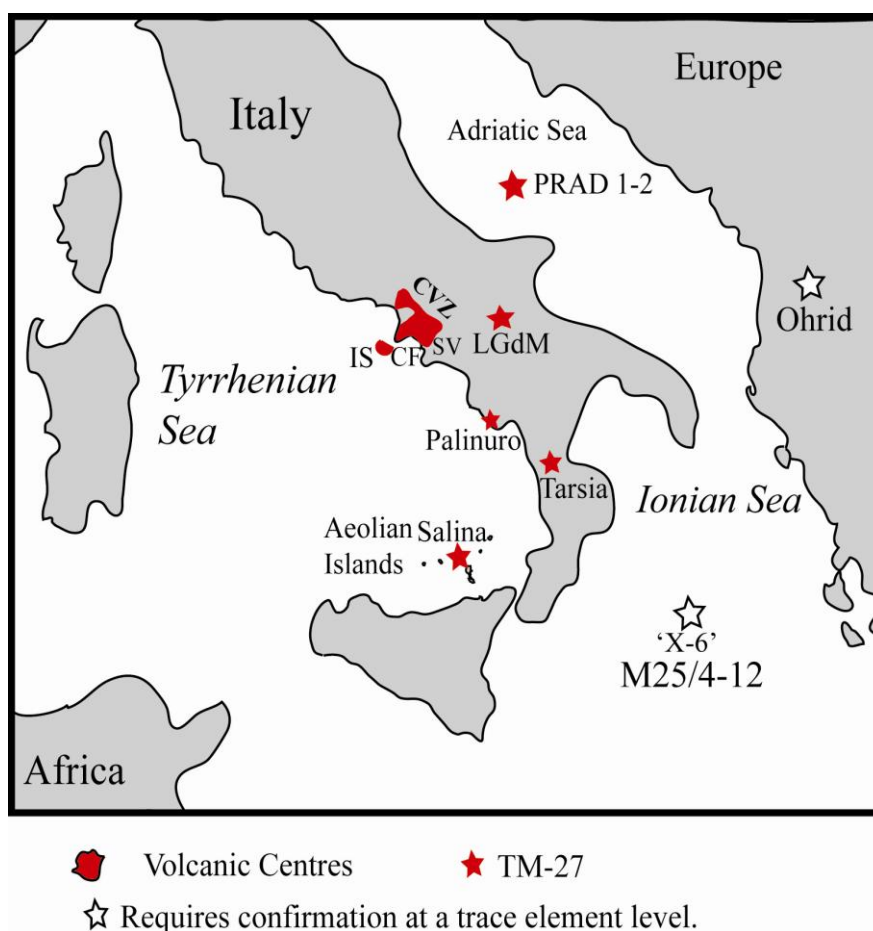


Figure 6.20: Stars marked in red are the localities of the tephras precisely correlated to TM-27 at LGdM using diagnostic major, minor and trace element bi-modality in the glass compositions. This eruption is likely to include X-6 (M25/4-12) and OT0702-9 (Lake Ohrid) tephra layers, however these require confirmation at a multi-elemental level.

6.3.4 Summary:

- The Panarea Pink ash recorded at Punta Falcone, Panarea, ranges from tephri-phonolite to phonolite and does not compositionally correspond to either of the previously proposed correlatives, the X-5 marine tephra (Lucchi et al., 2008) or the Pomici di Base, Vesuvius (De Rita et al., 2008). Its provenance/age remains unresolved.
- The HAR trachytic pyroclastic deposits sampled at Le Saline 1 (LeS1), Palinuro, cannot be precisely linked to any of the HAR tephra at a multi-element level. Trace element analyses do enable its distinction as a compositionally separate tephra to the TM-24 layers, the PRAD1-2 tephra (2525 cm/2605 cm) and SA03-03-925cm layer. Whilst detailed trace element data for the remaining prominent markers in the HAR group X-5, TM-25 and C-27 are not available, they do present more restricted K-trachytic major element compositions consistent with the Le Saline 1 glasses leaving a potential correlation open.
- The HAR MIS 5 tephra recorded in the Adriatic core PRAD 1-2 previously correlated to TM-24 and X-5 (Bourne et al., 2010) display significantly more elevated trace element compositions and are instead considered to record geochemically distinct volcanic events.
- The heterogeneous MIS 5 HAR tephra reported in the southern Adriatic core SA03-03-925cm has trace element concentrations that confirm previously established correlations with the TM-24 layers at LGdM (Bourne, 2012).
- Due to a high frequency of HAR tephra reported in the central Mediterranean archives during MIS 5, best illustrated by the thick TM-24a TM-24b and TM-25 layers at LGdM (Fig. 6.4), multi-element data is beginning to illuminate some erroneous distal-distal tephra correlations incorporating these compositionally similar tephra.
- All the tephra recognised as LAR within MIS 5 settings, including the Barone tephra, Salina, were correlated to the 2m thick TM-27. Major and trace element bimodality within the glass compositions is defined as an important diagnostic feature of this tephra.
- Multi-element data reinforce the previous correlation of Keller (1980) and Morche (1988) linking the Barone tephra/Salina I layer to tephra recorded at Palinuro (i.e., LeS2).

- TM-27 appears to present an important tephrochronological marker, which can be confidently linked over wide geographical distances (Fig.6.20), owing to its unique LAR composition and distinctive trace element geochemistry. Furthermore it dramatically differs geochemically from other prominent tephras produced in MIS 5 period and is constrained to an important period of climatic cooling.
- The Palinuro pyroclastic levels demonstrate the complexities of using tephras recorded in colluvial deposits as stratigraphic markers. Stratigraphically it appeared that the two localities represented the same volcanoclastic level. However geochemical data presented herein indicates the two deposits represent temporally separate eruptive events; LeS1 is a HAR tephra probably related to TM-25/X-5 (105 ± 2 ka; Kraml 1997) and LeS2 is LAR tephra related to TM-27 (ca. 108.3 ka BP; Wulf et al., submitted).

6.4 Conclusions

Three prominent external tephra outcropping in the Aeolian Islands have been geochemically characterised using major, minor and trace element glass analyses. This has been used to test provenance solutions or in the absence of well constrained proximal deposits, assessment of distal-distal links.

1) The '*Ischia tephra*' layer on Stromboli is assigned to the MEGT caldera forming eruption of Ischia. MEGT is one of the most widespread late Quaternary tephra layers recorded in central Mediterranean archives, enabling the synchronisation of distal archives. MEGT is seemingly responsible for key central Mediterranean markers TM-19 and the Y-7. $^{40}\text{Ar}/^{39}\text{Ar}$ dating from both distal TM-19 and Y-7 layers means this tephra is a particularly powerful chronological tool beyond the limits of more conventional dating (^{14}C).

2) The Panarea Pink Ash (PPA) remains unresolved. Links to both younger Somma-Vesuvian activity and the older X-5 marine tephra are refuted based on glass data presented herein.

3) Combined major and trace element data confirm that the LeS1 HAR tephra recorded at Palinuro is not the equivalent of either of the TM-24 tephras reported at LGdM. Major element data might suggest that TM-25 is a potential correlative but this requires confirmation at a trace element level.

4) Owing to the closely spaced, geochemically overlapping eruptions recorded at LGdM (TM-24/25), problematic correlations associated with these LGdM tephras and the X-5 exist in the literature. Trace element data presented herein might indicate that there is potential to provide diagnostic features for some of these tephras. Whilst in other instances data indicates some temporally separate MIS 5 HAR tephras have indistinguishable major and trace element geochemistries (i.e. The TM-24 layers and PRAD2525/2605cm) (Fig. 6.17). This demonstrating a problem of repeatedly produced glass geochemistries.

5) In the absence of detail proximal stratigraphies it seems imperative to utilise LGdM as a reference tephrostratigraphy, given that it presents probably the most detail record of Italian explosive eruptions between 60-130 ka (Wulf et al., submitted). Furthermore it offers an independent chronology so that when precise correlations are established age can be exported.

6) The LAR Barone tephra layer, Salina, represents a southern equivalent of the LGdM TM-27 tephra, reinforcing its widespread dispersal in which it can be linked to other archives in the central Mediterranean region. This eruption presents a more unique and diagnostic glass chemistry than the younger TM-24/25 tephras at LGdM. This eruption can be used to precisely correlate distal archives (Fig. 6.20). This tephra presents a particularly widespread and important stratigraphic marker, dispersed within the central Mediterranean, enabling the synchronisation of archives over hundreds of kilometres.

Abstract

Biancavilla ignimbrites represent an explosive episode in the dominantly effusive volcanic history of Mount Etna (Italy) and are responsible for widespread ash dispersal throughout the central Mediterranean region. Distal tephras recorded within marine and lacustrine archives spanning termination 1 are attributed to this explosive activity on Etna (Y-1/Et-1). However, no major, minor and trace element data exists for the juvenile component of proximal deposits, which are fundamental to precise proximal-distal correlations. Here, geochemical data (EPMA and LA-ICP-MS) are presented for juvenile glasses in clasts from (a) fall (Acireale & Giarre) and flow deposits (Biancavilla) outcropping around Mount Etna and (b) distal tephras recorded at Lago Grande di Monticchio (LGdM) & Lago di Mezzano (LMZ), Italy, a Ionian Sea marine core and a cave site in Libya, North Africa.

Matching proximal and distal chemistries precisely, allow us to revise the extent of volcanic ash footprints and to better determine eruptive histories. At least two widespread ash dispersal events are confirmed from Mount Etna during this period of explosive activity. The older is associated with the lower Acireale Plinian Fall and the Biancavilla ignimbrites (D1b/BF) and it correlates to TM12-1 (LGdM), Y-1 (Ionian Sea) and distal ash at Haula Fteah, Libya. Whilst a younger Plinian phase is tentatively linked to Acireale D2b Plinian fall, this second Plinian dispersal corresponds distally to TM-11 (LGdM), Y-1 (Lago di Mezzano; the Central Adriatic and the Bannock basin). Identification of Acireale D1b Plinian fall and Biancavilla flow tephra compositions/morphologies in distal layers illustrates that both eruptive mechanisms were responsible for the first major ash dispersal. Links between the second Plinian fall (D2b) episode and the upper most Biancavilla flow deposits cannot be ruled out. Careful assessment of distal Etnean tephras means that the Biancavilla explosive episodes present two important distal tephrostratigraphical markers during Termination 1.

7.1 Introduction:

Mount Etna is the largest active volcano in Europe and is well renowned for its quasi persistent effusive activity (Coltelli et al., 2000). Historical activity has been dominated by lava flows from the summit crater or monogenetic vents on the flanks of the volcano, whilst violent Strombolian eruptions are also common, all are dominated by basaltic compositions. However, over the last 100 ka Coltelli et al. (2000) identified numerous explosive tephra recorded in stratigraphies surrounding the volcano. Identification of these varying explosive deposits within the predominantly effusive history of the volcano have been used to infer changing eruptive mechanisms operating through time (Duncan, 1976, Kieffer, 1979 Chester et al., 1987, De Rita et al., 1991 and Coltelli et al., 2000). Coltelli et al. (2000) subdivided the explosive activity of the last 100 ka into the following erupted units; (a) ~100 ka Strombolian to sub-Plinian activity; (b) 100-80 ka Plinian activity; (c) 80-16 ka Strombolian to sub-Plinian; (d) 15.5 to 15 ka Plinian activity; and (e) 15 ka to present Strombolian to sub-Plinian. During the last 100 ka, erupted magma compositions included basalts, hawaiite, mugearite and benmoreite (Coltelli et al., 2000).

The focus of this investigation is the most recent Plinian episode, unit D of Coltelli et al., (2000). Coltelli et al. (2000) proposed a link between the Plinian deposits and the Biancavilla ignimbrites, a succession of four “block and ash” flow deposits recorded to the south-west of Etna (De Rita et al., 1991). The onset of explosive activity is constrained at $18,289 \pm 270$ cal. yrs. B.P (Coltelli et al., 2000) by a ^{14}C date from beneath the lowermost proximal fall deposits at Giarre. A radiocarbon age from the base of the Biancavilla flow is reported as $17,363 \pm 554$ cal. yrs. BP ($14,180 \pm 260$ uncal yrs B.P; Delibrias, 1972).

Herein, the focus is principally the juvenile glass geochemistry of this Plinian activity on Mount Etna (Unit D) and the Biancavilla Ignimbrites to confirm links between the eruptive successions. Previously published chemical data on the proximal deposits were derived from bulk rock analyses, potentially masking some compositional variability (Coltelli et al., 2000). The significance of the switch from effusive to explosive volcanism associated with the Biancavilla eruptive phase is considered by interpreting the geochemical signature of this particularly unique phase in the eruptive history of Mount Etna.

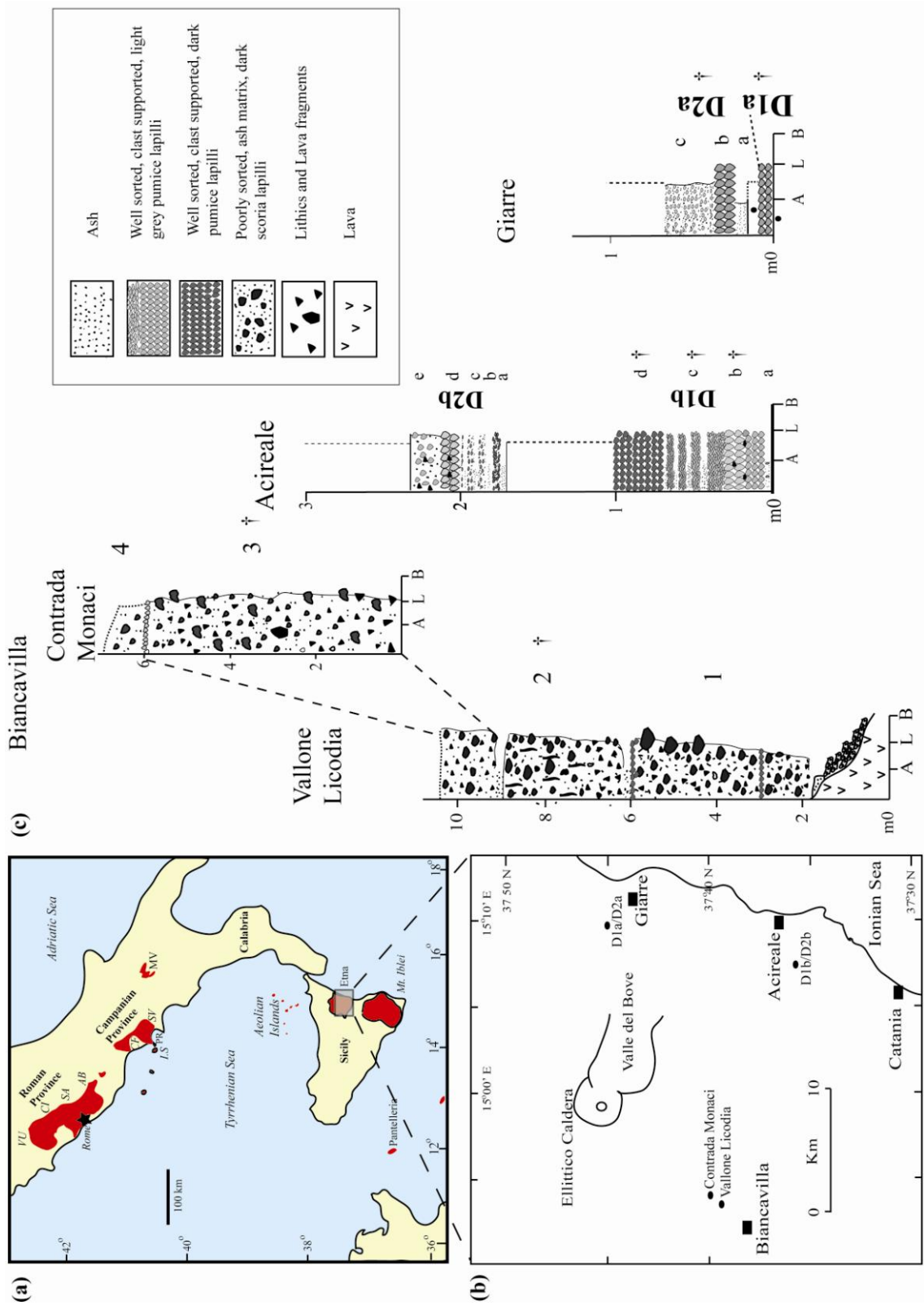


Figure 7.1: (a) Location of Mount Etna on Sicily; (b) Map of Etna; black dots represent sampled localities. (c) Stratigraphic logs represent the stratigraphies from which juvenile glasses were sampled. Sampled units are marked by †. (see Table 7.1).

Given the chronological constraints of the Unit D/Biancavilla Ignimbrite explosive episode it holds significant importance to distal tephrochronological studies. This explosive activity occurs during a period of important environmental change and the onset of the last glacial interglacial transition (LGIT) or termination 1. The first recognised occurrences of distal Etnean tephra within this stratigraphic context was reported in the type locality for the Y-1 in the Ionian Sea (Keller et al., 1978). Keller et al. (1978) correlated the Y-1 to the Biancavilla Ignimbrites based on its unique Na-alkali composition. Subsequently Etnean ash has been reported across the Central Mediterranean and is either termed as (1) the Y-1 consistent with the Ionian Sea or (2) Et-1 in the case of the Tyrrhenian Sea (Paterne et al., 1988; Vezzoli 1991; Calanchi et al. 1996, Calanchi et al., 1998; Ramrath et al. 1999; Siani et al., 2004; Wulf et al., 2004; Wulf et al., 2008).

New proximal geochemical glass data will be used to evaluate distal correlations in the context of Unit D/Biancavilla ignimbrite, incorporating new distal trace element glass data from the Y-1 Ionian Sea (M25/4-11), Lago di Mezzano (LMZ) in the Roman comagmatic province (central Italy) & Haula Fteah, Libya. Two distal ashes in Lago Grande di Monticchio, TM-11 'Biancavilla Ignimbrite' & TM-12-1 'Ante-Biancavilla' are re-investigated. The relationships between the distal ash dispersals and the different phase of explosive volcanism on Mount Etna are assessed, evaluating their potential to precisely synchronise distal archives.

7.2 Geological Setting

Mount Etna is a 3340 m high stratovolcano, which extends over 1250 km² (Viccaro et al., 2010). Located along the eastern coast of Sicily, Mount Etna is positioned at the intersection of two major faults trending NNW-SSE (Tindari-Letojanni-Malta NNE-SSW (Messina-Giardini) (Viccaro et al., 2010). Etna volcanic activity began ~ 500 ka BP (Gilliot et al., 1994) and around 200 ka BP erupted products began to display the Na-alkalic compositions so characteristic of Mount Etna. The construction of a central-conduit stratovolcano started about 130 ka BP. Effusive activity was prevalent but interrupted by explosive episodes associated with caldera collapse.

7.3 Volcanostratigraphy and sampling:

Proximal field sampling on Mt Etna focussed on juvenile clasts in stratigraphically coherent units. Outcrops to the east and south-west of Mount Etna were targeted including block and ash flows and pumice fall deposits. Samples were selected from flow units at Vallone di Licodia and Lower Contrada Monaci near Biancavilla (Table 7.1; Fig. 7.1). Fall units were targeted in the medial-proximal localities of Acireale and Giarre to the east of Mt Etna along the Ionian Sea coast (Fig. 7.1). Details of all the pumices sampled and their stratigraphic context are summarised in Table 7.1.

7.3.1 Biancavilla Area

Proximal sampling of the ignimbrite deposits concentrated on the region of Vallone di Licodia and Contrada Monaci, near Biancavilla on the lower SW flank of Etna (Fig. 7.1, Fig. 7.4a). The pyroclastic deposits rest on an autoclastic lava dome related to ‘ancient Mongibello’, which are in turn covered by the lavas of the ‘recent Mongibello’. The Biancavilla ignimbrite is subdivided into four major flow units (Table 7.1) and each unit is characterised by a fine grained basal deposit (Sparks et al., 1973; De Rita et al., 1991). The lower flow deposits were sampled at Vallone di Licodia and the upper flow deposits were sampled at Contrada Monaci, with details of the stratigraphy outlined by Di Rita et al. (1991) in Table 7.1.

7.3.2 Eastern flank, Etna:

Coltelli et al. (2000) recognise four pumice lapilli beds on the eastern flank of Mount Etna (Fig. 7.3). Due to their widespread dispersal these fall units are adopted as regional stratigraphic markers used to correlate Mount Etna volcanic stratigraphies. These pumice beds form two couplets, outcropping in different areas of the eastern flank of the volcano, at Acireale and Giarre (Fig. 7.1). At Acireale sampling of these pumice lapilli beds concentrated on the volcano-stratigraphy of Coltelli et al., (2000) (Fig. 7.3). The stratigraphy comprises two fall successions, the lower D1b and the upper D2b (Fig. 7.3). The deposits are separated by a volcanoclastic deposit. Details of the sampled stratigraphy are summarised in Table 7.1. D2b phenocryst and microcrystal assemblage differs from the D1b (Table 7.1), amphibole is absent from D2b pumices (Coltelli et al., 2000).

| Region | Sample Locality | Sub-units | Thickness (meters) | Description | Phenocrysts | Micro-cryst | Sampled | GPS | Interpretation | Dispersal | Proximal Age | Reference |
|-------------|------------------------------|-----------|--------------------|--|-------------|-------------|---------|----------------------------|--|-----------|--|-----------------------|
| Biancavilla | Contrada Monaci, Biancavilla | 4 | 0.5 | Poorly sorted, matrix supported (coarse ash) lapilli tuff. Heavily eroded from above | plag, cpx | - | | N 37 39 402 E014 55 256 | Four block and ash Ignimbrite deposits | SW | Tree stub in the base of the flow 17,363 ± 554 yrs BP cal. (uncalibrated: 14,180 ± 260) | De Rita et al. (1991) |
| | | 3 | 6 | Poorly sorted, matrix supported (coarse ash) lapilli tuff. Lava fragments. Structureless except for a 10cm thick scoria/pumice rich clast supported horizon the boundary between units 3 and 4 | plag, cpx | - | † | | | | | |
| | Vallone Licodia, Biancavilla | 2 | 3 | Poorly sorted, matrix supported (Coarse ash), Scoriaceous lapilli unstratified tuff. Lithic rich at the base. De-gassing pipes. Coarse grained ash tuff at the base. | plag, cpx | - | † | N 3739 320 E014 54870 | | | | |
| | | 1 | 6 | Poorly sorted, matrix supported, scoriaceous lapilli tuff, subdivided into inversely graded tuffs (a) lithic rich capped by a pumice top (b) scoria lapilli tuff with fewer lithics, again capped by pumice rich upper portion | plag, cpx | - | | | | | | |

Table 7.1: Stratigraphic information of proximally investigated samples from the Biancavilla flow deposits and the Unit D fall deposits of Coltelli et al. (2000).

| | Sample Locality | Outcrop Thickness (m) | Sub-units | Thickness | Description | Pheno-crysts | Micro-crysts | Sampled † | GPS | Interpretation | Dispersal | Proximal Age | |
|--------------|-----------------|-----------------------|-----------|---|---|--------------|----------------------------|--------------|----------------------------------|----------------|-----------|--|--|
| Eastern Etna | Acireale | 3 | D2b | 0.6 | Comprises of; (a) grey ash massive (b) clast supported fine pumice lapilli (dark-grey); (c) alternating ash and clast supported, well sorted pumice lapilli (d) clast supported coarse light grey banded pumice deposits; (e) ash matrix supported pumice lapilli bed | plag, cpx | ol, Ti-mag, plag, cpx | Inaccessible | | Plinian Fall | SE | - | |
| | | | | 0.6 | Volcanogenic sedimentary deposit | | | | | | | | |
| | | | D1b | 1 | Comprises of (a) grey ash and accretionary lapilli; (b) clast supported, well sorted coarse pumice lapilli bed of banded grey pumice; (c) four alternations of ash and well sorted millimetric pumice lapilli (grey); (d) clast supported, well sorted pumices (dark) | plag, cpx | amp, plag, cpx, ol, Ti-mag | † b, c, d | N37 35 847 E015 07 616 | Plinian Fall | SE | - | |
| | | | | Undefined stratigraphic relationship | | | | | | | | | |
| | Giarre | 0.8 | D2a | 0.5 | Bedded and comprises of (a) grey vesiculated tuff and accretionary lapilli; (b) clast supported, well sorted, grey pumice lapilli; (c) alternating, well sorted ash and dark grey pumices within ash matrix (d) clast supported, well sorted, coarse light grey pumice lapilli; (e) Poorly sorted ash and light grey pumice bed | | amp, plag, cpx, ol, Ti-mag | † | N 37 35 847 E015 07 616 | Plinian Fall | E | - | |
| | | | | 0.1 | Volcanogenic sedimentary deposit | | | | | | | | |
| | | | | | | | | | | | | 18,289 ± 270 yrs BP cal (uncal 15,050 yrs BP) | |
| | | | D1a | 0.05 | Thin layer of clast supported, well sorted, light grey banded pumice lapilli | | amp, plag, cpx, ol, Ti-mag | † | N 37 35 847 E015 07 616 | ? | ? | 18,675 ± 285 yrs B.P cal (uncal; 15,420±60 yrs BP) | |

Cotelli et al. (2000)

Table 7.1: continued.

At Giarre the second couplet of tephra fall identified by Coltelli et al., (2000) was sampled from the following stratigraphy (Fig. 7.1). The lowermost deposit D1a comprises banded pumices, these light grey pumices only form a thin layer often only a few cm thick. D2a comprises a thicker fall bed and details of both are given in Table 7.1 and shown in Figure 7.1. The Giarre pumices (Fig. 7.2c) display greater vesicularity and crystallinity than the Acireale fall deposits (Fig. 7.2b) and both contain micro-crysts of amphibole and magnetite in addition to the main phenocryst assemblage (Table 7.1).

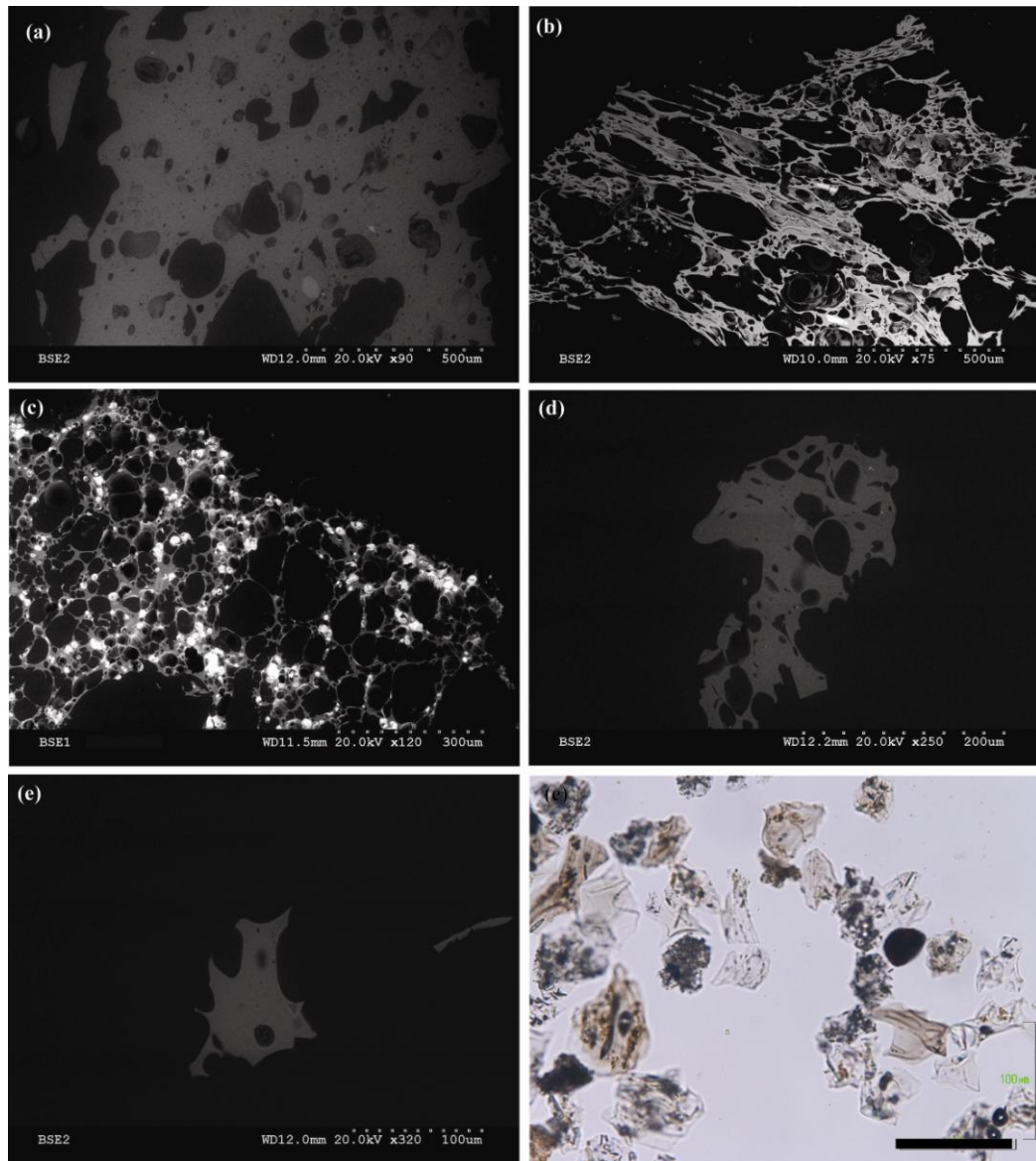


Figure 7.2: SEM and light microscope images of Etnean tephras. (a) Contrada Monaci flow scoriaceous lapilli; (b) Acireale D1b pumices; (c) Giarre D1a highly vesicular pumices; (d) Y-1 Ionian Sea (M25/4-11); (e) Y-1 Lago di Mezzano (LMZ); (f) Glass shards identified with The Haua Fteah cave (Barker et al., in prep).

7.3.3 Stratigraphic interpretations:

From the grain-size distribution, areal dispersal and lithofacies outlined in Coltelli et al., (2000) at least three of the fall units identified on the eastern flank of Etna are interpreted as Plinian fall (D2a, D1b, D2b). Consequently, they have been associated with the same eruptive events that produced the flow deposits at Biancavilla (De Rita et al., 1991). Due to the presence of four flow units at Biancavilla it may be tempting to assume direct correspondence with the four fall units. However, due to the limited thickness of unit D1a, it is considered a smaller, perhaps sub-Plinian eruption, with a less sustained eruptive column. This would suggest a more complex proximal fall-flow relationship.

7.4 Results and discussion

7.4.1 Proximal glass chemistry

Representative proximal glasses are given in Table 7.2 full geochemical data sets are presented in appendix 5 and whole rock analysis in Table 7.3. Glasses from clasts found in both fall and flow deposits have compositions ranging from trachy-andesitic to trachyte and are also termed benmorite (Fig. 7.3). Major and minor element chemistries are heterogeneous with 59.4-64.5 wt.% SiO₂, 4.0-6.6 wt.% FeO 1.4-5.5 wt.% CaO (Table 7.2). These deposits are characterised by particularly high concentrations of Na₂O (5.1-6.8 wt.%), where Na₂O > K₂O (2.8-4.4 wt.%). A TAS diagram (Fig. 7.3a) reveals that the investigated Biancavilla flow and Unit D fall are significantly more evolved than the explosively produced FL tephra, which represents the most widespread tephra produced at Mount Etna during the Holocene (Wagner et al., 2008).

| Locality Unit Sample Material | Vallone di Licodia (Flow unit 2) | | | Contrada Monaci (Flow 3) | | | Acireale D1b-(003) | |
|--|-------------------------------------|--------------|---------------|-----------------------------|--------------|---------------|-----------------------|--------------|
| | 2A Scoria | 5A Scoria | 13C Scoria | 2A Scoria | 3A Scoria | 14C Scoria | 2A Pumice | 6B Pumice |
| Major elements | | | | | | | | |
| SiO ₂ | 63.79 | 63.89 | 62.82 | 61.75 | 62.58 | 62.96 | 62.17 | 61.41 |
| TiO ₂ | 1.24 | 1.21 | 1.29 | 1.60 | 1.20 | 1.35 | 1.14 | 1.32 |
| Al ₂ O ₃ | 17.24 | 17.02 | 17.51 | 16.90 | 16.93 | 17.15 | 17.27 | 16.87 |
| FeOt | 4.91 | 4.61 | 4.56 | 5.80 | 5.11 | 4.35 | 4.70 | 5.32 |
| MnO | 0.17 | 0.27 | 0.16 | 0.18 | 0.18 | 0.19 | 0.20 | 0.22 |
| MgO | 1.75 | 1.43 | 1.13 | 1.53 | 1.68 | 1.68 | 1.49 | 1.79 |
| CaO | 1.41 | 2.02 | 3.08 | 3.23 | 3.36 | 3.18 | 3.15 | 3.64 |
| Na ₂ O | 5.73 | 5.57 | 6.26 | 5.77 | 5.59 | 5.93 | 6.10 | 6.08 |
| K ₂ O | 3.76 | 3.97 | 3.18 | 3.25 | 3.36 | 3.23 | 3.78 | 3.35 |
| Analytical Total | 95.92 | 95.36 | 94.29 | 97.64 | 98.05 | 94.82 | 98.50 | 98.97 |
| K ₂ O/Na ₂ O | 9.49 | 9.54 | 9.44 | 9.01 | 8.96 | 9.15 | 9.88 | 9.42 |
| Trace elements | | | | | | | | |
| Spot size (µm) | 34 | 34 | 34 | 34 | 34 | 34 | 25 | 20 |
| Rb | 82.3 | 95.1 | 70.2 | 76.7 | 89.6 | 76.2 | 88.9 | 80.9 |
| Sr | 685 | 399 | 812 | 714 | 708 | 719 | 755 | 750 |
| Y | 34.4 | 36.1 | 36.4 | 35.3 | 35.2 | 37.3 | 35.8 | 35.9 |
| Zr | 433 | 419 | 415 | 414 | 423 | 434 | 435 | 420 |
| Nb | 114 | 120 | 111 | 111 | 115 | 115 | 119 | 117 |
| Ba | 1419 | 1349 | 1446 | 1307 | 1329 | 1391 | 1490 | 1371 |
| La | 121 | 124 | 120 | 118 | 123 | 127 | 128 | 119 |
| Ce | 226 | 234 | 224 | 222 | 231 | 236 | 230 | 224 |
| Pr | 22.6 | 22.8 | 23.2 | 22.36 | 23.3 | 24.0 | 23.3 | 22.6 |
| Nd | 86.1 | 89.0 | 84.5 | 80.4 | 86.2 | 92.3 | 87.6 | 83.6 |
| Sm | 13.6 | 14.4 | 13.6 | 14.2 | 14.9 | 16.0 | 12.2 | 13.0 |
| Eu | 3.4 | 3.3 | 3.4 | 3.2 | 3.3 | 3.5 | 3.4 | 3.3 |
| Gd | 8.9 | 10.3 | 9.8 | 10.0 | 10.8 | 10.2 | 9.9 | 10.4 |
| Dy | 7.2 | 7.6 | 7.5 | 7.04 | 7.4 | 7.6 | 7.4 | 7.5 |
| Er | 3.6 | 3.9 | 3.9 | 3.4 | 3.7 | 3.7 | 3.6 | 3.5 |
| Yb | 3.1 | 3.4 | 3.3 | 3.4 | 3.3 | 3.6 | 3.1 | 3.4 |
| Lu | 0.44 | 0.52 | 0.48 | 0.47 | 0.46 | 0.53 | 0.47 | 0.51 |
| Ta | 5.4 | 5.3 | 5.4 | 5.2 | 5.1 | 5.4 | 5.0 | 5.1 |
| Pb | 19.8 | 20.9 | 17.2 | 19.1 | 21.8 | 19.0 | 27.0 | 20.9 |
| Th | 21.6 | 22.1 | 22.1 | 22.1 | 22.3 | 22.4 | 23.8 | 22.4 |
| U | 6.5 | 6.8 | 6.3 | 6.4 | 6.5 | 6.5 | 7.0 | 6.8 |

Table 7.2: Representative major, minor and trace element data from proximal scoriaceous flow deposits in the Biancavilla area and Unit D fall deposits from Acireale and Giarre. Full data is available in appendix eVI.

| Locality | Acireale | | Acireale | | Giarre | | Giarre | |
|------------------------------------|-----------|--------|-----------|--------|-----------|--------|-----------|--------|
| | D1b-(004) | | D1b (005) | | D1a (006) | | D2a (007) | |
| | 3A | 2A | 18D | 8B | 11C | 2A | 6B | 12C |
| Sample | Pumice | Pumice | Pumice | Pumice | Pumice | Pumice | Pumice | Pumice |
| Material | Pumice | Pumice | Pumice | Pumice | Pumice | Pumice | Pumice | Pumice |
| Major elements | | | | | | | | |
| SiO ₂ | 61.87 | 62.17 | 62.32 | 62.09 | 59.97 | 60.99 | 61.33 | 61.45 |
| TiO ₂ | 1.31 | 1.29 | 1.12 | 1.21 | 0.88 | 0.82 | 0.82 | 0.84 |
| Al ₂ O ₃ | 17.03 | 16.92 | 17.17 | 16.65 | 17.91 | 17.86 | 16.97 | 17.90 |
| FeOt | 5.16 | 5.09 | 5.06 | 5.00 | 5.77 | 5.15 | 6.00 | 5.62 |
| MnO | 0.12 | 0.17 | 0.17 | 0.13 | 0.19 | 0.15 | 0.24 | 0.12 |
| MgO | 1.84 | 1.64 | 1.66 | 1.76 | 1.89 | 1.42 | 1.56 | 1.25 |
| CaO | 3.49 | 3.24 | 3.78 | 3.66 | 4.54 | 3.90 | 3.86 | 3.32 |
| Na ₂ O | 5.84 | 6.05 | 6.13 | 6.08 | 6.07 | 6.56 | 5.77 | 6.13 |
| K ₂ O | 3.34 | 3.43 | 2.60 | 3.43 | 2.79 | 3.13 | 3.45 | 3.37 |
| Analytical Total | 98.67 | 99.13 | 98.28 | 95.40 | 98.19 | 97.98 | 97.78 | 95.32 |
| K ₂ O/Na ₂ O | 9.18 | 9.48 | 8.72 | 9.51 | 8.85 | 9.70 | 9.22 | 9.50 |
| Trace elements | | | | | | | | |
| Spot size (µm) | 25 | 20 | 25 | 25 | 20 | 20 | 20 | 20 |
| Rb | 84.0 | 79.1 | 82.1 | 82.1 | 82.5 | 82.3 | 85.3 | 94.4 |
| Sr | 751 | 713 | 771 | 692 | 860 | 675 | 788 | 436 |
| Y | 37.7 | 37.5 | 34.7 | 34.0 | 25.3 | 26.5 | 22.9 | 27.9 |
| Zr | 454 | 438 | 427 | 421 | 319 | 360 | 337 | 397 |
| Nb | 115 | 119 | 115 | 113 | 102 | 108 | 99 | 117 |
| Ba | 1381 | 1409 | 1478 | 1365 | 977 | 1003 | 969 | 1011 |
| La | 127 | 123 | 120 | 119 | 98 | 103 | 98 | 108 |
| Ce | 233 | 230 | 229 | 215 | 174 | 185 | 161 | 189 |
| Pr | 24.4 | 25.6 | 22.4 | 21.1 | 17.4 | 18.9 | 15.9 | 18.7 |
| Nd | 92.3 | 88.7 | 78.0 | 74.6 | 60.8 | 64.9 | 56.0 | 64.9 |
| Sm | 14.3 | 14.1 | 12.6 | 15.2 | 10.3 | 9.9 | 8.4 | 11.2 |
| Eu | 3.7 | 3.1 | 3.4 | 3.3 | 2.5 | 2.3 | 2.4 | 2.4 |
| Gd | 10.9 | 11.0 | 11.0 | 9.5 | 6.4 | 6.6 | 6.4 | 9.8 |
| Dy | 8.3 | 7.1 | 7.4 | 7.1 | 5.4 | 5.5 | 4.6 | 5.4 |
| Er | 3.9 | 3.7 | 3.5 | 3.6 | 2.6 | 2.7 | 2.3 | 3.0 |
| Yb | 3.6 | 3.9 | 3.6 | 3.1 | 2.6 | 2.8 | 2.2 | < LOD |
| Lu | 0.51 | 0.52 | 0.46 | 0.51 | 0.36 | 0.41 | 0.38 | < LOD |
| Ta | 5.6 | 5.2 | 5.7 | 4.7 | 4.4 | 4.9 | 5.0 | 5.6 |
| Pb | 17.9 | 18.9 | 21.4 | 18.0 | 15.6 | 16.5 | 18.0 | 14.7 |
| Th | 22.8 | 21.9 | 20.4 | 22.0 | 19.7 | 21.0 | 18.9 | 21.7 |
| U | 7.0 | 7.0 | 6.6 | 6.9 | 6.0 | 6.1 | 5.9 | 6.1 |

Table 7.2: Continued.

Mantle normalised trace element patterns (Fig. 7.4) for proximal glasses in both fall and flow deposits show enrichments in the large ion lithophile elements (LIL) relative to high field strength elements (HFSE). Consequently, the glasses display a slight trough at Nb and Ta (Fig. 7.4). Glasses also show strong depletions in Ti. Overall, all proximal glasses display a similar trace element signature and are up to more than 300 times more enriched than primitive mantle (Fig.7.4). Glasses show LREE enrichment relative to the HREE (La/Yb = 31-45; Fig. 7.4). Sr shows a range in compositions from 860-398 ppm and the depletion is attributed to high level fractionation associated with Ca rich phases like plagioclase and clinopyroxene. Vallone Licodia glasses are some of the most fractionated glasses associated with low CaO wt. % (Fig. 7.3c) and a marked Sr anomalies ($Sr/Pr_N = 0.34 \pm 0.09$; Fig. 7.4). Given that Al_2O_3 , K_2O and Na_2O do not show a marked decrease with increasing SiO_2 it is more likely that clinopyroxene was the dominant fractionating phase effecting the glass compositions (Fig. 7.3).

Geochemical data indicate that the glasses/magmas linked to explosive activity on Mount Etna are in marked contrast to the mafic compositions that feed effusive activity (i.e., hawaiites/basanites). Glasses in the Unit D/Biancavilla deposits show depletions in Nb, Ta, and Ti (Fig. 7.4) which imply a subduction influence. Indeed, it has been suggested that this is linked to slab detachment or roll back triggering a switch from intra-plate mantle sources (Schiano et al., 2001; Tonarini et al., 2001; De Astis et al., 2003).

7.4.1.1 Biancavilla Flow Deposits

Glasses from within the flow units at Biancavilla are trachytic (Fig. 7.3). The lowermost ignimbrite scoriaceous deposits at Vallone Licodia (Flow unit 2) display the most fractionated glass compositions with 62.4-64.5 wt.% SiO_2 , 4.3-1.4 wt.% CaO. The Monaci Contrada (Flow unit 3) overlaps with the less evolved component of flow unit 2 at a major element level with 61.7-63.4 wt.% SiO_2 , 3.0-3.7 wt.% CaO and 4.1-5.8 wt.% FeO. Scoriaceous deposits within both flow units respond to increasing fractionation with decreasing FeO and CaO, whilst the remaining major and minor element concentrations remain relatively consistent (Fig. 7.3). Trace element concentrations within the Vallone Licodia glasses show some variation with 34-39 ppm Y; 415-455 ppm Zr; 111-119 ppm Nb; 1446-1338 ppm Ba.

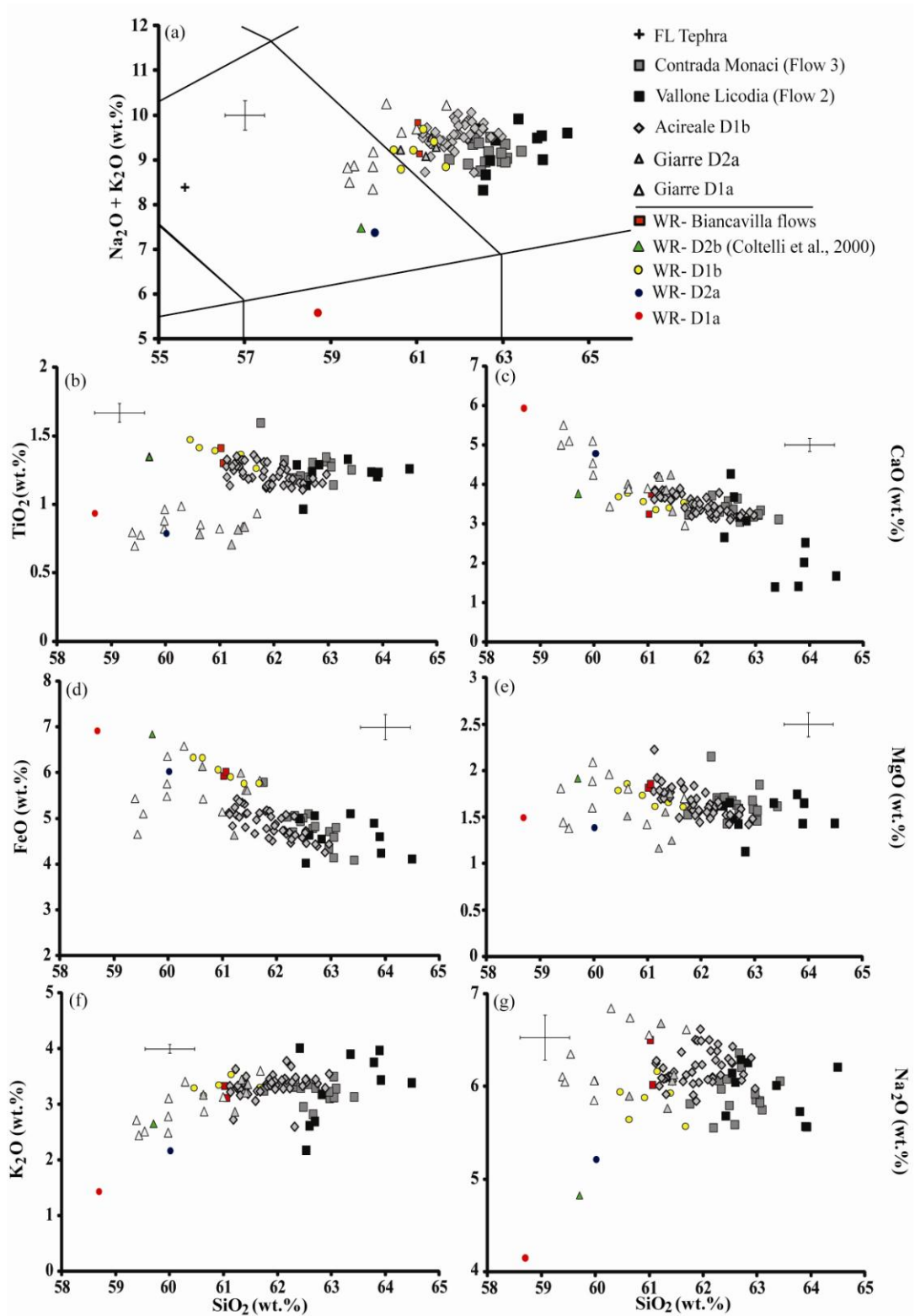


Figure 7.3: Major element bi-plots for the proximal glasses from the Biancavilla flow deposits and the unit D fall. Also shown for comparison are the whole rock analyses of the same deposits. Errors given are 2 x standard deviation of analyses of the StHs6/80G secondary standard.

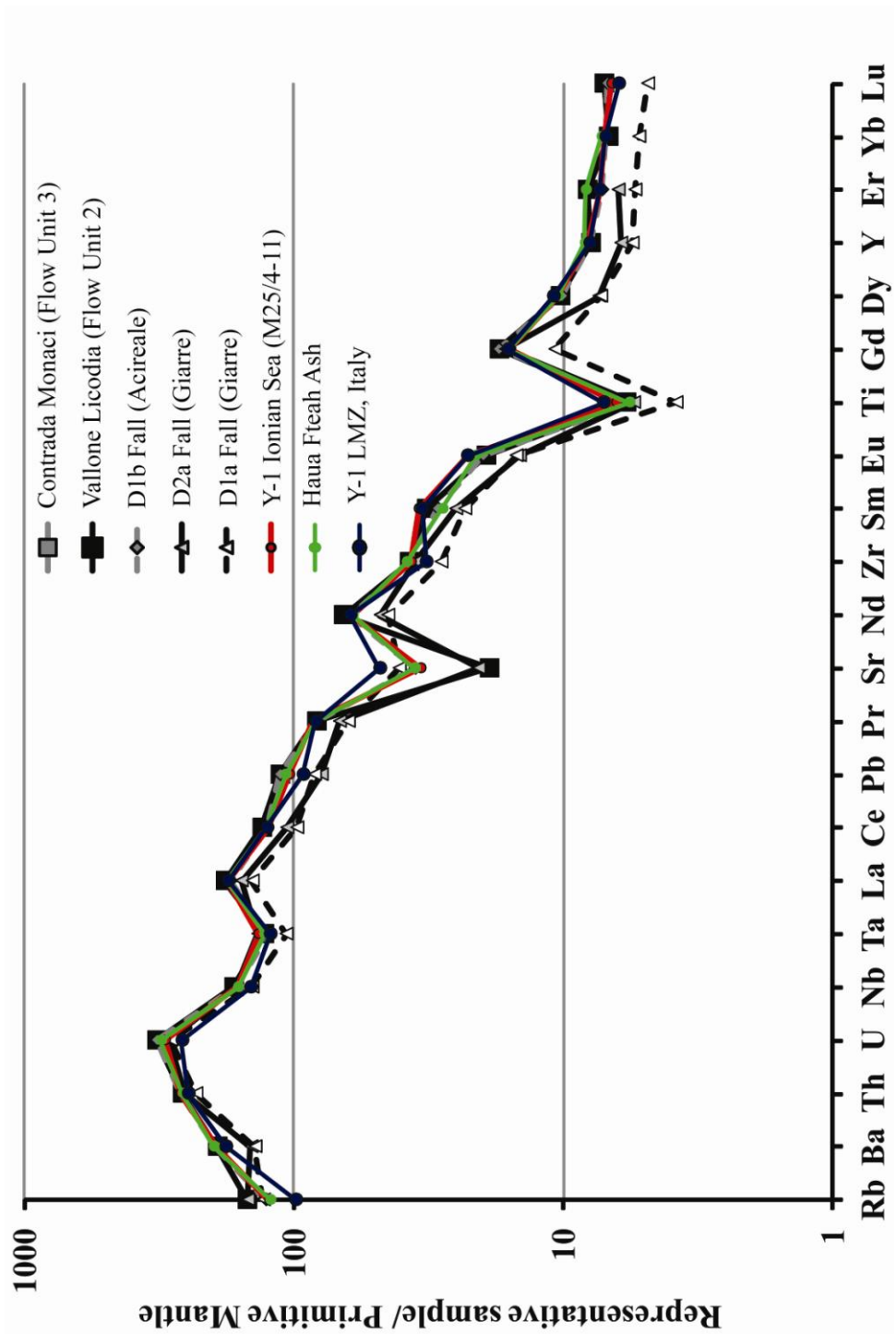


Figure 7.4: Mantle normalised diagram displaying representative proximal glasses of the Biancavilla flow deposits and the Unit D fall deposits (Sun and McDonough, 1989). Also given are representative Etnean glasses reported distally from Y-1 tephras recorded in the Ionian Sea (M25/4-11), Lago di Mezzano, Italy and finally an ash deposit recorded in the Haua Fteah cave site, Libya (Barker et al., in prep).

The most variability is in Sr as outlined above (Fig.7.5). In addition the trace element concentrations within the Monaci Contrada flow (unit 3) glasses are homogeneous with 36 ± 1 ppm Y; 423 ± 16 ppm Zr; 114 ± 3 ppm Nb; 1358 ± 69 ppm Ba and consistent with the least fractionated component of the lower Vallone Licodia flow deposits (Fig. 7.5). They do not display the lower Sr (658-833 ppm) values seen in the Vallone Licodia deposits. HFSE ratios to Th are consistent between the flow units (Table 7.4).

7.4.1.2 Unit D Fall Deposits

Acireale Fall

The varicoloured glasses in the lower fall deposits of Acireale D1b have a slight compositional variation defining a bi-modal population. Compositions range from 61.1-63.0 wt.% SiO₂, 4.3-5.4 wt.% FeO and 3.1-4.2 wt.% CaO. All D1b glasses are trachytes (Fig. 7.3). The light coloured low SiO₂ pumices of sub-unit b and c are in contrast with the darker higher SiO₂ glasses (Table 7.2). The latter also display lower CaO, FeO and MgO (Fig. 7.3).

The glasses in the D1b fall unit display some trace element variation (Fig. 7.5) with 33-41 ppm Y; 390-487 ppm Zr; 105-126 ppm Nb; 1278-1499 ppm Ba; 211-254 ppm Ce. They show LREE enrichment relative to the HREE (La/Yb = 33-43). HFSE/Th ratios are constant within the D1b glasses (Table 7.4). There is no systematic relationship between trace element concentrations and SiO₂ variation.

Giarre Fall

D1a the lowermost fall deposit outcropping in the Giarre area comprise the least fractionated glass compositions with 59.4-61.7 wt.% SiO₂, 4.7-6.6 wt.% FeO and 3.0-5.5 wt.% CaO. Glasses range from trachy-andesites to trachytes (5.9-6.6 wt.% Na₂O and 2.4-3.6 wt.% K₂O Fig. 7.3). Although these glasses display some scatter probably related to their high micro-cryst content, the data are believed to be representative of the magma compositions related to this eruptive phase. Trace element concentrations in the glasses display limited variation but were restricted to only two successful analyses due to high micro-cryst concentrations in the glass. The D1a glasses display the least incompatible trace element enrichment (Fig. 7.4).

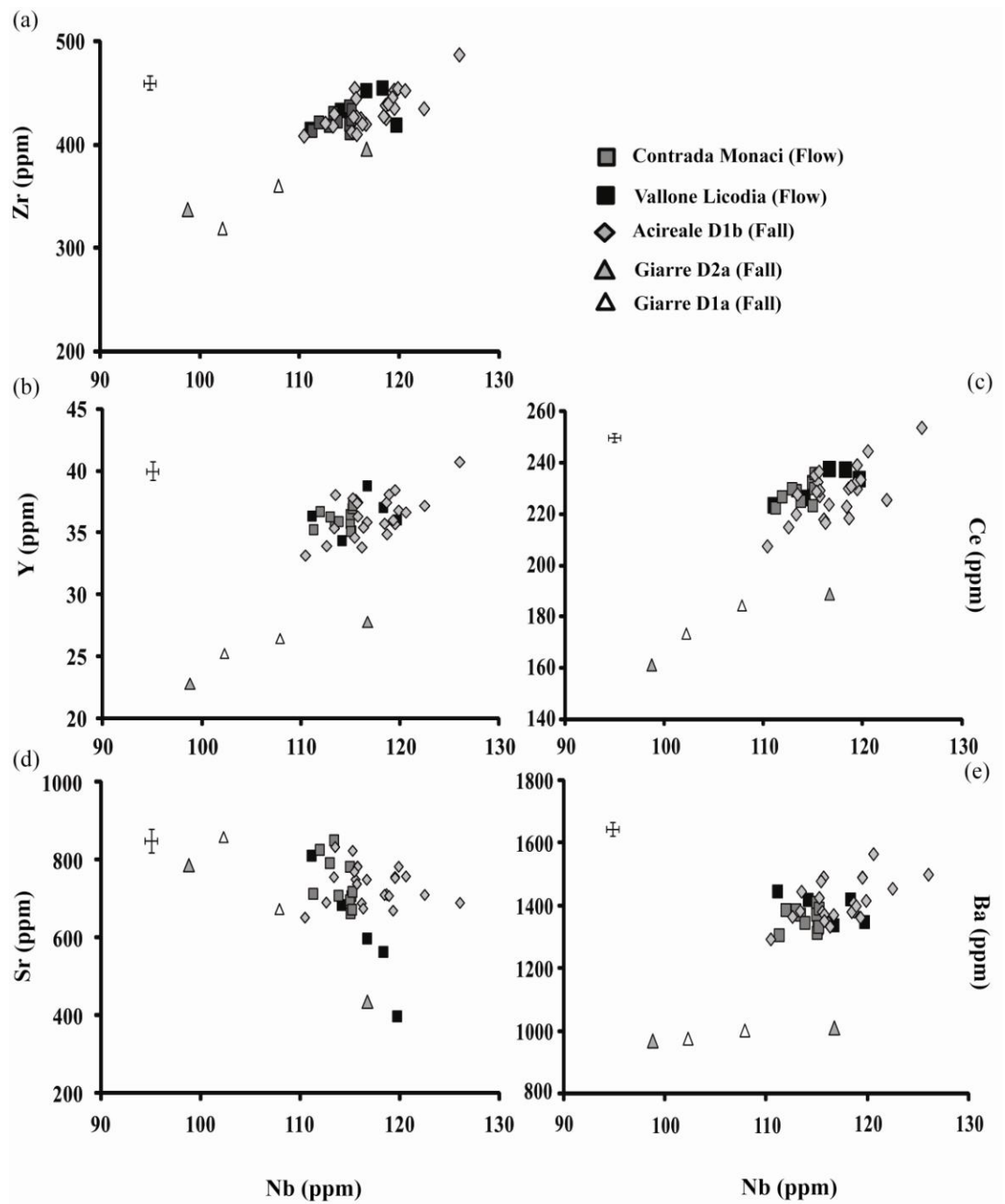


Figure 7.5: Trace element bi-plots for the proximal glasses of the Biancavilla flow deposits and the Unit D fall. Errors given are 2 x standard deviation on repeat analyses of the StHs/6-80-G standard glass.

Concentrations are consistently lower in these two glasses than the other unit D tephras (Fig. 7.5; Table 7.2). Sr behaves compatibly within these glasses (Fig. 7.5d). HFSE/Th ratios remain constant within the D1a glasses (Table 7.4).

The upper pumice fall unit D2a in the Giarre region display glasses relatively homogeneous compositions with 60.6-61.5 wt.% SiO₂, 4.6-6.1 wt.% FeO and 3.3-4.2 wt.% CaO. Alkalis element concentrations range from 5.8-6.7 wt.% Na₂O and 2.9-3.4 wt.% K₂O and are classified as trachytes (Fig. 7.3). D2a shows more variability in the trace element concentrations than the underlying D1a (Fig. 7.5a-e). Strontium behaves compatibly within the D2a glasses (Fig. 7.5d). HFSE element ratios to Th remain fairly constant within these glasses (Table 7.4).

7.4.1.3 Proximal relationships and diagnostic features for distal identification:

Proximal relationships are assessed in the following section and diagnostic geochemical features of the proximal units are identified. Proximal relationships are verified using statistical distance tests (Perkins et al., 1995).

Vallone Licodia - Contrada Monaci - Acireale D1b

There is significant overlap in the composition of the glasses from the Vallone Licodia and Contrada Monaci flows sampled in the Biancavilla region. The lower most scoriaceous deposits extend to more elevated SiO₂ and K₂O but most noticeably lower CaO (Fig. 7.3). Statistical distance tests on the glasses from the two flow units indicates they are indistinguishable at a major and minor level ($D^2 = 1.08$; Table 7.5) given their overlapping geochemistries. Stratigraphically, these flow deposits have been correlated by Coltelli et al. (2000) to the unit D Plinian fall deposits recorded in the composite Etna stratigraphy (Table 7.1). Glasses from the D1b lower Plinian fall deposits overlap with the less evolved components of the Vallone Licodia ($D^2 = 2.48$) flow deposits and match the Contrada Monaci flow deposits ($D^2 = 1.62$). D1b tephras are indistinguishable from the Contrada Monaci and Vallone Licodia glasses at a 95% confidence limit (Table 7.5). The darker glasses recorded in the D1b Plinian fall (sub-unit d) represent particularly similar compositions to the flow deposits at Contrada Monaci ($D^2 = 1.3$), therefore both components are represented.

Trace element concentrations in the glasses reinforce the geochemical link between D1b Plinian fall and the flow deposits of the Biancavilla region (Fig. 7.5). The most noticeable variation is that the D1b Plinian fall glasses do not display the lower Sr contents observed within the Vallone Licodia population. D1b glasses are indistinguishable from the Contrada Monaci ($D^2 = 0.97$) and Vallone Licodia ($D^2 = 2.77$) flow glasses at a 95% confidence limit (Table 7.5). They share similar levels of

incompatible trace element enrichment and LREE enrichment relative to HREE (Fig. 7.4). Furthermore, concentrations appear to follow similar evolutionary paths (Fig. 7.5) and this is reflected in consistent incompatible trace element ratios (Table 7.4).

The geochemical data presented here confirms that the magma involved in the D1b Plinian phase (Acireale) is indistinguishable from that of the Biancavilla block and ash flows (units 2 and 3). This is consistent with the suggestion of Coltelli et al. (2000) that the Plinian activity (Unit D) and the flow deposits in the Biancavilla area are linked in time and space. They propose (1) an initial Plinian phase, (2) waning eruptive intensity with formation of a spatter rampart and (3) over steepening of the hot spatter rampart with resultant collapse to form block and ash flows (i.e. Biancavilla Ignimbrites).

Giarre D1a and D2a

Coltelli et al., (2000) recognised uncertainties associated with the intensity of explosive activity producing the lower fall at Giarre D1a. The Giarre pumices have greater vesicularity and micro-cryst contents so can be distinguished from those found at Acireale (Fig.7.2). Greater vesicularity makes glass analysis more problematic, hence the lower number of analytical points and the greater scatter in the D1a analyses. D1a glass compositions are easily distinguished from those of the Acireale D1b Plinian fall and Biancavilla flow deposits. D1a fall glasses extend from lower SiO₂ and K₂O, whilst higher CaO and FeO than the Acireale/Biancavilla glasses (Fig.7.3). Giarre D1a glasses consistently display lower TiO₂, even at overlapping SiO₂ concentrations (Fig. 7.3b). These major element variations are insufficient to enable statistical difference to be determined between the Giarre D1a and Acireale D1b glasses ($D^2 = 4.76$), probably related to the scatter increasing the standard deviation of the glass population, although this elevated D^2 value is greater than those between D1b and Biancavilla flow deposits, it highlights the differences seen in D1a glasses (Table 7.5). Furthermore, D1a glasses differ more significantly from these scoriaceous flow deposits of Vallone Licodia ($D^2 = 9.36$) and Contrada Monaci ($D^2 = 9.74$).

| | Biancavilla | | Acireale | | | | | | Giarre | |
|--------------------------------------|--|---|---------------------------------|---------------------------------|---------------------------------|--------------------------------|--------------------------------|--------------------------------|--------------------------|--------------------------|
| | Vallone Licodia Flow unit 2 Scoria | Contrada Monaci Flow unit 3 scoria | D1b | D1b | D1b | D1b | D1b | D1b | D1a | D2a |
| | | | sub-unit b pumice (light) | sub-unit b pumice (light) | Sub-unit c pumice (light) | Sub-unit c pumice (dark) | Sub-unit c pumice (dark) | Sub-unit d pumice (dark) | D1a pumice (light) | D2a pumice (light) |
| SiO ₂ | 61.0 | 61.1 | 60.9 | 61.1 | 60.6 | 60.5 | 61.4 | 61.7 | 58.7 | 60.0 |
| Al ₂ O ₃ | 16.5 | 16.7 | 16.9 | 16.8 | 17.0 | 16.9 | 16.8 | 17.1 | 20.3 | 19.5 |
| FeOt | 5.9 | 6.0 | 6.1 | 5.9 | 6.3 | 6.3 | 5.8 | 5.8 | 6.9 | 6.0 |
| MgO | 1.8 | 1.9 | 1.7 | 1.6 | 1.9 | 1.8 | 1.7 | 1.6 | 1.5 | 1.4 |
| CaO | 3.2 | 3.8 | 3.6 | 3.3 | 3.8 | 3.7 | 3.4 | 3.5 | 5.9 | 4.8 |
| Na ₂ O | 6.5 | 6.0 | 5.9 | 6.2 | 5.6 | 5.9 | 5.9 | 5.6 | 4.2 | 5.2 |
| K ₂ O | 3.3 | 3.1 | 3.3 | 3.5 | 3.1 | 3.3 | 3.5 | 3.3 | 1.4 | 2.2 |
| TiO ₂ | 1.4 | 1.3 | 1.4 | 1.3 | 1.4 | 1.5 | 1.4 | 1.3 | 0.9 | 0.8 |
| MnO | 0.2 | 0.2 | 0.2 | 0.2 | 0.2 | 0.2 | 0.2 | 0.2 | 0.2 | 0.2 |
| Total | 101.4 | 99.5 | 98.4 | 98.9 | 97.3 | 98.4 | 97.4 | 96.3 | 94.3 | 95.2 |
| K ₂ O + Na ₂ O | 9.8 | 9.1 | 9.2 | 9.7 | 8.8 | 9.2 | 9.4 | 8.8 | 5.6 | 7.4 |

Table 7.3: ICP-AES whole rock analysis of the Biancavilla flow deposits and the unit D fall deposits from Acireale and Giarre.

The upper D2a Giarre trachytic Plinian fall is characterised by glasses that overlap with the least evolved glasses of the Acireale D1b Plinian fall. Consequently, they are indistinguishable at a 95% confidence limit (Table 7.5). However, again important compositional differences are observed and not fully translated in statistical separation of glass populations. Indeed, as with the D1a glasses, the D2a glasses display significantly lower TiO_2 than the Acireale D1b fall at a given SiO_2 wt.%. Therefore both Giarre fall episodes can be distinguished from the Acireale fall D1b and the Biancavilla flow deposits based on their lower TiO_2 (Fig. 7.3; Table 7.4). These differences in glass data are confirmed in whole rock analyses (Table 7.3) where TiO_2 is again lower (Fig. 7.3). Lower TiO_2 concentrations cannot be attributed to the late stage formation of magnetite microlites given that these microlites would be incorporated in the whole rock compositions.

Trace element concentrations observed in the Giarre D1a and D2a fall deposits have lower levels of incompatible trace element enrichment (Fig. 7.4) and consequently lower concentrations than those observed in Acireale and Biancavilla glasses (Fig. 7.4). Rb, Th and U concentrations in the Giarre glasses are consistent with the Acireale fall/Biancavilla flow glasses (Table 7.2). However, other elements Ba (Fig. 7.5e; Table 7.4), the LREE (Fig. 7.5c), Y (Fig. 7.5b) and HREE (Fig. 7.4) display significantly lower concentrations in the Giarre fall deposits. Furthermore, some incompatible trace element ratios indicate subtle differences between the Giarre glasses and the Acireale D1b fall – Biancavilla flows (Table 7.4) These ratios include Nb/Zr, Ce/Th, La/Th and Y/Th (Table 7.4).

Statistically the Giarre D1a glasses are different to glasses in the Acireale D1b Plinian fall at a 99 % confidence limit ($D^2 = 30.05$). Also the D1a glasses are significantly different to both the Vallone Licodia flow glasses ($D^2 = 17.99$) and the Contrada Monaci flow glasses ($D^2 = 24.77$) at a 95 % confidence limit (Table 7.5). As the diagnostic features of the Giarre D1a and D2a glasses are similar (Table 7.4), these two units are indistinguishable at a major and trace element level (Table 7.5), this might indicate tephra deposits derive from a similar magma batch.

| Locality | Biancavilla | | Acireale | Giarre | | Ionian Sea | Haua Fteah Ash | Lago di Mezzano | Lago Grande di | Monticchio |
|-----------------------|-----------------|-----------------|-------------|-------------|-------------|----------------|----------------|-----------------|----------------|------------|
| Sample | Licodia Vallone | Contrada Monaci | D1b | D1a | D2a | Y-1 (M25/4-11) | HF | Y-1 LMZ | TM-12-1 | TM-11 |
| Deposit | Flow | Flow | Fall | Fall | Fall | Fall | Fall | Fall | Fall | Fall |
| Classification | Tra | Tra | Tra | T.A-Tra | Tra | Tra | Tra | T.A-Tra | Tra | T.A-Tra |
| TiO ₂ wt.% | >1 wt.% | >1 wt.% | >1 wt.% | < 1wt.% | < 1wt.% | >1 wt.% | >1wt.% | >1wt.% | >1wt.% | >1wt.% |
| Ba (ppm) | 1395 ± 48 | 1359 ± 69 | 1412 ± 65 | 990 ± 18 | 990 ± 29 | 1336 ± 40 | 1357 ± 33 | 1300 ± 37 | - | - |
| Nb/Th | 5.1 ± 0.2 | 5.2 ± 0.1 | 5.2 ± 0.2 | 5.2 ± 0.03 | 5.3 ± 0.1 | 5.2 ± 0.2 | 5.2 ± 0.10 | 5.1 ± 0.3 | - | - |
| Zr/Th | 19.3 ± 0.6 | 19.2 ± 0.3 | 19.2 ± 0.6 | 16.7 ± 0.7 | 17.8-18.3 | 17.0-19.5 | 19.5 ± 0.4 | 18.4 ± 0.7 | - | - |
| Ta/Th | 0.24 ± 0.01 | 0.24 ± 0.01 | 0.24 ± 0.01 | 0.23 ± 0.01 | 0.26 ± 0.1 | 0.24 ± 0.01 | 0.24 ± 0.01 | 0.24 ± 0.01 | - | - |
| Y/Th | 1.62 ± 0.02 | 1.64 ± 0.03 | 1.61 ± 0.07 | 1.28 ± 0.01 | 1.25 ± 0.05 | 1.61 ± 0.06 | 1.67 ± 0.04 | 1.74 ± 0.10 | - | - |
| La/Th | 5.5 ± 0.1 | 5.6 ± 0.1 | 5.5 ± 0.2 | 5.0 ± 0.1 | 5.1 ± 0.2 | 5.4 ± 0.1 | 5.5 ± 0.1 | 5.8 ± 0.3 | - | - |
| Ce/Th | 10.3 ± 0.3 | 10.4 ± 0.42 | 10.0 ± 0.3 | 8.8 ± 0.01 | 8.6 ± 0.1 | 10 ± 0.4 | 10.3 ± 0.2 | 10.7 ± 0.6 | - | - |
| Nb/Zr | 0.27 ± 0.1 | 0.27 ± 0.005 | 0.27 ± 0.01 | 0.31 ± 0.02 | 0.29 | 0.28 ± 0.1 | 0.27 ± 0.003 | 0.28 ± 0.1 | - | - |

Table 7.4: Incompatible trace element ratios and other diagnostic features of the Etnean tephras analysed. Tra = trachytic; T.A-Tra = trachy-andesitic to trachytic.

Combined major and trace element data demonstrate that the Giarre glasses are geochemically distinct from the Acireale D1b and Biancavilla flow deposits. They indicate subtly different evolutionary trends and incompatible trace element ratios (Table 7.4).

Calibrated radiocarbon ages beneath the D1a ($18,675 \pm 285$ cal yrs B.P; Table 7.1) and D2a ($18,289 \pm 270$ cal yrs BP) are significantly older than a calibrated age from a carbonised tree at the base of the Biancavilla flow ($17,363 \pm 554$ cal yrs BP; Table 7.1). Proximal age determinations confirm that the Giarre fall was erupted prior to the emplacement of the Biancavilla ignimbrites. Differences between the Giarre glasses and the Acireale and Biancavilla glasses might be link to the temporal gap between the eruptions. Possible mechanisms might include longer residency of magmas in high level sub-volcanic chambers or replenishment with new magma.

Andronico et al. (2001) report evidence of an 18.7 ka flank eruption on the eastern slopes of Etna just to the north of the Giarre area. The age of this explosive activity is in better accordance with the Giarre ages (Table 7.1). However, stratigraphic links between fall recorded at Giarre and fall recorded in the summit region of Etna might make such a link to the flank eruption problematic. That said, links between Giarre and the summit region are highly speculative, due to (1) a lack of intermediate sections; (2) complex and repetitive pyroclastic successions; (3) homogeneous mineral assemblages and whole rock major element chemistries (Coltelli 2012 *pers comm.*). Indeed, correlations are based largely on physical parameters of the pumices (vesicularity, crystalinity; Coltelli et al., 2000). Currently, links between the glass geochemistry of the pumices at Giarre and in the summit region remain untested and do not conclusively preclude links between the Giarre fall and the flank eruption reported by Andronico et al. (2001).

Acireale D2b

The stratigraphy at Acireale indicates the presence of a temporal gap between D1b and the second Plinian fall D2b (Coltelli et al., 2000). Unfortunately, D2b samples were unavailable due to a loss of exposure reported in Coltelli et al., (2000). Consequently, glass compositions for this upper Plinian fall episode are uncharacterised. However, the

| Sample | D1b | D2a | D1a | Contrada Monaci | Vallone Licodia |
|--|------|-------|-------|--------------------|--------------------|
| Trace element ($f=10$) | | | | | |
| D1b | 0.00 | 11.18 | 30.05 | 0.97 | 1.91 |
| D2a | 2.55 | 0.00 | 1.20 | 9.04 | 7.54 |
| D1a | 4.76 | 1.43 | 0.00 | 24.77 | 17.99 |
| Contrada Monaci | 1.62 | 7.89 | 9.74 | 0.00 | 2.77 |
| Vallone Licodia | 2.48 | 6.71 | 9.36 | 1.08 | 0.00 |
| Major elements ($f=8$) | | | | | |

(a)

| | | |
|------------------------|------------------------|--|
| p (confidence limit) | D^2 critical, $f=8$ | |
| 0.995 | 1.344 | < 0.5 % probability that the two samples are compositionally different if D^2 is less than 1.344 |
| 0.990 | 1.646 | < 1% probability that the two samples are compositionally different if D^2 is less than 1.646 |
| 0.950 | 2.733 | < 5% probability that the two samples are compositionally different if D^2 is less than 2.733 |
| 0.050 | 15.507 | > 95% probability that the two samples are compositionally different if D^2 is greater than 15.507 |
| 0.010 | 20.090 | > 99% probability that the two samples are compositionally different if D^2 is greater than 20.090 |
| p (confidence limit) | D^2 critical, $f=10$ | |
| 0.995 | 2.156 | < 0.5 % probability that the two samples are compositionally different if D^2 is less than 2.156 |
| 0.990 | 2.558 | < 1% probability that the two samples are compositionally different if D^2 is less than 2.558 |
| 0.950 | 3.940 | < 5% probability that the two samples are compositionally different if D^2 is less than 3.940 |
| 0.050 | 18.307 | > 95% probability that the two samples are compositionally different if D^2 is greater than 18.307 |
| 0.010 | 23.209 | > 99% probability that the two samples are compositionally different if D^2 is greater than 23.209 |

(b)

Table 7.5: Statistical distance values (D^2) matrix based on major and minor element compositions of the Biancavilla flow deposits and the unit D fall recorded from Acireale and Giarre; (b) The p (confidence limits) values and the D^2 critical values for the statistical distance, where $f = 8$ (Major and minor elements).

Acireale D2b whole rock (WR) analysis (Coltelli et al., 2000) are compared to new whole rock and glass data from the remaining units and this enables some observations to be made. WR analyses of pumice and scoria display systematic offsets to lower SiO₂ than the glass compositions of the same sample (Fig. 3). D2b WR pumice analyses display lower SiO₂, K₂O and Na₂O whilst higher MgO, FeO, CaO than those of WR D1b pumices (Fig. 3). Given the systematic offset between glass and WR pairs observed it is suggested that D2b glasses might be less evolved than the lower D1b glasses. This remains to be tested as WR analyses may vary largely based on phenocryst proportions in the pumices. Importantly WR D2b pumices display TiO₂ contents similar to the Acireale and Biancavilla WR deposits rather than the lower values observed in the Giarre deposits (Fig. 3b). In the absence of glass data for Acireale D2b, WR data provides evidence to support geochemical links with the lower Acireale fall and Biancavilla flows magma rather than the Giarre fall.

Summary:

- (1) Acireale lower D1b Plinian fall is geochemically indistinguishable from the Biancavilla flow deposits, suggesting they were fed by the same magma and are co-genetic.
- (2) Glasses from the Giarre D1a fall and D2a Plinian fall are geochemically distinguishable from the Acireale D1b fall and Biancavilla flow deposits on the basis of significantly lower TiO₂ and incompatible trace element concentrations.
- (3) Given the geochemical links between the Biancavilla flows and D1b Plinian fall it is proposed that the D1b fall post-dates the Giarre fall (D1a, D2a).
- (4) In the absence of glass analyses, higher TiO₂ in WR pumice analyses (Coltelli et al. 2000) reveals that the upper D2b Plinian fall is likely to have been derived from a similar magma to the D1b fall and Biancavilla flows rather than the Giarre fall. Thus D2b second Plinian and Biancavilla flows may be co-genetic.

Redefined below is the nomenclature of Coltelli et al. (2000) Unit D stratigraphy to incorporate the Biancavilla ignimbrites (Table 7.6);

| | |
|--------|------------------------------------|
| D2b | Acireale D2b/ Biancavilla flow (?) |
| D1b/BF | Acireale D1b/ Biancavilla flows |
| D2a | Giarre D2a |
| D1a | Giarre D1a |

Table 7.6: Revised nomenclature, integrating the proximal Unit D and Biancavilla flow deposits.

7.4.2 Distal Etnean tephra deposits:

7.4.2.1 Results

Distal tephtras attributed to the explosive volcanism of Mount Etna occurring during the last glacial interglacial transition (Termination 1) are given in Table 7.7. Presented herein are new major, minor and trace element data for the Y-1 tephra from its type locality in the Ionian Sea (Keller et al., 1978), Y-1 recorded in Lago di Mezzano (LMZ), central Italy (Ramrath et al., 1999) and the first occurrence of Etnean ash from a cave site in NE Libya, at Haua Fteah. New major element glass data are presented for two tephtras layers recorded at Lago Grande di Monticchio (LGdM), Italy. Wulf et al., (2004) correlated TM-11 to the Y-1/Biancavilla Ignimbrite, whilst the older TM-12-1 is termed the ‘Ante Biancavilla’. Representative analyses are presented in Table 7.8 and full data set are reported in Appendix 5.

Geochemical data presented below are compared and contrasted with the proximal glass data presented in section 4.1 in order to define correlations to proximally dated units. As such the distal data are used to help to refine the proximal event stratigraphy. Characteristics of the distal deposits are given summarised in Table 7.7. All distal tephtras display a similar mantle normalised profiles characterised LILE enrichment relative to the HFSE to the proximally presented glasses (Fig. 7.4). Showing a small trough at Nb and Ta (Fig. 7.4), whilst a further depletion in Ti (Fig. 7.4).

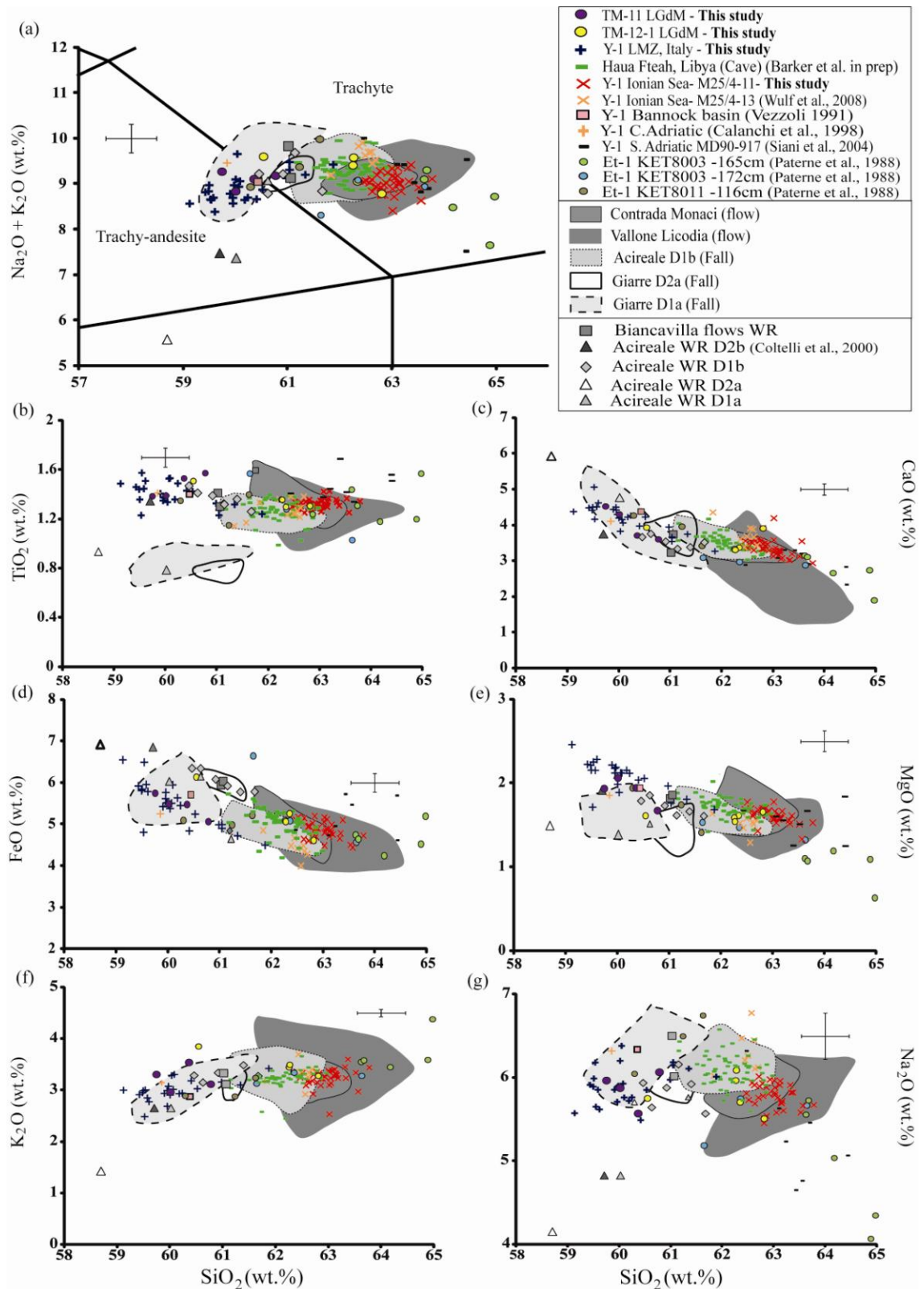


Figure 7.6: Major element bi-plots showing distal Etnean tephras from across the central Mediterranean and North Africa compared to new proximal glass data sets. Also shown are the whole rock analyses of the proximal deposits characterised. Errors associated with the glasses analyses are 2 x standard deviation of repeat analyses of the StHs/6-80-G standard.

| Name | Location | Co-ordinates | Sediments | Thickness | Shard Colour | | Presented in this Study | | Age | Ref |
|-----------------------|-----------------------------------|----------------------------------|-------------------|----------------|--------------|--------------|-------------------------|--------|--|-------|
| | | | | | mm | Clear/vitric | Dark/brown | Majors | | |
| TM-11 | Lago Grande di Monticchio | N 40, 56 E 16, 34 | Lacustrine | 0.55 | | x | x | | 16,440 ± 820 varve years BP | (1) |
| TM-12-1 | Lago Grande di Monticchio | N 40, 56 E 16, 35 | Lacustrine | 1.44 | | x | x | | 17,980 ± 900 varve years BP | (2) |
| LMZ | Lago di Mezzano (C .Italy) | N 42, 37 E 26, 35 | Lacustrine | 100 | | x | x | x | - | (3) |
| Y-1-Ionian Sea | M25/4-11-Ionian Sea | N 36, 44 75 E17, 43 05 | Marine | 100 | | x | x | x | 17,350 ±200 cal yrs BP (¹⁴C 14,290 ± 110)* | (4,5) |
| Y-1-B.basin | Bannock-84 | N 34, 20 E 20, 02 | Marine | | x | x | | | | (6) |
| Y-1-Pal 94-66 | C. Adriatic | N 42, 39 59.1 E14 56 21.4 | Marine | | - | - | | | | (7) |
| Y-1-MD90917 | S. Adriatic | N 41, 17 E17, 37 | Marine | | - | - | | | 17,768 ± 303 cal yrs BP | (8) |
| Et-1- KET8003 | Tyrrhenian Sea | N 38, 49,2 E 14, 29,5 | Marine | | - | - | | | | (9) |
| Et-1- KET8011 | Tyrrhenian Sea | N39, 40,1 E1 5, 04,5 | Marine | | | | | | | (9) |
| Haua Fteah | N.E Libya | N 32, 42 280 E 21, 54 574 | Cave | 300-400 | x | x | x | x | | (10) |

Table 7.7: Reported Etnean tephtras identified in distal archives from the Mediterranean Region, their depositional settings and other characteristics. Those samples in bold are geochemically characterised in this study. (1) Wulf et al. 2004; (2) Wulf et al. 2008; (3) Ramrath et al., (1999); (4) Keller et al., (1978); (5) Kraml (1997); (6) Vezzoli et al., (1991); (7) Calanchi et al., (1998); (8) Siani et al., (2004); (9) Paterne et al., (1988) (10) Barker et al., (in prep). X = the presence, * extrapolated radiocarbon age based on the extrapolation of two radiocarbon determinations above and below the Y-1 Ionian Sea (Kraml, 1997).

| Shard I.D | Y-1 M25/4-11 | | | Haua Fteah Ash | | | Y-1 LMZ | | | TM11 (n=4) | | TM12-1 (n=5) | |
|------------------------------------|--------------|------|------|----------------|------|------|---------|------|------|------------|------|--------------|------|
| | 14B | 16B | 27C | 64 | 28 | 60 | 14B | 25C | 4A | | | | |
| Majors (wt.%) | | | | | | | | | | | | | |
| SiO ₂ | 63.2 | 63.1 | 62.8 | 61.6 | 61.6 | 62.8 | 59.5 | 59.6 | 61 | 59.7 | 60.0 | 62.3 | 62.3 |
| TiO ₂ | 1.4 | 1.3 | 1.3 | 1.2 | 1.3 | 1.3 | 1.4 | 1.5 | 1.2 | 1.4 | 1.4 | 1.3 | 1.4 |
| Al ₂ O ₃ | 16.8 | 17 | 17 | 16.6 | 16.7 | 16.7 | 17.6 | 17.7 | 17.9 | 17.2 | 17.7 | 16.9 | 16.7 |
| FeOt | 4.7 | 4.9 | 4.8 | 5.5 | 5.6 | 4.9 | 5.8 | 5.8 | 5 | 5.7 | 5.5 | 5.3 | 5.1 |
| MnO | 0.2 | 0.1 | 0.2 | 0.2 | 0.1 | 0 | 0.2 | 0.1 | 0.1 | 0.2 | 0.2 | 0.1 | 0.2 |
| MgO | 1.7 | 1.6 | 1.7 | 1.7 | 1.8 | 1.7 | 2.2 | 2.3 | 1.8 | 1.9 | 2.1 | 1.6 | 1.5 |
| CaO | 3.1 | 3.4 | 3.5 | 3.8 | 3.7 | 3.3 | 4.4 | 4.6 | 3.7 | 4.5 | 4.3 | 3.4 | 3.3 |
| Na ₂ O | 5.6 | 5.6 | 5.5 | 6 | 5.9 | 5.9 | 5.9 | 5.6 | 6.2 | 6.0 | 5.9 | 5.7 | 6.1 |
| K ₂ O | 3.2 | 3.1 | 3.3 | 3.3 | 3.2 | 3.3 | 2.9 | 2.8 | 3.1 | 3.3 | 3.0 | 3.4 | 3.5 |
| Analytical Total | 99.5 | 99.1 | 98.9 | 98.1 | 98.1 | 97.5 | 96.8 | 98.1 | 97.6 | 95.6 | 96.9 | 94.2 | 96.7 |
| K ₂ O/Na ₂ O | 8.8 | 8.7 | 8.8 | 9.3 | 9.1 | 9.2 | 8.8 | 8.4 | 9.3 | 9.3 | 8.8 | 9.1 | 9.6 |
| Trace (ppm) | | | | | | | | | | | | | |
| Rb | 81 | 78 | 78 | 80 | 77 | 78 | 68 | 63 | 70 | - | - | - | - |
| Sr | 711 | 716 | 725 | 670 | 728 | 754 | 888 | 1016 | 881 | - | - | - | - |
| Y | 36 | 36 | 36 | 37 | 36 | 38 | 35 | 36 | 36 | - | - | - | - |
| Zr | 427 | 413 | 419 | 439 | 416 | 439 | 357 | 363 | 396 | - | - | - | - |
| Nb | 119 | 115 | 109 | 114 | 112 | 118 | 104 | 103 | 108 | - | - | - | - |
| Ba | 1362 | 1351 | 1375 | 1350 | 1318 | 1379 | 1247 | 1254 | 1331 | - | - | - | - |
| La | 125 | 122 | 122 | 122 | 118 | 125 | 116 | 121 | 118 | - | - | - | - |
| Ce | 229 | 224 | 225 | 233 | 220 | 233 | 216 | 224 | 220 | - | - | - | - |
| Pr | 23.7 | 23 | 23.2 | 23 | 22.4 | 24.4 | 21 | 23 | 21.4 | - | - | - | - |
| Nd | 82 | 81 | 88 | 85 | 80 | 85 | 74 | 84 | 79 | - | - | - | - |
| Sm | 14.1 | 16.6 | 13.9 | 14.2 | 14.4 | 14.5 | 13.9 | 14.9 | 14 | - | - | - | - |
| Eu | 3.3 | 3.4 | 3.4 | 3.9 | 3.4 | 3.8 | 3.3 | 3.8 | 3.9 | - | - | - | - |
| Gd | 10.1 | 11.2 | 11.6 | 11.4 | 10.5 | 10.1 | 7.7 | 9.6 | 9.4 | - | - | - | - |
| Dy | 8 | 7.4 | 7.4 | 7.7 | 7.5 | 7.6 | 6.7 | 8 | 8 | - | - | - | - |
| Er | 4 | 3.8 | 3.9 | 3.7 | 3.5 | 3.9 | 3.6 | 3.5 | 3.7 | - | - | - | - |
| Yb | 3.7 | 3.4 | 3 | 3.5 | 3.3 | 3.4 | 2.4 | 3.4 | 3.8 | - | - | - | - |
| Lu | 0.52 | 0.48 | 0.58 | >LOD | <LOD | <LOD | 0.42 | 0.46 | 0.49 | - | - | - | - |
| Ta | 5.3 | 5.3 | 5.1 | 5.1 | 5 | 5.5 | 4.5 | 5 | 5 | - | - | - | - |
| Th | 23.2 | 21.8 | 21.4 | 22.3 | 21 | 22.6 | 18.3 | 21 | 21.2 | - | - | - | - |
| U | 6.5 | 6.6 | 6.4 | 6.8 | 6.3 | 6.4 | 5.8 | 5.5 | 6.3 | - | - | - | - |

Table 7.8: Representative major, minor and trace element data from distal Etnean Tephra layers recorded within the Mediterranean region. Full data is available in Appendix e.VI

Y-1 M25/4-11 Ionian Sea (*type locality*):

Glasses observed in this Y-1 Ionian Sea tephra layer span a narrow range with 62.5-63.8 wt.% SiO₂, 4.4-5.2 wt. FeO and 2.9-4.1 wt.% CaO. Glasses have Na₂O (5.5-6.0 wt.%) > K₂O (2.5-3.6 wt.%) and are classified as trachytes (Fig. 7.6). Glasses display some trace element variability including 384-438 ppm Zr, 109-123 ppm Nb, 1274-1396 ppm Ba (Fig. 7.7). LREE are enriched relative to the HREE (La/Yb = 36 ± 2; Fig. 7.4). Strontium appears to be behaving compatibly with the lowest concentrations in the most enriched glasses (Fig. 7.7a). HFSE ratios to Th and other diagnostic incompatible trace element ratios remain constant (Table 7.4).

Y-1 Lago di Mezzano (LMZ- *Central Italy*)

Glasses from this tephra layer are relatively heterogeneous with 59.1-61.8 wt. SiO₂, 4.5-6.5 wt. % FeO and 3.3-5.1 wt.% CaO. Glasses display Na₂O (5.5-6.4 wt.%) > K₂O (2.5-3.4 wt.%) and range from trachy-andesite to trachyte (Fig.7.6). Y-1 reported at LMZ have a less enriched trace element composition than Y-1 in the type locality (Fig. 7.4), but again display LREE enrichment relative to the HREE (La/Yb = 37 ± 5). Trace element concentrations observed in the glasses display some significant variability (i.e., 357-402 ppm Zr, 1247-1335 ppm Ba, whilst other incompatible trace elements concentrations are homogeneous (i.e. 36 ± 1 ppm Y) (Fig. 7.7). Strontium appears to remain fairly constant with increasing fractionation (Fig. 7a). HFSE/Th ratios and other diagnostic incompatible trace elements ratios remain constant (Table 7.4).

Haua Fteah tephra (*Libya*)(*Barker et al., in prep*)

Glasses in the visible tephra layer recorded in Haua Fteah (HF) cave stratigraphy show a narrow compositional range with 61.1-62.9 wt.% SiO₂, 4.2-5.7 wt.% FeO and 3.0-4.17 wt.% CaO. Glasses display Na₂O (5.6-6.6 wt.%) > K₂O (2.4-3.7 wt.%) and are all trachytes (Fig. 7.6). Glasses display LREE enrichment relative to the HREE (La/Yb = 35 ± 1). Trace element concentrations generally show only limited variation (i.e., 72-80 ppm Rb, 35-38 ppm Y; 20-23 ppm Th), whilst there is some significant variability in others elements (i.e., 890-670 ppm Sr and 1276-1403 ppm) (Fig. 7.7). HFSE ratios to Th and other diagnostic incompatible trace element ratios remain constant (Table 7.4).

Lago Grande di Monticchio (LGdM)

New analyses of the two LGdM layers were conducted on tephra layers within the thin sections of the varved sediments, these analyses were more challenging than mounted glass separates. As a result the numbers of analyses were limited and restricted to major and minor elements.

TM-11 glasses are homogeneous with 60.2 ± 0.8 wt.% SiO_2 , 5.4 ± 0.3 wt.% FeO and 4.0 ± 0.4 wt.% CaO . Glasses display Na_2O (5.9 ± 0.2 wt.%) $>$ K_2O (3.2 ± 0.2 wt.%) and range from trachy-andesites to trachytes (Fig. 7.6).

TM-12-1 glasses are more heterogeneous than TM-11 with 62.0 ± 0.9 wt.% SiO_2 , $5.2 \pm$ wt.% FeO and 3.6 ± 0.3 wt.% CaO . Glasses display Na_2O (5.8 ± 0.2 wt.%) $>$ K_2O (3.5 ± 0.2 wt.%) and range from trachy-andesites to trachytes (Fig. 7.6). This variability is largely due to a single less evolved outlying analysis that plots in the trachy-andesitic field.

7.4.2.2 Proximal-distal correlations:

Major, minor and trace element data from the distal tephra layers are compared to proximal tephtras. To aid in the interpretation of proximal-distal correlations, sample pairs have been examined using statistical distance tests (Perkins, 1995). Importantly this statistical treatment incorporates the compositional variability within the sample sets. Consequently, in addition to the data presented herein, published data with standard deviations have been incorporated in the statistical treatment. The statistical distance matrix is given in Table 7.9 and D^2 values are referenced within the discussion.

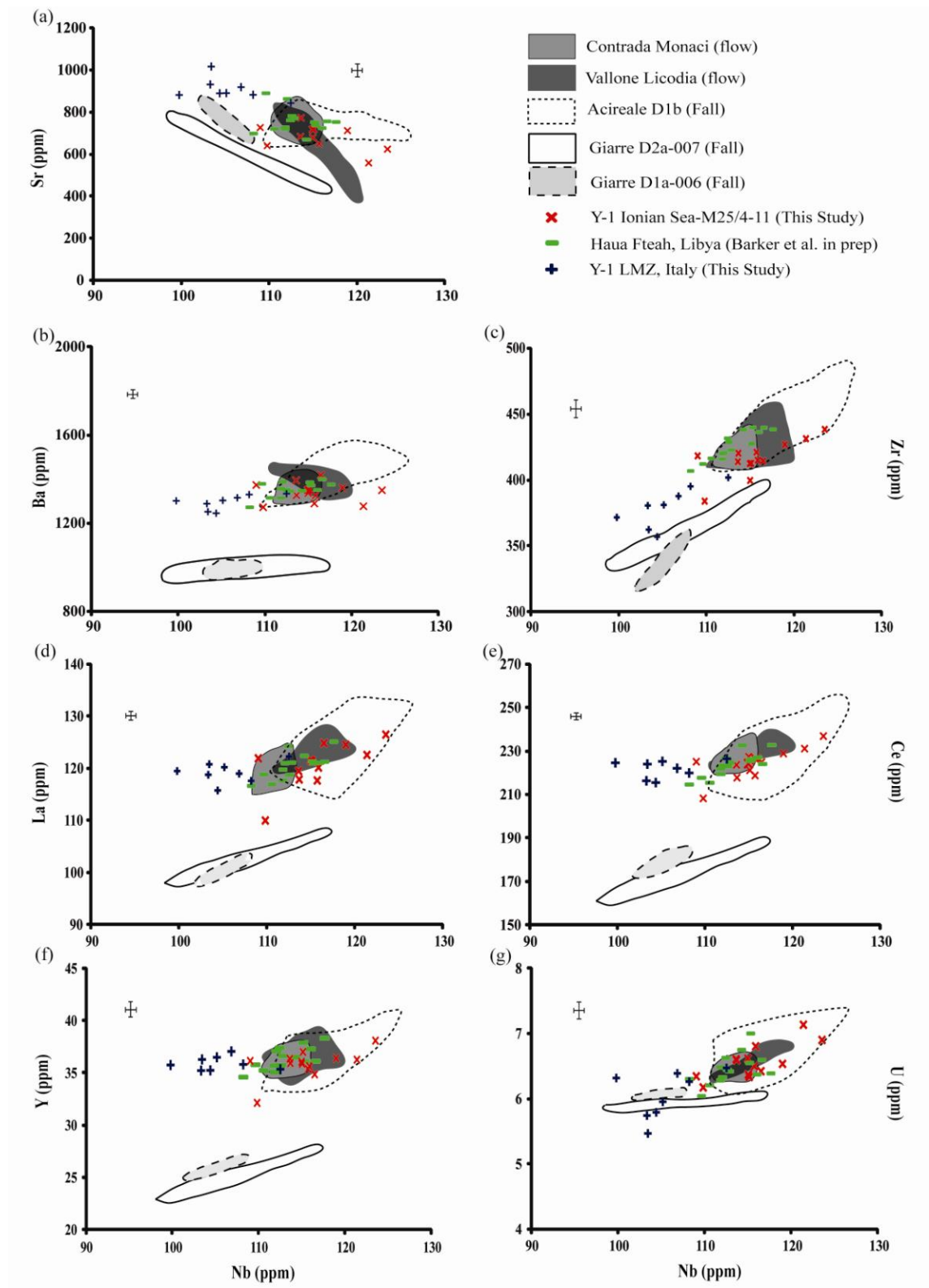


Figure 7.7: Trace element bi-plots for distal Etnean tephras from across the central Mediterranean and North Africa compared to new proximal glass data sets. Errors reported are 2 x standard deviation of repeat analyses of the StHs/6-80-G standard.

| Sample | D1b | D2a | D1a | Contrada Monaci | Vallone Licodia | Y-1 Ionian Sea M25/4-12 | Y-1 Ionian Sea ¹ M25/4-13 | Haua Fteah | Y-1 LMZ | TM-11 | TM12-1 | Y-1 C. Adriatic ² | Y-1 S. Adriatic ³ | Y-1 Bannock basin ⁴ |
|-------------------------|-----------------------------|-------|-------|--------------------|--------------------|-------------------------------|--|---------------|---------|-------|--------|---------------------------------|---------------------------------|-----------------------------------|
| | Trace element (f=10) | | | | | | | | | | | | | |
| D1b (Acireale) | 0.00 | 11.18 | 30.05 | 0.97 | 1.91 | 3.03 | - | 1.24 | 15.79 | - | - | - | - | - |
| D2a (Giarre) | 2.55 | 0.00 | 1.20 | 9.04 | 7.54 | 7.35 | - | 9.28 | 10.72 | - | - | - | - | - |
| D1a (Giarre) | 4.76 | 1.43 | 0.00 | 22.77 | 17.99 | 22.83 | - | 25.17 | 21.05 | - | - | - | - | - |
| Contrada Monaci | 1.62 | 7.89 | 9.74 | 0.00 | 2.27 | 1.62 | - | 0.12 | 13.80 | - | - | - | - | - |
| Vallone Licodia | 2.48 | 6.71 | 9.36 | 1.08 | 0.00 | 1.06 | - | 2.90 | 12.98 | - | - | - | - | - |
| Y-1 Ionian Sea M25/4-11 | 4.06 | 12.80 | 13.22 | 0.87 | 1.37 | 0.00 | - | 2.57 | 22.41 | - | - | - | - | - |
| Y-1 Ionian Sea M25/4-13 | 0.70 | 2.83 | 4.29 | 1.39 | 2.28 | 2.55 | 0.00 | - | - | - | - | - | - | - |
| Haua Fteah | 0.47 | 4.59 | 6.73 | 1.43 | 2.73 | 4.23 | 1.36 | 0.00 | - | - | - | - | - | - |
| Y-1 LMZ | 7.94 | 3.51 | 0.65 | 19.39 | 13.65 | 29.07 | 6.29 | 13.57 | 0.00 | - | - | - | - | - |
| TM-11 | 7.94 | 3.51 | 0.96 | 22.51 | 13.72 | 36.41 | 6.21 | 15.62 | 0.26 | 0.00 | - | - | - | - |
| TM12-1 | 0.69 | 3.24 | 5.74 | 1.64 | 2.78 | 2.85 | 1.54 | 0.57 | 8.98 | 9.00 | 0.00 | - | - | - |
| Y-1 C. Adriatic | 5.66 | 2.81 | 0.51 | 12.36 | 10.89 | 17.11 | 4.96 | 8.57 | 0.42 | 0.51 | 6.88 | 0.00 | - | - |
| Y-1 S. Adriatic | 14.99 | 22.31 | 22.18 | 15.12 | 7.72 | 14.53 | 11.66 | 18.42 | 33.14 | 34.85 | 11.62 | 25.22 | 0.00 | - |
| Y-1 Bannock basin | 9.21 | 4.21 | 1.51 | 23.91 | 15.27 | 37.65 | 7.85 | 13.66 | 2.24 | 3.29 | 8.80 | 1.89 | 13.90 | 0.00 |
| | Major elements (f=8) | | | | | | | | | | | | | |

(a)

| <i>p</i> (confidence limit) | $D^2_{critical, f=8}$ | |
|-----------------------------|------------------------|--|
| 0.995 | 1.344 | < 0.5 % probability that the two samples are compositionally different if D^2 is less than 1.344 |
| 0.990 | 1.646 | < 1% probability that the two samples are compositionally different if D^2 is less than 1.646 |
| 0.950 | 2.733 | < 5% probability that the two samples are compositionally different if D^2 is less than 2.733 |
| 0.050 | 15.507 | > 95% probability that the two samples are compositionally different if D^2 is greater than 15.507 |
| 0.010 | 20.090 | > 99% probability that the two samples are compositionally different if D^2 is greater than 20.090 |
| <i>p</i> (confidence limit) | $D^2_{critical, f=10}$ | |
| 0.995 | 2.156 | < 0.5 % probability that the two samples are compositionally different if D^2 is less than 2.155 |
| 0.990 | 2.558 | < 1% probability that the two samples are compositionally different if D^2 is less than 2.558 |
| 0.950 | 3.940 | < 5% probability that the two samples are compositionally different if D^2 is less than 3.940 |
| 0.050 | 18.307 | > 95% probability that the two samples are compositionally different if D^2 is greater than 18.307 |
| 0.010 | 23.209 | > 99% probability that the two samples are compositionally different if D^2 is greater than 23.209 |

(b)

Table 7.9: Statistical distance values (D^2) matrix based on major, minor and trace element compositions of the proximal deposits and distal Etnean tephra; (b) The *p* (confidence limits) values and the $D^2_{critical}$ values for the statistical distance, where *f* = 8 (Major and minor elements).

Comparisons to D1b/BF

Figure 7.6 reveals that the trachytic glasses of the Ionian Sea Y-1 (M25/4-11), Haua Fteah and LGdM TM-12-1 overlap the proximal glasses of D1b/BF (see Table 7.6). All glasses display more elevated TiO_2 at a given SiO_2 than the Giarre glasses (Fig. 7.6b) and they display greater incompatible trace element enrichment than the Giarre glasses (Fig. 7.4), excluding correlation with Giarre D1a, D2a.

The Y-1 Ionian Sea glasses and the Contrada Monaci flow deposits are indistinguishable in major and trace element geochemistry (Fig. 7.6; 7.7) at a 99 % confidence limit (Table 7.9). Furthermore, this distal tephra has a close affinity to the Vallone Licodia flow (Table 7.9). There is a less precise match with the major element compositions of the Acireale D1b Plinian fall reflected in slightly higher D^2 value ($D^2 = 4.06$). However, at a trace element level Y-1 tephra (M25/4-11) is indistinguishable from D1b Acireale (Table 7.9). Given the co-genetic links identified proximally between Acireale D1b Plinian fall and the Biancavilla flow deposits, the Y-1 Ionian Sea (M25/4-11) tephra is attributed to the D1b/BF event. Indeed, a greater co-ignimbritic association of this tephra layer is supported by the glass data and the dominance of darker black and brown glass shards similar to the scoriaceous block and ash flow deposits.

The ash from the Haua Fteah (HF) cave can also be correlated to the D1b/BF Plinian activity. These glasses comprise clear and brown shards (Fig. 7.2) and their trachytic chemistry is similar to the Acireale D1b Plinian fall and the Contrada Monaci flow deposits. Indeed, at a major and trace element level they are indistinguishable at a 99.5 % confidence limit (Table 7.9). HF lies on the SE dispersal axis of D1b Plinian fall (Coltelli et al., 2000), given the chemical affinities and mixed shard colours (Fig. 7.2) it is plausible that the HF deposit comprises of both Plinian fall and co-ignimbrite ash related to both phases of the D1b/BF event.

TM-12-1 trachytic glasses are broadly consistent with those reported by Wulf et al., (2008), whilst the new analyses presented herein display less variability. The previously termed 'Ante Biancavilla', TM-12-1 glasses overlap precisely with the compositions of Acireale D1b Plinian fall ($D^2 = 0.69$), they are indistinguishable at a 99 % confidence limit. Furthermore they are indistinguishable from Contrada Monaci flow glass composition at a 95 % confidence limit ($D^2 = 1.64$).

The precise proximal correlation of Haua Fteah ash and TM-12-1 to D1b/BF is supported by their geochemical affinity to one another. TM-12-1 major element compositions are indistinguishable ($D^2 = 0.57$) from the Haua Fteah ash layer at a 99 % confidence limit. Y-1 Ionian Sea also shares an affinity to TM12-1 although statistically this is less convincing ($D^2 = 2.85$) due to the greater dominance of a co-ignimbritic ash component in this Y-1 sample (M25/4-11).

Previously published Y-1 major element data from a neighbouring Ionian Sea core M25/4-13 (Wulf et al., 2008) is trachytic and overlap with the D1b/BF episode. Statistical distance values reveal that this particular Y-1 layer is indistinguishable from the Acireale D1b Plinian fall and the Contrada Monaci flow deposits at a 99 % confidence limit (Table 7.9). This published Y-1 data is indistinguishable from the Y-1 tephra reported here (M25/4-11) and TM-12-1 at a 95 % confidence limit.

Comparisons to Giarre D1a and D2a

Figure 7.6 reveals that the glasses observed the LMZ Y-1 tephra and TM-11 are less evolved than those observed than in the trachytic D1b/BF glasses. These trachyandesites to trachytes compare more favourably on most major element bi-plots with the fall deposits found at Giarre (D1a and D2a). This is reflected in major statistical distance values (Table 7.9). Whilst the Giarre fall D1a offers the best proximal counterpart statistically, the TiO_2 contents in the LMZ Y-1 and TM-11 are significantly higher than the Giarre glasses (Fig. 7.6b). Consequently, a correlation to Giarre fall for these less evolved tephtras is not supported by data here (Table 7.4).

Trace element data from the LMZ Y-1 tephra reinforce the rejection of proximal links to Giarre D1a. LMZ Y-1 glasses display greater level of incompatible trace element enrichment than the Giarre glasses (Fig. 7.4). Indeed LREE, Y/HREE and Ba concentrations in the LMZ glasses are more elevated than the Giarre glasses (Fig. 7.7). The LMZ Y-1 glasses are statistically different from the Giarre glasses at a 95% confidence limit ($D^2 = 21.05$). Giarre glasses do not present a satisfactory proximal correlative for the LMZ Y-1.

Incompatible trace element concentrations are lower in the LMZ Y-1 glasses than the D1b/BF glasses, consistent with their lower SiO_2 . However, these LMZ Y-1 glasses are more akin to the D1b/BF glasses than the Giarre compositions. Indeed, the LMZ glasses appear to fall upon more similar evolutionary trends to the more enriched D1b/BF

glasses (Fig. 7.7) and they share similar diagnostic incompatible trace element ratios (Table 7.4).

Glass data presented herein for TM-11 and LMZ Y-1 are clearly linked to Etnean activity and unit D, both based on chemistry and chronological/stratigraphic constraints. However, neither can be linked to precise proximal units on Etna.

Comparisons with published distal tephras

Distal Etnean type tephras with glass compositions that are not currently recognised in the proximal setting are not limited to the TM-11 and LMZ Y-1 tephra layers. Published data indicates Y-1 tephra from the central Adriatic (Calanchi et al., 1998) and the Bannock basin (Vezzoli, 1991), both contain trachy-andesite glasses (Fig. 7.6). These compositions correspond to TM-11 at LGdM and the LMZ Y-1 glasses and are indistinguishable at a 95 % confidence limit (Table 7.9). These tephras all have TiO₂ contents that are more elevated than the trachy-andesites reported at Giarre precluding a correlation (Fig. 7.6b). The geochemical consistency between TM-11, Y-1 LMZ and Y-1 in the central Adriatic cores is important for distal-distal marine – lacustrine correlations in this particular region of the central Mediterranean (Table 7.9; Fig. 7.8).

Y-1/Et-1 glasses reported from the southern Adriatic (Siani et al., 2004) and the southern Tyrrhenian Sea are more difficult to link to proximal equivalents or with other known distal Etnean tephras. Y-1/Et-1 glass compositions reported from the southern Adriatic (Siani et al., 2004) are more scattered (Fig. 7.6). Although the glasses are most similar to the Vallone Licodia flow deposits; this southern Adriatic tephra does not present a precise correlative to any of the proximal glasses reported herein. These glasses are clearly derived from a highly fractionated Etnean magma that is most similar to the composition of the most evolved end-member of the flow deposits and is thus more likely to relate to a co-ignimbrite eruptive phase.

In the southern Tyrrhenian sea, the situation is more complex. Paterne et al. (1988) report a single tephra layer in KET8011 displaying glass compositions ranging from trachy-andesites to trachytes (Fig. 7.6). Consequently, these glasses correspond to the distal least evolved compositions (i.e., TM-11/Y-1 LMZ compositions) and also overlap the least evolved D1b Acireale glasses (Fig. 7.6). This tephra layer might represent two compositionally separate eruptive episodes, given that these two glass components are not found together elsewhere in a single tephra layer (Fig. 7.6). Interestingly, no

evidence of a more evolved trachytic co-ignimbrite ash was reported in this layer (Paterne et al., 1988). In KET8003 two distinct layers were identified (Paterne et al., 1988), providing further evidence for temporally separate explosive events. The lower (i.e., oldest) at 170-172cm contains glasses which correspond to analyses of D1b/BF; and two distal layers (i.e., TM-12-1 and the Ionian Sea Y-1 (M25/4-11)). A stratigraphically higher layer (i.e., younger) is similar to that of the southern Adriatic (Siani et al., 2004). Although it does not match an exact proximal unit, its geochemistry is more comparable to the highly evolved trachytic end-members associated with the co-ignimbrite ash. The stratigraphic superposition of this upper layer might support the possibility of an intervening block and ash flow collapse event in the Biancavilla region between the two Plinian events. None of the distal trachy-andesitic glasses (i.e., TM-11, LMZ, Y-1 central Adriatic or the Bannock basin) show evidence of the more evolved trachytic co-ignimbrite components. This might indicate that this younger Plinian episode may not be directly associated with the proximal ignimbrite deposits at Biancavilla. Distal localities and their associations are shown in Figure 7.8.

7.4.3 Towards an integrated proximal – distal event stratigraphy:

This section evaluates the potential of distal archives to help constrain the age and dispersals of Etnean eruptions during termination 1.

Giarre D1a/D2a

Giarre fall glasses (D1a and D2a) are not present in any of the distal archives reported herein and in published work. Proximal ages derived from the Giarre deposits (Table 7.1) appear to pre-date the D1b/BF episode. Consequently, proximal ages (Coltelli et al., 2000) should not be imported to distal archives unless the specific diagnostic chemistry of the Giarre fall is identified (Table 7.4). The absence of Giarre fall in any of the distal archives supports the assertion that these explosive episodes may have been more localised with restricted more local dispersal compared to the Acireale Plinian fall. Indeed, the D1a activity is poorly constrained in terms of dispersal and magnitude due to its limited proximal thickness (Coltelli et al., 2000). One could propose that the Giarre fall deposits originated from an older flank eruption on the eastern flanks of Etna predating the Plinian activity (18.7 ka, Andronico et al., 2001). Indeed a vent proximal to Giarre might explain the thickness of the pumice (i.e., near vent sub-Plinian). As

demonstrated in section 4.1.3, Giarre glasses are compositionally less evolved with differing incompatible trace element ratios, this geochemical evidence might support their origin from a separately residing parasitic magma batch. This magma differs to that feeding the later Plinian Acireale fall and Biancavilla flow deposits. This is consistent with models for the current plumbing system beneath Etna, where it is proposed that there is a complex high level magma storage system residing beneath Mount Etna, rather than a single magma chamber (Ferlito et al., 2008).

Acireale Unit D and Biancavilla flows

The high resolution distal archive at LGdM is particularly important for the assessment of the proximal event stratigraphy given the evidence for two discrete tephra layers with geochemically different glasses. Indeed, distal glass geochemistry for Etnean type eruptions recorded across the central Mediterranean region largely reflects the two compositionally distinguishable glass components (Table 7.10);

(a) D1b/BF- The older TM12-1 correlates to the proximal D1b/BF first Plinian glass compositions. This is distally linked to the Y-1 layers in the Ionian Sea (type locality) and Haua Fteah ash layer, Libya. Proximal ages from the base of the Biancavilla flows ($17,363 \pm 554$ cal yrs BP) provides the best age constraint from the source region, indeed this age is younger than the Giarre age and fairly consistent with the interpolated radiocarbon age from the Ionian Sea (Table 7.7).

(b) D2b? – Based on links above (a), stratigraphic superposition proximally at Acireale and the absence of Giarre composition distally would indicate that the younger TM-11 and its geochemically defined correlatives; Y-1 reported in LMZ, the Central Adriatic and the Bannock basin belong to a younger second Plinian episode recorded at Acireale D2b.

| Age | Eruptive event & Proximal deposit | Classification | Distal Deposit | Axis of Dispersal |
|--|---|----------------|---|-------------------|
| 16 440 ± 820 varve years BP | Plinian 2 - D2b - Sustained eruptive column, links to Flow deposits un-confirmed | T.A to Tra | TM-11, Y-1 LMZ, Y-1 C. Adriatic, Y-1 Bannock Basin | SE, N |
| ca.1500 varve years (LGdM) | Proximal Volcanogenic sediments/Palaesol | | | |
| 16,809-17916 cal yrs BP/ 17980 ± 900 varve years BP | Plinian 1 - D1b/BF - Sustained eruptive column & contemporaneous ignimbrite (block and ash) flows. | Tra | Y-1 Ionian Sea (M25/4-11; M25/4-13); TM-12-1, Haua Fteah Ash (N. Africa). | SE, E, N |
| | Undefined stratigraphic relationship Flank eruptions? | | | |
| 18,289 ± 270 cal yrs BP | D2a -Localised fall? | Tra | Not recorded | E |
| 18,675 ±285 cal yrs BP | D1a -Localised fall? | T.A to Tra | Not recorded | Not determined |

Table 7.10: Suggest event stratigraphy for the unit D Plinian activity on Etna and the associated Biancavilla Ignimbrites based on the integration of proximal and distal information. T.A =Trachy-andesite; Tra = Trachyte.

The glass-whole rock compositional offset observed in the lower Acireale Plinian fall deposits (D1b; Fig. 7.3), might indicate that the D2b fall deposit are likely to present less evolved glass compositions than those of D1b. Consequently, they are likely to be more comparable with the less evolved compositions recorded in these distal layers including TM-11, Y-1 in LMZ, the central Adriatic and Bannock basin glasses. D2b pumices display higher TiO₂, consistent with the proximal D1b/BF pumice and scoria and the less evolved distal tephras (Fig. 7.6b). Thus it is proposed that this second Plinian deposit recorded at Acireale (D2b) is the proximal equivalent of a second ash dispersal recorded in some central Mediterranean archives (i.e., TM-11; Y-1 LMZ, central Adriatic and Bannock basin).

The varve chronology separating TM-11 and TM-12-1 at LGdM represents a period of 1500 varve years. Since TM-12-1 is confidently correlated to proximal D1b/BF it is possible to extrapolate a 1500 varve year gap between the two Plinian eruptions recorded at Acireale (D1b and D2b).

The presence of distal deposits which display purely co-ignimbritic components Y-1 southern Adriatic (Siani et al., 2004) and Tyrrhenian Sea, KET8003-165cm; Paterne et al., (1988)), does raise the possibility that separate spatter rampart/collapses triggered co-ignimbritic flow events that were temporally independently of the two main Plinian episodes. This is supported by the fact that at Lago Grande di Monticchio TM-12-1 correlated to the lower Acireale (D1b) is stratigraphically below the Greenish tephra from Vesuvius (Wulf et al., 2008). However, in the Southern Adriatic, a purely co-ignimbritic type ash lies stratigraphically above the same Greenish Vesuvius tephra (Siani et al. 2004). Based on ages from this Southern Adriatic Y-1 (Table 7.7) and from below the lowermost proximal flow deposits (Table 1) it is possible to suggest that there would not be a significant time period between the D1b/BF event and any subsequent collapse producing co-ignimbrite ash.

Glass geochemistry enables us to confirm at least two Plinian widespread ash dispersals events from Mount Etna during the time of termination 1 (Table 7.10).

- a) D1b/BF- Isopach thicknesses define a SE dispersal for the lower D1b Plinian fall recorded proximally (Coltelli et al. 2000), distal glasses recorded at Haua Fteah, Libya, represent compositions consistent with this first Plinian episode confirming a south easterly dispersal (Fig. 7.8).

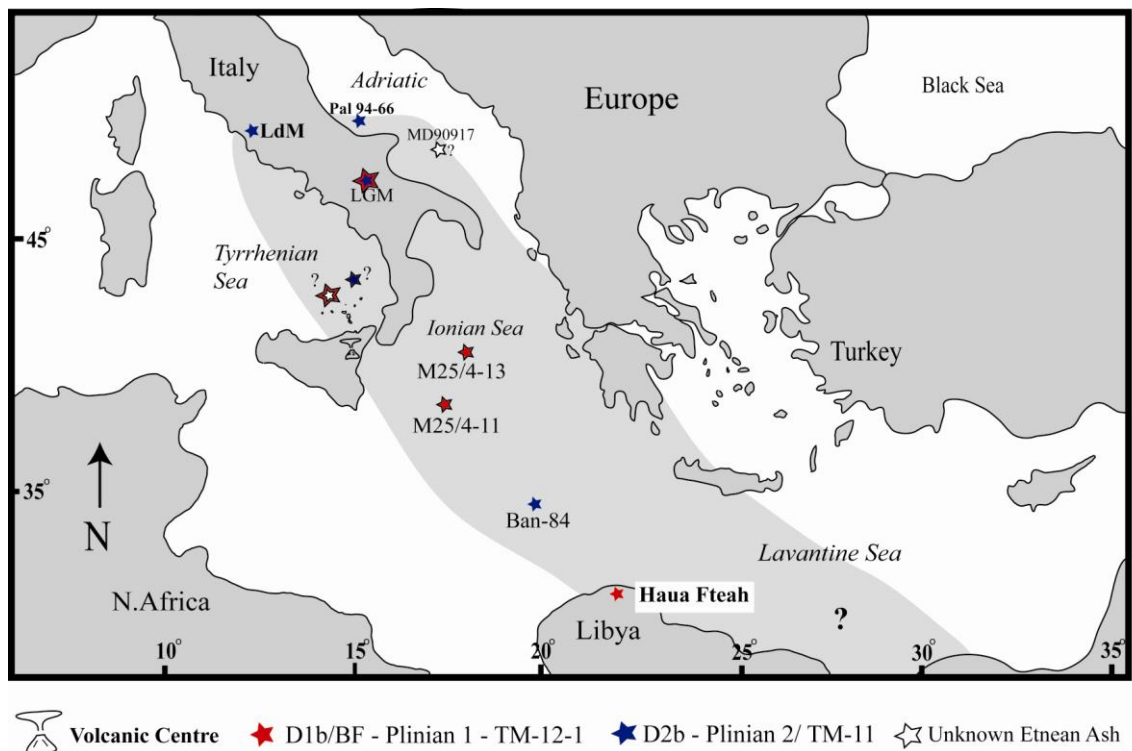


Figure 7.8: A map of the Mediterranean outlining the extended fall footprint of the Etnean ash associated with the Biancavilla/Unit D activity on Mount Etna during termination 1. Highlighting the care required when attempting to synchronise distal archives using Y-1/ Et-1 tephras. Correlations to proximal deposits are shown, in the absence of glass data for the upper Plinian fall D2b, links to LGdM tephras are reported.

b) D2b – Isopach thicknesses define a SE dispersal for the upper D2b Plinian fall. Y-1 data reported from the Bannock basin (Vezzoli 1991) demonstrates a second chemically distinct eruption on a similar SE trajectory from Mount Etna.

The presence of two tephras at Lago Grande di Monticchio corresponding to two Plinian episodes highlights the complexities of ash dispersal. Coltelli et al. (2000) suggested the finer material recorded north of Etna was probably transported at higher atmospheric levels rather than consistent with the main dispersal axis.

Combining proximal-proximal, proximal-distal and distal-distal geochemical correlations; stratigraphic superposition and associated chronological constraints we propose a revised event stratigraphy of explosive events on Etna associated with the Unit D/Biancavilla explosive episode (Table 7.10).

7.4.4 Tephrostratigraphical Implications

At least two Plinian explosive events from Mount Etna (D1b/BF and D2b) occur during the last glacial-inter-glacial transition (Termination 1) within resultant ash dispersal recorded in distal central Mediterranean archives. They relate to the two major Plinian episodes recorded at Acireale and link to the Biancavilla ignimbrite deposits. This is best illustrated distally where two temporally separate Etnean tephra layers are recorded in the high resolution record at Lago Grande di Monticchio (Wulf et al., 2008).

Data presented herein has significant implications for the use of the ‘Y-1’ tephra as a tephrostratigraphic marker in the central Mediterranean. Assessing the synchronicity of environmental responses to termination 1 climatic forcing across the central Mediterranean is dependent on the assumption that the Y-1 tephra represents a single volcanic event in time. Data herein clearly demonstrates that this is not the case with a time gap of ca.1500 varve years. This supports the previous concerns of Wulf et al. (2008). Using the ‘Y-1’ to assess the synchronicity of climatic change between the central Adriatic and the Ionian Sea archives may lead to erroneous interpretations. Two geochemically identifiable ‘Y-1’ tephras were erupted during temporally separate explosive episodes, consequently imprecise correlations might lead to incorrect deductions about the “leads and lags” in climatic variability during this abrupt transition. However, these distal tephra layers can be used to synchronise distal archives but only after careful multi-elemental geochemistry and correlations to proximal deposits (Fig. 7.8).

Both of the Acireale Plinian eruptions are particularly widespread, but not uniformly dispersed. Where precise correlations are made, using glass geochemistry, physical parameters (morphology and colour) and stratigraphy, then distal archives can be linked over thousands of kilometres. A case in point is linking tephra recorded at LGdM, TM-12-1 and the ash layer recorded in the Haua Fteah cave, Libya (Fig. 7.8).

The presence of geochemically separate Plinian eruptions in the Ionian Sea and the Bannock basin cores would indicate that the fall footprints of these two eruptions are not uniform and result in complex dispersal patterns. Herein Y-1 is presented from Ionian Sea cores (M25/4-11 and M25/4-13), yet no evidence of Etnean ash was found at the neighbouring core M25/4-12 (Keller et al., 1978), despite a detailed cryptotephra investigation of the sediments (Chapter 5).

7.5. Conclusions:

(1) Dual explosive eruptive events on Mount Etna (ca.18-16ka) involving fractionated trachytic magmas with Nb, Ta and Ti depletions is indicative of a subduction influence. Given the predominantly intra-plate chemistry of Etna perhaps these explosive events coincide with a switch from relatively non-explosive intra-plate to more hydrous and explosive (Plinian) supra-subduction activity.

(2) Geochemistry confirms a co-genetic relationship between the Unit D Acireale Plinian fall (Coltelli et al., 2000) and the Biancavilla ignimbrites (i.e., block and ash flows) (De Rita et al. 1991).

(3) Trachytic block and ash flows are believed to be contemporaneous with Plinian activity because distal tephras contain evidence (i.e., geochemistry, morphologies and colour) consistent with input from both.

(4) Distal data confirm at least two major Plinian Ash dispersals sourcing from Etna spanning Termination 1 interval. The 'Y-1' across the central Mediterranean does not represent a single contemporaneous ash dispersal. Thus great care must be exercised when synchronising distal archives.

(5) Fall recorded at Giarre appears to predate the Acireale Plinian episodes given their links to the Biancavilla flows. Giarre fall geochemistry is not identified in any of the reviewed distal tephra layers.

(6) It is suggested that two Plinian dispersals to the SE, identified at Acireale, can be correlated to distal ash layers both following these main dispersal but also to the North of Etna, enabling the synchronisation of distal archives over wide geographical areas.

(7) Proximal-distal correlations to high resolution archives enable us to infer that this explosive phase on Mount Etna spans a minimum of 1500 varve years, we suggest that the first be attributed to Acireale D1b and the second once confirmed by glass geochemistry to Acireale D2b.

Chapter 8: Conclusions

The overall aim of this thesis was to test proximal-distal tephra correlations within the central Mediterranean region using additional grain-specific trace element geochemistry of volcanic glasses. A summary of the main conclusions of the thesis follow with detailed conclusions given at the end of each chapter;

- **Proximal Aeolian Island Eruptions:** Glass geochemistries from the major explosive episodes in the Aeolian Islands are diverse. Where overlaps in major element geochemistries exist between volcanic islands, trace element signatures of the magmas from individual islands are diagnostic. For example potassic shoshonitic/K-series glasses from Vulcano and Stromboli can be distinguished using HFSE/Th ratios. On an island specific basis the integration of major, minor and trace element data is often essential for resolving diagnostic geochemistries for individual eruptions. (Chapter 3).
- **Marsili Basin marine core:** Using the Marsili Basin core as a test-bed for proximal-distal tephra correlation revealed that some of the existing correlations were erroneous because they were based solely on major elements. A multi-elemental approach to proximal-distal tephra correlations offers a more precise means of validating correlations. The identification of unknown Aeolian Island derived glasses reveals that yet further proximal characterisation of tephras is required. Monogenetic turbidites recorded in the Marsili Basin core can be used as tephrostratigraphic markers when correlated to precise source volcanics but polygenetic turbidites offer very little tephrochronological information (see Chapter 4).
- **Aeolian ash dispersal patterns:** Limited tephra fall from Aeolian Island explosive volcanism is recorded in the Marsili basin core. The paucity of Aeolian tephras in the Tyrrhenian Sea and their greater abundance within the Aeolian Islands to the south and east, on Sicily and in the Ionian Sea marine core might suggest that ash dispersals are influenced by prevailing circulation patterns in the Mediterranean which are westerly during most of the year (see Chapter 3, 4, 5).

- **Ionian Sea marine core:** Two Aeolian Island explosive eruptions (7-40ka) are present in the Ionian Sea core M25/4-12. Ash from the Gabelotto-Fiume bianco HKCA eruption on Lipari is identified in the Ionian Sea core M25/4-12 within sapropel 1 (28 cm b.s.f) early Holocene sediments. This provides a new chronostratigraphic marker of 8730–8400 cal yrs BP (7770 ± 70 ^{14}C yrs BP). A second, older tephra (44 cm) is compositionally identical and from an unknown late glacial eruption on Lipari. Contributing to growing evidence for more numerous ash dispersal sourcing from the Island (see Chapter 5).
- **The distal Y-3 marker:** Trace element data confirm that the VRa eruption, from Campi Flegrei within the Tufi Biancastri series of eruptions is not the proximal counterpart of the Y-3 in the Ionian Sea. Consequently, proximal ages associated with the VRa should not be imported to the Ionian Sea core. In the absence of a proximal counterpart for the Y-3 tephra, the geochemistry presented from its type locality should be used to determine distal-distal correlation for what represents an important tephrostratigraphic marker in the central Mediterranean (Chapter 5).
- **The distal Y-5 marker:** The Y-5 Ionian sea layer previously correlated to the Campanian Ignimbrite (Kraml, 1997) has been validated using new proximal glass data (Tomlinson et al., 2012). This confirms the southern dispersal of ash was associated with the first Plinian eruptive phase rather than the subsequent co-ignimbrite ash (Chapter 5). This illustrates that where significant compositional heterogeneity is observed proximally detailed glass geochemistry can be used to establish precise links between distal tephras and individual eruptive phases.
- **‘External’ ash layers recorded in the Aeolian Islands:** Ages can be imported into the proximal Aeolian Island stratigraphies by precisely linking ‘external’ ash layers to dated proximal or distal deposits. For example the *‘Ischia tephra’* layer displays glass geochemistry with variability corresponding to the MEGT caldera forming eruption of Ischia (ca. 55 ka). The Barone tephra layer, Salina, is assigned to the LGdM tephra, TM-27 (108.3 ka) (Wulf et al., submitted). A pink ash layer on the island of Panarea, which has been used as an important age

constraint for explosive activity on the island, does not appear to correspond to either of the published correlatives and remains currently unresolved. These external ash layers can also be integrated into and contribute to the known dispersal of major explosive episodes in the central Mediterranean region (See chapter 6).

- **Proximal Biancavilla Mount Etna:** Volcanic glass geochemistry confirms a co-genetic relationship between the Acireale Plinian fall (unit D) and the Biancavilla ignimbrites (i.e., block and ash flows). (see Chapter 7).
- **Y-1/Biancavilla central Mediterranean marker:** Deposits from two Plinian Etnean eruptions are evident in the distal record at LGdM spanning the Termination 1 time interval. Consequently, the Y-1 found in the central Mediterranean does not represent a single contemporaneous tephra layer. Statistically different geochemistries are seen in the glasses of the Y-1 recorded in the Ionian Sea and Y-1 recorded in Lago di Mezzano (Italy). Distal archive synchronisation using these Etnean ashes should incorporate major, minor and trace element data to ensure precise correlations (Chapter 7).
- **Etna Proximal-distal correlations:** proximal-distal correlations with Lago Grande di Monticchio suggest a temporal gap of ca. 1500 varve years might be inferred between the two Acireale (Unit D) Plinian episodes on Mont Etna. TM-12-1 is confidently assigned to the lower Acireale D1b fall/Y-1 (Ionian Sea), whilst the Giarre fall geochemistries are absent distally, the younger TM-11 at LGdM is linked to the upper Acireale D2b fall.

The integration of major, minor and trace element glass data provides the most robust basis for proximal-distal tephra correlations. Statistically valid tephra correlations allow for the exchange of tephrochronological and tephrostratigraphical information; (a) with proximal ages assigned to distal tephras; (b) distal age/stratigraphic information can be imported back to help unravel proximal eruptive sequences; (c) comparisons of proximal and distal ages can enable the cross validation of age information. A caveat-trace element analyses is not always able to define diagnostic geochemistry for temporally separate explosive eruptions from the same volcanic source. A feature that becomes apparent within this research is that the larger magnitude Plinian eruptions,

whilst displaying overlapping chemistries (major and trace) with inter-Plinian activities, can typically be defined by their significantly greater geochemical variability (i.e., Campanian Ignimbrite, MEGT; TM-27).

Future work:

- Presented in chapter 3 is a significant contribution of proximal glass geochemical data for many of the major explosive Aeolian Island eruptions. Whilst this is crucial to determining and refining proximal-distal tephra correlations, many of these tephras remain poorly dated at source, thus whilst defining provenance of distal tephras can be achieved, assigning a reliable age is remains problematic. Although challenging, future investigation need to focus on chronologically constraining some of the more poorly dated eruptive episodes (i.e., Secche di Lazzaro, Stromboli).
- The occurrences of distal Lipari tephras temporally constrained between the major explosive episodes reported on the island might infer that small volume/localised eruptions have the potential to distally disperse ash significant distances. Consequently, future proximal investigations might target some of the smaller volume deposits for geochemical characterisation.
- The identification of cryptotephra layers from the upper sediments of M25/4-12 in the Ionian Sea, demonstrate the potential to extend this investigation into the older sediments of the core, providing the potential to identify further chronological markers.
- A systematic multi-elemental re-investigation of proposed occurrences of Y-3 tephras within the Mediterranean region would help refine distal-distal tephra correlations. Geochemical and chronological data associated with reported ‘Y-3’ tephras indicated that some erroneous correlations exist, owing to numerous explosive episodes with overlapping geochemistries sourcing from Campi Flegrei (Tufi Biancastri). Precise distal-distal correlations would enable the accurate application of this tephra as crucial stratigraphic marker coinciding with the MIS 2/3 transition.

- In order to further validate Y-1 proximal-distal links in the central Mediterranean glass analyses of the upper Acireale D2b fall unit is essential. The sample has recently been retrieved from archived material in the absence of available proximal exposure and is being prepared for analysis.

References

Albert, P.G., Tomlinson, E.L., Smith, V.C., Di Roberto, A., Todman, A., Rosi, M., Marani, M., Muller, W., Menzies, M.A., 2012. Marine-continental tephra correlations: Volcanic glass geochemistry from the Marsili Basin and the Aeolian Islands, Southern Tyrrhenian Sea, Italy. *Journal of Volcanology and Geothermal Research*, 229-230, 74-94.

Allan, A.S.R., Baker, J.A., Carter, L., Wysoczanski, R.J., 2008. Reconstructing the Quaternary evolution of the world's most active silicic volcanic system: insights from a similar to 1.65 Ma deep ocean tephra record sourced from Taupo Volcanic Zone, New Zealand. *Quaternary Science Reviews* 27 (25–26), 2341–2360.

Allen, H.D., 2003. Response of past and present Mediterranean ecosystems to environmental change. *Progress in Physical Geography*, 27(3), 359 – 377.

Alley, R.B., Meese, D.A., Shuman, C.A., Gow, A.J., Taylor, K. C., Grootes, P. M., White, J. W. C., Ram, M., Waddington, E. D., Mayewski, P. A., Zielinski, G. A., 1993. Abrupt increase in Greenland snow accumulation at the end of the Younger Dryas event. *Nature*, 362, 527 – 529

Andronico, D., Branca, S., Del Carlo, P., 2001. The 18.7 ka phreatomagmatic flank eruption on Etna (Italy): relationship between eruptive activity and sedimentary basement setting. *Terra Nova*, 13, 235-240.

Andronico, D., Calderoni G., Cioni, R., Sbrana, A., Sulpizio, R., Santacroce, R., 1995. Geological map of Somma-Vesuvius volcano. *Periodico Mineralogia* 64, 77-78.

Anikovich, M.V., Sinitsyn, A.A., Hoffecker, J.F., Holliday, V.T., Popov, V.V., Lisitsyn, S.N., Forman, S.L., Levkovskaya, G.M., Pospelova, G.A., Kuz'mina, I.E., Burova, N.D., Goldberg, P., Macphail, R.I., Giaccio, B., Praslov, N.D., 2007. Early Upper Paleolithic in eastern Europe and implications for the dispersal of modern humans. *Science* 315, 223–226.

Arienzo, I., Heumann, A., Worner, G., Civetta, L., Orsi, G., 2011. Processes and timescales of magma evolution prior to the Campanian Ignimbrite eruption (Campi Flegrei, Italy). *Earth Planet Science Letters*, 306 (3-4), 217-228.

Barker, G., Albert, P.G., Armitage, S., Aubert, M., Cullen, V., Douka, K., Farr, L., Grün, R., Hill, E., Hunt, C., Inglis, R., Jacobs, Z., Kinsley, L., Lane, C., Reynolds, T., Roberts, R., Russell, R., Simpson, S., Tomlinson, E.L., Wulf, S. (in prep). Redating the Haua Fteah cave (Cyrenaica, north eastern Libya) and its implications for the prehistory or North Africa. In prep.

Bertagnini, A., Landi, P., 1996. The Secche di Lazzaro pyroclastics of Stromboli volcano: a phreatomagmatic eruption related to the Sciara del Fuoco sector collapse. *Bulletin of Volcanology*, 58, 239-245.

Bigazzi, G., Coltelli, M., Norelli, P., 2003. Nuove eta delle ossidiane di Lipari determinate con il metodo delle tracce di fissione. *GEOITALIA 2003*; Federazione Italiana di Scienze della Terra, 444-446.

Blockley, S.P.E., Pyne-O'Donell, S.D.F., Lowe, J.J., Matthews, I.P., Stone, A., Pollard, A.M., Turney, C.S.M., Molyneux, E.G. 2005. A new and less destructive laboratory procedure for the physical separation of distal glass tephra shards from sediments. *Quaternary Science Reviews*, 224, 16-17, 1952-1960.

Borchardt, G.A., Harward, M.E. and Schmitt, R.A., 1971. Correlation of volcanic ash deposits by activation analysis of glass separates. *Quaternary Research* 1(2): 247-260.

Bourne, A.J., 2012. The late Quaternary tephrochronology of the Adriatic region: implications for the synchronisation of marine records. Unpublished Thesis; Royal Holloway University of London.

Bourne, A., Lowe, J.J., Trincardi, F., Asioli, A., Blockley, S.P.E, Wulf, S., Matthews, I.P. Piva, A., Vigliotti, L. 2010. Distal tephra record for the last 105, 000 years from the core PRAD 1-2 in the Adriatic Sea: implications for marine tephrostratigraphy. *Quaternary Science Reviews*, 29, 23-24. 1-16.

Brauer, A., Allen, J.R.M., Mingram, J., Dulski, P., Wulf, S., Huntley, B., 2007. Evidence for last interglacial chronology and environmental change from Southern Europe. *PNAS*, 104, 450-455. Bronk-Ramsey, C., 2009. Bayesian analysis of radiocarbon dates. *Radiocarbon*. 51, 337-360.

Brown, R.J., Orsi, G., de Vita, S., 2008. New insights into Late Pleistocene explosive volcanic activity and caldera formation on Ischia (southern Italy). *Bulletin of Volcanology* 70, 583–603.

Busacca, A., Nelstead, K.T., McDonald, E.V., Purser, M., 1992. Correlation of distal tephra layers in Loess in Channeled Scabland and Palouse of Washington state. *Journal of Quaternary Research* 37 (3), 281-303.

Calanchi, N., De Rosa, R., Mazzuoli, R., Rossi, P.L., Santacroce, R., Ventura, G., 1993. Silicic magma entering a basaltic magma chamber: eruptive dynamics and magma mixing — an example from Salina (Aeolian Islands, southern Tyrrhenian Sea). *Bulletin of Volcanology* 55, 504–522.

Calanchi, N., Gasparotto, G., Romagnoli, C., 1994. Glass chemistry in volcanoclastic sediments of ODP Leg 107, Site 650, sedimentary sequence: provenance and chronological implications. *Journal of Volcanology and Geothermal Research* 60, 59–85.

Calanchi, N., Dinelli, E., Gasparotto, G., Lucchini, F., 1996. Etnean tephra layer in Albano lake and Adriatic Sea cores: new findings of Y1-layer in the Central Mediterranean area. *Acta Vulcanologica* 8, 7–13.

Calanchi, N., Cattaneo, A., Dinelli, E., Gasparotto, G., Lucchini, F., 1998. Tephra layers in Late Quaternary sediments of the Central Adriatic Sea. *Marine Geology* 149, 191–209.

Calanchi, N., Peccerillo, A., Tranne, C.A., Lucchini, F., Rossi, P.L., Kempton, P., Barbieri, M and Wu, T.W. 2002. Petrology and geochemistry of volcanic rocks from the island of Panarea: implications for mantle evolution beneath the Aeolian Island arc

(Southern Tyrrhenian Sea). *Journal of Volcanology Geothermal Research* 115, 367-395.

Calanchi, N., Dinelli, E., 2008. Tephrostratigraphy of the last 170 ka in sedimentary successions from the Adriatic Sea. *Journal of Volcanology and Geothermal Research*, 177, 81- 95.

Carey, S. N. & Sigurdsson, H. (1982): Influence of particle aggregation on deposition of distal tephra from the May 18, 1980, eruption of Mount St. Helens volcano.- *Journal of Geophysical Research* 87, 7061- 7072.

Cas, R. A. F., Wright, J. V. 1987. *Volcanic Successions, Modern and Ancient*. Allen and Unwin, London.

Carobene, L., Cirrincione, R., De Rosa, R., Gueli, A.M., Marino, S., Troja, S.O. 2006. Thermal (TL) and optical stimulated (OSL) techniques for dating Quaternary colluvial volcanoclastic sediments: An example from the Crati Basin (Northern Calabria). *Quaternary International* 148, 149-164.

Caron, B., Siani, G., Sulpizio, R., Zanchetta, G., Paterne, M., Santacroce, R., Tema, E., Zanella, E. 2012. Late Pleistocene to Holocene tephrostratigraphic record from the Northern Ionian Sea. *Marine Geology*, 311-314. 41-51.

Chester, D.K, Duncan, A.M., Guest, J.E. 1987. The pyroclastic deposits of Mount Etna volcano, Sicily. *Geological Journal* 22, 225-243.

Cimarelli, C., De Rita, D., Dolfi., M., Procesi., M., 2008. Coeval strombolian and vulcanian type explosive eruptions at Panarea (Aeolian Islands, Southern Italy). *Journal of Volcanology and Geothermal Research* 177, 797-811.

Civetta, L., Orsi., G., Pappalardo, L., Fishher., R.V., Heiken G., Ort., M. 1997. Geochemical zoning, mingling, eruptive dynamics and depositional processes- The Campanian Ignimbrite, Campi Flegrei Caldera, Italy. *Journal of Volcanology and Geothermal Research* 75 (3-4), 183-219.

Clift, P., Blusztajn, J., 1999. The trace-element characteristics of Aegean and Aeolian volcanics arc marine tephra. *Journal of Volcanology and Geothermal Research* 92, 321-374.

Coltelli, M., Del Carlo, P., Vezzoli, L., 2000. Stratigraphic constraints for explosive activity in the past 100 ka at Etna Volcano, Italy. *International Journal of Earth Sciences* 89, 665-667.

Cortes, J.A., Wilson, M., Condliffe, E., Francalanci, L., Chertkoff, D.G., 2005. The evolution of the magmatic system of Stromboli volcano during the Vancori period (26-13.8 ky). *Journal of Volcanology and Geothermal Research* 147, 1-2, 1-38.

Crisci, G.M., De Rosa, R., Esperanca, S., Mazzuoli, R., Sonnino, M. 1981. Temporal evolution of a three component system: The island of Lipari (Aeolian Arc, southern Italy). *Bulletin of Volcanology* 53. 207-221.

Crisci, G.M., Delibrias, G., De Rosa, R., Mazzuoli, R., Sheridan, M.F., 1983. Age and petrology of the Late-Pleistocene brown tuffs on Lipari, Italy. *Bulletin of Volcanology* 46, 241-391.

Dansgaard, W., 1985. Greenland Ice Core Studies. *Palaeogeography, Palaeoclimatology, Palaeoecology* 50, 185-187.

Dansgaard, W., Johnsen, S.J., Clausen, H.B., Dahljensen, D., Gundestrup, N.S., Hammer, C.U., Hvidberg, C.S., Steffensen, J.P., Sveinbjornsdottir, A.E., Jouzel, J., Bond, G., 1993. Evidence for General Instability of Past Climate from a 250-KYR Ice-Core record. *Nature*, 364, 218 – 220.

Davi, M., De Rosa, R., Donato, P., Sulpizio, R., 2011. Lami pyroclastic succession (Lipari, Aeolian Islands): A clue for unraveling the eruptive dynamics of the Monte Pilato rhyolitic pumice cone. *Journal of Volcanology and Geothermal Research* 201, 285-300.

Davies, S.M., Wohlfarth, B., Wastegard, S., 2004. Were there two Borrobol Tephra during the early Lateglacial period: implications for tephrochronology. *Quaternary Science Reviews* 23 (5-6), 581-589.

de Alteriis, G. Insinga, D.D. Morabito, S. Morra, V. Chiocci, F.L. Terrasi, F. Lubritto, C. Di Benedetto, C. Pazzanese, M., 2010. Age of submarine debris avalanches and tephrostratigraphy offshore Ischia Island, Tyrrhenian Sea, Italy. *Marine Geology* 278 (1-4), 1-18.

De Astis, G., Dellino, P., De Rosa, R., La Volpe, L., 1997. Eruptive emplacement mechanism of fine grained pyroclastic deposits widespread on Vulcano Island. *Bulletin of Volcanology* 59, 87-102.

De Astis, G., Peccerillo, A., Kempton, P.D., La Volpe, L., Wu, T.W., 2000. Transition from calc-alkaline to potassium-rich magmatism in subduction environments: geochemical and Sr, Nd, Pb isotopic constraints from the island of Vulcano (Aeolian arc). *Contributions to Mineralogy and Petrology* 139 (6), 684-703.

De Astis, D., Dellino, P., La Valop, L., Lucchi., F., Tranne, C.A., 2006. Geological Map of the Island of Vulcano (Aeolian Islands), scale 1:10,000 University of Bari, University of Bologna and INGV.

Deino, A. L., Orsi, G., De Vita, S., Piochi, M., 2004. The age of the Neapolitan Yellow Tuff caldera –forming eruption (Campi Flegrei caldera-Italy) assessed by $^{40}\text{Ar}/^{39}\text{Ar}$ dating method. *Journal of Volcanology Geothermal Research* 133, 1-4, 157-170.

Delibrias, G., Guiller, M.T., Labeyrie, J., 1972. Gif natural. Radiocarbon measurements VII. *Radiocarbon*, 14: 280-320.

Dellino, P., De Astis, G., La Volpe, L., Mele, D. and Sulpizio, R., 2011. Quantitative hazard assessment of phreatomagmatic eruptions at Vulcano (Aeolian Islands, Southern Italy), as obtained by combining stratigraphy, event statistics and physical modelling. *Journal of Volcanology and Geothermal Research* 201, 264-384.

Del Moro, A., Gioncada, A., Pinarelli, L., Sbrana, A., Joron, J.L., 1998. Sr, Nd and Pb isotope evidence for open system evolution at Vulcano, Aeolian Arc, Italy. *Lithos* 43, 81-106.

De Rita, D., Frazzetta, G., Romano, R., 1991. The Biancavilla-Montalto Ignimbrite (Etna, Sicily). *Bulletin of Volcanology* 53, 121-131.

Di Rita, D., Dolfi, D., Cimarelli, C. 2008. Occurrence of Somma-Vesuvius fine ashes in the tephrostratigraphy record of Panarea, Aeolian Islands. *Journal of Volcanology and Geothermal Research* 177 (1), 197-207.

De Rosa, R., Donato., Gioncada. A., Masetti, M., and Sactacroe, R., 2003a. The Monte Guardia eruption (Lipari, Aeolian Islands): an example of a reversely zoned magma mixing sequence. *Bulletin of Volcanology* 65, 530-543.

De Rosa, R., Guillou, H., Mazzuoli, R., ventura, G., 2003. New unspiked K-Ar ages of volcanic rocks of the central and western sectors of the Aeolian Islands: Reconstruction of the volcanic stages. *Journal of Volcanology and Geothermal Research* 120, 161-178.

Di Roberto, A., Rosi, M., Bertagnini, A., Marani, M.P., Gamberi, F., Del Principe, A., 2008. Deep water gravity core from the Marsili Basin (Tyrrhenian Sea) records Pleistocene-Holocene explosive events and instabilities of the Aeolian Island Archipelago, (Italy). *Journal of Volcanology and Geothermal Research* 177 (1), 133-144.

Di Roberto, A., Rosi, M., Bertagnini, A., Marani, M.P., Gamberi, F. 2010. Distal turbidites and Tsunamigenic landslides of Stromboli Volcano (Aeolian Islands, Italy). *Adv. Nat. Tech. Hazards Res.* 28, IV, 719-731.

Di Traglia, F., 2011. "The last 1000 years of eruptive activity at the Fossa Cone (Island of Vulcano, Southern Italy)", PhD Thesis, University of Pisa, Italy, unpublished thesis.

Di Vito, M.A., Isaia, R., Orsi, G., Southon, J., de Vita, S., D'Antonio, M., Pappalardo, L., Piochi, M., 1999. Volcanism and deformation since 12000 years at the Campi Flegrei caldera (Italy). *Journal of Volcanology and Geothermal Research* 91, 221-246.

Di Vito, M.A., Sulpizio., Zanchetta, G., D'Orazio. 2008. The late Pleistocene pyroclastic deposits of the Campanian plain: New insights into the explosive activity of the Neapolitan volcanoes. *Journal of Volcanology and Geothermal Research* 177 (1) 19-48.

Di Vivo, B., Rolandi, G., Gans, P.B., Calvert, A, Bohrson, W.A., Spera, F.J., Belkin, H.E., 2001. New constraints on the pyroclastic eruptive history of the Campanian volcanic Plain (Italy). *Mineralogy and Petrology*. 73, 47-65.

Dolfi, D., de Rita, D., Cimarelli, C., Mollo, S., Soligo, M., Fabbri, M. 2007. Dome growth rates, eruption frequency and assessment of volcanic hazard: Insights from new U/Th dating of the Panarea and Basiluzzo dome lavas and pyroclastics, Aeolian Islands, Italy. *Quaternary International* 162-163, 182-194.

Donato, P., Behrens, H., De Rosa, R., Holtz, F., Parat, F., 2006. Crystallization conditions in the Upper Pollara magma chamber, Salina Island, Southern Tyrrhenian Sea. *Mineralogy and Petrology* 86, 89-108.

Duncan, A. M., 1976. Pyroclastic flow deposits in the Adrano area of Mount Etna, Sicily. *Geol Mag* 113:357-363

Ellam, R.M., Menzies, M.A., Hawkesworth, C.J., Leeman, W.P., Rosi, M., and Serri, G., 1988. The transition from calc-alkaline to potassic orogenic magmatism in the Aeolian Islands, Southern Italy. *Bulletin of Volcanology* 50. 387-398.

Favalli, M., Karatson, D., Mazzuoli, R., Pareschi, M.T., Ventura, G., 2005. Volcanic geomorphology and tectonic of the Aeolian archipelago (Southern Italy) based on integrated DEM data. *Bulletin of Volcanology* 68, 157-170.

Fertilo, C., Viccaro, M., Cristofolini, R., 2008. Volatile-induced magma differentiation in the plumbing system of Mt. Etna volcano (Italy): evidence from glass in tephra of the 2001 eruption. *Bulletin of Volcanology* 70, 4, 455-473.

Francalanci, L., Taylor, S.R., McCulloch, M.T., Woodhead, J.D., 1993. Geochemical and isotopic variations in the calc-alkaline rocks of Aeolian arc, southern Tyrrhenian Sea, Italy: constraints on magma genesis. *Contributions to Mineralogy Petrology* 113, 300–313.

Frazzetta, G., La Volpe, L., Sheridan, M.F., 1983. Evolution of the Fossa cone, Vulcano. *Journal of Volcanology and Geothermal Research* 17, 329-360.

Gabbianelli, G., Romagnoli, C., Rossi, P.L., Calanchi, N., 1993. Marine geology of the Panarea-Stromboli area (Aeolian Archipelago, Southeastern Tyrrhenian Sea). *Acta Vulcanologica* 3,11–20.

Gamberi, F., Marani, M., 2007. Downstream evolution of the Stromboli slope valley (south eastern Tyrrhenian Sea). *Marine Geology* 243 (1), 180–199.

Gertisser, R. Keller, J. 2000. From basalt to dacite: origin and evolution of the calc-alkaline series of Salina, Aeolian Arc, Italy. *Contributions to Mineralogy and Petrology*. 139 (5), 607-626.

Gertiser, R., Self, S., Gaspar, J., Kelley, S.P., Pimental, A., Eikenberg, J., Barry, T., Pacheco, J., Queiroz, G., Vespa, M., 2010. Ignimbrite stratigraphy and chronology on Terceira Island, Azores. In Gropelli, G., and Viereck-Goette, L., eds *Stratigraphy and Geology of Volcanic Areas*. Geological S.America Special paper. 464, pp133-154.

Giaccio, B., Hajdas, I., Peresani, M., Fedele, F.G., Isaia, R., 2006. The Campanian Ignimbrite and its relevance for the timing of the Middle to Upper Palaeolithic shift. In: Conard, N.J. (Ed.), “When Neanderthals and Modern Humans Met”. *Tübingen Publications in Prehistory*. Kerns Verlag, Tübingen, pp. 343–375.

Giaccio, B., Isaia, R., Sulpizio, R., Zanchetta, G. 2008. Explosive volcanism in the central Mediterranean are during the late Quaternary- linking sources and distal archives. *Journal of Volcanology and Geothermal Research* 177, v-vii.

Gillot, P. Y 1987. Histoire volcanique des iles eolinned; arc insulaire ou complexe progenique annulair? *Doc Trav IGAL Paris* 1: 25-42.

Gillot, P.Y., Chiesa, S., Pasquare, G., Vezzoli, L., 1982 <33000 yr K/Ar dating of the volcano-tectonic horst of the isle of Ischia, Gulf of Naples. *Nature* 229:242

Gillot, P.Y., Keller, J., 1993. Radiochronological dating of Stromboli. *Acta Vulcanologia* 3, 69-77.

Gioncada, A., Mazzuoli, R., Bisson, M., Pareschi, M.T., 2003 Petrology of volcanic products younger than 42 ka on the Lipari-Vulcano complex (Aeolian Islands, Italy): an example of volcanism controlled by tectonics. *Journal of Volcanology and Geothermal Research* 122, 191–220.

Gioncada, A., Mazzuoli, R., Milton, A.J., 2005. Magma mixing at Lipari (Aeolian Islands, Italy): Insights from textural and compositional features of phenocrysts. *Journal of Volcanology and Geothermal Research* 145, 1-2, 97–118.

Giordano, G., Porreca, M., Musacchio, P. and Mattei., 2008. The Holocene Secche di Lazzaro phreatomagmatic succession (Stromboli, Italy): evidence of pyroclastic density current origin deduced by facies analysis and AMS flow directions. *Bulletin of Volcanology* 70, 1221-1236.

Grams, I., 1999. Kartierung und Interpretation der marinen und terrestrischen Quartarablagerungen, unter besonderer Beachtung der Tuffvorkoomme, bei Palinuro (Suditalien). Dipl. Thesis, University of Freiburg, 127pp.

Haflidason, H., Eiriksson, J., Van Kreveld, S., 2000. The tephrochronology of Iceland and the North Atlantic region during the middle and late Quaternary: a review. *Journal of Quaternary Science* 15, 3-22.

Hall, V. A., Pilcher, J., 2002. Late-Quaternary Icelandic tephtras in Ireland and Great Britain: detection, characterization and usefulness. *The Holocene* 12 (2), 223-230.

Hornig-Kjarsgaard, I., Keller, J., Kobersky, U., Stadlbauer, E., Francalanci, L., Lenhart, R., 1993. Geology, stratigraphy and volcanological evolution of the island of Stromboli, Aeolian Island arc, Italy. *Acta Vulcanologia* 3, 21-68.

Hunt, J.B., Hill, P.G., 1993. Tephra geochemistry: a discussion of some persistent analytical problems. *The Holocene* 3, 271–278.

Isaia, R., di Vito, M.A., de Vita, S., Rosi, M., Sbrana, A., 2012. Comment on “ $^{40}\text{Ar}/^{39}\text{Ar}$ dating of tuff vents in the Campi Flegrei caldera (southern Italy): towards a new chronostratigraphic reconstruction of the Holocene volcanic activity” by Fedele et al. [*Bulletin of Volcanology*; 73: 1323-1336]. *Bulletin of Volcanology* 74, 293-296.

Jochum, K.P. et al., 2006. MPI-DING reference glasses for in situ microanalysis: 581 New reference values for element concentrations and isotope ratios. 582 *Geochemistry Geophysics Geosystems*. 7, (2).

Keller, J., 1980a. The island of Vulcano. *Rendiconti della Società Italiana di Mineralogia e Petrologia*. 36, pp 369-414.

Keller, J., 1980b. The island of Salina. *Rendiconti della Società Italiana di Mineralogia e Petrologia*. 36, pp 489–524.

Keller, J., 2002. Lipari's Fiery Past: Dating the Medieval Pumice Eruption of Monte Pelato, Internat. Conference UNESCO-Reg Siciliana, Lipari, September 29–October 2

Keller, J., Leiber, J., 1974. Sedimente, Tephra-Lagen und Basalte der sudtyrrhenischen Tiefsee-Ebene im Bereich des Marsili-Seeberges. *Met. Forsch.- Ergebniss. Reihe C*. 19, 62-76.

Keller, J., Ryan, W.B.F., Ninkovich, D., Altherr, R., 1978. Explosive volcanic activity in the Mediterranean over the past 200,000 yr as recorded in deep-sea sediments. *Geological Society of America Bulletin* 89, 591–604.

Keller, J., Kraml, M., 2004. Tephrochronological archives for known and unknown paroxysms in Italian explosive volcanism of the upper Quaternary. IAVCEI General Assembly Nov. 2004, Pucón, Chile.

Kieffer G (1979) L'activite de l'Etna pendant les dernires 20000 ans. CR Acad Sci Paris 288D: 1023-1026

Kokelaar, P., Romagnoli, C., 1995. Sector collapse, sedimentation and clast population, evolution at an active island-arc volcano: Stromboli, Italy. *Bulletin of Volcanology* 57 (4), 240-262.

Kraml, M., 1997. Laser $^{40}\text{Ar}/^{39}\text{Ar}$ - Datieringen an distalen marinen Tephren desjung-quartaren Mediterranean Vulkanismus (Ionisches Meer, METEOR-Fahrt 25/4). Ph.D Thesis Albert-Ludwings-Universitat Freiburg. pp.216.

Lambeck, K., Bard, E., 2000. Sea-level change along the French Mediterranean coast for the past 30000 years. *Earth and Planetary Science Letters* 175, 203–222.

Le Bas, M.J., Le Maitre, R.W., Streckeisen, A., Zanettin, B., 1986. A chemical classification of volcanic rocks based on the total alkali-silica diagram. *Journal of Petrology* 27, pp 745–750.

Lirer, L., Pescatore, T., Scandone, P., 1967. Livelli di piroclastiti nei depositi continentali post-tirreniani del litorale Sud-tirrenico. *Atti Accademia Gioenia Scienze Naturali - Serie VI - 18*, 85–115.

Lowe, J.J., Blockley, S.P.E., Trincardi, F., Asioli, A., Cattaneo, A., Matthews, I.P., Pollard, M., Wulf, S., 2007. Age modelling of late Quaternary marine sequences from the Adriatic: towards improved precision and accuracy using volcanic event stratigraphy. *Continental Shelf Research*. 27, 560–582.

Lowe, J., Barton, N., Blockley, S., Ramsey, C.B., Cullen, V., Davies, W., Gamble, C., Grant, K., Hardiman, M., Housley, R., Lane, C.S., Lee, S., Lewis, M., MacLeod, A., Menzies, M., Muller, W., Pollard, M., Price, C., Roberts, A.P., Rohling, E.J., Satow, C., Smith, V.C., Stringer, C.B., Tomlinson, E.L., White, D., Albert, P.G., Arienzo, I., Barker, G., Boric, D., Carandente, A., Civetta, L., Ferrier, C., Guadelli, L., Karkanis, P., Komuzelis, M., Muller, C., Orsi, G., Pross, J., Rosi, M., Shalamanov-Korobar, L., Sirakov, N., Tzedakis, C., 2012. Volcanic ash layers illuminate the resilience of

Neanderthals and early Modern Humans to natural hazards. PNAS 109 (34) 13432-13537.

Lucchi, F., Tranne, C.A., Calanchi, N., Rossi, P.L., Keller, J. 2007. The stratigraphic role of marine deposits in the geological evolution of the Panarea volcano (Aeolian Islands, Italy). *Journal of the Geological society of London*, Vol 164, pp 983-996.

Lucchi, F., Tranne, C.A., De Astis, G., Keller, J., Losito, R., Morche, W., 2008. Stratigraphy and significance of Brown Tuffs on the Aeolian Islands (southern Italy). *Journal of Volcanology and Geothermal Research* 177, 49–70.

Lucchi, F., Tranne, C.A., Rossi, P.L., 2010. Stratigraphic approach to geological mapping of the Late Quaternary island of Lipari (Aeolian archipelago, Southern Italy). In Groppelli, G., Viereck-Grotte, L., 2010. *Stratigraphy and Geology of Volcanic Areas*. The Geological society of America. Special Paper 464.

Lucchi, R.G., Kidd, R.B., 1998. Sediment provenance and turbidity current processes at the Lametini Seamounts and Stromboli Canyon, SE Tyrrhenian Sea. *Geo-Marine Letters* 18, 155–164.

Magri, D., Sadori, L., 1999. Late Pleistocene and Holocene pollen stratigraphy at Lago di Vico, central Italy. *Vegetation History and Archaeobotany* 8, 247-260.

Mariciano, R., Munno, R., Paola, P., Santangelo, N., Santo, A., Villa, I. 2008. Late Quaternary tephra layers along the Cilento coastline (southern Italy). *Journal of Volcanology and Geothermal Research* 177, 227-243.

Masson, D.G., Harbitz, C.B., Wynn, R.B., Pedersen, G., Loveholt, F. 2006. Submarine landslides: processes, triggers and hazard prediction. *Royal Society of Philosophical Transactions* 364, 2009-2039.

McCoy, F.W., 1981. Areal distribution, redeposition and mixing of tephra within deep-sea sediments of the Eastern Mediterranean Sea. In: Self, S., Sparks, R.S.J. (Eds.), *Tephra Studies*. Reidel, Dordrecht, pp 245–254.

- McCoy, F.W., Cornell, W., 1990. In: Kastens, K.A., Mascle, J., et al. (Eds.) *Volcaniclastic Sediments in the Tyrrhenian Basin*. Proc. ODP Sci. Res. 107, pp 291-305.
- Morche, W., 1988. *Tephrochronologie der Aolischen Inseln*. Unpublished PhD Thesis, Albert-Ludwigs-Universität Freiburg, Germany.
- Munno, R., Petrosino, P., 2004. New constraints on the occurrence of Y-3 Upper Pleistocene tephra marker layer in the Tyrrhenian Sea. *Il Quaternario*, 17, 11–20.
- Narcisi, B., 1996. Tephrochronology of a Late Quaternary lacustrine record from the Monticchio maar (Vulture volcano, Southern Italy). *Quaternary Science Reviews* 15, 155-165.
- Narcisi, B., 2002. Tephrostratigraphy of the Late Quaternary lacustrine sediments of Lago di Pergusa (central Sicily). *Bollentino della Societa geologica italiana*. 12 (2), 211-219.
- Narcisi, B., Vezzoli, L., 1999. Quaternary stratigraphy of distal tephra layers in the Mediterranean- an overview. *Global and Planetary Change* 21, 31–50.
- Negri, A., Capotondi, L., Keller, J., 1999. Calcareous nannofossils, planktonic foraminifera and oxygen isotopes in the Late Quaternary Sapropels of the Ionian Sea. *Marine Geology* 157. 89-103.
- Norin, E., 1958. The sediments of the central Tyrrhenian Sea. In: Pettersson, H. (Ed.), *Sediment cores from the Mediterranean Sea and the Red Sea*. Reports of Swedish Deep-Sea Expeditions 1947–1948: 8 (1), 1–136
- Orsi, G., DeVita, S., Di Vito., 1996. The restless, resurgent, Campi Flegrei nested caldera (Italy): Constraints on its evolution and configuration. *Journal of Volcanology and Geothermal Research* 74 (3-4) 179-214.
- Pappalardo, L., Civetta., L., D'Antonio, M., Deino, A., Di Vito, M., Orsi, G., Carandente, A., De Vita, S., Isaia, R., Piochi, M. 1999. Chemical and Sr-isotopical

evolution of the Phlegraean magmatic system before the Campanian Ignimbrite and Neapolitan Yellow Tuff eruptions, *Journal of Volcanology and Geothermal Research* 91 (2-4) 141-166.

Pasquare, G.L., Francalanci, V.H., Garduno, V.H., Tibaldi 1993. Structure and geological evolution of the Stromboli volcano, Aeolian Islands, Italy. *Acta Vulcanologica* 3. 79-89.

Paterne, M., Guichard, F., Labeyrie, J., Gillot, P. Y. & Duplessy, J. C. 1986. Tyrrhenian Sea tephrochronology of the oxygen isotope record for the past 60,000 years. *Marine Geology* 72, 259-285.

Paterne, M., Guichard, F., Labeyrie, J. 1988. Explosive activity of the South Italian volcanoes during the past 80,000 years as determined by marine tephrochronology. *Journal of Volcanology and Geothermal Research* 34, 153–172.

Paterne, M., Labeyrie, J., Guichard, F., Mazaud, A., Maitre, F. 1990. Fluctuation of the campanian explosive activity (South Italy) during the past 190,000 years as determined by marine tephrochronology. *Earth and Planetary Science Letters*. 98, 166–174.

Paterne, M., Kallel, N., Labeyrie, L., Vautravers, M., Duplessy, J.-C., Rossignol-Strick, M., Cortijo, E., Arnold, M., Fontugne, M. 1999. Hydrological relationship between the North Atlantic Ocean and the Mediterranean Sea during the past 15 – 75 kyr. *Paleoceanography*, 14, 5, 626 – 638.

Paterne, M., Guichard, F., Duplessy, J.C., Siani, G., Sulpizio, R and Labeyrie, J., 2008. A 90,000-200, 000 yrs marine tephra record of Italian volcanic activity in the Central Mediterranean Sea. *Journal of Volcanology and Geothermal Research* 177 (1), 187-196.

Pearce, N.J.G., Westgate, J.A., Perkins, W.T., Eastwood, W.J., Shane, P., 1999. The application of laser ICP-MS to the analysis of volcanic glass shards from tephra deposits: bulk and single shard analysis. *Global and Planetary change* 21, 1-3, 151-171.

Pearce, N.J.G., Westgate, J.A., Perkins, W.T., Preece, S.J., 2004. The application of ICP-MS methods to tephrochronological problems. *Applied Geochemistry*. 19, 289-322.

Pearce, N.J.G., Denton, J.S., Perkins, W.T., Westgate, J.A., Alloway, B.V., 2007. Correlation and characterisation of individual glass shards from tephra deposits using trace element laser ablation ICP-MS analyses: current status and future potential. *Journal of Quaternary Science* 22 (7), 721–736.

Peccerillo, A and Wu, T.W., 1992. Evolution of Calc-alkaline magmas in continental arc volcanoes: Evidence from Alicudi, Aeolian arc (Southern Tyrrhenian Sea, Italy). *Journal of Petrology* 33 (6), 1295-1315.

Perkins, M.E., Nash, W.P., Brown, F. H. and Fleck, R.J., 1995. Fallout tuffs of Trapper Creek, Idaho: A record of Miocene explosive volcanism in the Snake River Plain volcanic province. *Geological society of America Bulletin* 107 (12), 1484-1506.

Perkins, W.T., Pearce, N.J.G., Mineral microanalysis by laser probe inductively coupled plasma mass spectrometry. IN Potts, P.J., Bowles. J.F.W., Reed, S.J.B., Cave, M.R., (e.ds) *Microprobe techniques in Earth Sciences*. The mineralogical society pp 291-325.

Petrone, C.M., Braschi, E., Francalanci, L., 2009. Understanding the collapse–eruption link at Stromboli, Italy: A microanalytical study on the products of the recent Secche di Lazzaro phreatomagmatic activity. *Journal of Volcanology and Geothermal Research* 188 (4), 315-332.

Poli, S., Chiesa, S., Gillot, P.Y., Gregnanin, A., Guichard, F., 1987. Chemistry versus time in the volcanic complex of Ischia (Gulf of Naples, Italy): evidence of successive magmatic cycles. *Contributions to Mineralogy and Petrology* 95, 322–335.

Preece, S.J., Pearce, N.J.G., Westgate, J.A., Froese, D.G, Jensen, B.J.L., Perkins, W.T., 2011. Old cow tephra across eastern Beringia: a single cataclysmic eruption at the close of marine isotope stage 6. *Quaternary Science Reviews* 30, 2069-2090.

Pyle, D.M., Ricketts, G.D., Margari, V., Van Andel, T.H., Sinitsyn, A.A., Praslov., N.D., Lisitsyn, S., 2006. Wide spread dispersal and deposition of distal tephra during the Pleistocene Campanian Ignimbrite/Y-5 eruption, Italy. *Quaternary Science Reviews* 25 (21-22), 2713-2728.

Ramrath, A., Zolitschka, B., Wulf, S., Negendank, F.W., 1999. Late Pleistocene climatic variations as recorded in two Italian maar lakes (Lago di Mezzano, Lago Grade di Monticchio) *Quaternary Science Reviews* 18, 977-992.

Rasmussen, S.O., Andersen, K.K., Svensson, A.M., Steffensen J.P., Vinther, B., Clausen, H.B., Siggaard-Andersen, M.L., Johnsen, S.J., Larsen, L.B., Dahl-Jensen, D., Bigler, M., Röthlisberger, R., Fischer, H., Goto-Azuma, K., Hansson, M., Ruth, U., 2006. A new Greenland ice core chronology for the last glacial termination. *J. Geophysical Research*, 111, p. D06102.

Reimer, P.J., Reimer, R.W., 2007. Radiocarbon Dating: Calibration, In Elias, S.A., 2007. *Encyclopaedia of Quaternary Science*, Elsevier, 2941 – 2950.

Reimer, P.J., Bailliem, M.G.L, Bard, E., Bayliss, A., Beck, W.J., Blackwell, P.G., Bronk-Ramsey, C., Buck, G.S., Burr, G.S., Edwards, R.L., Friedrich, M., Grootes, P.M., Guilderson, T.P., Hajdas, I., Heaton, T.J., Hogg, A.G., Hughen, K.A., Kaiser, K.E., Kromer, B., McCormac, F.G., Manning, S.W., Reimer, R.W., Richards, D.A., Southon, J.R., Talamo, S., Turney, S.C.M., van der Plicht. J., Weyhenmeyer, C.E., 2009. IntCal09 and marine 09 radiocarbon age calibration curves, 0-50, 000 years cal BP. *Radiocarbon* 51, 1111-1150.

Rohling, E. J., Hayes, A., De Rijk, S., Kroon, D., Zachariasse, W.J., Eisma D., 1998. Abrupt cold spells in the northwestern Mediterranean, *Paleoceanography* 13(4), 316–322.

Rolandi, G., Petrosino, P., McGeehin, J., 1998. The interplinian activities at Somma-Vesuvius in the last 3,500 years. *Journal of Volcanology and Geothermal Research* 17, 249-271.

Rossi, M. 1980. The island of Stromboli. *Rend Soc Ital Mineral Petol* 36:345-368.

Rosi, M., Sbrana, A., (Eds.), 1987. Phlegrean Fields. CNR Quaderni Ricerca Scientifica. 114 (9), 175pp

Rosi, M., Sbrana, A., Vezzoli, L., 1988b Correlazioni tefrostratigrafiche di alcuni livelli di schia, Procida e Campi Flegrei. Mem Soc Geol It 41:1015–1027

Rosi, M., Bertagnini, A., Landi, P., 2000. Onset of the persistent activity at Stromboli Volcano (Italy). Bulletin of Volcanology 62 (4–5), 294–300.

Santacroce, R., Cioni, R., Marianelli, P., Sbrana, A., Sulpizio, R., Zanchetta, G., Donahue, D. J., Joron, J.L., 2008. Age and whole rock-glass compositions of proximal pyroclastics from the major explosive eruptions of Somma-Vesuvius: A review as a tool for distal tephrostratigraphy. Journal of Volcanology and Geothermal Research 177, 1-18.

Schiano, P., Clocchiatti, R., Ottolini, L., Busa, T., 2001. Transition of Mount Etna lavas from a mantle-plume to island-arc magmatic source. Nature 41, 900-904

Schneider, J.L., Le Ruyet, A., Chanier, F., Buret, C., Ferriere, J., Proust, J.N., Rosseel, J.B., 2001. Primary or secondary distal volcanoclastic turbidites: how to make the distinction? An example from the Miocene of New Zealand (Mahia Peninsula, North Island). Sedimentary Geology. 145, 1–22.

Shane, P., 2000. Tephrochronology: New Zealand a case study. Earth Science reviews. 49, 223-259.

Siani, G., Paterne, M., Michel, E., Sulpizio, R., Sbrana, A., Arnold, M., Haddad, G., 2001. Mediterranean sea surface radiocarbon age changes since the Last Glacial Maximum. Science 294, 1917-1920.

Siani, G., Sulpizio, R., Paterne, M., Sbrana, A., 2004. Tephrostratigraphy study for the last 18,000 ¹⁴C years in a deep-sea sediment sequence for the South Adriatic. Quaternary Science Reviews 23, 2485–2500.

Smith, V.C., Isaia, R., & Pearce, N.J.G., 2011. Tephrostratigraphy of post-15 kyr Campi Flegrei eruptions: implications for eruption history and chronostratigraphic markers. *Quaternary Science Reviews* 30 (25-26), 3638-3660.

Soligo, M., De Astis, G., Delitala, M.C., La Volpe, L., Tadderucci, A., Tuccimei, P., 2000. Diequilibri nella serie dell uranio nei prodotti dell isola di Vulcano: cronologia isotopica e implicazioni magmatologiche. 2 *Forum Italiano di Scienze della Terra Riassunti, Plinius*. 22, 347-349.

Sparks, R.S.J., Self, S., Walker, G.P.L., 1973. Products of ignimbrite eruptions. *Geology* 1: 115-118.

Speranza, F., Pompilio, M., D'Ajello Caracciolo, F., Sagnotti, L., 2008. Holocene eruptive history of the Stromboli volcano: constraints from palomagnetic dating. *Journal of Geophysical Research* 113, B09101.

Sulpizio, R., Zanchetta, G., Paterne, M., Siani, G., 2003. A review of tephrostratigraphy in central and southern Italy during the last 65 ka. *Il Quaternario*, 16 (2003), pp. 91–108

Sulpizio, R., De Rosa, R., Donato, P., 2008. The influence of variable of topography on the depositional behavior of pyroclastic density currents: The examples of the Upper Pollara eruption. *Journal of Volcanology and Geothermal Research* 175, 367-385.

Sun, S., McDonough, W.F., 1989. Chemical and isotopic systematics of 630 oceanic basalts: implications for mantle composition and processes. In: 631 A.D. Saunders, Norry, M.J. (Editor), *Magmatism in Ocean Basins*.

Tamburrino, S., Insinga, D.D., Sprovieri, M., Petrosino, P., Tiepolo, M., 2012. Major and trace element characterisation of tephra layers offshore Pantelleria Island: insights into the last 200 ka of volcanic activity and a contribution to Mediterranean tephrochronology. *Journal of Quaternary Science* 27 (2), 129-140.

Tibaldi, A., 2001. Multiple sector collapses at Stromboli volcano, Italy: how they work. *Bulletin of Volcanology* 63, 112-125.

Thunnell, R., Federman., A., Sparks. R.S.J., Williams. D. 1979. The age of volcanic significance of the Y-5 ash layer in the Mediterranean. *Quaternary Research*. 12, 241-253.

Todman, A. 2012. Temporal and spatial variations in the geochemistry of recent (< 2ka) volcanic rocks Vulcano, Aeolian Islands, Italy. Unpublished thesis Royal Holloway, University of London. MPhil.

Tommasini, S, Heumann, A., Avanzinelli, R., Francalanci, L. 2007. The Fate of High-Angle Dipping Slab in the Subduction Factory: an Integrated Trace Element and Radiogenic Isotope (U, Th, Sr, Nd, Pb) Study of Stromboli Volcano, Aeolian Arc, Italy. *Journal of Petrology*, 48, 12, 2404-2430.

Tomlinson, E.L., Thordarson, T., Muller, W., Thirlwall, M., Menzies, M.A., 2010. Microanalysis of tephra by LA-ICP-MS- Strategies, advantages and limitations assessed using the Thorsmork ignimbrite (Southern Iceland). *Chemical Geology* 279, (3-4), 73-89.

Tomlinson, E.L., Kinvig, H.S., Smith, V.C., Blundy, J.D., Gottsmann, J., Muller, W., Menzies, M.A. 2012a: The Upper and Lower Nisyros Pumices: Revisions to the Mediterranean tephrostratigraphic record using micron-beam glass geochemistry. *Journal of Volcanology and Geothermal Research*. *Available Online*

Tomlinson, E., Arienzo, I., Civetta, L., Wulf, S., Smith, V.C., Hardiman, M., Lane, C.S., Carandente, A., Orsi, G., Rosi, M., Muller, W., Thirlwall, M.F., Menzies, M. 2012b. Geochemistry of the Phlegraean Fields (Italy) proximal sources for major Mediterranean tephra: implications for the dispersal of Plinian and co-ignimbritic components of explosive eruptions. *Geochimica et Cosmochimica Acta*. *Available Online*

Tonarini, S., Armienti, P., D'Orazio, M., Innocenti, F., 2001. Subduction-like fluids in the genesis of Mt. Etna magmas: evidence from boron isotopes and fluid mobile elements. *Earth and Planetary Science Letters* 192, 4, 471-483.

Turney, C.S.M., et al., 2004. Tephrochronology of Last Termination Sequences in Europe: a protocol for improved analytical precision and robust correlation procedures (a joint SCOTAV-INTIMATE proposal). *Journal of Quaternary Science* 19 (2), 111–120.

Turney, C.S.M., Blockley, S.P.E., Lowe, J.J., Wulf, S., Branch, N.P., Mastrolorenzo, G., Swindle, G., Nathan, R., Pollard, M.A., 2008. Geochemical characterization of Quaternary tephras from the Campanian Province, Italy. *Quaternary International* 178 (1), 288-305.

Tzedakis, P.C., Andrieu, V., de Beaulieu, J.-L., Crowhurst, S., Follieri, M., Hooghiemstra, H., Magri, D., Reille, M., Sadori, L., Shackleton, N.J., Wijmstra, T.A., 1997. Comparison of terrestrial and marine records of changing climate of the last 500,000 years. *Earth and Planetary Science Letters*, 150, 171–176.

Tzedakis, P.C., McManus, J.F., Hooghiemstra, H., Oppo, D.W., Wijmstra, T.A., 2003. Comparison of changes in vegetation in northeast Greece with records of climate variability on orbital and suborbital frequencies over the last 450 000 years. *Earth and Planetary Science Letters*, 212, 197 – 212.

Ukstins Peate, I., et al., 2003. Correlation of Indian Ocean tephra to individual Oligocene silicic eruptions from Afro-Arabian flood volcanism. *Earth and Planetary Science Letters* 211 (3–4), 311–327.

Ukstins Peate, I., Kent, A.J.R., Baker, J.A., Menzies, M.A., 2008. Extreme geochemical heterogeneity in Afro-Arabian Oligocene tephras: preserving fractional crystallization and mafic recharge processes in silicic magma chambers. *Lithos, Continental Volcanism and the Chemistry of the Earth's Interior, International Conference on Continental Volcanism* 102 (1–2), 260–278.

Vezzoli L (1988) Island of Ischia: *Quaderni de La Ricerca Scientifica*, 114(10). Consiglio Nazionale delle Ricerca, Rome, p 133

Vezzoli, F., 1991. Tephra layers in the Bannock Basin (Eastern Mediterranean). *Marine Geology* 100, 21-34.

Viccaro, M., Giacomoni, P.P, Fertilo, C., Cristofolini, R. 2010. Dynamics of magma supply at Mt. Etna volcano (Southern Italy) as revealed by textural and compositional features in plagioclase phenocrysts. *Lithos* 116. 77-91.

Villari, L. 1980. The Island of Alicudi. *Rendiconti Societa Italiana di Mineralogia e Petrologia*, 36 (1) pp 441-466.

Vogel, H., Zanchetta, G., Sulpizio, R., Wagner, B., Nowaczyk, N., 2010a. A tephrostratigraphic record for the last glacial-interglacial cycle from Lake Ohrid, Albania and Macedonia. *Journal of Quaternary Science* 25, 320-338.

Voltaggio, M., Barbieri, M., Castorina, F., Taddeucci, A., Tecce, F., Tuccimei, P., Turi, B., Vesica, P., 1997. Calcite in fractures in a volcanic environment (Vulcano Island, Italy): contribution of geochronological and isotopic studies to volcano tectonics. *Journal of Volcanology and Geothermal Research* 75, 271- 282.

Voltaggio, M., Branca, M., Tuccimci, P., Tecce, F. 1995. Leaching procedure used in dating young potassic volcanic rocks by the $^{226}\text{Ra}/^{230}\text{Th}$ method. *Earth and Planetary Science Letters* 136, 123-131.

Vinci, A. (1985): Distribution and chemical composition of tephra layers from Eastern Mediterranean abyssal sediments. *Marine Geology* 64, 143-155.

Wagner, B., Sulpizio, R., Zanchetta, G., Wulf, S., Wessels, M., Daut, G., Nowackzick, H., 2008. The last 40 ka tephrostratigraphic record of Lake Ohrid, Albania and Macedonia: a very distal archive for ash dispersal from Italian volcanoes. *Journal of Volcanology and Geothermal Research* 177, 71–80.

Watts, W.A., Allen, J.R.M., Huntley, B., 1996. Vegetation history and palaeoclimate of the last glacial period at Lago Grande di Monticchio, southern Italy. *Quaternary Science Reviews* 15, 133–153.

Wortel, M.J.R., Spakman, W., 2000. Subduction and slab detachment in the Mediterranean-Carpathian region. *Science* 290 (5498), 1910-1917.

Wulf, S., 2000. Das tephrochronologische Referenzprofil des Lago Grande di Monticchio - Eine detaillierte Stratigraphie des suditalienischen explosiven Vulkanismus der letzten 100.000 Jahre. Ph.D. Thesis, University of Potsdam, Germany, Scientific Technical Report STR01/03, pp 19.

Wulf, S., Kraml, M., Brauer, A., Keller, J., Negendank, J.F.W., 2004. Tephrochronology of the 100 ka lacustrine sediment record of Lago Grande di Monticchio (southern Italy). *Quaternary International* 122, 7–30.

Wulf, S., Brauer, A., Mingram, J., Zolitschka, B., Negendank, J.F.W. 2006. Distal tephros in the sediments of Monticchio Marr lakes. In: Principe, C (E.d.), *La geologia del Mone Vulture*. Regione Basilicata- Consiglio Nazionale delle Ricerche pp 105-122.

Wulf, S., Kraml, M., Keller, J., 2008. Towards a detailed distal tephrostratigraphy in the Central Mediterranean: The last 20,000 yrs record of Lago Grande di Monticchio. *Journal of Volcanology and Geothermal Research* 177, 118-132.

Wulf, S., Keller, J., Paterne, M., Mingram, J., Lauterbach, S., Opitz, S., Sottit, G., Giaccio, B., Albert, P., Satow, C., Viccaro, M., Brauer, A. (2012; submitted). The 100-133 ka record of Italian explosive volcanism and revised tephrochronology of Lago Grande di Monticchio. *Quaternary Science Reviews*.

Zanchetta, G., Sulpizio, R., Di Vito, M.A. 2004. The role of volcanic activity and climate in alluvial fan growth at volcanic areas: an example from southern Campania Italy. *Sedimentary Geology* 168. 249-280.

Zanchetta, G., Sulpizio, R., Giaccio, B., Siani, G., Paterne, M., Wulf, S. D’Orazio, M. 2008. The Y-3 tephra: A last glacial stratigraphic marker for the central Mediterranean basin. *Journal of Volcanology and Geothermal Research* 177, 145-154.

Zanchetta, G., Sulpizio, R., Roberts, N, Cioni, R., Eastwood, W.J., Siani, G., Caron, B., Paterne, M and Santacroce, R., 2011. Tephrostratigraphy, chronology and climatic events of the Mediterranean basin during the Holocene: An overview. *The Holocene*. 21, 33-52.

Zanella, E., De Astis., G and Lanza, R 2001. Palaeomagnetism of welded, pyroclastic-fall scoriae at Vulcano, Aeolian Archipelago. *Journal of Volcanology and Geothermal Research* 107 (1-3), 71-86.

Zanon, V., Frezzotti, M.L., Peccerillo, A., 2003. Magmatic feeding system and crustal magma accumulation beneath Vulcano Island (Italy): evidence from CO₂ fluid inclusions in quartz xenoliths. *Journal of Geophysical Research. Solid Earth* 108.

Appendix I

See:

Albert, P.G., Tomlinson, E.L., Smith, V.C., Di Roberto, A., Todman, A., Rosi, M., Marani, M., Muller, W., Menzies, M.A., 2012. Marine-continental tephra correlations: Volcanic glass geochemistry from the Marsili Basin and the Aeolian Islands, Southern Tyrrhenian Sea, Italy. *Journal of Volcanology and Geothermal Research*, 229-230, 74-94.

Appendix II

Detailed description of results from investigated tephra compared with the 'Ischia tephra' layer Stromboli:

Y-7 Ionian Sea – M25/4-11

Major element glass compositions display some major element variability with 61.4-63.1 wt.% SiO₂, 2.2-2.9 wt.% FeO, 0.9-1.5 wt.% CaO. Glasses display elevated alkalis (5.9-8.4 wt.% Na₂O and 5.9-7.4 wt.% K₂O) and range from phonolitic to trachytic compositions (Fig. 6.8a). The tephra deposits comprise of glasses with both Na₂O > K₂O and also K₂O ≥ Na₂O (K₂O/Na₂O = 0.72-1.32). K₂O ≥ Na₂O is typically restricted to the higher SiO₂ glasses analysed. Trace element concentrations reflect highly evolved melt compositions (Zr/Sr = 7-385) and the glasses display significant LREE enrichment relative to the HREE (La/Yb = 21.7 ± 1.7). Significant trace element heterogeneity is observed in the trace element concentrations of this tephra layer with 261-512 ppm Rb, 29-70 ppm Y, 227-803 ppm Zr, 41-127 ppm Nb, 66-155 ppm La, 124-293 ppm Ce and 16-53 ppm Th (Fig. 6.20d-f). Glasses display significant depletions in Ba, Sr and Eu relative to other incompatible trace elements indicative of K-feldspar fractionation (3-25 ppm Ba, 3-32 ppm Sr and Eu/Eu**N* = 0.2; Table 6.3). HFSE element ratios to Th are constant within these glasses (Nb/Th = 2.54 ± 0.16; Zr/Th = 15.0 ± 0.7; Ta/Th = 0.13 ± 0.01) (Fig. 6.10e).

Lago Grande di Monticchio (LGdM)

TM-19 (38.63 m; 60, 060 varve years BP; Ar/Ar = 55 ± 2 yrs BP)

TM-19 major element glass compositions display some significant variability with 61.3-63.2 wt.% SiO₂, 2.3-2.8 wt.% FeO, 0.9-1.4 wt.% CaO. Glasses display elevated alkalis (6.2-8.4 wt.% Na₂O and 6.1-7.2 wt.% K₂O) and range phonolitic to trachytic compositions (Fig. 6.7a). The tephra deposits comprises of both glasses with both Na₂O > K₂O and also K₂O ≥ Na₂O (K₂O/Na₂O = 0.72-1.17). K₂O ≥ Na₂O is typically restricted to the higher SiO₂ glasses analysed as both Na₂O subsequently total alkalis decrease with increasing SiO₂. Trace element concentrations reflect highly evolved melt compositions (Zr/Sr = 17-261) and the glasses display significant LREE enrichment relative to the HREE (La/Yb = 22.2 ± 1.9). Significant heterogeneity is observed in the trace element concentrations of this tephra layer with ranges of 287-541 ppm Rb, 30-68 ppm Y, 258-778 ppm Zr, 46-123 ppm Nb, 68-149 ppm La, 136-289 ppm Ce and 18-51 ppm Th (Fig. 6.10d-f). Glasses display significant

depletions in Ba, Sr and Eu relative to other incompatible trace elements indicative of K-feldspar fractionation (3-29 ppm Ba, 3-36 ppm Sr and $Eu/Eu^*_N = 0.2$). HFSE element ratios to Th are fairly constant within these glasses ($Nb/Th = 2.6 \pm 0.16$; $Zr/Th = 15.3 \pm 0.8$; $Ta/Th = 0.13 \pm 0.01$) (Fig. 6.10e).

TM-20 (39.34 m; 61,370 varve yrs BP);

TM-20 major element glass compositions are homogenous with 61.3-62.4 wt.% SiO_2 , 2.0-2.8 wt.% FeO, 1.0-1.3 wt.% CaO. Glasses display elevated alkalis (6.9-7.9 wt.% Na_2O and 6.2-6.8 wt.% K_2O) and are classified as phono-trachytes (Fig. 6.9a). $Na_2O > K_2O$ in all the shards investigated within TM-20 ($K_2O/Na_2O = 0.82-0.91$) (Fig. 6.10a). Trace element concentrations indicate a highly evolved melt composition ($Zr/Sr = 44-231$) with LREE enrichment relative to the HREE ($La/Yb = 20.3 \pm 0.8$). Trace element concentrations observed in these glasses are homogeneous 61-65 Y, 649-698 ppm Zr, 106-113 ppm Nb, 132-141 ppm La, 249-276 ppm Ce and 44-46 Th (Fig. 6.10d; f). HFSE element ratios to Th remain constant within these glasses ($Nb/Th = 2.4 \pm 0.4$; $Zr/Th = 14.6 \pm 0.4$; $Ta/Th = 0.12 \pm 0.02$) (Fig. 6.10e).

TM-20-1b (40.68 m; 64,140 varve yrs BP);

TM-20-1b major element glass compositions are homogenous with 61.5-62.5 wt.% SiO_2 , 2.3-2.8 wt.% FeO, 1.0-1.2 wt.% CaO. Glasses display elevated alkalis (6.9-7.7 wt.% Na_2O and 6.3-6.8 wt.% K_2O) and are classified as phono-trachytes (Fig. 6.9a). $Na_2O > K_2O$ in all the shards investigated within TM-20-1b ($K_2O/Na_2O = 0.82-0.94$) (Fig. 6.10a). Trace element concentrations indicate a highly evolved melt composition ($Zr/Sr = 54-198$) with LREE enrichment relative to the HREE ($La/Yb = 20.8 \pm 1.0$). Trace element concentrations observed in these glasses are homogeneous 56-64 ppm Y, 569-641 ppm Zr, 94-106 ppm Nb, 118-135 ppm La, 237-274 ppm Ce and 35-43 ppm Th. HFSE element ratios to Th remain constant within these glasses ($Nb/Th = 2.5 \pm 0.1$; $Zr/Th = 15.2 \pm 0.6$; $Ta/Th = 0.13 \pm 0.002$) (Fig. 6.10e).

TM-20-1c (41.05 m; 64,470 varve yrs BP);

TM20-1c major element glass compositions are homogenous with 61.6-62.8 wt.% SiO_2 , 2.0-2.9 wt.% FeO, 0.9-1.3 wt.% CaO. Glasses display elevated alkalis (7.0-7.7 wt.% Na_2O and 5.9-6.7 wt.% K_2O) and are classified as phono-trachytes (Fig. 6.9a). $Na_2O > K_2O$ in all the shards investigated within TM-20-1c ($K_2O/Na_2O = 0.82-0.92$). Trace element concentrations

indicate a highly evolved melt composition ($Zr/Sr = 65-255$) with LREE enrichment relative to the HREE ($La/Yb = 20.1 \pm 1.4$). Trace element concentrations observed in these glasses are homogeneous 60-65 ppm Y, 604-650 ppm Zr, 99-108 ppm Nb, 123-136 ppm La, 245-278 ppm Ce and 40-45 ppm Th (Fig. 6d-f). HFSE element ratios to Th remain constant within these glasses ($Nb/Th = 2.4 \pm 0.1$; $Zr/Th = 14.5 \pm 0.5$; $Ta/Th = 0.12 \pm 0.01$) (Fig. 6.10e).

Central Adriatic

PRAD1-2 1870 cm

Major element glass data for this phono-trachytic tephra are presented in Bourne et al. (2010). The layer is attributed by Bourne et al. (2010) to Ischia and linked with either TM19 or TM20 LGdM layers. The ash layer at 1870cm is characterised by shards displaying both $Na_2O > K_2O$ and $K_2O \geq Na_2O$ ($K_2O/Na_2O = 0.80-1.11$) (Fig. 6.9a). Trace element concentrations indicate a highly evolved melt compositions ($Zr/Sr = 12-351$) with LREE enrichment relative to the HREE ($La/Yb = 21.2 \pm 2.1$). Trace element concentrations observed in these glasses display dramatic heterogeneity 31-73 ppm Y, 247-819 ppm Zr, 42-130 ppm Nb, 67-157 ppm La, 133-303 ppm Ce and 17-53 ppm Th (Fig. 6.10d; f). HFSE element ratios to Th remain constant within these glasses ($Nb/Th = 2.5 \pm 0.1$; $Zr/Th = 14.9 \pm 1.0$; $Ta/Th = 0.12 \pm 0.02$) (Fig. 5e).

SA03-03 685 cm

Major element glass data for this phono-trachytic to trachytic tephra are presented in Bourne (2012). The layer is attributed by Bourne (2012) to Ischia and linked with either TM19 or the TM-20 layers. The ash layer at 1870cm is characterised by shards displaying both $Na_2O \gg K_2O$ and $K_2O = Na_2O$ ($K_2O/Na_2O = 0.80-1.0$). Trace element data for SA03-03 685 cm were normalised based on average SiO_2 values as major element analysis on the sample had already been completed (Bourne 2012). Trace element concentrations indicate a highly evolved melt composition ($Zr/Sr = 67-312$) with LREE enrichment relative to the HREE ($La/Yb = 22.0 \pm 1.7$). Trace element concentrations observed in these glasses are heterogeneous with 48-75 ppm Y, 414-824 ppm Zr, 71-125 ppm Nb, 101-159 ppm La, 202-303 ppm Ce and 28-51 ppm Th (Fig. 6.10d-f). HFSE element ratios to Th remain constant within these glasses ($Nb/Th = 2.5 \pm 0.1$; $Zr/Th = 15.3 \pm 0.5$; $Ta/Th = 0.12 \pm 0.01$) (Fig. 6.10e).